Vitalii Ivanov · Justyna Trojanowska ·
Ivan Pavlenko · Erwin Rauch ·
Dragan Peraković   *Editors*

Advances in Design, Simulation and Manufacturing V

Proceedings of the 5th International
Conference on Design, Simulation,
Manufacturing: The Innovation
Exchange, DSMIE-2022,
June 7–10, 2022, Poznan, Poland –
Volume 1: Manufacturing and
Materials Engineering

Springer

Lecture Notes in Mechanical Engineering

Lecture Notes in Mechanical Engineering (LNME) publishes the latest developments in Mechanical Engineering—quickly, informally and with high quality. Original research reported in proceedings and post-proceedings represents the core of LNME. Volumes published in LNME embrace all aspects, subfields and new challenges of mechanical engineering. Topics in the series include:

- Engineering Design
- Machinery and Machine Elements
- Mechanical Structures and Stress Analysis
- Automotive Engineering
- Engine Technology
- Aerospace Technology and Astronautics
- Nanotechnology and Microengineering
- Control, Robotics, Mechatronics
- MEMS
- Theoretical and Applied Mechanics
- Dynamical Systems, Control
- Fluid Mechanics
- Engineering Thermodynamics, Heat and Mass Transfer
- Manufacturing
- Precision Engineering, Instrumentation, Measurement
- Materials Engineering
- Tribology and Surface Technology

To submit a proposal or request further information, please contact the Springer Editor of your location:

China: Ms. Ella Zhang at ella.zhang@springer.com
India: Priya Vyas at priya.vyas@springer.com
Rest of Asia, Australia, New Zealand: Swati Meherishi at swati.meherishi@springer.com
All other countries: Dr. Leontina Di Cecco at Leontina.dicecco@springer.com

To submit a proposal for a monograph, please check our Springer Tracts in Mechanical Engineering at https://link.springer.com/bookseries/11693 or contact Leontina.dicecco@springer.com

Indexed by SCOPUS. All books published in the series are submitted for consideration in Web of Science.

More information about this series at https://link.springer.com/bookseries/11236

Vitalii Ivanov · Justyna Trojanowska ·
Ivan Pavlenko · Erwin Rauch ·
Dragan Peraković
Editors

Advances in Design, Simulation and Manufacturing V

Proceedings of the 5th International
Conference on Design, Simulation,
Manufacturing: The Innovation Exchange,
DSMIE-2022, June 7–10, 2022, Poznan,
Poland – Volume 1: Manufacturing
and Materials Engineering

Springer

Editors
Vitalii Ivanov
Sumy State University
Sumy, Ukraine

Justyna Trojanowska
Poznan University of Technology
Poznan, Poland

Ivan Pavlenko
Sumy State University
Sumy, Ukraine

Erwin Rauch
Free University of Bozen-Bolzano
Bolzano, Italy

Dragan Peraković ⓘD
University of Zagreb
Zagreb, Croatia

Preface

This volume of Lecture Notes in Mechanical Engineering contains selected papers presented at the 5th International Conference on Design, Simulation, Manufacturing: The Innovation Exchange (DSMIE-2022), held in Poznan, Poland, on June 7–10, 2022. The conference was organized by the Sumy State University, Poznan University of Technology, and International Association for Technological Development and Innovations, in partnership with Technical University of Kosice (Slovak Republic), Kielce University of Technology (Poland), University of West Bohemia (Czech Republic), Association for Promoting Innovative Technologies—Innovative FET (Croatia), and Society for Robotics of Bosnia and Herzegovina (Bosnia and Herzegovina).

DSMIE Conference Series is the international forum for fundamental and applied research and industrial applications in engineering. The conference focuses on a broad range of research challenges in the fields of manufacturing, materials, mechanical, and chemical engineering, addressing current and future trends in design approaches, simulation techniques, computer-aided systems, innovative production approaches, Industry 4.0 strategy implementation for engineering tasks solving, and engineering education. DSMIE-2022 brings together researchers from academic institutions, leading industrial companies, and government laboratories worldwide to promote and popularize the scientific fundamentals of engineering.

DSMIE-2022 received 159 contributions from 20 countries around the world. After a thorough peer-reviewed process, the Program Committee accepted 84 papers written by 337 authors from 16 countries. Thank you very much to the authors for their contribution. These papers are published in the present book, achieving an acceptance rate of about 53%. Extended versions of selected best papers will be published in scientific journals: Management and Production Engineering Review (Poland), Journal of Engineering Sciences (Ukraine), Advances in Thermal Processes and Energy Transformation (Slovak Republic), Assembly Techniques and Technology (Poland), Machines (Switzerland), and a special issue of Sustainability (Switzerland) "Industry 4.0 Technologies for Sustainable Asset Life Cycle Management."

We would like to thank members of the Program Committee and invited external reviewers for their efforts and expertise in contributing to reviewing, without which it would be impossible to maintain the high standards of peer-reviewed papers. One hundred five Program Committee members and 23 invited external reviewers devoted their time and energy to peer-reviewing manuscripts. Our reviewers come from all over the world, represent 19 countries, and are affiliated with more than 80 institutions.

Thank you very much to keynote speakers: Prof. George-Christopher Vosniakos (National Technical University of Athens, Greece), Prof. Dariusz Mazurkiewicz (Lublin University of Technology, Poland), Prof. Szymon Wojciechowski (Poznan University of Technology, Poland), Prof. Sahin Yildirim (Erciyes University, Turkey), Dr. Valdimir Dolgikh (Seco Tools AB, Sweden), and Mr. Krystian Kogut and Przemyslaw Pasich (InterMarium, Poland).

The book "Advances in Design, Simulation and Manufacturing V" was organized in two volumes according to the main conference topics: Volume 1—Manufacturing and Materials Engineering, and Volume 2—Mechanical and Chemical Engineering. Each volume is devoted to research in design, simulation, and manufacturing in the main conference areas.

The first volume consists of five parts. The first part includes recent developments in smart and sustainable manufacturing. Notably, it presents mechatronic systems for adaptive machining control and a feeding system for systematic production. This part also includes ways to increase production processes' efficiency using lean tools and systems for quality control monitoring. Recent developments in rider assistance systems, surface defects detection by machine learning and machine vision, and cybersecurity in the industry are presented in this part. An advanced methodology for solving production problems, issues of sustainable manufacturing, and applications of an automated diagnostic system are also presented. Finally, the first part includes studies in ensuring road infrastructure safety, the organization of an enterprise energy management system, and the implementation of intelligent mechatronic systems in engineering.

The second part includes studies in applying an open-source finite element software, designing an automated workstation for manufacturing control, and developing anti-collapse safety systems. Studies in designing drive systems, interference fits, and vibroturning devices are additionally presented. Notably, ways to implement approaches in the compositional interpolation of spatial curves are analyzed in this part.

The third part is devoted to reinforcement approaches and their impact on measuring accuracy, an up-to-date method for the monitoring cutters states in finishing turning of hard materials, decreasing turbine blade deformation during machining and ensuring the quality of surfaces under processing by diamond honing. Also, it presents studies aimed at lifetime prediction in composite manufacturing, simulation and optimization in grinding advanced materials. This part also includes recent developments in quality assurance for detonation coatings of aircraft engine parts, improved machining effectiveness by applying composite cutting tools, and clarification of the deforming broaching model. Finally, issues of

increasing the accuracy of threads, improving the efficiency of fine boring, simulation of high-speed machining, ensuring characteristics of working surfaces for rolling bearings, and investigation of the surface layer hardness when grinding porous materials are presented in this part.

The fourth part is based on studies in control of mixtures' physical and mechanical properties, catalytic growth of carbon nanostructures, metallographic determination of grain parameters for welded joints, and additives' influence on tribotechnical properties of polymer composites. Ways for studying thermomechanical phenomena in the surface layer of functional materials, mechanisms of the structure formation for composite solders, and modeling processes and equipment for the manufacture of electrode carbon graphite products are also presented in this part. This part includes recent developments in ultrasonic treatment, increasing corrosion resistance, and surface protection. Moreover, the fourth part provides research on hybrid composites, the structure of coatings, oxide layers, and nanostructures in plasma. Finally, ways for an increase in tribocharacteristics for highly loaded friction units of modern equipment and theoretical and experimental studies of porous materials obtained from industrial waste are included in this part.

The fifth part aims to design laboratories using virtual and augmented reality to increase the quality of engineering education. Also, ways to improve the quality of professional training for future engineers and systems to advise staff in manufacturing engineering enterprises are proposed in this part.

We appreciate the partnership with Springer Nature, iThenticate, EasyChair, and our sponsors for their essential support during the preparation of DSMIE-2022.

Thank you very much to DSMIE team. Their involvement and hard work were crucial to the success of the conference.

DSMIE's motto is "*Together we can do more for science, technology, engineering, and education*."

June 2022
<div align="right">
Vitalii Ivanov
Justyna Trojanowska
Ivan Pavlenko
Erwin Rauch
Dragan Peraković
</div>

Organization

Steering Committee

General Chair

Vitalii Ivanov   Sumy State University, Ukraine

Co-chair

Justyna Trojanowska   Poznan University of Technology, Poland

Members (in alphabetical order)

Olaf Ciszak   Poznan University of Technology, Poland
Oleksandr Gusak   Sumy State University, Ukraine
Oleksandr Liaposhchenko   Sumy State University, Ukraine
Slawomir Luscinski   Kielce University of Technology, Poland
Ivan Pavlenko   Sumy State University, Ukraine

Program Committee (in alphabetical order)

Katarzyna Antosz   Rzeszow University of Technology, Poland
Yevheniia Basova   National Technical University "Kharkiv
                                 Polytechnic Institute," Ukraine
Kristina Berladir   Sumy State University, Ukraine
Vladimira Binasova   University of Zilina, Slovak Republic
Jozef Bocko   Technical University of Kosice, Slovak Republic
Ricardo Branco   University of Coimbra, Portugal
Dagmar Caganova   Slovak University of Technology,
                                 Slovak Republic
Emilia Campean   Technical University of Cluj-Napoca, Romania

Robert Cep	VSB-Technical University of Ostrava, Czech Republic
Yelizaveta Chernysh	Sumy State University, Ukraine
Olivian Chiver	Technical University of Cluj-Napoca, Romania
Vasile George Cioata	Polytechnic University of Timisoara, Romania
Olaf Ciszak	Poznan University of Technology, Poland
Oguz Colak	Eskisehir Technical University, Turkey
Radu Cotetiu	Technical University of Cluj-Napoca, Romania
Nadezda Cubonova	University of Zilina, Slovak Republic
Ivan Cvitic	University of Zagreb, Croatia
Predrag Dasic	University Union "Nikola Tesla," Serbia
Yuliia Denysenko	Sumy State University, Ukraine
Oleksandr Derevianchenko	Odessa Polytechnic National University, Ukraine
Sergey Dobrotvorskiy	National Technical University "Kharkiv Polytechnic Institute," Ukraine
Milan Edl	University of West Bohemia, Czech Republic
Sulaymon Eshkabilov	North Dakota State University, USA
Mathieu Gautier	University Lyon, France
Renata Gnatowska	Czestochowa University of Technology, Poland
Mihaly Gorbe	John von Neumann University, Germany
Marta Grabowska	Poznan University of Technology, Poland
Jakub Grabski	Poznan University of Technology, Poland
Marek Gucwa	Czestochowa University of Technology, Poland
Domenico Guida	University of Salerno, Italy
Oleksandr Gusak	Sumy State University, Ukraine
Michal Hatala	Technical University of Kosice, Slovak Republic
Ihor Hrytsay	Lviv Polytechnic National University, Ukraine
Ihor Hurey	Lviv Polytechnic National University, Ukraine
Jozef Husar	Technical University of Kosice, Slovak Republic
Vitalii Ivanov	Sumy State University, Ukraine
Maryna Ivanova	National Technical University "Kharkiv Polytechnic Institute," Ukraine
Reza Jazar	Royal Melbourne Institute of Technology, Australia
Lydmila Kalafatova	Donetsk National Technical University, Ukraine
Isak Karabegovic	University of Bihac, Bosnia and Herzegovina
Gennadii Khavin	National Technical University "Kharkiv Polytechnic Institute," Ukraine
Lucia Knapcikova	Technical University of Kosice, Slovak Republic
Kateryna Kostyk	National Technical University "Kharkiv Polytechnic Institute," Ukraine
Jan Krmela	Alexander Dubcek University of Trencin, Slovak Republic
Ivan Kuric	University of Zilina, Slovak Republic
Yaroslav Kusyi	Lviv Polytechnic National University, Ukraine

Maria Lazar	University of Petrosani, Romania
Vladimir Lebedev	Odessa Polytechnic National University, Ukraine
Oleksandr Liaposhchenko	Sumy State University, Ukraine
Slawomir Luscinski	Kielce University of Technology, Poland
Jose Mendes Machado	University of Minho, Portugal
Ole Madsen	Aalborg University, Denmark
Angelos Markopoulos	National Technical University of Athens, Greece
Dariusz Mazurkiewicz	Lublin University of Technology, Poland
Mykola Melnychuk	Lutsk National Technical University, Ukraine
Ronald Mersky	Widener University, USA
Viktor Molnar	University of Miskolc, Hungary
Ronald Iosif Moraru	University of Petrosani, Romania
Dmitriy Muzylyov	Kharkiv Petro Vasylenko National Technical University of Agriculture, Ukraine
Arun Nagarajah	University of Duisburg-Essen, Germany
Marek Ochowiak	Poznan University of Technology, Poland
Daniela Onofrejova	Technical University of Kosice, Slovak Republic
Oleh Onysko	Ivano-Frankivsk National Technical University of Oil and Gas, Ukraine
Vitalii Pasichnyk	National Technical University of Ukraine "Igor Sikorsky Kyiv Polytechnic Institute," Ukraine
Ivan Pavlenko	Sumy State University, Ukraine
Dragan Perakovic	University of Zagreb, Croatia
Marco Perisa	University of Zagreb, Croatia
Oleksandr Permiakov	National Technical University "Kharkiv Polytechnic Institute," Ukraine
Jan Pitel	Technical University of Kosice, Slovak Republic
Grigore Marian Pop	Technical University of Cluj-Napoca, Romania
Oleksandr Povstyanoy	Lutsk National Technical University, Ukraine
Erwin Rauch	Free University of Bolzano, Italy
Michal Rogalewicz	Poznan University of Technology, Poland
Andrii Rogovyi	Kharkiv National Automobile and Highway University, Ukraine
Yiming Rong	Southern University of Science and Technology, China
Joanna Rosak-Szyrocka	Czestochowa University of Technology, Poland
Alessandro Ruggiero	University of Salerno, Italy
Vira Shendryk	Sumy State University, Ukraine
Lesya Shkitsa	Ivano-Frankivsk National Technical University of Oil and Gas, Ukraine
Robert Sika	Poznan University of Technology, Poland
Dusan Simsik	Technical University of Kosice, Slovak Republic
Volodymyr Sokolov	V. Dahl East Ukrainian National University, Ukraine
Marcin Sosnowski	Jan Długosz University of Częstochowa, Poland

Vadym Stupnytskyy	Lviv Polytechnic National University, Ukraine
Antoni Swic	Lublin University of Technology, Poland
Anastasiia Symonova	Kremenchuk Mykhailo Ostrohradskyi National University, Ukraine
Marek Szostak	Poznan University of Technology, Poland
Yuliia Tarasevych	AGH University of Science and Technology, Poland
Volodymyr Tonkonogyi	Odessa Polytechnic National University, Ukraine
Justyna Trojanowska	Poznan University of Technology, Poland
Michael Tseitlin	National Technical University "Kharkiv Polytechnic Institute," Ukraine
Nicolae Ungureanu	Technical University of Cluj-Napoca, Romania
Alper Uysal	Yildiz Technical University, Turkey
Leonilde Rocha Varela	University of Minho, Portugal
George-Christopher Vosniakos	National Technical University of Athens, Greece
Jerzy Winczek	Czestochowa University of Technology, Poland
Szymon Wojcechowski	Poznan University of Technology, Poland
Oleg Zabolotnyi	Lutsk National Technical University, Ukraine
Jozef Zajac	Technical University of Kosice, Slovak Republic
Volodymyr Zavialov	National University of Food Technologies, Ukraine
Przemyslaw Zawadzki	Poznan University of Technology, Poland
Jan Zdebor	University of West Bohemia, Czech Republic
Lianyu Zheng	Beihang University, China
Predrag Zivkovic	University of Nis, Serbia
Justyna Zywiolek	Czestochowa University of Technology, Poland

Invited External Reviewers (in alphabetical order)

Iryna Ablieieva	Sumy State University, Ukraine
Tygran Dzhuguryan	Maritime University of Szczecin, Poland
Oksana Gaponova	Sumy State University, Ukraine
Kateryna Ivanova	Sumy State University, Ukraine
Nikolaos Karkalos	National Technical University of Athens, Greece
Nadiia Kharchenko	Sumy State University, Ukraine
Vitalii Kolesnyk	Sumy State University, Ukraine
Sergii Kotliar	National Technical University of Ukraine "Igor Sikorsky Kyiv Polytechnic Institute," Ukraine
Oleksandr Kupriyanov	Ukrainian Engineering Pedagogics Academy, Ukraine
Iurii Merzliakov	Sumy State University, Ukraine
Panagiotis Karmiris Obratanski	National Technical University of Athens, Greece

Emmanouil Papazoglou   National Technical University of Athens, Greece
Vita Pavlenko   Sumy State University, Ukraine
Emanuala Pop   Technical University of Cluj-Napoca, Romania
Serhii Sharapov   Sumy State University, Ukraine
Dimitrios Skondras-Giousios National Technical University of Athens, Greece
Olexii Solovar   National Technical University of Ukraine "Igor
                            Sikorsky Kyiv Polytechnic Institute," Ukraine
Sebastian Sonntag   University of Duisburg-Essen, Germany
Valentin Tikhenko   Odessa Polytechnic National University, Ukraine
Anatolii Tkachuk   Lutsk National Technical University, Ukraine
Iryna Vaskina   Sumy State University, Ukraine
Tatiana Volina   National University of Life and Environmental
                            Sciences of Ukraine, Ukraine
Dmytro Zhyhylii   Sumy State University, Ukraine

DSMIE Team (in alphabetical order)

Kristina Berladir   Sumy State University, Ukraine
Olaf Ciszak   Poznan University of Technology, Poland
Yuliia Denysenko   Sumy State University, Ukraine
Oleksandr Gusak   Sumy State University, Ukraine
Vitalii Ivanov   Sumy State University, Ukraine
Oleksandr Liaposhchenko   Sumy State University, Ukraine
Slawomir Luscinski   Kielce University of Technology, Poland
Ivan Pavlenko   Sumy State University, Ukraine
Justyna Trojanowska   Poznan University of Technology, Poland

Contents

Manufacturing Technology

Advanced Materials

ICT for Engineering Education

Smart and Sustainable Manufacturing

Mechatronic Actuator for Adaptive Machining Control

Anatoly Gushchin[1] , Vasily Larshin[1(✉)] , Oleksandr Lysyi[2] ,
and Igor Dudarev[3]

[1] Odessa Polytechnic National University, 1, Shevchenko Avenue, Odessa 65044, Ukraine
vasilylarshin@gmail.com
[2] Odessa Military Academy, 10, Fontanskaya doroga Street, Odessa 65009, Ukraine
[3] Odessa State Agrarian University, 13, Panteleymonovskaya Street, Odessa 65012, Ukraine

Abstract. The paper discusses the principles of operation and fundamentals of the theory of a lineal mechatronic actuator for adaptive machining control (cutting, grinding, polishing, etc.). Structurally, the actuator is made according to the scheme of a linear DC electric motor containing a fixed stator field winding and a movable armature winding. Both windings (fixed and movable) are located coaxially on one cylindrical ferromagnetic core and interact in such a way that the movable armature is in a dynamic equilibrium state under the action of two oppositely directed forces: electromagnetic and electrodynamic ones. The electromagnetic force is due to the non-symmetrical arrangement of the armature winding on the ferromagnetic core relative to the center of its mass. The electrodynamic force is caused by the action of the magnetic field of the field winding on the armature winding through which the regulated current flows. The armature winding is rigidly connected to an axially displaced actuating element carrying a cutting or pressing tool, including a rotating one. It is established that the electromagnetic force is proportional to the difference in the magnetic permeability of the ferromagnetic core and the vacuum, and the electrodynamic force is proportional to the magnitude of the currents in the field and armature windings. The mechatronic actuator operating characteristics showing the effect of the regulated currents on the axial force are experimentally constructed.

Keywords: Industrial growth · Process innovation · Linear actuator · Power mechanism · Dynamic equilibrium · Reciprocating motion · Cutting force · Field winding · Mechanical machining

1 Introduction

Any mechanical machining to remove the stock allowance from the workpiece to be machined (cutting, grinding, polishing, superfinish, etc.) ultimately comes down to creating the necessary mechanical cutting force and torque while ensuring the required kinematics (e.g., speed, acceleration) and the trajectory of the tool relative to the workpiece to be machined. Adaptive and intelligent control of the cutting force allows creating control systems focused on the mechanical machining, based on which fundamentally

new technological methods of machining are possible, for example, drilling holes with adaptation to adjustable axial force and torque.

For a long time, such an adaptation was tried to be implemented by controlling the load on the electric motor of the tool or workpiece drive. However, the long kinematic chain and the high inertia of the actuator did not allow for the required quality of automatic control. Therefore, adaptive load feedback control on the main motion electric motor has not found practical application in mechanical engineering technology. We need a new approach that provides a breakthrough in solving the problem of adaptive and intelligent control. A possible way out of this situation is using a mechatronic linear displacement power mechanism built into the machine spindle. The power characteristic of the machining process can be adjusted. Such a mechatronic power mechanism controls and provides not kinematic (e.g., speed, acceleration, displacement), but power parameters of mechanical processing, for example, axial cutting force and cutting torque. The paper proposes a new mechatronic power linear actuator (hereinafter LA), which belongs to the class of DC electric machines with the rectilinear motion of the linear electric motors type.

The need for linear power mechanisms oriented towards the machining process (i.e., machining by purpose) arises when machining parts are made of difficult-to-machine, superhard, ceramic, and polymer composite materials, including complex-shaped parts and parts with an arbitrary (freeform) shape. The proposed LA design can be built into the motor spindle of a modern CNC machine, through which the elastic technological system of the machine is closed. In this case, such an LA should be equivalent to a series link with adjustable stiffness, which provides the force-and-torque parameters during machining, for example, when cutting or grinding.

The LA operation principle in its essence does not differ from a conventional DC motor with a rotational movement of the armature. The fundamental difference is only one. Namely, the rotational motion of a conductor in a magnetic field is replaced by its linear motion. It is possible to control force-and-torque parameters in the LA adaptive tracking drive by changing the stator field and armature winding currents.

2 Literature Review

The prototype of the LA proposed design contains a field winding and two armature movable windings, which are rigidly connected by the working body of the technological system and are designed to create conditions for dynamic equilibrium of the working (e.g., cutting) tool in space (levitation type equilibrium) when machining, e.g., superhard materials and CFRP [1]. However, this design has large both overall dimensions and weight.

The problem of reducing the dimensions and weight of the design is partially solved by replacing two movable armature windings with one winding while maintaining the dynamic equilibrium of the opposing forces created by the stator and armature windings [2].

There is a kind of LA in which the stator winding consists of two parts, between which a movable armature winding is located [3]. However, in all the above works, there is no theoretical justification for the operation of the mechatronic power mechanism, including the justification of distributed and hierarchical control [4]. It hinders the

effective improvement of this mechanism, which can be part of a hierarchical control system.

The area of application of adaptive machine control technology is extremely wide [1]. It is crucial when machining parts made of polymer composite materials or CFRP [5, 6] to ensure the high quality of the parts [7, 8].

To establish LA design and calculation principles, it is necessary to use electromagnetism's laws [9, 10] and the electric machines theory fundamentals [11]. In addition, the most significant effect can be obtained when developing a multi-level control system [4, 12], in which a mechatronic motor spindle with a built-in LA belongs to the lower level of the control of a technological system.

The analysis of literature sources has shown that the available LA analogs, including those described in our previous developments, are used in the adaptive motor spindle of CNC metal-cutting machines. However, the known LA designs were created empirically, i.e., by the "trial and error" method. And as a result, the known technical solutions for new LA designs, including the mentioned above, are not always effective. Therefore, the research aims to develop the principles of LA structure and the theory of their design and calculation, which is an urgent task of the current level of adaptive machining control development, as one of the stages of creating sensitive technological systems with artificial intelligence.

3 Research Methodology

At first glance, the correct idea of using two movable armature windings (rigidly interconnected by the working body of a technological system) to balance forces, as well as to realize reciprocating motion in two opposite directions (analogous to a checks and balances system), is accompanied by large LA dimensions and its substantial mass. Studies have shown that a similar function of LA can be realized based on one unmovable stator field winding and one movable armature winding. To do this, you can use the well-known physical phenomena of electromagnetism, for example, the force effect of a magnetic field on a current-carrying conductor according to Ampere's law.

For the theoretical justification of this approach, we consider the effect of the electrodynamic force interaction of two current-carrying windings, which are coaxially located on one cylindrical ferromagnetic core. According to Ampere's law, a mechanical force acts on a rectilinear current-carrying conductor located in an external (relative to it) magnetic field. The magnitude of the force can be found as follows [9, 11]

$$\overline{F} = I[\overline{l}, \overline{B}] = I[\boldsymbol{l} \times \boldsymbol{B}] \tag{1}$$

where $\overline{F}$ is the force vector, N; I is the current strength, A, $\overline{l}$ or $\boldsymbol{l}$ is the conductor length vector in the current direction, A; $\overline{B}$ or $\boldsymbol{B}$ is the magnetic flux density vector (or magnetic field induction vector), Wb/m^2 or T.

By changing the direction of the induction vector $\overline{B}$ of the external magnetic field, you can change the direction of the force acting on the conductor with an electric current flowing in the same direction (Fig. 1). This manifests the principle of superposition, for example, of two independent magnetic fields. It is possible to provide a dynamic equilibrium condition of oppositely directed forces (forces F_1 and F_2 in Fig. 1).
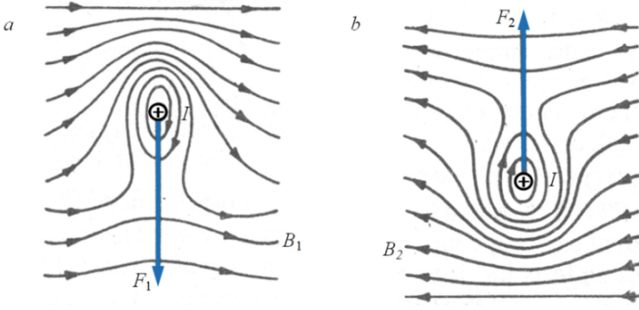
Fig. 1. Resultant field due to current-carrying conductor and magnetic field with inductions B_1 and B_2 having direction from left to right (*a*) and on the contrary (*b*), respectively.

In general, with the simultaneous action of multidirectional magnetic fluxes (one of which is created by the stator field winding) on a current-carrying conductor, the resulting mechanical force acting on this conductor can be found based on vector summation and multiplication, i.e.

$$\overline{F}_\Sigma = \sum_{j=1}^{k} I_j \left[\overline{l}_j, \left(\sum_{i=1}^{m} \overline{B}_i \right) \right], \tag{2}$$

where $\sum_{i=1}^{m} \overline{B}_i$ is the total induction (resultant vector) of magnetic field sources in the LA field winding, T; $\left[\overline{l}_i, \left(\sum_{i=1}^{m} \overline{B}_i \right) \right]$ is the vector product of the vector $\overline{l}_j$ (conductor length j-th vector) and resulting vector $\sum_{i=1}^{m} \overline{B}_i$; I_j is the current strength in the j-th conductor $(j = 1, 2, \ldots, k)$, A; $\overline{l}_j$ is the length of the j-th conductor, m.

Equation (2) opens up ways to control the force acting on the current-carrying conductor (or the conductor turns) located in the total magnetic field from the action of magnetic field independent sources. To create a dynamic balance of forces, in the form of one equivalent force, at least two independently acting magnetic flows with inductions $\overline{B}_1$ and $\overline{B}_2$ directed in opposite directions are necessary (Fig. 1).

In this case, by increasing or decreasing the value, for example, $\overline{B}_2$ it is possible to reverse the direction of movement of the current-carrying conductor in the total magnetic field without changing the direction of current in the second independent source of the magnetic field $\overline{B}_1$.

Let us consider the force interaction of a ferromagnetic core and a current-carrying winding or a coil with turns (hereinafter solenoid) based on the following positions of electrodynamics.

1. A solenoid, i.e., a set of tightly pressed cylindrical turns with direct current (DC), creates a symmetrical magnetic field inside itself. The "cork-screw" rule determines the direction of the magnetic field induction vector.

2. A ferromagnetic core placed in the magnetic field area is magnetized and forms its magnetic field with the same direction of the magnetic flux. Moreover, the induced field in this core can have a more extensive magnetic power due to the ferromagnetic properties of the core.

3. A magnetic core with magnetic permeability μ_a pushes into the solenoid, having the area of the circular cross-section S, the length l_s, and the field winding with n turns per one meter of length [13]. If a current I flows through the solenoid field winding, let's find the force F_1 acting on the magnet core, neglecting the edge effects (Fig. 2).
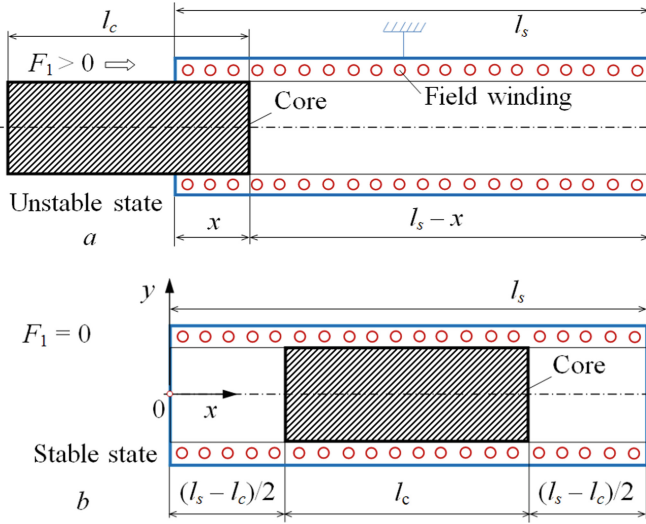
Fig. 2. Magnetic system unstable state with electromagnetic force $F_1 > 0$ (a) and the stable system state with $F_1 = 0$ (b).

Since the magnetic susceptibility of a magnetic core $\chi \ll 1$, then in the first approximation, the magnetic field intensity in a vacuum and a magnetic core can be considered equal, i.e., $H_0(x) = H(x) = nI$. Therefore, the magnetic field energy of the magnetic system will be

$$W = 0.5\,[H(x)B(x)x + H_0(x)B_0(x)(l_s - x)]S, \tag{3}$$

where $B(x)$ and $B_0(x)$ are the induction in a magnetic and a vacuum, respectively, T. Given that $B(x) = \mu_a H(x)$ and $B_0(x) = \mu_0 H_0(x)$, we get

$$W = 0.5(n^2 I^2)\,[\mu_a x + \mu_0(l_s - x)]S. \tag{4}$$

Therefore, according to [13], the electromagnetic force can be found as follows

$$F_1(x) = \left(\frac{\partial W}{\partial x}\right) = \frac{1}{2}(\mu_a - \mu_0)n^2 I^2 S. \tag{5}$$

Or we have

$$F_1 = \frac{1}{2}\mu_0(\mu_r - 1)n^2 I^2 S, \tag{6}$$

where F_1 is the traction force developed by the field winding, N; μ_a and μ_r are the absolute (in N/A^2 or H/m) and relative (dimensionless) magnetic permeability of the magnetic core substance, respectively, $\mu_r = \mu_a/\mu_0$; μ_0 is the magnetic permeability of vacuum (magnetic constant), $\mu_0 = 4\pi \cdot 10^{-7}$ N/A^2 or H/m); n is the number of turns of the winding on the current coil (i.e., the number of turns of the armature winding) per unit length of this winding, 1/m; I is the current in the coil winding (current in the armature winding), A; S is the area of the circular cross-section of the coil winding (armature winding), m^2.

4. The solenoid moves under the influence of force F_1. The solenoid moves, putting on the core. During this movement, more and more turns of the solenoid fall into the zone of action of the core magnetic field. As a result, there is an increase in force F_1, which occurs until the solenoid turns, located at the edges of the solenoid, fall into the action zone of the core magnetic field with a different (opposite) direction of this field. This physical phenomenon begins to act when the extreme (or edge) turns of the solenoid intersects the symmetry axis of the core having finite dimensions. As a result, a force F_2 appears and begins to increase. It acts on the same solenoid (armature winding) but in the opposite direction. When $F_1 = F_2$ the movement of the solenoid relative to the core stops (Fig. 2, b), the magnetic fields of the two sources are combined (mixed) and acquire a common axis of symmetry.

5. When the core is located on the other side of the solenoid, but with the current direction in the solenoid unchanged (i.e., with the same polarity of the current source), the solenoid also moves on the core (puts on the core) but moves at the same time under the action of a force F_1 that already has the opposite direction. The described tendency of movement to an equilibrium state from a non-equilibrium one can be called the "solenoid law" (or "solenoid principle"), and this law can be formulated as follows: "the equilibrium state of the coaxially arranged a solenoid and a core takes place with complete symmetry of their own magnetic fields, regardless of their initial location on the same axis".

   Corollaries from the "solenoid law" are the following:

   5.1) with the practical use of the "solenoid law", the "solenoid-core" system must always be in a non-equilibrium state in which it has the potential to move, i.e., this system creates a thrust or pressure force;

   5.2) the solenoid working movements zone (in the LA design) should be located in the zone of maximum force F_1 action (Fig. 2);

   5.3) the tendency for the solenoid to move to an equilibrium state (from a non-equilibrium one) is manifested in any direction of DC (flowing through the solenoid winding) and any orientation of the magnetic core in space.

6. When two solenoids (the field winding and the armature winding) are located with oppositely directed currents (or with the same direction of currents, but with opposite directions of winding turns) on one ferromagnetic core, the said solenoids will be

affected by oppositely directed axial forces F_{01} and F_{02}, bringing the "solenoid-core-solenoid" system into equilibrium condition. The imbalance of these forces in the LA mechatronic mechanism with the load of the latter axial cutting force and cutting torque can be used in practice for adaptive computer control of the machining process, with cutting, grinding, polishing, etc.

4 Results

The described principles of converting the power characteristics of an external DC magnetic field and a current-carrying conductor located in this magnetic field into a reciprocating movement of the tool in space with program control of the cutting force and torque depending on the magnitude of the axial movement of the tool are implemented in the operating LA mechatronic mechanism (Fig. 3). This mechanism includes a fixed cylindrical ferromagnetic core *FC* (magnetic core) with two solenoids: armature winding *AW* (movable armature) and field winding *FW* (stator). The armature winding *AW* can reciprocate movements along the longitudinal axis of the ferromagnetic core *FC*. The field winding *FW* (stator) is fixed to the magnetic circuit motionlessly. To control the movements of the armature, an adjustable DC source *PS1* with a tuning resistor *R1* is built into its electrical circuit, which allows changing the armature current I_a over a wide range with the required accuracy, i.e., changing the force F_{01}.

The magnitude of this force must be sufficient to carry out mechanical machining. Namely, cutting, grinding, polishing, etc. To implement programmable movements of the armature winding *AW*, i.e., the LA armature, it is necessary to create a force F_{02} that must be directed against the force F_{01}, and the following condition must be fulfilled (Fig. 3).

$$F_{01} + Q > F_{02} + F_{CUT}, \tag{7}$$

where Q and F_{CUT} are the weight of the mechanism moving parts and cutting force analog, respectively, N.

For computer programming of the force F_{02}, the field winding *FM* (stator) is designed, in the electrical circuit of which a DC power supply with an adjustment resistor *R2* and a control unit CU is included. The latter transmits control signals from peripheral devices and a computer.

The mechatronic LA works as follows. The power supplies *PS1* and *PS2* are switching on. The tuning resistors *R1* and *R2* set such values of forces F_{01} and F_{02}, at which the armature (with armature winding *AW*) is suspended at the beginning of its working stroke, for example, in the upper position. This position is limited by a mechanical stop or a zero position sensor (not shown in Fig. 3). The suspended state of the armature (with armature winding *AW*) provides the potential for both its programmable movements and the forces developed by it in the range from several nanonewtons (nN) to several kilonewtons (kN).

A working tool of a technological system (e.g., the system based on themetal-cutting machine) is fixed on a movable armature, which is given the movements necessary for performing a machining operation, e.g., turning, grinding, etc.
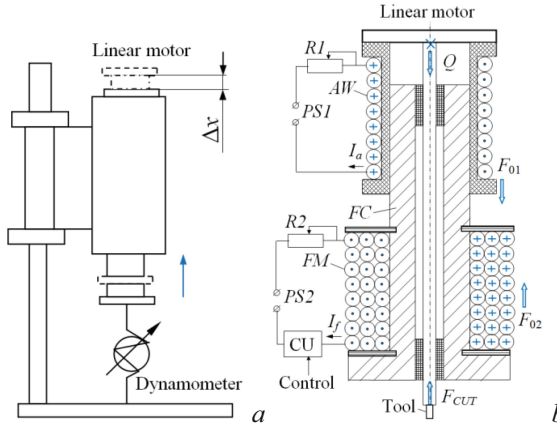
Fig. 3. Experimental stand (*a*) for studying a linear actuator (*b*).
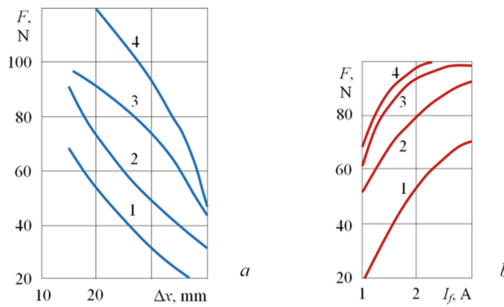
Fig. 4. Dependence of the armature traction force F on the magnitude Δx of its linear displacement (*a*) and the magnitude of the current I_f in the field winding (*b*).

To obtain the LA operating characteristics, the regulation of currents in the armature and field windings is carried out using resistors *R1* and *R2* (Fig. 3).

The LA mechanical force was measured using a spring dynamometer with a measurement range of 0–200 N. The dependence of the traction force F on the position Δx of the armature winding at the field current $I_f = 3$ A is obtained by changing the armature current (Fig. 4, *a*): $1 - 5$ A, $2 - 6$ A, $3 - 7$ A and $4 - 8$ A. The dependence of the traction force F on the field current (I_f in Fig. 4) with a fixed armature position of $\Delta x = 15$ mm, it is obtained at the same armature currents (Fig. 4, *b*): $1 - 5$ A, $2 - 6$ A, $3 - 7$ A and $4 - 8$ A. Besides, diagrams of changes in the axial force in various axial positions of the stator coil (from 5 to 30 mm) and the armature coil, allow determining the LA effective range of operation for use in a drilling device are experimentally obtained.

Experimental LA performance characteristics in Fig. 4 show the fundamental possibility of constructing a new class of mechatronic LA which have the possibility of stepless force-and-torque regulation in technological systems of various purposes. The short kinematic chain of these power mechanisms (along with a DC electrical circuit)

allows building the low-inertia tracking systems for adaptive computer control of technological systems, for example, for the implementation of multi-level adaptive control of metal-cutting machines [14, 15].

5   Conclusions

A scientific direction in the field of adaptive control of technological systems has been formulated, which consists in the development of a new class of mechatronic power mechanisms – linear actuators (LA) – for mechanical machining the freeform parts of materials with unique physical and mechanical properties, when these parts machining must be performed with strictly force-and-torque regulation of the main movement of mechanical or combined (electro-physical) machining, to wit: cutting, grinding, polishing, electroerosion, spot welding, etc.

When these LA are embedded in the motor spindles of modern CNC metal-cutting machines, they can work effectively as part of adaptive tracking systems with program control of the force-and-torque parameters, implementing robust algorithms of the lower control level in the hierarchical control of the technological systems.

The developed LA design is similar to the corresponding design of an electric machine with a rotating rotor: there is an unmovable field winding (stator) and a movable armature with an armature winding. However, the main purpose of such a power mechanism (motor) is to create and regulate machining axial force and torque, for example, during cutting or abrasive machining of parts made of superhard materials. Stepless regulation of the force-and-torque parameters is carried out by changing the electric currents in the stator and armature windings.

The LA performance characteristics were experimentally obtained: the dependence of the axial force on the working tool linear displacement magnitude at fixed currents in the stator and armature windings and the dependence of the axial force on the field winding current at a fixed axial position of the armature.

An experimental CNC machine has been developed with an adaptive mechatronic mechanism of the tool pressing force with automatic adjustment of the force "by disturbance" in a two-level control system of a CNC metal cutting machine: at the lower level – a robust system of automatic control "by disturbance" based on LA, at the upper one – a CNC system of this machine.

References

1. Larshin, V.P., Gushchin, A.M.: Mechatronic technological system information support. Appl. Aspects Inf. Technol. **4**(2), 153–167 (2021). https://doi.org/10.15276/aait.02.2021
2. Dobrinski, A., Möhring, H.-C., Stehle, T.: Development of an adaptronic spindle for a faultless machining of homogeneous and inhomogeneous materials. J. Mach. Eng. **21**(2), 5–23 (2021). https://doi.org/10.36897/jme/136277
3. Dobrinski, A., Dudarev, A.: Intelligent automated drilling in the laminate composites and hybrid materials. Mater. Today Proc. **38**(4), 1980–1983 (2021). https://doi.org/10.1016/j.matpr.2020.09.723
4. De Silva, C.W.: Mechatronics: A Foundation Course. CRC Press/Taylor & Francis, Boca Raton (2010). https://www.twirpx.com/file/1725202/

5. Duntschew, J., Eschelbacher, S., Schluchter, I., Möhring, H.-C.: Discrete wavelet transformation as a tool for analysing the borehole quality when drilling carbon fibre reinforced plastic aluminium stack material. J. Mach. Eng. **21**(1), 78–88 (2021). https://doi.org/10.36897/jme/132930

6. Shimana, K., et al.: Surface integrity of machined surface in simultaneous cutting of CFRP. J. Mach. Eng. **20**(1), 98–106 (2020). https://doi.org/10.36897/jme/117781

7. Sultana, I., Shi, Z., Attia, M.H., Thomson, V.: Surface integrity of holes machined by orbital drilling of composites with single layer diamond tools. Procedia CIRP **45**, 23–26 (2016)

8. Fleischer, J., Teti, R., Lanza, G., Mativenga, P., et al.: Composite materials parts manufacturing. CIRP Ann. Manuf. Technol. **67**(2), 603–626 (2018)

9. Gaur, R.K., Gupta, S.L.: Engineering Physics (for B.Sc. and B.E. students). Dhanpat Rai & Sons, Delhi (1993)

10. Bleaney, B.I., Bleaney, B.: Electricity and Magnetism, 2nd edn. London (1965)

11. Savelyev, I.V.: Physics. A General Course in Three Volumes. V.II. Electricity and Magnetism, Waves, Optics. MIR Publishers, Moscow (1980)

12. Mitrishkin, Y., Rodolfo, E.: Hierarchical control system for complex dynamical plants. In: Proceedings of the 6th International Conference on Informatics in Control, Automation and Robotics, Intelligent Control Systems and Optimization, ICINCO 2009, Milan, Italy, pp. 56–65 (2009)

13. Matveev, A.N.: Electricity and Magnetism: Textbook. Higher School, Moscow (1983). (in Russian)

14. Tonkonogyi, V., Sidelnykova, T., Dašić, P., Yakimov, A., Bovnegra, L.: Improving the performance properties of abrasive tools at the stage of their operation. In: Karabegović, I. (ed.) NT 2019. LNNS, vol. 76, pp. 136–145. Springer, Cham (2020). https://doi.org/10.1007/978-3-030-18072-0_15

15. De Silva, C.W.: Sensors and Actuators: Engineering System Instrumentation, 2nd edn. CRC Press, Boca Raton (2015). https://doi.org/10.1201/b18739

Design and Validation of a Feeding System for the Systematic Production of Needle Beds

Luis Freitas[1] , Divo Pinto[1] , José Vicente[2] , Katarzyna Antosz[3] ,
and José Machado[1(✉)]

[1] MEtRICs Research Centre, University of Minho, Guimarães, Portugal
`jmachado@dem.uminho.pt`
[2] InsideLimits, Canidelo, Vila Nova de Gaia, Portugal
[3] Rzeszow University of Technology, Rzeszów, Poland

Abstract. With the increasing quality standards of the electronic industry, especially in Printed Circuit Boards, the In-Circuit-Test Machines are becoming one of the most important systems on the production lines. Higher requirements are being set, pressing the In-Circuit-Test Machines production process to meet the necessary quality parameters, mainly precision and reliability. One of the possible approaches to update the manufacturing process of the In-Circuit-Test Machines is to automatize the process from a technological point of view. The automation of the process was divided into several sub-functions, one of them and the paper's focus, the feeding system. To achieve a desirable solution, the problem was analyzed, several solutions were studied within the state of the art, and two original solutions were proposed to solve the problem. The decision process followed engineering criteria through simulation and efficiency parameters, and it culminated in the proposal of a final solution. A prototype for the final solution was tested, and the results were presented.

Keywords: Industrial growth · Product innovation · In-circuit-test machines · Machine design · Feeding systems

1 Introduction

Due to the constant technology evolution, the complexity of machines, production systems, and mechatronic components has increased, and the size of Printed Circuit Boards (PCB) is getting smaller. One of the PCB production steps is the electrical quality testing phase of In-Circuit Test (ICT) systems. Since the manufacturing process of ICT systems is mainly performed manually, the production of PCBs is sometimes negatively affected, which can result in stoppages on the PCB production lines. Directly related to the increasing complexity of PCBs is the increase in the number of test points leading to the increase in the complexity of the ICT system. Thus, the manufacturing process of these systems struggles to guarantee the high quality demanded by the automotive industry. One of the solutions to avoid part of the problems in the manufacture of PCBs is to improve the production process of ICT systems.

This paper is focused on the development and design process of a feeding system that will be applied on an automatized system for the most critical production phase of the ICT system production – needle receptacle insertion.

To achieve the proposed goals, the paper is organized as follows: Sect. 2 presents a brief ICT description and its current manufacturing process by highlighting the goals proposed for the system to be developed and the proposed methodology to do it; Sect. 3 presents the research methodology of the design and evaluation phase; Sect. 4 describes the selection process of the solution to implement. Finally, the last section presents the conclusions by summarizing the prototype evaluation and the steps forward.

2   Literature Review

As part of an article aiming to present an original conceptual solution to solve a well-known problem, this chapter presents in 2.1 subchapters, a description of the current systems and manufacturing used process. The proposed goals are also presented, in the 2.1 subchapter, based on the problems previously explained, as well as an analysis of current methodologies, on the 2.2 subchapter to achieve these goals.

2.1   ICT Systems Manufacturing

Regarding the hardware part of an ICT system – the Fixture, it is characterized as electromechanical equipment roughly consisting of a mobile plate and a Needle Bed. Over this Needle Bed, it is placed on a Device Under Test (DUT – this paper addresses PCBs as DUT) [1].

Notably, a Needle Bed consists of three main components: the bed itself (called test plate), the receptacles, and the needles. The test plate is a custom manufactured plate with several through-holes where, on its top side, the receptacles are inserted and hosts the needles. On the bottom side of test plate, the receptacles-needle sets are connected to Wiring System that measures electrical parameters in the DUT and is the bridge between the hardware and software parts shows both top and bottom plate sides (Needle Bed and Wiring System) [2]. Figure 1 shows both sides of the test plate, bottom, and top, the Needle Bed and the Wiring system, respectively.
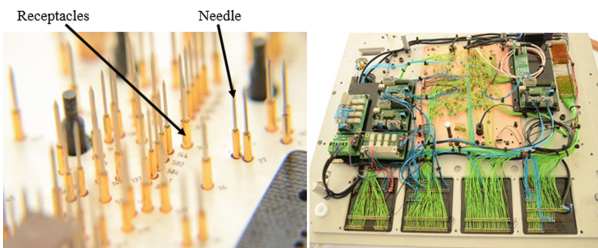
Fig. 1.   Needle beds [3].

The manufacturing process consists of two main tasks: the wiring process, which creates an entire network of electrical connections, and the insertion process of the receptacles and needles. This paper will focus on the receptacles insertion process.

The receptacles are manually inserted into the test plate, and then the needles are also manually inserted into these receptacles, which serves as guidance for the needles. The following figure presents a technical drawing of a receptacle (Fig. 2 - a) and photos of the receptacles, needles, and receptacles-needle set sizes compared to an ordinary pen (Fig. 2 - b).
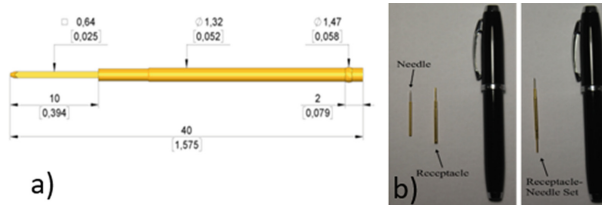
Fig. 2. a) Receptacle technical drawing (KS-075 47 E03 Ingun) [4] b) compared sizes.

Note that receptacle diameter and size are, in themselves, a problem since precision levels are around hundredths of a millimeter.

Receptacle insertion is done using a press-in tool (Fig. 3), which helps the technician press the receptacles to their final position.
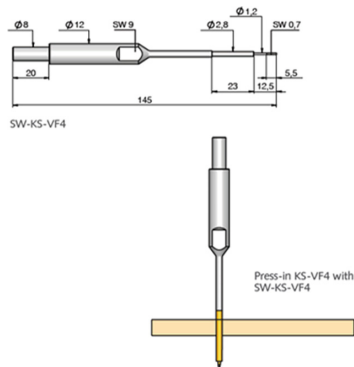
Fig. 3. Press-in tool (SW-KS-VF4, Ingun) [5].

This manufacturing process can take more than a week of work, depending on the PCB to be tested, defining the Needle Bed configuration. It is a repetitive process, requiring high concentration and sensitivity levels from the technicians throughout the whole process.

This dependence on the operator's ability and experience is a competitive disadvantage. Being the position and the perpendicularity between the needles and the PCB is an important requirement, to what concerns the ICT quality validation, the probability of

production errors due to the handcrafted production process is a truly concern. Hence, it is important to highlight that a misplaced receptacle-needle set can be undetectable by a human-eye inspection. Consequently, this quality failure detection is postponed to the production line phase, causing a considerable delay in the ICT production once the Needle Bed needs to be reworked.

All the conditions inherent to the abovementioned process resemble more a hand-crafted process than an industrial one. Therefore, the automation of the ICTs production process is a path to ensure both position tolerances and perpendicularity of the receptacles-needle sets, consequently reducing both time and cost of production.

This upgrade is expected to create a competitive advantage in this manufacturing process and achieve significant goals, such as those presented in Table 1.

Table 1. Project goals.

Features	Current market situation	Project goals
Fixtures production process optimization	Handmade receptacles insertion	An automated system of receptacles insertion and quality checking
Fixtures production time reduction	$100\% = 104$ h	$50\% = 52$ h
Receptacle insertion repeatability process	The handmade process makes repeatability impossible	An automated system that allows receptacle insertion repeatability process

This specific paper will focus on the feeding system that will provide the receptacles to the insertion system. Therefore, the project goals can be transformed in the engineering requirements for the feeding system, as presented in the following table (Table 2).

Table 2. Engineering requirements.

Engineering requirements	Values
Number of receptacles per cycle	200
Number of different receptacles	4
Position tolerance	0.1 mm

2.2 Methodology

Several authors have stressed the importance of using a well-established methodology in the design process of a mechatronic system. The advantages are numerous and are well documented in the scientific literature [6, 7].

In this paper, the authors wanted to introduce to these models the simulation component that will allow better development and optimize cost-efficiency, mainly in the design phase [8].

For the feeding systems, there are also authors who proposed evaluation parameters for assembly solutions based on efficiency analysis through the use of matrix operations [9].

Unlike most studies on vibratory bowls, the purpose of this study is not to study the effects of the vibration on the movement of part nor to study the forces in action in the system [10, 11].

3   Research Methodology

The process started with developing the conceptual solution, followed by further analysis. The following two designs that the team decided to go through among several. This pre-selection is a normal part of the design process and comes from the experience and know-how of the authors.

3.1   Conceptual Solution

The first solution consists of two orientation devices, the first is a chute with passive orientation type (numbered with 1 in Fig. 4a), and the second is a narrow cut with active orientation type (numbered with 2 Fig. 4a).
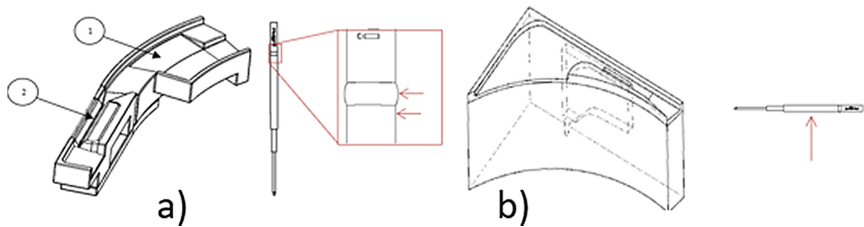
Fig. 4. a) Schematics for solution 1; b) Schematics for solution 2.

The chute identified with the number 1 has a very narrow surface that only lets a receptacle pass, that is, rejects all those who are too much so as not to cause jamming situations. The narrow cut has the function of orienting the receptacles. Due to the difference between the diameters identified in Fig. 4, the receptacle is always supported by the ring allow obtaining the desired orientation.

The second solution presents a different concept. It consists in two parts, the top that has the first orientation device (Slot) and the bottom that has a cavity where the receptacles fall (Fig. 4 – b).

The working principle of this solution is the center of gravity of the receptacle (Fig. 4 – b) the receptacle only enters in the slot if it moves with the largest mass part forward, otherwise the receptacle proceeds to the escape. In the event of falling, the part of the largest mass clashes first in the second part of the guidance device that will provide

a vertical posture to the receptacle. Important to mention that this solution must be integrated with the first orientation device of the first solution.

3.2 Simulation

The purpose of this simulation is to evaluate the behavior of the receptacles in the designed orienting devices.

The simulation was performed on Inventor Dynamic Simulation module, and for both systems the same pre-conditions were used. The effect of the vibrating bowl was neglected and the movement was achieved through gravity by introducing a decline on the track around *yy* and *xx* axis, according to the reference on Fig. 5.

Several tests were made, for both systems where the receptacle was placed in the beginning of the track, as presented in the below figure.
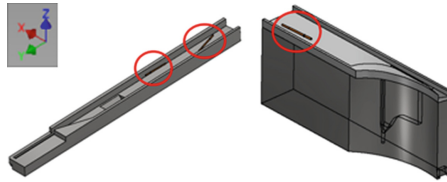
Fig. 5. CAD input of solution 1 and 2 for simulation.

With the gravity effect the receptacles slide into the orientation devices area, where its behavior is analyzed.

The first system, as mentioned before, has two orientation devices: one that only allows one receptacle to pass and another that will place the receptacle in the required position for the Robot handling. In the design phase it was expected that, when more than one receptacle reaches the first orientation device, just one would pass through. The simulation did confirm this assumption, as presented in the Fig. 6 with a screen shot after 1, 2 and 3 s from the start of the simulation, respectively a), b) and c).
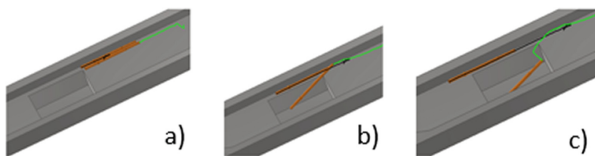
Fig. 6. Receptacle movement on simulation in the first orientation device of the solution 1.

The next and final orientation device needs to position the receptacle vertically and with the thin surface pointing down. The simulation did confirm this expectation as presented next in Fig. 7 - a:

Solution 2 presented in Fig. 7 - b, as mentioned before, works on a different principle, but uses the first orientation device. For saving time purpose, it was only simulated the second orientation device.
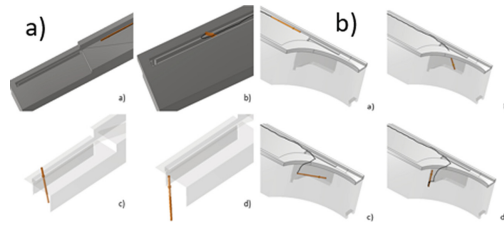
Fig. 7. a) Receptacle movement on simulation in the second orientation device of the solution 1; b) Receptacle movement on simulation of the solution 2.

In this solution, the receptacle has more degrees of freedom, and that makes its behavior somewhat unpredictable. Depending on the orientation of the receptacle when it hits this orientation device, the final orientation could be on the opposite of the desire position (Fig. 8).
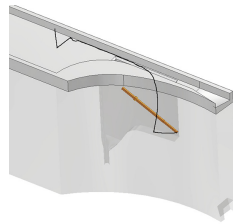
Fig. 8. Receptacle movement on simulation in the second orientation device of the solution 2.

3.3 Efficiency Analysis

In order to assess the possible orientations that the receptacles can take when entering the vibrating bowl track, an experimental test was carried out in which 25 receptacles were placed in a bowl without any modification (Fig. 9), in order to understand which orientations that resulted in the end of the course (zone A – Fig. 9).

Fig. 9. Vibratory bowl.

After 9 tests with 25 receptacles, the following data were obtained and is presented in Fig. 10:

	Test 1	Prob	Test 2	Prob	Test 3	Prob	Test 4	Prob	Test 5	Prob
Normal	9	35%	11	46%	7	37%	13	59%	10	45%
Inverse	17	65%	11	46%	5	26%	6	27%	8	36%
2x Normal	0	0%	0	0%	0	0%	0	0%	1	5%
2x Inverse	0	0%	1	4%	1	5%	0	0%	0	0%
Pair	0	0%	1	4%	6	32%	3	14%	3	14%

Test 6	Prob	Test 7	Prob	Test 8	Prob	Test 9	Prob		Prob
9	39%	7	33%	6	33%	11	52%		**42%**
11	48%	9	43%	7	39%	5	24%		**39%**
0	0%	0	0%	0	0%	0	0%		**1%**
0	0%	2	10%	2	11%	1	5%		**4%**
3	13%	3	14%	3	17%	4	19%		**14%**

Fig. 10. Orientations probabilities.

As can be seen in Table 3, the receptacles have five possible orientations plus the final one:

Table 3. Receptacles orientations.

Code	Scheme	Code	Scheme
a - Normal		d – Inverse	
b – 2x Normal		e – 2x Inverse	
		f – Final Position	
c – Pair			

Both normal and reverse orientation, as expected, have almost the same chance of occurring (42% and 39%). It is noteworthy that, according to the study, the possibility of the needles inserting each other is low ($1 + 4 = 5\%$) and occurs more often when they assume the reverse position (4%) than when they assume the normal position (1%).

With this data is possible to build the system matrix based on the orientation devices for each feeding system.

For the solution A, considering the slope with curve and the narrow cut, the matrix goes as follow (Fig. 11):

$$
\begin{array}{c}
\text{Slope with curve} \\
\begin{array}{cc} a & b \end{array} \\
\begin{array}{c} a \\ b \\ c \\ d \\ e \end{array}
\begin{bmatrix}
1 & 0 \\
0 & 0 \\
0,5 & 0,5 \\
0 & 1 \\
0 & 0
\end{bmatrix}
\end{array}
\quad
\begin{array}{c}
\text{Narrow Cut} \\
f \\
\begin{array}{c} a \\ b \end{array}
\begin{bmatrix} 1 \\ 1 \end{bmatrix}
\end{array}
\quad = \quad
\begin{array}{c}
\text{Final} \\
f \\
\begin{bmatrix} 1 \\ 0 \\ 1 \\ 1 \\ 0 \end{bmatrix}
\end{array}
$$

Fig. 11. Matrix for orientation devices in system 1.

The matrix value are the values of the probability that an orientation can turn into other orientation when passes that specific orientation device. For example, for the [1] position in the first matrix with the value 1, that means that the orientation a will stay at that orientation when it passes in the "slope with curve" orientation device.

$$[0,42\ 0,39\ 0,01\ 0,04\ 0,14]\begin{bmatrix}1\\0\\1\\1\\0\end{bmatrix} = 0,47$$

Fig. 12. Efficiency calculation for system 1.

Multiplying the matrix with the probabilities for each orientation (Fig. 12):

These method results on an efficiency of 47%. That means that for each 100 receptacles placed randomly on the bowl, 47 will come out in the desired position.

For the solution B, considering the slope with curve and narrow groove the matrix goes as presented in Fig. 13 – a. Multiplying the matrix with the probabilities for each orientation (Fig. 13 – b).

Fig. 13. a) Matrix for orientation devices in system 2; b) Efficiency calculation for system 2.

These method results on an efficiency of 23.5%. That means that for each 100 receptacles placed randomly on the bowl, 23 will come out in the desired position.

4   Results

With the information presented in the previous chapters it was possible to develop a selection table for both solutions:

Table 4. Solution score comparison.

	Flexibility (0.1)	Machinability (0.2)	Efficiency (0.2)	Performance (0.5)
Solution 1	●●	●●●	●●	●●●
Solution 2	●	●●	●	●

As presented in Table 4, the solution 1 gathers the best score in the overall performance. The evaluation parameters were:

- Flexibility – How easy is to apply this solution to a different receptacle.
- Machinability – The simplicity and the expected cost of the production process.

- Efficiency – For a certain number of receptacles how many will be placed in the desire orientation.
- Performance: How the solution performs as expected in the design phase.

As concluded in the simulation phase, the performance from solution 2 does not meet the criteria since some of the receptacles, in a certain condition, could exit the system upside down. Even with an auxiliary function that could solve that issue, the efficiency would be even lower. Adding to that lower flexibility, this solution is harder to manufacture, resulting in the choice of solution 1. This solution is simple to produce, since the second orientation device is just a simple narrow cut and a hole. Flexibility comes from the ease of adding a system that would allow to change this orientation device, depending on the receptacle used.

After selecting the solution 1 as the solution to go forward, the team decided to build a prototype and test the behavior of the receptacle and compare with the previous tests.

The purpose was to validate the results of the simulation, now with the vibrating effect of a real vibrating bowl. The orientation devices of the solution were prototype via 3D print and applied into the bowl, as presented in Fig. 14.

Fig. 14. Vibratory bowl.

As expected, the prototype replicated the result of the simulation, both orientation devices worked as pretended. After 9 tests with 25 receptacles, it was achieved a result of 100% receptacles in the desire position.

5 Conclusions

This paper reports a specific challenge of finding an accurate answer for a well-defined problem. The presented solution highlights the necessity of the development of a specific design when facing the lack of a valid market alternative.

The final solution, obtained through simulation optimization and physical validation of the prototype, met the main requirement since all containers were oriented in the desired position. As for the requirements mentioned above, the vibrating bowl system offers a wide range of sizes where the developed system can be applied and by modifying the slot, different types of receptacles can be used. Position tolerance is easily achieved when producing in a final technology – CNC Machining.

Also, this paper stressed the importance of a well-defined methodology, based on the evaluation and comparison of engineering parameters and simulation factors for a better design method. With this approach it is possible to design and develop a system that will meet all the requirements and achieve the project goals in a cost-effective way.

The next steps include the production of the final feeding system. With this, it is possible to introduce this functionality into the final automation system for receptacles insertion. For future research it is proposed to study the final orientation position tolerance to ensure that it meets the mentioned requirements.

References

1. Bateson, J.: In-Circuit Testing. Company, Van Nostrand Reinhold (1994). https://doi.org/10.1016/c2013-0-04561-6
2. Professional Plastic, "Bed of Nails type Test Fixtures" (2019)
3. I.-T. Solutions, "InsideLimits company website"
4. Ingun, "Ks-075 47 e03," (2021). https://ingun.com/en/Products/Productfinder/GKS_KS/KS-075/KS-07547E03. Accessed 15 Oct 2021
5. Ingun, "SW-KS-XXX"
6. Tan, P.S., Ngoi, B.K.A., Lee, S.S.G., Lim, L.E.N.: A knowledge-based advisor for the automatic selection and sequencing of orienting devices for vibratory feeding. Eng. Appl. Artif. Intell. **8**(1), 1–13 (1995). https://doi.org/10.1016/0952-1976(94)00053-P
7. Jänsch, J., Birkhofer, H.: The development of the guideline VDI 2221 - the change of direction. In: 9th International Design Conference, DESIGN 2006, pp. 45–52 (2006)
8. Chang, K.-H.: Design Theory and Methods using CAD/CAE: The Computer Aided Engineering Design Series. Academic Press (2014)
9. Boothroy, G.: Assembly Automation and Product Design. Taylor & Francis Group (2005)
10. Vilán Vilán, J.A., Robleda, A.S., García Nieto, P.J., Placer, C.C.: Approximation to the dynamics of transported parts in a vibratory bowl feeder. Mech. Mach. Theory **44**(12), 2217–2235 (2009). https://doi.org/10.1016/J.MECHMACHTHEORY.2009.07.004
11. Maul, G.P., Thomas, M.B.: A systems model and simulation of the vibratory bowl feeder. J. Manuf. Syst. **16**(5), 309–314 (1997). https://doi.org/10.1016/S0278-6125(97)88461-0

An Increase in the Efficiency of Selected Production Processes Using Lean Tools

Lucia Knapčíková(✉) ⓘ, Matúš Martiček, Jozef Husár ⓘ, and Jakub Kaščak ⓘ

Technical University of Košice, 1, Bayerova Street, 080 01 Prešov, Slovak Republic
`lucia.knapcikova@tuke.sk`

Abstract. The uncertainty of today's globalized economy requires prompt responses by companies, responding to rapid changes in customer demand. The last thing a company wants is an inflexible production system that cannot respond quickly. Companies' situation largely depends on reacting promptly to changing customer requirements. Of course, all these activities must also generate some profit for society. In achieving its objectives, the company must pay particular attention to reducing production costs. Therefore, improving production processes is becoming increasingly important. The improvement consists in identifying and eliminating losses that occur in production. Managing and improving business processes is a regular part of a successful company, no matter which segment the company operates. With increasing competition in a market economy, it is essential to optimize production processes. The textile market is oversaturated, supply exceeds demand, and companies have to put an even bigger stop on streamlining internal processes. It is mainly a matter of eliminating waste from various sources and does not add value for consumers' willingness to pay. This paper aims to use selected lean manufacturing tools to minimize inefficient work activities and time losses.

Keywords: Lean tools · Manufacturing · Efficiency · Production process · Industrial innovation

1 Introduction

Taiichi Ohno interprets the essence of the Lean approach as follows: "All we do is track the timeline from the moment a customer places an order with us until the moment we pick up cash. And we shorten this timeline by removing waste without added value" [1]. In short, the principle of lean manufacturing is aimed at eliminating waste and continuous improvement. John Krafcik coined the common term Lean in his 1988 article "Triumph of the Lean Production System". The term "lean production" was first published by Womack et al. in his book The Machine that Changed the World [2]. In their book, Lean Thinking, Womack and Jones present five well-known basic principles [3]: identification of customer values; value flow identification; development of continuous production capabilities; use of traction mechanisms to support material flow; striving for excellence by reducing all forms of waste to zero.

It should not be forgotten that lean manufacturing is a waste elimination process in every production area, including customer relationships (sales, supply, invoicing, service, product flow, machine maintenance, management, and logistics) to respond to customer demand the shortest possible time for developing products with minimal space and the best possible output [3].

Value is a critical starting point for lean thinking. The value of a product can only be defined by the end customer whose need is satisfied at a specific price at a particular time [2, 3]. Lean Management is the successor to Toyota Production System and Lean Manufacturing. It is currently considered one of the most popular management systems globally. Many recognized scientists and practitioners have repeatedly confirmed and defined its effectiveness. One of the basic rules of lean management is the constant pursuit of faultlessness, thanks to which the system is constantly evolving [4].

2 Literature Review

The philosophy associated with lean manufacturing is based on the fact that the customer is willing to pay only what satisfies its needs [4]. In practice, this approach means that if there are two products of the same quality on the market (there may not necessarily be products, there may be services), you choose ten with a low price [5]. The lower price is due to better, more efficient use of the necessary resources to implement the product [5].

Reducing the quality of inputs (purchase of cheaper raw materials, machines, or the use of more affordable, less qualified labor, reduction of labor causes a decrease in product quality [6, 7]. The customer already considers two factors, price and quality, while the price does not always decide. Despite the assumptions, the customer prefers high quality for the same price [8]. Therefore, it is more appropriate to reduce costs inside the organization and look for savings potential there [9]. The leanness of a business means doing only the needed things, doing them right the first time, doing them faster than others, and spending less money [8, 10]. However, the essence of a lean business does not lie in saving. It is about increasing the company's performance by producing more than competitors in a given area [11]. We will create higher added value than others with a given number of people and equipment.

3 Research Methodology

To eliminate waste from the production process, optimization of production operations times was used. This tool can be implemented in different situations, and there is usually a direct link between them. It is not possible to apply them in isolation but as a set of tools. The input data for the evaluation of increasing the efficiency of production operations are in the following Table 1. The presented data are average from a tested sample.

Table 1. Increasing the efficiency of production operations [3].

Operation	Operation time [s]
1. Manipulation with cardboard products	405
2. Manipulation with an empty carton	150
3. Carton unloading and sorting	1132
4. Removing the label	4077
5. Fixing the label and removing the old price	3895
6. Removing the sticky surface	1900
7. Storage of goods in boxes	364
8. Scanning	575
9. Pairing	3000
10. Manipulation with full strapping box	700
11. Disassembly of old cardboard	250
12. Preparation of new carton	400
13. Cleaning labels	800
14. Cutting tapes	340

4   Results

The monitoring revealed that it was necessary to remove unnecessary shelves with labels at the workplace. Instead, it was required to create a new place for cartons of goods that were freely thrown on the ground. A system of shelves and signage has been introduced. Each carton stored on the shelf was marked with its own number (Fig. 1). A color method of numbering according to the length of time the goods are in stock has been introduced on the cartons. The employees know that if cardboard marked in blue is stored in a week, green is stored in a month, and red means it is in storage for more than three months and needs to be exported, even if it is not complete. In this way, the overcrowded warehouse was eliminated, and the goods were shipped more quickly and flexibly [12]. The warehouse was also divided into a section where there are places to work and an area to handle. These essential factors were utterly absent before the adjustment. There was a high potential for shortening transport times and movements at the workplace, so reorganizations were made. The desks were centralized in one line, where the employees sat one after the other, and not arbitrarily rotated, as was the case in the original state.

4.1   Optimization of Workplace

The workplace reorganization [13], which is shown in (Fig. 1), has been introduced. It offers the removal of tables from the center of the workplace and their relocation to the already mentioned line. The relocation of the label racks to a compact set of racks with a clear marking system and a change in the material supply will not occur through the

main entrance to the workplace, as before. Still, a handling truck has created a new entry for the supply of goods [14]. This will significantly facilitate employees' handling and shorten the transport time [15]. While until now the operators worked in 3 positions, the change took place in the first and second positions, where the operators walked around the box with the goods and subsequently processed it [16]. Now a new position has been proposed, the job position of the so-called manipulator, who will bring the goods to the number one position (processing) and she will only process it, thus checking the individual workplaces and carrying the goods as needed [17]. For the second position (strapping), there was a change that the operator of the goods no longer goes to sort the rest boxes, but the goods only strap five pieces, all work with removal and sorting into boxes is done by the manipulator. State before and state after optimization is presented in Fig. 1.
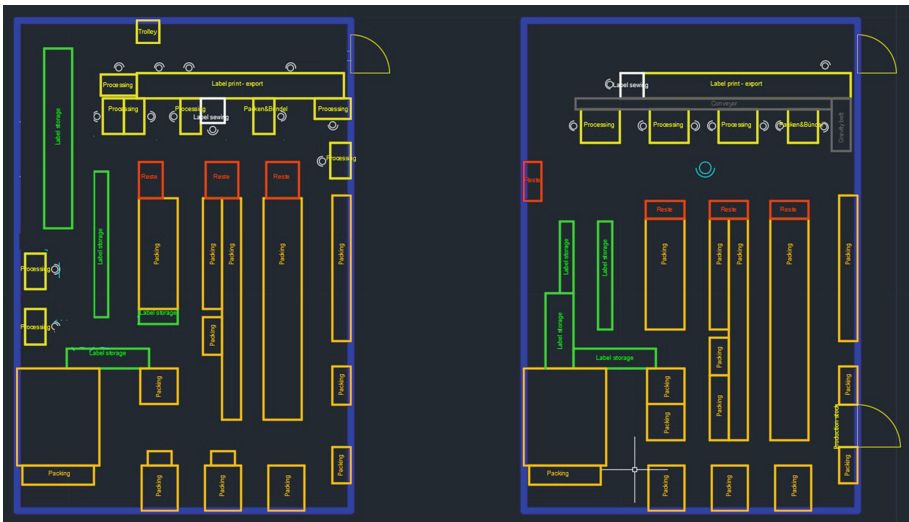
Fig. 1. The workplace layout before and after optimization (left-before, right-after) [3].

A carton marking system has been introduced to create a clean workplace. Thanks to this measure, we have introduced a state of sustainable cleanliness in the workplace. We marked using color lines and spaces according to the operation determined in space. Workplace operators [18] do not have many machines, so there was no need to introduce regular maintenance. The figures below (Fig. 2, Fig. 3) show the condition at the workplace after introducing the maintenance system. Gradual implementation of the above measures has reduced the time required to perform individual operations. As shown in (Fig. 2), a graph of the time pool display before the optimization is compiled.

Following the implementation of Lean methods and procedures, the individual operations wholly disappeared or were significantly reduced, thanks to a conveyor belt and the position of a manipulator, which is more economical for the company than a professional. Due to the optimization [19], as seen in the graph (Fig. 3), the work that does not add value to the product is significantly eliminated. The most significant values remained
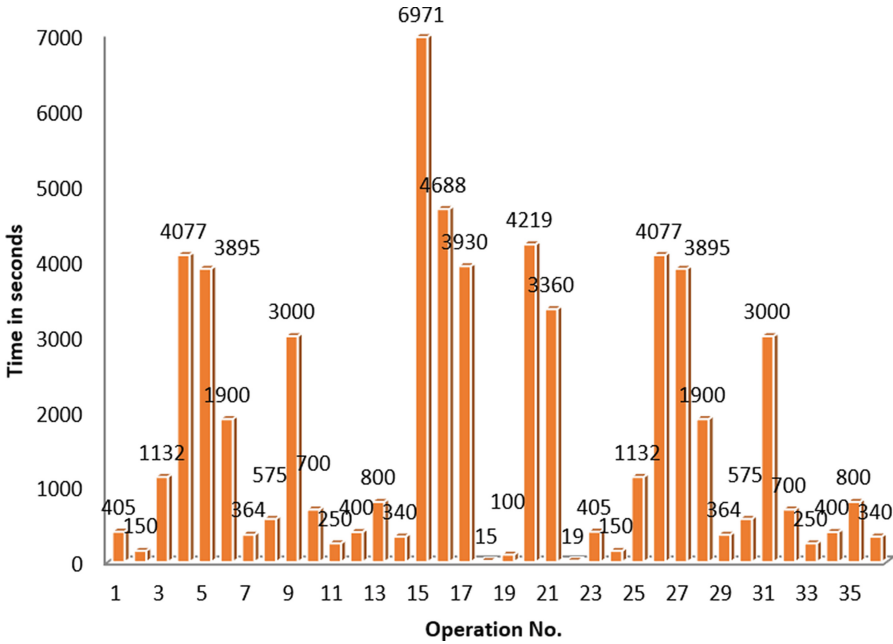
Fig. 2. A timetable of individual operations before optimization [3].

on the chart, as this process could no longer be regulated without negatively impacting product quality and staff overload.
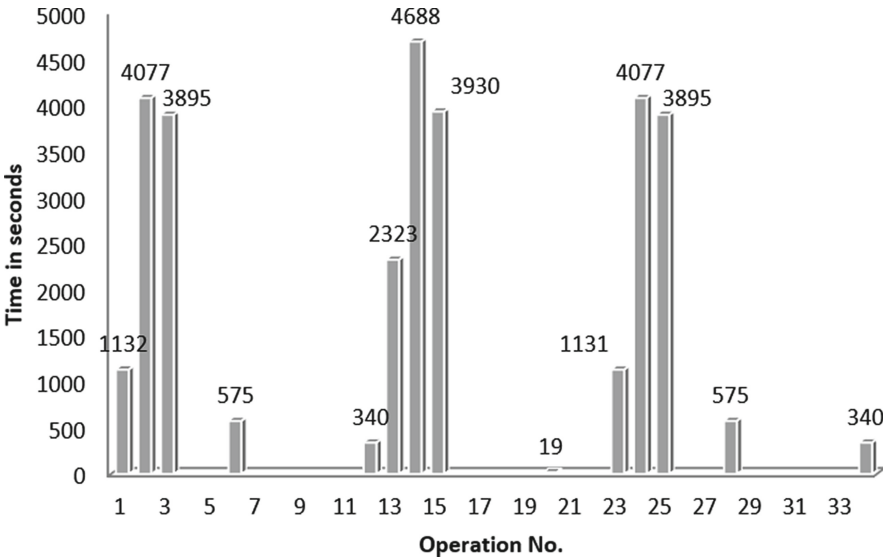
Fig. 3. Elimination of inefficient work activities [3].

Workflow optimization is the foundation of modern business management and is supported by continuous technology improvement and rapid innovation [20]. As more and more companies begin to leverage automation into their business processes and take advantage of it, the workflow optimization market will only continue to grow [21]. As this technology becomes more widespread and sophisticated, more companies will use workflow automation to create elegant and efficient working methods, disrupting more industries and creating competitive advantages in their markets.

5   Conclusions

Every company that teaches the principles of Lean methods in production has its concept, which includes a set of tools, techniques, and processes with which it works in this construction, e.g., a house, under the roof of which are all used tools or a grinder, into which tools fall (enter) and the product of lean production. The set of tools, techniques, and methods is, in principle, always very similar, only the form of their presentation changes, classification into offered products.

Waste is defined as everything (activity, activity, process) that does not add value to a product and increases its cost. And it is these types of activities, activities, and techniques that we should try to eliminate. However, it must be recognized in the production process before removing waste.

Therefore, we divided the individual methods and tools from the field of lean production according to my focus on techniques for identification and strategies for the elimination of waste. In our future research, we will focus on using other possible solutions, e.g., optimizing the material flow.

References

1. Kiyko, S., Druzhinin, E., Prokhorov, O., Ivanov, V., Haidabrus, B., Grabis, J.: Logistics control of the resources flow in energy-saving projects: case study for metallurgical industry. Acta Logistica **7**(1), 49–60 (2020). https://doi.org/10.22306/al.v7i1.159
2. Pinto, J.L., Matias, J.C.O., Pimentel, C., Azevedo, S.G., Govindan, K.: Just in Time Factory: Implementation Through Lean Manufacturing Tools. Springer, Heidelberg (2018)
3. Lengvarská, I.: Optimization of production process in the manufacturing enterprise. FVT TUKE (2020)
4. Rother, M., Shook, J.: Learning to See: Value Stream Mapping to Add Value and Eliminate Muda, 1st edn. Lean Enterprise Institute (1999)
5. Scotchmer, A.: 5S Kaizen in 90 Minutes. Management Books (2008)
6. Kotliar, A., et al.: Ensuring the economic efficiency of enterprises by multi-criteria selection of the optimal manufacturing process. Manag. Prod. Eng. Rev. **11**(1), 52–61 (2020). https://doi.org/10.24425/mper.2020.132943

7. Ivanov, V., Dehtiarov, I., Pavlenko, I., Kosov, M., Hatala, M.: Technological assurance and features of fork-type parts machining. In: Ivanov, V., et al. (eds.) DSMIE 2019. LNME, pp. 114–125. Springer, Cham (2020). https://doi.org/10.1007/978-3-030-22365-6_12

8. Smith, K., Hanover, D.: Experiential Marketing: Secrets, Strategies, and Success Stories from the World's Greatest Brands. Wiley, Hoboken (2016)

9. Pacaiova, H., Sinay, J., Turisova, R., et al.: Measuring the qualitative factors on copper wire surface. Measurement **109**, 359–365 (2017)

10. Mesaros, P., et al.: The impact of information and communication technology on cost reducing in the execution phase of construction projects. TEM J. **9**(1), 78–87 (2020)

11. Lebedev, V., Tonkonogyi, V., Yakimov, A., Bovnegra, L., Klymenko, N.: Provision of the quality of manufacturing gear wheels in energy engineering. In: Ivanov, V., et al. (eds.) DSMIE 2018. LNME, pp. 89–96. Springer, Cham (2019). https://doi.org/10.1007/978-3-319-93587-4_10

12. Peña Miñano, S., et al.: A review of digital wayfinding technologies in the transportation industry. In: Advances in Transdisciplinary Engineering, pp 207–212. IOS Press BV (2017)

13. Camacho, T.D., Foth, M., Rakotonirainy, A.: Pervasive technology and public transport: opportunities beyond telematics. IEEE Pervasive Comput. **12**, 18–25 (2013). https://doi.org/10.1109/MPRV.2012.61

14. Nagyova, A., Pacaiova, H., Markulik, S., et al.: Design of a model for risk reduction in project management in small and medium-sized enterprises. Symetry-Basel **13**(5) (2021). https://doi.org/10.3390/sym13050763

15. Lasinska, N.: Hybrid management methodology for transport projects related to rolling stock. J. Eng. Sci. **8**(2), B7–B11 (2021). https://doi.org/10.21272/jes.2021.8(2).b2

16. Straka, M., Khouri, S., et al.: Utilization of computer simulation for waste separation design as a logistics system. Int. J. Simul. Model. **17**(4), 83–596 (2018). https://doi.org/10.2507/IJSIMM17(4)444

17. Fiebig, S., Sellschopp, J., Manz, H., Vietor, T., Axmann, K., Schumacher, A.: Future challenges for topology optimization for the usage in automotive lightweight design technologies. In: Proceedings of the 11th World Congress on Structural and Multidisciplinary Optimization, Sydney, Australia, vol. 142, pp. 1–8 (2015)

18. Singh, R., Davim, J.P.: Additive Manufacturing: Applications and Innovations, 1st edn. CRC Press, Boca Raton (2018)

19. Walker, N.L., Williams, A.P., Styles, D.: Key performance indicators to explain energy and economic efficiency across water utilities and identifying suitable proxies. J. Environ. Manag. **169**, 1–10 (2020)

20. Rosova, A., Behun, M., Khouri, S., Cehlar, M., Ferencz, V., Sofranko, M.: Case study: the simulation modeling to improve the efficiency and performance of production process. Wirel. Netw. **28**, 863–872 (2020). https://doi.org/10.1007/s11276-020-02341-z

21. Gerber, B.: 12 Key Financial Performance Indicators You Should Be Tracking. https://www.accountingdepartment.com/blog/12-key-performance-indicators-you-should-be-tracking. Accessed 03 Nov 2019

Quality Control Monitoring in 3D Printing

Natalia Lishchenko[(✉)], Peter Lazorik, Jakub Demčák, Ján Piteľ, and Kamil Žídek

Technical University of Kosice, 1 Bayerova, 08001 Prešov, Slovak Republic
`natalia.lishchenko@tuke.sk`

Abstract. Online monitoring of the 3D printing process is one of the keys to ensuring product quality and improving the efficiency of the printing process. The technological system of 3D printing presented in the paper can be considered as an information system that has basic parameters: input, state, and output. The analysis of sensors and devices of online monitoring systems was summarized in two directions, as their state parameters or output parameters. In contrast to the first one, the second direction has excellent prospects since it allows direct monitoring of the object quality parameters. Still, the decision-making algorithms must be fast and reliable. A computer vision approach has become widespread to implement the direction of online monitoring of surface quality. The detection of defects using computer vision at various stages of the printing process, especially at the initial stage (the formation of the first layer), will help to take timely corrective measures and prevent the printing of low-quality parts. A defect "stringy first layer" is often observed in the FDM method. Computer vision method to detect this defect has been investigated. The method allows determining the defect presence quickly and quantifying it by the number of detected pixels. This method can successfully serve the purpose of real-time quality monitoring of a 3D printing process.

Keywords: Additive manufacturing · 3D printing · FDM method · First layer · Quality monitoring · Process innovation · Sustainable manufacturing

1 Introduction

Today, the degree of development of the "smart factory" direction within the Industry 4.0 concept is an indicator of the country's development aimed at increasing the competitiveness of its products. The key components of Industry 4.0 include: Cyber-Physical Systems, Big Data, Model Simulation, Cloud Technology, Augmented Reality, Virtual Reality, 3D Printers/Additive Manufacturing (AM), Industrial Internet of Things (IIoT), Artificial Intelligence, Autonomous Robots, and Cyber Security [1]. The development of each of these components contributes to the development of the Smart Factory concept.

AM, also referred to as 3D printing, allows producing complex- and irregular-shaped three-dimensional (3D) parts without the use of expensive molds and conventional tooling [2]. The quality of a product manufactured via the AM can be characterized by various aspects, such as dimensional accuracy, surface quality, mechanical properties, and conformance to specifications. AM encounters challenges such as adhesion, warping, porosity, gaps between layers, clogged nozzles, distortion due to shrinking, and poor

dimensional accuracy. These defects could lead to dimensional deviations between the 3D CAD (Computer-Aided Design) model and the physical printed part and the lowest surface finish.

The development and integration of monitoring and error detection techniques in AM processes is a crucial step towards fully exploiting these state-of-the-art technologies. Sometimes 3D printing takes several hours to print large objects, so the continuation of the printing process in case of the presence of some unacceptable surface distortions may be unreasonable. So, the necessity of quality monitoring seems to be obvious. In addition, the detection of defects at various stages of the printing process, especially at the initial stage (the formation of the first layer), will help to take timely corrective measures and prevent the printing of low-quality parts. At the same time, the use of non-contact quality control methods during printing will lead to the fact that the AM process will become more reliable stable and will find widespread adoption in the industry.

Therefore, a quantitative method for assessing the first layer quality, based on the computer vision method, while investigating defect so-called "stringy first layer" is proposed in this article.

2   Literature Review

To date, the most common methods of 3D printing are stereolithography (SLA), Jet prototyping (JP) [3], selective laser sintering (SLS) [4], and fused deposition modeling (FDM) [5] (see Fig. 1). The FDM is the most common technique where these materials are used: ABS-plastic, PLA-plastic, PETG/PET/PETT-plastic, PC- plastic, and others. An important aspect that determines the quality of the printed object is the printing parameters of the FDM machine.

At least three parameters must be considered to get good characteristics of the final product with the FDM process. The first type involves the geometry parameters (nozzle diameter, filament size). The second aspect is processing parameters (extrusion temperature, bed temperature, printing speed, build orientation, setting of retraction). The third one – structural parameters (layer thickness, infill pattern, infill density, number of layers, raster angle, air gap, raster width, contour width, number of contours) are also important. The combination of these parameters is critical in determining the printing product characteristics.

FDM operations encounter problems and challenges that are associated with warping, blistering [6], stringy first layer [7], scrapped surface, cracking or delamination [8], porosity, layer shift, curling, and rough corners [9], etc.

A technical 3D printing system, like any technical system, can be represented as a model of a control system, which has an input, a state, and an output [10]. Therefore, a technological 3D printing system has the same parameters (Fig. 2). The quality of a 3D object can be ensured using a quality monitoring system, state parameters, or output parameters.

To implement the first direction (state parameters monitoring), researchers use thermal camera [11–14], thermocouple [15], acoustic emission (AE) signal [16, 17], current sensor [18], vibration signal [19], accelerometer [20], etc. During FDM printing, the object is formed layer-by-layer, so it is important to support thermal energy to ensure

proper inter-layer bonding. The layer bonding mechanism is absent when the filament temperature falls below the glass transition point. In the papers [11–14], an IR camera was used to measure the object temperature for observing the change of the temperature map of the printing object [11], fixing special and temporal variations of temperature based on a combined experimental-numerical approach [12]. The physically-based model is first built and simulated using 3D transient FEA (Finite Element Analysis), then it is compared with actual experimental measurements [13]. Temperature-measuring sensors were embedded in the plane of the printed polymer object [14]. In this way, temperature profiles generated during printing are obtained. This information can then be used to calculate the developed strain fields.

To implement the second direction (output parameters monitoring), cameras are widely used, which can detect delamination, the blob, void, crack, misalignment, infill, and contour profile defects; to identify the product surface roughness, geometric deviations, under- and over-extrusion, etc. [21]. The feature of image-based monitoring is image processing after the end of printing N layers [8, 22–25] when installing one or more cameras from one or more angles. SVM algorithms allow classifying parts as either "good" or "bad" [22]. A method based on determining the entropy of an image is presented in [8]. After printing N layers, the camera captures a clear point cloud of the printed part and compares it with the STL file. If the image differs by more than 5%, the subject is defective [23, 24]. Specially created defects (detachment, missing material flow) are compared with the current printing layer in the STL file [25].
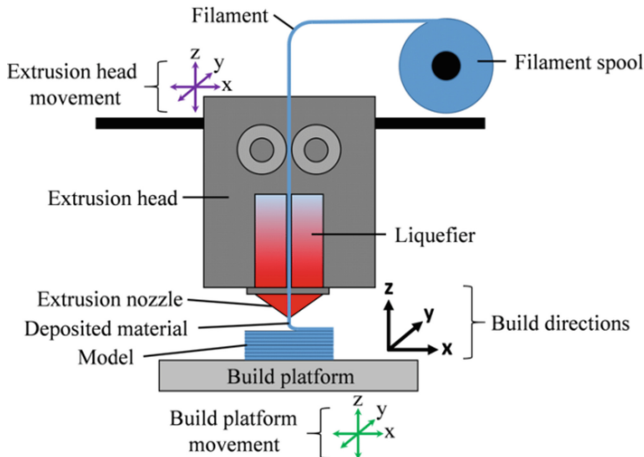
Fig. 1. The schematic diagram of fused deposition modeling (FDM) [5].

To implement the first direction, it is necessary to establish the relationship between the state parameters and the output parameters characterizing the product quality. The second direction is promising since it allows direct monitoring of the object quality parameters, but the decision-making algorithms must be fast and reliable. Particular attention must be paid to the first layer quality monitoring [26–28] as defects in printing can lead to waste in material and time. A new technique for online detection of first

layer print bonding failures during FDM is described in [29]. The first layer, good or bad bond quality, is reflected on signal energy and reconstructed vibroacoustic signals in the time domain. To identify the failure modes in printing the first layer, time-domain features of AE (to detect the occurring time of major process failures) and frequency domain (to identify different failures modes) are observed [30]. The review showed that researchers propose methods for assessing the bonding quality between the first layer and build platform, rather than assessment methods of the structural first layer defects. The existing methods are primarily associated with such defects as peeling, dragging, warping, scratching, etc. That is why the first layer's quality assessment with a structural defect was studied at the beginning of our research.

3   Research Methodology

Process management ensures the expedient functioning of the process based on the insurance of the necessary technological parameters. Management can be carried out in two forms: direct and indirect. Direct management includes control and regulation, indirect control - monitoring of state parameters or output parameters (see Fig. 2).

Research in 3D printing systems can be performed differently, depending on the goals. When the object of study is the 3D printing process, different properties can be the subject of research, such as the method of object formation (SLA, JP, SLS, and FDM), the choice of system elements, and the development of a process monitoring system.

The information system (see Fig. 2) has input, state, and output parameters. Input parameters include parameters such as 3D printer type and filaments properties. State parameters are the temperature of the layers, the extruder, the build platform, and ambient air; vibration of the mechanical components of the 3D printer; acoustic emission; motor current; force and pressure of extrusion head elements. Output parameters include 3D object geometry, surface finish, material properties. Printing control parameters are geometry, processing, and structural parameters.

Monitoring based on computer vision has two main applications, which can be distinguished and proposed for process control and assessing the manufactured object's quality. The latter is used for a surface quality assessment (the presence of defects on the surface - voids, cracks, blobs, and misalignment), determination of the output parameters of the print: layer, height, layer contour, material color, etc., and determination of geometric deviations of the dimensions of the printed object by comparison with the CAD model.

Defect detection of the printed product first layer helps to eliminate waste of material and time and prevents the need to reprint the whole part. In this study, a defect "stringy first layer" is simulated on specially made samples, and part quality is being checked with the help of images taken by a camera. Quality is represented in terms of a numerical value.

The 3D printer used for this experiment was Creality Ender-3 with PLA filament and using the FDM method. The samples were designed by software Autodesk Inventor Professional 2021. The conversion of a CAD model into STL format is necessary for the slicer software Ultimaker Cura to generate the G-code for object printing. The process
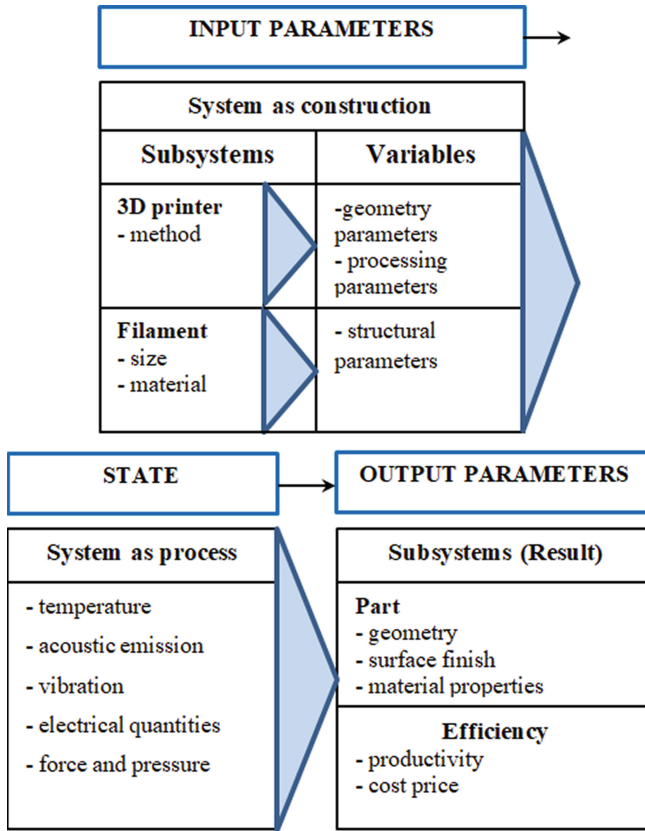
Fig. 2. The 3D printing information system.

parameters were selected according to Table 1. KEYENCE equipment was used for image analysis: Camera CA-H048MX (16x Speed, High Performance, 0.47 Megapixel Monochrome); CV-X Series Terminal Software; Light CA-DRM10X (see Fig. 3).

Table 1. Printing process parameters.

Parameter	Value	Units
Nozzle diameter	0.4	mm
Filament size	1.75	mm
Layer thickness	0.2	mm
Raster angel	45	degree
Raster width	0.4	mm
Bed temperature	60	°C
Printing temperature	210	°C
Printing speed	45	mm/s
Infill density	20	%
Infill flow	20, 50, 100	%

<center>*a*   *b*</center>
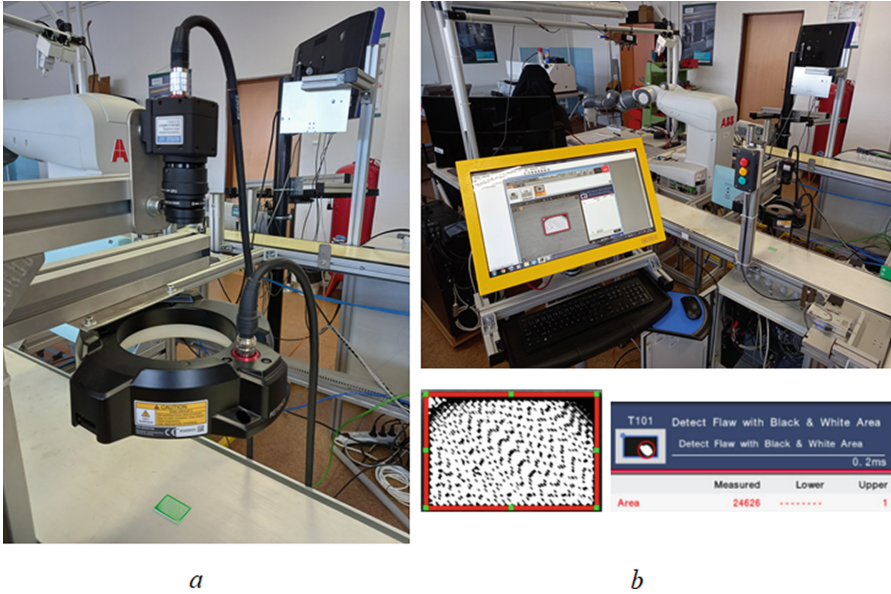
Fig. 3. Setup for quality assessment of the samples: *a* – hardware and *b* – software.

4   Results

The defect was artificially created on the samples to develop a method for evaluating the first layer quality that has a defect "stringy first layer" (the lines will not match each other, spaces between them). At the same time, by changing one of the printing parameters, Infill Flow, a different quantitative assessment of the defect is achieved. We have printed four rectangular samples (30 × 20 × 5 mm): without defects – bi-colored

(Fig. 4a) and one-colored (Fig. 4d), with defects – two bi-colored (Fig. 4b, c). Bi-colored samples were printed by green layer on the gray substrate.

In real printing, the part's first layer is printed on the 3D printer bed, with a natural contrast between two colors: the bed color and part color. When a defect appears, the gaps between the filament lines are observed. To study the developed method for assessing the quality of the first layer, the bed was replaced with a gray substrate, and the first layer was replaced with a green layer printed on the substrate. Thus, bi-colored samples consisting of two contrasting colors (gray and green) simulate the printer bed and the first layer of the printed part lying on it.

The choice of two colors (gray and green) was due to the ability of the camera software tool "Detect flaw with the black and a gray area" to recognize two types of contrasting areas on the object's surface. In this case, the number of detected pixels on the sample without defects is 0 for the green object (Fig. 4a) or the maximum one for the gray object (Fig. 4d). The number of detected pixels between 0 and maximum indicates some defects on the surface, as for example, for samples in Fig. 4b, c.
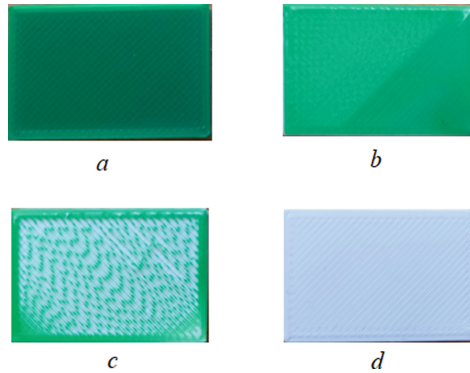
Fig. 4. Samples for study: *a* – bi-colored without defects (Infill Flow set up to 100%); *b* – with defects (Infill Flow set up to 50%); *c* - with defects (Infill Flow set up to 20%); *d* – one-colored without defects (Infill Flow set up to 100%).

The surface quality of the evaluated samples is characterized by the number of detected pixels in Table 2.

Table 2. Experiment results.

Sample	Number of detected pixels	Number of detected pixels in %
1 (Fig. 4a)	0	0
2 (Fig. 4b)	705	1.93
3 (Fig. 4c)	24626	67.4
4 (Fig. 4d)	36517	100

Changing of the Infill Flow parameter from 50% to 20% caused an increase of distances between the print lines in this way: a percentage of the number of detected pixels increased from 1.93% (Infill Flow set up to 50%) to 67.4% (Infill Flow set up to 20%) which indicates poor quality of the printed layer.

The need for two contrasting colors, which the 3D printer bed and filament have, limits the application of this method. The method can only be used to detect defects in the first layer, characterized by the presence of a distance between the filament lines. Among the disadvantages of computer vision-based monitoring, the need to interrupt the printing process to capture an image can be noted.

5   Conclusions

The modeling of the "stringy first layer" defects has been carried out, and a method for a quick assessment of the first layer quality has been proposed based on the number of detected pixels. In the above experiment, decreasing the print parameter Infill Flow from 50% to 20% led to a change in the number of detected pixels from 1.93% to 67.4%, indicating poor printed layer quality.

The proposed method can detect defects on the first layer, characterized by the distance between filament lines, for example, so-called "stringy first layer" and "under-extrusion". It was verified by the experiment the usability of this method for quick quality assessment of the printed surface for further research in 3D printing online quality monitoring.

The main drawback of the proposed method is that the printing process of the first layer is over when quality control is really applied. Another drawback is that the printing process needs to be paused while the images of a semi-finished part are taken.

In the future, it is necessary to develop a method that allows assessing the quality of the first layer in the printing process online, for example, using a Laser Displacement Sensor embedded on the print head. This gives us a direction for future research.

References

1. Žídek, K., Pitel', J., Adámek, M., Lazorík, P., Hošovskỳ, A.: Digital twin of experimental smart manufacturing assembly system for Industry 4.0 concept. Sustainability **12**, 3658 (2020). https://doi.org/10.3390/su12093658
2. Kaščak, J., et al.: Design of an atypical construction of equipment for additive manufacturing with a conceptual solution of a printhead intended for the use of recycled plastic materials. Appl. Sci. **11**, 2928 (2021). https://doi.org/10.3390/app11072928
3. Ngo, T.D., Kashani, A., Imbalzano, G., Nguyen, K.T.Q., Hui, D.: Additive manufacturing (3D printing): a review of materials, methods, applications and challenges. Compos. B Eng. **143**(15), 172–196 (2018). https://doi.org/10.1016/j.compositesb.2018.02.012

4. Becker, P., Gebert, J., Roennau, A., Finsterwalder, F., Dillmann, R.: Online error detection in additive manufacturing: a review. In: IEEE 8th International Conference on Industrial Engineering and Applications (ICIEA 2021), pp. 167–175. IEEE (2021). https://doi.org/10.1109/ICIEA52957.2021.9436729

5. Gordelier, T.J., Thies, P.R., Turner, L., Johanning, L.: Optimising the FDM additive manufacturing process to achieve maximum tensile strength: a state-of-the-art review. Rapid Prototyping J. **25**(6), 953–971 (2019). https://doi.org/10.1108/rpj-07-2018-0183

6. Fu, Y., Downey, A., Yuan, L., Pratt, A., Balogun, Y.: In situ monitoring for fused filament fabrication process: a review. Addit. Manuf. **38**(5–8), 101749 (2020). https://doi.org/10.1016/j.addma.2020.101749

7. Kadam, V., Kumar, S., Bongale, A., Wazarkar, S., Kamat, P., Patil, S.: Enhancing surface fault detection using machine learning for 3D printed products. Appl. Syst. Innov. **4**, 34 (2021). https://doi.org/10.3390/asi4020034

8. Okarma, K., Fastowicz, J.: Improved quality assessment of colour surfaces for additive manufacturing based on image entropy. Pattern Anal. Appl. **23**(3), 1035–1047 (2020). https://doi.org/10.1007/s10044-020-00865-w

9. Kaščák, J., Gašpár, Š, Paško, J., Husár, J., Knapčíková, L.: Polylactic acid and its cellulose based composite as a significant tool for the production of optimized models modified for additive manufacturing. Sustainability **13**, 1256 (2021). https://doi.org/10.3390/su13031256

10. Klocke, F.: Manufacturing Process 2. Grinding, Honning, Lapping. Springer, Heidelberg (2009)

11. Zhou, X., Hsieh, S.-J.: Thermal analysis of fused deposition modeling process using infrared thermography imaging and finite element modeling. In: Conference: SPIE Commercial + Scientific Sensing and Imaging Thermosense 10214, Florida, USA (2017). https://doi.org/10.1117/12.2262796

12. Ferraris, E., Zhang, J., Hooreweder, B.V.: Thermography based in-process monitoring of fused filament fabrication of polymeric parts. CIRP Ann. **68**(1), 213–216 (2019). https://doi.org/10.1016/j.cirp.2019.04.123

13. Li, J., Jin, R., Hang, Y.: Integration of physically-based and data-driven approaches for thermal field prediction in additive manufacturing. Mater. Des. **139**(4), 473–485 (2018). https://doi.org/10.1016/J.MATDES.2017.11.028

14. Lu, Y., Wang, Y.: Monitoring temperature in additive manufacturing with physics-based compressive sensing. J. Manuf. Syst. **48**(C), 60–70 (2018). https://doi.org/10.1016/j.jmsy.2018.05.010

15. Kousiatza, C., Chatzidai, N., Karalekas, D.: Temperature mapping of 3D printed polymer plates: experimental and numerical study. Sensors **17**(3), 456 (2017). https://doi.org/10.3390/s17030456

16. Wu, H., Yu, Z., Wang, Y.: Experimental study of the process failure diagnosis in additive manufacturing based on acoustic emission. Measurement **136**, 445–453 (2019). https://doi.org/10.1016/j.measurement.2018.12.067

17. Li, F., Yu, Z., Shen, X., Zhang, H.: Status recognition for fused deposition modeling manufactured parts based on acoustic emission. In: E3S Web Conference, vol. 95 (2019). https://doi.org/10.1051/e3sconf/20199501005

18. Kim, C., Espalin, D., Cuaron, A., Perez, M.A., MacDonald, E., Wicker, R.B.: A study to detect a material deposition status in fused deposition modeling technology. In: IEEE International Conference on Advanced Intelligent Mechatronics (AIM), Busan, Korea, pp. 779–783. IEEE (2015). https://doi.org/10.1109/AIM.2015.7222632

19. Li, Y., Zhao, W., Li, Q., Wang, T., Wang, G.: In-situ monitoring and diagnosing for fused filament fabrication process based on vibration sensors. Sensors **19**(11), 2589 (2019). https://doi.org/10.3390/s19112589

20. Oleff, A., Küster, B., Stonis, M., Overmeyer, L.: Process monitoring for material extrusion additive manufacturing: a state-of-the-art review. Progress Addit. Manuf. **6**(4), 705–730 (2021). https://doi.org/10.1007/s40964-021-00192-4

21. Wu, D., Wei, Y., Terpenny, J.: Surface roughness prediction in additive manufacturing using machine learning. In: ASME 2018 13th International Manufacturing Science and Engineering Conference. Manufacturing Equipment and Systems (3), Texas, USA (2018). https://doi.org/10.1115/MSEC2018-6501

22. Delli, U., Chang, S.: Automated process monitoring in 3D printing using supervised machine learning. Procedia Manuf. **26**, 865–870 (2018). https://doi.org/10.1016/j.promfg.2018.07.111

23. Kopsacheilis, C., Charalampous, P., Kostavelis, I., Tzovaras, D.: In situ visual quality control in 3D printing. In: Proceedings of the 15th International Joint Conference on Computer Vision, Imaging and Computer Graphics Theory and Applications - IVAPP, pp. 317–324 (2020). https://doi.org/10.5220/0009329803170324

24. Nuchitprasitchai, S., Roggemann, M., Pearce, J.M.: Factors effecting real-time optical monitoring of fused filament 3D printing. Progress Addit. Manuf. **2**(3), 133–149 (2017). https://doi.org/10.1007/s40964-017-0027-x

25. Chen, W.J., Ho, J.-H., Mustapha, K.B., Chai, T.-Y.: A vision based system for anomaly detection and classification in additive manufacturing. In: Conference: 2019 IEEE Conference on Sustainable Utilization and Development in Engineering and Technologies (CSUDET), pp. 87–92. IEEE (2019)

26. Dynnyk, O., Denysenko, Y., Zaloga, V., Ivchenko, O., Yashyna, T.: Information support for the quality management system assessment of engineering enterprises. In: Ivanov, V., et al. (eds.) DSMIE 2019. LNME, pp. 65–74. Springer, Cham (2020). https://doi.org/10.1007/978-3-030-22365-6_7

27. Araújo, A.F., Varela, M.L.R., Gomes, M.S., Barreto, R.C.C., Trojanowska, J.: Development of an intelligent and automated system for lean industrial production, adding maximum productivity and efficiency in the production process. In: Hamrol, A., Ciszak, O., Legutko, S., Jurczyk, M. (eds.) Advances in Manufacturing. LNME, pp. 131–140. Springer, Cham (2018). https://doi.org/10.1007/978-3-319-68619-6_13

28. Lasinska, N.: Hybrid management methodology for transport projects related to rolling stock. J. Eng. Sci. **8**(2), B7–B11 (2021). https://doi.org/10.21272/jes.2021.8(2).b2

29. Bhavsar, P., Sharma, B., Moscoso-Kingsley, W., Madhavan, V.: Detecting first layer bond quality during FDM 3D printing using a discrete wavelet energy approach. Procedia Manuf. **48**, 718–724 (2020). https://doi.org/10.1016/j.promfg.2020.05.104

30. Wu, H., Yu, Z., Wang, Y.: A new approach for online monitoring of additive manufacturing based on acoustic emission. In: ASME 2016 11th International Manufacturing Science and Engineering Conference (2016). https://doi.org/10.1115/MSEC2016-8551

Motorcycle Rider Assistance System
for Obstacle Detection with Visualization
in the Rider's Visual Area

Václav Mašek(✉) 🆔 and Roman Čermák 🆔

University of West Bohemia, 2732/8, Univerzitní St., 301 00 Pilsen, Czech Republic
`vmasek@kks.zcu.cz`

Abstract. This work describes a design study of motorcycle rider's assistant system. The main reason was to design affordable and useful safety devices for every motorcycle rider. The study includes a detailed design of a sensory unit placed on the motorcycle and a visualization unit with HUD (Head-Up Display) placed on the rider's helmet. The sensory unit contains an infrared sensor for range detection of vehicles in front of the motorcycle, a camera for pedestrian detection and traffic sign recognition, and a combination of IMU (inertial measurement unit) and GPS (global positioning system) sensors for independent speed determination both in open and enclosed areas. Displaying unit contains two displays and a head-up display with a single combiner without a collimating lens. The microcontroller of the sensory unit is Raspberry Pi 3b+ and of displaying unit is ESP 32. Mutual communication is via Bluetooth connection. Work contains stress analysis and fatigue analysis of stress parts, and modal analysis of sensory unit. An ergonomic study of the rider's field of view is also included. The general software design of control software is also described.

Keywords: Sustainable manufacturing · Product innovation · Advanced rider · Assistance system · Head-up display · Prevention · Sensor fusion · Design · Simulation · Raspberry Pi · ESP 32 · OpenCV

1 Introduction

In the Czech Republic, a total of 107,572 traffic accidents were registered in 2019, in which 547 people were killed. In almost 1/5 of the accidents, the driver's misconduct while driving was the cause [1].

The second most common cause of accidents is driver misconduct. Most misconduct is caused by inattention, failure to observe a safe distance, or failure to adjust the speed of the road condition.

Motorcycle drivers are the most vulnerable group of motorists. Per 100,000 registered motorcycles, there is an average of six times more accidents than the same number of cars [2]. In addition, a motorcyclist has almost 30 times less chance of survival than a car's passengers in a collision [3].

Using an appropriate assistance system to inform motorcyclists of the impending danger could reduce the number of fatal accidents.

This work aims to create a low-cost motorcycle driver assistance system using commercially available components and Open Source-based software.

2 Literature Review

The history of autonomous driving dates to 1939, when General Motors introduced a concept car capable of following a predetermined track. In 1977, attempts were made to capture the car's surroundings using cameras [4]. Between 1987 and 1995, the most significant one-off project to date for the development of autonomous vehicles, the Eureka Prometheus project, took place. Its ascent was the first car capable of at least partial autonomous movement on public roads (the average distance between the necessary driver interventions in the steering was 9 km) [5].

Since then, most automakers have been developing autonomous or assistance systems that try to make it easier, at least partially, for the driver to operate the car while making driving safer. The developers of these systems soon understood that an autonomous or assistance system is not necessarily just the domain of two-track vehicles. Gradually, assistance and autonomous technologies began to appear in the field of motorcycles.

However, autonomous driving is neither suitable nor advantageous for a motorcycle for the following reasons:

- Complex technical problem (motorcycle naturally unstable, changes in the position of the center of gravity of the driver-motorcycle system when passing corners)
- Limited space for sensors and actuators, at the same time more complex "ride by wire", technology for automatic balancing
- Lower practicality of an autonomous motorcycle than in a car
- Reduce user attractiveness (many users take a motorcycle for the enjoyment of operating the machine)

Therefore, there are many more driver's assistants for single-track vehicles, not directly interfering with the steering.

Using an appropriate assistance system to inform motorcyclists of the impending danger could reduce the number of fatal accidents.

This work aims to create a low-cost motorcycle driver assistance system using commercially available components and Open Source-based software.

The only solution currently available comparable to the proposed assistance system is the system from NUVIZ.

Samsung introduced the "Samsung Smart Windshield" windshield in 2016 in collaboration with Yamaha, equipped at the bottom of HUD. The shield is connected to a mobile phone and displays navigation, speed, and mobile notifications [6].

The Bosch Advanced Rider Assistance System includes adaptive cruise control, a front-forward collision warning system, and lane detection [7].

Students developed the MoNa (Motorcycle Navigation) system at the University of Salzburg. The driver is directed using arrows displayed using HUD. Since 2017, the

developers have not provided any product information, so further system development is uncertain (Mona website in German: https://mona-navigation.codingtub.eu/).

Nuviz's assistance system solution is already offered on the market for about $700. In addition to traffic data, the system can also display basic notifications from a mobile phone and act as a security camera [8] (Fig. 1).
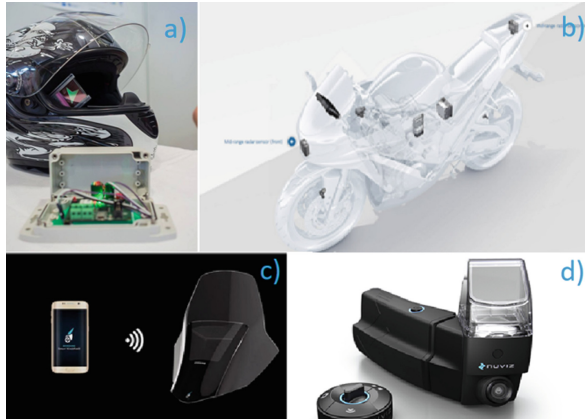
Fig. 1. Currently developed and marketed systems (MoNa, [13] (a), Bosch, [7] (b), Samsung, [6] (c), Nuviz, [8] (d)).

3   Research Methodology

The aim was to develop a system that allows the measurement of the motorcycle's speed without interfering with its electronics. Detection of the objects of interest (persons, animals, traffic signs…) and measuring the distance from the obstacle/car/vehicle in front of the motorcycle are also required. The mechanical design of the developed system was planned to ensure the protection of electronic components against external influences, cooling of electronic components, and easy mounting on the motorcycle/helmet while maintaining sufficient holding. The system also must ensure that relevant information is displayed to the driver.

The system is planned to be opened to be extended in the future with additional modules and functional units that can communicate with intelligent infrastructures, such as vehicle-to-everything (e.g., [11] and [12]), which will increase the safety of both motorcycle riders and other road users (pedestrians, etc.).

The microcontroller of the sensory unit was chosen based on the desired computational power for image processing. In the case of displaying units, low power consumption was preferred so smaller and lighter batteries could be used.

Proper sensors for visual detection of objects of interest, measuring the distance in front of the motorcycle, and independent speed measurement was chosen.

The block diagram of the functions of the whole system is shown in Fig. 2. (power supply marked in red, information flows in blue). The following electronic components were selected based on the requirements – see Table 1.
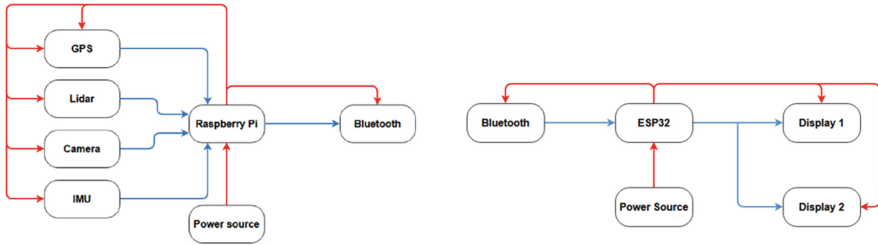
Fig. 2. Sensory block schematics (top) and display units.

Table 1. List of electronic components.

Type of component	Model
GPS	NEO – 6M
IMU	MPU 6050
Camera	Waveshare RPi
Infrared sensor	Teraranger Evo 60 m
Display	ST7789
Controller of the sensory unit	Raspberry Pi 3b+
Controller of the display unit	ESP 32
The power source of the sensory unit	ADATA AT10000
Display unit power source	Eloop Ultraslim E30

4   Results

Based on the specification of the requirements, a mechanical design of the sensory unit (attached to the construction of the front fork of the motorcycle) and a display unit (attached to the rider's helmet) were created – see Fig. 3.
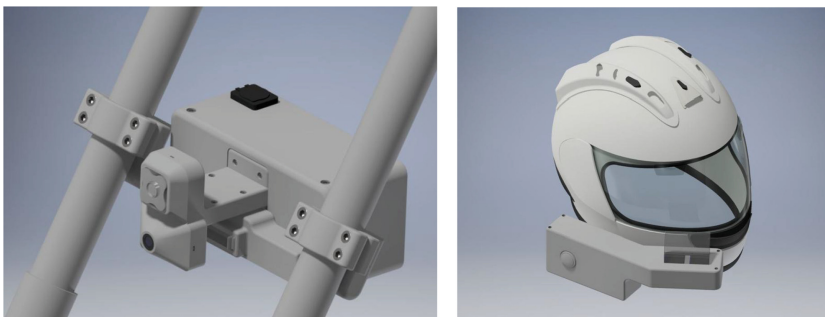
Fig. 3. 3D model sensory (left) and display unit.

4.1 Sensory Unit

Both the camera and the laser range finder are placed above each other, reducing the risk of damage to the range finder. The Raspberry Pi, together with the IMU and GPS sensor, is located on the front of the case. These components are cooled while driving through the flowing air. Since the proposed system is universal, adjust the unitholder according to the steering angle (Fig. 4).
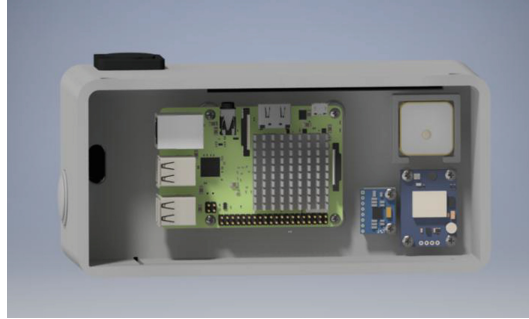
Fig. 4. Location of Raspberry Pi and sensors.

4.2 Display Unit

Due to the design and price demands, a HUD solution without collimating optics was chosen for the purpose of this work. Only one combiner was used, common to both displays. This allows to use both displays for displaying more comprehensive information. At present, the right display is used for displaying traffic signs and the display, located more in the field of view, displays warning pictograms (Fig. 5).
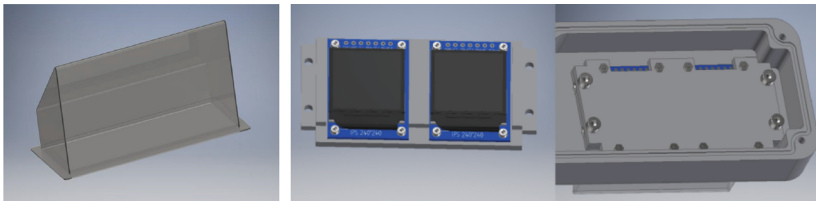
Fig. 5. The combiner, the fixing of the displays, and their location.

4.3 Software

For the software development was used: Python 3.7 (Sensory Unit); Wiring 1.0 (Display Unit).

The software architecture of the assistance system has three parts:

- obtaining the necessary data from sensors and processing them: infrared sensor; camera (Python: OpenCV); GPS + IMU (Python: MPU6050 a PyNmea2);
- sending the obtained information from the sensory unit to the display unit: Bluetooth interface (Wiring: BluetoothSerial and Python: PyBluez);
- displaying information to the driver (Wiring: TFT_eSPI).

The source code for infrared sensor was taken from the manufacturer's GitHub. The return value is the distance in meters (x). For the calculation of the safe distance from the front of the moving vehicle, a calculation assuming a safety gap of 2 s was chosen (https://github.com/Terabee):

$$x \geq d = \frac{2 \cdot v}{3{,}6} \tag{1}$$

- d = required minimum safe distance in m
- v = vehicle speed in km/h

IMU return values are acceleration and angular speed values around the acceleration axes. Since the sensory unit is located on the motorcycle fork, the acceleration vector is considered for calculating speed only in the direction of the motorcycle's movement direction. The equation was used:

$$\vec{a} = \frac{d\vec{v}}{dt} = \dot{v} \tag{2}$$

The return values of the GPS sensor are latitude and longitude values. For a distance of two points (the x) orthodrome equation was used:

$$\sin\left(\frac{x}{2r}\right)^2 = \sin\left(\frac{\Delta\varphi}{2}\right)^2 + \cos\ \varphi 1 \cdot \cos\ \varphi 2 \cdot \sin\left(\frac{\Delta\lambda}{2}\right)^2 \tag{3}$$

- r = radius of geoid of the approximated sphere (6371 km)
- $\varphi 1$, $\varphi 2$ = start and end latitude, $\Delta\varphi = \varphi 1$ and $\varphi 2$ difference,
- $\Delta\lambda$ = difference of the initial and the end longitude

Speed is calculated:

$$\vec{v} = \frac{d\vec{x}}{dt} = \frac{\vec{x_1} - \vec{x_0}}{\Delta t} \tag{4}$$

The moving average function is used to filter deviations caused by measurement inaccuracies in the case of driving without GPS correction.

A cascade classifier was used to classify significant objects in the image, using Haar-like features [9]. Pedestrian detection gives good results to walking pedestrians. However, it cannot detect non-standing persons, e.g., persons in the wheelchair, etc. (Fig. 6).

The potential risk of collision with a pedestrian, with animals, or too little distance from the front of a moving vehicle can also be highlighted by pictograms (Fig. 7).

Fig. 6. Pedestrian recognition app.

Fig. 7. Possibilities of signaling a collision with a vehicle, pedestrian, or animal.

Table 2. Examples of simplified traffic signs (pictograms) [14].

Group of traffic signs	Pictogram

Since some road signs have the same or similar meaning, it was decided to use simplistic symbolism to interpret signs of similar meaning. The following simplifications can be adopted for selected traffic sign groups – see Table 2.

All pictograms displayed are stored in the ESP32 in hexadecimal notation, currently having a capacity of 10 symbols. The selection of a specific, displayed image or pictogram is controlled by the program's internal logic based on the sensory unit's data (Fig. 8).
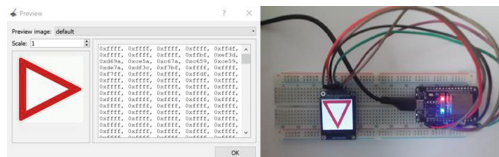
Fig. 8. Hexadecimal color writing (left) and pictogram displayed.

4.4   Simulation Verification

For the sensory unit, it was necessary to verify resistance to resonances arising from vibrations while driving. The following assumptions were based:

- Low-speed motor (chopper type motorcycle)
- Both forks and handlebars are solid bodies (vibrate with the same frequency)
- Motorcycle suspension design respects ISO 2631 and ISO 5349 standards

Of the above facts, the expected safe frequency is 100 Hz. According to the modular analysis of the report, the higher non-zero custom frequency of the assembly is about 130 Hz, which meets the requirements. Furthermore, a finite element analysis of static load was performed, and the MATLAB program environment was used to calculate the fatigue strength of the joints. The sensor unit holder can withstand 10,000 disassemblies, and the display unit holder has 3000 disassemblies (Fig. 9). Mechanical properties of the used material were taken from [10].
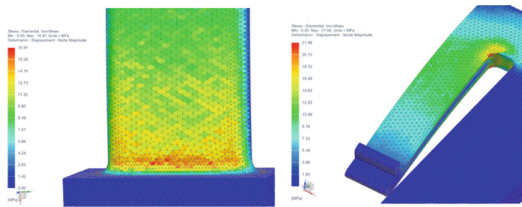
Fig. 9. Calculation of stress in sensory unit latch (left) and display unit latch.

The NX Human module was used to verify the view from the helmet. A right-hand composition was used. The model of a person consists of a figure 175 cm high. The driver will detect any vehicle coming from the right (Fig. 10).

Fig. 10. Field of view of the left and right eye.

5   Conclusions

A prototype motorcycle rider assistant has been developed, which currently implements several basic functions to increase rider safety – eliminating inattention. It consists of

two key elements – a sensor unit and a display unit. The system is generally applicable because it is entirely independent of the type of motorcycle and does not interfere with the construction and wiring in any way. Since the location is chosen on the front fork, this unit is suitable for motorcycle models with sufficient space for mounting above the front wheel (e.g., chopper type). The display unit is located on the motorcycle driver's helmet. HUD realized data display. The software covers several basic security features that can be further expanded.

The assistant prototype will be tested on a test polygon and in real road traffic. Based on the results of the tests, the mechanical design will be optimized, and the software will be adjusted and improved. The prototype can be further expanded with other functional elements, such as night vision, detection of a vehicle approaching from the side, or communication with smart infrastructures, e.g., vehicle-to-everything or pedestrian-to-infrastructure networks. It would be possible to predict better the occurrence of pedestrians and other objects in the drive track of the motorcycle.

References

1. Transport Accidents - Time Series (2020). https://www.czso.cz/csu/czso/transport_accidents_time_series. Accessed 14 Oct 2021
2. Facts + statistics: Motorcycle crashes (2019). https://www.iii.org/fact-statistic/facts-statistics-motorcycle-crashes. Accessed 14 Oct 2021
3. Dimovski, A.: Motorcycle accidents - statistics, facts, and trends in 2021 (2021). https://carsurance.net/blog/motorcycle-accidents/. Accessed 14 Oct 2021
4. Gringer, B.: History of the autonomous car (2020). https://www.titlemax.com/resources/history-of-the-autonomous-car/. Accessed 14 Oct 2021
5. Dhawan, C.: Autonomous Vehicles Plus: A Critical Analysis of Challenges Delaying AV Nirvana. FriesenPress, Victoria (2018)
6. Courts, Z.: First look: Samsung head-up display smart windshield for motorcycles (2016). https://www.motorcyclistonline.com/first-look-samsung-head-up-display-hud-smart-windshield-for-motorcycles/. Accessed 14 Oct 2021
7. Advanced rider assistance systems (2018). https://www.bosch-mobility-solutions.com/en/solutions/assistance-systems/advanced-rider-assistance-systems-2w/. Accessed 14 Oct 2021
8. Taylor, R.: Nuviz motorcycle head-up display review (2017). https://www.bennetts.co.uk/bikesocial/reviews/products/motorcycle-technology/nuviz-motorcycle-head-up-display-review. Accessed 14 Oct 2021
9. Arunmozhi, A., Park, J.: Comparison of hog, LBP and Haar-like features for on-road vehicle detection. In: 2018 IEEE International Conference on Electro/Information Technology (EIT), pp. 0362–0367 (2018). https://doi.org/10.1109/eit.2018.8500159
10. Ezeh, O.H., Susmel, L.: On the fatigue strength of 3D-printed polylactide (PLA). Procedia Struct. Integrity **9**, 29–36 (2018). https://doi.org/10.1016/j.prostr.2018.06.007
11. Periša, M., Perakovic, D., Vaculik, J.: Adaptive technologies for the blind and visual impaired persons in the traffic network. Transport **30**, 247–252 (2015). https://doi.org/10.3846/16484142.2014.1003405
12. Periša, M., Cvitić, I., Perakovic, D., Husnjak, S.: Beacon technology for real-time informing the traffic network users about the environment. Transport **34**, 373–382 (2019). https://doi.org/10.3846/transport.2019.10402

13. Mona - motorcycle navigation system. Eindrücke vom mona-Stand! 1.0 (2014). Facebook. https://www.facebook.com/photo/?fbid=254832078037690&set=pb.100042175 286138.-2207520000. Accessed 14 Oct 2021
14. Cesty.cz, B. (n.d.): Dopravní znacky. www.bezpecnecesty.cz. https://www.bezpecnecesty.cz/cz/autoskola/dopravni-znacky. Accessed 20 May 2021

Surface Defects Detection on Pressure Die Castings by Machine Learning Exploiting Machine Vision Features

Zoe Papagianni and George-Christopher Vosniakos(✉)

National Technical University of Athens, 9, Iroon Polytechniou St., 15780 Athens, Greece
vosniak@central.ntua.gr

Abstract. Detection of surface defects in high-pressure aluminum die castings is of paramount importance for maintaining product quality. Visual inspection by humans is time-consuming and subject to errors and oversights. A machine vision system has been set up to capture part surface images in this work. Afterimage quality enhancement using standard transformations and filtering Regions of Interest were defined in the areas where defects are expected to appear. Noise elimination extended edge extraction followed. Corresponding descriptors were employed to identify statistical features associated with defective parts. An advanced learning process has been developed to classify parts as defective or normal, based on Feedforward Artificial Neural Networks (ANNs), which were compared to typically used Support Vector Machines. Different combinations of descriptors were tried as input to determine the best four ANNS, which were used as an ensemble to enhance robustness at overall positive recognition rates of the order of 90% despite the restricted dataset.

Keywords: Die casting · Surface defects · Machine vision · Artificial neural networks · Support vector machines · Industrial innovation

1 Introduction

Manufactured parts may develop surface defects, irregularities, and discontinuities, e.g., shrinkage, stains, and porosity in the case of castings, greatly influencing part properties and functional behavior, let alone esthetic acceptability. Different manufacturing processes may impart various defects to manufactured parts. Thus, suitably trained human operators in quality control departments are necessarily employed. However, their intervention is prone to error, ill-judgment and subjectivity.

Thus, computer vision coupled with image analysis and statistical feature calculations that can be uniquely connected to the presence of defects have been examined for years as an automation solution to the problem. There are two main approaches [1]: the first is based on matching techniques, in which surfaces are evaluated, after comparison with an ideal surface, deviations pointing to defects, while the second approach seeks out predefined types of defects. Both methods are considered to be relatively unreliable.

Recently, machine learning has been added as a possible extension promising higher reliability.

The present work takes this latter approach with some peculiarities in each step, to be explained next. Section 2 describes the state-of-the-art for defect detection in castings. Section 3 outlines image acquisition and analysis techniques employed here in the context of high-pressure die castings. Section 4 presents the machine learning techniques processing image analysis features to detect defective parts. Section 5 provides a succinct discussion and pertinent conclusions.

2 Literature Review

Numerous methods focusing on machine vision have been reported in the last decade or more. For instance, a method of categorizing defects using pixel statistics and histogram balancing has been demonstrated in the study [2]. A comprehensive review of automated visual defect detection on flat steel surfaces typically produced by rolling processes is given in the research [3], bearing some resemblance to casting defect detection. Real-time defect-recognition in rolled workpieces using support vector machines (SVM) had been implemented successfully even long ago [4]. A method for texture calibration was proposed in the study [5], employing color texture description parameters. However, the color quality of the texture may be affected by other surface defects. In the research [6], Otsu's method was revised for optimizing the limit value in histograms with one or two distributions. In the study [7], Mie light scattering was used. A vision system analyzed inequalities/contrasts created by defects. An automatic thresholding algorithm based on histograms of defective areas outperforming Otsu's method has been reported [8]. In the same direction, recognition has been proposed based on shadows created by surface defects independent of resolution and depth of field [9]. A 3D vision system was advocated in [10] to detect defects, focusing on laser beam system analysis and elevation profiling.

More recently, machine learning methods were fostered in combination with machine vision. A surface defect recognition system for copper rods used CCD cameras to capture images, which are converted to binary and, then, search areas are located from which defects are extracted [11]. A neural network has been trained for automatic categorization. Automatic detection and categorization of defects in ceramic tiles used the Rotation Invariant Measure of Local Variance (RIMLV) operator and then morphological operators to complete and normalize the identified areas. A data vector machine with the 'winner-takes-all' strategy was employed to categorize the data [12]. The efficient design of machine vision systems and advanced algorithms for surface defect detection in aluminum castings was focused on in [13]. Neural networks were used for categorization. A separation method was reported in [14] employing a Gaussian filter, a comparison filter and a binary image. Geometric data and statistics of the binary image are input to machine learning algorithms. In a revised version, the defects in the cast parts are examined by collective categorization methods [15]. In another study, a combination of filters and a Quality Threshold Clustering algorithm were proposed to improve efficiency in a machine learning framework [16]. In [17], small image datasets were used with Wasserstein generative adversarial nets, feature-extraction-based transfer learning techniques,

and multi-model ensemble framework, achieving a false-negative detection rate as low as 2%. In Convolutional Neural Networks (CNN) that dominate computer vision tasks in manufacturing inspection [18], large annotated datasets are required, which constitutes a bottleneck. Typically, this is overcome by generating synthetic images of defective surfaces, e.g., using Generative Adversarial Networks (GANs) [19] or Auto-annotated deep segmentation using cycle consistent GANs [20].

3   Research Methodology

The part examined is a 'flange', see Fig. 1(a), an automotive part made of Al-Mg-Si alloy standardized as AC 51500. Its overall dimensions are $230 \times 210 \times 10$ mm.
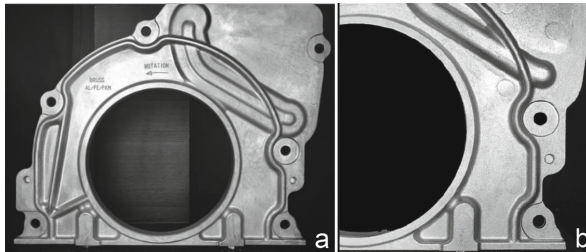
Fig. 1. Part front side (a) general aspect (b) image of the lower right section after preprocessing.

52 parts of this type were photographed, of which 15 had no defects, while the remaining 37 had at most two surface defects of the type: surface crack, stain, shrinkage, unfilled region, see Fig. 2. For a full presentation of defects and explanation of their causes in metallurgical terms, the reader is referred to [21].
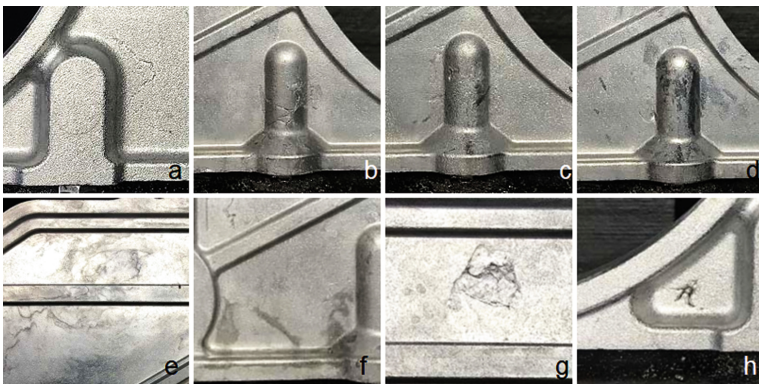
Fig. 2. Characteristic types of defects in part 'flange': (a-b) surface crack (c-d) shrinkage and stain (e-f) stain (g-h) unfilled region.

3.1   Image Acquisition and Pre-processing

A simple part-holding jig was designed and manufactured in-house, see Fig. 3, restricting the influence of ambient light. The jig is illuminated by a 333×444 mm LED panel with power 44 W/m and color temperature 4500 °K aiming to diffuse light and possessing a central hole of 44 mm $\times$ 55 mm where the camera is fixed.

An iPhone 6™ mobile phone camera was used to take photographs of each part's upper, left, and right sides separately. For a field of view of approximately 30×40 cm, the size of the smallest possible defect being estimated at 1 mm, camera resolution should be at least 25 pixels/cm.

Images were transformed to acquire the same position and rotation and then preprocessed with standard techniques such as grayscale conversion, contrast enhancement, sharpening, and background removal, see Fig. 1(b).
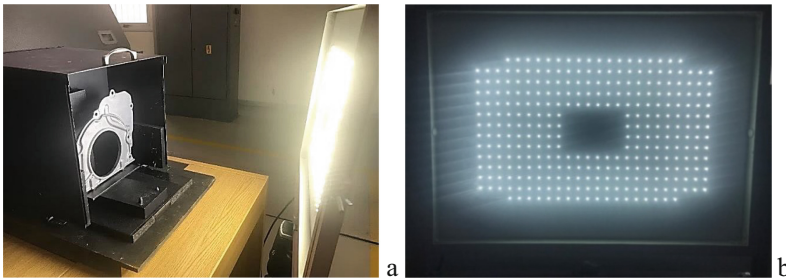
Fig. 3. (a) Part-holding jig with typical part mounted (b) led panel.

3.2   Image Processing

All image processing is carried out in Matlab™. The defects to be detected are expected, by previous experience, to lie in particular areas of the part; see Fig. 2 for examples. This fact is exploited to lower the computational load by isolating the corresponding Regions of Interest (ROIs). ROI extraction is based on descriptor vectors, see Fig. 4(a) consisting of pixels placed around the area of interest; the pertinent coordinates are determined, see Fig. 4(b). The particular descriptor vectors employed are of type SURF.

ROIs are processed further to eliminate noise. ROI edges consist of dark pixels, similarly to the defects, and as a result, it is preferable to remove them to prevent errors during image analysis. Thus, a binary mask was applied, which discriminates between image pixels belonging to either the ROI or the background. Then, a filter was used to eliminate dark enough pixels, i.e., those with brightness value in greyscale lower than 140–180, see Fig. 4(c). The threshold was determined by trial and error based on the experience and perception of the user.

In edge detection, the pixels where the brightness gradient is comparatively large are identified, which happens, typically in areas with defects rather than in non-defective areas. For this reason, the edge detection function is applied to ROIs where contour edges have been removed, see Fig. 5.
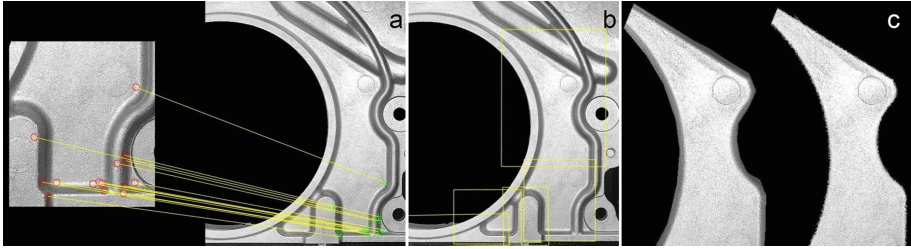
Fig. 4. ROI processing (a) Extraction descriptor vector (b) box detection (c) binary mask and filter application.
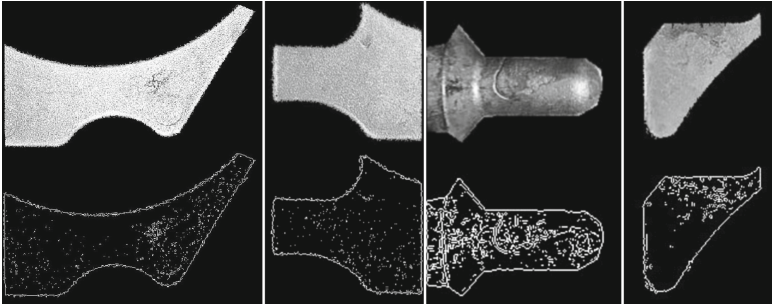
Fig. 5. Sample result of edge extraction in four different ROIs.

3.3   ROI Image Analysis

For every ROI image, the following statistical features are computed.

a. Mean (F_1) and standard deviation (F_2) of the brightness of all pixels.
b. The brightness gradient represents the mean (F_3) and standard deviation (F_4).
c. A number of pixels (F_5) and their mean brightness (F_6) provided that brightness is lower than a threshold.
d. A number of white pixels (F_7) derived from edge detection.

In addition, the feature 'weight' (F_8) is also computed to serve in classification next:

$$\text{weight} = (\text{mean2} + \text{stdev2}) \text{ for brightness}/(\text{mean2} + \text{stdev2}) \text{ for brightness gradient} \tag{1}$$

Note that each pixel has a brightness value from 0 to 255 in greyscale. The sum of the above feature values is calculated for each individual ROI. It is presented in Fig. 6, particularly defective parts represented by an orange line and normal ones by a blue line.

Based on these diagrams, it is obvious that defective parts correspond to lower mean pixel value of non-defective parts except for some cases, which may be due to the small defect size or the brighter illumination of the surrounding area. However, such exceptions may not influence the result, compensating for other features like the high gradient value or a high number of white pixels.

a

b

c

d

e
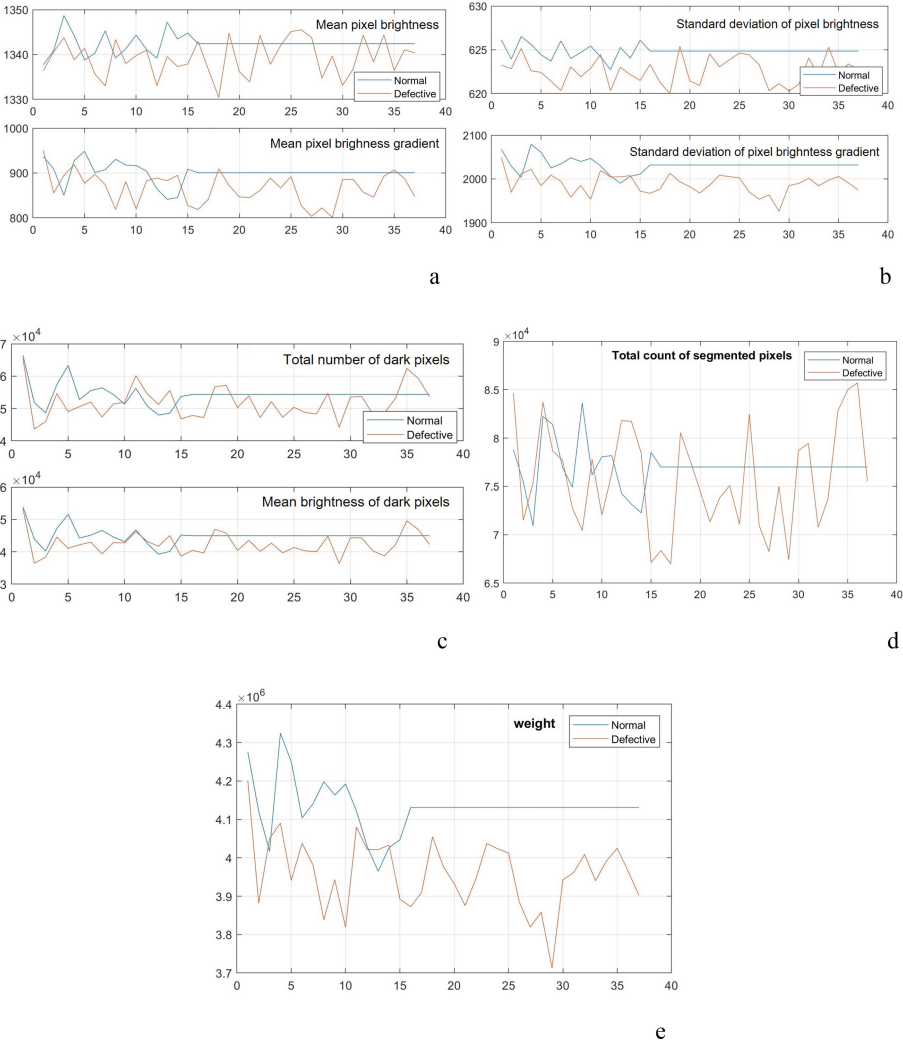
Fig. 6. Feature value sum over ROIs, see Sect. 3.3 (a) F1-F3 (b) F2-F4 (c) F5-F6 (d) F7 (d) F8.

4   Results

Support Vector Machines (SVM) and Artificial Neural Networks (ANN) were investigated for classifying a part as defective or not. They use as input all or some of the features presented in Sect. 3.3. SVMs are typically employed as classifiers; hence they were used to form a baseline for comparison, whereas the development of ANNs as classifiers was a more intricate task.

4.1 Support Vector Machines

Implementation was done on Classification Learner of Matlab$^{\text{TM}}$. In particular, quadratic Support Vector Machines with cross-validation of 5 sets were used. In Fig. 7, the normalized value range of inputs is presented. Non-defective parts are depicted in blue line color, whereas defective ones are in orange. Two combinations of input variables were tested: for combination S1: F_1, F_3, F_5, F_7, F_8 and for combination S2: F_1, F_2, F_3, F_4, F_5 F_7, F_8. The achieved positive recognition rates are 90.4% and 88.6%, respectively (Fig. 8).
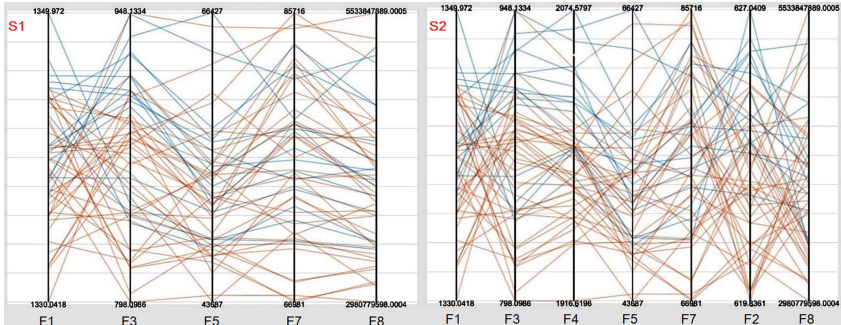
Fig. 7. SVM feature input value ranges for S1 (left) and S2 (right) combinations.
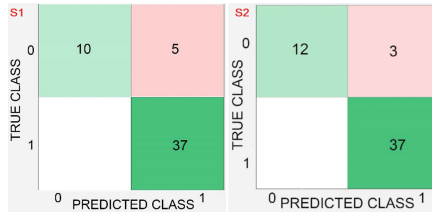
Fig. 8. SVM results for combinations S1 (left) and S2 (right).

4.2 Artificial Neural Networks

A two-layer feed-forward network with a sigmoid activation function was implemented on the Neural Network Toolbox of Matlab™. Two output neurons were used corresponding to the classification error and the classification probability as such being expressed in the range 0 to 1 representing the defect domain. Different numbers of neurons were also tried for the hidden layer ranging from 20 to 60. As far as input neurons are concerned, it was not clear which of the eight available features F_1 to F_8 should be used; hence a number of different ANNs were constructed, each corresponding to a different combination of features, see Sect. 3.3.

The data were divided into training, validation, and testing sets. In all cases, 70% of the input values were used for training, 15% for validation, and 15% for testing. This

distribution was adopted due to the limited number of available parts. Apart from the positive recognition rate, overfitting was considered in evaluating alternative architectures. The four architectures shown in Table 1 emerged as the best ones, all corresponding to a single hidden layer with 30 neurons and exhibiting no overfitting. Characteristic results for the ANN corresponding to best performing combination A1 are given in Fig. 9. In the confusion matrices, diagonal cells correspond to correctly classified observations, and off-diagonal cells correspond to incorrectly classified ones. The number of observations and the percentage of the total number of observations are shown in each cell. The column on the far right shows the total percentage predicted to belong to each correctly or incorrectly classified class.

Table 1. Best ANN architectures.

ID	Feature combination	Classification success rate (%)
A1	F_1, F_3, F_5, F_7, F_8	98.1
A2	$F_1, F_2, F_3, F_5, F_6, F_7, F_8$	84.6
A3	$F_1, F_2, F_3, F_4, F_5, F_7, F_8$	92.3
A4	F_1, F_3, F_5, F_7	90.4
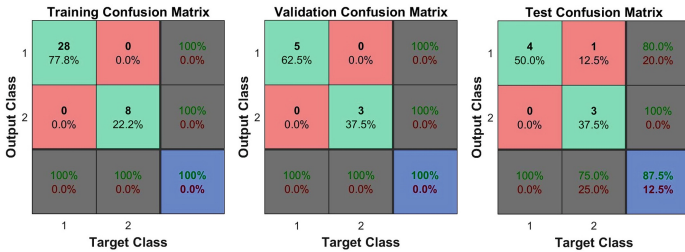
Fig. 9. Confusion matrix results for ANN corresponding to input feature combination A1.

Instead of the best ANN, all four ANNs were used as an ensemble, see Fig. 10. It was decided because of the small dataset to enhance robustness.
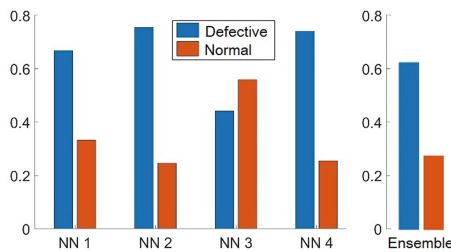
Fig. 10. Classification example for each one of the four ANNs and their ensemble.

Note that the separation of the training, validation and testing sets is random; therefore, a part belonging to the training set of one ANN may belong to the validation or testing set of another ANN. Accordingly, we also compensate for cases of false classification by one of the ANNs. To illustrate, in the case depicted in Fig. 10, NN3 has misclassified the part. Nevertheless, all other ANNs have classified it correctly, resulting in ultimately correct classification. Thus, the final output is the mean positive classification rate of the four ANNs and the mean classification vector.

$$class = \frac{\sum_{n=1}^{4} Accuracy_n \cdot Classification_n}{4} \tag{2}$$

5 Conclusions

When developing a system for recognizing surface defects on die casting parts using machine vision, emphasis should be placed on the robustness of capturing and analyzing the surface images to support automatic classification. In this context, it should be mentioned that no special equipment was used in this work, except for a work-holding jig that also catered for relatively stable lighting conditions. It proved to be sufficient for obtaining uniform images; any slight variations between them were eliminated by image processing without disturbing ROIs. With improved equipment, even better precision and reliability of acquired images should be attained.

Regarding the classification of parts as defective or not, it has to be noted that the number of parts used to deploy the machine learning methods was small in this work. Indeed, manufacturing applications are notorious for small machine learning datasets. In this light, both methods are considered to be promising. ANNs are superior to SVM due to performance, flexibility, and robustness, yet high classification precision does not necessarily mean that the system is robust enough to be of practical use. The small size of available data was dealt with by exploiting an ensemble of four ANNs.

Future steps involve augmenting the dataset with new cases of defective parts as and when they become available and using the new dataset for retraining the ANNs. Further evolution of the system involves identifying and classifying individual defects according to ROI labels or some grouping of ROIs.

References

1. Mery, D., Jaeger, T., Dieter, F.: A review of methods for automated recognition of casting defects. Insight-wigst. Northhampton **44**(7), 428–436 (2002)
2. Singh, S., Kaur, M.: Machine vision system for automated visual inspection of tile's surface quality. IOSR J. Eng. **2**, 429–432 (2012)
3. Luo, Q., et al.: Automated visual defect classification for flat steel surface: a survey. IEEE Trans. Instrum. Meas. **69**, 9329–9349 (2020). https://doi.org/10.1109/TIM.2020.3030167

4. Jia, H., Murphey, Y.L., Shi, J., Chang, T.-S.: An intelligent real-time vision system for surface defect detection. In: Proceedings of the 17th International Conference on Pattern Recognition, pp. 239–242. Cambridge (2004). https://doi.org/10.1109/ICPR.2004.1334512

5. López, F., Valiente, J.M., Prats, J.M., Ferrer, A.: Performance evaluation of soft color texture descriptors for surface grading using experimental design and logistic regression. Pattern Recogn. **41**, 1761–1772 (2008). https://doi.org/10.1016/j.patcog.2007.09.011

6. Ng, H.: Automatic thresholding for defect detection. Pattern Recogn. Lett. **27**, 1644–1649 (2006). https://doi.org/10.1016/j.patrec.2006.03.009

7. Gamage, P., Xie, S.Q.: A real-time vision system for defect inspection in cast extrusion manufacturing process. In: Proceedings of the 14th International Conference on Mechatronics and Machine Vision in Practice (IEEE), pp. 240–245 (2007). https://doi.org/10.1109/MMVIP.2007.4430750

8. Wakaf, Z., Jalab, H.A.: Defect detection based on extreme edge of defective region histogram. J. King Saud Univ.-Comput. Inf. Sci. **30**, 33–40 (2018). https://doi.org/10.1016/j.jksuci.2016.11.001

9. Galan, U., Orta, P., Kurfess, T., Ahuett-Garza, H.: Surface defect identification and measurement for metal castings by vision system. Manuf. Lett. **15**, 5–8 (2018). https://doi.org/10.1016/j.mfglet.2017.12.001

10. Kowal, J., Sioma, A.: Surface defects detection using a 3D vision system. In: Proceedings of the 2012 13th International Carpathian Control Conference, ICCC 2012 (IEEE), pp. 382–387 (2012). https://doi.org/10.1109/CarpathianCC.2012.6228672

11. Lei, W., Shen, Y.: Design of machine vision applications in detection of defects in high-speed bar copper. In: Proceedings of the International Conference on E-Product E-Service and E-Entertainment (Henan), pp. 1–4 (2010)

12. Hanzaei, S.H., Afshar, A., Barazandeh, F.: Automatic detection and classification of the ceramic tiles' surface defects. Pattern Recogn. **66**, 174–189 (2017). https://doi.org/10.1016/j.patcog.2016.11.021

13. Nielsen, D.R., Pitchumani, R.: Control of flow in resin transfer molding with real-time preform permeability estimation. Polym. Compos. **23**, 1087–1110 (2002). https://doi.org/10.1002/pc.10504

14. Pastor-Lopez, I., Santos, I., Santamarıa-Ibirika, A., Salazar, M., De-la-Pena-Sordo, J.G., Bringas, P.: Machine-learning-based surface defect detection and categorisation in high-precision foundry. In: Proceedings of the 2012 7th IEEE Conference on Industrial Electronics and Applications, pp. 1359–64 (2012). https://doi.org/10.1109/ICIEA.2012.6360934

15. Pastor-Lopez, I., Santos, I., De-la-Pena-Sordo, J., Salazar, M., Santamarıa-Ibirika, A., Bringas, P.G.: Collective classification for the detection of surface defects in automotive castings. In: Proceedings of the IEEE 8th Conference on Industrial Electronics and Applications, pp. 941–946 (2013). https://doi.org/10.1109/ICIEA.2013.6566502

16. Pastor-Lopez, I., Santos, I., De-la-Pena-Sordo, J., Garcıa-Ferreira, I., Zabala, A.G., Bringas, P.G.: Enhanced image segmentation using quality threshold clustering for surface defect categorisation in high precision automotive castings. In: Herrero, Á., et al. (eds.) SOCO'13-CISIS'13-ICEUTE'13, pp. 191–200. Springer, Cham (2014). https://doi.org/10.1007/978-3-319-01854-6_20

17. Le, X., Mei, J., Zhang, H., Zhou, B., Xi, J.: A learning-based approach for surface defect detection using small image datasets. Neurocomputing **408**, 112–120 (2020). https://doi.org/10.1016/j.neucom.2019.09.107

18. Nguyen, T.P., Choi, S., Park, S.-J., Park, S.H., Yoon, J.: Inspecting method for defective casting products with convolutional neural network (CNN). Int. J. Precis. Eng. Manuf.-Green Technol. **8**(2), 583–594 (2020). https://doi.org/10.1007/s40684-020-00197-4

19. Jain, S., Seth, G., Paruthi, A., Soni, U., Kumar, G.: Synthetic data augmentation for surface defect detection and classification using deep learning. J. Intell. Manuf. **33**, 1–14 (2020). https://doi.org/10.1007/s10845-020-01710-x
20. Tsai, D.M., Fan, S.K.S., Chou, Y.H.: Auto-annotated deep segmentation for surface defect detection. IEEE Trans. Instr. Meas. **70**, 5011410 (2021). https://doi.org/10.1109/TIM.2021.3087826
21. Walkington, W.G.: Die Casting Defects - Causes and Solutions. Wheeling, North American die Casting Association (NADCA) (2007)

Cybersecurity Validation in the Online Gambling Industry

Dragan Peraković(✉) , Leon Cetinić, Ivan Cvitić , and Marko Periša

University of Zagreb, 4, Vukelićeva Street, 10000 Zagreb, Croatia
`dragan.perakovic@fpz.unizg.hr`

Abstract. With the development of information and communication technologies and their application in the field of the gambling industry, consequently, there is a development and expansion of the electronic form of this type of service, better known as online gambling, which can be observed as a part of Industry 4.0 concept. Significant progress in online gambling has been monitored during the COVID-19 pandemic and numerous lockdowns worldwide. In such conditions, this form of service is growing in popularity, accompanied by a sharp increase in users. This also increases the risk of numerous cyber-attacks, the successful implementation of which can cause several negative consequences for end-users and the service provider. One example of maintaining security is penetration testing, in which an expert is placed in the role of an attacker to find security vulnerabilities within the system. This research aims to establish a straightforward penetration testing process applicable in the online gaming environment. Periodic and high-quality defined penetration testing can timely detect cyber vulnerabilities, mitigate cyber threats and reduce cybersecurity risks.

Keywords: Penetration testing · Methodology · Attack vectors · Online gambling · Online betting · Smart city · Industrial growth

1 Introduction

Information security is essential in organizations' business because it offers confidentiality, availability, and integrity of data and systems necessary for safe and sustainable operation. With the development of technology, the number of cyberattacks on computer systems is increasing; to avoid unwanted events, it is necessary to protect the system with certain security aspects.

With the development of information and communication technologies and their application in gambling, the development and expansion of the electronic form of this type of service known as online gambling consequently occur. The digitalization of the online gambling industry (whose architecture is shown in Fig. 1) strongly contributes to the growth in innovations and offers of all forms of gambling, making it a part of a more comprehensive concept of Industry 4.0 [1]. Thus, in the past couple of years, the players have been attracted to online betting, live betting, online casinos, and online lottery games, either through the offer of such gambling games on personal computers

or smartphones. Significant progress in online gambling has been observed during the COVID-19 pandemic and numerous lockdowns worldwide. In such conditions, this service is growing in popularity, accompanied by a sharp increase in users. Figure 2 shows an increase in Gross Gambling Revenue for online gambling. Such conditions also influenced the increase in the complexity of the information communication systems in charge of providing this type of service [2].
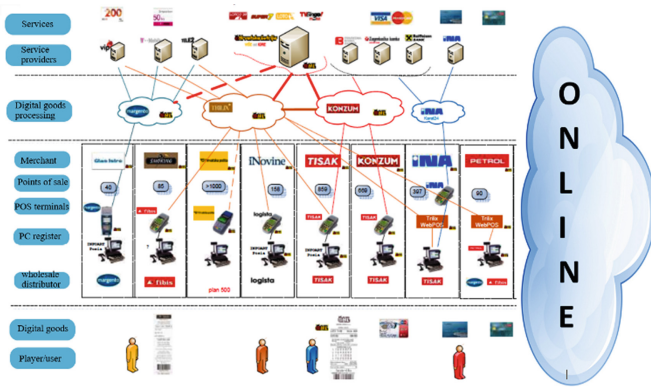
Fig. 1. Example of online gambling industry architecture.

This also increases the risk of numerous cyber-attacks, the successful implementation of which can cause several negative consequences for end-users and the service provider. One example of maintaining security is penetration testing, in which an expert is placed in the role of an attacker to find security vulnerabilities within the system.
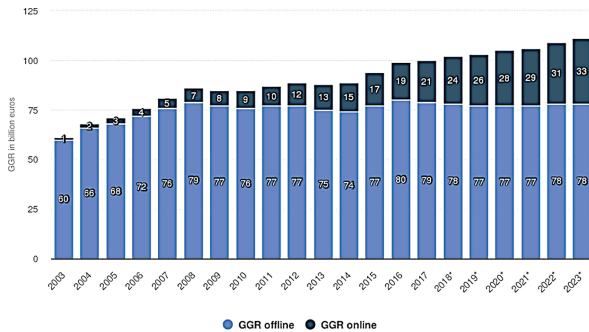
Fig. 2. Gross gambling revenue (GGR) online and offline in Europe from 2003 to 2023 [3].

In addition to existing knowledge, experience, tools, and methodology, the penetration tester tries to find system vulnerabilities such as unauthorized access to the system and data, disabling the system, or obtaining the privileges needed to control the system. After testing, the knowledge about individual vulnerabilities and possible harms to the

system is analyzed. The knowledge and information gathered are documented in the report as a review related to penetration testing. The report describes the stages of execution, the efficiency of the used tools, and the advantages and disadvantages of the test. Based on the conclusion reached in the document, the necessary action is determined to secure the system further and prevent the exploitation of identified vulnerabilities.

This research goal is to establish cybersecurity validation methodology applicable in the online gambling sector. Online gambling is a specific Industry 4.0 representative dealing with susceptible transactions and manipulating sensitive user information [4]. As such, it requires a well-defined methodology for assessing the efficiency of its currently implemented cybersecurity mechanisms.

2 Literature Review

The frequency of use and development of information and communication (IC) systems in the public and private sectors requires strategic approaches in protecting the privacy of users and organizations. Over the last 40 years, the need for remote communication and data transmission, and exchange has constantly increased. The advantages achieved by IC systems are developing new services, technologies, and various terminal devices such as IoT and Cloud Computing. Also, the amount of data generated by users and devices is increasing, and traffic content often contains confidential and sensitive information of private and business users. National programs define information security's organizational and managerial aspects at the national level to develop information security laws, regulations, methods, and procedures. Many devices and complex systems require a combination of different approaches to enable the safe operation of the system [5, 6].

The perimeter of performing penetration testing varies from client to client, as do the procedures, methods, and tools used in testing. There are different requirements that organizations may request from pentesters depending on their information and system security needs. The need for organizations to conduct penetration testing may be aimed at protecting the financial sector, protecting personal and critical data, preventing system protection, or enforcing protection against an already committed cyber-attack. Various companies, organizations, and entities have a great need to protect their information system. The demand for penetration testing is from public and financial sector organizations whose unauthorized access can create a significant financial deficit or threaten national security [7, 8]. Most organizations are not aware, sufficiently informed, or do not know the quality protection of actual complex communication structures and have little or almost no control over them [9]. Furthermore, the risks of organizations are increased by using applications or databases within their infrastructure. Such additional risks that are not sufficiently controlled can increase the number of security attacks that leave significant consequences for companies [10].

The growing advent of devices has enabled the creation of the Internet of Things (IoT) environment, contributing to the increase in security threats in the world. Suppose IoT environments are viewed from the perspective of an information and communication system. In that case, each element of this system can be described through the vulnerabilities, which creates an exceptional security threat to the environment. In a survey by US Business Insider, 39% of respondents indicated that security and privacy

are the main problems of the IoT environment. However, to respond to security threats, the IoTSF (Internet of Things Security Foundation) organization was established to promote knowledge and provide security methods to protect the IoT environment [5]. IoT devices are vulnerable to many cyber-attacks, and one of the attack vectors is phishing, which is used to try to access information within the IoT environment. One way to protect devices is using artificial intelligence [11], augmented reality [12, 13], blockchain structures [14], virtual reality [15], and the goal of defense is to protect IoT devices from unwanted messages by using certain functions [16].

2.1 The Need to Conduct Penetration Testing

The need to conduct penetration testing comes from the increasing number of attacks on organizations, most often to steal the financial resources of these organizations. An illustration of this can be seen in Fig. 3, which presents the value of the damage in millions of US dollars caused by cybercrime between 2001 and 2020. The graph refers to the area of the whole world and for those cyber attacks that have been reported. The data was collected by IC3 (Internet Crime Complaint Center), an organization responsible for accepting, developing, and filing criminal charges related to the occurrence of cybercrime.
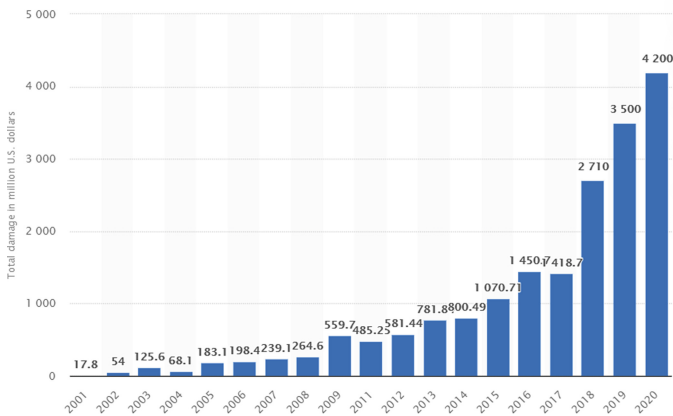
Fig. 3. Amount of monetary damage caused by cybercrime from 2001 to 2020.

The graph in Fig. 3 shows the exponential growth of financial losses due to cybercrime, and a similar exponential increase is expected in the coming years. Compared to 2020, when the total damage amounted to over 4 billion US dollars, in 2010, the total damage amounted was almost nine times less.

The United States has the most significant financial damage, accounting for 83.96% of all reported losses caused by cybercrime in 2014 [17]. Testing provides a proactive approach by investigating the real risks and the actual state of infrastructure safety even before the damage occurs. Examiners adapt their methodologies and tools to the type of testing, adapt to change, and determine the attack adapted to real environments. Based

on the test results, companies can make plans and estimates for further investment and progress of the organization.
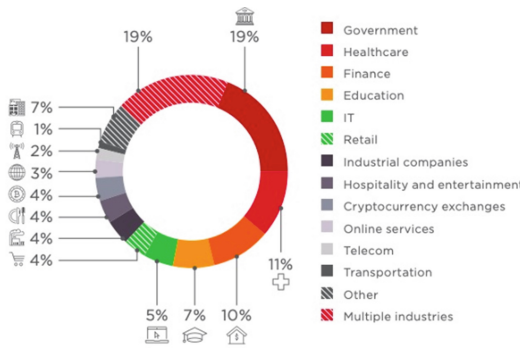
Fig. 4. Victim categories among organizations.

Figure 4 shows the frequency of cyber attacks on different organizations. Data from 2018 show that the riskiest are government organizations, which is 19% of cases are the target of attackers. Along with government organizations, 19% of attacks are suffered by multiple industries. The target of attacks on government organizations is mainly to obtain sensitive information without authorization, while in most other organizations, the most common causes of attacks are financial. Unauthorized attacks on cryptocurrencies are gaining momentum because it is easier to hide stolen cryptocurrencies from real money [18].

2.2 Classification of Information Systems Threats

The system's vulnerability is due to the weakness of specific subsystems used by potential attackers. Smaller organizations can plan on one or two threat classification criteria. For example, smaller organizations do not have complete internal system protection due to fewer employees. In comparison, larger organizations must identify all sources of threats to protect their system on the highest level. Classification allows an organization to identify threats that affect their assets to protect them in advance. The quality approach can enable the construction of security systems or help to create hybrid protection techniques by analyzing a combination of different classifications of threats [19].

The actors in implementing threats are people, natural disasters, and technological impacts. According to research published in Computer Crime: A Crimefighter's Handbook, the highest percentage of risk to organizations is caused by the human factor in the internal part of the network, which most often occurs due to insufficient attention and education of employees. To prevent this threat, it is necessary to introduce educational measures that reduce the likelihood of their mistakes [20]. Natural threats are caused by natural disasters such as earthquakes, floods, fires, winds, and storms, and threats such as wars and terrorist attacks. Technological threats are caused by a physical or chemical process over equipment and other system assets. Physical processes include using

physical means to enter restricted areas and the theft or damage of hardware or software [21]. Chemical threats are processes over hardware and software elements that result in a malfunction. This type of technological threat is most often caused by accidental but also incorrect management of employees of organizations.

3   Research Methodology

3.1   Stages of Penetration Testing Process

The practical part of the paper refers to the virtual environment with specific vulnerabilities that are exploited and presented in this paper. The penetration testing process is divided into 5 phases: Collecting information, network mapping, vulnerability identification, exploitation of vulnerabilities, and documentation.
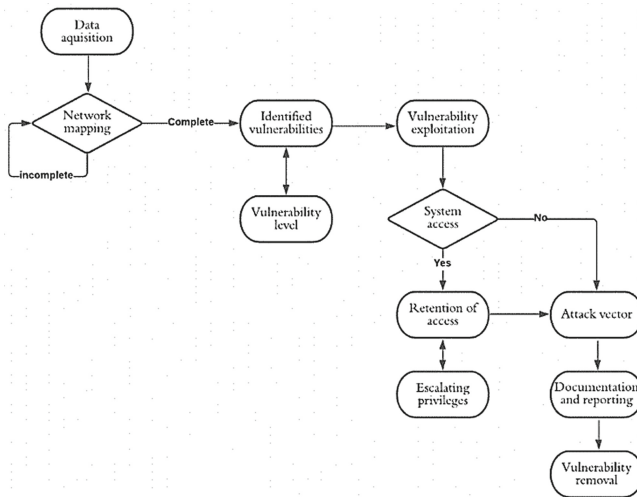
Fig. 5. Flow chart of penetration testing process.

Figure 5 shows a flow diagram describing the stages of the penetration testing process. The first step of penetration testing is to collect data crucial in further testing and complete the entire network mapping. Once a complete network mapping has been performed and all data has been collected, it is necessary to identify vulnerabilities and determine their threat levels. Furthermore, it is essential to exploit vulnerabilities that may access the system. It will be required to maintain access and, if possible, do privilege escalation to extend access to the entire system. If the vulnerability exploitation phase did not aim to access the system (example of a DoS attack), attack vectors are implemented automatically. The whole process needs to be documented and reported; after the reporting process, all vulnerabilities in the system must be eliminated.

3.2   Collecting Information

The implementation of the practical part begins with the phase of gathering information by accessing the website. The website displays daily newspapers with a brief description of the article. It is necessary to find as much information about the website as possible to comprehensive the vulnerability identification phase. The website uses the HTTP (HyperText Transfer Protocol) protocol, which means that the site is not encrypted and that it will be easier to carry out penetration testing attacks.
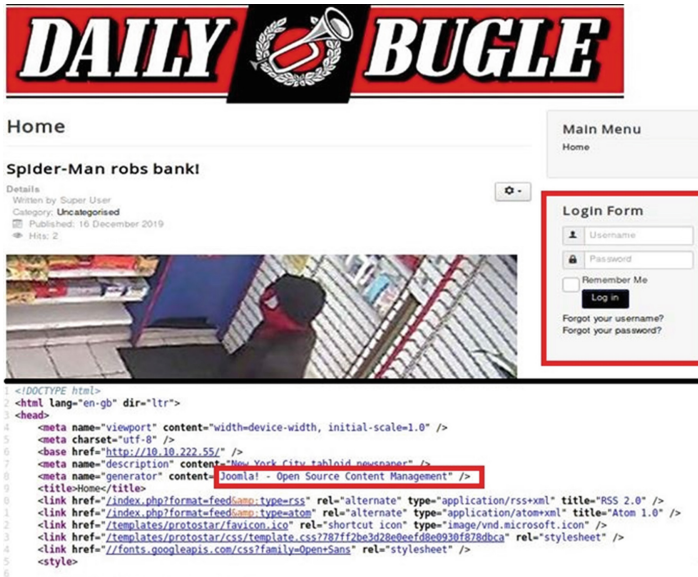
Fig. 6. The appearance of a vulnerable system website.

The possibility of logging in is visible on the website, which can be used to continue the work to gain access. Furthermore, it is necessary to find the type and version of the website with the need to analyze and find vulnerabilities. Using the View Page Source option, it is possible to access the page's source code, which often contains the critical data needed to collect information. Figure 6 shows the code in which the data was found that the website includes a Joomla open source web content management system. It is also possible to search the robots.txt directory, which, in addition to confirming that it is a Joomla system, also displays specific directories that will be analyzed.

4   Results

Every system is vulnerable and cannot be fully protected. However, this is not a reason not to set the strategies to the maximum level of security. Automated tools enabled data collection and mapping of the target system network and were used as attack vectors in the system penetration phase. The practical part of the work was successfully performed

and found vulnerabilities that allowed remote access to the system. Upon testing, examiners offer organizations a report and suggestions for resolving security vulnerabilities. The system vulnerability was caused by incorrect configuration and incomplete system updates. Various vulnerability solutions are provided through better firewall configuration, access control methods, the latest system versions, and protection against SQLi attacks using parameterized queries and input checking. Also, it is recommended to upgrade web applications with SSL (Secure Socket Layer) protocol and set it up to redirect traffic to a secure HTTPS protocol automatically.

4.1 Network Mapping and Vulnerability Identification

The results of using the Nmap tool for scanning the entire system range are presented in Fig. 7. The following tools that gather new information about the system are Dir-Buster. The results collected by the DirBuster tool show several directories on the server that need to be explored. By searching one of the directories, more precisely the directory/administrator, we accessed the website for logging in with administrator privileges.


```
root@kali:~# nmap 10.10.65.247 -sV
Starting Nmap 7.80 ( https://nmap.org ) at 2021-08-27 10:28 CDT
Nmap scan report for 10.10.65.247
Host is up (0.053s latency).
Not shown: 997 closed ports
PORT     STATE SERVICE VERSION
22/tcp   open  ssh     OpenSSH 7.4 (protocol 2.0)
80/tcp   open  http    Apache httpd 2.4.6 ((CentOS) PHP/5.6.40)
3306/tcp open  mysql   MariaDB (unauthorized)

Service detection performed. Please report any incorrect results at https://nmap.org/submit/ .
Nmap done: 1 IP address (1 host up) scanned in 8.29 seconds
root@kali:~# _
```

Fig. 7. Results of the map tool.

Individual vulnerabilities were found using searchsploit Joomla 3.7.0 and searchsploit OpenSSH 7.4. The result shows how Joomla version 3.7.0 is vulnerable to SQL Injection attacks and Cross-Site Scripting. By retrieving the document (PHP/web apps/42033.txt) for additional explanation of SQL, vulnerability suggested attack using SQLmap tool.

4.2 Exploitation of Vulnerabilities

The primary and most demanding phase of penetration testing is the exploitation of vulnerabilities. The first attempt to exploit the vulnerability is performed using the SQLmap tool to conduct SQL injection attacks over the Joomla 3.7.0 version, as seen in Fig. 8. After exploiting the SQLi attack, five databases were found, and after analyzing each of them, it was determined that the Joomla database is vulnerable. The information granted to access the website administrator is a username: jonah and a hash password that needs to be cracked by finding the appropriate format. After seeing the form, it is necessary to break the hash record with the help of the John The Ripper tool.

Fig. 8. Results of SQLmap tool.

After collecting credentials for access to the website administrator, it is necessary to set up and run a reverse shell to gain remote access to the system. After joining the system, it is essential to gain privilege escalation, which is achieved using a lines script that finds the necessary credentials to access greater authority. After accessing a higher-level user, it is required to run the sudo -l command, which shows commands run as root. Taking advantage of the wrong configuration and running the code makes it possible to achieve root privileges, which completes the practical part of the work.

5   Conclusions

The number of cyberattacks is increasing every day, and the development of new threats to the system, so protecting the information system becomes imperative for all organizations. In addition to computer and network systems, the targets of cyber attacks are people and new types of technologies, such as IoT devices. The growing presence of new devices requires new protection mechanisms, and one example is the use of artificial intelligence in system protection. It is necessary to emphasize the importance of security and present specific protection mechanisms to secure their property significantly to individuals and organizations. The statistics in this paper show that the most influential interest groups of cyber-attacks are organizations of great importance, such as online gambling as part of the Industry 4.0 concept. Therefore, preventive protection of the system using a safety mechanism such as penetration testing is required. Penetration tests require certified professionals to use their knowledge to simulate an attack to protect the information system. The development of new technologies and new threats creates the need for constant improvement of examiners' knowledge to protect the system as much as possible. The penetration testing methodology aims to give the examiner insight into the steps and procedures when performing testing. Standardization and legal aspects are not fully regulated, and this problem is sought to be solved using a standardized methodology. The positive side of standardization is that recently great importance has been given to choosing the correct methodology with quality tools and methods to provide quantitative and comprehensive information system protection.

References

1. Šimović, H., Bajo, A., Davidović, M., Jelavić, F.: Gambling market in Croatia: financial performance and fiscal effect. Fiscus **4**(9), 1–32 (2019). https://doi.org/10.3326/efiscus.2019.9
2. EGBA. European Online Gambling Key Figures 2020. Brussels, Belgium (2020)
3. Eggeling, H.: Company presentation. In: 57th Annual AGIFORS Symposium (2017)
4. Varela, L., Putnik, G.D., Manupati, V., Rajyalakshmi, G., Trojanowska, J., Machado, J.: Collaborative manufacturing based on cloud, and on other I4.0 oriented principles and technologies: a systematic literature review and reflections. Manag. Prod. Eng. Rev. **9**(3), 90–99 (2018). https://doi.org/10.24425/119538
5. Geer, D., Harthorne, J.: Penetration testing: a duet. In: Annual Computer Security Applications Conference, vol. 18, no. 1, pp. 185–195 (2002)
6. Hertzog, R,. O'Gorman, J., Aharoni, M.: Kali Linux Revealed: Mastering the Penetration Testing Distribution. Offsec Press (2017)
7. Božić, K., Penevski, N., Adamović, S.: Penetration testing and vulnerability assessment: introduction, phases, tools and methods. In: Proceedings of the International Scientific Conference - Sinteza 2019, pp. 229–234. Singidunum University, Novi Sad (2019)
8. Abu-Dabaseh, F., Alshammari, E.: Automated penetration testing: an overview. In: Nagamalai, D., et al. (eds.) NATL, CSEA, DMDBS, Fuzzy, ITCON, NSEC, COMIT – 2018. Computer Science & Information Technology, pp. 121–129. Academy & Industry Research Collaboration Center (AIRCC) (2018). https://doi.org/10.5121/csit.2018.80610
9. Weidman, G.: Penetration Testing: A Hands-On Introduction to Hacking. 1st edn. No Starch Press (2014)
10. Creasey, J.: A guide for running an effective penetration testing programme. Crest (2017). https://www.crest-approved.org/wp-content/uploads/CREST-Penetration-Testing-Guide.pdf. Accessed 24 Sept 2021
11. Pavlenko, I., Trojanowska, J., Ivanov, V., Liaposhchenko, O.: Scientific and methodological approach for the identification of mathematical models of mechanical systems by using artificial neural networks. In: Machado, J., Soares, F., Veiga, G. (eds.) HELIX 2018. LNEE, vol. 505, pp. 299–306. Springer, Cham (2019). https://doi.org/10.1007/978-3-319-91334-6_41
12. Ivanov, V., Pavlenko, I., Liaposhchenko, O., Gusak, O., Pavlenko, V.: Determination of contact points between workpiece and fixture elements as a tool for augmented reality in fixture design. Wirel. Netw. **27**(3), 1657–1664 (2019). https://doi.org/10.1007/s11276-019-02026-2
13. Ivanov, V., Pavlenko, I., Trojanowska, J., Zuban, Y., Samokhvalov, D., Bun, P.: Using the augmented reality for training engineering students. In: 4th International Conference of the Virtual and Augmented Reality in Education, VARE 2018, pp. 57–64 (2018)
14. Chernobrovchenko, V.S., Dyadyura, K.O., Panda, A.: Investigation of the blockchain structure for hydroxyapatite-based scaffolds. J. Eng. Sci. **8**(2), C30–C35 (2021). https://doi.org/10.21272/jes.2021.8(2).c5
15. Bun, P., Trojanowska, J., Ivanov, V., Pavlenko, I.: The use of virtual reality training application to increase the effectiveness of workshops in the field of lean manufacturing. In: 4th International Conference of the Virtual and Augmented Reality in Education, VARE 2018, pp. 65–71 (2018)
16. Peraković, D., Cvitić, I., Kuljanić, T., Brletić, L.: Analysis of wireless routers vulnerabilities applied in the contemporary networks. In: Mokrys, M, Badura, S., Peraković, D. (eds.) Proceedings of the 6th International Virtual Research Conference in Technical Disciplines (RCITD-2018), pp. 31–37. Publishing Society, Zilina (2018). https://doi.org/10.18638/rcitd.2018.6.1.123

17. Gupta, B.B., Tewari, A., Cvitić, I., Peraković, D., Chang, X.: Artificial intelligence empowered emails classifier for Internet of Things based systems in industry 4.0. Wirel. Netw. **28**(1), 493–503 (2021). https://doi.org/10.1007/s11276-021-02619-w
18. Statista. https://www.statista.com/statistics/267132/total-damage-caused-by-by-cyber-crime-in-the-us/. Accessed 19 July 2021
19. Ptsecurity. https://www.ptsecurity.com/ww-en/analytics/cybersecurity-threatscape-2018/. Accessed 22 Aug 2021
20. Geric, S., Hutinski, Z.: Information system security threats classifications. J. Inf. Organ. Sci. **31**, 51 (2007)
21. Icove, D., Seger, K., VonStroch, W.: Computer Crime: A Crimefighter's Handbook. O'Reilly Media, Newton (1995)

8D Methodology for Solving Problems in the Production of PVC Pipes

Marta Popowska, Natalia Marzec, and Justyna Trojanowska[(✉)]

Poznan University of Technology, 3, Piotrowo St., 60-965 Poznan, Poland
justyna.trojanowska@put.poznan.pl

Abstract. The paper aims to apply the 8D methodology in problem-solving in the production process. The research project has been carried out at a manufacturing site of PVC pipes. The authors propose a methodology that eliminates deviations from the company's work standards and helps achieve a new target state. The 8D methodology, extended by additional steps, was proposed to find effective solutions based on the lean management concept. Extension of the 8D methodology with additional steps has facilitated the building of a team with key competencies necessary for solving the identified problem, clear definition of goals, and analysis of the sequence in which the proposed solutions have been implemented, to ensure that the return on investment is achieved within the shortest possible time. The implemented solutions improve the pipe extrusion process by reducing the amount of generated waste by 12.6% and shortening the extrusion head gap adjustment process during the start-up of the manufacturing line by 16.5%.

Keywords: 8D methodology · Problem solving · Production process · Process innovation

1 Introduction

The key objective of manufacturing companies nowadays is making a profit by satisfying the needs of consumers. Enterprises face the challenge of continuous development, enabling quick adaptation to market changes, which is the key to success. Development entails continuous problem-solving. Following the Lean Transformation Framework (LTF), problem-solving is an integral part of a lean organization [1], while skillful problem solving is indispensable for the achievement of strategic goals [2]. The efficiency of implemented solutions depends on identifying types of problems and finding the right tools to solve them. The literature offers various structured problem-solving methodologies, such as, e.g., the A3 methodology [3], the 8D methodology [4], or the Kepner-Tregoe method [5]. According to Smalley [3] and Denysenko [6], the problem-solving process comprises the following stages: define the problem, set a goal, analyze the root cause, apply remedies, control, set standards and follow up actions. At each stage, different tools are applied, such as an Ishikawa diagram, a process map, a Pareto diagram, or a priority matrix. Skillful implementation of these methods boosts the effectiveness of the developed solutions.

2   Literature Review

One of the underlying assumptions of lean management is the strive for continuous improvement [7] and eliminating waste [8]. Most problem-solving methodologies are founded on the Deming cycle (plan-do-check-act, PDCA). This four-stage process, also called the Deming wheel [9], comprises planning the product, manufacturing, selling and testing, and market research [10].

A methodology applied to solve a particular problem must be adjusted to the type of irregularity [11]. A selection of problem-solving methods enables enterprises to evolve a proper reaction [12]. The 8D is one of the methodologies supporting efficient root cause analysis (RCA) performance according to a defined and structured pattern. The 8D methodology has a structure defined in eight steps (Fig. 1).
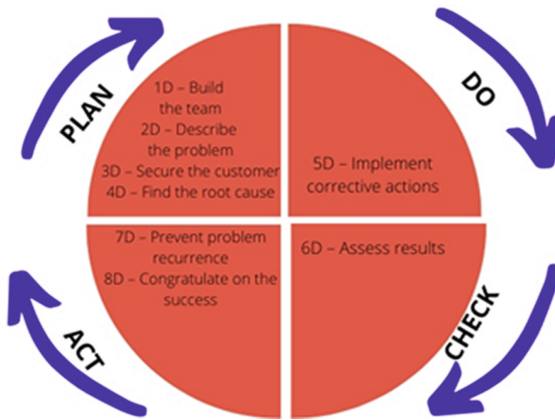
Fig. 1. Stages of the 8D methodology in sequential order following the PDCA cycle.

Problem-solving methodologies comprise a structured path to be followed by the team searching for solutions.

3   Research Methodology

3.1   Production Processes

The research project has been carried out at a manufacturing site of PVC pipes, comprising two manufacturing lines for home sewage systems, five manufacturing lines for outdoor sewage lines, and two manufacturing lines for rainwater drainage systems. All pipes are extruded from PVC compounds. Extrusion is a continuous process consisting of the plasticization of PVC compounds and forming the shape through the nozzle of an extrusion head. A diagram of an extrusion line for home sewage system pipes is shown in Fig. 2.
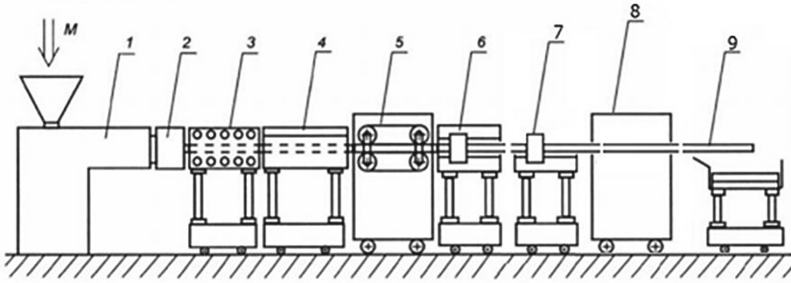
Fig. 2. Extrusion line: M – PVC compound, 1 – extruder, 2 – extrusion head, 3 – calibrator, 4 – vacuum bath, 5 – extractor, 6 – saw, 7 – inkjet printer, 8 – flare tool, 9 – extruded pipe. Source: company source.

3.2   Research Problem

The company was examined for wastage. For this purpose, a timekeeping system was introduced at all workstations to establish the working time necessary to perform specific actions in certain conditions. A problem with adjusting the pipe diameter during the start-up of the home sewage pipe extrusion line was identified. Pipe diameters outside the tolerances generated large quantities of waste and protracted the start-up of the extrusion line. It was noted that improvement of the diameter adjustment could contribute to achieving a new target state of the extrusion process.

To validate the significance of the problem, the quantity of waste generated on the line under analysis was analyzed. A graph covering 8 months was drawn based on the data retried from the ERP SAP (Fig. 3). Another reason causing 14.9% of waste was the wrong thickness of the pipe wall.

3.3   Proposed Solution

The 8D methodology, extended by additional steps, was proposed to find effective solutions based on the lean management concept. The flowchart in Fig. 4 shows the procedure. The original steps of the methodology are marked in blue, the added steps – in yellow.

The original 8D methodology has been extended by step zero. In this step, even before the team is built, the irregularity is identified and matched with a certain type of problem. Step 6 added comprises the development of possible solutions.

Considering the probability that each of the causes can affect the problem independently of other causes, a solution for each cause must be developed. In step 7, the sequence of implementation of solutions is determined. Step 8 comprises additional elaboration of a plan to implement each of the solutions.
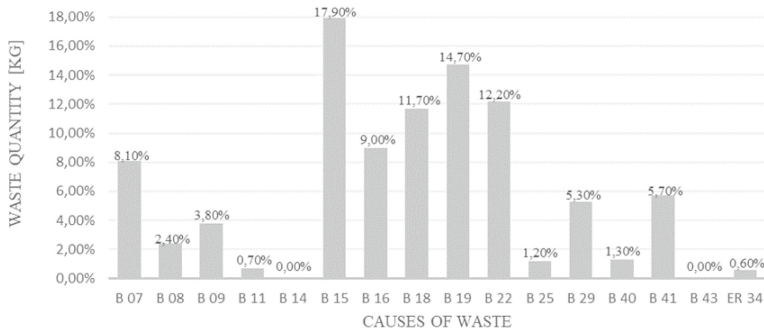
Legend: B07 – Cleaning of the saw; B08 – The saw getting stuck; B09 – Bad quality of cutting/bevelling; B11 – External deformation; B14 – Scorch; B15 – Scheduled start-up; B16 – Scratches; B18 – Downtime; B19 – Wrong thickness of the pipe wall; B22 – Wrong shape of the flare; B25 – Failure of the flare tool; B29 – Breakage of the pipe; B40 – Study samples; B41 – Cleaning the vacuum; B43 – Start-up after a breakdown; ER34 – Failure of the extractor.

Fig. 3. Waste, by cause, for January–July 2020. Source: company data.
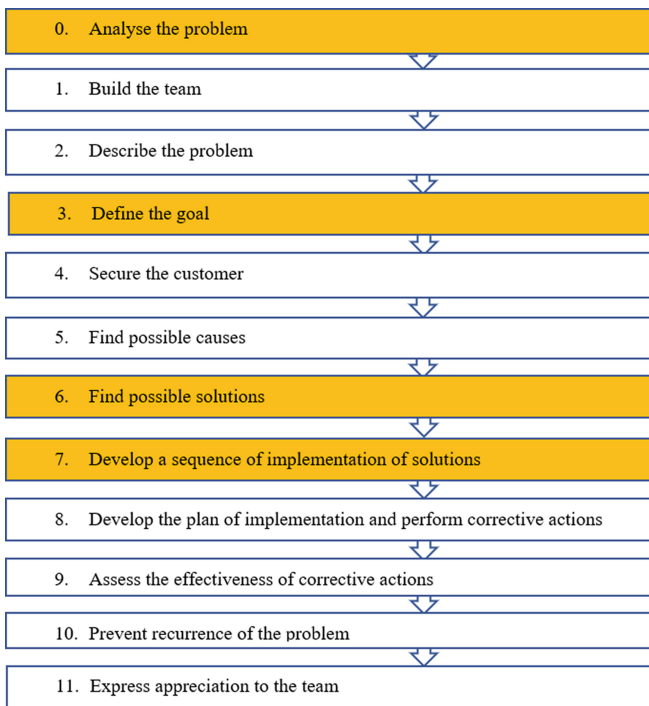
Fig. 4. Methodology flowchart. Source: own elaboration.

4 Results

Data retrieved from the ERP SAP was analyzed to validate the significance of the problem. The analysis included verifying the frequency with which the wrong thickness of the wall pipe occurred. The results show that the problem occurred each month from January to August 2020 (Fig. 5).
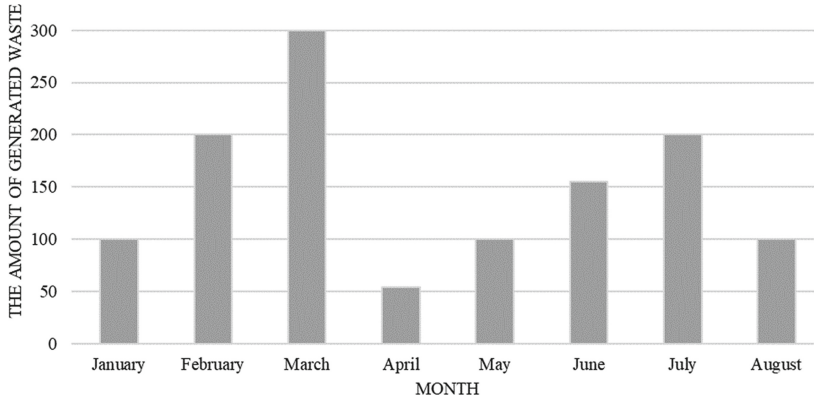
Fig. 5. Quantity of waste generated by wrong pipe wall thickness for eight months. Source: company data.

1. *Build the team.*
   Implementation of the 8D methodology was initiated with building the team. As a result of an analysis of the tasks to be performed by the team members, a team of ten was appointed.
2. *Describe the problem.*
   Information was gathered on-site (gemba) during observation of the tools and machines used (genbutsu) and in an analysis of the actions taken in the process (genjitsu).
3. *Define the goal.*
   A team meeting was held to:

   - Brief the team members on the problem and present (visualize) the gathered data and facts,
   - Develop the goal to be achieved,
   - Discuss the 8D process structure,
   - Schedule the follow-up meetings.

   The goal was scheduled to be achieved within 3 months. The goal was unambiguous, measurable, feasible, important for all the team members, and defined in time.

4. *Secure the customer.*

   The problem occurring on line 110 did not directly negatively impact the customer. Pipe diameter irregularities would be discovered in the verification performed before the manufacturing process was completed. Improvement of standards and process conditions would stimulate the internal development of the enterprise.

5. *Find possible causes.*

   All possible causes of the problem were examined logically using a cause-and-effect diagram. Publications describing similar technical problems in areas of quality of castings indicators [13], topological optimization [14], operational reliability [15], the efficiency of the manufacturing process [16], fixture design [17, 18], and machine tools [19] were analyzed before the meeting. The Ishikawa diagram in Fig. 6 shows the possible causes of the problem.
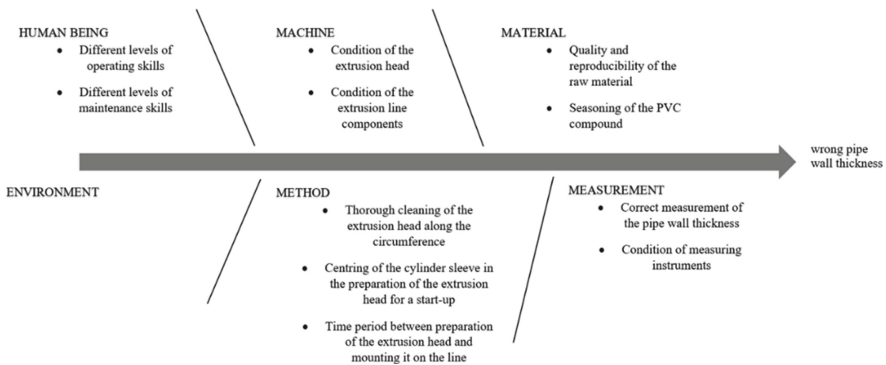
Fig. 6. Ishikawa diagram. Source: own elaboration.

6. *Find possible solutions.*

   A team meeting was held to find possible solutions. Ideas for the solutions were generated in a brainstorming session. All the solutions are listed in Table 1.

7. *Develop a sequence of implementation of solutions.*

   A priority matrix was used to determine a sequence of implementation of the solutions. All solutions were analyzed for the forecast results and feasibility of implementation. The solutions were marked with numbers, as shown in Table 1. They are presented in Fig. 7.

Table 1. Generated solutions. Type of solution: A – administrative, P – preventive.

Category	No	Cause	Solution	Type of solution
Human being	1	Different levels of operating skills	Sharing of knowledge and skills among operators	A

(*continued*)

Table 1. (*continued*)

Category	No	Cause	Solution	Type of solution
	2	Different levels of maintenance skills	Sharing of knowledge and skills among maintenance personnel	A
Machine	3	Condition of the extrusion head	Establishment of a schedule of technical inspections	A
	4	Condition of the extrusion line components	Additional inspection of thermal control components, cleaning of hoppers and dosing systems, inspections of the gas injection installation, checking the plastifying system for wear	A
Material	5	Quality and reproducibility of the raw material	Analysis of the results of raw material examination and comparison with the results gathered in the manufacturing process	A
Method	6	Seasoning of the PVC compound	Verification of compliance with the compound seasoning procedure	A
	7	Thorough cleaning of the extrusion head along the circumference	Verification of the extrusion head cleaning process	A
	8a	Centering of the cylinder sleeve in the preparation of the extrusion head for a start-up	Use of a caliper for adjusting the extrusion head gap	P
	8b		Setting the gap using a brass gap gauge	P
	9	The time period between preparation of the extrusion head and mounting it on the line	Verification of compliance with the standard of preparing the extrusion head 2–3 days before a start-up	A
Measurement	10	Correct measurement of the pipe wall thickness	Verification of the measurement method applied by all operators	A
	11	Condition of measuring instruments	Checking the verification of the measuring instrument	A
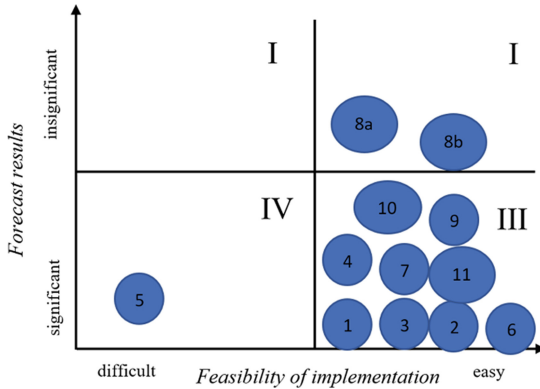
Fig. 7. Stages of the 8D methodology in sequential order under the PDCA cycle.

Solution no. 7 was selected to be implemented first. A Gantt chart was created, including deadlines and persons responsible for completing particular actions (Fig. 8).

Fig. 8. Gantt chart. Source: own elaboration.

8. *Develop the plan of implementation and perform corrective actions.*
   The solution selected to be implemented first is a low-cost tool called the caliper. An implementation plan was created, comprising the following stages:

- Design of the tool
- Manufacturing of the tool
- Testing
- Use of the tool for adjustment of the extrusion head gap
- Registration of the time spent on adjusting the suitable pipe wall thickness/pipe diameter
- Analysis of the generated waste
- Meeting to debrief the testing phase

- Introduction of a standard for the caliper use
- Training the employees
- Dissemination of the solution to other manufacturing lines.

9. *Assess the effectiveness of corrective actions.*

   To ensure the proper course of the testing phase, all manufacturing equipment maintenance personnel were trained in using the caliper. To validate the efficacy of the implemented solution, data on waste was generated after the implementation was analyzed. Based on the data retrieved from the ERP SAP, waste generated due to the wrong thickness of the pipe wall accounted for 2.1% of all irregularities. Implementation of the tool reduced the number of irregularities and the time required for adjustment of the head gap. The results are shown in Table 2 and Fig. 9.

Table 2. Results. Source: own elaboration.

Parameter	Measurement before implementation of the solution [%]	Target [%]	Result [%]
Waste caused by a wrong thickness of the pipe wall	14.7	<3	2.1
Time spent on adjusting the head gap relative to the total start-up time	24	<10	7.5
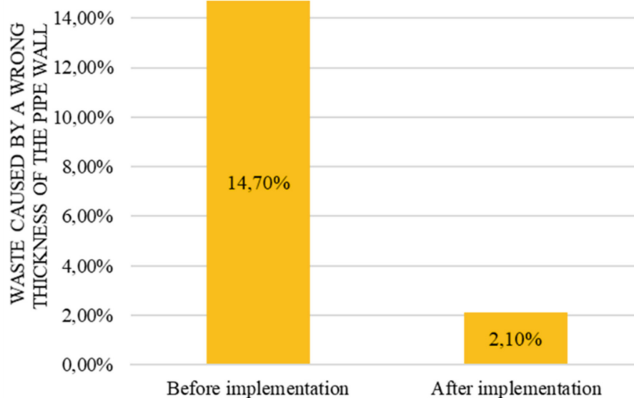
Fig. 9. Waste caused by a wrong thickness of the pipe wall before and after implementation of the solution. Source: Own elaboration.

10. *Prevent recurrence of the problem.*

     For the new rules to be abided by, standard use of the new tool was drawn up and put up in a visible place in the extrusion head warehouse. Effects of the implementation were monitored for the following six months. At the end of each month, the Pipe Manufacturing Coordinator analyzed the quantity of waste generated on the extrusion lines for home sewage system pipes. The time spent adjusting the head gap during each start-up of the line was registered by the Lean CI Engineer once a month.

11. *Express appreciation to the team.*

     A team meeting was held to complete the process where the results obtained were presented, and the team members were congratulated on their success. Conclusions were drawn from the process, and the usefulness of implementation of the 8D methodology was acknowledged.

5 Conclusions

As a result of the implementation of the solutions, waste generated in the extrusion of pipes for home sewage systems caused by a wrong thickness of the pipe wall has been reduced by 12.6%, and the duration of the process of adjustment of the extrusion head gap during the start-up of the line has been shortened by 16.5%. The problem has been eliminated by implementing an original methodology based on the classic 8D methodology. The results demonstrate that the goal set has been achieved, and the solution has been implemented in other pipe extrusion processes for home sewage systems. Extension of the 8D methodology with additional steps has facilitated the building of a team with key competencies necessary for solving the identified problem, clear definition of goals, and analysis of the sequence in which the proposed solutions have been implemented, to ensure that the return on investment is achieved within the shortest possible time.

References

1. Kuusela, R., Koivuluoma, M.: Lean transformation framework for software intensive companies: responding to challenges created by the cloud. In: 37th EUROMICRO Conference on Software Engineering and Advanced Applications, pp. 378–382 (2011). https://doi.org/10.1109/SEAA.2011.74
2. Ivanov, V., Liaposhchenko, O., Denysenko, Y., Pavlenko, I.: Ensuring economic efficiency of flexible fixtures in multiproduct manufacturing. Eng. Manag. Prod. Serv. **13**(1), 53–62 (2021)
3. Smalley, A.: Four types of problems, Lean Enterprise Institute (2018)
4. Starzynska, B., Szajkowska, K., Diering, M., Rocha, A., Reis, L.P.: A study of raters agreement in quality inspection with the participation of hearing disabled employees. In: Hamrol, A., Ciszak, O., Legutko, S., Jurczyk, M. (eds.) Advances in Manufacturing. LNME, pp. 881–888. Springer, Cham (2018). https://doi.org/10.1007/978-3-319-68619-6_85
5. Govindarajan, V.: A contingency approach to strategy implementation at the business-unit level: integrating administrative mechanisms with strategy. Acad. Manag. J. **31**(4), 828–853 (1988)

6. Denysenko, Y., Kysylevska, A., Panchenko, O., Zaloga, V., Dynnyk, O.: Decision-making based on prediction of oil quality indicators in the enterprise's information system. In: Tonkonogyi, V., et al. (eds.) InterPartner 2019. LNME, pp. 25–31. Springer, Cham (2020). https://doi.org/10.1007/978-3-030-40724-7_3

7. Liker, J.K., Meier, D.: The Toyota Way Fieldbook: A Practical Guide for Implementing Toyota's 4Ps. McGraw-Hill (2004)

8. Kaščak, J., et al.: Design of an atypical construction of equipment for additive manufacturing with a conceptual solution of a printhead intended for the use of recycled plastic materials. Appl. Sci. **11**, 2928 (2021)

9. Dynnyk, O., Denysenko, Y., Zaloga, V., Ivchenko, O., Yashyna, T.: Information support for the quality management system assessment of engineering enterprises. In: Ivanov, V., et al. (eds.) DSMIE 2019. LNME, pp. 65–74. Springer, Cham (2020). https://doi.org/10.1007/978-3-030-22365-6_7

10. Szczepaniak, M., Trojanowska, J.: Methodology of manufacturing process analysis. In: Hamrol, A., Kujawińska, A., Barraza, M.F.S. (eds.) MANUFACTURING 2019. LNME, pp. 281–294. Springer, Cham (2019). https://doi.org/10.1007/978-3-030-18789-7_24

11. Denysenko, Y., Dynnyk, O., Yashyna, T., Malovana, N., Zaloga, V.: Implementation of CALS-technologies in quality management of product life cycle processes. In: Ivanov, V., et al. (eds.) DSMIE 2018. LNME, pp. 3–12. Springer, Cham (2019). https://doi.org/10.1007/978-3-319-93587-4_1

12. Kujawinska, A., Vogt, K., Diering, M., Rogalewicz, M., Waigaonkar, S.D.: Organization of visual inspection and its impact on the effectiveness of inspection. In: Hamrol, A., Ciszak, O., Legutko, S., Jurczyk, M. (eds.) Advances in Manufacturing. LNME, pp. 899–909. Springer, Cham (2018). https://doi.org/10.1007/978-3-319-68619-6_87

13. Gašpár, Š, et al.: Influence of gating system parameters of die-cast molds on properties of Al-Si castings. Materials **14**, 3755 (2021). https://doi.org/10.3390/ma14133755

14. Kaščak, J., Gašpár, Š, Paško, J., Husár, J., Knapčíková, L.: Polylactic acid and its cellulose based composite as a significant tool for the production of optimized models modified for additive manufacturing. Sustainability **13**, 1256 (2021). https://doi.org/10.3390/su13031256

15. Trojanowski, P., Trojanowska, J.: Reliability of road transport means as a factor affecting the risk of failure – the transport problem case study. In: Ivanov, V., Trojanowska, J., Pavlenko, I., Zajac, J., Peraković, D. (eds.) DSMIE 2021. LNME, pp. 253–261. Springer, Cham (2021). https://doi.org/10.1007/978-3-030-77719-7_26

16. Kujawińska, A., Diering, M.: The impact of the organization of the visual inspection process on its effectiveness. Int. J. Adv. Manuf. Technol. **112**(5–6), 1295–1306 (2021). https://doi.org/10.1007/s00170-020-06543-9

17. Ivanov, V., Dehtiarov, I., Pavlenko, I., Kosov, M., Hatala, M.: Technological assurance and features of fork-type parts machining. In: Ivanov, V., et al. (eds.) DSMIE 2019. LNME, pp. 114–125. Springer, Cham (2020). https://doi.org/10.1007/978-3-030-22365-6_12

18. Ivanov, V., Pavlenko, I., Kuric, I., Kosov, M.: Mathematical modeling and numerical simulation of fixtures for fork-type parts manufacturing. In: Knapčíková, L., Balog, M. (eds.) Industry 4.0: Trends in Management of Intelligent Manufacturing Systems. EICC, pp. 133–142. Springer, Cham (2019). https://doi.org/10.1007/978-3-030-14011-3_12

19. Shvets, S.V., Machado, J.: Numerical model of cutting tool blade wear. J. Eng. Sci. **8**(2), A1–A5 (2021). https://doi.org/10.21272/jes.2021.8(2).a1

Towards Sustainable Manufacturing: A Case Study for Sustainable Packaging Redesign

Erwin Rauch[1]([✉]) , Matthias Rofner[1] , Cristian Cappellini[1] ,
and Dominik T. Matt[1,2]

[1] Free University of Bolzano, Universitätsplatz 1, 39100 Bolzano, Italy
erwin.rauch@unibz.it

[2] Innovation Engineering Center (IEC), Fraunhofer Italia Research s.c.a.r.l., Via A. Volta 13b,
39100 Bolzano, Italy

Abstract. In the past decades, research was predominantly conducted to increase the operational efficiency and productivity of production processes. Currently, from a global perspective, a profound change in values in society is discernible. Starting from purely economic objectives of the last years, preserving the environment and a human-oriented design of socio-technical systems such as factories are becoming more and more important. In the future, this change emanating from society will also represent a major challenge for manufacturing companies to design processes and systems more sustainably. The organization's objectives are changing so that manufacturing should be more resource-efficient, generate less or no waste, and allow a safe, ergonomic, and ethically correct work environment for employees. In this article, the authors show an example of the future symbiosis between economic, ecological, and social sustainability using the example of a case study from a real SME manufacturer. This case study aims to identify more sustainable alternatives for polystyrene-based packaging and thus contribute to more sustainable manufacturing.

Keywords: Sustainability · Sustainable manufacturing · Dual transformation · Case study · Industry 4.0

1 Introduction

In the past ten years, a great deal of attention has been paid to digital transformation. Since the introduction of the Fourth Industrial Revolution (also Industry 4.0) in 2011 [1], research and practice have sought to apply digital technologies to manufacturing increasingly and thereby make production more efficient [2]. Industry 4.0 should help high-wage countries like Germany keep value creation in their own country and prevent outsourcing manufacturing to low-cost countries. In addition to this Digital Transformation, Sustainable Transformation will also be a challenge in the future, which is why the authors can also speak of a Dual Transformation (digital and sustainable).

In the last decade, in addition to purely economic goals, social aspects were also taken into account, since the aim was to put people at the center of Industry 4.0 [1] and

to develop concepts and technologies that make work easier, more ergonomic, and more attractive [3]. Despite all efforts in this direction, the use of digital technologies also brings many challenges to minimize negative impacts on people and their environment and reap the benefits of digitalization. This concerns, for example, the development of trustworthy AI systems [4] that promote social interaction and participation of employees instead of turning employees into pure command takers by intelligent AI systems and not using their cognitive abilities in a meaningful way. Furthermore, there is still much space for development in consideration of human values [5] for the design of manufacturing systems and processes, aiming in particular to increase inclusivity [6] and a human-centric production [3, 7].

Environmental sustainability has usually played an insufficient role as an objective of corporate decision-making. In addition to the fact that ecologically challenging processes were often outsourced to other countries to get rid of the problem, many efforts to achieve more sustainable supply chains often served for greenwashing, i.e., to create the image of a "green company" without seriously pursuing environmental objectives and activities [8]. As the problems surrounding climate change increase and the public becomes more aware of this issue, industrial companies are also under pressure to become more active in this direction and contribute to more sustainable manufacturing. On a global societal level, the United Nations (UN) presented the Sustainable Development Goals (SDG) that are a universal call to action to end poverty, protect the planet and improve the lives and prospects of everyone, everywhere. All UN Member States adopted the 17 SDGs in 2015 as part of the 2030 Agenda for Sustainable Development which set out a 15-year plan to achieve those goals [9].

Similarly, the World Manufacturing Forum 2021 also focused on sustainability discussing digital technologies as a key enabler for circularity and exploring their crucial role to achieve environmental sustainability [10]. According to the report, the circular economy relies on several strategies that extend the product life cycle through reusing, recycling, remanufacturing, and redesigning circular products and materials to reduce waste. The Report identified key drivers to the circular economy for achieving the SDGs defined by the UN. Enablers at the consumer level include environmental awareness, increasing trust and transparency in relation to service providers, convenience and accessibility of sustainable products, and digital literacy. At the company level, enablers include demand for sustainable products, digital technologies, and circular skills. At the value chain level, there is a need to improve data sharing, enhance infrastructure and networks, and standardize requirements [10].

In Europe, the European Commission (EC) defined with the European Green Deal a strategy to transform the EU into a modern, resource-efficient, and competitive economy, ensuring: (i) no net emissions of greenhouse gases by 2050, (ii) economic growth decoupled from resource use and (iii) no person and no place left behind. This new industrial strategy for Europe will lead the twin green and digital transitions and make Europe even more competitive globally [11].

2 Literature Review

According to the UN Brundtland Commission [12], sustainable development can be defined as 'development that meets the needs of the present without compromising

the ability of future generations to meet their own needs'. The manufacturing sector is important for the sustainable development of the global society since it helps address global challenges such as needs for renewable energy sources, green buildings, etc. [13]. The term Sustainable Manufacturing is defined by the United States Environmental Protection Agency (EPA) as 'the creation of manufactured products through economically-sound processes that minimize negative environmental impacts while conserving energy and natural resources. Sustainable manufacturing also enhances employee, community and product safety' [14].

The main concept in sustainability is the Triple Bottom Line (TBL) put on the global agenda by Elkington in 1997 [15]. TBL foresees three dimensions of sustainability. The economic dimension of sustainability deals with an organization's implications on its most important stakeholders. These include employees, families, customers, suppliers, communities, and any other person influencing or affecting the organization. The environmental dimension discusses the impact an organization has on its natural environment. This includes reducing its carbon footprint, using natural resources, toxic materials, and so on, and the active removal of waste, reforestation, and restoration of natural harm. The third dimension is the social one explaining an organization's possible impact on the local, national and international economy. This includes creating employment, generating innovation, paying taxes, wealth creation, and any other economic impact an organization has.

Figure 1 shows the current trend towards a more balanced target paradigm in manufacturing by raising environmental and social objectives on the same level as objectives related to efficiency and productivity.

Several examples of sustainable packaging redesign were described in the literature. In the example of the study [16], the authors define environmental performance, cost, quality, market acceptance, and user-friendliness as main requirements. The research [17] confirms that most customers and companies want to increase environmental/social sustainability while not wanting to pay more for it. This leads to a balancing problem.
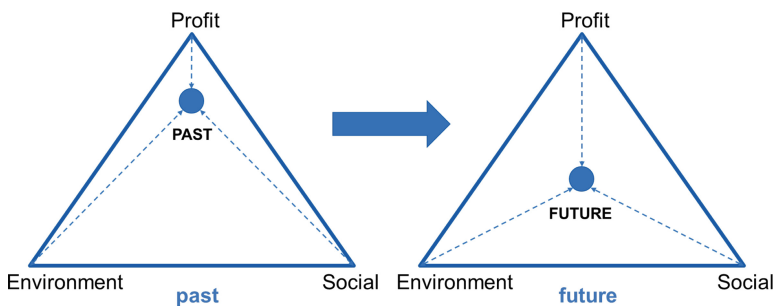
Fig. 1. Paradigm shift – towards a more balanced target paradigm.

3   Research Methodology

Achieving sustainability in manufacturing requires a holistic view spanning the product, the manufacturing processes involved in its fabrication, and the entire supply chain [18]. In this work, the authors concentrate on a specific part of the manufacturing process: the packaging. Based on case study research at a manufacturer of sanitary ware products, the procedure for the redesign of packaging material with the objective to achieve a more balanced combination of economic, environmental, and social sustainability is shown. The applied methodology for this research is a combination of case research, market search, and multi-criteria utility analysis to select the most promising solutions for the redesign of the packaging.

Case study research is one of the most powerful research methods for better understanding the applicability of theoretical concepts in practice [19]. Case research has been recognized as being particularly suitable to ask "what" and "how", but also "why" questions, usually when doing research in a very dynamic, experiential, and complex context [20]. Case studies allow investigating a certain phenomenon in a real-life context, especially when the boundaries between a phenomenon and its context are not clearly evident [21]. Data collection in this case study is based mainly on the observation of the packaging process, the analysis of historical data regarding the product, packaging material, and the process, and interviews with managers and process engineers.

Market research has been conducted through a web search of alternative packaging materials, participation at fairs/exhibitions, and interviews with potential suppliers for innovative and sustainable packaging materials. The information retrieved from case research and the market research has to be used to compare the identified solutions and select a set of candidate alternatives to the current packaging.

Multi-criteria utility analysis establishes preferences between options by referencing an explicit set of objectives that the decision-making body needs to identify. It has established measurable criteria to assess the extent to which the objectives have been achieved. In simple circumstances, the process of identifying objectives and criteria may alone provide enough information for decision-makers [22].

4   Results

4.1   Case Study Description and Analysis

The company for which the case study is being evolved is operating with highly voluminous, large, flat products, generally made of glass and metal profiles. The products are easily breakable and are positioned vertically into an external packaging that consists of cardboard. To prevent damage due to external forces or vibrations. Overall, there are 23 different types of elements, which can be divided into two subgroups:

- Filling elements
- Positioning/position-fixing elements.

All out of the 23 elements are entirely made of expanded polystyrene (EPS) foam. This material has the benefits of being cheap having good isolation properties. It is known for

its low density, which additionally lowers the transport cost for the final product, even if the volume is high. It reinforces the edges of the external cardboard since there are some potential weaknesses when punctual forces are applied to the packaging during handling, transportation, and installation.

Since all the 23 types have different functions and hence, different properties and geometries, it is complex to replace all these elements in one single moment with the same alternative solution. To validate the importance of single elements for the company in a pilot project, it was necessary to compare the different types of packaging elements in terms of the yearly volumina and purchasing cost. By doing that, two of them, one of the filling elements and one of the positioning elements, could be detected as outstandingly important for the company. These two elements combined make an impact of 56.1% in the total volume and 43.3% in the total purchasing cost spend every year for internally used packaging elements.

Before starting with the research for eco-sustainable alternatives, the specific function of these two elements had been analyzed.

- Packaging element A (PEA)

    Packaging element A has the dimensions shown in Fig. 2 and a total length of 1,950 mm. It is placed into the packaging to fill blank spaces between the final product and the surface of the external cardboard. With the properties given by the EPS, the risk of the product being broken by vibrations and external forces is reduced.
- Packaging element B (PEB)

    The packaging element B has the dimensions shown in Fig. 3 and a total length of 1,600 mm. It is placed into the packaging to fix the product's position inside the cardboard and again, with the properties given by the EPS, to reduce the risk that the product is being broken or damaged due to vibrations and external forces.

The company's long-term goal is to replace all the existing packaging elements with an eco-sustainable alternative that does not particularly change their function, geometry, and property. The authors only considered these two mostly used elements for the case study.
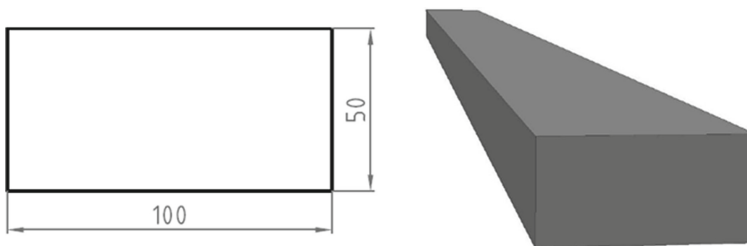
Fig. 2. Dimensions of PEA.
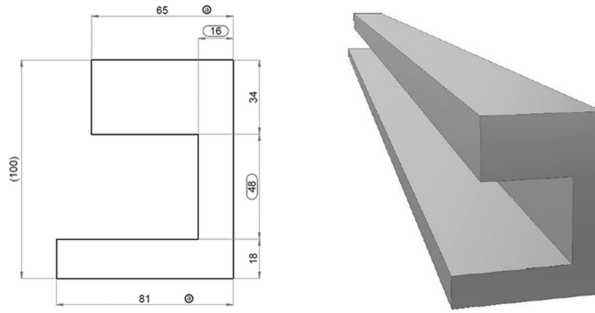
Fig. 3. Dimensions of PEB.

4.2 Identified Alternative Packaging Solutions

First, a general overlook of all potential materials is generated by scanning the market for packaging materials used in similar industrial applications. In this step of market research, the following alternative packaging materials have been identified:

- Paper
- Cardboard
- Air cushions
- Biological foam
- Self-expanding foam
- Honeycomb cardboard

Since the market for sustainable packaging is growing very fast, the listed material alternatives might not be exhaustive, and recently developed alternatives may have been neglected. Once detected all the alternatives, data collection has been started through a web search, fairs, and supplier interviews and quotations. It is important to respect the individual material properties and overthink the eventual application of the material while fulfilling all the specific use case requirements, which gives different possibilities for the two prioritized packaging elements, PEA and PEB.

The following ones are taken into consideration for the substation of PEA:

- Paper cushions
- Folded cardboard
- Biological/Paper air cushions
- Biological foams
- Self-expanding foams.

Since PEB is more complicated in terms of geometry, fewer alternative materials could be defined as suitable for substituting PEB:

- Folded cardboard
- Biological foam
- Honeycomb cardboard.

4.3   Comparison and Selection

In the next step, an evaluation system has been established in a multi-criteria utility analysis to compare the candidate solutions for PEA and PEB identified in Sect. 4.2. To keep the comparison between the provided solutions as simple as possible and refer to the dimensions of the TBL, without compromising in terms of the required properties, four evaluation criteria have been taken into consideration:

1. Technical performance
2. Economic Sustainability (Profit)
3. Eco-Sustainability (Environment)
4. Social Sustainability (Social)

A numeric value between 1 and 3 is assigned for each of these criteria to compare the specific solutions. Additionally, the numeric values assigned are weighted with a numeric factor 1.00 ('less important'), 1.25 ('important'), or 1.50 ('very important') to assign a specific higher or lower importance for each of the criteria. The value of the numeric factor also reflects the evolution towards a more balanced target paradigm in manufacturing. The sum of the four evaluation values as mentioned above results in a final score for each candidate packaging solution. The evaluation is conducted in a team consisting of the process engineer collecting the data and managers from production, logistics, and purchasing.

For the evaluation of the technical performance, the following points have been discussed and used for defining a value between one and three:

- Attenuation properties
- Geometric applicability
- Stability
- Integrability in production
- Manufacturing impact

This criterion is considered important for the application in the case study, and thus the weighting factor of 1.25 has been assigned to it.

The second criterion for evaluating the alternatives is economic sustainability and has been quantified as the total cost of ownership. Therefore, it refers to the purchasing cost and considers storage cost, personal cost, and external/internal transportation cost. For confidentiality reasons, this cost overview is not shown in this paper. This criterion is considered important for the case study, and therefore the weighting factor 1.25 is assigned to it.

The third evaluation criterion is the eco-sustainability and is based on the following considerations:

- Eco-Sustainability of the raw material
- Recycling properties
- Environmental impact of transportation
- The energy needed during production

Since this criterion is considered the most important for this specific case study, the weighting factor 1.50 is assigned.

The last criterion is social sustainability, which deals with the impact of the packaging elements on people (e.g., safety, physical/mental ergonomics, wellbeing, and workers' acceptance). This attribute is assigned the multiplicator 1.00, since all the provided alternatives do not show critical implications in weight, chemical effects, etc.

For the evaluation, a simple multi-criteria utility analysis tool has been created in Microsoft Excel, which facilitates the calculation of the final score for each candidate solution. Table 1 shows the results and ranking for PEA.

Table 1. Results and ranking of the multi-criteria analysis for PEA.

Pos.	Provided solution	Technical performance	Economical sustainability	Eco-sustainability	Social sustainability	Total score
	Weighting factor	1.25	1.25	1.50	1.00	
1	Folded cardboard	2.50	1.75	2.50	2.25	11.31
2	Biological foams	3	1	2.25	2.50	10.88
3	Paper cushions	1.25	2.25	2.50	2.50	10.63
4	Biological/ air cushions	1.50	2	2	2.50	9.88
5	Self-expanding foams	2	1.75	1.25	2	8.56

Similarly, an evaluation for PEB has been conducted (see Table 2).

Table 2. Results and ranking of the multi-criteria analysis for PEB.

Pos.	Provided solution	Technical feasibility	Economical aspect	Eco-sustainability	Social sustainability	Total score
	Multiplicator	1.25	1.25	1.50	1.00	
1	Folded cardboard	2.25	1.75	2.50	2.25	11
2	Biological foams	3	1	2.25	2.50	10.88
3	Honeycomb cardboard	2	1.50	2	2.25	9.63

Finally, the two first-ranked provided solutions for both elements, PEA and PEB, are taken for further analysis as in both cases, folded cardboard and biological foams

were ranked first. The company decided to possibly define a single packaging solution for PEA and PEB for standardization purposes. The overall cost still plays an important role for the company. Since the folded cardboard provides better performance from an economic and ecological viewpoint, the company chose this solution (see Fig. 4). Since the major problem of biological foams is the current high market price, the analysis will be redone again in 2–3 years to monitor the economic development of this material since it is the most promising technical properties with nearly identical technical properties as the actually used EPS.

Fig. 4. Final redesign of sustainable packaging material for PEA and PEB in folded cardboard.

5 Conclusions

This work aims to encourage researchers/practitioners from manufacturing companies to rethink their manufacturing processes and make them more sustainable. The practical case study of packaging was used to show how the approach for the redesign towards a more sustainable production process and value chain could look like. It was also important to show that companies should be attributing an increasingly higher weighting and importance to environmental and social sustainability than traditional economic objectives in process and product optimization. It was particularly interesting to see that although the case study company wanted to achieve a more sustainable solution than the current polystyrene packaging, it stated as a constraint that the costs should possibly remain the same or, in the case of a highly sustainable solution, be only slightly (max. 5%) above the costs of the current solution. This shows that the path to a greener and more socially responsible production still depends heavily on cost and efficiency. Manufacturers are still susceptible when deciding whether or not to adopt a more sustainable solution. Limitations of the study are that results are based on a subjective evaluation of the criteria by the project team. The main contribution is to show a TBL-based approach for evaluating redesign alternatives for more sustainable packaging.

References

1. Kagermann, H., Wahlster, W., Helbig, J.: Securing the future of German manufacturing industry: recommendations for implementing the strategic initiative INDUSTRIE 4.0. Final report of the Industrie 4.0 (2013)

2. Matt, D.T., Rauch, E.: SME 4.0: the role of small-and medium-sized enterprises in the digital transformation. In: Matt, D.T., Modrak, V., Zsifkovits, H. (eds.) Industry 4.0 for SMEs: Challenges, Opportunities and Requirements, pp. 3–36. Palgrave Macmillan, Cham (2020)

3. Rauch, E., Linder, C., Dallasega, P.: Anthropocentric perspective of production before and within Industry 4.0. Comput. Ind. Eng. **139**, 105644 (2020)

4. Shneiderman, B.: Human-centered artificial intelligence: reliable, safe & trustworthy. Int. J. Hum.-Comput. Interact. **36**(6), 495–504 (2020)

5. Umbrello, S., van de Poel, I.: Mapping value sensitive design onto AI for social good principles. AI Ethics **1**(3), 283–296 (2021). https://doi.org/10.1007/s43681-021-00038-3

6. Viola, S.: Technological innovation, design and inclusiveness for the manufacturing landscapes. Eur. J. Sustain. Dev. **6**(3), 271 (2017)

7. Longo, F., Padovano, A., Umbrello, S.: Value-oriented and ethical technology engineering in industry 5.0: a human-centric perspective for the design of the future factory. Appl. Sci. **10**(12), 4182 (2020)

8. Kopnina, H.: Green-washing or best case practices? Using circular economy and Cradle to Cradle case studies in business education. J. Clean. Prod. **219**, 613–621 (2019)

9. United Nations: The Sustainable Development Agenda. https://www.un.org/sustainabledevelopment/development-agenda/. Accessed 13 Nov 2021

10. The 2021 World Manufacturing Report: Digitally Enabled Circular Manufacturing. https://worldmanufacturing.org/wp-content/uploads/WMF2021_E-Book_b.pdf. Accessed 10 Nov 2021

11. European Commission: A European Green Deal - Striving to be the first climate-neutral continent. https://ec.europa.eu/info/strategy/priorities-2019-2024/european-green-deal_en. Accessed 11 Nov 2021

12. UN World Commission on Environment and Development. Our Common Future, Oxford University Press (1987)

13. Moldavska, A., Welo, T.: The concept of sustainable manufacturing and its definitions: a content-analysis based literature review. J. Clean. Prod. **166**, 744–755 (2017)

14. United States Environmental Protection Agency: Sustainable Manufacturing. https://www.epa.gov/sustainability/sustainable-manufacturing. Accessed 13 Nov 2021

15. Elkington, J.: Enter the triple bottom line. In: The triple bottom line, pp. 23–38. Routledge (2013)

16. Svanes, E., Vold, M., Møller, H., Pettersen, M.K., Larsen, H., Hanssen, O.J.: Sustainable packaging design: a holistic methodology for packaging design. Packag. Technol. Sci.: Int. J. **23**(3), 161–175 (2010)

17. Ma, X., Moultrie, J.: Understand sustainable packaging design in practice. In: DS 92: Proceedings of the 15th International Design Conference, pp. 2693–2704 (2018)

18. Jayal, A.D., Badurdeen, F., Dillon, O.W., Jr., Jawahir, I.S.: Sustainable manufacturing: modeling and optimization challenges at the product, process and system levels. CIRP J. Manuf. Sci. Technol. **2**(3), 144–152 (2010)

19. Matt, D.T.: Application of Axiomatic Design principles to control complexity dynamics in a mixed-model assembly system: a case analysis. Int. J. Prod. Res. **50**(7), 1850–1861 (2012)

20. Yin, R.: Case Study Research. Sage Publications, Beverly Hills (1994)

21. Rymaszewska, A., Helo, P., Gunasekaran, A.: IoT powered servitization of manufacturing–an exploratory case study. Int. J. Prod. Econ. **192**, 92–105 (2017)

22. Dodgson, J.S., Spackman, M., Pearman, A., Phillips, L.D.: Multi-criteria analysis: a manual (2009)

An Automated Diagnostic and Surveillance System for Eliminating the Community Spread of Infectious Respiratory Diseases in the Industry

Milan Sága Jr.[1(✉)] ⓘ, Michal Bartoš[1] ⓘ, Ivan Zajačko[1] ⓘ, Ivana Klačková[1] ⓘ, and Dariusz Wiecek[2] ⓘ

[1] University of Zilina, Univerzitna 8215/1, 010 26 Zilina, Slovakia
milan.saga2@fstroj.uniza.sk
[2] Faculty of Mechanical Engineering and Computer Science,
University of Bielsko-Biala, ul. Willowa 2, 43-309 Bielsko-Biala, Poland
wiecekd@ath.bielsko.pl

Abstract. The article focuses on the definition of risk management in industry, which is linked to developing an automated diagnostic and inspection system based on artificial intelligence designed to eliminate risks in industrial companies. The thesis outlines the risk management process according to the current ISO standard, and the following section of the article summarizes the risk management options available to businesses. The article also discusses the numerous strategies that can be used to lessen the risk of working with automated systems in industrial settings. A critical element in the spread of COVID-19 is the failure to maintain a sufficient distance between people (workers) and the late detection of the symptoms of this disease. Monitoring unjustifiable aggregation of workers and early detection of symptoms such as characteristic cough and temperature makes it possible to reduce or significantly eliminate the spread of this disease in the engineering company.

Keywords: Engineering · Industry · Safety · Sustainable manufacturing · Industrial growth

1 Introduction

The manufacturing industry is the backbone of the economies of many nations. This is especially true for Slovakia, where their share in total economic performance is much higher than in several other national economies. With the growth of new technologies and ways of working, traditional production is facing enormous changes, which place enormous challenges on established business models and the way of today's production processes. At the same time, these developments create many opportunities that lead to new business models, such as individualization of production and cost and efficiency due to shorter innovation cycles, reduced time to market, or in-house production adaptation. Given the ever-changing economic scenario, risk management is becoming increasingly

critical. Negative market developments and societal risks can lead to significant financial losses and, in the worst case, to business closures. As a result, risks must not be overlooked, and risk management should be part of every company's activities. Even though the company faces risks, the company also has opportunities that, if properly used, can help it compete or gain a better position in the market.

The pandemic has caused businesses and governments to face confusing supply chain collections and logistical failures. More than a year ago, we knew that we were facing a revolution in the system of healthcare, education, and workplaces. Consequences, such as the lack of semiconductors, were more difficult to predict. Measures to protect workers from exposure to and infection with the SARS-CoV-2 virus, which causes COVID-19, depend on the risk of exposure. This risk varies depending on the type of work performed, the possibility of long-term interaction with people, and contamination of the work environment. Employers have a minimum prevention strategy, and control is based on a thorough assessment of workplace hazards through routine combinations of technical and administrative controls, safe working practices, and personal protective equipment to prevent workers from being exposed to risks. These measures are based not only on wearing robes and on a gauge but also on cameras to monitor the migration of people in operation or record the increased body temperature of employees, which is one of the most common symptoms of COVID-19.

The article shall consist of the possibility of using automated systems in the field of security, risk management in industry, and developing an automated diagnostic and surveillance system to eliminate the community spread of infectious respiratory diseases in the industry.

2   Literature Review

In most modern sectors, automation is the most important engine of change. Automation is expected to replace over 800 million jobs by 2030 entirely, and in the meanwhile, automation will revolutionize the way we work, organize our businesses, and collaborate with others. The most significant benefit of automation is cost savings: if you pay $ 500 per month for a machine to do the work of a salaried employee earning $ 3,000 per month, you can easily save $ 2,500 per month ($ 30,000 per year). And because of widespread technological advancements, applications like automated payment systems, security software, and even automated trading software are becoming increasingly accessible to small and medium-sized firms. However, with the rise of automation, there will be new security concerns and certain security benefits [1].

2.1   Monitoring People Aggregation

In practically all of the nations afflicted by the viral sickness, which has spread into a pandemic, we can currently notice a drop in industrial productivity. Customer demand for produced items was significantly lowered, and the virus affected the logistical supply chain of material and people, which is scarce in many sectors, resulting in a drop in output. Situations like these may arise again in the future, but not identical to them. As a result, all essential production components (i.e., man, machine, and energy) must be

carefully monitored. It is necessary to have a model for assessing the threat to an industrial enterprise in various crisis situations (viral diseases, natural disasters, and energy crisis), quantifying the impact on the enterprise itself (economic and other indicators), and proposing alternative solutions quickly and effectively. With the advancement of artificial intelligence methods [2, 3], camera systems, and automation tools, it is now possible to design a diagnostic and inspection automation system based on rope robots that will use camera systems to monitor material flow in production, as well as legitimate migration of people within the production system [4, 5] (Fig. 1).
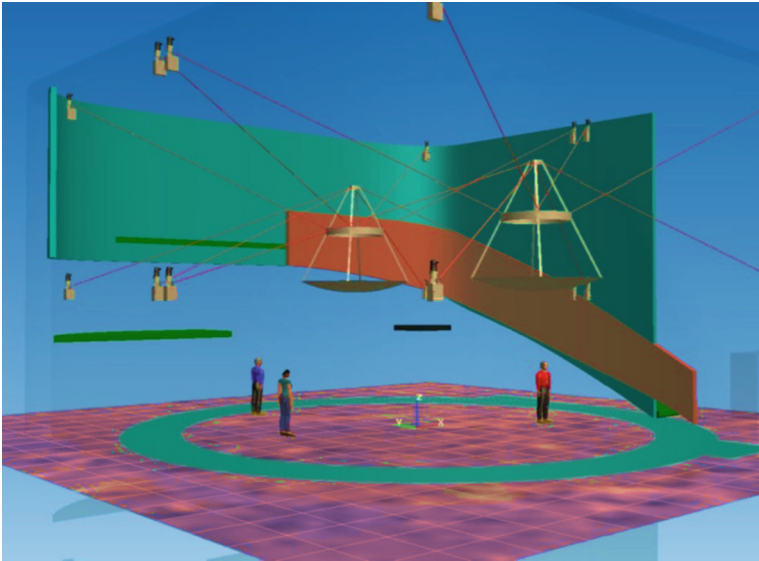
Fig. 1. Draft of the cable robot (Modified from: [6])

2.2 Acoustic Camera

It is a device with which we can identify in detail the source of acoustic emission with the help of a special microphone system and then measure the acoustic data and graphically present them. The application of an acoustic camera in the case of sound localization is possible thanks to its modular composition and technical properties in various fields of human activity in both indoor and outdoor environments. The acoustic camera system consists of several microphone units arranged according to measurement needs in a circle (so-called Ring), a triangle (so-called Star), or a sphere. Sound sources are crucial and are negligible. The acoustic camera enables the optimal investment of funds, e.g., based on noise in the required places. In this way, we can detect sound sources and hear them quickly, elegantly, and precisely. These noise measures can over a wide range of distant distances, in detail, short distances, also distances up to 800 m from the noise source itself [6].

2.3 Diagnostics of COVID-19 Disease with Advanced Cough Analysis Based on AI Methods

The assumption is that people with COVID-19, particularly asymptomatics, may be accurately discriminated against using artificial intelligence merely from their cough mobile phone records. A COVID-19 cough record data collection channel was developed through a website between April and May 2020 to train the MIT Open Voice model, and a COVID-19 cough cough data set containing 5320 data was created. An AI speech processing framework has been created to pre-examine COVID-19 from cough records using acoustic biomarker function extractors and produces a personalized map of patient testimonials for real-time longitudinal patient monitoring with minimal variable costs. Cough recordings are converted with the Mel Frequency Cepstral Coefficient and fed into a convolutional neural network-based architecture that includes a single layer of the Poisson biomarker and three pre-trained ResNet50s running in parallel, yielding binary preliminary screening diagnoses. The remaining 1064 subjects in the data set were used to test CNN-based models trained on 4256 subjects. The roles of biomarkers have been learned using transfer learning on more extensive data sets that have previously been successfully validated in an Alzheimer's laboratory, considerably boosting the accuracy of COVID-19 identification in our design. The sensitivity to COVID-19 is 98.5%, with a specificity of 94.2% when the model is validated in participants diagnosed using an approved test (AUC: 0.97). The sensitivity is 100% in asymptomatic people, with a specificity of 83.2% [6, 7].

Artificial intelligence techniques can be used to create a free, non-invasive, real-time, ever-distributable, large-scale asymptomatic COVID-19 screening tool that can be used to supplement current COVID-19 control efforts. Daily screenings of students, employees, and the general public when schools, employment, and transit reopen or testing associations to warn of group breakouts quickly might be helpful to use cases [7].

3   Research Methodology

Risk management is defined as a process in which management tries to prevent the impact of current and future risks by proposing appropriate solutions to mitigate the negative consequences. On the other side, it allows you to take advantage of beneficial benefits [8].

Risk management is a technique for identifying possible dangers that might result in a decline in safety. Risk management is a method of analyzing, assessing, and classifying the risks that an organization faces, from which priorities are established, and processes for mitigating those risks are developed. We define risk management as a systematic, ongoing strategy to deal with risk and uncertainty that employs a variety of tools, methodologies, and approaches. It is a component of management that ensures the system, process, project, or business activity's safety and stability [9].

Organizational risk management is used to assess and manage the organization's uncertainty in business strategy, people, processes, and technological compliance. The following principles must be followed for risk management to be applied in the organization:

- full top-level support,
- enterprise-wide implementation,
- familiarization of all human resources in the organization with risk management implementation,
- creation of effective risk-monitoring systems [10].

Risk management is responsible for safeguarding and enhancing an organization's assets. These objectives are met by risk management, which supports the organization's objectives as follows:

- given the ever-changing economic scenario, risk management is becoming increasingly critical.,
- helps the firm use and allocate funds and resources more efficiently;
- decreases business volatility in non-core areas,
- the company's assets and reputation are protected and strengthened,
- employees' expertise and the company's knowledge base are developed and supported,
- improves operating efficiency [10].

Various standards and norms can be used to execute risk management in the workplace. These standards and norms are chosen by each organization depending on their demands or those of its partners.
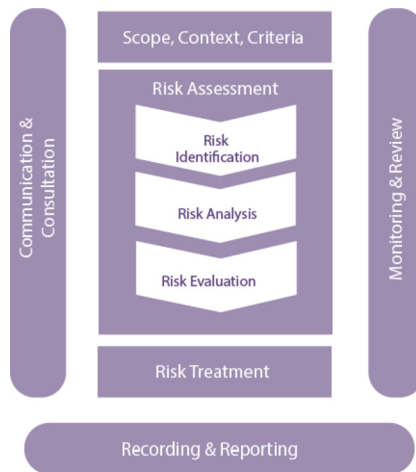
Fig. 2. Process of risk management (modified from [11])

ISO 31000: 2018 Risk management is an international standard that outlines generic risk management processes. The standard's Slovak adaptation, STN ISO 31000: 2019 Risk management - instructions, is adapted from it. The standard is developed for specific categories in the industry, but it may be used by anybody or any group - private, public, or social - without prejudice [11].

The risk management process steps depicted in Fig. 2 are listed in this standard list. The stages of the risk management process are a series of actions and outputs that form a cycle at the end. This procedure is an essential component of company management, and it has to be tailored to existing practices and corporate culture [11].

The risk database or the risk checklist are used to keep track of the hazards that have been identified. It is not advisable to rely on this database and checklist to identify risks [12].

The risk database is a collection of well-organized data from previously completed projects. A structured risk information file is a good way to keep track of data for future initiatives.

The risk checklist is a list of potential issues. The issues are unique to one business. The list is tailored to a certain sector or business. Identification is not a one-time event for us; it is a process that we engage in regularly or continually, depending on the situation. This is accomplished through the use of monitoring or early warning systems. They call attention to the increasing values of the responsible person's risk based on selected indicators that monitor the growth of selected risks at regular intervals and alert them when they surpass the established limitations [13].

To sum up, the most critical and time-consuming element of the risk management process is risk identification. It necessitates past expertise, systematicity, the capacity to foresee even unknown occurrences, collaboration, and a focus on the future [9, 14].

4   Results

The main problem, particularly at this time, is to prevent the pandemic illness from spreading. COVID-19. The human being is a crucial component of the process, and its replacement is challenging. There is a need to decrease or eradicate this hazard based on the understanding that this sort of sickness will continue to exist in the community.

4.1   Design of a Cable-Driven Parallel Robot for Industrial Inspection and Risk Reduction

Basic Idea for a Cable-Driven Parallel Robot. We can build a planar rope robot with 2 degrees of freedom by using 4 winding devices positioned in the corners of the supporting framework. The rope robot may move horizontally above the manufacturing line once the ropes have been appropriately tensioned. The vertical distance between the working plane and the production line may be adjusted by tightening or relaxing the haul ropes [15, 16].

4.2   Cable-Driven Parallel Robot

The most significant difference between a cable-driven parallel robot (CDPR) and a traditional parallel robot is the replacement of fixed guide chains with ropes of various materials and sizes. The motors and actuators are placed on the base, platform, or in the corners of the supporting structure and are not part of the guiding chain. Actuators are motors with a winding device, pulleys, ropes, and components to secure the rope.

The ropes are connected to a platform that can accommodate an additional gadget. Additional equipment can be employed for handling or other technical operations due to the machine's intended usage.

The most significant benefit of CDPR is its exceptionally lightweight (in comparison to the size of the workspace) and ability to operate across large areas. Because of its negligible weight, the platform can move rapidly and accelerate up to 40 g.

Furthermore, the permanent guide chains employed in parallel mechanisms are replaced by ropes, CDPRs cannot transfer compressive pressures, pressure on the platform cannot be created, and therefore the robot is unable to make a movement that would push the platform in front of it. Because bending the rope would result in incorrect placement and other problems during winding, the ropes must function under continuous strain [17, 18].

4.3   Requirements for Using a CDPR in Industry to Eliminate Risks and Regulate Processes

A concept for implementing a robotic device is provided below for the demands of production process control and risk elimination in the automobile sector. A cable-driven parallel robot was created as a suitable kind for this purpose, as its structure ensures that the robot device does not obstruct the manufacturing line's area. It is feasible for a robot to move quickly and with high dynamics in a reasonably big space. It will be essential to complete the following tasks throughout the inspection process:

- *Visual inspection of the production process* - a camera device will be installed on the robot platform during the visual inspection, communicating the optical output to the robot operator. The video will be captured for archiving with the possibility of retrieving the record.
- *Control of technological production parameters* - sensors for measuring various parameters (temperature sensor, flue gas concentration sensor, vapor composition sensor) can be placed on the robot platform, which will regularly record these parameters according to the operator's requirements to avoid errors in the production process.
- *Employee control* - utilizing a robot with a camera, it is possible to monitor and regulate the movement of employees in the production hall and their health, using an inspection system that can identify specific irregularities in the employees' motions and behavior. This system would inform the operator if an employee made motions that may indicate a health concern, and the operator could then summon medical assistance [19–21].

4.4   Conceptual Design

Robot Working Area - The most basic requirement for reducing risks in the manufacturing process was to design a device that would control the manufacturing process in a predetermined location, be fully programmable, and have parts and components that would not interfere with the production hall's built-up area or limit workers and equipment in performing their tasks. The floor layout for the automobile production line where
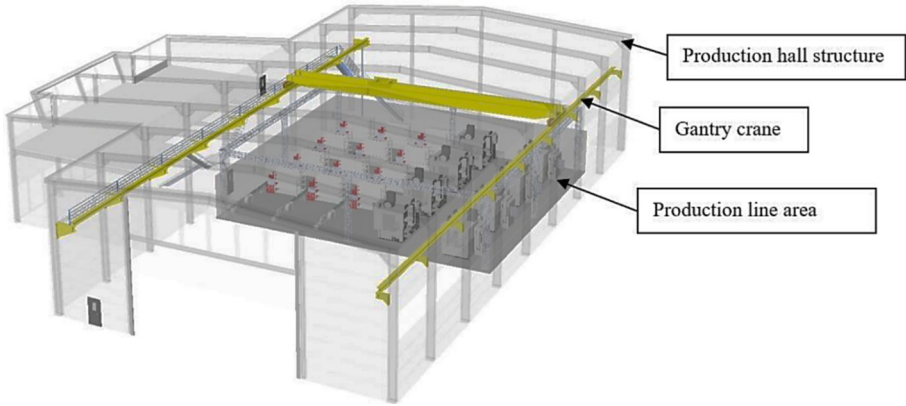
Fig. 3. Working area of designed robot

the robot will be used is in the shape of a square. The built-up area is around 20×20 m. The height of the production CNC machines in the line is no more than 3 m [19] (Fig. 3).

In its workplace, the robot platform will travel above the manufacturing line. Figure 4 depicts the robot's working environment. The robot winches might be put in the higher corners of the production hall under ideal circumstances, but because the production hall for which the robot is intended as a gantry crane, it is not viable to position the winders in the corners. The working space is restricted from the top by the device's supporting structure or the structure's circumferential dimensions. The working space is restricted below by manufacturing machines, which constitute a built-up region where the robot should not be [22–24].
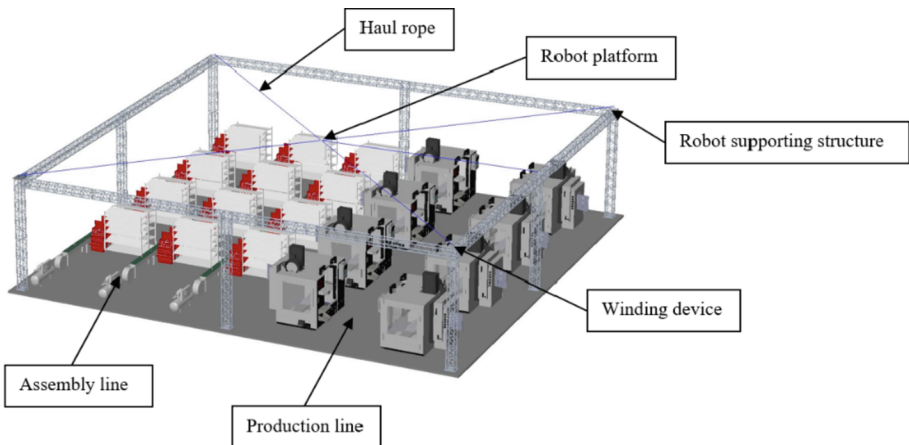
Fig. 4. Design of a cable-driven parallel robot used for risk elimination in the automotive industry [25]

5   Conclusions

Neglecting safety concerns often lead to additional expenditures, such as accidents and mechanical failures, which may be catastrophic to a business. As a result, it is essential to address removing risks and hazards caused by equipment design and construction, technical operations, and dangers systematically provided by the external environment. The inability to maintain appropriate space between people/workers/, as well as the late diagnosis of illness signs, are both critical factors in the spread of COVID-19 [26, 27].

Other anti-epidemiological tactics include maintaining a safe distance, wearing veils, and so forth. The goal is to give a scientific solution for lowering workplace infectivity. For this reason, no one has ever published an idea like this, and it's a first in the field [28].

References

1. Alton, L.: Automated systems and security: ISACA 2018. https://www.isaca.org/resources/news-and-trends/isaca-now-blog/2018/automated-systems-and-security-threats-and-advantages
2. Bun, P., Trojanowska, J., Ivanov, V., Pavlenko, I.: The use of virtual reality training application to increase the effectiveness of workshops in the field of lean manufacturing. In: 4th International Conference of the Virtual and Augmented Reality in Education, VARE 2018, pp. 65–71 (2018)
3. Ivanov, V., Pavlenko, I., Trojanowska, J., Zuban, Y., Samokhvalov, D., Bun, P.: Using the augmented reality for training engineering students. In: 4th International Conference of the Virtual and Augmented Reality in Education, VARE 2018, pp. 57–64 (2018)
4. Wiecek, D., Burduk, A., Kuric, I.: The use of ANN in improving efficiency and ensuring the stability of the copper ore mining process. Acta Montan. Slovaca **24**(1), 1–14 (2019)
5. Pavlenko, I., et al.: Parameter identification of cutting forces in crankshaft grinding using artificial neural networks. Materials **13**(23), Article number 5357 (2020)
6. Skycam, skycam.tv (2020). http://skycam.tv/
7. Laguarta, J., Hueto, P., Subirana, B.: COVID-19 artificial intelligence diagnosis using only cough recordings. IEEE Open J. Eng. Med. Biol. **1**, 275–281 (2020)
8. Moosa, I.: Operational Risk Management. Palgrave MacMillan, London (2007)
9. Atef, M., Moneim, A.: Risk assessment and risk management. Cairo University (2005)
10. Riadenie rizika v priemysle. ATP Journal (2011)
11. Brown, J.: Enterprise risk management (2019)
12. Liaposhchenko, O., et al.: Improvement of parameters for the multi-functional oil-gas separator of 'HEATER-TREATER' type. In: 2019 IEEE 6th International Conference on Industrial engineering and applications (ICIEA), Waseda Univ, Tokyo, Japan, 12–15 April 2019, pp. 66–71 (2019)
13. Tlach, V., Ságová, Z., Kuric, I.: Circular and quasi-circular paths for the industrial robots measuring with the Renishaw Ballbar QC20-W. In: MATEC Web of Conferences. EDP Sciences, vol. 254, no. 05007 (2019). ISSN 2261-236X. https://doi.org/10.1051/matecconf/201925405007

14. Radojicic, J., Surdilovic, D., Krüger, J.: Application challenges of large-scale wire robots in agricultural plants (2016). https://doi.org/10.3182/20130327-3-JP-3017.00021
15. Rengevič, A., Kumičáková, D., Kuric, I., Tlach, V., Dróźdiel, P.: Approaches to the computer vision system proposal on purposes of objects recognition within the human-robot shared workspace collaboration. Commun. Sci. Lett. Univ. Žilina **19**(2A), 68–73 (2017). ISSN 1335-4205
16. Pott, A.: Cable-driven parallel robots. In: Pott, A. (ed.) Springer Tracts in Advanced Robotics, vol. 120, pp. 1–13. Springer, Cham (2018). https://doi.org/10.1007/978-3-319-76138-1_1
17. EXPO 2015, Weltaustellung Seilroboter, Universität Stuttgart (2015)
18. Jung, J.: Workspace and stiffness analysis of 3D printing cable driven parallel robot with a retractable beam-type end-effector. School of Electronic and Electrical Engineering Daegu Catholic University, Korea (2020). https://www.mdpi.com/2218-6581/9/3/65
19. Pratima, B.: Chapter 24 - Process control. In: Biermann's Handbook of Pulp and Paper, 3rd edn. Elsevier (2018). https://doi.org/10.1016/B978-0-12-814238-7.00024-6
20. Gladwell, G.M.L.: Parallel robots, 2nd edn. Department of civil engineering. University of Waterloo (2006)
21. Harikrishna, V., Kumar, K.V.: Investigation of the blockchain structure for hydroxyapatite-based scaffolds. J. Eng. Sci. **8**(2), C30–C35 (2021). https://doi.org/10.21272/jes.2021.8(2).c5
22. Taghirad, H.D.: Parallel Robots: Mechanics and Control. CRC Press (2013). ISBN 9781466555761
23. Cone, L.L.: Skycam: an aerial robotic camera system. Byte Mag. **10**(10), 122–132 (1985)
24. Petapixel (2020). petapixel.com, https://petapixel.com/2011/10/26/japanese-flying-ball-could-be-the-future-of-aerial-camera-systems/
25. Akustická kamera. Avekol (2014). http://www.avekol.sk/sluzby/akusticka-kamera
26. Fedak, W., et al.: Influence of spray nozzle operating parameterson the fogging process implemented to preventthe spread of SARS-CoV-2 virus. Energies **14**(14), 4280 (2021). https://doi.org/10.3390/en14144280
27. Figiel, A., Klačková, I.: Safety requirements for mining complexes controlled in automatic mode. Acta Montan. Slovaca **25**(3), 417–426 (2020). ISSN 1335-1788. https://doi.org/10.46544/AMS.v25i3.13
28. Kuric, I., Klačková, I., Nikitin, Y.R., Zajačko, I., Císar, M., Tucki, K.: Analysis of diagnostic methods and energy of production systems drives. J. Process. **9**, 843 (2021). https://doi.org/10.3390/pr9050843

Correlation Between Accidents on Selected Roads as Fundamental for Determining the Safety Level of Road Infrastructure

Piotr Trojanowski[1](✉) 🔵, Aleksandra Trusz[2], and Borys Stupin[3]

[1] West Pomeranian University of Technology in Szczecin, 17, Piastów Ave., 70-310 Szczecin, Poland
`piotr.trojanowski@zut.edu.pl`
[2] University of Gdańsk, 119, Armii Krajowej St., 81-824 Sopot, Poland
[3] Sumy State University, 2, Rymskogo-Korsakova St., Sumy 40007, Ukraine

Abstract. The objective of the present publication was to determine whether the application of a statistical tool, analysis of the correlation between accidents that occur on roads before and after their modernization, can constitute the basis for creating a method for assessing the safety level of road infrastructure. It constitutes an entirely new approach to the methods used so far, aiming to determine high-risk zones/sections based solely on the number of accidents in the area covered by the analysis. Due to the general availability of data, the presented method can be both widely applied in practice and a tool to verify the correctness of specific risk factors contributing to the occurrence of undesirable road incidents. The conducted research allowed us to determine the correlation between the average number of accidents on alternative roads before the expressways/motorways were constructed and the average number of accidents on alternative routes after their completion is high. The situation is different in the case of the correlation between the average annual number of accidents on an alternative road before the completion of an expressway/motorway and the yearly average number of accidents on newly constructed sections. The results of our research suggest that the analysis of the correlation between accidents may constitute the basis for the development of a new method for assessing the level of road infrastructure safety.

Keywords: Industrial growth · Transport · Transportation engineering · Transport systems · Highway engineering

1 Introduction

The road infrastructure is constantly affected by degradation factors, such as the influence of the environment in the form of changing weather conditions or human impact. The human factor concerns mainly the use of means of transport, especially trucks. The level of road safety decreases in pair with the deterioration of the quality of the infrastructure. Bearing this in mind, it is necessary to take measures to restore the full functionality of roads.

These activities can be divided into immediate, resulting from a sudden requirement, such as the need to fill a pothole in the road, and thorough, i.e., including comprehensive changes that improve the quality of the sections changed. The activities of a thorough nature include the modernization of road infrastructure. This term has been defined as activities leading to the modernization and permanent improvement of the refurbished object.

The scope of modernization activities usually includes the reconstruction or renovation of the existing section. They are carried out to facilitate access to a significant point or junction, improve driving comfort, increase safety at the respective section and in terms of environmental protection (e.g., by reducing exhaust emissions and noise in a designated area). Due to the research methodology applied, i.a., the comparative analysis, the research covered only those modernized objects, at least partially, in 2013 and 2014. The study was conducted on the example of road infrastructure in Poland. In 2011–2014, many sections of high significance for the national communication grid were modernized in Poland (Table 1).

Table 1. List of selected sections of roads modernized in 2011–2014.

No.	Project name	Years	Section length [km]
1	Renovation of the A4 motorway between Katowice and Chorzów	2013	ca. 9
2	Construction of the "Tczewska" junction together with the reconstruction of the A6 motorway	2011–2014	2.87
3	Reconstruction of the S8 Piotrków Trybunalski - Warsaw expressway on the Rawa Mazowiecka - Radziejowice section	2010–2014	32.15
4	Reconstruction of the S8 expressway, Powązkowska junction - Miarki junction section	2012–2015	ca. 4
5	Renovation on the national road No. 1 on the section from the border of the Łódzkie/Śląskie Voivodeship to Częstochowa	2013	19
6	Renovation of NR no. 3 on the Skwierzyna - Międzyrzecz section	2013	ca. 13
7	Extension of the national road No. 8 to the parameters of the dual carriageway expressway on the Jażewo - Białystok section	2011–2014	24.51
8	Modernization of road access to the Port of Szczecin (reconstruction of Struga)	2011–2013	ca. 2.5
9	Renovation of the road surface of NR 12 on the Bobrzany - Szprotawa section	2013	ca. 6
10	Renovation of national road No. 19	2013–2014	ca. 16
11	Improving safety on the national road No. 43	2012	ca. 4

The modernizations mentioned above included the reconstruction of approx. 133 km of roads throughout Poland. They focused mainly on improving safety and driving comfort, e.g., upgrading the road class, eliminating dangerous intersections, or repairing the surface.

Road infrastructure constitutes one of the transport system elements, and it can be considered a coherent whole. Regarding the cited definition of modernization as "activities leading to the modernization and permanent improvement of the refurbished object", it can be assumed that the construction of new road sections constitutes a kind of "modernization and permanent improvement" of the road infrastructure considered as a whole.

2 Literature Review

Road traffic safety [1, 2] depends on numerous factors [3–5]. It can be assumed that most road incidents have their origins in human errors [6]. Therefore, the aspect of the human factor [7] as an element determining the level of road safety is a frequent object of research in subject literature [8], also in the case of cyclists [9]. However, we shall not omit other factors [10], that is, first of all, environmental issues (e.g., weather) [11] and the technical environment [12–14] (e.g., materials [15] and road infrastructure [16]). The technical environment affecting [17] the road safety level includes the reliability [18] of means of transport [19, 20], the location of vehicle diagnostics and repair sites [21], emergency services, and the condition of the road infrastructure [22].

The road infrastructure safety level analysis is carried out in many ways [23]. These methods are often aimed at identifying the so-called risk areas, risk zones, black spots [24], etc. In this case, the analysis of undesirable road events [25] (collisions, accidents [26]) that took place on the analyzed sections within a specified time is usually performed [27]. Depending on the adopted criteria, road incidents are most often investigated in the context of:

– number of events,
– place of occurrence,
– types of events, e.g., frontal collisions or hitting a solid obstacle,
– the circumstances of the occurrence, e.g., time,
– participants.

The result of the conducted research usually links the occurrence of road accidents and collisions to specific sections of infrastructure. By narrowing the infrastructure analysis to sections with an above-average concentration of adverse events, it is possible to research to determine specific factors causing accidents/collisions [28, 29]. It seems, however, that these factors and their impact on the occurrence of undesirable road events may be in a strong relationship with the traffic volume. Therefore, there is a need to apply tools that would enable the verification of such a research approach. Therefore, a study of the correlation between road accidents was proposed as the basis for determining the safety level of road infrastructure, including the designation of high-risk zones.

3   Research Methodology

As already mentioned, based on the literature review, the determination of the safety level of road infrastructure often adopts the form of determination of high-risk zones based on a higher incidence of accidents. Nevertheless, it should be noted that the number of accidents largely depends on the intensity of road traffic. Therefore, by limiting ourselves only to comparing the number of accidents on individual sections of the road infrastructure, we will be unable to acquire the complete picture.

This publication aims to supplement the knowledge on determining the level of road infrastructure safety based on the correlation between accidents before and after the modernization of road infrastructure. This approach allows us to determine whether the number of accidents has actually decreased after the modernization of the road, for example, by removing an element considered a risk factor. An interesting case is a situation where, due to the expansion of the road infrastructure, the road, which previously constituted the main section of a given infrastructure connection, has been replaced by a higher-class road. This, in turn, results in a significant reduction of traffic volume at the "old section". It allows conducting a study consisting of a comparative analysis of the number of accidents before and after the modernization of the transport system and then checking whether there is a correlation between the accidents that have occurred. A strong correlation coefficient may indicate the actual influence of a predefined risk factor favoring the occurrence of undesirable road events. On the other hand, a weak correlation coefficient may indicate that the risk factor was incorrectly designated.

As shown in Fig. 1, the preliminary stage of the proposed methodology is to analyze the current condition of road infrastructure in the selected area. This is made possible thanks to materials of state organizations responsible for road infrastructure management. The area covered by the study was the territory of Poland, the entity responsible for the road infrastructure is the General Directorate for National Roads and Motorways (GDDKiA). Industry publications can also be considered a valuable source of information. The analysis of the road infrastructure condition has been divided into two parts. The first one divided the infrastructure according to the criteria adopted by the entity responsible for road infrastructure management in the respective territory. Then, it was analyzed how the infrastructure has changed in recent years.

Based on the analysis, it was established that in 2019 there was 307 065.9 km of paved public roads in the area covered by the study (Poland). Moreover, between 2007 and 2019, the total length of motorways increased by 253% and expressways by 619%.

The subsequent stage of the research concerned the identification of sections of road infrastructure under modernization in a selected area. We adopted the following selection criteria:

– modernization time in the years 2013 and 2014 - such a choice was dictated by the need to obtain reliable data (for 4–5 years) both before and after the introduction of changes to the road infrastructure;
– high importance for the region, which is associated with a significant volume of road traffic;
– section length exceeding at least 20 km - to reduce the influence of a random factor.
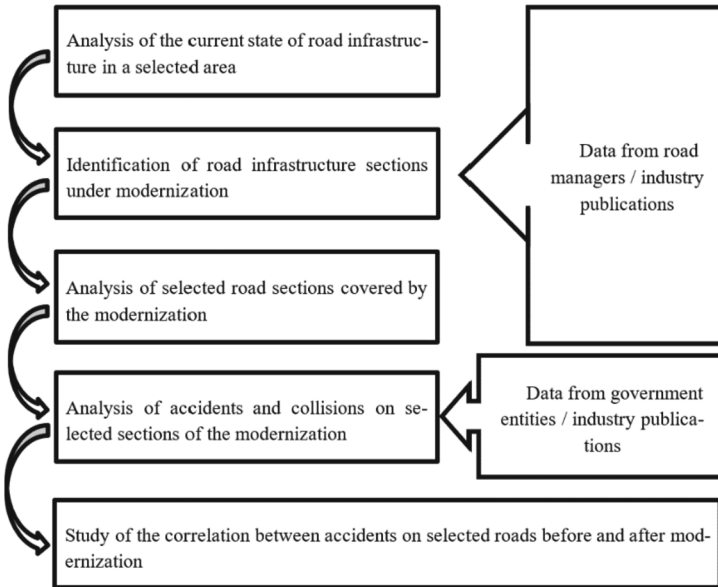
Fig. 1. Research scheme.

The next step is to analyze the previously identified sections in terms of the possibility of including them in further research. The decisive factor was, above all, the occurrence of a situation where the section previously used as the main road connection has been replaced by a higher-class road (motorway or expressway), and its role has been reduced - which was also associated with a significant decrease in road traffic volume. Each of the sections selected in this way was considered in terms of changes made to it and the analysis of accidents in the years before and after the works were performed, which was the next stage of the research. The final part of the research was to determine, using the Statistica software suite, the correlation between accidents that occurred on the previously defined sections of the road infrastructure.

4   Results

Regarding the number of accidents, we analyzed 12 sections of newly built roads (including 8 sections of expressways and 4 sections of highways) along with alternative routes. In line with the methodology mentioned above, we selected sections located in various parts of Poland, measuring between 20 and 45 km in length.

Table 2 presents the average annual number of accidents (based on [30]) on alternative routes before and after the commissioning of expressways/motorways and new roads after their commissioning. The total average number of accidents on both routes for the period after their opening was also calculated. In the tables, the sections were marked with the following reference numerals:

1.   Kurów Zachód - Jastków section of the S12 and S17 expressway, and road No. 874,

Table 2. Summary of the average annual number of accidents on the discussed expressways/motorways and alternative routes.

No.	The average annual number of accidents on the alternative road prior to the opening of an expressway/motorway	The yearly average number of accidents on the alternative road after the express road/motorway was opened	The yearly average number of accidents on the expressway/motorway	The total yearly average number of accidents on both routes
1	17.75	4	2.2	3.1
2	6	3.4	3	3.2
3	53.5	30.2	6	18.1
4	18.75	8	4.6	6.3
5	12.2	4.75	4.5	4.63
6	16.6	6	3.25	4.63
7	10	3.75	4.25	4
8	33.2	12.75	3.75	8.25
9	13.75	4.8	5	4.9
10	26.25	10.8	4.6	7.7
11	4.5	1.4	0.2	0.8
12	35.6	10	3.75	6.88

2. Sulechów - Świebodzin section of the S3 expressway, and the route running through: Rosin, Kalsk, Brzezie near Sulechów,
3. Kielce Północ - Kielce Południe section of the S7 expressway, and the road running through the center of Kielce (ul. Radomska, al. Solidarności, ul. Świętokrzyska, ul. Jesionowa, ul. Zagnańska, ul. Przemysław Gosiewskiego, ul. Żelazna, ul. Amii Krajowej, ul. Krakowska and road No. 762),
4. Syców Wschód - Wieluń section of the S8 expressway, and road No. 482,
5. Gorzów Wielkopolski Południe - Międzyrzecz Północ section of S3 expressway, and roads Nos. 158 and 159,
6. Kaczkowo - Korzeńsko section of the S5 expressway, and road No. 309,
7. Wieluń - Sieradz Południe section of the S8 expressway, and road No. 482,
8. Sieradz Południe - Łask section of the S8 and S12 expressway, and roads Nos. 83 and 482,
9. Toruń Południe - Włocławek Zachód section of the A1 motorway, and NR 91,
10. Dębica Wschód - Rzeszów Północ section of the A4 motorway, and NR 94,
11. Przemyśl - Korczowa section of the A4 motorway, and National Roads NR 77 and 94,
12. Tarnów Północ - Dębica Wschód section of the A4 motorway, and NR 94.

The study includes a tiny research sample (12 cases), and therefore the analyzes presented in Figs. 2 and 3 are only illustrative. They were elaborated to formulate preliminary conclusions, the verification of which will only become possible after conducting comprehensive research.
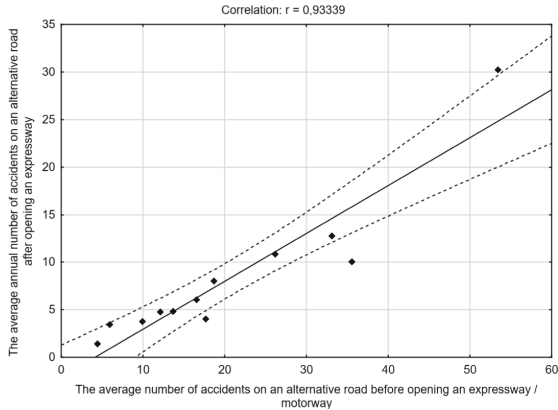
Fig. 2. Correlation between the average number of accidents on an alternative road before opening an expressway/motorway and the average annual number of accidents on an alternative road after opening an expressway.

The correlation between the average number of accidents on an alternative road before opening an expressway/motorway and the average annual number of accidents on an alternative road after opening (Fig. 2) is 0.93339, which means that it is high. Despite the small research sample, the correlation between the results is strong. It proves that the decrease in the annual average number of accidents on alternative roads due to the commissioning of expressways/motorways is proportional. It is impossible to state whether this dependence is constant for every case of a new section of a high-class road being constructed. Still, in the discussed cases, such a relationship existed.

The situation is different in the case of the correlation between the average annual number of accidents on an alternative road before the completion of an expressway/motorway and the yearly average number of accidents after its opening. In this case, it is only 0.56105, which is a much lower level. The proportionality of the number of accidents in the first case, compared to its absence in the second case, may indicate differences in the causes of accidents.

The number of accidents on alternative roads after the commissioning of high-class roads has clearly decreased, directly related to a significant reduction in road traffic volume. Still, it is surprising that there is a significant correlation between the occurrence of accidents before and after opening the new road.

On the other hand, in the case of expressways and motorways, the causes of accidents are unrelated, so a reduction in their number is disproportionate. The construction of an expressway/motorway eliminates many of the threats present on routes consisting of lower-class roads, at the same time generating new threats, resulting, for example, much higher speeds than the drivers are reaching.
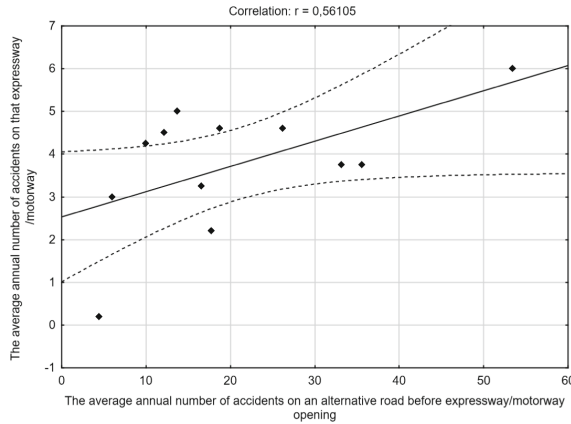
Fig. 3. Correlation between the average annual number of accidents on an alternative road before expressway/motorway opening and the yearly average number of accidents on that expressway/motorway.

Accidents occurring on motorways are characterized by greater randomness, making it more difficult to identify specific factors.

5   Conclusions

The modernization of the road infrastructure is carried out for several reasons. In addition to individual causes depending on a given section subjected to changes, there are three crucial and recurring factors: improving road safety, increasing the comfort of travelers, and reducing the travel time between the endpoints of the section.

In line with the assumed objective, the road infrastructure was analyzed before and after modernization. The accidents occurring in the discussed sections in the period covered by the analysis (using data from 9 years) were also presented and discussed. The results of the conducted research prove that the modernizations bring about a decrease in the average number of accidents. Statistical analysis was carried out, proving the correlation between the occurrence of accidents before and after the opening of new roads on the alternative route and the correlation between the number of accidents before the road construction and their number on new S and A-class roads. It proves that on older routes, where motorways and expressways were constructed, there is a strong correlation between the occurrence of accidents in the period before and after the opening of the new roads. The situation is different when it comes to linking the number of accidents on expressways and motorways to accidents on alternative routes before new roads were opened. In this case, the correlation is low, proving that accidents that occur on newly built sections are not related to those that occurred earlier on the routes subjected to our research.

Summing up, the study of the correlation between accidents before and after road modernization may constitute the basis for developing a new method for assessing the safety level of road infrastructure, which is a new approach to the works cited in the literature review.

References

1. Losurdo, F., Dileo, I., Siergiejczyk, M., Krzykowska, K., Krzykowski, M.: Innovation in the ICT infrastructure as a key factor in enhancing road safety: a multi-sectoral approach. In: 2017 25th International Conference on Systems Engineering (ICSEng), pp. 157–162 (2017)

2. Martins, M.A., Garcez, T.V.: A multidimensional and multi-period analysis of safety on roads. Accid. Anal. Prev. **162**, 106401 (2021)

3. Benlagha, N., Charfeddine, L.: Risk factors of road accident severity and the development of a new system for prevention: new insights from China. Accid. Anal. Prev. **136**, 105411 (2020)

4. Filina-Dawidowicz, L., Możdrzeń, D., Stankiewicz, S.: Integrated approach for planning of intermodal food transport chains considering risk factors. In: Rodriguez Morales, G., Fonseca C., E.R., Salgado, J.P., Pérez-Gosende, P., Orellana Cordero, M., Berrezueta, S. (eds.) TICEC 2020. CCIS, vol. 1307, pp. 319–332. Springer, Cham (2020). https://doi.org/10.1007/978-3-030-62833-8_24

5. Kascak, J., Baron, P., Torok, J., Pollak, M., Teliskova, M.: Macrostructure digitalization of the roadway surface profiles. MM Sci. J **2019**, 2839–2844 (2019)

6. Adanu, E.K., Smith, R., Powell, L., Jones, S.: Multilevel analysis of the role of human factors in regional disparities in crash outcomes. Accid. Anal. Prev. **109**, 10–17 (2017)

7. Lyu, N., Cao, Y., Wu, C., Xu, J., Xie, L.: The effect of gender, occupation and experience on behavior while driving on a freeway deceleration lane based on field operational test data. Accid. Anal. Prev. **121**, 82–93 (2018)

8. Rolison, J.J., Regev, S., Moutari, S., Feeney, A.: What are the factors that contribute to road accidents? An assessment of law enforcement views, ordinary drivers' opinions, and road accident records. Accid. Anal. Prev. **115**, 11–24 (2018)

9. Useche, S., Montoro, L., Alonso, F., Oviedo-Trespalacios, O.: Infrastructural and human factors affecting safety outcomes of cyclists. Sustainability **10**(2), 299 (2018)

10. Malin, F., Norros, I., Innamaa, S.: Accident risk of road and weather conditions on different road types. Accid. Anal. Prev. **122**, 181–188 (2019)

11. Theofilatos, A.: Incorporating real-time traffic and weather data to explore road accident likelihood and severity in urban arterials. J. Safety Res. **61**, 9–21 (2017)

12. Ivanov, V., Pavlenko, I., Kuric, I., Kosov, M.: Mathematical modeling and numerical simula-tion of fixtures for fork-type parts manufacturing. In: Knapčíková, L., Balog, M. (eds.) Indus-try 4.0: Trends in Management of Intelligent Manufacturing Systems. EICC, pp. 133–142. Springer, Cham (2019). https://doi.org/10.1007/978-3-030-14011-3_12

13. Ivanov, V., Dehtiarov, I., Pavlenko, I., Kosov, M., Hatala, M.: Technological assurance and features of fork-type parts machining. In: Ivanov, V., et al. (eds.) DSMIE 2019. LNME, pp. 114–125. Springer, Cham (2020). https://doi.org/10.1007/978-3-030-22365-6_12

14. Krol, O., Sokolov, V.: Research of toothed belt transmission with arched teeth. Diagnostyka **21**(4), 15–22 (2020). https://doi.org/10.29354/diag/127193

15. Knapcikova, L., Husar, J., Herzog, M., Pesek, L.: Testing of new composite materials based on fabric from used tires. Chem. Listy **106**, S450–S452 (2012)

16. Papadimitriou, E., Filtness, A., Theofilatos, A., Ziakopoulos, A., Quigley, C., Yannis, G.: Review and ranking of crash risk factors related to the road infrastructure. Accid. Anal. Prev. **125**, 85–97 (2019)

17. Knapcikova, L., Husar, J., Kascak, P.: Automatic Identification applications for smart railway concept. In: Knapcikova, L., Balog, M., Perakovic, D., Perisa, M. (eds.) 4th EAI International Conference on Management of Manufacturing Systems. EICC, pp. 83–91. Springer, Cham (2020). https://doi.org/10.1007/978-3-030-34272-2_8

18. Repin, S., Evtiukov, S., Maksimov, S.: A method for quantitative assessment of vehicle reliability impact on road safety. Transp. Res. Proc. **36**, 661–668 (2018)

19. Trojanowski, P., Trojanowska, J.: Reliability of road transport means as a factor affecting the risk of failure – the transport problem case study. In: Ivanov, V., Trojanowska, J., Pavlenko, I., Zajac, J., Peraković, D. (eds.) DSMIE 2021. LNME, pp. 253–261. Springer, Cham (2021). https://doi.org/10.1007/978-3-030-77719-7_26

20. Lasinska, N.: Hybrid management methodology for transport projects related to rolling stock. J. Eng. Sci. **8**(2), B7–B11. https://doi.org/10.21272/jes.2021.8(2).b2

21. Trojanowski, P., Filina-Dawidowicz, L.: Diagnostic and repair centers locating methodology for vehicles carrying sensitive cargo. Transp. Res. Proc. **55**, 410–417 (2021)

22. Reynolds, C.C., Harris, M.A., Teschke, K., Cripton, P.A., Winters, M.: The impact of transportation infrastructure on bicycling injuries and crashes: a review of the literature. Environ. Health **8**(1), 1–19 (2009)

23. Dereli, M.A., Erdogan, S.: A new model for determining the traffic accident black spots using GIS-aided spatial statistical methods. Transp. Res. Part A: Policy Pract. **103**, 106–117 (2017)

24. Ghadi, M., Török, Á.: A comparative analysis of black spot identification methods and road accident segmentation methods. Accid. Anal. Prev. **128**, 1–7 (2019)

25. Yang, C., Chen, M., Yuan, Q.: The application of XGBoost and SHAP to examining the factors in freight truck-related crashes: an exploratory analysis. Accid. Anal. Prev. **158**, 106153 (2021)

26. Zhang, G., Tan, Y., Zhong, Q., Hu, R.: Analysis of traffic crashes caused by motorcyclists running red lights in Guangdong Province of China. Int. J. Environ. Res. Public Health **18**(2), 553 (2021)

27. Kurakina, E., Rajczyk, J.: Potential for improving the procedure of inspecting road traffic accident black spots. Archit. Eng. **5**(3), 56–62 (2020)

28. Santos, B., Trindade, V., Polónia, C., Picado-Santos, L.: Detecting risk factors of road work zone crashes from the information provided in police crash reports: the case study of Portugal. Safety **7**(1), 12 (2021)

29. Touahmia, M.: Identification of risk factors influencing road traffic accidents. Eng. Technol. Appl. Sci. Res. **8**(1), 2417–2421 (2018)

30. Polish Road Safety Observatory: Reports and statistical data (2021)

Principles of Forming the Organizational Structure of the Enterprise Energy Management System

Liudmyla Kamenska[1] , Valentyn Moiseenko[1] , Vira Shendryk[2(✉)] ,
Sergii Shendryk[3] , and Oleksandr Shendryk[4]

[1] Ukrainian State University of Railway Transport, 7, Feijerbakh Square, Kharkiv 61050,
Ukraine
[2] Sumy State University, 2, Rymskogo-Korsakova Street, Sumy 40007, Ukraine
v.shendryk@cs.sumdu.edu.ua
[3] Sumy National Agrarian University, 60, Herasyma Kondratieva Street, Sumy 40000, Ukraine
[4] National Technical University of Ukraine "Igor Sikorsky Kyiv Polytechnic Institute", 37,
Peremohy Avenue, Kyiv 03056, Ukraine

Abstract. The paper describes the problems and contradictions description in the formation of the organizational structure of energy management systems. This work covers the Ukrainian regulatory acts and international standards that are providing methodologies of implementation and evaluation of effective energy management systems. Problems of implementation of these systems are highlighted. The effectiveness of enterprise energy management is provided by the common use of information systems, which can only increase through flexible data management and adopting the basic principles of organizational methods. To reduce the influence of the 'human' factor, it is necessary to transfer to the lower level the issues of monitoring or control and the issues of decision-making, thereby changing the concept of building and developing the system. In such conditions, the energy management process does not become a unique process established to achieve specific goals - it becomes an integral part of any production, technological, social process in which energy resources are directly or indirectly involved. Modern trends in energy management demand integration between the existing informational subsystems providing support to the decision-making process at the operational level and at the strategic management level to create a comprehensive Enterprise Energy Management System.

Keywords: Industry 4.0 · Energy efficiency · Energy consumption · Enterprise energy management system · Organizational structure

1 Introduction

Reasonable and economically sound energy use is one of the priority tasks of enterprises' operating activities.

Energy management is perceived as a concept, not as a separate one, but as a complex of concepts, methods, approaches, and tools for the energy resource management process

from the point of energy conservation. In other words, according to [1], energy management is described as a body of knowledge, tools, principles, and forms of energy-saving management which aim to reduce the energy resources' costs. This vision of energy management is present both in research, in the work of leading analytical centers [1], developing national directions for the development of independent economies, as well as in the work of numerous analysts and audit companies offering programs for the management of energy resources incompetent, flexible, uninterrupted and scientifically sound way of production in the different levels such as shops at an enterprise, concern, industry [2].

There are two main approaches to implementing energy management, each of which is provided by different organizational and technical methods. The first approach is provided by the modernization of the existing assets of the enterprise to achieve energy savings. The purpose of the second approach is planning and operational control of the distribution and consumption of energy resources. It is energy management in the literal sense. To ensure effective energy management, it is necessary to introduce an energy management system as a tool to reduce energy consumption through its rational use.

2   Literature Review

The energy management system (EMS) model for industrial enterprises was proposed by prof. V.P. Rosen et al. [3]. This paper has developed a model of EMS activity for industrial enterprises. The methodology for the formation and operation of EMS is based in [3] as the EMS function, which relies on a spiral that reiterates a cycle aimed at steadily developing the management system. EMS is characterized by a strong feedback loop that is basically separated from formal energy management.

The authors of this work propose to develop an EMS concept based on the management principles laid down in the international standards ISO 9000 and ISO 14000, as well as on the principles of process control automation laid down in the standards of the GOST series "Automated control systems" and "Information Technology". This is since EMS includes a personnel management system and a set of technical means for registering, monitoring, analyzing, and planning data on the competence of the fuel and energy resources utilization by an enterprise.

In the concept of constructing an EMS for the implementation purposes of these provisions, it is proposed to establish the efficiency markers of the fuel and energy resources consumption by groups (workshops, sections, etc.), to announce a system of material and moral incentives. To save energy, widely use various internal control and monitoring methods for the efficiency of the fuel and energy resources consumption. In addition, the EMS concept proposes to distinguish from general management such specific functions as control, analysis, accounting, assessment, planning, and stimulation of enhancing the efficiency of the fuel and energy resources consumption. This EMS model is shown in Fig. 1.

Regulating the development and implementation of EMS at industrial enterprises in the form of automated systems for handling the efficiency of fuel and energy resources consumption is the concept that underlies the creation of standards DSTU 4472: 2005 [4] and DSTU 4715: 2007 [4]. In DSTU 5077: 2008 "Energy saving. Energy management

systems for industrial enterprises. Checking and control of operability" [4] establishes general requirements for the energy management system and the principles of its formation and audit. It should be noted that these standards were introduced between 2005 and 2008. According to the main provisions of the DSTU 4472–2005 methodology [4], EMS is the baseline for the methodology for building an energy management system on the methodologies' basis of the product quality management system [5, 6] and the environmental management system, which is reflected in the national standards of Ukraine.

The methodology for the formation and implementation of energy management system activities, as defined above, can be applied to the formation and implementation of energy management activities in the form of energy conservation management, which should cover all relevant aspects of energy activities following [7, 8].
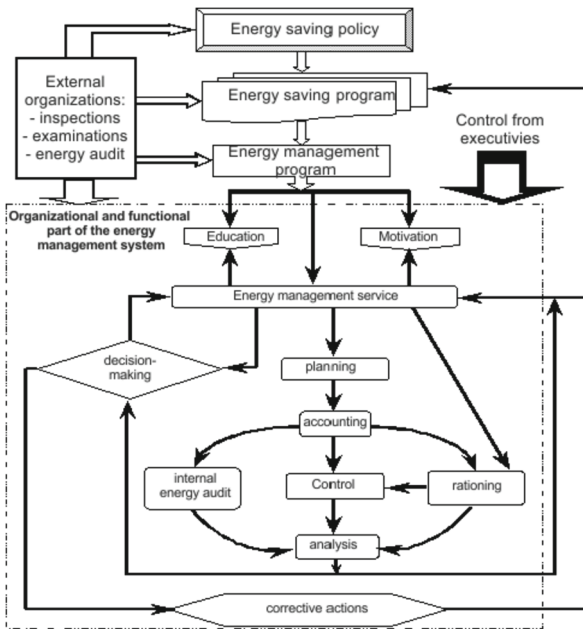
Fig. 1. Diagram of the energy management system according to [3].

This model implements three control cycles (see Fig. 1):

- energy efficiency management (life cycle of energy management service);
- improving energy efficiency (customer requirements);
- improvement of the energy management system.

This model explicitly addresses the requirements of different organizations.

The issues of rational use of energy resources in the EU countries, Canada, and the USA require a lot of attention. At the same time, both national requirements and standards and international ones are established. For example, in Sweden and Germany, national

standards and guidelines for energy management have been adopted [9]. An overview of the energy management standards of foreign countries is given by S. Khokhlyavin in his book [10].

The European Union has introduced several standards governing the rational use of fuel and energy resources (FER). In 2009, the European standard EN 16001: 2009 Energy Management Systems was adopted. Requirements with the instruction for use [4]. In 2011, the International Organization for Standardization ISO/FDIS introduced ISO/FDIS 50001: 2011 (E) Energy Management Systems - Requirements with the instruction for use [11]. This standard was further developed in a series of additional standards, which were also introduced in Ukraine on September 1, 2016. The peculiarity of the standards in this series is that they are based on the methodology of the ISO 9000 and ISO 14000 series of standards.

The fundamental drawback of the quality management methodology implemented in the ISO 9000 series standards, and therefore in other standards based on this methodology, is the absence of requirements for its formation as an automated system.

On the other hand, the national standards DSTU 4472: 2005 and DSTU 4715: 2007 require forming an energy management system as an automated system. At the same time, standards for automated systems that were developed in the 80s of the last century are the basis for the formation of such systems.

A promising direction in the development of automated control systems used by enterprises for energy management is the integration of all aspects of the organization and their management based on modern intelligent information technologies, both in the field of technological process control and in the management of the organization as a whole.

Thus, the analysis of the existing approaches and standards made it possible to find out that there are two mutually contradictory approaches to the organization of energy management systems, which affect the formation of organizational principles and the energy management system's functioning:

- on one side, the methodology for the system deployment and management cycle is under the jurisdiction of the ISO 9000 series of standards;
- on the other side, the creation and functioning of energy management systems should be solved due to the principles applicable to automated control systems using information technology.

Therefore, the purpose of this study is to analyze approaches to the application of energy management at industrial enterprises to identify the basic principles of the formation of organizational structures of energy management systems. Such organizational structures should reflect possible directions for further sustainable development, actions, and established measures that contribute to their implementation.

3 Research Methodology

Modern energy management systems are developing to manage the energy efficiency of technological processes, i.e., for structured decision-making tasks [11]. At the same

time, energy management faces several urgent decision-making problems, for which it is impossible to form a mathematical model of the control unit. Thus, decision-making in integrated energy management systems is carried out under conditions of risk and uncertainty. According to Marko Boganek [12], information technology should be used to solve problems in poorly structured or unstructured decision-making processes.

The decision-making process should be considered well-structured when a mathematical model of the control object can be formed. Investigation of the behavior of a control unit under the influence of appropriate input signals makes it possible to form an appropriate control system for this object. According to this, energy management systems for technological processes can be formed following the principles of forming industrial automatic control systems (IACS), which are currently being actively developed within the framework of the Industry 4.0 concept.

Significant difficulties arise when solving problems of energy efficiency management of energy resources at the enterprise scale. In this case, intelligent information technology is used to structure the decision-making process. That is the fact that companies that have integrated their own computer systems for storing and processing purposes achieved more success than companies that haven't. That is because of using the information gathered from those information systems and their participation in the decision-making process [13]. The basis of this approach lies in the fact that the method of structuring decisions includes a description of the subject area, namely, a description of a control unit by forming a database and forming an appropriate knowledge base based on this data. As a rule, such decision support systems are unique precisely because the database, and therefore the knowledge base, is formed for a specific control object.

For the formation of energy management systems across the enterprise, that is, for the upper strategic level of management, it was proposed to use the intelligent systems presented in [14]. The division of the intelligent system into two parts, proposed by K.O. Pupkov is important for further systems research. In Fig. 2 shows a diagram of the system, on which its two main blocks are highlighted: the synthesis of the goal and its implementation [14].
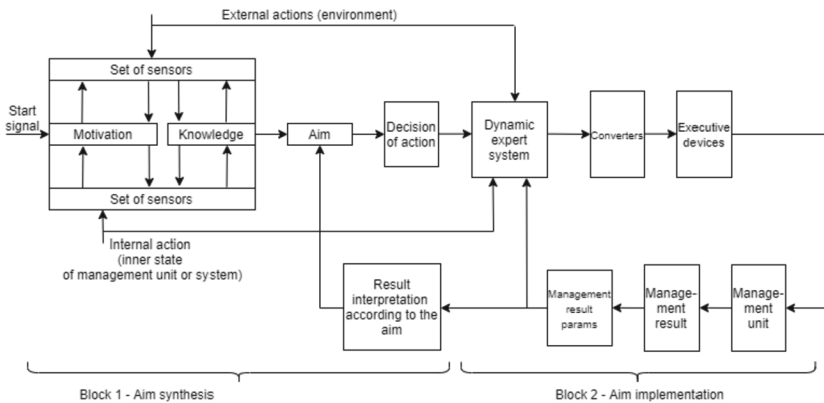
Fig. 2. Scheme of the division of an intelligent system [14].

This consideration of the management process, dividing it into two main stages, allows us to understand how the decision-making process is formed what are its main components.

Formally, the mathematical model of this intelligent decision-making system is described by the following six equations [14]:

$$(T \times X \times S) \xrightarrow{\alpha^1} (M \times T); \tag{1}$$

$$(T \times X \times S) \xrightarrow{\alpha^2} (C \times T); \tag{2}$$

$$(C \times T \times X \times S) \xrightarrow{\alpha^3} (R \times T); \tag{3}$$

$$T \times \overline{X} = A \times T\overline{X} \times T + B \times T\overline{U} \times T; \tag{4}$$

$$T \times Y = D \times T\overline{X} \times T; \tag{5}$$

$$(T \times R \times Y) \xrightarrow{\alpha^4} (C \times T); \tag{6}$$

where T – a set of points in time, X – a set of states of the system, S – a set of environmental conditions, M – a set of states of motivation, C – set of goal states, R –the set of states of the predicted result, Y – a set of states of a real result, A, B, D –matrices of parameters, U – a set of control actions, $\alpha^1 - \alpha^2$ – intelligent transformation operators using knowledge.

Equation (1) describes the process of forming motivation M for activity through specific sets of environmental states S and sets of states of system X by using the intelligent transformation operator α^1.

Based on the generated set of motivations M, Eq. (2) describes the formation of the activity goal C for a certain set of environmental states S by applying the intelligent transformation operator α^2. After forming the goals, the set of states of the predicted result R of the activity is determined based on Eq. (3) using the operator of intelligent transformation α^3. Equation (6) allows you to set the level of achievement of the activity goal by comparing the predicted result R and the actual result Y using the intelligent transformation operator α^4. K.O. Pupkov defines the mathematical model of the intellectual system as follows [14]: "Intellectual operators, realizing perception, representation, formation of concepts, judgments, and conclusions in the process of cognition, are formal means of processing information and knowledge, as well as making decisions. These aspects should be the basis for constructing DES (dynamic expert system), functioning in real-time and in the real world".

We propose to use this approach when determining the organizational structure of the energy management system.

4   Results

The introduction of energy management systems at the stage of production processes, where information processes are supported by the automated control systems of technological processes (APCS) or Manufacturing Execution System (MES), is aimed at

implementing the functions of monitoring, accounting, and analyzing the state of energy processes. At this stage, the result of the decisions ensures only technological processes' efficiency. In this regard, it is often believed that the main direction of the development of automated control systems in the energy sector is the automation of energy efficiency management processes in production processes.

The concept of Industry 4.0 becomes the methodological basis of this direction and concentrates its activities exclusively on the stage of the formation of automated control systems for production processes. In this case, one of the governing factors is the energy efficiency indicator of technological processes. Implementing the energy efficiency management methodology does not imply the formation of a management loop with the involvement of top management, which formulates strategic goals in this type of activity, makes appropriate decisions. Thus, a problem arises, which is that in the energy management systems of enterprises, a management cycle is implemented for management, in which there is no stage of forming the goal of the activity, strategic planning, analysis of the results obtained, correction of goals and, accordingly, their further implementation. To overcome this problem, dialogue management systems are being developed and implemented, which belong to the class of Decision Support Systems.

Today, the Manufacturing Execution System (MES) records the amount of energy consumed. This indicator is an indirect confirmation of the serviceability of technological equipment and is not used in the subsequent stages of planning and strategic management of the enterprise. Most often, the aggregate of accumulated information on the amount of consumed energy is used only for static statistical reports, although based on the accumulated data, it is possible to analyze energy needs and formulate recommendations for efficient energy consumption and over-standardized consumption. Thus, in the scheme of intellectual activity shown in Fig. 2, the necessary information does not fall into the dynamic peer-review stage.

Lack of information in making management decisions is the main problem in implementing the organizational and economic mechanism for managing the development of energy management systems of enterprises [15].

The problem of the incomprehensibility of information can be overcome by introducing an intermediate information system (SCADA), which would ensure the transfer of processed information from the Manufacturing Execution System (MES) subsystems that control energy consumption to the upper level of strategic decision formation in the decision expert evaluation unit.

The low-efficiency level of implementation of energy-saving measures is because of the lack of a systematic approach to making managerial decisions [16]. The adoption of balanced strategic management decisions is possible only with enough information obtained from the stage of technological process control and with a comprehensive consideration of all aspects of management. The low level of automation of energy management tasks at the stage of forming strategic decisions by the administration of enterprises reduces the efficiency and adequacy of management decisions. This process must be intelligently supported in the form of intelligent decision support systems.

Energy management should be carried out considering the close relationships of a significant number of factors influencing the process of energy consumption. Consequently, when studying energy management systems of enterprises to find methods of

strategic management, it is advisable to use the methodology of systems analysis. A systematic research approach allows considering the connections of the system under study with external systems relative to it, taking into account the hierarchy of such systems and their control processes, and also allows taking into account the uncertainties caused by the incompleteness of the incoming information, multi-criteria and other factors [17].

To reduce the influence of the "human" factor in decision-making and avoid the problems of excessive centralization, it is necessary to move to the lower level not only the issues of monitoring or control but also the issues of decision-making that correspond to the support of functional states, thereby changing the concept of building and developing the system. This changes the traditional management model and moves from a divisional linear model to an integrated project approach when building an organizational management structure at all levels.

5   Conclusions

Thus, the following conclusions can be drawn by summarizing and analyzing the research results.

There are two approaches to support energy efficiency in enterprises: modernization of enterprise assets to save energy and energy management and control energy distribution and consumption.

When implementing energy management, two main approaches are used. One of them is based on the principles of process management based on the ISO 9000 standards. The other proposes to build the management of the energy management system as an automated control system.

You can carry out energy management in process control systems using the latter approach. But this has significant limitations since the information for making strategic decisions is not transferred to the upper levels of management. To overcome this problem, it is suggested:

– organize the transfer of information from technological systems to decision support systems through SCADA systems;
– use intelligent decision-making technologies;
– to form, on their basis, decision support systems for senior management;
– to avoid the problems of excessive centralization, to transfer to the lower level of decision-making support for decisions that ensure the current state of the energy-saving object.

The use of such a methodology will allow in the future to form new principles for organizing the structure of energy management of enterprises and move on to the following actions to develop them:

• to provide coverage of all more or less significant objects of the system with globally distributed networks of "downstream";
• implement an advanced low-level process control architecture;
• introduce artificial intelligence at every level of management;

- to carry out the transition to autonomous management of lower-level objects according to previously prepared or newly created scenarios;
- create accessible interfaces for public access to the energy management system;
- organize cloud services for access to the energy management system for senior management.

References

1. Energy management. http://kazakhaudit.kz/energomenedjment. Accessed 12 Oct 2021
2. Energy management definition. https://msd.com.ua/osnovy-energosberezheniya/ponyatie-energeticheskogo-menedzhmenta/. Accessed 12 Oct 2021
3. Rozen, V.P., Solovei, A.I., Inshenkov, E.N., Cherniavsky, A.V.: Introduction of energy management system at industrial enterprises of Ukraine. Bull. KhNTUSG "Probl. Energy Supply Energy Saving Agro-Ind. Complex Ukr." **27**, 188–189 (2004)
4. Rozen, V.P., Cherniavsky, A.V.: Energy management standardization, implementation and functioning. PromElectro **2**, 47–54 (2011)
5. Dynnyk, O., Denysenko, Y., Zaloga, V., Ivchenko, O., Yashyna, T.: Information support for the quality management system assessment of engineering enterprises. In: Ivanov, V., et al. (eds.) DSMIE 2019. LNME, pp. 65–74. Springer, Cham (2020). https://doi.org/10.1007/978-3-030-22365-6_7
6. Lasinska, N.: Hybrid management methodology for transport projects related to rolling stock. J. Eng. Sci. **8**(2), B7–B11 (2021). https://doi.org/10.21272/jes.2021.8(2).b2
7. BS EN 16001:2009 Energy management systems - requirements with instructions for use. https://smartcons.org/standards/bs16001/. Accessed 12 Oct 2021
8. ISO/FDIS 50001:2011(E) Energy management systems - requirements with guidance for use. https://www.iso.org/standard/51297.html. Accessed 12 Oct 2021
9. SS 627750:2003 Energy Management Systems – Specification. https://www.sis.se/en/produkter/management-system/energy-management-systems/ss627750/. Accessed 12 Oct 2021
10. Khokhliavin, S.: Energy management standards: USA, Korea EU and other countries. Energyaudit **2**, 34–39 (2009)
11. Nakhodov, V., Borychenko, O., Cherniavskyi, A.: The methodical issues of industrial energy monitoring systems implementation. Power Eng.: Econ. Tech. Ecol. **3**, 47–56 (2020). https://doi.org/10.20535/1813-5420.3.2020.228616
12. Mladenić, D., Lavrac, N., Bohanec, M., Moyle, S.: Data Mining and Decision Support. Integration and Collaboration. Springer, Boston (2003). https://doi.org/10.1007/978-1-4615-0286-9
13. Tole, A.A., Matei, N.C.: Executive information systems' (EIS) structure and their importance in decision-making. A comparison between decision support computer systems. J. Inf. Syst. Oper. Manag. Roman. Econ. Bus. Rev. **10**(1), 194–207 (2016)
14. Pupkov, K.O., Konkov, V.G.: Intelligent Systems. Bauman MGTU, Moskow (2003)
15. Doroshenko, V.: Improving the organizational-economic mechanism for managing the development of the city's heat supply system. Socio-Econ. Probl. State **1**(6), 48–58 (2012)
16. Yevtukhova, T.O., Simborskiy, A.I.: The current state of communal energy in Ukraine. Probl. Gener. Energy **17**, 31–36 (2008)
17. Voropai, N.I.: Systemic research in energy. Retrospective of scientific directions SEI-ISEM. Nauka (2010)

Intelligent Mechatronic Systems Applications in Engineering

Sahin Yildirim[(✉)] [ID]

Erciyes University, 1, Yenidoğan Mahallesi Turhan Baytop Sokak, Talas/Kayseri 38280, Turkey
`sahiny@erciyes.edu.tr`

Abstract. This paper presents some experimental applications using intelligent systems such as sensors, controller, robotic systems, and crane systems. A Mobile robot design, path planning, and applications in real-time is proposed for blind people. A proposed A* algorithm is used for path planning of the mobile robot. Moreover, an image processing structure predicts the path without touching obstacles. An industrial robot is used with image processing to classify universal materials. On the other hand, a new walking performance six-legged mobile robot control is proposed to analyze the stability and walking conditions of the robot by using an open dynamic engine solution. Furthermore, a designed and controlled crane system is proposed for vibration and amplitude analysis of the double bridge crane system. On the system, a prosed neural predictor is used to analyze performance. Analysis and control of the welding position of an industrial robot are also utilized to compare with operator-based welding process structure. The results improved that all the proposed analyze has superior performance in real-time applications for all approaches.

Keywords: Intelligent systems · Robotic system · Path planning · Crane systems · R&D investment · Product innovation

1 Introduction

Nowadays, some researchers have been proposed, studied, and investigated algorithms for the path planning of mobile robots. Satapathy and Kumar have been focused on the path planning algorithm for a proposed mobile robot with a comparative study in a different environment. In their investigation, the proposed algorithm has good performance for following exact trajectories [1]. Another approach was a kind of simple local path planning algorithm for autonomous mobile robots [2]. A based on the occupancy grid map of the environment has been used for the path planning algorithms for a mobile robot [3]. There has been some investigation related to intelligent path planning of mobile robot agents by using breadth-first search algorithm [4]. Guruji et al. proposed an A* Algorithm for Robot Path Planning. The proposed algorithm has superior performance to follow the prescribed trajectory with disturbances [5]. Another approach has been related to a totally film-based multi-path algorithm for recognition. [6]. Some indoor applications have been studied. A path planning algorithm for low-cost autonomous robot navigation in indoor environments [7]. On the other hand, some virtual approaches have been

proposed, such as Web-Assisted laboratory for control education: remote and virtual environments [8].

2 Literature Review

It is aimed to design and implement a mobile robot that will enable blind people to travel easily from one place to another (Fig. 1). The study consists of mobile robot design, mapping of working environment, mobile robot localization, path planning, and controller design.
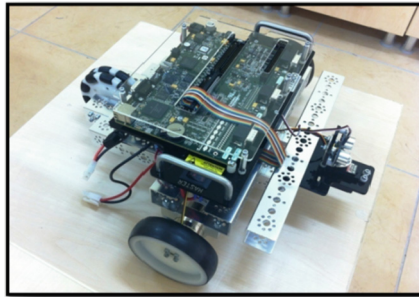
Fig. 1. The proposed designed and controlled mobile robot.

The main target of this project is designing the robotic system and control approach, which enables blind persons to go from one place to someplace on a determined path with a minimum error by the guidance of a mobile robot (Fig. 2).
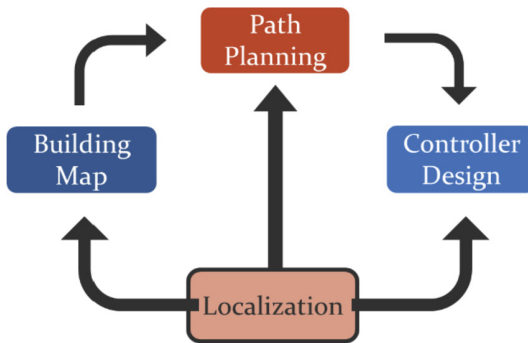
Fig. 2. Flow process diagram of the mobile robots.

The optimum path is planned to use a proposed algorithm based on the traditional A* algorithm, and its performance is tested for different situations. An avoidance area is calculated on the map for the mobile robot, and curve fitting methods are applied to the path calculated by the A* algorithm to generate a smooth trajectory with continuous

headings. National Instruments LabView Robotics software development environment is used during all programming processes [9, 10]. Finally, the controller design is carried out to track the trajectory with minimum error, and the performance is tested experimentally (Fig. 3). In that sense, the project is presented as an important and innovative study that eases the life of blind people.
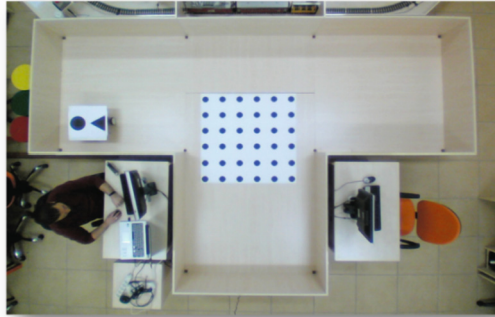
Fig. 3. Representation of experimental setup [11].

A proposed algorithm is presented to improve the capabilities of the A* algorithm which is a best-first path planning algorithm (Fig. 4). An avoidance area is calculated for the mobile robot, and curve fitting methods, general polynomial, and b-spline are applied to the path the A* algorithm calculates to generate a smooth trajectory with continuous headings.
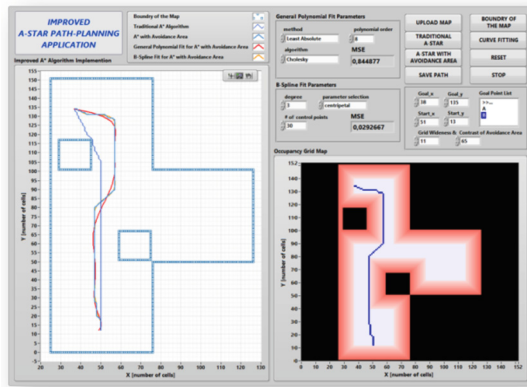
Fig. 4. View of the improved path-planning window [11].

3   Research Methodology

The dynamic model required for model-based control is designed on the ODE (Open Dynamics Engine) platform to represent the exact system. In this control process, where a layered architecture is preferred, the joint controllers of the six-legged mobile robot were developed first. Then, using these developed joint controllers, a balance control layer was created in which the robot would automatically compensate according to the external disturbance slope effects.

In addition to this layer, a gait controller has been added to the system, which allows the application of the standard walking gaits (Tripod-Quadruped-Tetrapod) to the robot. Afterward, the performance increase achieved by this walk controller was investigated, a two-axis steerable test platform. Finally, to improve the walking performance, a walking simulator with parallel programming support was developed, and the parameters of the controllers were tuned by using this simulator (Fig. 5).
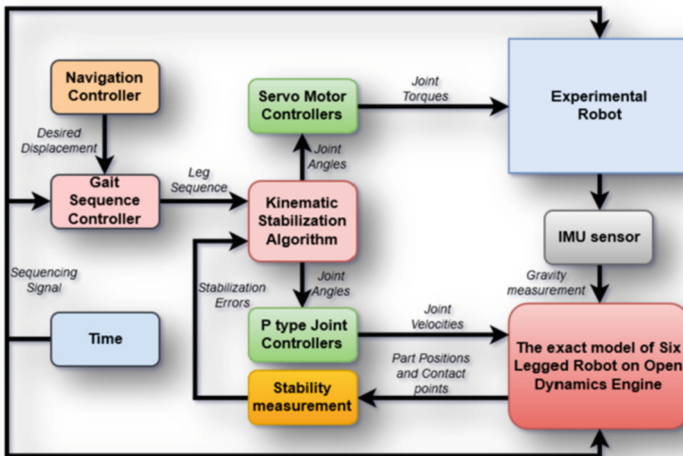
Fig. 5. The proposed control structure [12].

An ODE-based dynamic model is used in this model-based control system instead of the reference system model. Using a physical simulator in the reference model, dynamic factors such as inertia effects or friction forces caused by motion can be easily compensated during the control process. In this study, a performance criterion required to evaluate the results of the ODE-based balance and gait control that we developed earlier has been developed. Most of the stabilization margins used in legged mobile robots represent how stable the robot is in its current state. In this proposed method, based on the resemblance of the repetitive steps, a stability margin representing the quality of the entire walk has developed.

The six-legged robot we use in our experiments has shown in Fig. 6. The RaspBerry Pi SoC, which ODE-based walking control algorithm coded on it. The IMU (Inertial Measurement Unit) sensor is located at the center of the robot's trunk, also seen from the

figure. The total weight of the robot is 2.4 kg, and it is controlled by a total of 18 servo motors, 3 in each leg. The servo motors used on the robot are Dynamixel AX-12. Many data such as load, speed, and position can be read simultaneously from these servos. For communication between RaspBerry Pi SoC and servos, a USB2 Dynamixel converter is used.
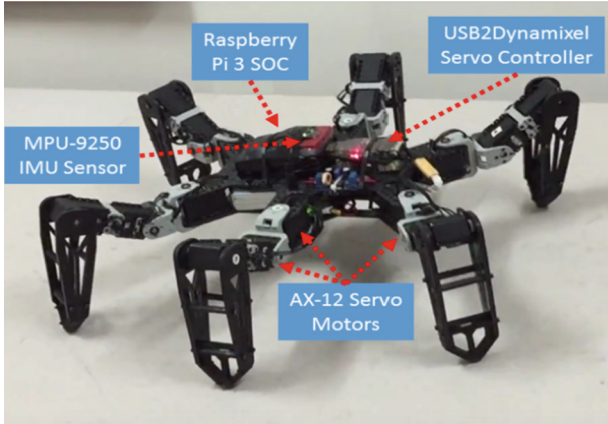
Fig. 6. The proposed six-legged walking robot [12].

A lot of walking patterns can be used in legged mobile robots. These walking patterns are also named walking gaits in technic. For six-legged mobile robots, there are three basic walking modes. These are known as walking tripod, quadruped, and pentapod, respectively. The walking gaits are formed by moving the legs sequentially (Fig. 7).
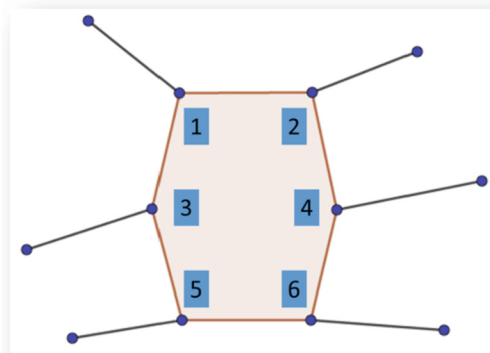
Fig. 7. Walking leg sequent of the robot [12].

As a result of the experiments, it was seen that the most stable movement was made in the quadruped walking gait (Table 1).

Table 1. Velocity variations with different walking types [12]

Gait type	Proposed margin	Area (mm*s)	Velocity (mm/s)
Tripod	7,27	35,73	10
Quadruped	0,07	19,56	5
Pentapod	60,84	52,52	3,33

4   Results

4.1   Dynamic of Crane Systems Three Car Crane System with Moving Load

The dynamic effects that occurred during the experimental loading of one or more carriages on a double bridge overhead crane system were tested under different carriage speeds and different loads. Also, vibration measurements were carried out at different points on the bridges.

The front view of the overhead crane system used in this work and operating phases are given in Fig. 8. This study was conducted to study the case where the carriage moves on bridges of crane system (Fig. 9).
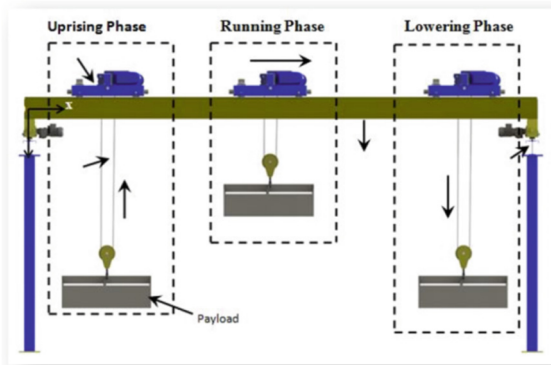
Fig. 8. The front view of the overhead crane system and operating phases [13].

Performance analysis of the proposed three-car crane system is investigated by using two types of neural network predictors. These are the backpropagation neural network (BPNN) and radial basis neural network (RBNN). As shown in Table 2, the proposed RBNN has superior performance for predicting vibration of 3 car crane systems with 700 kg and 1260 kg loads. Furthermore, this kind of neural predictors can be employed in such systems in real-time applications for the good performance of cranes.
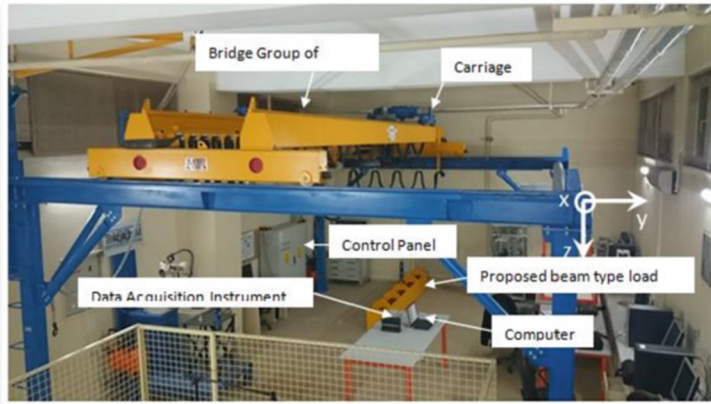
Fig. 9. Experimental crane system apparatus [13].

Table 2. Experimental and simulation results with two types of neural network types.

Operating conditions			NN type	Neuron numbers			RMSEs
Case	Load (kg)	Car speed (m/s)		Input (n_I)	Hidden (n_H)	Output (n_O)	
One car	700	0,3	BPNN	3	10	5	0,1942
			RBNN	3	10	5	0,0952
	1260	0,3	BPNN	3	10	5	0,1493
			RBNN	3	10	5	0,0778
Two cars	700	0,3	BPNN	3	10	5	0,1375
			RBNN	3	10	5	0,0574
	1260	0,3	BPNN	3	10	5	0,0796
			RBNN	3	10	5	0,0682

4.2   Analysis of Material Classification

In this study, using computer and image processing, the classification of materials with different shapes and sizes on the belt conveyor has been performed using a Motoman robot manipulator. The computer, Labview, Universal Gripper, and Motoman SV3X model robot manipulator were used for this process (Fig. 10, 11).

Lab-view software was used to predict the position of the different types of objects on the movement of the conveyor systems with constant speed (Fig. 12). The classification process was improved by analyzing the materials' field information and shape properties to be classified with the developed image processing techniques. A universal gripper was employed to grasp different types of objects with good performance.
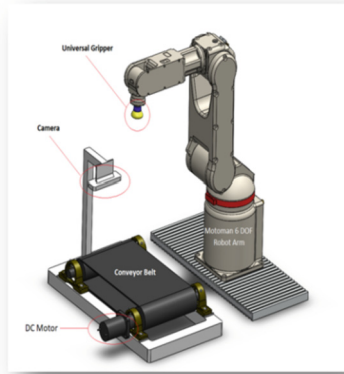
Fig. 10. Designed system view.

Fig. 11. Experimental setup.
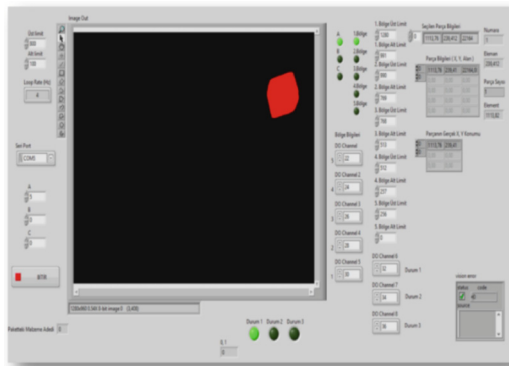
Fig. 12. Lab-view window representation [14].

Two different methods have been used for classification. These methods apply area calculation and shape matching operations (Tables 3, 4). If the area values are close to each other, but the shape properties are different from each other, the shape matching method is suitable. It is suitable to use the area calculation method to classify materials that are similar to each other but have different area values.

Table 3. Particle analysis results.

	A	B	C
Mass Center X Position	601,34886 pixel	253,76225 pixel	990,50005 pixel
Calibrated Mass Center X Position	117,54278 mm	49,60169 mm	193,60830 mm
Mass Center Y Position	476,12284 pixel	457,71959 pixel	501,09352 pixel
Calibrated Mass Center Y Position	93,06545 mm	89,46825 mm	97,94635 mm
Area	18039,00 pixel × pixel	35904,00 pixel × pixel	42032,00 pixel × pixel

Table 4. Shape matching results.

	A	B	C
Center X Position (pixel)	601	254	990
Center Y Position (pixel)	476	458	501
Score (Max. 1000)	1000	996	1000

4.3   Analysis and Control of Welding Trajectory in Industrial Robots

This section is proposed to compare the operator-based welding process and the automated robot manipulator-based gas welding process on a prescribed trajectory. As shown in Fig. 13, the material is steel with a sudden prescribed welding trajectory position.

This experimental work used an industrial KUKA-type robot manipulator as an automated welding robot manipulator for joining steel plates. Fronius arc welding apparatus was also used for supplying arc, a high definition camera, a steel welding table, and steel material pieces as experimental pieces for testing and computer (Fig. 14).

The following diagram is an overview of the trajectory determination method and neural network predictor (Fig. 15).

As shown from Fig. 15, image processing is employed to ignore the edge of the welding positions. The proposed trajectory has a sudden change of welding positions (Fig. 16).
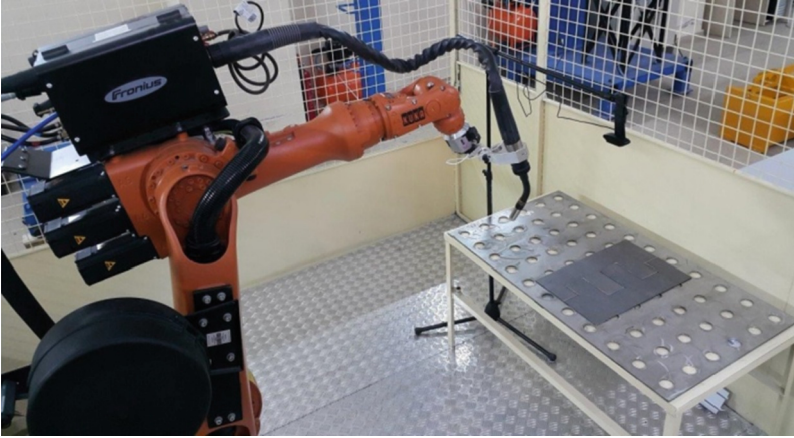
Fig. 13. The view of the industrial robot manipulator system with welding torch [15].
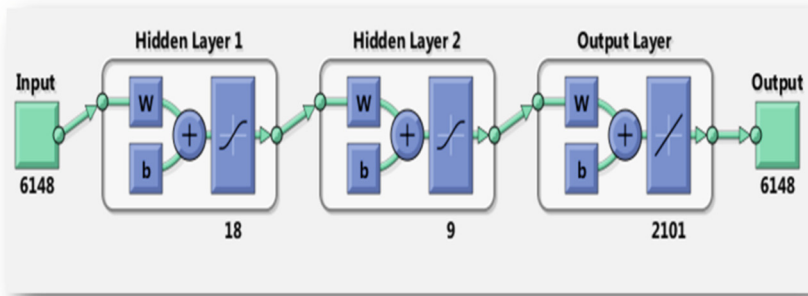
Fig. 14. Representation of the proposed neural network schematic view.
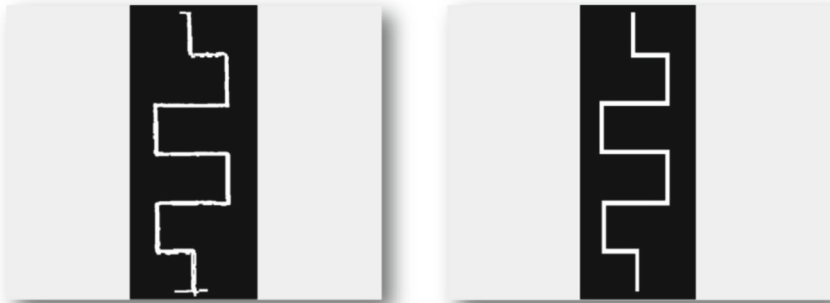
Fig. 15. Experimental result and edging the faults [14].
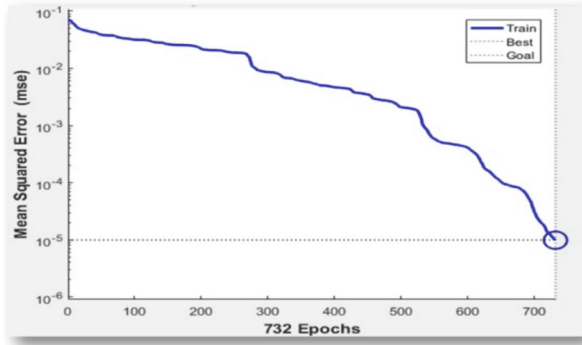
Fig. 16. The best training performance with 9.8454e−06 at 732 iterations [14].

5 Conclusions

This paper has presented some novel approaches to developing mechatronic systems for improving automation systems. Especially, the proposed systems have been investigated in real-time applications such as analysis of three car crane systems, trajectory planning intelligent mobile robots, analysis of welding process with a robot manipulator. On the other hand, material classification has been improved by using an intelligent universal gripper with an industrial robot manipulator. Stability and leg walking movement position have been analyzed using the ODE method for a six-legged mobile robot.

The results of these investigations have shown that the proposed approaches have good performance rather than standard methods. Furthermore, the neural networks predictors have superior performance for analyzing the mechatronic systems' performance of real-time applications.

References

1. Satapathy, D., Kumar, G.J.R.: Path planning algorithm for a mobile robot – a comparative study in different environment. IJCTA **9**, 453–459 (2016)
2. Čikeš, M., Đakulović, M., Petrović, I.: The path planning algorithms for a mobile robot based on the occupancy grid map of the environment - a comparative study. In: 2011 XXIII International Symposium on Information, Communication and Automation Technologies, Sarajevo, Bosnia and Herzegovina, pp. 1–8 (2011)
3. Subramanian, M.B., Sudhagar, D.K., RajaRajeswari, G.: Intelligent path planning of mobile robot agent by using breadth first search algorithm. In: 2014 IEEE International Conference on Innovations in Engineering and Technology (ICIET 2014), pp. 1951–1955. Madurai, Tamil Nadu, India (2014)
4. Subramanian, M.B., Sudhagar, D.K., Rajarajeswari, G.: Autonomous mobile robot agent path planning based on VFH method using heuristic based optimal algorithm. Int. J. Appl. Eng. Res. **10**, 5189–5194 (2015)
5. Guruji, A.K., Agarwal, H., Parsediya, D.K.: Time-efficient A* algorithm for robot path planning. Procedia Technol. **23**, 144–149 (2016)
6. Yin, W., Yang, X.: A totally Astar-based multi-path algorithm for the recognition of reasonable route sets in vehicle navigation systems. Procedia Soc. Behav. Sci. **96**, 1069–1078 (2013)

7. Pala, M., Osati, N., López-Colino, F., Sanchez, A., Castro, A., Garrido, J.: HCTNav: a path planning algorithm for low-cost autonomous robot navigation in indoor environments. ISPRS Int. J. Geo Inf. **2**, 729–748 (2013)
8. Leão, C.P., et al.: Web-assisted laboratory for control education: remote and virtual environments. In: Uckelmann, D., Scholz-Reiter, B., Rügge, I., Hong, B., Rizzi, A. (eds.) The Impact of Virtual, Remote, and Real Logistics Labs. ImViReLL 2012. Communications in Computer and Information Science, vol. 282, pp. 62–72. Springer, Heidelberg (2012). https://doi.org/10.1007/978-3-642-28816-6_7
9. General Polynomial Fit VI - LabVIEW 2014 Help, National Instruments Corporation (2014)
10. B-Spline Fit VI - LabVIEW 2011 Help, National Instruments Corporation (2011)
11. Savas, S.: Mobile robot design, path planning and control for blind people. Ph.D. thesis, Graduate School of Natural and Applied Sciences, Erciyes University, Kayseri, Turkey (2019)
12. Arslan, E.: Parallel programming supported balance and walk control for six legged mobile robot. Ph.D. thesis, Graduate School of Natural and Applied Sciences, Erciyes University, Kayseri, Turkey (2018)
13. Esim, E.: Design, implementation and dynamic analysis of experimental multi carriage crane systems. Ph.D. thesis, Graduate School of Natural and Applied Sciences, Erciyes University, Kayseri, Turkey (2019)
14. Ozak, B.: Robot manipulators design and an experimental application with image processing for materials classification. MSc thesis, Graduate School of Natural and Applied Sciences, Erciyes University, Kayseri, Turkey (2017)
15. Ulu, B.: Analysis and control of weld seam trajectory on the robot manipulator. MSc thesis, Graduate School of Natural and Applied Sciences, Erciyes University, Kayseri, Turkey (2017)

Design Engineering

An Element Deletion Algorithm
for an Open-Source Finite Element Software

Zaki Alomar$^{(\boxtimes)}$, Cristian Cappellini , and Franco Concli

Free University of Bolzano/Bozen, Universitätsplatz 1, 39100 Bolzano, Italy
zalomar@unibz.it

Abstract. In a fracture analysis, predicting the fracture location and the progression of the failure is of high importance. An element deletion algorithm is a powerful tool used to visualize the failure evolution and get rid of the distorted elements that prevent the simulation from converging. Primarily, such an algorithm is only found in commercial software such as Abaqus. A similar algorithm was developed and implemented into the Code_Aster platform in this work. The algorithm's effectiveness was tested through a non-linear analysis on a Cor-Ten specimen with notches under uniaxial tension. The element deletion functionality was implemented by defining a virtual material with low stiffness to the deleted elements. The results obtained demonstrated the code's capability in accurately representing the failure progress along the notches. Moreover, by assigning a virtual material to the deleted elements, a complete fracture of the specimen is observed without facing any convergence issues. Overall, the shape of the fracture for a notched specimen conforms well to the physical failure of a ductile material such as Cor-Ten.

Keywords: Code_Aster · Fracture modeling · Numerical analysis · Sustainable manufacturing

1   Introduction

Finite Element Analysis (FEA) is an essential tool in the arsenal of many industrial sectors. The importance of FEA lies in its ability to provide all the necessary information about the structural integrity of a complex design under various load scenarios. The ability to predict the failure of a structure prior to physically building it reduces the industries' need for extensive prototyping. The structure can be iteratively tested and optimized until a satisfactory design is achieved, which subsequently leads to a huge cut in the manufacturing costs (in terms of both time and money).

A variety of FEA software currently exists. Generally, the software can be divided into two main categories: commercial and open-source platforms. The commercial FEA software is reliable and user-friendly, but the license costs of such software are significantly high, and it is fundamentally a 'black-box' for the users. Conversely, open-source FEA software is license-free characterized by a high level of transparency. For instance, one can easily access the source code and modify it to implement new functionalities and

attributes typically unavailable in other commercial software [1–3]. The characteristics mentioned above have shifted the interest of many industries and academic institutes towards open-source platforms, especially for the structural analysis of solids.

This paper aims to introduce an elements-deletion algorithm into an open-source FEA software to visually identify the progression of failure in a structure under a specific load. To achieve this target, "Code_Aster" was utilized in this study. The French Department of Energy (EDF) developed and maintained this software. It is based on the Python scripting language, which was employed to introduce our algorithm and expand the functionality of the Code_Aster software.

2 Literature Review

The element deletion technique has already been implemented in a couple of well-known commercial software such as "ABAQUS" and "LS-DYNA". Nevertheless, the use of this technique is still somewhat limited owing to the high level of expertise needed to exploit its functionality reliably. The main purpose of utilizing element deletion is to get rid of the highly distorted elements in an explicit analysis to reach numerical convergence and subsequently proceed with the simulation. However, deleting elements in standard or implicit simulation leads to severe convergence difficulties. Therefore, element deletion is mostly used in explicit simulation, such as the simulation of a crash [4], an impact [5, 6], machining [7], and damage evolution in ductile materials [8, 9]. Additionally, the excessive deletion of elements often results in energy and mass losses from the system, leading to underestimating the expected results.

Marco et al. [10] modeled the femur bone fracture using Abaqus/Explicit while enabling the element deletion algorithm to track the crack growth. The user subroutine employed in that study compares the maximum principal strain with the critical strains of each material. When the maximum principal strain ratio to the critical one reaches a unity, the corresponding elements are deleted. The results of the simulation, shown in (Fig. 1), proved the capability of the element deletion subroutine to model the crack growth up to a certain extent. Yet, it failed to adequately represent the fracture morphology due to convergence difficulties faced when simulating long crack paths.

(a)   (b)
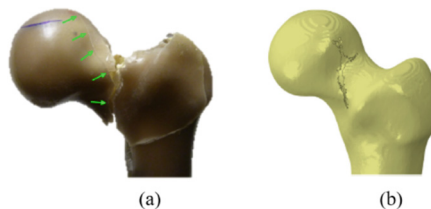
Fig. 1. The path of the crack growth obtains (a) experimentally and (b) numerically using the element deletion subroutine [10].

Similarly, Belda et al. [11] modeled the quasi-static compression fractures of cancellous bone. The authors used a combination of continuum damage mechanics and

the element deletion technique to simulate the local fracture of the trabeculae at the micro-scale level. Using the continuum damage approach, the failure was modeled as a material degradation to describe the progressive stiffness loss due to the progression of micro-defects in the model. After that, the complete fracture was introduced by element deletion Abaqus/explicit subroutine. The fracture pattern predicted by the FEA analysis was relatively in good agreement with the experimental outcomes.

Element deletion is also helpful in machining and cutting tool modifications. Muaz and Choudhury [12] were able to numerically model and simulate multiple rotations of modified milling inserts using coupled-temperature-displacement analysis. The excessively damaged elements were removed from the mesh during the cutting simulation. The model was validated by comparing the numerically predicted temperature with the experimental outcomes. The error obtained was just about 6.1%.

Woldman et al. [13] modeled the abrasive wear modes in machine components operating in sandy environments. Element deletion introduces volumetric wear through a shear damage criterion based on both fracture strains and equivalent plastic displacement. The abrasive modes observed experimentally were accurately represented numerically following the latter approach.

Generally, the element deletion is a powerful tool with enormous potential yet to be fully exploited. This work focuses on creating a simple element deletion algorithm similar to the Abaqus subroutine for the open-source software "Code_Aster".

3   Research Methodology

The Code_Aster platform does not have the option to remove elements during post-processing. This option is only available in the mesh module, making the development of element deletion difficult. However, the software allows for the addition of elements. The latter can be exploited to extract only the elements needed and use them in a new model, which typically implies removing unwanted elements. Luigi Giaccari [14] wrote a script that performs structure optimization by material removal following the abovementioned approach. Herein, the code written follows the same approach, and it is intended to delete elements once they reach the material's tensile yield strength.

3.1   The Framework of the Code

The code is divided into two main functions. The first function extracts the values of the quantity of interest (in our case, the von Mises values at the nodes) and identifies the number of nodes with a higher value than a user-specified threshold. The second function groups together all the elements whose nodes did not reach the critical value.

Figure 2 shows the flow chart of the first function. The von Mises Value of each node is extracted from the Code_Aster table obtained via the simulation. An empty list is created, so the number of each node deleted is appended there. A for loop is used to screen through all the von Mises values and compare them to the yield strength of the material. The designated numbers of nodes with a higher stress value than the threshold are saved in the empty list.

The flow chart (Fig. 3) depicts how the new model elements are grouped together. In the beginning, a new empty list is created to accommodate the new group of elements. In Code_Aster, it is possible to obtain the connection of each element in the mesh in terms of the nodes where each node has a designated number. Using a for loop, it was possible to go through all the elements and check whether any of the elements has in its connection one of the numbers appended in the list of the first function. If the latter holds, the element is ignored; otherwise, it is added to the new list as a string (i.e., M12). The new list is then used as the basis of the new model in a new mesh.
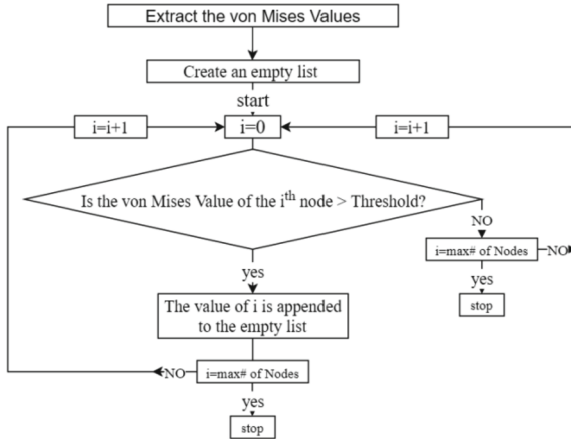
Fig. 2. The flowchart of the first part of the element deletion code describes the method in which the nodes with high stresses are identified.
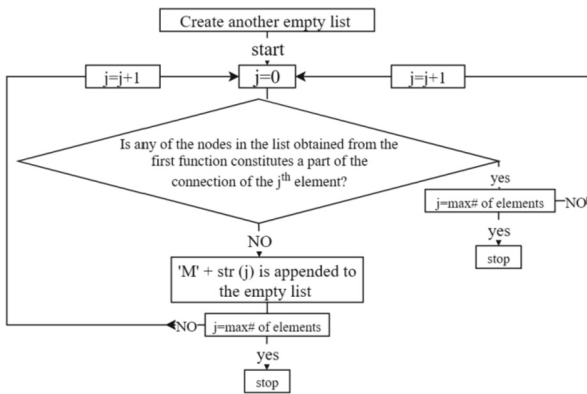
Fig. 3. The flowchart of the second part of the element deletion code describes the method in which the new model elements are identified and grouped together.

3.2   Simulation Setup

To test the effectiveness of the element deletion code, a two-dimensional non-linear analysis was carried out on a specimen under uniaxial tension. The specimen is designed with 2 notches, as shown in (Fig. 4a). Knowing that the stresses will be the highest at the notches, the mesh is refined only in that location (Fig. 4b) to better showcase the functionality of the element deletion code without drastically increasing the computational cost.
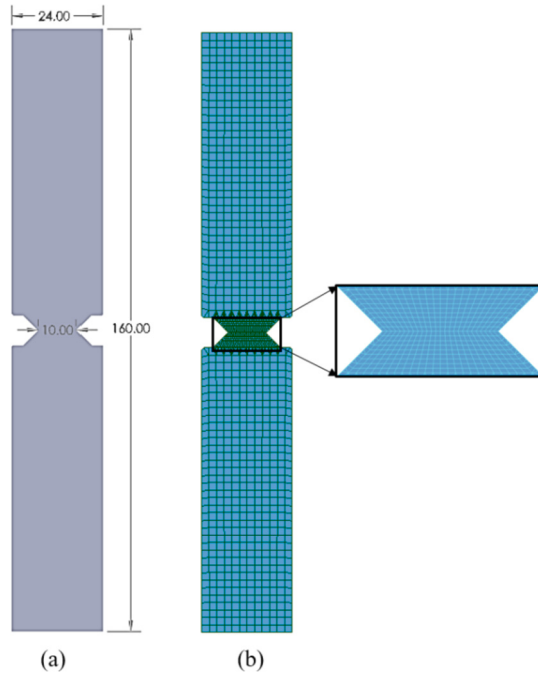
Fig. 4. (a) CAD drawing of the specimen and (b) the corresponding mesh. The dimensions are in mm.

The material used in this study is Cor-Ten having a modulus of elasticity of 210 GPa, a Poisson ratio of 0.30, and a yield strength of 375 MPa (the threshold value in this work). The non-linear behavior of the material was also introduced in the simulation according to the data provided in [15]. The tensile test is performed by applying an incremental displacement of 0.4 mm at the top edge of the specimen every 1 s. The bottom edge was completely fixed.

Implementing the new group of elements acquired from the code requires the creation of a new mesh and subsequently a whole new simulation. Therefore, fields of stresses and displacements are created in between the simulations and projected into the new mesh or model. In this way, the energy of the system is somehow conserved. Also, removing the element completely resulted in convergence issues since it is an implicit simulation.

To solve this issue, the element that should be deleted is assigned a virtual material with 1% stiffness of the actual material. That group was excluded from the results output.

4   Results

A total displacement of 5.2 mm is imposed in 13 steps where each step corresponds to 1 s. After each step, the results are reported in the form of equivalent von Mises stresses. Figure 5 presents the von Mises stresses distribution in the specimen at 9 different time steps at the vicinity of the notches.
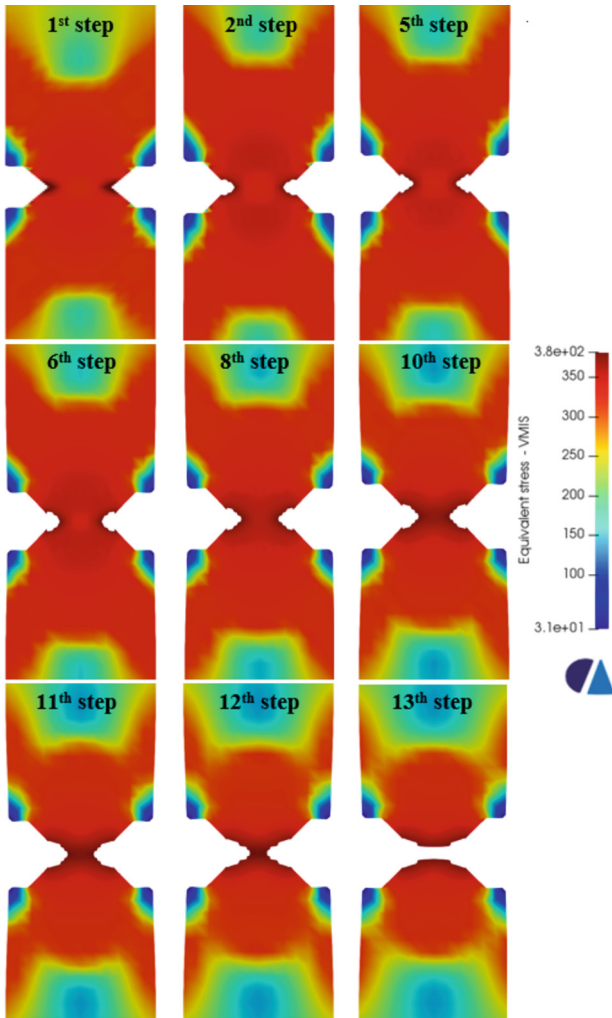
Fig. 5. The equivalent von Mises stresses at different time steps at the proximity of the notches. The stresses are displayed in MPa.

The initial number of elements in the model was 2034. After the first simulation, the number of elements decreased to 1536 and became 1440 at the last simulation. It should be noted that between the second and third simulations and between the fourth and the fifth, the number of elements did not change since the threshold value was never reached.

Evidently, it was clear that the element deletion code effectively removed the proper element and predicted the failure path. The 13th step in (Fig. 5) shows a complete fracture of the specimen. The shape of the fracture for a notched specimen conforms well to the failure of a ductile material such as the Cor-Ten material studied herein. The complete fracture of elements was made possible due to the integration of a virtual material in our code. The same simulations were also tested without assigning a virtual material. The results of only two-time steps were obtained before the ending of the simulation due to a convergence error. However, this should not be an issue in an explicit simulation, and the code should theoretically work fine. This will be investigated thoroughly in the near future.

The results obtained in this study are just an example of the capabilities of the element deletion code. Different failure criteria can be chosen according to the required analysis and to the material behavior. For instance, the temperature can be the failure criterion in the case of thermal analysis. Considering the material behavior, dedicated failure criteria should be implemented for evaluating and testing the fracture evolution of a wider range of different materials. Further investigations will be performed in this direction. The options are just limitless, especially with the freedom offered by the open-source software.

5   Conclusions

This work presents a new element deletion algorithm based on the assignment of a virtual material with very low stiffness to elements with stresses higher than the yield strength. The code is implemented into the open-source software Code_Aster to simulate the fracture behavior of a Cor-Ten specimen with notches under tension. From the results of the simulations conducted, the following points are concluded:

- The element deletion algorithm alone is not sufficient for implicit simulation as it leads to many convergence issues.
- The expected deleted elements are assigned with virtual material having lower stiffness. This approach prevents convergence errors in implicit simulation, allowing us to visualize the complete fracture of the specimen.
- The developed code was capable of predicting the failure path of the specimen as the stresses increased in each simulation.
- The complete fracture of the specimen adopted in this study conforms well to the physical fracture of the ductile materials such as Cor-Ten.
- The algorithm presented offers a high potential in fracture analysis and other fields of computational modeling.

References

1. Zaheer, M., Lindh, P., Aarniovuori, L., Pyrhonen, J.: Comparison of commercial and open-source FEM software: a case study. IEEE Trans. Ind. Appl. **56**, 6411–6419 (2020). https://doi.org/10.1109/TIA.2020.3015827

2. Huo, Z., Mei, G., Xu, N.: juSFEM: a Julia-based open-source package of parallel smoothed finite element method (S-FEM) for elastic problems. Comput. Math. Appl. **81**, 459–477 (2021). https://doi.org/10.1016/J.CAMWA.2020.01.027

3. Meng, Q.X., Xu, W.Y., Wang, H.L., Zhuang, X.Y., Xie, W.C., Rabczuk, T.: DigiSim – an open source software package for heterogeneous material modeling based on digital image processing. Adv. Eng. Softw. **148**, 102836 (2020). https://doi.org/10.1016/J.ADVENGSOFT.2020.102836

4. Shi, D., Xiao, X.: An enhanced continuum damage mechanics model for crash simulation of composites. Compos. Struct. **185**, 774–785 (2018). https://doi.org/10.1016/j.compstruct.2017.10.084

5. Takazawa, H., Hirosaka, K., Miyazaki, K., Tohyama, N., Saigo, S., Matsumoto, N.: Numerical simulation of impact loading for reinforced concrete wall. Int. J. Press. Vessel. Pip. **167**, 66–71 (2018). https://doi.org/10.1016/J.IJPVP.2018.10.010

6. Dewangan, M.K., Panigrahi, S.K.: Finite element analysis of hybrid 3D orthogonal woven composite subjected to ballistic impact with multi-scale modeling. Polym. Adv. Technol. **32**, 964–979 (2021). https://doi.org/10.1002/pat.5143

7. Priest, J., Ghadbeigi, H., Avar-Soberanis, S., Gerardis, S.: 3D finite element modelling of drilling: the effect of modelling method. CIRP J. Manuf. Sci. Technol. **35**, 158–168 (2021). https://doi.org/10.1016/j.cirpj.2021.06.001

8. Seupel, A., Hütter, G., Kuna, M.: An efficient FE-implementation of implicit gradient-enhanced damage models to simulate ductile failure. Eng. Fract. Mech. **199**, 41–60 (2018). https://doi.org/10.1016/j.engfracmech.2018.01.022

9. Estrada, Q., Szwedowicz, D., Silva-Aceves, J., Majewski, T., Vergara-Vazquez, J., Rodriguez-Mendez, A.: Crashworthiness behavior of aluminum profiles with holes considering damage criteria and damage evolution. Int. J. Mech. Sci. **131–132**, 776–791 (2017). https://doi.org/10.1016/j.ijmecsci.2017.07.042

10. Marco, M., Giner, E., Larraínzar-Garijo, R., Caeiro, J.R., Miguélez, M.H.: Modelling of femur fracture using finite element procedures. Eng. Fract. Mech. **196**, 157–167 (2018). https://doi.org/10.1016/j.engfracmech.2018.04.024

11. Belda, R., Palomar, M., Peris-Serra, J.L., Vercher-Martínez, A., Giner, E.: Compression failure characterization of cancellous bone combining experimental testing, digital image correlation and finite element modeling. Int. J. Mech. Sci. **165**, 105213 (2020). https://doi.org/10.1016/j.ijmecsci.2019.105213

12. Muaz, M., Choudhury, S.K.: A realistic 3D finite element model for simulating multiple rotations of modified milling inserts using coupled temperature-displacement analysis. Int. J. Adv. Manuf. Technol. **107**(1–2), 343–354 (2020). https://doi.org/10.1007/s00170-020-05085-4

13. Woldman, M., Van Der Heide, E., Tinga, T., Masen, M.A.: A finite element approach to modeling abrasive wear modes. Tribol. Trans. **60**, 711–718 (2017). https://doi.org/10.1080/10402004.2016.1206647

14. Structure Optimization with Code_Aster/Code_Aster usage/Code_Aster forums. https://www.code-aster.org/forum2/viewtopic.php?id=14692. Accessed 21 Oct 2021

15. Concli, F., Maccioni, L.: Experimental–numerical calibration of the fracture locus of weathering steel. WIT Trans. Eng. Sci. **124**, 219–227 (2019)

Conceptual Design of an Automated Workstation for the Control of Manufactured Products in Single-Purpose Machines

Martin Bohušík$^{(\boxtimes)}$, Vladimír Bulej , Ivan Kuric , Milan Sága ,
and Vladimír Stenchlák

University of Žilina, 8215/1, Univerzitná Street, Žilina, Slovak Republic
martin.bohusik@fstroj.uniza.sk

Abstract. The article describes the solution of an automated line for the industrial company, where there was a requirement for inspection of manufactured parts and inspection of assembly of parts, including the design of an automated workstation (robotic workcells, assembly stations, inspection stations, operators, etc.). Camera systems that use artificial intelligence to determine the contour can check the shape of the gears involved. The main requirement to control production by camera systems arose because of human resources' time-consuming nature of the visual inspection. The article provides an overview of camera systems used in engineering companies that capture images of objects, and then these images are further processed in detail through software tools. Properly designing the automated workplace inspection through cameras consisted of collecting data from the company - lighting in production, material reflectivity, etc. Based on the obtained data, specific types of cameras from specific manufacturers were selected and placed at the necessary locations in the automated production.

Keywords: Sustainable manufacturing · Camera systems · Automated manufacturing · Machine vision · R&D Investment

1 Introduction

Machine vision belongs to the automation process where input information is obtained by recording images through industrial cameras. These cameras process the image by computing devices. Subsequently, algorithms are used through which it is possible to create different design applications for product inspection.

Recently, machine vision systems have become more efficient and affordable. Cameras alleviate time-consuming and increase accuracy over a human inspection. Machine vision through cameras is applied in various industries. It is used from inspection to process operations. Machine vision has also found application in various types of robots – cartesian robots [1], scara robots [2], snake robots, etc., because of their wide range of applications [3].

The article creates an inspection workplace in the Visual Components program for BROKKEM s.r.o. The requirement for implementing a machine vision system arose to

reduce the time consumption of inspection. In the literature review, an analysis of the current state of the camera systems was made.

In the practical part, a workplace concept is designed, in which camera systems from the manufacturer COGNEX were used. The cameras were selected according to the specified parameters from the company, where there was a requirement for partial automation of the workplace - inspection requirements, working distances, choices of lighting and lenses, etc. In the 3D design of the workplace, specific models under investigation are shown, made on actual machines used in the workplace.

The paper's contribution consists of designing an automated workstation for the inspection and assembly of a specific product, according to the company's requirements.

The superstructure to the presented solution is to replace the motion sensors placed in the robotic cell with a camera system that can detect the worker's movement through artificial intelligence (computer vision). Automated production will be suspended if a worker moves in close proximity to the industrial robot.

2   Literature Review

Computer vision, as the automatic analysis of images and video by computers, has a wide range of applications - use in the engineering industry, food industry, medical industry, etc. A specific application of machine vision is, e.g., in checking the position of parts in automotive production, checking the use of correct parts or fasteners, categorizing objects, checking printed circuit boards, checking for defects on products, finding imprints on apples, detecting chocolates on a conveyor and placing them in a box by a delta robot, automatic reading of license plates on vehicles, the ability to record multiple players on the ice (during hockey) and then give a penalty to that team, security checks at the airport, inserting virtual objects into movies, helping drivers by warning them (vibrating the steering wheel) when they are drifting out of their lane, creating 3D models from old photos, classifying plant species, etc. In the case of a trained artificial neural network for detection and categorization of objects in an image, artificial intelligence can also be used for other types of digitized image processing - control of separation processes in multifunctional devices [4–6], application of artificial neural networks (ANN) in the copper ore mining process to increase efficiency and ensure stability [7], cutting force determination based on integrated application of fixtures [8].
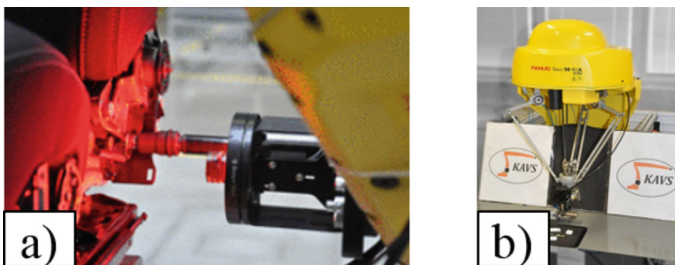
Fig. 1. Machine vision applications – a) installation of screws [1] b) assembly of the USB key [2].

Some of the published projects (solved at the Department of Automated Manufacturing Systems in Žilina - KAVS) in which machine vision was used are:

a) application of a camera system (Sony XC-56 camera) for the detection and subsequent assembly of bolts in automotive production by means of the FANUC M-20iA/20M industrial robot (installation of screws into car seats). This application is shown in Fig. 1a [9, 10]
b) assembly of the USB key through the FANUC M-1iA parallel robot, where the detection of the individual parts of the USB key is detected by the Sony XC-56 camera Fig. 1b [11]
c) application of machine vision for tire defect detection, integration of camera systems into serial and parallel robot control, detection of adhesive buildup on the product, visual product inspection based on deep learning methods, and more.

Due to the experience gained in solving the above-mentioned projects (in which machine vision is used), we were able to work on solving the assignment from the company BROKKEM s.r.o.

The company focuses, among other things, on the production of components for single-purpose machines. There will also have to be a complete assembly for the latest order. Figure 2 shows the product, which will be manufactured, inspected, and assembled directly on a single automated line.
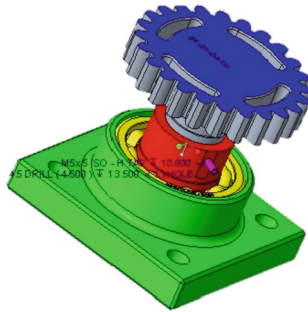
Fig. 2. Product covered by camera inspection.

The company had only a few requests for the design of an automated workplace and the selection of suitable cameras to inspect their products. Company requirements are the following:

1. The automated workstation can't be larger than 12 × 16 m
2. Design of the location of the assembly stations for the product
3. Maximum number of workers - 3 persons
4. Camera systems must be used to control products
5. Only cameras from COGNEX may be used for product inspection

3   Research Methodology

3.1   Smart Cameras

Products are often inspected through visual inspection by human workers. Visual inspection by human operators can be considered a critical element susceptible to errors resulting, e.g., from fatigue, insufficient reaction speed, stereotyped process, etc. In certain types of tasks, this human cognitive function can be replaced by a 2D or 3D camera system. The inspection of products through machine vision (contour inspection, object categorization, etc.) is becoming more and more widespread in the industry.

Smart machine vision cameras differ from standard industrial cameras in that they have storage and processing capability built into the camera housing. A standard camera takes an image and then sends it to another device for storage and analysis - a smart camera doesn't need to do this. I/O and communication are frequently built-in to smart cameras. It allows them to operate autonomously and to interface with other automation equipment. Smart cameras don't need a computer to operate, which makes them compact and robust, which is why they are one of the most emerging machine vision cameras in the industry [12].
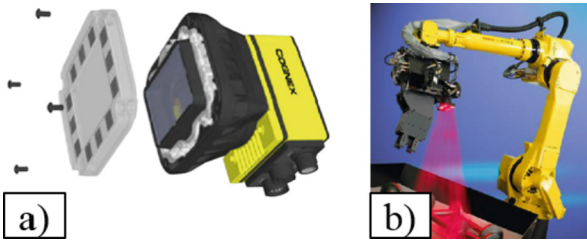
Fig. 3. Cameras with integrated lighting from COGNEX – a) In-Sight 7000 b) guiding the robot through the camera [13].

Some types of smart cameras have built-in lighting, so there is no need for additional lighting as with peripheral machine vision sensing devices. LED lighting is the most common type of lighting used for smart cameras. Figure 3 shows cameras with integrated lighting from COGNEX. The lighting is placed around the lens.

3.2   Lighting

Humans have been exposed to lighting that is referred to as "daylight" since the beginning of time. Various factors affect the efficiency of a person working in a particular room, such as office furniture placement, the lack/abundance of air in the room, or even the lack/abundance of light. Before designing the workspace (where the person will work), all of the above factors should be considered, and daylight should be preferred to artificial lighting (if possible). Researchers have conducted various studies where they have found that artificial lighting (fluorescent, incandescent, etc.) increased worker fatigue. The worker made more mistakes, and a longer latency time of the motion response to the light signal has been demonstrated [14].

Choosing the right type of lighting application is very important for people and industrial cameras. Lighting placed in areas where employees perform certain types of work (e.g., assembly products) can significantly increase work efficiency. Improper use of lighting in the workplace can create, for example, a strobe effect, which can cause serious injury to an employee. The lighting for industrial cameras is selected according to the specific type of task – checking microchips on a computer motherboard, scanning the contour of a gear-wheel, scanning objects with a reflective surface, etc. One of the main tasks of proper object inspection on an automated workstation was precisely to evaluate the use of a particular type of lighting in a specific product inspection.

Figure 4 graphically depicts four types of lighting commonly employed in machine vision (LED, Quartz halogen, fluorescent, and xenon strobe).
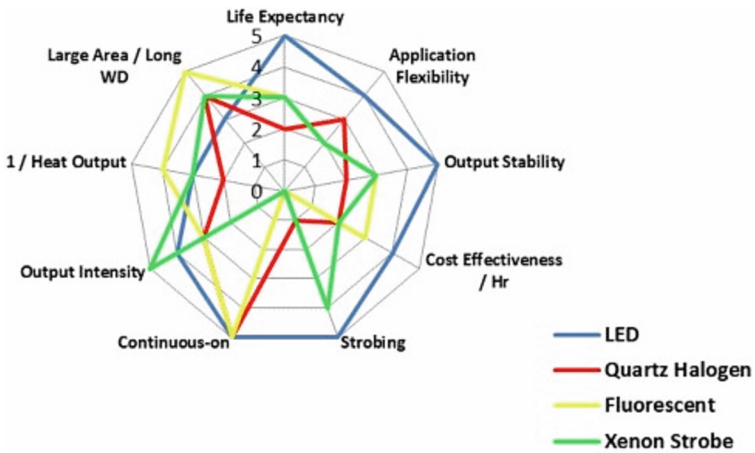
Fig. 4. Common vision lighting sources are compared and contrasted [15].

3.3   Specific Information of the COGNEX Cameras Used

Cognex's vision sensors and 2D and 3D vision systems all use machine vision technology to perform inspections, but they're built for various purposes.

Comparison of Vision Sensor, 2D vision, and 3D vision cameras in terms of application is shown in Table 1. Visual tools of used cameras in the automated line design are shown in Table 2.

Table 1. Comparison of vision sensor, 2D vision, and 3D vision cameras, in terms of application: [13].

	Vision sensors	2D vision	3D vision
Presence/Absence	✓	✓	✓
Defect Detection	✓	✓	✓
Assembly Verification	✓	✓	✓
Gauge/Measure	✓	✓	✓
Cosmetic Inspection		✓	✓
Guide/Align		✓	✓
OCR/OCV	✓	✓	
Code Reading		✓	

Table 2. Visual tools of used cameras [13].

	In-sight 2000 camera	In-sight 7500 camera
Pattern Matching	✓	✓
Blob	✓	✓
Edge	✓	✓
Measurement	✓	✓
1D/2D Code Reading	✓	✓
OCR	✓	✓
Flaw Detection	✓	✓
Color Verification	✓	✓
Color Identification	✓	✓
Histogram	✓	✓
Brightness	✓	✓
Pixel Counting	✓	✓
Contrast	✓	✓
Image Filters	✓	✓

4 Results

In this chapter, a conceptual design of the workplace is created (Fig. 5). The products of BROKKEM s.r.o. are digitally recorded, processed, and evaluated using camera systems (machine vision). The single parts to be assembled in the assembly process are machined by CNC machines [16–18]. The requirement arose for the following types of product inspection – (a) checking the bearing house, (b) inspection of the pressed-in bearing, (c) gear check, (d) palletizing through QR code. For all the above-mentioned product

inspections, cameras from COGNEX were chosen, for which we also designed mounts (welded profiles) for the automated line. The entire conceptual design of the workplace was created in Visual Components [19, 20]. The dimensions of the designed automated workplace are approximately 8.5×10 m.

In the future, we want to implement all the above-mentioned cameras on an automated line at BROKKEM s.r.o. In the phase of testing the use of camera systems, products (in addition to correct and non-conforming products) with defined defects, such as a defect on a gear wheel (damage to a tooth), will be randomly placed on the conveyor belt. The de-signed system will remain implemented in production when the desired product control success rate is achieved. If it is necessary to make the robotic workplace more efficient, it is possible to design robot-human cooperation (collaborative robotics) when assembling a gear with a shaft [21].
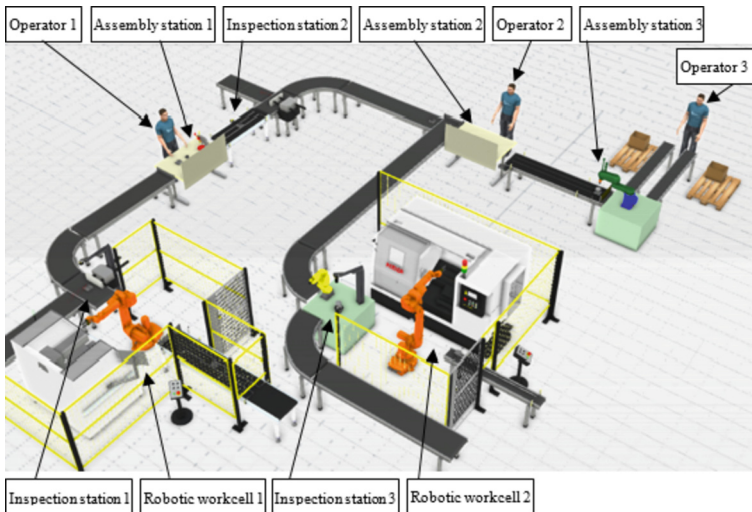
Fig. 5. Robotic workstation with human operators designed in visual components.

4.1   Checking the Bearing House

A Cognex In-sight 7500 camera (Fig. 6b) with planar scanning was used to inspect the bearing house. This camera has integrated 4000 K white LED illumination to save the cost of external light sources. The working distance of the subject was 604 mm, from which a 12 mm/f2.3 lens was chosen. The lens features self-focusing, which makes it easy to mount the system. The sensor is a CMOS with a pixel size of 4.5×4.5 m per pixel, and the image is taken at a resolution of 800×600 pixels in black and white. The shutter speed is 500 ms. Therefore, the checking procedure will not be slowed down significantly. An 8 gigabyte SD card can be inserted into the camera to record the time of the inspection and recorded images that have not been inspected for possible time information. The power supply of the camera is 24VDC 1.5 A. The device provides IP 67

protection, which is sufficient protection in a collision with a robot. Communication with the software is through an Ethernet cable connected to the In-sight Explorer software. The camera placement design for detecting the bearing house contour is shown in Fig. 6a [13].
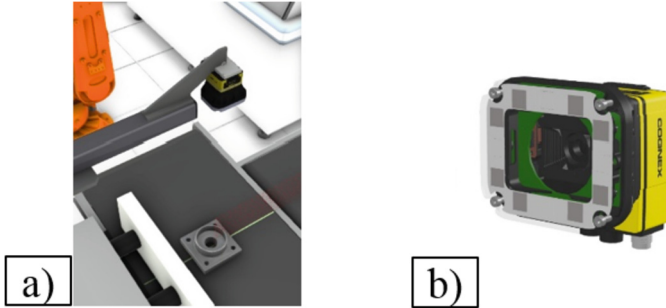
Fig. 6. Checking of the bearing house - a) design of the camera placement for detection of the bearing house contour b) Cognex In-sight 7500 camera [13].

4.2   Checking Bearing Installation

The In-sight 2000 camera (Figure 7b) was used to inspect the correct bearing installation by the operator. This is one of the most cost-effective camera sensors available. The camera employs the edge detection capability to inspect the bearing installation. If a bearing edge is caught in the image, the conveyor moves it out of the process. The camera has modularity, so it has integrated white LED lighting to reduce costs. The lens's working distance is 200 mm, while the image's field of view is 100 mm. The lens was chosen with an 8 mm focal length. The device uses a CMOS sensor whose size per pixel is 1.93 μm with an output image resolution of 800 × 600 pixels. The output image is black and white, and communication with the software is done through an Ethernet cable with the In-Sight Explorer software. The supply voltage is 24 V/DC. Checking bearing installation is shown on Fig. 7a.

4.3   Gear Wheel Inspection Using Deep Learning

An In-sight D902M series camera (Fig. 8b) was used for the repeating tooth features on the gear with the serial number on the shaft face, supported by artificial intelligence over conventional cameras used in the workplace. The choice of this camera was suitable for checking surface scratches, burrs, number of teeth, and OCR (optical character recognition) at different positions. Artificial intelligence allows these defects to be detected at different rotations compared to the convex ones that require a precise position for sensing. The working distance is 362 mm, where the field of view is 120 × 120 mm from these parameters, a lens with a C-aperture and a focal length of 12.5 mm was chosen. The camera sensor is a CMOS whose size per pixel is 3.45 μm × 3.45 μm. The camera
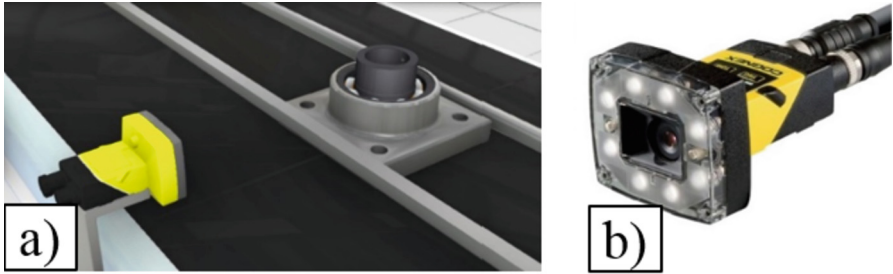
Fig. 7. Checking bearing installation – a) design of camera placement for bearing assembly inspection b) Cognex In-sight 2000 camera [13].

provides an image resolution of 1900 × 1200 pixels whose image is in black and white format. The storage memory of the camera is 16 gigabytes which can be expanded with an additional SD card up to a maximum of 8 gigabytes when pairing the camera with a local network is non-limited storage space. The process memory of the camera is 3 gigabytes. A GiGE interface attached to the In-Sight ViDi software facilitates communication. The supply voltage is 24 VDCLighting is provided by STEMMER IMAGING with CSS LAK type. This type belongs to the category of dark field lighting, which is ideal for searching for defects. Gear wheel inspection is shown in Fig. 8a [13].
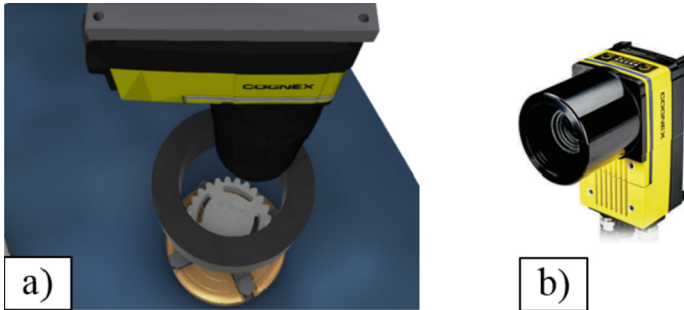
Fig. 8. Gear wheel inspection – a) design of camera placement for gear wheel inspection b) Cognex In-sight D902M camera [13].

4.4 Palletizing Products Through QR Code

For proper distribution of products by SCARA robot, a fixed QR code reader Dataman 260X (Fig. 9b) rectangular version was used for compactness of the system. The camera works based on Cognex 2Dmax and Powergrid algorithms. These algorithms make it possible to recognize codes even on curved surfaces. The device provides an image resolution of 752 × 480 pixels, which is a sufficient resolution at a working distance of 90 mm. The reader has a built-in CMOS image sensor. The camera offers 60 frames per second which it can decode in an average of 0.45 s. From the tabulated values provided

by the manufacturer for the field of view of the QR code, which is 15×15 mm, a lens with a focal length of 6.2 mm was chosen, which can read 105 million characters from the QR code at the above working distance. The lighting is integrated in the camera, where a polarizing filter was chosen to highlight the QR code and reduce the shine of the metal material. Communication with the software is realized by an Ethernet cable connected to the In-Sight Explorer. The camera provides IP-65 protection [13].
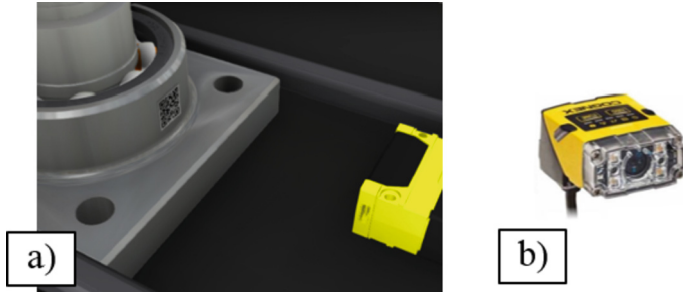
Fig. 9. QR code scanning – a) design of camera placement for QR code scanning b) Dataman 260X camera [13].

5   Conclusions

In the practical part of the article, at the company's request, a conceptual proposal for the use of camera systems in a robotic workplace was developed. The practical part was realized in Visual Components. This proposal consists of the correct choice of industrial cameras that have been provided by the manufacturer Cognex. According to the inspection requirements, suitable cameras were selected within the application and parameters for the given component inspection.

The automated workplace design meets all the company's requirements and is ready for practical implementation in the company.

References

1. Virgala, I., Kelemen, M., Prada, E., et al.: A snake robot for locomotion in a pipe using trapezium-like travelling wave. Mech. Mach. Theory **158**, 104221 (2021). https://doi.org/10.1016/j.mechmachtheory.2020.104221

2. Svetlik, J., Demec, P.: Methods of identifying the workspace of modular serial kinematic structures. Appl. Mech. Mater. **309**, 75–79 (2013). https://doi.org/10.4028/www.scientific.net/AMM.309.75

3. Puškár, M., Jahnátek, A., Kuric, I., Kádárová, J., Kopas, M., Šoltésová, M.: Complex analysis focused on influence of biodiesel and its mixture on regulated and unregulated emissions of motor vehicles with the aim to protect air quality and environment. Air Qual. Atmos. Health **12**(7), 855–864 (2019). https://doi.org/10.1007/s11869-019-00704-w

4. Ivanov, V., Dehtiarov, I., Pavlenko, I., Kosov, M., Hatala, M.: Technological assurance and features of fork-type parts machining. In: Ivanov, V., et al. (eds.) DSMIE 2019. LNME, pp. 114–125. Springer, Cham (2020). https://doi.org/10.1007/978-3-030-22365-6_12

5. Pavlenko, I., Liaposhchenko, A., Ochowiak, M., Demyanenko, M.: Solving the stationary hydroaeroelasticity problem for dynamic deflection elements of separation devices. Vibr. Phys. Syst. **29**, 2018026 (2018)

6. Pavlenko, I., et al.: Effect of superimposed vibrations on droplet oscillation modes in prilling process. Processes **8**(5), 566 (2020). https://doi.org/10.3390/pr8050566

7. Wiecek, D., Burduk, A., Kuric, I.: The use of ANN in improving efficiency and ensuring the stability of the copper ore mining process. Acta Montanistica Slovaca **24**(1), 1–14 (2019)

8. Ivanov, V., Pavlenko, I., Kuric, I., Kosov, M.: Mathematical modeling and numerical simulation of fixtures for fork-type parts manufacturing. In: Knapčíková, L., Balog, M. (eds.) Industry 4.0: Trends in Management of Intelligent Manufacturing Systems. EICC, pp. 133–142. Springer, Cham (2019). https://doi.org/10.1007/978-3-030-14011-3_12

9. Sága, M., Bulej, V., Čuboňová, N., Kuric, I., Virgala, I., Eberth, M.: Case study: performance analysis and development of robotized screwing application with integrated vision sensing system for automotive industry. Int. J. Adv. Rob. Syst. **17**(3), 1729–8814 (2020). https://doi.org/10.1177/1729881420923997

10. Kuric, I., Tlach, V., Císar, M., Ságová, Z., Zajačko, I.: Examination of industrial robot performance parameters utilizing machine tool diagnostic methods. Int. J. Adv. Robot. Syst. **17**(1), 1–11 (2020). https://doi.org/10.1177/1729881420905723

11. Bulej, V., Stanček, J., Kuric, I.: Vision guided parallel robot and its application for automated assembly task. Adv. Sci. Technol. Res. J. **12**(2), 150–157 (2018)

12. Fisher, S.: Smart Camera. Machine Vision. Smart cameras for OEM (2021). https://fishersmith.co.uk/components/smart-cameras. Accessed 15 Oct 2021

13. COGNEX, 2020. Area Scan vs. Line Scan. Cognex. https://www.cognex.com/what-is/machine-vision/system-types/area-scan-vs-line-scan. Accessed 15 Oct 2021

14. Špes, M.: Daylighting of interior workspaces (2016)

15. Daryl, M.: A Practical Guide to Machine Vision Lighting (2013). https://www.advancedillumination.com/. Accessed 15 Oct 2021

16. Dodok, T., Čuboňová, N., Kuric, I.: Workshop programming as a part of technological preparation of production. Adv. Sci. Technol. Res. J. **11**(1), 111–116 (2017). https://doi.org/10.12913/22998624/66504

17. Prydalnyi, B.I., Sulym, H.T.: Mathematical model of the tensioning in the collet clamping mechanism with the rotary movable input link on spindle units. J. Eng. Sci. **8**(1), E23–E28 (2021). https://doi.org/10.21272/jes.2021.8(1).e4

18. Krol, O., Sokolov, V.: Modeling of spindle node dynamics using the spectral analysis method. In: Ivanov, V., Trojanowska, J., Pavlenko, I., Zajac, J., Peraković, D. (eds.) DSMIE 2020. LNME, pp. 35–44. Springer, Cham (2020). https://doi.org/10.1007/978-3-030-50794-7_4

19. Holubek, R., Ružarovský, R., Sobrino, D.R.D.: An innovative approach of industrial robot programming using virtual reality for the design of production systems layout. In: Trojanowska, J., Ciszak, O., Machado, J.M., Pavlenko, I. (eds.) MANUFACTURING 2019. LNME, pp. 223–235. Springer, Cham (2019). https://doi.org/10.1007/978-3-030-18715-6_19

20. Klačková, I., Kuric, I., Zajačko, I., Tucki, K.: Energy and economical aspects of implementation of virtual reality in robotized technology systems. In: 18th International Conference on Emerging eLearning Technologies and Applications (ICETA), pp. 318–322. IEEE, Denver (2020)

21. Tlach, V., Kuric, I., Ságová, Z., Zajačko, I.: Collaborative assembly task realization using selected type of a human-robot interaction. Transp. Res. Procedia **40**, 541–547 (2019). https://doi.org/10.1016/j.trpro.2019.07.078

The Anti-collapse Safety System
for Hydraulically Operated Docking Levelers

Bogdan Dorel Cioroagă and Vasile George Cioată(✉) ®

Politehnica University Timisoara, 5, Revolution Street, 331128 Hunedoara, Romania
`vasile.cioata@fih.upt.ro`

Abstract. During the crossing of the docking leveler by the logistics equipment, there is a risk that the truck stationed in the docking station will advance far enough so that the support lip of the leveler will no longer be in contact with the floor of the truck causing the leveler to fall while being crossed by the forklift. The paper focuses on sizing a security system that eliminates the risk presented. This system consists of installing a safety valve that blocks the flow of fluid through the hydraulic motors that operate the leveler. Valve blockage occurs when a limit flow is reached. The maximum drop at the tip of the leveler's lip is h = 6% of the docking leveler platform length (in the vertical plane) until the valve is blocked. It must be taken into consideration that the safety valve should not be actuated during the operation of the leveler not to influence its operating sequences. The paper presents the kinematic diagram of the docking leveler, its functional sequences, the calculation of the actuation and sizing of the safety valve, and the indication of a type of valve recommended following the sizing calculations of the safety system. This paper aims to solve a problem in the industry of docking levelers and their operation in safe warehouses.

Keywords: Product innovation · R&D investment · Valve · Flow · Kinematic · Velocity · Leveler · Safety · System · Hydraulic

1 Introduction

Docking levelers are devices designed to provide a smooth passage of logistics equipment from the logistics warehouses to the interior of vehicles taking over or delivering goods to these warehouses. These docking products can be found in a wide variety of types and sizes adapted to the needs of the field [1].

The main constructive elements that make up most of the docking levelers are:

- The frame (Fig. 1, position 1) - aims to fix the leveler to the floor of the warehouse and has the role of supporting the platform;
- The platform (Fig. 1, position 2) - is the subassembly of the leveler that acts as a crossing bridge for logistics equipment; it is installed in the frame by a hinge and at the opposite end is installed a lip;
- The lip (Fig. 1, position 3) - has the role of connecting the truck with the leveler; it is supported during the operation of the leveler on the floor of the vehicle [2].
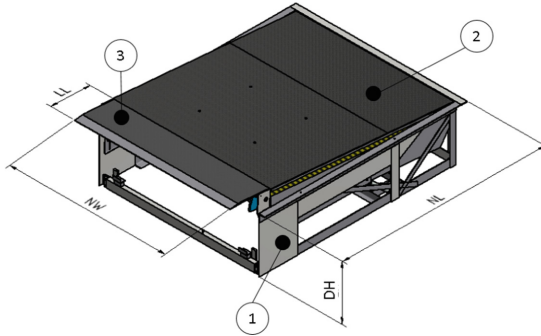
Fig. 1. Docking leveler.

Both the platform and the lip are equipped with linear hydraulic motors to perform the necessary movements to bring the leveler to the operating position. They are controlled by a control unit that can be found in a wide range of varieties; the operating sequences found in most levelers are the following starting from the resting position of the leveler (when the platform is perfectly horizontal and the lip is not extended, the platform is supported on exceptional support from the frame):

- Sequence 1 – performs the lifting or lowering movement of the platform;
- Sequence 2 – the lip is actuated, it can be performed simultaneously with sequence one or after it has stopped;
- Sequence 3 – consists in retracting the platform from the operating position;
- Sequence 4 – the lip closes;
- Sequence 5 - the leveler reaches the platform to the resting position.

The execution time of sequences necessary to place the leveler in the operating position and retract it to the rest position is 120 s [3].

To eliminate the risk of the leveler platform falling due to accidental retraction of the vehicle (see Fig. 2) on which it rests while being crossed by the logistics equipment, a safety system is necessary to prevent this risk. The safety system recommended by the EN 1398: 2009 standard consists of installing a safety valve on the exhaust of the hydraulic motors that operate the leveler platform [4].
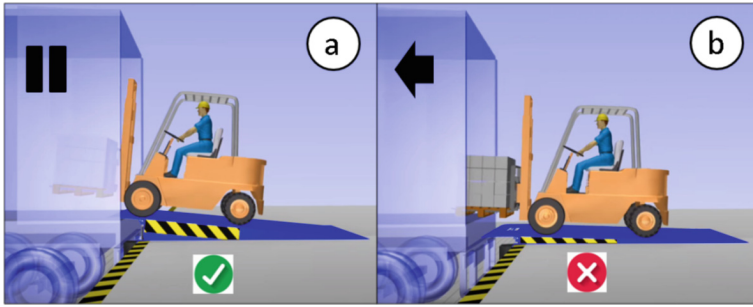
Fig. 2. The case of the leveler that loses support during operation.

The operation principle of the safety valve is that it closes automatically when a limit flow is reached, having the effect of blocking the hydraulic motors that support the platform of the leveler, avoiding the fall of the logistic machines that cross it [4].

According to EN 1398: 2009, the docking levelers must be secured with automatic protection systems against dangerous level drops, which act when detecting values of 25% of the load-bearing capacity of the leveler. The fall of the leveler is allowed within the limit of 6% of the length of the platform or for the continuous fall with a velocity of less than 0.05 m/s [5].
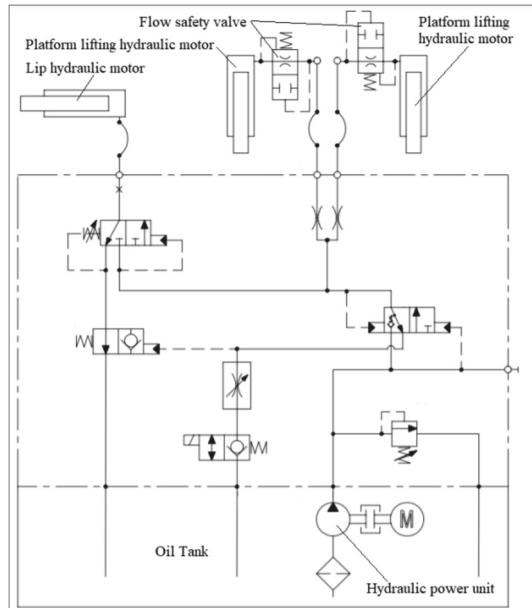
Fig. 3. The general hydraulic circuit of docking levelers.

Figure 3 shows the hydraulic circuit used for hydraulically operated docking levelers. It can be seen that the leveler contains two linear hydraulic motors designed to lift the platform and one designed to operate the lip.

The retraction of the lifting cylinders is achieved by depressurizing them due to the weight of the platform that presses on them; two drosels adjust the retraction velocity. The lifting cylinders have a standard supply and evacuation, on which the safety valve is installed [6].

2   Literature Review

The purpose of the review is to find a practical solution for a problem found in the industry of manufacturing docking equipment applied on hydraulic dock levelers. Docking levels must be equipped with an anti-falling system according to the safety standard EN 1398:2009. The paper presents the approach and the design of an anti-falling system according to the mentioned standard, creating a universal guideline that explains systematically which parameters are involved and the way of thinking about the problem to obtain a series of steps that define the design process of the hydraulic anti-falling system.

Recent studies are not applied directly to this type of product. Still, similar principles and knowledge are used for other mechanical safety systems and can be found in the technical literature. The literature does not have many documentation of knowledge in this direction, the problem being harvested directly from the specific manufacturing industry of docking levelers, products that are not very popular and do not present a high constructive and technological complexity.

Summary of research. The anti-falling safety system is designed to determine the leveler platform's falling velocity at a certain distance. The velocity resulting by the falling of the platform has a direct effect on the hydraulic cylinders that are depressurized in the first stage, and in the second stage, they become pressured by activating a flow blocking valve, the trigger of the system is the falling velocity and the controlled parameter is the resulting flow in the safety valve. All this system is calculated based on the configuration parameters of the leveler and the cinematic scheme of the platform lifting system.

Ideas of where research might go next are finding other mechanical anti-falling systems that can be applied to this case, triggered by gravity. Creating a design concept for a universal automatic anti-falling system based on contact sensors and has a backup mechanical blocking sensor in case of a power outage.

3   Research Methodology

To determine the parameters that influence the flow developed in the linear hydraulic motors with a simple action that takes over the platform's fall, it is necessary to analyze the kinematic operation of the system (Fig. 4).

During the operati,on of the leveler it is supported on the end which means that point A_0 has a travel velocity 0 as well as point B_0 wwhich is a kinematic pivot in the area where the platform hydraulic motor operates [7].
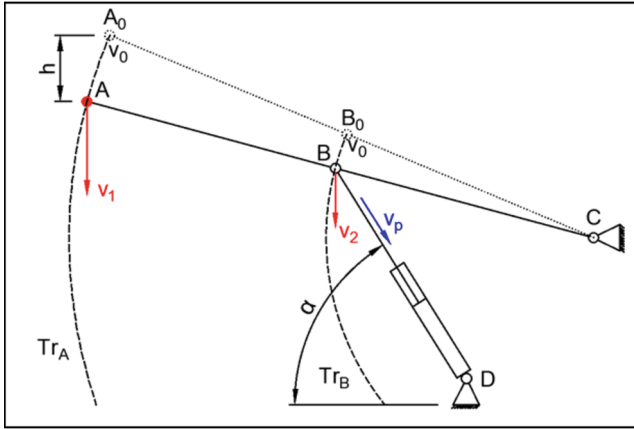
Fig. 4. General kinematic scheme of docking levelers.

The expected faonel of the platform in the absence of support is represented by the vertical height h, following this distance by the falling point A located on the end of the platform, will have a velocity v_1 and v_2 for point B. Points C and D represent the articulated supports of the platform and the hydraulic motor in the frame area. Tr_A and Tr_B represents the trajectories of the two points A and B during the fall of the platform, the angle α is the inclination angle of the hydraulic motor after the fall of the platform. [8].
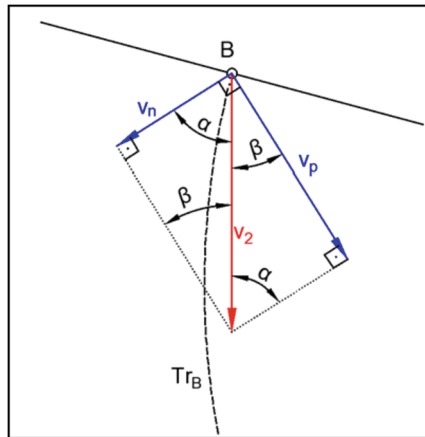
Fig. 5. Detail of intoity v_2 decompositions.

Figure 5 shows in detail the breaking in to components of the velocity v_2 for determining the retraction velocity v_p of the hydraulic motor piston until the safety valve is blocked. The flow Q_{mh} developed in the hydraulic installation during theis of the

platform being directly influenced by the variable parameter v_p and the constructive parameter which is constant S representing the active surface of the piston.

The calculation approach of the sizing problem of the safety system represented by the shut-off valve actuated by the flow Q_{mhn} necessary to block is performed in two distinct stages [9]:

Step 1 - Determining the law of variation of the flow Q_{mh} within the system, as a function that depends on the vertical fall of the platform h.

Determination of travel velocities v_1, v_2 and v_p:

$$v_1 = \sqrt{2 \cdot g \cdot h} \tag{1}$$

$$v_2 = v_1 \cdot i \tag{2}$$

$$v_p = v_2 \cdot \sin\alpha \tag{3}$$

where $i = \frac{(BC)}{(AC)}$ is the gear ratio of $v_1 > v_2$ the value of this velocity v_2 depending on its position on the segment (AC).

The friction with the air was not taken into account in calculating the velocities, this being negligible in this case [10].

Determination of valve reaction time:

$$t = \frac{h}{v_1} \tag{4}$$

Flow determination Q_{mh} developed in the hydraulic motor:

$$Q_{mh} = \frac{S}{v_p} = \frac{\pi \cdot D^2}{\frac{4}{v_p}} = \frac{\pi \cdot D^2}{4 \cdot v_p} \tag{5}$$

Extension of the formula for framing all parameters:

$$Q_{mh} = \frac{\pi \cdot D^2}{4 \cdot v_2 \cdot \sin\alpha} = \frac{\pi \cdot D^2}{4 \cdot v_1 \cdot \frac{(BC)}{(AC)} \sin\alpha} = \frac{\pi \cdot D^2 \cdot (AC)}{4 \cdot v_1 \cdot (BC) \cdot \sin\alpha} = \frac{\pi \cdot D^2 \cdot (AC)}{4 \cdot \sqrt{2 \cdot g \cdot h} \cdot (BC) \cdot \sin\alpha} \tag{6}$$

Step 2 - Determining the falling distance according to a standardized valve closing flow rate Q_{mhs} [11].

$$Q_{mhs} = \frac{\pi \cdot D^2 \cdot (AC)}{4 \cdot \sqrt{2 \cdot g \cdot h_s} \cdot (BC) \cdot \sin\alpha} \tag{7}$$

$$h_s = \sqrt{\frac{\pi \cdot D^2 \cdot (AC)}{Q_{mhs} \cdot 4 \cdot \sqrt{2 \cdot g} \cdot (BC) \cdot \sin\alpha}} \tag{8}$$

4 Results

The sizing of the valve will take place for a standard docking leveler with the technical characteristics presented in Table 1.

The determination of the flow developed during the fall of the platform is performed starting from the determination of the maximum allowed fall h according to EN 1398: 2009 [12]:

$$h = NL \cdot 6\% = 3000 \cdot 0{,}06 = 180 \ \text{mm} = 0{,}18 \ \text{m} \tag{9}$$

Determination of travel velocities v_1 and v_2 of points A and B when the maximum drop limit is reached:

$$v_1 = \sqrt{2 \cdot g \cdot h} = \sqrt{2 \cdot 9{,}81 \cdot 0{,}18} = 1{,}878 \ \frac{\text{m}}{\text{s}} \tag{10}$$

$$v_2 = v_1 \cdot i = 1{,}878 \frac{(BC)}{(NL) + (LL)} = 1{,}878 \frac{1300}{3000 + 500} = 0{,}698 \ \frac{\text{m}}{\text{s}} \tag{11}$$

Determination of the compression velocity v_p of the linear hydraulic motor with simple action:

$$v_p = v_2 \cdot \sin\alpha = 0{,}698 \cdot \sin 56 = 0{,}578 \ \frac{\text{m}}{\text{s}} \tag{12}$$

Table 1. Technical characteristics of the docking leveler.

Description	Symbol	Value	U.M
Platform nominal length	NL	3000	mm
Lip length	LL	500	mm
Leveler nominal width	NW	3600	mm
Frame height (dock height)	DH	600	mm
Platform thickness	LH	280	mm
Maximum extended hydraulic motor slope angle	α	56	deg
Segment (BC) according to Fig. 4	(BC)	1300	mm
Hydraulic motor – nominal working pressure	P_n	200	bar
Hydraulic motor - lifting force	F_n	150000	N
Hydraulic motor-stroke		300	mm
Hydraulic motor - maximum length		700	mm
Hydraulic motor - inner diameter	D_i	40	mm
Hydraulic motor - outer diameter	D_e	50	mm
Hydraulic motor - piston rod diameter	D_r	35	mm

Determination of the reaction time of the valve for the maximum permissible drop rate h:

$$t = \frac{h}{v_1} = \frac{0.18}{1,878} = 0,096 \text{ s} \tag{13}$$

Determination of the flow Q_{mh} developed in the hydraulic motor: [13]

$$Q_{mh} = \frac{\pi \cdot D^2}{4 \cdot v_p} = \frac{\pi \cdot \left(10^{-3} \cdot 40\right)^2}{4 \cdot 0,578} = 0,002172 \frac{\text{m}^3}{\text{s}} = 130,32 \frac{\text{l}}{\text{min}} \tag{14}$$

Determination of the pressure developed in the linear hydraulic motor following the fall of the platform using Bernoulli's law, neglecting the influence of the height difference:

$$\frac{v_p^2}{2} = -\frac{P}{\rho} \tag{15}$$

$$P = -\frac{v_p \cdot \rho}{2} = \frac{0,578 \cdot 860 \cdot 10^3}{2} = 248540 \frac{\text{N}}{\text{m}^2} = 2,48 \text{ bar} \tag{16}$$

The hydraulic fluid is considered Divinol DHG ISO 10 which has a density at 15 °C equivalent to $\rho = 860 \frac{\text{kg}}{\text{m}^3}$ [14].

It results that the pressure developed after the fall of the platform does not exceed the maximum working pressure of the hydraulic motor $P_n = 200$ bar [15].

For the leveler configuration that has been presented, a flow blocking valve with actuation below the limit flow of $130 \frac{\text{l}}{\text{min}}$ and a minimum working pressure of 200 bar can be used [16].

5   Conclusions

It was found that the main factor influencing the flow developed in the hydraulic motor during the fall of the platform is its falling velocity; a significant factor is also the angle of inclination of the hydraulic motor and its position of actuation on the leveler platform.

It was found platform's mass does not influence the flow developed during the fall of the platform. From the application side it resulted that for the chosen standard configuration of the leveler the reaction time of the system is very short $t = 0,096$ s and the pressure developed due to the fall of the platform is 2.48 bar which does not present the risk of destruction of the hydraulic circuit by overload.

References

1. ASSA ABLOY Homepage. https://www.assaabloyentrance.co.uk/en/products/loading-bay-equipment/dock-levelers/, Accessed 23 Sept 2021
2. https://www.hormann.co.uk/industry-commerce-and-public-authorities/loading-technology/dock-levellers, Accessed 20Nov 2021
3. Product datasheet dock leveler, ASSA ABLOY, DL6120TA

4. European standard, EN 1398, Dock levellers safety requirements (2009)
5. Cioroagă, B.D., Cioată, V.G., Kiss, I.: Redesign of docking swingdock levers for increasing load capacity in resting position. In: International Conference on Applied Sciences ICAS 2021, Hunedoara, Romania (2021)
6. Xu, B., Cheng, M., Yang, H., Zhang, J., Yang, M.: Safety brake performance evaluation and optimization of hydraulic lifting systems in case of overspeed dropping. Mechatronics **23**(8), 1180–1190 (2013). https://doi.org/10.1016/j.mechatronics.2013.10.005
7. Blaschuk, M., Dronov, A., Koperchuk, A., Chernukhin, R., Litvinenko, V.: Kinematic parameters of rotary transmission with hydraulic cylinders. In: E3S Web of Conference, vol. 15, p. 03003 (2017). https://doi.org/10.1051/e3sconf/20171503003
8. Asok, K.M., Amitabha, G., Günter, D.: Kinematic Analysis and Synthesis of Mechanisms. CRC Press, Florida (1994)
9. Dong, L., Zhu, C.: Distributed control strategy for large-scale hydraulic synchronous lifting systems. J. Syst. Control Eng. **232**(3), 213–222 (2018). https://doi.org/10.1177/095965181 7744958
10. Damerow, P., Freudenthal, G., Mclaughlin, P.: Exploring the limits of preclassical mechanics. Springer Science+Business Media, New York (1992). https://doi.org/10.1007/978-1-4757-3994-7
11. Chapple, P.: Principles of Hydraulic Systems Design, 2nd edn. Momentum Press Engineering, Boston (2015)
12. Marghitu, D.B.: Mechanical Engineer's Handbook. Academic Press, Boston (2001)
13. Ilango, S., Soundararajan, V.: Introduction to Hydraulics and Pneumatics, 2nd edn. Eastern Economy Edition, New Deli (2011)
14. Ruqiong, Q., Chunyi, D.: The principle and applications of Bernoulli equation. J. Phys. Conf. Series **916**, 012038 (2017). https://doi.org/10.1088/1742-6596/916/1/012038
15. Scherer, M., Geimer, M., Weis, B.: Contribution on control strategies of flow-on-demand hydraulic circuits. In: The 13th Scandinavian International Conference on Fluid Power, SICFP2013, Sweden, vol. 92, pp. 531–540 (2013). https://doi.org/10.3384/ecp1392a53
16. Șcheaua, F.D.: Theoretical aspects regarding the pressure safety valves operation within a hydraulic circuit. Maga. Hydraul. Pneum. Tribol. Ecol. Sensorics Mechatron. **1**, 1–6 (2018)

Development of the Disk Tool Magazine
with Modified Gear Drive

Oleg Krol[(✉)] and Volodymyr Sokolov

Volodymyr Dahl East Ukrainian National University, 59-a, Central Pr., 93400 Severodonetsk,
Ukraine
krolos@snu.edu.ua

Abstract. The problems of modeling and research of disk tool magazines
of drilling-milling-boring machining centers are considered. Three-dimensional
modeling of the tool magazine structures and auto operator devices (manipulator)
as the main components of the automatic tool change system during processing
body parts has been carried out. The integrated computer-aided design system and
specialized applied libraries in the express mode of 3D modeling were used. A
new approach to improving the drive device of the tool magazine is proposed,
based on the modification of the gear drive design using an incline-arched pro-
file of the teeth. The design technique of its closest analogue – a cylindrical gear
transmission with helical teeth according to the criterion of contact endurance of
the teeth as the main method for the calculation was adopted. An experiment is
carried out to assess the main kinetic-geometric parameters of spur gears with
incline-arched teeth. The relationship between the engagement parameters and
the size of the gear cutting head has been established. The extreme values of the
inclination angles for the incline-arched teeth for the given basic dimensions of the
transmission have been determined. Dependences for calculating the longitudinal
curvature and length of the cut teeth are obtained to research the bending strength
of the transmission teeth.

Keywords: Disk tool storage · 3D modeling · Gear transmission · Teeth profile ·
Incline-arched form · Product innovation

1 Introduction

The effectiveness of the embedding of machining centers and multi-operation CNC
machines is associated mainly with developing a system for changing workpieces and
tools. As you know, the productivity of machining centers is 3–8 times higher than that of
conventional machines due to a sharp reduction in auxiliary time and thereby increasing
the share of machine time up to 60–70% in the total processing cycle.

Auxiliary time is reduced due to automatic tool change, high-speed positioning of
the machine operation devices, etc. In modern machine tools, the changeover time is
further reduced due to the use of interchangeable Machine Tool Magazines (MTM) with
a pre-adjusted cutting tool.

Modern metal cutting tools and systems present complex assembly designs, including tool magazines, auto operators, auxiliary and cutting tools. In the practice of mechanical engineering, the classification of tooling systems is used, in particular, for CNC machines of drilling-boring-milling groups, and the concept of a tool module is considered [1, 2]. In the case of this module, a variety of instrument blocks are mounted, which gives the MTM technological flexibility. Modular MTM for multipurpose drilling-milling-boring machines with CNC (Machining Center, MC) is characterized by auxiliary tools – unified basic mandrels with a taper of 7:24. The design of such an MC auxiliary tool is determined by its attachment surfaces for mounting to the machine and for fastening the cutting tool, and the design of the shank end is interconnected with devices that carry out automatic tool changing.

2 Literature Review

In the layouts of machining centers, Automatic Tool Changers (ATC) with an autooperator are used. The disk and chain tool magazines are used as drives, which are removed from the working area of the machine tool [3]. Auto-operators perform loading and unloading operations as part of the ATC system with a rigidly specified work cycle.

At the same time, designing an MC tooling system is a complex task. Designing documentation (drawings, specifications, diagrams) for MC tooling is a laborious and time-consuming process. The presence of 3D modeling with the principle of associativity allows you to generate any necessary views and cross-sections, generate basic drawings, and obtain initial data for calculations and related tasks. To implement 3D modeling of MTM, the rapidly progressing KOMPAS-3D system with the technology of integrated end-to-end 3D design and rendering, developed by the ASCON group of companies, is used [4, 5].

The following basic requirements are imposed on automatic tool changing systems: sufficient storage capacity for tools (turret, tool magazine); reliable identification of tools in the store; minimal time spent on changing tools.

In work [6], the optimal tool support strategy for machine-building production was conducted. For this purpose, based on a systematic approach, a number of factors (divided into static, quasi-static, and dynamic) have been identified that influence the choice of a stable production process in the direction of two aspects:

1. Compliance with the production schedule of orders increased inventory and transportation costs. In this regard, the research work [7] proposed a mathematical model reflecting the minimum stock of the tool and the value of the average delay associated with the identification of the tool. This model most adequately reflects the situation associated with the tools storage in a centralized tool plant or localized storage [6].
2. High tool availability and reduced machining time. Resolution of this conflict of goals lies, according to the authors [6], in determining the optimal storage area within a set of options: a) centralized tool plant; b) localized storage; and c) machine tool magazine The authors of [6] proposed 8 main selection factors, including binding to a production order, frequency of use for processing a similar group of parts, taking into account several orders, and possibility of recycling.

The MC efficiency and productivity are related mainly to the system ATC interrupted operation and the accuracy of forming blanks with the level of errors arising from the interaction of "tool magazine-autooperator-machine tool spindle".

A number of works are related to the analysis of errors in the functioning of the MC tool system. So, works [8, 9] are devoted to analyzing errors associated with the positioning of tools in the MTM, which can lead to failures in the ATC of the MC. In this regard, it is essential to have an early warning system for tool magazine failures. Such a system for analyzing vibration signals in situations of removing tool blocks from the magazine slot and mounting it in the conical mating hole of the spindle is presented in [8, 10].

In turn, the positioning indicators – positioning accuracy, positioning resolution, positioning repeatability- depend on the design characteristics of the MTM drive, the main mechanical transmission of which is a toothed gear. In the reversing mechanisms of machine tools and machine-tool complexes, the use of classical mechanical transmissions is problematic due to the problem of strict synchronization of the power and driving shafts rotations [11, 12]. The inconsistency of movement is associated, among other things, with increased clearances in the engagement. The mismatch of the gear elements rotations causes inaccuracy in the positioning of the MTM. Another feature of the driven gear is that its design is presented in a toothed sleeve with a thin-walled rim, which implies the need to research both positioning accuracy and strength in the contact zone with the pinion. In this regard, improving the design of the MTM drive device with a gear transmission is urgent.

The analysis of the reviewed works devoted to the study of automatic tool change devices and systems has shown that in the strategy of optimal tool supply for machine-building production, an important direction is the observance of the production order schedule, which directly depends on the uninterrupted operation of the tool magazine and its driving device. Impressive results have been achieved in determining the minimum tool stock, the tool change sequence, and the degree of overlap. Simultaneously, in terms of constructive improvement of the ATC components, there is the potential to improve the performance of the MTM drive mechanism. Therefore, improvement of the design of the mechanical drive transmission and the geometry of the engagement zone is the subject of this research.

Statement of the research task. The analysis of the considered works in the field of creating the components of the automatic tool change system of machining center allows us to formulate the goal of the research: To develop a complex procedure for modeling a disk tool magazine with a modified gear drive that ensures a decrease in the level of contact stresses in the engagement and increases its service life.

Step-by-step algorithm to realize this research:

1. Selection of the tool magazine as the ATC main component.
2. Formation of criteria for assessing the effectiveness of the MTM
3. Identification of the main structural elements of the tool system, influencing the level of performance criteria
4. Development of 3d model of MTM, as a basis for further modeling of the design.
5. Improvement of the MTM drives through modification of the gear transmission.
6. Experimental evaluation for improvement of continuous service life of the MTM.

3   Research Methodology

The choice of the tool magazine type is determined by the multi-operation machine's purpose, type, and layout. The processing of medium-sized housing parts on multioperation machines shows that disk magazines with a capacity of up to 30 tools are more often used.

For specialized MC of the drilling-milling-boring type, a layout with a disk magazine mounted on the machine upright, and a two-grip manipulator (autooperator) is used. Such magazines are equipped with a small number of tools (no more than 18), provided that the tools are located in one row.

For studying the properties of the MC tool system based on the SVM1HF4 model in the integrated CAD KOMPAS-3D, a 3D project of the main components of the ATC device with a disk tool magazine was developed [13, 14], including 1330 3D models of parts and assemblies. In creating the project, the parameterization toolkit with the C3D Toolkit core [15, 16] and the application package "Shafts and mechanical transmissions-3D". A three-dimensional model of a disk magazine mounted on a machine upright with a vertical spindle head is shown in Fig. 1. KOMPAS provides export and import (with further editing) of 3D geometry and model data via STEP, ACIS, IGES, Parasolid, and other internationally known formats. The software is available in English and German.

a)   b)

c)   d)
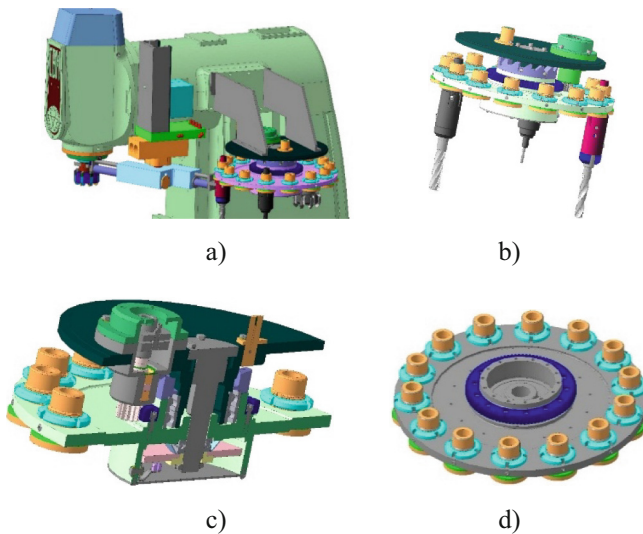
Fig. 1. 3D models of disk magazine: a – general view; b – assembly; c – section; d – disk with tool slots.

The MTM kinematics involves the transmission of a movable housing part rotation carrying the tool from the hydraulic motor through a toothed gear [17, 18]. In this position (when the autooperator grips tool approaches) the tool is unclamped in the magazine by a hydraulic cylinder, and the tool is changed.

The ATC autooperator [19, 20] consists of mechanisms: a gripper (including a housing, a retainer, a pusher, and a key), a rotation (which is carried out only when the grippers are extended), and is fastening with a support bracket to the machine bed.

Their advantage is associated with an increase in strength, a decrease in the wear level, and an increase in positioning accuracy [21–23].

In this paper, we propose a constructive modification of a Spur Gear with Incline Arched Teeth (SGIAT) and research the geometric and kinematic characteristics of these gears and the features of their gear cutting.

The main parameters of SGIAT $[a_W, m_n, b_W, z_1, z_2, \beta]$ are found by the method of calculating its closest analogue – a helical bevel gear transmission, that is, from the criterion of contact endurance of teeth, [24, 25]. For this reason, the listed parameters of the SGIAT engagement are considered given in this article. One of the features of the SGIAT is that the angle of its teeth inclines β changes along the width of the engagement. Therefore, the value of the angle β for SGIAT found from the specified performance criterion will be only in the middle section of the engagement width b_W, that is, for $\beta = \beta_n$ (Fig. 2). We assume that the angle of inclination of the SGIAT teeth at one end of the gear (wheel) is equal to zero, that is, β_{min}. At the same time, at the other end of the gear (wheel), the angle takes on the maximum value, that is, $\beta = \beta_{max}$.
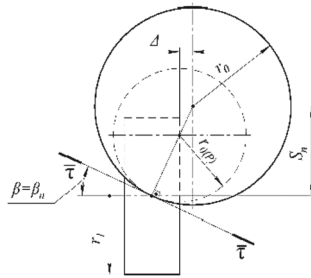
Fig. 2. The teeth' inclination angle in the middle section of the engagement width.

The accepted condition β_{min} (Fig. 3, a) will be performed if the axis of the cutting head is located at one of the ends of the gear (wheel).

For the given parameters β_n and b_W the calculated radius of the gear cutting head $r_{o(P)}$, which provides the condition β_{min}, is determined by the equality $r_{o(P)} = 0.5 \cdot b_W / sin\beta_n$, Fig. 3a.

According to the calculated value $r_{o(P)}$ from [11], the nearest larger nominal radius of the standard gear-cutting head $r_o = d_o/2$ is taken [25]; (in a particular case, the values $r_{o(P)}$ and r_o may coincide).

Further calculations are carried out using the standard r_o. Since $r_o \geq r_{o(P)}$, the center of the gear head circle with the nominal radius r_o will be displaced from the right end of the pinion being cut by an amount $\Delta = r_o \cdot sin\beta_n - 0.5 \cdot b_W$, as a result of which the minimum angle of the teeth inclination β_{min} will no longer be zero, Fig. 3, a.

$$\sin \beta_{min} = \frac{\Delta}{r_o} = \frac{r_o \cdot \sin \beta_n - 0.5 \cdot b_W}{r_o} = \sin \beta_n - 0.5 \cdot b_W / r_o \qquad (1)$$
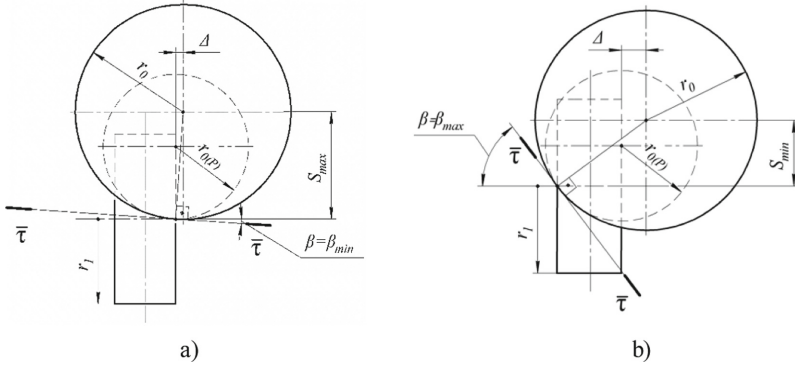
Fig. 3. The angles of the teeth inclination along the width of the engagement: a – minimum; b – maximum.

hence, the minimum angle of inclination, is equal to:

$$\beta_{\min} \arcsin(\sin \beta_n - 0.5 \cdot b_W / r_o) \tag{2}$$

Similarly, β_{max}, Fig. 3, b:

$$\sin \beta_{\max} = \frac{\Delta + b_W}{r_o} = \frac{r_o \cdot \sin \beta_n + 0.5 \cdot b_W}{r_o} = \sin \beta_n + 0.5 \cdot b_W / r_o, \tag{3}$$

from where: $\beta_{\max} \arcsin(\sin \beta_n + 0.5 \cdot b_W / r_o)$.
Using the equation of the longitudinal line of the incline-arched teeth:

$$\vec{R}_1 = -\vec{i}_1 \cdot r_1 \cdot \cos \phi - \vec{j}_1 \cdot r_1 \cdot \sin \phi + \vec{k} \cdot \left(\sqrt{r_o^2 - r_1^2 \cdot \phi^2} - r_o \cdot \sin \beta_n \right), \tag{4}$$

determine the initial ϕ_i and finite ϕ_f angles of the pinion rotation for cutting one cavity between two adjacent teeth. To do this, it is enough to equate the coordinate sequentially z_1 in Eq. (5) to its two extreme values: $z_1 = \pm 0.5 \cdot b_W$. As a result:

$$\phi_{H,K} = \sqrt{r_o^2 \cdot \cos^2 \beta_n - b_W \cdot (0.25 \cdot b_W \pm r_o \cdot \sin \beta_n)} / r_1, \tag{5}$$

where $r_1 = 0.5 \cdot m_n \cdot z_1 / \cos \beta_n$ is the pitch radius of the pinion.

For the term under the root with a double sign "$\pm$", the "plus" sign is taken during the calculation ϕ_i and the "minus" sign is taken during the calculation ϕ_f.

In Fig. 2, 3 symbol $\bar{\tau}$ denotes the tangent to the circle with the radius r_o at the point of its intersection with the middle-end section, the pinion's right and left end of the pinion, respectively.

4   Results

Cutting SGIAT teeth is carried out by the generation method therefore the rotation of the pinion with an angular velocity ω_1 and the translational movement of the gear-cutting

head with a speed V_o are interrelated movements: $V_o = \omega_1 \cdot r_1$. In this case, the distance between the axes of the gear and the cutting head in the direction of movement of the latter in the process of forming one cavity between two adjacent pinion teeth varies from S_{max} to S_{min}: $S_{max} = (r_o - r_{o(P)}) \cdot \cos \beta_{min}$; $S_{min} = (r_o - r_{o(P)}) \cdot \cos \beta_{max}$.

The angles of pinion rotation ϕ_i and ϕ_f make it possible to find the coefficient of the SGIAT end overlap:

$$\varepsilon = \frac{\phi_f - \phi_i}{P} = \frac{\phi_f - \phi_i}{(2 \cdot \pi / z_1)} = \frac{\sqrt{r_o^2 - b_W^2} - r_o}{(2 \cdot \pi / z_1) \cdot r_1}, \tag{6}$$

where $P = 2 \cdot \pi / z_1$ – circumferential pitch of the teeth.

At the same time, an increase in the overlap ratio ensures the smooth operation of the tool magazine even when using small-tooth gears.

The length L of the longitudinal line (4) of the incline-arched tooth lying on the pitch diameter of the pinion (the parameter L is necessary for the strength calculations of the tooth):

$$L = \int_{\phi_H}^{\phi_K} \sqrt{\dot{x}_1^2 + \dot{y}_1^2 + \dot{z}_1^2} \cdot d\phi, \tag{7}$$

where

$$\begin{cases} \dot{x}_1 = dx_1/d\phi = r_1 \cdot \sin \phi; \\ \dot{y}_1 = dy_1/d\phi = -r_1 \cdot \cos \phi; \\ \dot{z}_1 = dz_1/d\phi = -r_1^2 \cdot \phi / \sqrt{r_o^2 - r_1^2 \cdot \phi^2}. \end{cases} \tag{8}$$

After substituting (8) into (7), we obtain the required dependence for calculating the length of the longitudinal line (4):

$$L = r_o \cdot \int_{\phi_H}^{\phi_K} \frac{d\phi}{\sqrt{(r_o/r_1)^2 - \phi^2}} = r_o \cdot arcsin\left(\frac{r_1 \cdot \phi}{r_o}\right)\Big|_{\phi_H}^{\phi_K}. \tag{9}$$

An increase in the length of the entire line of engagement increases the carrying capacity of the transmission and its durability.

The radius of the longitudinal line curvature (4):

$$\rho = \frac{\sqrt{\left[(r_o^2 - r_1^2 \cdot \phi^2) \cdot \cos^2\phi + r_1^2 \cdot \phi^2\right]^3}}{|\phi \cdot (r_o^2 - r_1^2 \cdot \phi^2) \cdot \sin\phi + r_o^2 \cdot \cos\phi|} \tag{10}$$

The limits of variation of the curvature radius ρ are determined from Eq. (9) by substituting the values $\phi = \phi_i$ and $\phi = \phi_f$.

Let us illustrate the obtained analytical results concerning the parameters $[r_{o(P)}, \Delta, \beta_{min}, \beta_{max}, \theta_i, \theta_f, S_i, S_f, \varepsilon, L, \rho_{min}, \rho_{max}]$ modified gear drive of the disk tool magazine.

In the numerical calculation of SGIAT, the following engagement characteristics are used: $m_n = 4$ mm; $b_W = 85$ mm; $z_1 = 19$; $\beta_n = 17^0 49' 27''$; $r_1 = 0.5 \cdot m_n \cdot z_1 / \cos \beta_n = 39.92$ mm. The calculation results are shown in the table (Table 1).

Table 1. The calculated value of transmission parameters.

Parameter	$\frac{r_{0(P)}}{r_0}$	Δ	$\frac{\beta_{min}}{\beta_{max}}$	$\frac{\varphi_i}{\varphi_f}$	$\frac{S_{min}}{S_{max}}$	ε	L	$\frac{\rho_{min}}{\rho_{max}}$
Value	$\frac{138.8}{157.5}$	5.7	$\frac{2.1^0}{35.2^0}$	$\frac{184.8^0}{225.9^0}$	$\frac{15.3}{18.7}$	2.2	91.0	$\frac{28.4}{224.4}$

When obtaining experimental data in the table, it was taken into account that the calculated diameter of the gear cutting head $d_{o(P)} = 2 \cdot r_{o(P)} = 2 \cdot 138.8 = 277.6$ mm is between its two standard nominal diameters d_o, equal 250 and 315(mm). Since the condition must be met $r_o \geq r_{o(P)}$, a larger standard nominal diameter $d_o = 315$ mm is adopted, for which $r_o = d_o/2 = 315/2 = 157.5$ mm. Wherein $r_o = 157.5$ mm $> r_{o(P)} = 138.8$ mm. All linear dimensions in the table are given in mm.

5   Conclusions

A comprehensive project for creating a disk tool magazine with a modified drive device, which provides an increased service life of drive elements and more accurate positioning of tool blocks, has been developed.

3D project of a disk tool magazine for 14 tools in the environment of CAD KOMPAS-3D using the application program "Shafts and mechanical transmissions -3D" has been created. The project, which includes 1330 3D models of parts and assemblies, became a prize-winner of the International Competition "Future Aces of Computer 3D-Modeling". An idea of a constructive modification of spur gear with inclined-arched teeth with a variable angle of teeth inclination along the gearing width was put forward and implemented. As a limitation, it is assumed that at one end of the wheel, the axis of the gear-cutting head is located at one of the ends of the wheel.

An analytical form for calculating the relationship between the gearing parameters and the size of the gear cutting head has been developed. It has been proven that to increase the overlap ratio of the modified SGIAT, the closest larger standard size of the gear cutting head should be taken to its calculated value, which excludes negative angles of the teeth inclination in this gear.

An experimental calculation of a modified version of SGIAT has been used in a disk tool magazine drive. As a result, the durability of this device and the accuracy of positioning of tool blocks have been increased.

Creating promising drives with modified gears is one of the trends in developing ATC systems in modern machine-building production. Further development of works on this topic is planned to create a complex of parametrized three-dimensional models of drive structures and their elements for a wide range of magazines and develop relevant sections of databases for the machine-building industry.

References

1. Dervoort, W.H.: Modern Machine Shop Tools, Their Construction, Operation and Manipulation, Including Both Hand and Machine Tools. Creative Media, London, LLS (2018)

2. Borovik, A., Gorlachev, V., Lelyukhin, V., Cheboksarov, V.: Metal-cutting machines. Training and methodology complex. Prospect, Moscow (2019)
3. Lynch, M.: Machining Center. Setup and Operation. CNC Concept, Inc., Illinois (2013)
4. Platonov, L.: 15 novelties of KOMPAS-3D vol 15. CAD Graph. **6**, 7–21 (2014)
5. Nikonov, I.: KOMPAS-3D Creation of models. Progress book, Moscow (2020)
6. Schaupp, E., Abele, E., Metternich, J.: Evolution relevant factors for developing an optimal tool storage strategy. Procedia CIRP **55**, 23–28 (2016). https://doi.org/10.1016/j.procir.2016.08.047
7. Rochov, P., Hund, E., Gruss, M., Nuhuis, P.: Development of a mathematical model for the calculation of the tool appropriation delay depending on the tool inventory. Logist. J. referierte Veröffentlichungen **2015** (2015). https://doi.org/10.2195/lj_Rev_rochow_en_201503_01
8. Chen, C., Tian, H., Zhang, J., et al.: Study on failure warning of tool magazine and automatic tool changer. J. Vibroeng. **18**(2), 883–899 (2016)
9. Li, G., Wang, Y., He, J., et al.: Fault forecasting of a machining center tool magazine based on health assessment. Math. Prob. Eng., 1–10 (2020). DOI: https://doi.org/10.1155/2020/5796965
10. Yan, Y., Yin, Y., Xiong, Z., Wu, L.: The simulation and optimization of chain tool magazine automatic tool change process. Adv. Mater. Res. **834–836**, 1758–1761 (2014)
11. Litvin, F.L., Qi, Fan, Fuentes, A.: Computerized design, generation, simulation of meshing and contact of face-milled format cut spiral bevel gears (2001). https://doi.org/10.21236/ada394095
12. Janigova, S., Schurger, B.: Design optimization of the modified planetary carrier. J. Eng. Sci. **8**(1), E17–E22 (2020). https://doi.org/10.21272/jes.2021.8(1).e3
13. Zhilevski, M., Mikhov, M.: Study and performance improvement of the drive systems for a class of machine tools. In: 14th International Conference on Modern Technologies in Manufacturing, MATEC Web of Conferences, Cluj Napoca, Romania, vol. 299, p. 05003 (2019). DOI: https://doi.org/10.1051/matecconf/201929905003
14. Pavlenko, I., Ivanov, V., Kuric, I., Gusak, O., Liaposhchenko, O.: Ensuring vibration reliability of turbopump units using artificial neural networks. In: Trojanowska, J., Ciszak, O., Machado, J.M., Pavlenko, I. (eds.) MANUFACTURING 2019. LNME, pp. 165–175. Springer, Cham (2019). https://doi.org/10.1007/978-3-030-18715-6_14
15. Krol, O., Porkuian, O., Sokolov, V., Tsankov, P.: Vibration stability of spindle nodes in the zone of tool equipment optimal parameters. Compters rendus de l'Acade'mie bulgare des Sciences **72**(11), 1546–1556 (2019). https://doi.org/10.7546/CRABS.2019.11.12
16. Rogovyi, A., Korohodskyi, V., Medvediev, Y.: Influence of Bingham fluid viscosity on energy performances of a vortex chamber pump. Energy **218**, 119432 (2021)
17. Tsankov, P.: Modeling of vertical spindle head for machining center. J. Phys. Conf. Ser. **1553**, 012012 (2020). https://doi.org/10.1088/1742-6596/1553/1/012012
18. Krivosheya, A.V., Voznyy, V.V., Melnyk, V.E.: Analysis of the gear tooth gearing by the module m = 2625 mm of hydraulic pumps. J. Eng. Sci. **4**(1), A11–A15 (2017)
19. Ivanov, V., Dehtiarov, I., Pavlenko, I., Kosov, I., Kosov, M.: Technology for complex parts machining in multiproduct manufacturing. Manag. Prod. Eng. Rev. **10**(2), 25–36 (2019). https://doi.org/10.24425/mper.2019.129566
20. Syzyi, Y., Ushakov, O., Slipchenko, S., Basova, Y., Ivanova, M.: Simulation of the contact temperature in the cylindrical plunge grinding process. Diagnostyka **21**(2), 77–86 (2020). https://doi.org/10.29354/diag/122532
21. Radzevich, S.: Theory of Gearing: Kinematics, Geometry, and Synthesis, 2nd edn. CRC Press, Boca Raton (2018)
22. Krol, O., Sokolov, V.: Research of modified gear drive for multioperational machine with increased load capacity. Diagnostyka **21**(3), 87–93 (2020). https://doi.org/10.29354/diag/126026

23. Ivanov, V., Dehtiarov, I., Pavlenko, I., Kosov, M., Hatala, M.: Technological assurance and features of fork-type parts machining. In: Ivanov, V., et al. (eds.) DSMIE 2019. LNME, pp. 114–125. Springer, Cham (2020). https://doi.org/10.1007/978-3-030-22365-6_12
24. Kubo, A., Ueda, A.: Gear geometry as function of production method. In: The Proceedings of the JSME International Conference on Motion and Power Transmission, vol. 5, no. 1, pp. 27–44 (2017)
25. Solid cutters for bevel gears. Standard ASP 2023-special S390. Padova (2014)

Improvement of the Computer-Aided Design for Interference Fit Based on the Generalized Design Selection Criteria

Vladimir Nechiporenko(✉) [iD], Valentin Salo [iD], Petro Litovchenko [iD],
Vladislav Yemanov [iD], and Stanislav Horielyshev [iD]

National Academy of the National Guard of Ukraine, 3, Zakhysnykiv Ukrayiny Sq.,
Kharkiv 61001, Ukraine
`69nevlani@gmail.com`

Abstract. The paper proposes an improved approach to finding a rational combination of numerical values of geometric parameters (diameter and working length) of interference fit in the process of their analysis based on a scientifically grounded universal criterion in the automated design of the test joint. The mentioned search was carried out within the analytically described mathematical model, which is the most important in practical terms, of the area of existence of the fit parameters of the multiparametric complex, developed by the authors in previous publications. In this case, the object of the study is geometric spatial images, which are volumetric bodies of the specified complex in the quadrants of three-dimensional space. The influence of the values of the required parameters on other values of the specified complex of models was thoroughly studied. For the first time, a generalized criterion for selecting the final design solution (standard interference fit) for a shroud joint during its thermal assembly and operation was formulated. For the selected criteria, the mathematical apparatus of the theory of *R*-functions was used together with the authors' computer software that plays the role of an effective research tool. The specific numerical and analytical results presented in work can be used to modernize the software for the computer-aided design of interference fits.

Keywords: Product innovation · Mathematical modeling · Area existence · Theory *R*-functions · Complex parameters · Multi-parametric model

1 Introduction

In modern machines, there is a tendency to use more and more capacities to implement their working function, high speeds in transport simultaneously with increasing requirements for increasing the service life, efficiency, and environmental safety. The main technological operation responsible for this set of requirements is assembly, during which the quality of the connected parts and machine assemblies is ensured. One of the most common assembly operations is guaranteed interference on a smooth cylindrical or conical surface of power units and mechanical transmissions parts. Such joints most

often experience a joint action of axial force and torque. Therefore, they are one of the most critical machine units.

In this regard, creating and implementing effective methods and software tools for computer-aided design of interference fit for joints of machine elements is an urgent task of modern mechanical engineering. Automation of the design process of interference fits allows considering many loading, operational and technological factors to reduce the random factor during assembly and reduce the number of experimental studies and tests, improving the quality and shortening the design work time.

2   Literature Review

A significant number of scientific studies are devoted to the issues of mathematical modeling of friction smooth joints with an interference fit. So, in the article [1], one of the methods for calculating composite bolted joints was developed. From the analysis of the clamping force of the bolt and the friction of the contact surfaces, it was revealed that the most critical parameter of influence on the mechanical properties of the composite bolted joint is the hole tolerance. In [2], an experimental study of the mechanical response of composite joints made of carbon fiber reinforced plastic connected with overlapping bolts was carried out. Microscopic examinations of the interface and the bearing plane were carried out to understand the damage mechanism. As a result, it was found that the insertion of the bolt can act as cold expansion, facilitating the formation of a tightly connected interface and preventing the bolt from tilting. However, in papers [1] and [2], there is no information about the automation level for solving the problems under consideration, reducing the presented results' value.

The paper [3] describes a method for numerical simulation of the behavior of composite joints during an interference fit under the condition of pretensioning overlapped bolts in the event of extreme temperatures. The disadvantage of this method is the need to destroy the joint elements. In [4], the author proposes a method for compensating machining errors on the surface of arbitrary shape parts using a 3D model of a machining template in CAD. To evaluate this model, a methodology is proposed that uses regression analysis, spatial statistics methods, and NURBS modeling. By applying this method to an interference fit during the design phase, the quality of the mating joint surfaces can be improved.

The article [5] uses the method of stochastic analysis of the load distribution on bolt elements in composite joints using the Monte Carlo simulation method. This algorithm can be easily built into its structure as a separate module with a sufficiently high software versatility. In [6], the authors propose to use interior point algorithms to find solutions in a generalized continuum – a space bounded on all sides using finite element analysis based on the FEniCS package. However, it is irrational to apply the methods proposed in [5, 6] for the automated design of joints with interference since there are continuous functional connections between most of the model parameters of the area of existence of fits. In [7], it is proposed to transform the structure of the model into a topological one with a minimum number of geometric parameters using the numerical methods of Ritz and Galerkin. For models representing a closed area of space, these methods, in our opinion, are ineffective.

Finally, let's note that the issues of computer-aided design and mathematical modeling have received much attention in modern scientific research [8, 9] related to the design of permanent joints [10], in particular, interference fit. However, the issue of predicting the quality of the fit, which depends on its parameters, taking into account their probabilistic nature, remains relevant. Creating and implementing effective design methods and software to solve the stated problem is necessary. In [11], one of the many criteria for selecting a standard interference fit in the coordinate planes *dl*, *lN,* and *dN* of the *dlN* quadrant (*l* is the fit working length, *d* is the fit diameter, *N* is the interference) is proposed. Its essence lies in selecting one of the alternative localized fit models (as an example, this is *H7/v7*), which occupies the most significant part of the volume within the recommended area of existence of the friction joint parameters. The considered criterion effectively solves this problem but is not always sufficient for selecting a rational design solution since most of its parameters are interconnected for the adopted fit.

3   Research Methodology

This paper studies the influence of individual parameters of a multiparametric complex of a three-dimensional mathematical model (TDMM) based on the automated calculation of smooth cylindrical joints with interference when using the thermal assembly method carried out. These studies are based on the results of numerical-analytical methods of work [11] using the author's computer program Interference Fit. At the initial stage, a comprehensive study of the mutual influence of the geometric parameters d and l (in a wide range of values) was carried out, and a rational combination of their values was found. Depending on the values of these sought-for values from the area of existence of suitable standard fits (AEF), it becomes possible to determine other important parameters for the selected fit in any part of the multiparametric mathematical model complex. At the same time, the methodology for selecting a rational interference fit according to the proposed criterion is based on a qualitatively new study of a TDMM of AEF in the *dlN* quadrant. Note that the central values of these criteria [12, 13] are analytically described using the mathematical apparatus of the theory of R-functions [14, 15].

This research aims to study the influence of individual parameters of a complex of *n*-parametric TDMM of the area of existence of fit parameters (AEFP) on the qualitative selection of a smooth joint with an interference fit of the crown of a gear wheel with a hub, carried out in the thermal assembly method. The use of a multiparametric complex with mathematical modeling makes it possible to improve the author's software, make it possible to make the final design solution more accurate, and show rational combinations of its parameters.

4   Results

4.1   Generalized Criteria for Selecting a Rational Interference Fit Within the Quadrant *dlN*

The fit diameter d is the governing argument for the functions of the following series of friction joint parameters: fit working length l = f(d) (minimum critical value of working

length lcr and recommended maximum working length of the fit lr max), specific contact pressure p = f (d, l)) (limit permissible [pmin] and [pmax] and actual pa) on the mating surfaces of the joint and, as the final result of the calculation, the required interference N = f(p). Considering the above parameters is necessary to select the final design solution from the list of alternatives in their automated design.

In the presented numerical studies, the initial data and the results obtained by the authors of [11] in the form of three-dimensional graphical objects, which are mathematical models of the AEFP, were taken as a basis. However, the rational values of the diameter d and the working length l of the fit are determined in the proposed work. Within the analytically described in [11] area of existence of geometric parameters of fits (AEGPF), represented in the form of a flat figure *abcd* (two-dimensional model) in the coordinate plane *dl* (see Fig. 1), in this study, let's find the center of grouping of the sought quantities – points B (d_B; l_B), where d_B and l_B are coordinates. Point B represents the intersection of the segments of the range of variation of the rational values of the fit diameter $\delta_{d_{max}}$ and the range of variation of the rational values of the fit working length $\delta_{l_{max}}$.
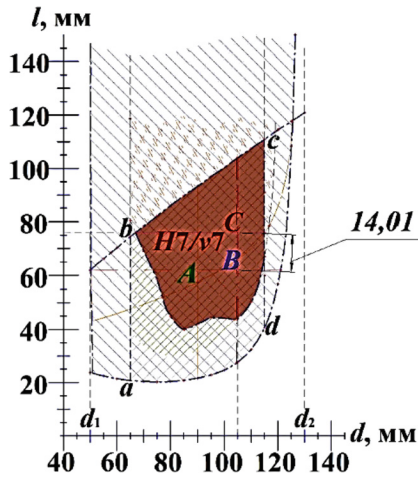
Fig. 1. The set (localized flat model) of the fit *H7/v7*, included in the AEGPF, depending on the diameter and working length.

The maximum values of the ranges of rational values of orthogonal segments within the plane model of AEGPF are determined by the formulas:

$$\delta_{l_{max}} = \frac{l_{r_{max}} - l_{cr}}{t_l}; \quad \delta_{d_{max}} = \frac{(d_2 - 15) - (d_1 + 15)}{t_d}, \quad (1)$$

where t_l and t_d – the length and diameter steps through which the corresponding maximum segments (ranges) of their rational values are set (at $t_l = t_d = 1$ mm); $(d_1 + 15)$ and $(d_2 - 15)$ – the minimum and maximum recommended limit values of the seating diameter of the joint, within which it is possible to ensure the specified strength of the

joint, respectively; d_1 – the diameter of the inner surface of the covered part; d_2 – the conventional outer diameter of the covering part.

For the example under consideration, initial data $d_1 = 50$ mm and $d_2 = 130$ mm were adopted, and values $d_1 + 15 = 50 + 15 = 65$ mm; $d_2 - 15 = 130 - 15 = 115$ mm – described in operation [11]; l_{cr} – the minimum critical value of the working length at which the condition for the strength of the joint is met [11]:

$$l_{cr} = \frac{[p_{min}]_k}{[p_{max}]} l_k, \tag{2}$$

where $[p_{min}]_k$ and $[p_{max}]$ respectively, are the allowable limiting minimum and maximum values of specific contact pressure on the working surfaces of the parts in the joint, at a particular actual value of the fit working length l_k.

After analyzing and enumerating the diameter and length values for the considered fit $H7/v7$, let's accept their rational combination: B (105; 60) ($d_B = 105$ mm and $l_B = 60$ mm). Analytically, this point is set using the mathematical apparatus of the theory of R-functions [12, 13] in the form:

$$\omega_B = d - d_B + l - l_B - \sqrt{(d - d_B)^2 + (l - l_B)^2}, \tag{3}$$

where $d - d_B$ and $l - l_B$ – are the distances from the origin of the coordinate axis $0d$ to the point d_B and from $0l$ to l_B, respectively, for the *abcd* figure model ($d - d_B = 105$ mm and $l - l_B = 60$ mm).

Let's note that the proposed method is effective from the point of view of covering not only one rational fit but also admissible alternative ones depending on the geometric parameters d and l of the two-dimensional AEGPF model. To formulate one of the many criteria associated with the choice of a suitable standard interference fit from the list of alternative ones, let's determine the center of a grouping of rational values of geometric parameters – points C_i (d_{C_i}; l_{C_i}), the localized set (flat model) of each selected standard i-th interference fit from among alternatives. The location of the point C_i, formed at the intersection of the segments of the maximum values of the change in the ranges of the fit diameter $\delta_{d_{C_i}}$ and fit the working length $\delta_{l_{C_i}}$ analytically described (according to the theory of R-functions [14, 15]) is similar to formula (3):

$$\omega_{C_i} = d - d_{C_i} + l - l_{C_i} - \sqrt{(d - d_{C_i})^2 + (l - l_{C_i})^2}, \tag{4}$$

where d_{C_i} and l_{C_i} – the actual coordinates of the point of the segment of the range of values of the fit diameter and fit working length, respectively.

Several suitable standard fits are superimposed on the AEGPF model as many localized flat models. For the example in question, Fig. 1 shows the fit of the $H7/v7$ included in the AEGPF, which are shaded areas. An important factor in our research is determining the segment BC_i, the smallest distance from point C_i to point B. In particular, for fit $H7/v7 - BC_{v7} = 14.01$ mm. The analysis of the results shows that the considered case is the most rational among all suitable fits, which can be taken as one of the main criteria for selecting a standard interference fit from the list of alternatives, depending on the parameters within *dlN* quadrant. This generalized selection criterion coincides with a particular criterion proposed in the study [11], confirming its effectiveness and reliability.

4.2   A Complex of Three-Dimensional Models of the Area of Existence of Fits

The combination of various criteria for selecting the final design solution is essential for the designer. However, in this case, it is necessary to consider how the main parameters of the adopted fit affect the values of other parameters, on which the value of the actual interference in the joint depends. In [11], for fit *H7/v7*, a particular criterion for selecting suitable interference fit in the coordinate planes *dl*, *lN*, and *dN* was considered (see Fig. 2), and before that (in previous works of the authors) – in the coordinate planes *lp*, *lN* and *pN* that have a standard adjacent plane *lN*. It is important to note that in the case of using the thermal method of assembling the joint, it is necessary to consider a significant technological factor – the temperature t_2 of heating of the covering part.
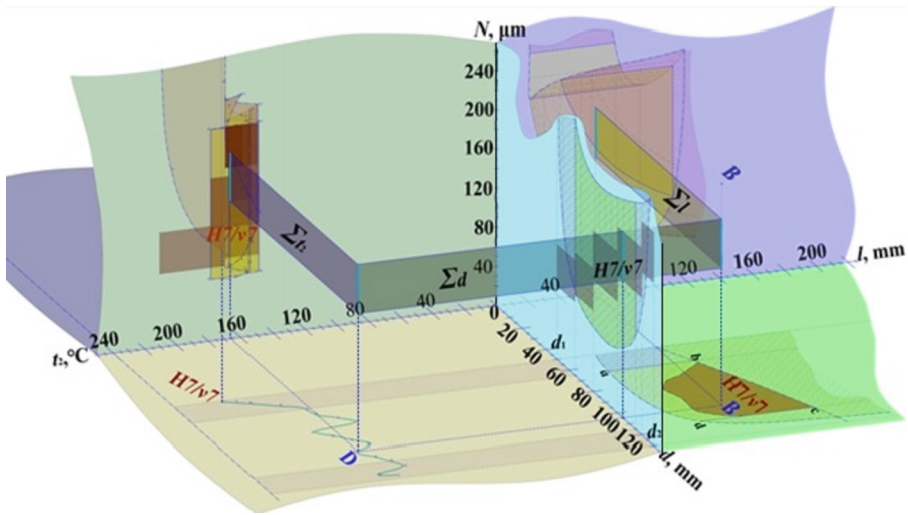
Fig. 2. Projections of TDMM of the AEF and secant parametric planes.

To construct the following spatial models of the AEF, as components of the general complex of the multiparametric image TDMM, the coordinate axis $0t_2$ (°C) is orthogonally extended to the coordinate planes *dN* and *pN* to form projection coordinate planes dt_2, t_2N and pt_2. Then the two-dimensional models constructed based on a numerical-analytical analysis of the research results in the form of graphs on the coordinate planes dt_2 and t_2N should be added to the previously studied model *dN*. As a specific applied example, a TDMM of the AEF and a localized model of the selected standard fit *H7/v7* (see Fig. 3) superimposed on it were considered in the case of the accepted values of the fit diameter $d = 105$ mm and the fit working length $l = 60$ mm. Such an AEF plotted in the coordinate axes dt_2N is a wavy surface projected onto the coordinate plane dt_2 in a curve with a decreasing character. This spatial surface is bounded by curves corresponding to the values of admissible interferences: from above – $[N_{max}]$ and from below – $[N_{min}]$ at $l_k \rightarrow l_{r\,max}$. The secant rectangular plane Σd (see Figs. 2 and 3) with a height equal to the limiting values of the probabilistic interferences of fit *H7/v7*, orthogonally intersects the projection of the two-dimensional recommended localized model (stepped shape) in

the coordinate plane dN. The Σd plane intersects the three-dimensional wavelike AEF model in the dt_2N quadrant.
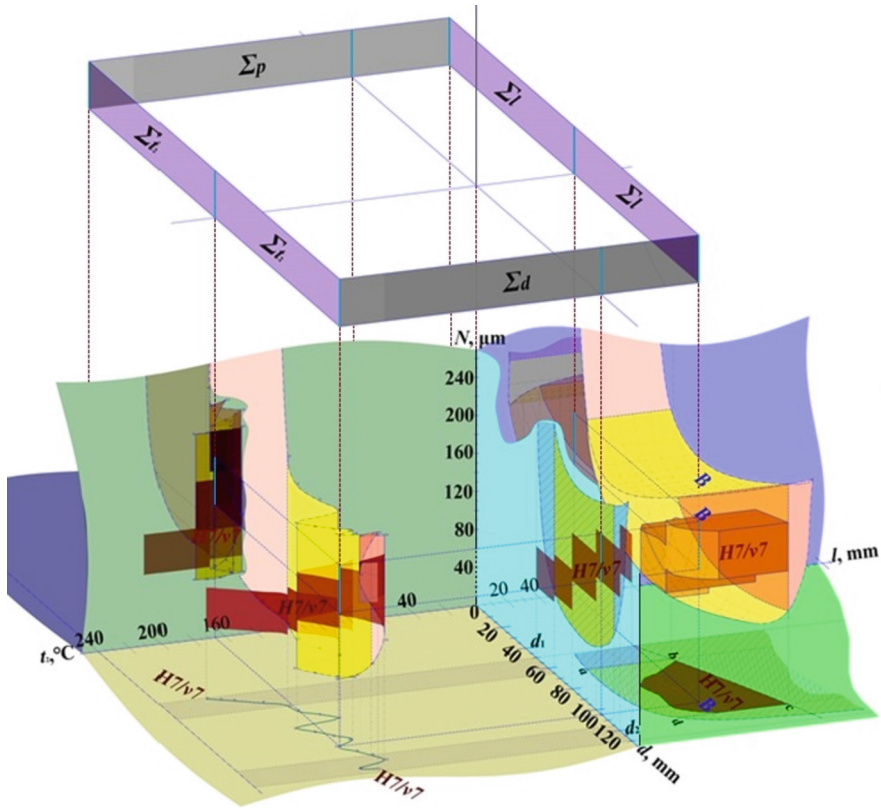
Fig. 3. Volumetric models of the AEF.

The secant parametric plane Σt_2 (see Fig. 2) orthogonally intersects the projection of the model in the coordinate plane t_2N, passing through the undulating surface model of the selected fit, and at the same time also intersects the plane Σd (Σt_2 is perpendicular to Σd, and the line of their intersection of these planes on the model is projected into point D of the coordinate plane dt_2). The secant planes Σl and Σp are formed similarly (see Fig. 3), with Σd parallel to Σp and Σt_2 parallel to Σl. These secant planes form a closed rectangle in the plan (perpendicular to the coordinate axis 0N). Its corners are always in the corresponding body of the AEF model for their quadrant. The result of all the above geometric operations shows a clear functional relationship of the parameters of the selected fit in a multiparametric complex of TDMM. The proposed generalized criterion for the considered example of fit $H7/v7$ allows visually determining the value of the heating temperature of the covering surface of part $t_2 = 167$ °C. Applying the method created by the authors, the user analyzes the graphic interaction of interference fit parameters to select a rational design solution.

5 Conclusions

When using the mathematical apparatus of the theory of *R*-functions to improve the methodology of computer-aided design of fit with interference, the ranges of the combination of rational values of the basic geometric parameters of the fit are analytically described.

As a result of the performed three-dimensional modeling, a visual representation of numerical calculations in the form of a graphical image was created, the practical use of which makes it possible to comprehensively take into account the *n*-th number of parameters for the selected fit in the spatial images of each quadrant with the coordinate axis 0*N*. This circumstance makes it possible to objectively assess the rationality of the adopted design solution in the automated design of interference fit.

When using the effective Interference Fit software to calculate interference fit in the numerical calculations, the authors formulated a generalized criterion for selecting the final design solution.

Based on the research results, it is planned to create methodological and software tools for implementing an integrated methodology for the computer-aided design of interference fits for joints of machine-building parts. In addition, it is planned to study the strength parameters of interference fits with their calculations based on the use of the various numerical and analytical methods of RVR, which will increase the qualitative level of their design.

References

1. Chao, C., Dean, H., Qiming, L., Xu, H.: Evaluation on the interval values of tolerance fit for the composite bolted. Compos. Struct. **206**, 628–636 (2018). https://doi.org/10.1016/j.compstruct.2018.08.062
2. Junshan, H., Kaifu, Z., Qingda, Y., Hui, C., Ping, L., Yu, Y.: An experimental study on mechanical response of single-lap bolted CFRP composite interference-fit joints. Compos. Struct. **196**, 76–88 (2018). https://doi.org/10.1016/j.compstruct.2018.05.016
3. Junshan, H., Kaifu, Z., Hui, C., Peng, Z.: Modeling on mechanical behavior and damage evolution of single-lap bolted composite interference-fit joints under thermal effects. Chin. J. Aeron. **34**(8), 230–244 (2021). https://doi.org/10.1016/j.cja.2020.09.023
4. Poniatowska, M.: Free-form surface machining error compensation applying 3D CAD machining pattern model. Comput. Aided Des. **62**, 227–235 (2015). https://doi.org/10.1016/j.cad.2014.12.003
5. Fengrui, L., Meijuan, S., Libin, Z., Jianyu, Z.: Probabilistic bolt load distribution analysis of composite single-lap multi-bolt joints considering random bolt-hole clearances and tightening torques. Compos. Struct. **194**, 12–20 (2018). https://doi.org/10.1016/j.compstruct.2018.03.100
6. Bleyer, J., Hassen, G.: Automated formulation and resolution of limit analysis problems. Comput. Struct. **243**, 106341 (2021). https://doi.org/10.1016/j.compstruc.106341
7. Ge, Y., Xiao, X., Fehmi, C.: Topologically robust CAD model generation for structural optimization. Comput. Methods Appl. Mech. Eng. **369**, 113102 (2020). https://doi.org/10.1016/j.cma.2020.113102
8. Cao, Y., Zhang, L., Sun, Y., Shi, Y., He, Y., Zhen, Y.: Strength analysis of the interference joint of the oval submarine pipeline to the mechanical connector. Appl. Ocean Res. Direct **101**, 102229 (2020)

9. Zhang, X., Jiang, H., Luo, T., Hu, L., Cui, J.: Theoretical and experimental investigation on interference fit in electromagnetic riveting. Int. J. Mech. Sci. **156**, 261–271 (2019)
10. Song, D., Li, Y., Zhang, K., Cheng, H., Liu, P., Hu, J.: Micromechanical analysis for microscopic damage initiation in fiber/epoxy composite during interference-fit pin installation. Mat. Des. **89**, 36–49 (2016)
11. Nechiporenko, V., Salo, V., Litovchenko, P., Rakivnenko, V., Horbunov, A.: Rational design solution based on mathematical modeling of an interference fit. In: Ivanov, V., Trojanowska, J., Pavlenko, I., Zajac, J., Peraković, D. (eds.) DSMIE 2021. LNME, pp. 73–80. Springer, Cham (2021). https://doi.org/10.1007/978-3-030-77719-7_8
12. Awrejcewicz, J., Kurpa, L., Shmatko, T.: Investigating geometrically nonlinear vibrations of laminated shallow shells with layers of variable thickness via the R-functions theory. Compos. Struct. **125**, 575–585 (2015)
13. Balestrino, A., Caiti, A., Crisostomi, E., Grammatico, S.: Stabilizability of linear differential inclusions via *R*-functions. IFAC Proc. **43**(14), 1092–1097 (2010)
14. Pokras, V., Rvachev, M.: Application of the *R*-functions method to visioplastic analysis in metal forming. J. Mater. Process. Technol. **60**(1–4), 493–500 (1996)
15. Varvak, M.: Ellipsoidal/radial basis functions neural networks enhanced with the Rvachev function method in application problems. Eng. Appl. Artif. Intell. **38**, 111–121 (2014)

Substantiation of the Design Calculation Method for the Vibroturning Device

Roman Obertyukh , Andrii Slabkyi(✉) , Oleksandr Petrov , Dmytro Bakalets ,
and Sergey Sukhorukov

Vinnytsia National Technical University, 95, Khmelnytske Shose, Vinnytsia 21021, Ukraine
Slabkiyandrey@gmail.com

Abstract. The method of design calculation of the hydropulse device for radial vibration turning with the built-in generator of pressure pulses is presented in work. The structure is built based on a hydropulse vibrating drive, which provided a large specific power on the cutting tool and high compactness of the construction. The device's design calculation method is based on the results of experimental and theoretical studies of vibrating machines. The proposed method of construction calculation provides the ability to calculate the basic power, geometric, and energy parameters of the device for vibratory turning and can be used to calculate similar hydropulse devices for vibratory cutting and deformation hardening surfaces of machine parts. Based on the dependencies used in the proposed design calculation method, it is possible to optimize the design for a particular parameter, such as the speed of operation of the pressure pulse generator or the device's dimensions.

Keywords: Hydropulse device · Ring spring · Frequency · Amplitude · Device · Manufacturing innovation

1 Introduction

Creation of new designs of hydraulic impulse devices based on springs of increased rigidity (SR) – slotted springs, disk, and annular [1], expands the scope of using equipment with hydraulic impulse drive (HID). In particular, HID is used in the technological process of materials processing by vibration cutting (VC) (vibration rotation [2], vibration drilling [3], and vibration pressing [4]). Hardening of the surfaces of machine parts by surface hardening [5] and plastic deformation (SPD) can also be carried out using the HID [6, 7]. SHR-based hydro-pulse devices differ from the known devices for VC and SPD in small size and high intensity of impact on the technological object of treatment. In hydraulic-pulse devices based on SHR, the parameters of the force-vibration load (e.g., force, amplitude, and frequency of oscillations, and the form of oscillations of the actuator of the device) can be adjusted (if necessary, adaptability, in a wide range of simple mechanisms and means) [8, 9].

2   Literature Review

The expansion of technical and technological capabilities of hydropulse devices on SHR is closely related to the capacity of the pressure pulse generator (PPG), which controls the operation of the device (PPG, usually combined in one design with the power unit of the device [1, 10]). The necessity of small size (compactness) is not allowing the use of multi-stage PPG in the drive of these devices. So instead, it uses only single-stage parametric generators [1, 10, 11]. The requirement of small size (compactness) does not allow the use of multi-stage PPG in the drive of these devices [1, 11] and uses only single-stage parametric generators [12]. One of the possible ways to increase the throughput of single-stage PPG based on SHR is to reduce the stroke of the locking element of the PPG by eliminating its spool sealing at both levels (positive overlap h_d) and the use of bevel (valve) sealing and short SHR, the stiffness of which is determined by allowable stresses. In the springs elements that occur in the cross-sections of the SHR at maximum possible loads [9, 10].

This approach allows you to design parametric single-stage PPG [1, 8] with a bandwidth close to a two-stage generator [10]. Combining a PPG of this design with a power actuator (powerhead) based on a slotted spring and bellows sealing of the actuator (hydraulic plunger) allows creating a compact hydropulse device for vibration turning with a wide range of adjustment of vibration parameters.

A scientifically substantiated method of design calculation of a separate HD and device with HD is based on the results of theoretical [1, 11, 12] and experimental studies [13] of mechanical systems [14–16]. This method, in addition to the general principles and approaches to the calculation of HD machines and devices based on it [17], must consider the design of the pulse mechanism (device) structure [18] and their operating cycle [19].

The general purpose of developing methods of design calculation of PPG and devices based on it is to give a design engineer or researcher a set of relatively simple mathematical dependencies that allow determining all basic energy, power, and geometric parameters of PPG and device, and hydropulse.

3   Research Methodology

The structural scheme of the hydropulse device for radial vibroturning, is shown in Fig. 1 [11]. The device consists of a single-stage pressure pulse generator 1 of high throughput and a powerhead 2 that consists of a vibrating mover of the cutter 3, which performs vibratory cutting of part *D*.

The pressure pulse generator 1 consists of a housing 1.1, the shut-off element 1.2, which is in the form of a conical valve combined with a slotted spring, it placed in sleeve 1.3 and installed in housing 1.1, and contact with the conical bevel with the seat 1.4. Saddle 1.4 is located in the same bore as sleeve 1.3. In the axial direction, sleeve 1.3 and the saddle 1.4 are fixed by the cover 1.11 pressure pulse generator's 1. In cover 1.11, there is a plunger 1.10, the left spherical (according to the drawing) end of which rests on the support ring of the slotted spring 1, and the right end is in contact with the screw of the pre-deformation of the slotted spring 1 (pressure "opening" p_1 pressure pulse generator).
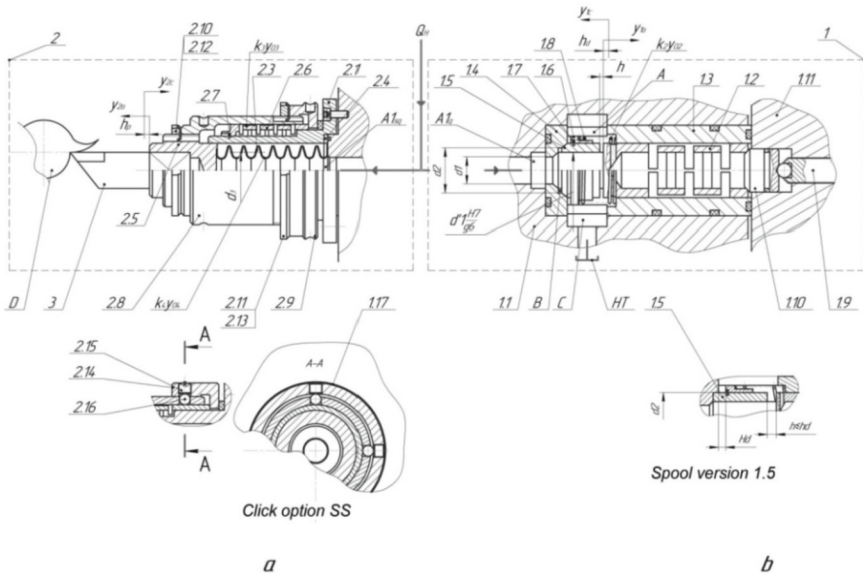
Fig. 1. Schematic diagram of a hydropulse device for radial vibrating turning.

The powerhead 2 of the device consists of a housing 2.1, which is connected to the housing 1.1 of the pressure pulse generator 1, for example, through screws 2.2. The inner bore of the housing 2.1 is a bellows 2.3, welded to the support ring 2.4 and the sleeve-holder 2.5. The support ring is located in the steel slotted spring bore of housing 2.1 and rigidly fixed by the guide protrusion of housing 1.1 of the pressure pulse generator 1. On the outer steel slotted cylindrical spring surface of housing 2.1 is a slotted spring 2.6 powerhead 2. Left thrust end installed in the recess of the case 2.1.

The thrust end of the slotted spring 2.6 is made in the form of a bore, which eliminates the possible inversion of the ring 2.7. The support ring on the inner surface is directed along the diameter of the greater degree of the cylindrical surface of the housing 2.1. Pre-deformation of the slotted spring 2.6 is carried out using sleeve 2.8, connected through a thread with the outer surface of the sleeve-holder 2.5 and a cap nut 2.9, the inner end of which is in contact with the end of the support ring of the slotted spring 2.6. The threaded connections of the sleeve 2.8 with the sleeve-holder 2.5 and the cap nut 2.9 are countered using slotted nuts 2.10 and 2.11 and the multi-bladed washers 2.12 and 2.13, respectively.

A variant of the mechanism of pressing on the slotted spring 2.6 is shown in Fig. 1, a. Instead of a cap nut 2.9, a sleeve cap 2.14 is installed, on the inner bore of which a spherical "running" track is formed (similarly to ball bearings), and in the tail part of the sleeve 2.8 through radial holes are made at the slotted spring-appropriate distance from its end (four or more). Through the threaded hole of the sleeve-cap 2.14, which is closed by the threaded plug 2.15, in the radial holes of the tail of the sleeve 2.8 install balls 2.16, which perform a kinematic-slotted circuit between the sleeve-cap 2.14 and the tail of the sleeve 2.8. To prevent accidental unscrewing of the threaded plug 2.15, a spring

ring 2.17 is used, located in the outer recess (groove) on the surface of the sleeve-cap 2.14.

To exclude possible impact interaction between the ends of the cap nut 2.9 (or sleeve-cap 2.14) and the mounting flange of the housing 2.1 between these ends, a damping rubber ring of the rectangular cross-section is installed.

The fixed seals of the sleeve 1.3, the saddle 1.4, the plunger 1.10, and the support ring 2.4 of the bellows 2.3 are made of standard rubber rings of round cross-section (not marked with positions in the drawing).

The maximum frequency ν of pressure pulses is determined by the design parameters of the pressure pulse generator 1, the total head of the device, the stiffness of the spring 1 and 2.6 (mainly), and the magnitude of the supplied energy flow of spring, usually the supply Q_p of the hydraulic pump and the modulus of elasticity K of the energy.

The developed hydropulse device's operating cycle can be divided by analogy with the known hydropulse devices and actuators into separate phases, which are usually combined in the forward and reverse strokes of the shut-off elements of the pressure pulse generator and power units (powerhead). For the beginning of reference of a direct course of a locking element 1.2 of the generator of pressure pulses (Fig. 1), for accurate fixing of coordinates of movement of this element, it is expedient to take an end plane of transition of a valve part of a locking element 1.2 in a direct cylindrical part of a slotted spring 1 (Fig. 1), when it is in the initial position (closed pressure pulse generator 1). The reverse stroke of the locking element 1.2 is carried out from the extreme position of the same end plane by moving the locking element 1.2 on the stroke h_d (coordinate y_{1c}, Fig. 1). For the coordinates y_{2o} and y_{23} counting of the beginnings of forward and reverse strokes of the cutter 3, as part of the powerhead of the device we take, respectively, the initial and extreme position of the outer end of the sleeve – cutter holder 2.5 (Fig. 1, here h_p – the working stroke of the cutter 3).

4　Results

In the dynamic process, the shut-off element 1.2 of the pressure pulse generator 1 performs two types of movement – dynamic and deformation. The valve part of element 1.2 moves kinematically, and the slotted spring 1 primarily participates in the kinematic and deformation movement. The fixed part of the slotted spring 1 can be considered only its support ring, which rests on the plunger 1.10 (Fig. 1).

Pressure pulse generator 1 and the cutter 3 of the powerhead 2 (Fig. 1) system of equations, which is presented on slide 4:

$$\begin{cases} A_{sp1} = \Delta E_{ss1} + \Delta E_{cs} + A_{f_1} + \Delta E_{gl} \\ A_{sp2} = \Delta E_{ss2.6} + \Delta E_s + A_{f_2}, \end{cases} \tag{1}$$

where

$$A_{sp1} = p_1 \cdot h_d \cdot A_2 \tag{2}$$

the average work of the energy pressure forces over time direct stroke of the shut-off element 1.2 together with the sleeve-valve 1.5 (Fig. 1);

$$\Delta E_{ss1} = 0{,}5k_1 h_d \tag{3}$$

ΔE_{ss1} – the increase in the potential deformation energy of the slit spring 1;

$$\Delta E_{cs1} = 0{,}5k_2h_d^2 \tag{4}$$

increase in the potential energy of deformation of the coil spring 1.8;

$$A_{f_1} = F_{f_1} \cdot h_d \tag{5}$$

total work of friction forces during movement on the direct course of the shut-off element 1.2 and the valve-sleeve 1.5;

$$\Delta E_{gl} = 0{,}5k_{0r} \cdot x_{01}^2 = 0{,}5p_1^2A_0^2 \cdot k_{0r}^{-1} \tag{6}$$

increase in the potential energy of deformation of the hydraulic link;

$$A_{sp2} = p_{p1} \cdot h_p \cdot A_s \tag{7}$$

the average work of the energy pressure forces during t_{pn} the direct stroke of the cutter 3;

$$\Delta E_{ss2.6} = 0{,}5 \, k_3h_p^2 \tag{8}$$

increase in the potential energy of deformations of the slit spring 2.6;

$$\Delta E_s = 0{,}5 \, k_4h_p^2 \tag{9}$$

increase in potential energy of bellows deformations 2.3;

$$A_{f_2} = F_{f_2} \cdot h_p \tag{10}$$

total work of friction forces during direct movement of the cutter 3, where $p_{p1} = 0{,}5(p_c + p_1)$ – average energy pressure in the time interval $t_{pn} = t_o - t_c + t_k = t_{kp}$; F_{f_1} – the average total friction force during the movement of the shut-off element 1.2 and the valve-sleeve 1.5; $F_{f_2} = R + \overline{F_y}$ – the average total force of resistance to the movement of the cutter 3 and the parts associated with it in the direction of direct movement.

At a given level of nominal pressure p_1 "opening" pressure pulse generator 1, pressure values p_2 "closing" and p_c (level of energy pressure in the pressure cavities $A1_g$ and $A1_{sg}$ at which the forces of elastic and dissipative resistance to movement of the moving parts of the pulse generator 1. 2 are balanced, see Sect. 3, Fig. 1) can be determined with a given accuracy only for known areas of degrees of sealing A_1 and A_2 pressure pulse generator 1, stiffness k_1 spring 1 and k_3 spring 2.6. At the stage of approximate calculations A_1 and A_2 under the assumption that the main operation of the investigated device will be carried out at vibration frequencies close to the maximum v_{max}, it is possible based on the results of theoretical and experimental studies of the hydropulse drive to accept $p_1/p_2 = 0{,}25...0{,}4$ and $p_c/p_2 = 0{,}5...0{,}8$. Taking the average values from these recommended ranges, we assign: $p_2 = 0{,}3p_2$ and $p_c = 0{,}6p_1$.

According to the structural scheme (Fig. 1) of the device, it is evident that the cross-sectional area determines the throughput of the pressure pulse generator 1 A_1 of the first degree of sealing. The diameter $d_1 = (4A_1/\pi)^{0,5} \cong 1{,}13A_1^{0,5}$ is the diameter of the

conditional passage of the pressure pulse generator 1 to determine which you want to determine the supply of the hydraulic pump Q_p station of the hydraulic pulse drive of the device.

The required feed Q_p can be calculated by the formula known for the hydropulse drive:

$$Q_h = K_{cp} v0^{-1} 0_{OH}^{-1} 1 max_{max} \tag{11}$$

where $K_{cp} = 1 + (t_{ot} + t_{ht} + t_{rt})/t_p$ – cyclic pressure pulse coefficient; $t_{ot}, t_{ht}, t_{rt}, t_p$ – time components (intervals) of pressure pulses; η_{0p} – volumetric efficiency of the hydraulic pump.

From the cyclogram of the operating cycle of the hydropulse drive of the device it is evident that $K_{cp} > 1$. With a given accuracy K_{cp} can be determined by the analysis of the mathematical model of the hydropulse drive of the device, the adequacy of which is confirmed by the results of experimental studies of the prototype device. It is possible to estimate a level K_{cp} approximately using the cyclogram of an operating cycle $p_r = f(t)$ relative values for time intervals, for example, the period of pressure pulses T_T based on the concept of pressure pulse scale:

$$\mu_{tp} = T_T/00_1 = 00_1 \cdot v_{max} \text{ s/mm}, \tag{12}$$

where 00_1 – the length of the segment on the cyclogram of the pressure pulse (Fig. 2) $00_1 = 0a' + a'b' + b'c' + c'd + d0_1$, mm.

Measuring these segments on the pressure pulse cyclogram (Fig. 2) and using (11), we find:

$$t_C = \mu_{tp} \cdot 0a'; \ t_p = \mu_{tp} \cdot ab'; \ t_{ht} = \mu_{tp} \cdot b'c'; \ t_{rt} = \mu_{tp} \cdot c'd; \ t_{ot} = \mu_{tp} \cdot d0_1. \tag{13}$$

Given (12) in, we obtain:

$$K_{cp} = 1 + (d0_1 + b'c' + c'd)/0b'. \tag{14}$$

Since the cyclogram of the operating cycle of the hydropulse drive device has the character of conditional, the coefficient K_{cp} also indicative (estimated), so in formula (10) it is advisable to enter the stock ratio $K_c = 1,1...1,25$:
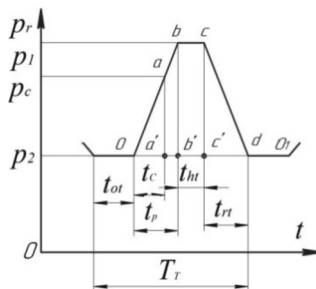
Fig. 2. To the concept of the scale of the energy pressure pulse.

$$Q_{pc} = K_c K_{cp} v0^{-1}{}_{OH}^{-1} 1max_{max} \qquad (15)$$

where is the specified value of the calculated feed of the hydraulic pump of the hydropulse drive device.

Time can be estimated by a dependence similar to:

$$t_p = (p_1 - p_2) \cdot W_0/(Q_p \cdot \kappa), \qquad (16)$$

we receive:

$$t_{rt} = (p_1 - p_2)W_0/(Q_g \cdot \kappa), \qquad (17)$$

where is the average energy consumption through the open slit of PPG 1 (Fig. 1). The level of slotted spring approximately can be found by the cyclogram of the operating cycle and assumptions about the linearity of the function $p_r = f(t)$. From the comparison of dependences (16) and (17), we find:

$$Q_g = Q_p \cdot t_p/t_{ct} = Q_H \cdot 0b'/c'd = Q_p \cdot \tau_{ct}, \qquad (18)$$

where τ_{rt} – the relative time of reduction of the energy pressure in the pressure cavity of the hydropulse drive device from level to level. According to the cyclogram of the operating cycle $t_{rt} < t_p$ ($\tau_{rt} > 1$), it follows that $Q_g > Q_p$.

To avoid negative phenomena during the operation of pressure pulse generator 1 (cavitation, etc.) and according to the generally accepted rules of design of hydraulic cylinders, the average speed of the energy carrier V_{g2} through the gap A_{gap} should not exceed the allowable $[V_\Gamma]$ [20]:

$$V_g = Q_g/(\pi d_2 h_d) \leq [V_g], \qquad (19)$$

from here:

$$Q_g \leq \pi d_2 h_d \cdot [V_g]. \qquad (20)$$

Flow rate V_{g1} energy carrier through a conditional passage $d_{cp} = d_1$ pressure pulse generator 1 also should not exceed the allowable $[V_\Gamma]$:

$$V_{\Gamma 1} = Q_{pc}/A_1 = 4Q_{pc}/\left(\pi d_{cp}^2\right) \leq [V_g], \qquad (21)$$

from here:

$$d_{cp} = d_1 \geq (4Q_{pc}/(\pi [V_g])^{0.5}; \qquad (22)$$

During the movement of the locking element 1.2 and the valve sleeve 1.5 in the gaps of their guides, there is only liquid friction, and the stiffness of the coil spring is $1.8k_2 << k_1$ – stiffness slotted spring 1 [21], so at the stage of design calculation of the increase in potential energy ΔE_{cs} and the total work of friction forces A_{f_1} (see

(1), compared with the components A_{mp_1} and ΔE_{gl} from the same equation of energy balance can be neglected. Based on these considerations, we write Eq. (1) in the form:

$$A_{ss_1} \geq \Delta E_{ss1} + \Delta E_{gl}, \tag{23}$$

Relative to the cross-sectional area of the average hydraulic line of the hydraulic pulse drive determine the stiffness of the elastic element of the hydraulic link according to a known formula:

$$k_{or} = A_0^2 \cdot \kappa \cdot W_0^{-1}, \tag{24}$$

or taking into account (3), (8), and (24)

$$h_d \cdot A_2 \geq 0{,}5k_1h_d^2 + 0{,}5p_1^2A_0^2 \cdot k_{0r}^{-1} = 0{,}5k_1h_d^2 + 0{,}5p_1^2\kappa^{-1} \cdot W_0, \tag{25}$$

where:

$$A_2 \geq 0{,}5\left(k_1h_dp_1^{-1} + p_1\kappa^{-1}h_d^{-1}W_0\right), \tag{26}$$

or

$$d_2 \geq 0{,}798(k_1h_Bp_1^{-1} + p_1\kappa^{-1}h_B^{-1}W_0)^{0{,}5}, \tag{27}$$

where $d_2 \geq 0{,}798(k_1h_dp_1^{-1} + p_1\kappa^{-1}h_d^{-1}W_0)^{0{,}5}$,

Under the accepted assumptions for calculation of rigidity of slotted spring 1 k_1 and slotted spring 2.6 k_3 equivalent voltage σ_{eq} in dangerous sections of the working rings of these springs can be calculated by the formula [2]

$$\sigma_{eq} = (1{,}22F_{ssi} \cdot R_i)a^{-3} \leq [\sigma], \tag{28}$$

where $F_{ssi} = k_i \cdot h_{max\ i} \cong p_1$ – the maximum effort that the load slotted spring 1 or slotted spring 2.6; $i = 1$; 3; $[\sigma]$ – permissible bending stress for the material of slotted spring 1 or slotted spring 2.6, here: $A_i = A_2$ for SS 1 and $A_i = A_s$ for SS 2.6. $h_{max\ i} = h_d$ for the locking element 1.2 pressure pulse generator1 i $h_{max\ i} = h_d$ for the locking element for cutter 3 (Fig. 1).

The stiffness of the slotted spring 1 and the slotted spring 2.6 was determined during a mathematical study:

$$k_i = \left(1{,}035Ea_i^4\right)/\left(R_i^3 \cdot n_i\right), \tag{29}$$

Taking $\sigma_{eq} = [\sigma]$ from formulas (28) and (29), we obtain the dependencies for calculating the limit loads $F_{max\ i}$ slotted spring 1 and the slotted spring 2.6, which ensures the strength of these springs and their maximum possible deformation $h_{max\ i}$:

$$F_{max\ i} = 0{,}82[\sigma]a^3R_i^{-1}; \tag{30}$$

$$h_{max\ i} = 0{,}79[\sigma]n_iR_i^2E^{-1} \cdot a_i^{-1}. \tag{31}$$

For slotted spring 1, the dependences (30) and (31) determine the significant value d_{CP}, approaching pressure pulse generator 1 (Fig. 1) in terms of bandwidth to two-stage pressure pulse generator.

Given in (27) (29) and (31), after algebraic transformations, we find:

$$d_2 \geq 0,722 \left[\frac{[\sigma]a_1^3}{R_1 \cdot p_1}(1 + 1,548 \frac{p_1^2 \cdot EW_0}{\kappa[\sigma]^2 n_1 R_1 a_1^2}) \right]^{0,5}.$$
(32)

For structural and technical reasons, it is advisable (Fig. 1) to assume that $d_2 = D_{lv1}$ (Fig. 3) for neglecting the gap δ_{gap} between the opening hole slotted spring 1 and the working part of this spring, then $d_2 = 2R_1 + a_1$.
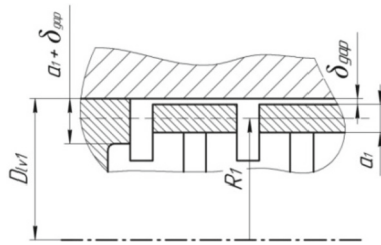
Fig. 3. Determining the diameter d_2 the second level of sealing PPG1.

The diameter of the second level of sealing pressure pulse generator 1 must also be consistent with the dependence obtained from (20) [11]:

$$d_2 \geq Q_g/(\pi h_d \cdot [V_\Gamma]) = Q_p \cdot \tau_{rt}/(\pi h_d[V_g]) \approx 0,318 \cdot Q_p \tau_{rt}/(h_d[V_g]).$$
(33)

Relative time τ_{rt} with a given accuracy can be found by the results of experimental studies of a prototype of the developed device.

Since $\tau_{rt} > 1$, not the initial stage of the design calculation of the pressure pulse generator 1, this relative time can be considered as a kind of stock factor K_{c1} and, for given values h_d and $[V_g]$ and found by the formula (15) the desired feed Q_{pc} hydraulic pump hydropulse drive device, pre-determine d_2, which must be consistent with the value d_2 found by (29) and Fig. 2.

Effective area A_s the cross-section of the bellows can be estimated by the equation of energy balance (1) if we neglect its member ΔE_s, because $k_4 << k_3$ and the average total force of resistance to movement of the cutter 3 (Fig. 1) is given as a dependence:

$$F_{f2} = R + \overline{F_y} = K_{C2} \cdot F_{ymax}$$
(34)

where $K_{C2} \cong 1,2...1,3$ – stock ratio; F_{ymax} – the maximum possible component of the cutting force, which is determined by known methods of the theory of cutting [20] by radial feed h_p, which is the maximum vibration amplitude of cutter 3 (Fig. 1). Under these considerations and assumptions, after algebraic transformations, with (1) considering (2) and (30), we find

$$A_s \geq (0,409a_2^3[\sigma] \cdot R_2^{-1} + K_{c2} \cdot F_{p1\,ymax}^{-1},$$
(35)

where for $p_c = 0.6p_1$, $p_{p1} = 0.5(0.6p_1 + p_1) = 0.8p_1$.

Other design calculations of the bellows 2.3 can be determined by the method and known recommendations [21–24]. According to the same recommendations, verification calculations of the bellows for strength are performed.

Other structural dimensions of the parts of the hydropulse device for radial vibration are in the process of developing its design based on the recommendations and experience of designing machines and devices with hydropulse drive.

5 Conclusions

The method of design calculation of the pulse device for radial for vibroturning and pressure pulse generator on its basis, allows, by relatively simple dependences, to find all the basic energy, power, and geometric parameters of hydropulse drive 1 and powerhead 2 (Fig. 1).

In the case of theoretical studies of the dynamics of the hydropulse drive device using its developed mathematical model and verification of the correctness and adequacy of this model by experimental studies of a prototype hydropulse drive device, to increase the reliability and accuracy of the calculation formulas of the developed method of project calculation, in them (formulas) can be introduced clarifying and correcting coefficients.

Principles and a slotted springroaches to the calculation of the parameters of the hydropulse drive device for radial vibration turning, controlled by a single-stage pressure pulse generator of high bandwidth, in the proposed method of design calculation, can be a basis for constructing methods of design calculation of other similar hydropulse drive and devices.

References

1. Obertyukh, R., Slabkyi, A., Andrukhov, S., Kudrash, V.: Parametric single-stage high-capacity pressure pulse generators. Bull. Mech. Eng. Transp. **9**(1), 40–48 (2019). https://doi.org/10.31649/2413-4503-2019-9-1-82-88
2. Lin, S., Deng, X.: Three-dimensional elliptical vibration cutting device based on the curved beam. IOP Conf. Ser. Earth Environ. Sci. **267**, 052044 (2019). https://doi.org/10.1088/1755-1315/267/5/052044
3. Overcash, J.: Tunable, ultrasonic, vibration assisted diamond turning. Charlotte (2006)
4. Haidong, Z., Ping, Z., Wenbin, M., Zhongming, Z.: A study on ultrasonic elliptical vibration cutting of inconel 718. Shock Vib. **2016**, 3638574 (2016). https://doi.org/10.1155/2016/3638574
5. Kostyk, K., et al.: Simulation of diffusion processes in chemical and thermal processing of machine parts. Processes **9**(4), 698 (2021). https://doi.org/10.3390/pr9040698
6. Kawasaki, M., Lee, H.J., Jang, J.I., Langdon, T.G.: Strengthening of metals through severe plastic deformation. Rev. Adv. Mater. Sci. **48**(1), 13–24 (2017)
7. Djema, M., Hamouda, K., Babichev, A., Saidi, D., Halimi, D.: The impact of mechanical vibration on the hardening of metallic surface. Adv. Mater. Res. **626**, 90–94 (2013). https://doi.org/10.4028/www.scientific.net/amr.626.90

8. Pavlenko, I., Ivanov, V., Gusak, O., Liaposhchenko, O., Sklabinskyi, V.: Parameter identification of technological equipment for ensuring the reliability of the vibration separation process. In: Knapcikova, L., Balog, M., Perakovic, D., Perisa, M. (eds.) 4th EAI International Conference on Management of Manufacturing Systems. EAI/Springer Innovations in Communication and Computing. Springer, Cham (2020). https://doi.org/10.1007/978-3-030-34272-2_24

9. Bocharov, Y.: Fundamentals of the general theory of hydraulic forge-stamping machines. Mach. Technol. Met. Process. Press. **330**, 12–40 (1980)

10. Arkhipchuk, M.: Speed pressure impulson generator for controlling hydropulse drivers of vibration technological machines. Vinnytsia (2006)

11. Obertyukh, R., Slabkyi, A., Petrov, O., Kudrash, V.: Mathematical modeling of the device for radial vibroturning. In: Advanced Manufacturing Processes II. InterPartner 2020. LNME. Springer, Cham (2021). https://doi.org/10.1007/978-3-030-68014-5_55

12. Iskovich-Lototsky, R., Matveev, I., Krat, V.: Vibration and vibro-impact action machines. Technics, Kiev (1982)

13. Gursky, V., Kuzio, I., Krot, P., Zimroz, R.: Energy-saving inertial drive for dual-frequency excitation of vibrating machines. Energies **14**(1), 71 (2021). https://doi.org/10.3390/en14010071

14. Onysko, O., Karabegović, I., Dašić, P., Penderetskyi, M., Melnyk, O.: The stress state of compact mechatronic satellites of a cycloidal reducer. J. Eng. Sci. **8**(2), D12–D17 (2021). https://doi.org/10.21272/jes.2021.8(2).d3

15. Virnuk, M., Iskovich-Lototsky, R., Veselovskaya, N.: Vibration and vibration processes and machines in foundry production. VNTU, Vinnytsia (2004)

16. Pavlenko, I., Trojanowska, J., Ivanov, V., Liaposhchenko, O.: Scientific and methodological approach for the identification of mathematical models of mechanical systems by using artificial neural networks. In: Machado, J., Soares, F., Veiga, G. (eds.) Innovation, Engineering and Entrepreneurship. HELIX 2018. LNEE, vol. 505, pp. 299–306. Springer, Cham (2019). https://doi.org/10.1007/978-3-319-91334-6_41

17. Amini, S., Aghaei, M., Lotfi, M., Hakimi, E.: Analysis of linear vibration in rotary turning of AISI 4140 steel. Int. J. Adv. Manuf. Technol. **91**, 1–10 (2017)

18. Shi, G., et al.: The finite element analysis and optimization of an elliptical vibration assisted cutting device. J. Appl. Mech. Eng. **4** (2015). https://doi.org/10.4172/2168-9873.1000170

19. Jamshidi, H., Nategh, M.J.: Theoretical and experimental investigation of the frictional behavior of the tool–chip interface in ultrasonic-vibration assisted turning. Int. J. Mach. Tools Manuf. **65**, 1–7 (2013). https://doi.org/10.1016/j.ijmachtools.2012.09.004

20. Abramov, F., Kovalenko, V., Lyubimov, A.: Handbook of Metal Cutting. Technology, Kiev (1983)

21. Zapletokhin, V.: Design of Parts of Mechanical Devices: Handbook Mechanical Engineering (1990)

22. Biederman, V.: Theory of Mechanical Oscillations: Textbook. Vysshaya shkola Publ., Moscow (1980)

23. Roganov, L., Karnaukh, S.: Calculation of Springs and Elastic Shock Absorbers. DSEA, Kramatorsk (2000)

24. Ponomarev, S., Andreeva, L.: Calculation of Elastic Elements of Machines and Instruments. Machine-building, Moscow (1980)

Compositional Interpolation of Spatial Discretely Presented Curves by Harmonizing Pointed Polynomials

Victor Vereshchaga[1] , Andrii Naydish[1] , Yevhen Adoniev[2] ,
Oleksandr Pavlenko[1(✉)] , and Kseniia Lysenko[1]

[1] Bogdan Khmelnitsky Melitopol State Pedagogical University,
20, Hetmanska St., Melitopol 72300, Ukraine
`alexander8944@gmail.com`
[2] Zaporizhzhia National University, 160-a, Heroiv Ukrainy St., Melitopol 72319, Ukraine

Abstract. This study defines the point calculus Balyuba-Naidysh (point BN-calculus). The principle of the geometric interpolation method, which is carried out only based on harmonized point polynomials, is explained. A record of the characteristic function is given in general. The sequence of transition from the characteristic function to BN-coordinates, which are components of harmonized point polynomials, is presented. To solve the problem of global interpolation of spatial discrete represented curves (DPC), the definition of the metric operator of three points (MOTP), the geometric scheme of its calculation, and one of its properties, which is the basis for calculating the length of segments in space, is provided. An interpretation of the terms composition and geometric composition is given. They define how they should be understood and applied in this study. Using the MOTP, a generalized record for determining the length of the section is shown, a record of the length of the section is shown in point form, and calculation formulas are given in the coordinate form, using which its length is calculated. It is indicated that the interpolation nodes are the vertices of the accompanying broken line (ABL), which is built on the basic points of the DPC through which the interpolation curve will pass in the form of a point polynomial. The CF harmonization method for forming a harmonized point polynomial continuously interpolates the spatial DPC.

Keywords: Point BN-calculus · Geometric composition · Characteristic functions · Curve · Industrial growth

1 Introduction

Usually, the curves in space are set in either coordinate or parametric form. You can submit both the first and second options in vector form. However, these methods of setting spatial curves are performed relative to the original coordinate system. The geometric models constructed in this way, which include spatial curves and their dimensions, also have the dimensions of the location of the geometric figure (GF) relative to the coordinate

system, which are necessarily included in the solutions, and which complicate these solutions. In addition, any movement of the GF, given by these traditional methods, in the coordinate system, requires the implementation of transformations of the solution of the problem, which leads to an increase in the cost of computer resources during testing or operation of the created model, which includes spatial curves.

On the traditional methods of constructing spatial curves, geometric models are created in the coordinate space. They cannot be used in coordinate spaces of higher dimensions without reconstruction. Also, these geometric models of the coordinate three-space cannot use multi-valued points "l"-valued parameter space.

The development of modern computer technology and information technology make it possible to study more complex processes that occur in coordinate spaces >3 and those that are "l"-significant in the parameter space, which in turn requires the creation of appropriate geometric models that do not it is possible to construct using traditional methods of modeling spatial curves.

Thus, the problem of developing new geometric modeling methods of spatial curves, which could meet modern requirements for research of complex systems, is relevant. Based on this, a particular problem is the creation of a new parametric method of interpolation of discrete spatial curves, which would allow the constructed geometric models in the coordinate three-space of impersonal rearrangements to be used in coordinate spaces larger than three-dimensional; which would allow, without changes in the constructed model, to change the significance of points (the number of coordinates that determine them) in the "l"-valued parameter space; which would, at the same time, reduce the resource consumption of construction, testing and operation of geometric models in terms of the application of spatial curves, which are part of these models.

2   Literature Review

Any curve can be best represented in a discrete situation in its set of points [1]. However, discrete representation requires the creation of large databases, and discrete curves do not fit well into transformations [2]. Analytical curves can be described in either coordinate or parametric arrangements [3]. Any analytical representation in coordinate mode remains free. Its projective or affine transformation needs appropriate recalculation of output data and constants, which determined the analytically presented curve in coordinate form. Besides, the difficulty of solving the task depends on the output coordinate system [4].

The parametric form of the curve representation assumes that any point on this curve is determined by the value of the parameters and does not depend on the choice of the original coordinate system. Therefore, the parametric curves are axis-independent, making it easy to perform affine transformations. Based on the above, we will analyze only the parametric curves in the future.

Any change in the initial conditions requires a mandatory recalculation of the created model [5]. The use of cubic splines does not allow for local correction of the simulated curve, which is very important for the interactive modeling mode. In the calculations of cubic splines, there is a need to rotate large matrices that depend on all elements simultaneously. Changing any of the elements of these matrices entails the need to change the rest of the others, in changing the geometric segment of the spline requires changes in the rest of the other segments.

Bezier curves. Pierre Bézier created the mathematical basis of Bézier curves (CB) based on geometric considerations. In our opinion, the disadvantages of Bezier curves are that their parameterization is not based on the initial geometric conditions. For them, Bernstein's basic functions are like a matrix into which the initial defining points are immersed, which generates a specific Bézier curve. Any effectiveness on the CB depends on all vertices of its defining polygon. Because of this, the change of any one of its vertices affects the whole CB, so CB is not subject to local changes.

The Koonsa's curves are constructed by applying the mixing function for the two forming lines of the placed polynomial and the line on each separate segment. The scalar value of "d", the mixing function, is considered a parameter function along the forming lines. The curve thus formed is less prone to uncontrolled oscillation and has continuous first and second derivatives along the entire curve. However, in our opinion, applying the Koons method to model piecewise curves has certain drawbacks, such as the inability to solve the inverse problem of modeling a segment of a parametric curve under predetermined conditions within the segment; and joining adjacent segments only at zero order of smoothness.

B-splines (BS) [6] are non-global curves because the Cox-de Boer formulas determine each determinant's essential function. However, when creating essential functions, a conditionality was introduced that it must be equal to zero in case of uncertainty "0"/"0". Such conditionality can lead to the appearance of related errors.

Rational B-splines or non-uniform rational B-splines (NURBS) are considered in [7], which are currently the standard for the exchange of design information between systems of machine design [8], as well as between design systems and automated production [9].

Uneven rational B-spline (NURBS) is a projection on the three-dimensional (3D) physical space of an irrational BS, defined in four-dimensional (4D) homogeneous coordinate space.

NURBS have almost all the same properties as irrational BS.

In addition, all medical, physical, geological processes, in most cases, are multifactorial, which can be described in the multidimensional space of parameters, although they occur in real physical space.

In this regard, the problem of developing new global interpolation methods of flat and spatial discrete represented curves, devoid of uncontrolled oscillation and suitable for use in n-dimensional parameter spaces, is relevant.

In our opinion, to the greatest measure for the determined problem, the compositional methods of modeling curves correspond [10], the geometric basis for which was the point calculus of Balyuba-Naidysh [11].

3   Research Methodology

To develop algorithms of global compositional interpolation of spatial discrete represented curves, which form a geometric composition of n-points, each of which is defined by l-coordinates.

For the global composition of interpolation of spatial discrete represented curves (DPC), geometric means of interpolation, built on methods of pointed calculation of Balyuba-Naidysh (PBN-calculation), will be offered.

Point BN-calculus, according to the well-known professor V. Vereshchaga, is the computational geometry of solving parts to the whole, which is taken from the composition (subset) of the existing geometric composition (existing geometric figure), using parameterization of base points that can be used at anyway, in the form of relationships, and is always represented in explicit or in the inexplicit form in ultimately by a simple ratio of points, in this situation, the sum of all defined parameters for base points should be equal to one.

The geometric way of homogeneous internal interpolation bypasses the process of adding system linear equations and solving them, relative to the coefficients, that provide the interpolation of the output DPC. This way is used to use harmonized exact polynomials, and they are mainly utilized according to characteristic parameters, which have the form:

$$P_j(t) = \frac{1}{\lambda_j} \cdot \prod_{\substack{i=1 \\ i \neq j}}^{n} (t_i - t), \tag{1}$$

for $j = \overline{1, n}$; $0 \leq t \leq 1$;
where $\lambda_j = \prod_{\substack{i=1 \\ i \neq j}}^{n} (t_i - t_j)$;

$\frac{1}{\lambda_j}$ — coefficient of transformation into a unit of the characteristic function $P_j(t)$ for $i = j$;

i – index, which makes the degree of rational function equal to $(n-1)$;

j – interpolation node number $j = \overline{1, n}$;

t – is the current parameter for the point polynomial;

t_j – meaning of parameters in nodes of interpolation.

In Eq. (1) abbreviated record of the product – means that the products are recorded for all parameters, except the difference in which $i = j$.

One-parameter point polynomial (PP) is not harmonized. It is a whole rational function with equal powers near each of the terms and has the following form [12]:

$$M = \sum_{j=1}^{n} A_j \cdot P_j(t), 0 \leq t \leq 1, \tag{2}$$

Harmonized characteristic functions of prof. V. Vereshchaga called BN-coordinates (Balyuba-Najdysh's coordinates), which are fractional-rational functions of degree $(n-1)$ in parametric form, which are used to continuously determine the position of the current point relative to all basis points A_j, $(j = \overline{1, n})$ DPC, or in other words, determines the share of participation of each of the basis points A_j in the formation of the coordinates of the current point M.

Taking into account, the one-parameter harmonized point polynomial (GPR) will have the form:

$$M = \sum_{j=1}^{n} A_j \cdot P_j, 0 \leq t \leq 1, \tag{3}$$

In the point BN-number [13], according to the interpretation of prof. I. Balyuba, MTPO is defined as a number calculated for three points and unambiguously corresponds to their relative position in the original geometric composition [14].
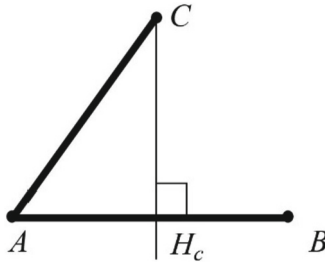
Fig. 1. Scheme for determination MTPO.

Consider a geometric composition of three points A, B, C (Fig. 1).

The point HC is the perpendicular base drawn from point C to the shade (AB).

The product of the lengths of equally oriented segments $(BA) \cdot (H_CA)$ and will determine the number of the metric operator of three points (MTPO). The exact orientation, in pointed BN-calculating, is determined by the direction of reading the notation of shades. If the directions of reading the notation of shades coincide, then the product of their lengths is positive; if they do not coincide – negative.

MTPO is noted by [15], the symbol Σ_{BC}^{A}, reads: "Sigma BC with vertex A". So, we have to write [16]:

$$\sum_{BC}^{A} = (BA) \cdot (H_CA). \tag{4}$$

In the research works of prof. I. Balyuba and prof. V. Vereshchaga proved that the geometric form of representation (4) corresponds to the point form of the MTPO:

$$\sum_{BC}^{A} = (B - A) \cdot (C - A). \tag{5}$$

If numbers denote the coordinates with the corresponding letter indices, then for n-space (6), you can write the MTPO as follows:

$$\sum_{BC}^{A} = \sum_{i=1}^{n} (i_B - i_A)(i_C - i_A). \tag{6}$$

In the works of professors I. Balyuba, V. Vereshchaga, V. Naidysh, the features, possibilities, and properties of MTPO, which relate to the general theory of MTPO, are considered in detail.

Consider a special case for the MTPO, which will relate to other presentations in this study.

4   Results

Suppose that in the coordinate three-space, the initial geometric composition consists of points A_j, for $j = \overline{1,n}$, which will be denoted by $A_j; j = \overline{1,n}$, which are discretely represented spatial curves (spatial DPC).

The implementation of composite interpolation of the spatial duodenum by a harmonized point polynomial will be provided in an algorithm of sequential actions.

1. Construct on the basis points $A_j; j = \overline{1, n}$ accompanying broken line (ABL), connecting them in a row, i.e., when each j-th point connects $(j + 1) - yu$ (Fig. 2).
2. Denote by "l" the length of the segments (Fig. 2).
3. Determine the distance from the first point A_1 to all the others, given that l_{11} and l_{21} are already known from point 2 of this algorithm.
4. Find the value of the length of the shades $l_{j(j-1)}; (j = \overline{1, n})$, denoted in paragraph 2 using the properties of the MTPO from (9).
5. Carry out the parameterization of the desired point polynomial through the parameterization ABL along with its links, thereby defining the parameters in the interpolation nodes, i.e., at the basic points of the desired point A_j of the desired point polynomial.
6. Having the values of the parameters in the interpolation nodes, we form the characteristic functions (CF) for each of the initial basis points $A_j; j = \overline{1, n}$ closing (1).

   The result is shown in Table 1. Characteristic functions for basis points $A_j; j = \overline{1, n}$

Table 1. Characteristic functions for basis points $A_j; j = \overline{1, n}$.

№	A_j	$P_j(t)$
1	A_1	$P_1(t) = \frac{1}{\lambda_1} \cdot (t_2 - t) \cdot (t_3 - t) \cdot (t_4 - t) \cdot \cdots \cdot (t_{n-2} - t) \cdot (t_{n-1} - t) \cdot (t_n - t),$
		де $\lambda_1 = (t_2 - t_1) \cdot (t_3 - t_1) \cdot (t_4 - t_1) \cdot \cdots \cdot (t_{n-2} - t_1) \cdot (t_{n-1} - t_1) \cdot (t_n - t_1)$
2	A_2	$P_2(t) = \frac{1}{\lambda_2} \cdot (t_1 - t) \cdot (t_3 - t) \cdot (t_4 - t) \cdot \cdots \cdot (t_{n-2} - t) \cdot (t_{n-1} - t) \cdot (t_n - t),$
		де $\lambda_2 = (t_1 - t_2) \cdot (t_3 - t_2) \cdot (t_4 - t_2) \cdot \cdots \cdot (t_{n-2} - t_2) \cdot (t_{n-1} - t_2) \cdot (t_n - t_2)$
3	A_3	$P_3(t) = \frac{1}{\lambda_3} \cdot (t_1 - t) \cdot (t_2 - t) \cdot (t_4 - t) \cdot \cdots \cdot (t_{n-2} - t) \cdot (t_{n-1} - t) \cdot (t_n - t),$
		де $\lambda_3 = (t_1 - t_3) \cdot (t_2 - t_3) \cdot (t_4 - t_3) \cdot \cdots \cdot (t_{n-2} - t_3) \cdot (t_{n-1} - t_3) \cdot (t_n - t_3)$
...	...	... ...
$n - 1$	A_{n-1}	$P_{n-1}(t) = \frac{1}{\lambda_{n-1}} \cdot (t_1 - t) \cdot (t_2 - t) \cdot (t_3 - t) \cdot (t_4 - t) \cdot \cdots \cdot (t_{n-2} - t) \cdot (t_n - t),$ де $\lambda_{n-1} = (t_1 - t_{n-1}) \cdot (t_2 - t_{n-1}) \cdot (t_3 - t_{n-1}) \cdot \cdots \cdot (t_{n-2} - t_{n-1}) \cdot (t_n - t_{n-1})$
n	A_n	$P_n(t) = \frac{1}{\lambda_n} \cdot (t_1 - t) \cdot (t_2 - t) \cdot (t_3 - t) \cdot (t_4 - t) \cdot \cdots \cdot (t_{n-2} - t) \cdot (t_n - t),$ де $\lambda_n = (t_1 - t_n) \cdot (t_2 - t_n) \cdot (t_3 - t_n) \cdot (t_4 - t_n) \cdot \cdots \cdot (t_{n-2} - t_n) \cdot (t_{n-1} - t_n)$

7. Find the sum μ_n of the current CF, written in Table 1.

8. Find the BN-coordinates (harmonized CF) for interpolation nodes $A_j; j = \overline{1, n}$, which we denote P_j:

   For the following BN-coordinates, we will not submit their expanded records:

$$P_2 = \frac{P_2(t)}{\mu_n}; P_3 = \frac{P_3(t)}{\mu_n}; \ldots; P_{n-1} = \frac{P_{n-1}(t)}{\mu_n}; P_n = \frac{P_n(t)}{\mu_n} \qquad (7)$$

9. Calculating the BN-coordinates, we can, following (4), write a harmonized point polynomial

$$M = \sum_{j=1}^{n} A_j \cdot P_j, 0 \leq t \leq 1; \sum_{j=1}^{n} P_j = 1, \qquad (8)$$

which continuously implements the current point M on the spatial curve that transports the original basis points A_j; $j = \overline{1,n}$.

Conventionally, the graphically harmonized exact polynomial (8) is shown in Fig. 2, in some sections of the arc A_2A_3 and $A_{n-2}A_{n-1}A_n$ of the curve do not intersect. Here are the sections of the arc $A_{n-2}A_{n-1}A_n$ remain either above the section of the arc A_2A_3 or below it.
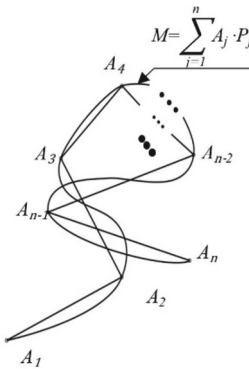
Fig. 2. Spatial harmonized point polynomial.

The use of point polynomials for interpolation of spatial DPC has a number of advantages. We list them:

1. All components of a point polynomial have the same degree, which reduces the probability of uncontrolled inflection points.
2. As the number of interpolation nodes increases, the error does not increase, making it possible not to increase the number of digits in the calculations, which improves the efficiency of modeling, testing, and operation of the geometric model.
3. Because the parameters of the harmonized point polynomial (BN-coordinates) are essentially a simple relationship of three points and because the harmonized point polynomial geometric and parametric components are separated from each other – the solution of any problem is carried out in the three-dimensional coordinate, and the result of development is projected on the axis of the space of parameters; on the plane of projections formed by the axes of the parameter space, on the subspaces of the parameter space. According to the results of these projections, the BN coordinates in all projections remain unchanged because they are invariants of parallel design.

4. With the change of the *l*-value of the starting points (the number of output coordinates of the parameter space), it is not necessary to change the solution model. Only the number of calculated (coordinate) equations changes in this case.

5. With the change of the number of n output points of the geometric composition, a discretely represented curve, the interpolation model remains unchanged, only the value of n changes in its records.

6. With a change in the position of the original geometric figure relative to the coordinate system of the three-dimensional coordinate, the solution of any problem does not change because the interpolation model based on a point polynomial is made relative to the base points of the original DPC, not relative to the three-dimensional coordinate.

7. Because the BN-coordinates of a harmonized point polynomial are invariants of parallel design, it is necessary to find the projection of a point polynomial on the axis of either a parameter space or a three-dimensional physical space to substitute the corresponding records of their coordinates in its point equation.

8. Because in a harmonized point polynomial, the geometric component is separated from its parametric component, the replacement of any of the points of the original geometric composition does not, in any case, change the created model of the problem solution.

9. In the equations of point polynomials, there are no constants in the form of coefficients that ensure the fulfillment of the initial conditions. To create the equation of a point, polynomial uses a geometric method of interpolation, which eliminates the stage of addition and solution of systems of linear equations relative to constants.

10. The use of point polynomials allows for local correction of the shape of the curve by changing the position of points or several in the area where it is necessary to correct the shape of the curve.

11. Since the equations of point polynomials are constructed not relative to the coordinate system but relative to the basic points of the original geometric composition, it is possible to ignore any movement of the original geometric figure - calculate as if it did not move and change its position.

12. Due to the fact that the solution of any problem, using point polynomials, occurs in space without the prior design of the initial conditions in the plane of projections and is carried out by geometric methods of interpolation, the solution itself and its stepwise implementation have clarity, which can always be represented in the form of geometric schemes.

13. Because any solution can be easily projected on all axes of the parameter space, using parametric connections between projections, it is easy to create two-, three-, …, *k*-dimensional projections, which will contribute to a deeper and more comprehensive analysis of the results of the obtained solution.

5   Conclusions

The analysis of interpolation methods made in this study showed that they are all piecewise rational and designed for local interpolation, which complicates creating models

of physical, social, natural, etc., multifactorial multidimensional processes. The harmonized point polynomials proposed in this study are designed to perform global interpolation in multidimensional parameter spaces. They are suitable for creating corresponding complex, multifactorial processes, each point of which is defined by l coordinates.

One of the main directions of further research, in our opinion, is the creation of methods and rules for point local change of the shape of the spatial curve, the graph of which is constructed for the corresponding harmonized point polynomial.

References

1. Konopatskiy, E., Bezditnyi, A., Litvinov, A.: Geometric modeling of torse surfaces in BN-calculus. J. Phys. Conf. Ser. **1791**, 012050 (2021). https://doi.org/10.1088/1742-6596/1791/1/012050

2. Pylypaka, S., Volina, T., Mukvich, M., Efremova, G., Kozlova, O.: Gravitational relief with spiral gutters, formed by the screw movement of the sinusoid. In: Ivanov, V., Pavlenko, I., Liaposhchenko, O., Machado, J., Edl, M. (eds.) DSMIE 2020. LNME, pp. 63–73. Springer, Cham (2020). https://doi.org/10.1007/978-3-030-50491-5_7

3. Konopatskiy, E., Bezditnyi, A., Shevchuk, O.: Modeling geometric varieties with given differential characteristics and its application. In: CEUR Workshop Proceedings, vol. 2744 (2020). https://doi.org/10.51130/graphicon-2020-2-4-31

4. Dubovoii, V., Kvetny, P., Mikhalov, O., Usov, A.: Modeling and optimization of systems: a textbook. PE TD "Edelweiss", Vinnytsia (2017)

5. Volina, T., Pylypaka, S., Nesvidomin, V., Pavlov, A., Dranovska, S.: The possibility to apply the Frenet trihedron and formulas for the complex movement of a point on a plane with the predefined plane displacement. East.-Eur. J. Enterp. Technol. **3**(7), 45–50, 111 (2021). https://doi.org/10.15587/1729-4061.2021.232446

6. Konopatskiy, E., Voronova, O., Shevchuk, O., Bezditnyi, A.: About one method of numeral decision of differential equalizations in partials using geometric interpolants. CEUR Workshop Proc. **2763**, 213–219 (2020). https://doi.org/10.30987/conferencearticle_5fce27708eb353.92843700

7. Pylypaka, S., Klendiy, M., Zaharova, T.: Movement of the particle on the external surface of the cylinder, which makes the translational oscillations in horizontal planes. In: Ivanov, V., et al. (eds.) DSMIE 2018. LNME, pp. 336–345. Springer, Cham (2019). https://doi.org/10.1007/978-3-319-93587-4_35

8. Volina, T., Pylypaka, S., Rebrii, A., Pavlenko, O., Kremets, Y.: particle movement on concave coulter of the centrifugal distributor with radially installed vertical blades. In: Tonkonogyi, V., et al. (eds.) InterPartner 2020. LNME, pp. 237–246. Springer, Cham (2021). https://doi.org/10.1007/978-3-030-68014-5_24

9. Pylypaka, S., Zaharova, T., Zalevska, O., Kozlov, D., Podliniaieva, O.: Determination of the effort for flexible strip pushing on the surface of a horizontal cylinder. In: Tonkonogyi, V., et al. (eds.) InterPartner 2019. LNME, pp. 582–590. Springer, Cham (2020). https://doi.org/10.1007/978-3-030-40724-7_59

10. Konopatskiy, E., Mashtaler, S., Bezditnyi, A.: Study of high-strength steel fiber concrete strength characteristics under the influence of elevated temperatures using mathematical modeling methods. IOP Conf. Ser.: Mater. Sci. Eng. **687**, 022040 (2019). https://doi.org/10.1088/1757-899X/687/2/022040

11. Pylypaka, S., Volina, T., Hryshchenko, I., Rybenko, I., Sydorenko, N.: Dynamics of a particle on a movable wavy surface. In: Tonkonogyi, V., et al. (eds.) InterPartner 2020. LNME, pp. 196–206. Springer, Cham (2021). https://doi.org/10.1007/978-3-030-68014-5_20

12. Konopatskiy, E., Bezditnyi, A.: Geometric modeling and optimization of multidimensional data in Radischev integrated drawing. IOP Conf. Ser.: J. Phys. Conf. Ser. **1260**, 072006 (2019). https://doi.org/10.1088/1742-6596/1260/7/072006
13. Konopatskiy, E., Bezditnyi, A.: Geometric modeling of multifactor processes and phenomena by the multidimensional parabolic interpolation method. IOP Conf. Ser.: J. Phys. Conf. Ser. **1441**, 012063 (2020). https://doi.org/10.1088/1742-6596/1441/1/012063
14. Pylypaka, S., Volina, T., Nesvidomin, A., Zakharova, I., Rebrii, A.: Particle movement in a centrifugal device with vertical blades. In: Ivanov, V., Pavlenko, I., Liaposhchenko, O., Machado, J., Edl, M. (eds.) DSMIE 2021. LNME, pp. 156–165. Springer, Cham (2021). https://doi.org/10.1007/978-3-030-77823-1_16
15. Konopatskiy, E., Bezditnyi, A.: Application of mixed geometric interpolants for modeling the strength characteristics of steel fiber concrete. IOP Conf. Ser.: J. Phys. Conf. Ser. **1546**, 012037 (2020). https://doi.org/10.1088/1742-6596/1546/1/012037
16. Konopatskiy, E., Bumaga, A., Bezditnyi, A.: Geometric approach to finding the best possible solutions based on composition optimization of the mixed aggregate of fine-grained concrete. IOP Conf. Ser.: Mater. Sci. Eng. **962**, 032031 (2020). https://doi.org/10.1088/1757-899X/962/3/032031

Manufacturing Technology

A New Method for the Monitoring Cutters States in Finishing Turning of Hard Materials

Oleksandr Derevianchenko(✉) , Oleksandr Fomin , and Natalia Skrypnyk

Odessa Polytechnic National University, 1, Shevchenko Ave., Odessa 65044, Ukraine
`algdrv@opu.ua`

Abstract. To the quality of parts finishing turning are presented high requirements. The process of hard materials finishing turning is characterized by the emergence of different cutters defects. That's why necessary to monitor cutters' states. The scientific novelty consists of creating a new method for monitoring cutters states in finishing turning of hard materials. This method makes it possible to detect a complex of defects in the cutting part of the tool, which appeared as a result of its wear and making tolls adjusting: formation of cutting tools adjusting on the wear value; formation correction, taking into account nose radius changing; formation and analysis of a section of cutting layer and calculation the necessary correction the feed value (S); estimation the state of flank face, estimate the distance from the extreme groove to the top, calculation the necessary termination of processing. The practical usefulness of the developed method consists of providing the possibility of adjusting the cutting toll and correction of cutting conditions (following results of monitoring cutters states) by the Computer Numerical Control (CNC) system of the machine tool.

Keywords: Concentrated wear · Nose radius changing · Radial wear · Cutting stability loss · Sustainable manufacturing · Industrial growth

1 Introduction

One of the crucial tasks of modern mechanical engineering, particularly within the Industry 4.0 strategy, is to increase the productivity of production processes, relevant modern technical and technological systems, machines, and devices.

In complex smart technical systems that operate with limited human participation, increasing productivity and failure reduction can be achieved by smart sensors [1].

Flexible fixtures provide a reducing number of technological operations and machining time, e.g., during holes machining in connecting rods [2].

An important and promising direction within Industry 4.0 is using service robots in different production and technological processes [3].

There is a clear need for corresponding improvement quality of machined parts. This is directly related to reducing failures and breakdowns in named systems and processes. So, the expediency of creating new monitoring methods and devices is obvious.

It should be noted that cutting finishing is an essential element of modern technologies. Preliminary research of authors showed that in the conditions of finishing turning of hard materials, forming a number of cutters specific defects.

They have reduced the quality of processing and the resource of tools. Therefore, the need for modern method development – for monitoring cutters states in finishing turning of complex materials – is obvious.

2   Literature Review

Many different factors are controlled in modern automated systems and the cutting process. For example, modern means of controlling the dynamics of the finishing boring are allowed to control the cutting process [4].

By the opinion of the authors of [5], knowledge of temperatures produced during drilling operation at various machining input parameters is required for the best quality product.

According to the research [6], many correction parameters of the cutting regime can be calculated quickly with minimum resources - fewer experiments and tests needed.

The study's authors [7] proposed the method for tool wear prediction (with chip color using). The means of the analysis of corresponding images were chosen fuzzy neural networks.

One of the important tasks in publication [8] is modern machine tools (MT) states diagnosis. The authors proposed to solve this problem with recurrent neural networks using. This approach provides MT wear diagnosis and prognosis of their states.

More and more widespread industrial applications are finding non-cutting processes. Research [9] was carried out to determine the influence of the laser treatment process parameters on the resulting roughness of the produced surface.

In the tasks of cutting tools (CT) states diagnosing, both direct and indirect control methods are widely used. More and more systems for monitoring cutting part (CP) states use modern vision systems. On modern machines, most technological and auxiliary operations are automated. Impotent operation in there is the CT identification. This task was successfully solved in the article [10]. Also, a method for an effective selection of tools and cutting conditions during precise machining was proposed in [11].

Worked by authors of paper [12], diagnostic systems may be used for control turning operations. Systems of discussed above types are analyzed in the research [13]. A connection of the manufacturing process with machine vision was presented.

Feature selection and method of improving the performance of cutting tools states monitoring are discussed in articles [14, 15].

According to [16], the current direction of modern research and developments is smart manufacturing creation. At modern factories, in metalworking technologies of such systems, it is appropriate to apply new data analyses methods. One of the important tasks is CT wear prediction. The authors proposed to solve this problem with random forests using.

In publication [17] analyzes a system for recognizing and predicting CT flank wear. A force sensor is used as an indirect device for receiving a signal from the cutting system. In the structure of data analysis processes is applied method of machine learning.

New results in CT wear recognition may be obtained with two methods [18]. The first of them is a method of time series imaging. The second is a method of deep learning. Also, in articles [19, 20], approaches based on chemical-thermal treatment were developed.

The literature analysis showed that known methods and monitoring systems provide diagnostics of certain types of CT defects. Not enough attention is paid to diagnosing the specific defects of cutters for finishing turning (when processing the hard materials).

According to the author's research, they are:

- significant changing's in shape and geometry of the main cutting edge (CE), including the changing value of the cutting angle in the base plane (ϕ) and position of the main cutting edge in the CP coordinate system (*LMN*);
- significant changing's in the shape and geometry of flank surface wear zones;
- the consequence in changing the thickness of the cut layer (a) – up to the loss of cutting process stability (due to situation: $a \leq a_{min}$));
- dislocation of CT top in the directions of each axis of the *LMN* coordinate system. Corresponding results are the appearance of the radial wear (h_Y) and nose radius (NR) changing.

The article's authors developed a smart monitoring system (SMS) for CP states monitoring and CT residual life prediction [21]. It includes special STV, which can register digital image sets – flank and rake worn surfaces, registration of projections of worn CE on the main plant, and others. Such a system provides getting all information for CP states monitoring.

The research aims to develop a new method for monitoring cutters' states and to recognize CP specific defects.

3   Research Methodology

Machine tool (lathe) model TPC - 125 BH1P was used. The cutting part material was composite 01 – material for treatment - hardened steel 115CrV3. Cutting conditions: V = 1,45–1,7 m/sec; t = 0,05–0,15 mm; S = 0,045–0,07 mm/rew.

The example on SMS work – to solve the problem of the formation of CE coordinates profile massive (by the results of the CT rake face digital image processing) – is shown in Fig. 1 (position E).
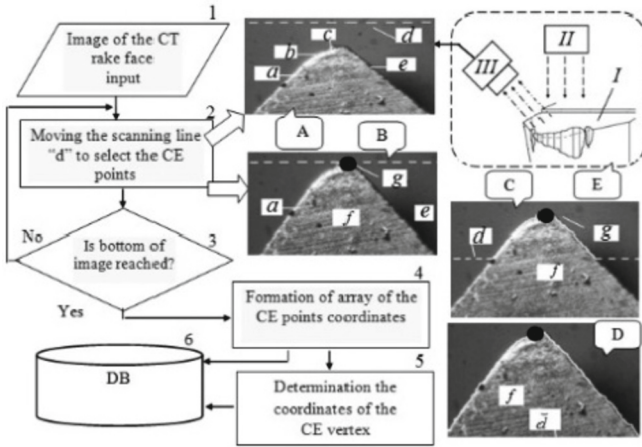
Fig. 1. Formation of CE coordinates profiles massive by the CT face surface digital image processing results.

There: I – worn-out CT; II – the source of special lighting; III – digital camera; A, B, C, D – stages of CE projection (on the main plane) forming (final projection profile is shown at D); A – beginning of the scan, D – end of a scan; g – recognized CT top; f – rake face; d – line of scan; a, b, c, e – regions of CE; 1 – 6: modules of the algorithm block diagram. Laboratory stand was developed for selective control results (CT monitoring with SMS). The general view of this stand, created on the base of profilograf, is shown in Fig. 2.
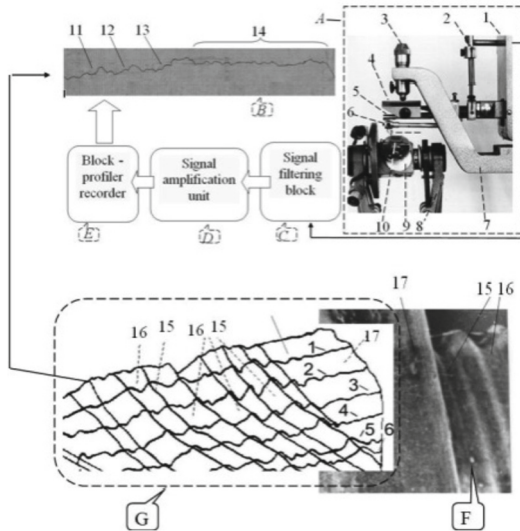
Fig. 2. General view of the laboratory stand for comparison results of monitoring cutters with SNS using and stand, created on the base of profilograf.

Here: A – a working area of profilograf; B – profilogramma of cutter wear zone at the flank surface with the tracks of concentrated wear; C, D, E – blocks of profilograf; scheme of the zone at the flank surface with the tracks of concentrated wear (CW); 1 – 10: stands components; 11 – 13: zones of concentrated wear tracks; 14 – zone without concentrated wear tracks; 15 – zones of CW protrusions; 16 – zones of CW cavity; 17 – zone without growing wear tracks.

Monitoring results with SMS using were controlled with a laboratory stand. Results divergence did not exceed 5–7%.

4 Results

A generalized scheme of a new method for monitoring CT states in finishing turning (and forming necessary correction for NCS) is shown in Fig. 3.

Block for the formation of cutting tools adjusting on the wear value is presented in position D.
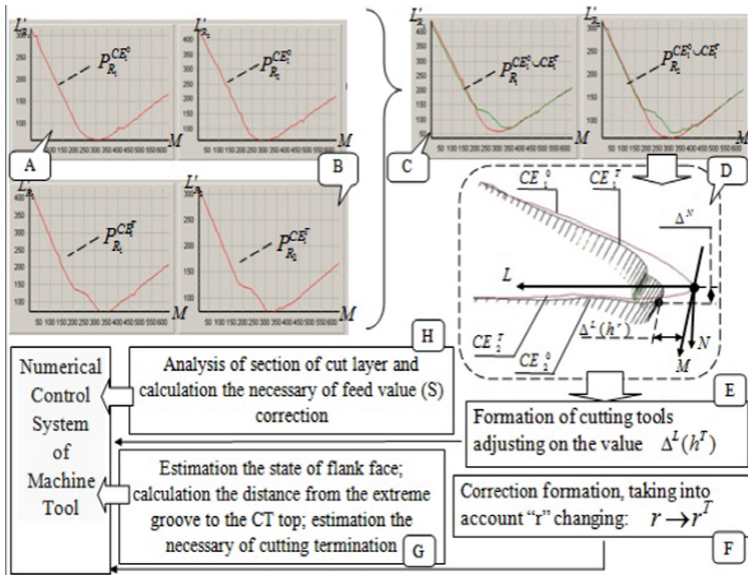
Fig. 3. Generalized results processing scheme of CT state monitoring (and forming necessary correction for the numerical control system of machine tool).

Positions A, B, C displays the process of combining CE projections. Blocks E, F, G, and H are forming necessary corrections for the NCS of the machine tool. The block diagram of an algorithm for CE projections combining the base plane and calculation of CT wear parameters is shown in Fig. 4.

Schemes (A, B) of CE changing and graphs (C, D, E) for new CT are shown in Fig. 5. Such conditions provide stability to the cutting process.
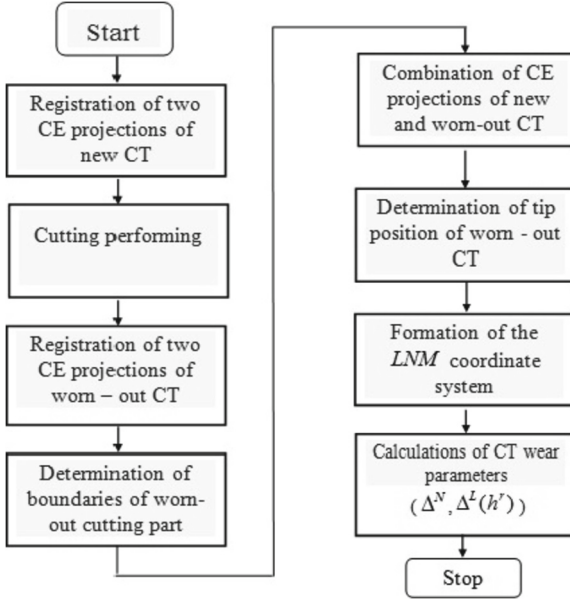
Fig. 4. Block diagram of an algorithm for CE projections combining in CT base plane.
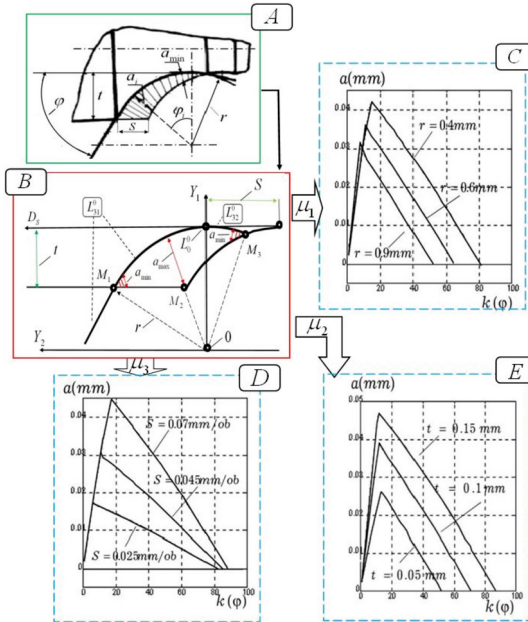
Fig. 5. Schemes of cutting thickness changing (A, B), and according to graphs for new CT (C, D, E). μ_1, μ_2, μ_3 - designation different types of graphs of cutting thickness changes.

Changes in CE geometric parameters (due to cutting part wearing) may lead to loss of cutting stability.

The analysis of cutting process stability is carried out according to the criterion of the minimum cut thickness - a_{min}.

If necessary, a signal is generated to NCS to stop treatment.

An example of cutting stability loss by the worn-out cutter in finishing turning is shown in Fig. 6.
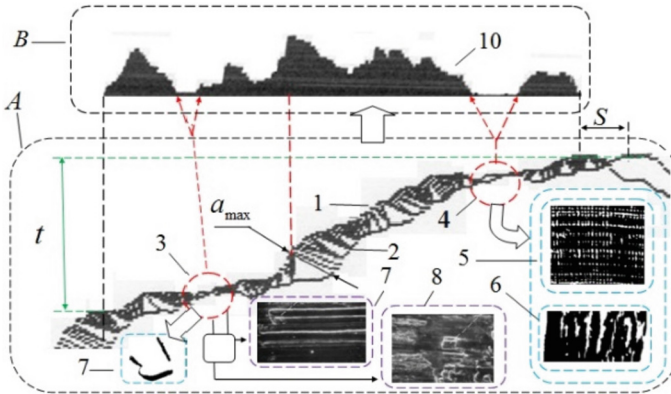
Fig. 6. Scheme of chip cutting stability loss in worn-out CE.

There A – the zone of two combined CE projections (1, 2) of worn-out CT, displaced on S value; 3, 4 – zones, where took place relation: $a \prec a_{min}$; 5, 6 – examples of according chips; 7, 8, 9 – examples of according zones on treatment surface; B – scheme of cut layer 10.

CE state in there is recognized as a failure state (due to the loss of cutting stability: the cut-off chips have an intermittent character). In some parts of the CE, cutting does not occur.

The graphs of a^T changes (for different values of the feed – positions A, B, C) and other values of cutting thickness are presented in Fig. 7.

Operations ψ_1, ψ_2 mean the a^T increasing. Positions D, E demonstrated the cheep types in zones, were take place relation: $a \prec a_{min}$.

The graphs in Fig. 6 and 7 were constructed using a special algorithm. CE state in there is recognized as a failure state – due to the loss of cutting stability.

There cut-off chips have an intermittent character (in some CE parts, cutting does not occur).

Block for formation and analysis of a section of cutting layer and calculation the necessary correction the feed value (S) is presented in Fig. 8.
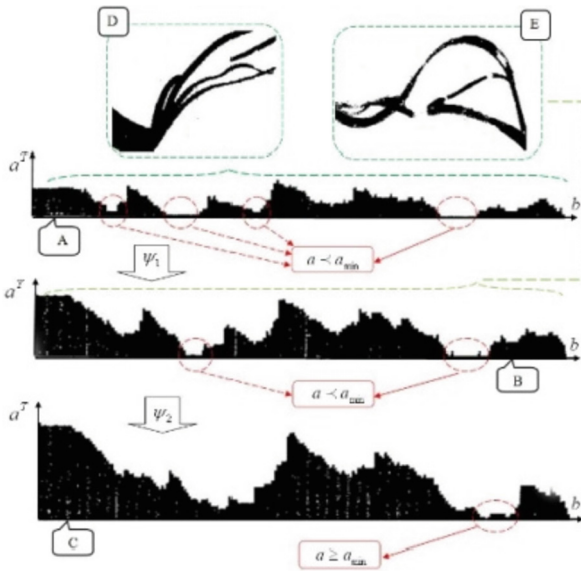
Fig. 7. Building schemes of cut layer for different values of cutting thickness (a^T).

This is a calculation scheme for determining the parameters of the section of the cut layer (to identify special elements of the CE structure and the boundary of their forming area). Here 1, 2 – two CE positions of a new tool, which are displaced on the S value; t – depth of cutting; 3 – a cross-section of cut layer; 4 – projections of CP top.

Accordingly, $1', 2', 3', 4'$ – analogs for worn-out CT. In addition, the analysis of cutting process stability is carried out according to the criterion of the minimum cut thickness. If necessary, the according to signal is generated to the numerical control system. Block for estimating the state of the flank face, estimating the distance from the extreme groove to the top, calculating the necessary termination of processing is presented in Fig. 9.
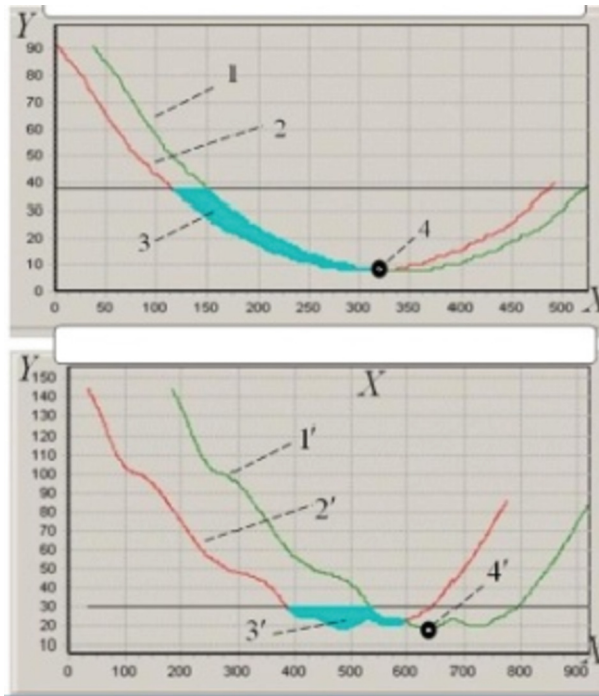
Fig. 8. Calculation scheme for determining the parameters of the section of the cut layer (for identification of special elements of CE structure and the boundary conditions of their forming section).
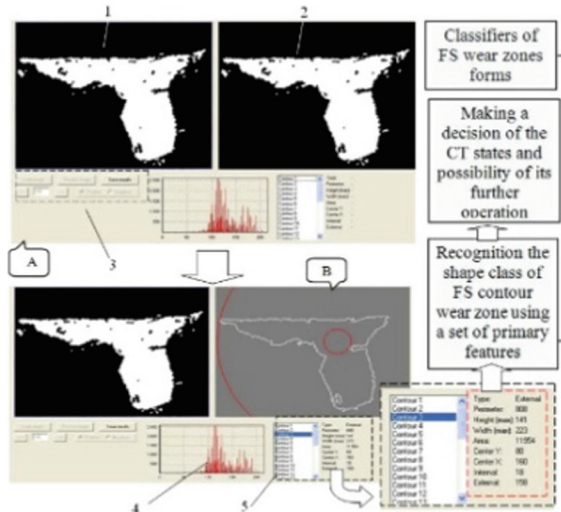
Fig. 9. Formation of the features set of wearing flank face form and CP state recognition; decide on the possibility of CT further exploitation.

5   Conclusions

A new method for monitoring CT states in finishing turning of hard materials is developed. The specific defects of CP were identified. The new method makes it possible to detect a complex of defects in the tools CP.

The method provided complex of necessary CT adjusting:

- formation of cutting tools adjusting on the wear value;
- formation correction, taking into account nose radius changing;
- formation and analysis of a section of cutting layer and calculation the necessary correction of feed value;
- estimation of the state of flank face, estimate the distance from the extreme groove to the top, calculation the necessary termination of processing.

A new method of CT states monitoring will allow increasing the processing quality and CT resource in finishing turning.

References

1. Karabegovic, I., Karabegovic, E., Mahmic, M., Husak, E.: The role of smart sensors in production processes and the implementation of industry 4.0. J. Eng. Sci. **6**(2), B6–B13 (2019). https://doi.org/10.21272/jes.2019.6(2).b2
2. Ivanov, V., Dehtiarov, I., Zaloga, V., Kosov, I., Savchuk, V.: Increasing productivity of connecting rods machining. In: Ivanov, V., Trojanowska, J., Pavlenko, I., Zajac, J., Peraković, D. (eds.) DSMIE 2020. LNME, pp. 264–275. Springer, Cham (2020). https://doi.org/10.1007/978-3-030-50794-7_26
3. Karabegović, I., Karabegović, E., Mahmić, M., Husak, E., Dašić, P.: The implementation of industry 4.0 supported by service robots in production processes. In: Ivanov, V., Trojanowska, J., Pavlenko, I., Zajac, J., Peraković, D. (eds.) DSMIE 2021. LNME, pp. 193–202. Springer, Cham (2021). https://doi.org/10.1007/978-3-030-77719-7_20
4. Orgiyan, A., Oborskyi, G., Ivanov, V., Balaniuk, A., Matzey, R.: Interaction of flexural and torsional shapes vibrations in fine boring with cantilever boring bars. In: Ivanov, V., Trojanowska, J., Pavlenko, I., Zajac, J., Peraković, D. (eds.) DSMIE 2021. LNME, pp. 481–489. Springer, Cham (2021). https://doi.org/10.1007/978-3-030-77719-7_48
5. Riaz, A., Muhammad, R., Ullah, N., Alkahtani, M., Akram, W.: Fuzzy logic-based prediction of drilling-induced temperatures at varying cutting conditions along with analysis of chips morphology and burrs formation. Metals **11**(2), 1–18 (2021). https://doi.org/10.3390/met11020277
6. Ghencea, D.P., Anania, F.D., Zapciu, M.: Research of fuzzy logic application on surfaces roughness prediction under finishing milling process. IOP Conf. Ser.: Mater. Sci. Eng. **1018**(1), 012020 (2021). https://doi.org/10.1088/1757-899x/1018/1/012020
7. Lin, C.-J., Jhang, J.-Y., Chen, S.-H.: Tool wear prediction using a hybrid of tool chip image and evolutionary fuzzy neural network. Int. J. Adv. Manuf. Syst. **118**(3–4), 921–936 (2021). https://doi.org/10.1007/s00170-021-07291-0

8. Zhang, J., Zeng, Y., Starly, B.: Recurrent neural networks with long term temporal dependencies in machine tool wear diagnosis and prognosis. SN Appl. Sci. **3**(4), 1–13 (2021). https://doi.org/10.1007/s42452-021-04427-5

9. Zuperl, U., Irgolič, T., Kovačič, M.: Minimum depth of milling to obtain the desired surface roughness in multi-layer materials. Mater. Tehnol. **54**(6), 747–753 (2020). https://doi.org/10.17222/mit.2019.263

10. Rifai, A.P., Fukuda, R., Aoyama, H.: Image based identification of cutting tools in turning-milling machines. J. Jpn. Soc. Precis. Eng. **2**(85), 159–166 (2018). https://doi.org/10.2493/jjspe.85.159

11. Ivchenko, O., et al.: Method for an effective selection of tools and cutting conditions during precise turning of non-alloy quality steel C45. Materials **15**(2), 505 (2022). https://doi.org/10.3390/ma15020505

12. Sun, W., Yeh, S.: Using the machine vision method to develop an on-machine insert condition monitoring system for computer numerical control turning machine tools. Materials **11**(10), 1977 (2018). https://doi.org/10.3390/ma11101977

13. Deac, G.C., Deac, C.N., Popa, C.L., Ghinea, M., Cotet, C.: Machine vision in manufacturing processes and the digital twin of manufacturing architectures. In: Annals of DAAAM and Proceedings of the International DAAAM Symposium, pp. 733–736. Vienna, Austria (2017). https://doi.org/10.2507/28th.daaam.proceedings.103

14. Xie, Z., Li, J., Lu, Y.: Feature selection and a method to improve the performance of tool condition monitoring. Int. J. Adv. Manuf. Syst. **100**(9–12), 3197–3206 (2018). https://doi.org/10.1007/s00170-018-2926-5

15. Kuric, I., Kandera, M., Klarák, J., Ivanov, V., Więcek, D.: Visual product inspection based on deep learning methods. In: Tonkonogyi, V., et al. (eds.) InterPartner 2019. LNME, pp. 148–156. Springer, Cham (2020). https://doi.org/10.1007/978-3-030-40724-7_15

16. Wu, D., Jennings, C., Terpenny, J., Gao, R.X., Kumara, S.: A comparative study on machine learning algorithms for smart manufacturing: tool wear prediction using random forests. J. Manuf. Sci. Eng. Trans. ASME **139**(7), 071018 (2017). https://doi.org/10.1115/1.4036350

17. Gouarir, A., Martínez-Arellano, G., Terrazas, G., Benardos, P., Ratchev, S.: In-process tool wear prediction system based on machine learning techniques and force analysis. Procedia CIR **77**, 501–504 (2018). https://doi.org/10.1016/j.procir.2018.08.253

18. Martínez-Arellano, G., Terrazas, G., Ratchev, S.: Tool wear classification using time series imaging and deep learning. Int. J. Adv. Manuf. Syst. **104**(9–12), 3647–3662 (2019). https://doi.org/10.1007/s00170-019-04090-6

19. Kostyk, K., et al.: Simulation of diffusion processes in chemical and thermal processing of machine parts. Processes **9**(4), 698 (2021). https://doi.org/10.3390/pr9040698

20. Hurey, I., Gurey, V., Bartoszuk, M., Hurey, T.: Formation of residual stresses during discontinuous friction treatment. J. Eng. Sci. **8**(1), C38–C44 (2021). https://doi.org/10.21272/jes.2021.8(1).c5

21. Derevianchenko, O., Fomin, O.: Complex recognition approach for cutting part of cutters in finishing turning. In: Ivanov, V., Trojanowska, J., Pavlenko, I., Zajac, J., Peraković, D. (eds.) DSMIE 2021. LNME, pp. 21–30. Springer, Cham (2021). https://doi.org/10.1007/978-3-030-77719-7_3

A Special Feature of Turbine Blade Deformation During Machining

Sergey Dobrotvorskiy , Yevheniia Basova(✉) , Serhii Kononenko ,
Ludmila Dobrovolska , and Abou Samra Youseff Mounif

National Technical University "Kharkiv Polytechnic Institute",
2, Kyrpychova St., Kharkiv 61002, Ukraine
`Yevheniia.Basova@khpi.edu.ua`

Abstract. Significant obstacles in machining surfaces of thin-walled parts are their deformation and oscillatory processes directly during machining. The same parameters subsequently determine the intensity of noise from aircraft engines and, accordingly, the amount of noise at airports. The work aimed to study the influence of the conditions of fixing the blade in the fixture during finishing machining on the change in its natural vibration frequencies. The article developed an approach to analyzing this problem based on the comparison of analytical and digital models. Computer simulation and determination of natural vibration frequencies of a turbine blade are carried out when fixed in the turbine disk lock and fixed to flat surfaces in a fixture. The distributions of stresses and deflections are determined by the distributed load increase. It turned out that the discrepancy between analytical and digital models calculations reaches 12–15%. It is concluded that the natural vibrations of the blade airfoil during machining strongly depend on the conditions of its fixation in the clamping device and differ significantly from the natural vibrations of the blade fixed in the turbine lock. Therefore, at the stage of creating a manufacturing process, it is necessary to determine the natural vibration frequencies and maximum deviations of the blade airfoil to avoid the occurrence of resonance vibrations when the machining conditions change and to carry out machining within the tolerance.

Keywords: Energy efficiency · Turbine blade · Free mode · Machining · Process innovation · Deviation · Aircraft noise

1 Introduction

Modern programs "Europe-Horizon" in the field of energy and transport development provide for the reduction of emissions of carbon dioxide, nitrogen oxides, and particulate matter to zero, as well as developing the airport noise-compatibility programs [1]. The solution to the first problem is planned to be obtained at the expense of the energy of hydrogen, wind, water. Almost all of the listed energy conversion processes use various turbines and devices containing blades. These paddles work in a wide variety of conditions. Aircraft engines that use hydrogen as a fuel are of particular interest. In

this case, the water and steam emissions create new problems in the atmosphere, and the turbine from a truly gas-dynamic one turns into a hybrid or steam turbine.

Moreover, since the noise of aircraft engines is closely related to the frequency and amplitude of natural vibrations of turbine blades, scientific interest is formed, among other things, from consideration of the conditions for machining the blades and their influence on the subsequent magnitude of aircraft engine noise. The problems mentioned above give rise to increased interest in the problems of manufacturing turbine blades. The last stage in the technology of manufacturing blades after polishing is to determine the spectrum of natural vibrations of products, which often differ significantly despite the same machining conditions. Therefore, it is relevant to consider the features of the distribution of the natural frequencies of the blade vibrations at the finishing operation of machining and the arising deviations of the console from the cutting forces to maintain the machining, as well as a preliminary assessment of the influence of the technology of manufacturing the blade apparatus on the noise level.

2 Literature Review

The production of aircraft gas turbine engines (GTE) and power plants based on GTE is developing in the direction of increasing their power and efficiency by increasing the operating temperatures, the efficiency of the aerodynamics of turbines and compressors [2, 3], and the use of lighter or harder materials [4, 5]. In paper [6], it was identified and evaluated the mutual influence of turbine objects on their optimal characteristics. Modern gas turbine engines must meet the following requirements: reliability, minimum weight, high performance, efficiency, and resource.

It should be noted that a variety of high requirements for an aircraft gas turbine engine (for example, in terms of reliability and durability, weight characteristics, etc.) predetermine several features of the GTE's production technology. This qualitatively distinguishes the technology of manufacturing such parts compared to other mechanical engineering products operated in-ground conditions.

From the analysis of technological processes of machining the blade apparatus, it was found that the most difficult process in manufacturing a blade is the machining of the blade airfoil [7, 8]. It is known that turbine and compressor blades are high-precision products that can have the following typical requirements for the accuracy of structural elements [9]:

- blade airfoil – deviation of the profile of the suction side and pressure side of the feather in the design sections from the given one: 0.06 … 0.40 mm; deviation of the profile of the inlet and exit edges of blade: 0.03 … 0.2 mm;
- deviation of the chord width of the blade airfoil b: $\pm (0.2 … 0.6)$ mm; the roughness of the blade's airfoil – Ra = 0.63 … 0.08 μm;
- the maximum deviation in the maximum section from the suction and pressure sides is 0.08–0.9 mm.

In work [8], it was indicated that the value of the radius of profile curvature significantly depends on the blade dimension-type and changes on blades with a feather

height of 40 mm from 6 to 24 mm; on blades with a feather height of 150 mm - from 52 to 400 mm. Such high demands on the accuracy of the blades require corresponding machining methods.

It is known that milling is difficult to obtain very thin blades. The roughness of the working surfaces of the blades after milling Ra = 1.5 microns. Therefore, during manufacturing mentioned parts at the final machining stages, grinding and polishing are used. With such machining technologies, the distribution of cutting forces during machining is not point-like but more distributed over the blade surface than the milling process. A feature of finishing polishing is a small machining allowance of 0.1–0.3 mm, small cut sections, and the clamping forces are in the range of 0.05–0.2 MPa. The width of the polishing wheel is 50–150 mm [10]. It is also important to note that due to the small depth of cut, the tangential component of the cutting force is 3–5 times less than the normal component. Therefore, to simplify the calculations, we will consider only the normal component in this work.

3 Research Methodology

3.1 Features of Blade Machining

When machining the surfaces of the gas channel blades, there is a continuous change in the power parameters of the cutting process [11, 12].

Changes in machining are subject to such parameters as the amount of allowance, depth of cut, contact angles between the tool and the part, surface curvature, rigidity of the machined surface, and other parameters that affect machining quality [13, 14]. The authors of the work [15] performed studies of the influence of the wear of the blade tool on the quality of the processed surface. In paper [16], issues were addressed of mechanical treatment of turbine blade cores are made of porous alumina ceramic. In research [17], the issues address the gap in the variety of the thin-walled parts computer-aided machining parameters calculation solutions that have been addressed. The research [18] touched upon issues related to the multitude of precise parts that are a necessity in reliable methods of surface finishing. The influence of the equipment assembly quality [19, 20] and its individual units [21, 22] on the quality of part machining should be highlighted.

Typical technological processes for manufacturing blades with a length of about 120 mm usually contain the following sequence of basic types of technological operations: milling, grinding, polishing, vibration polishing, static analysis of the frequency and amplitude of natural vibrations.

One of the main features of milling thin parts is that the cutting teeth of the tool periodically come into contact with the material being machined and can lead to deformation of the part during machining [23–26]. A single cut with a tool tooth is 0.5–2 ms. Chip thickness varies from minimum to maximum for top milling and from maximum to minimum for bottom milling and milling force and temperature. However, when milling, the cutting forces are localized [27]. The cutting forces are distributed over the surface with other finishing methods such as polishing and grinding (especially belt grinding). Thus, methods for assessing blade deformations during machining under a distributed load are needed to prevent loading that leads to fracture and rejection of the product.

When constructing an analytical model for calculating the deformation of the blade profile, it was represented as a rectangular plate. When calculating the static strength, the following assumptions were made:

- the blade was considered as a cantilever beam rigidly built into the rim of the disc;
- for simplicity, only the regular cutting forces component has been considered since the stiffness of the plate in the tangential direction of the cutting force component is deliberately many times higher, and the value of the tangential component of the cutting force is many times smaller than the normal component.

The purpose of calculating the static strength of the blade profile during machining is to determine the stresses and the safety factor in different sections along the length of the blade profile. For a plate, they have a physical meaning and can be set on the initial line the deflection W, the angle of rotation $\varphi_y = \frac{1}{h}\frac{\partial W}{\partial \eta}$, the moment $M_y = -\frac{D}{h^2}\left(\frac{\partial^2 W}{\partial \eta^2} + \nu\frac{\partial^2 W}{\partial \xi^2}\right)$ the reduced (according to Kirchhoff) shearing force $V_y = -\frac{D}{h^3}\left(\frac{\partial^3 W}{\partial \eta^3} + (2-\nu)\frac{\partial^3 W}{\partial \eta\partial \xi^2}\right)$ The stability problem was considered without a compressive force along the lateral surfaces [28, 29]. Therefore, the dependences of the parameters in the method of initial functions can be written in the form (1):

$$
\begin{aligned}
W &= h\big[L_{WW}W_0 + L_{W\varphi}\varphi_0 + L_{WM}M_0 + L_{WQ}Q_0\big],\\
\varphi_y &= \big[L_{\varphi W}W_0 + L_{\varphi\varphi}\varphi_0 + L_{\varphi M}M_0 + L_{\varphi Q}Q_0\big],\\
M_y &= \tfrac{D}{h}\big[L_{MW}W_0 + L_{M\varphi}\varphi_0 + L_{MM}M_0 + L_{MQ}Q_0\big],
\end{aligned}
\tag{1}
$$

where L_{ij} – transcendental linear differential operators that depend on the coordinate η.

The general solution of the problem, taking into account the external load, can be written in the form (2):

$$
\begin{aligned}
W &= h\big[L_{WW}W_0 + L_{W\varphi}\varphi_0 + L_{WM}M_0 + L_{WQ}Q_0 + W^*\big],\\
\varphi_y &= \big[L_{\varphi W}W_0 + L_{\varphi\varphi}\varphi_0 + L_{\varphi M}M_0 + L_{\varphi Q}Q_0 + \varphi_y^*\big],\\
M_y &= \tfrac{D}{h}\big[L_{MW}W_0 + L_{M\varphi}\varphi_0 + L_{MM}M_0 + L_{MQ}Q_0 + M_y^*\big],
\end{aligned}
\tag{2}
$$

where the last terms are particular solutions that take into account external influences.

We were interested in the degree of bending. Therefore, the work was limited to a more detailed consideration of this factor.

3.2 The Bending of the Plate, Rigidly Clamped Along One Longitudinal Side, the Second Can Be Supported, and the Other Two Are Free (There Are no Longitudinal and Transverse Forces), the Surface Load is Distributed

Having chosen the coordinate axes, as shown in Fig. 1, the condition on the initial line at $\eta = 0$ was written, $W_0 = \varphi_0 = 0$.

Below the solution to the bending problem was given (3):

$$
W = W^*_{(\eta)} + \overline{W} = \frac{Ph}{24}\left(\eta^4 - 4\eta^3 + 6\eta^2\right)2Re\sum_{n=1}^{\infty}(A_n shr_n\xi + B_n chr_n\xi)F_n(\eta),
\tag{3}
$$

where

$$F_n(\eta) = \frac{\eta}{2r_n^2} sinr_n\eta \left[\frac{1-\nu}{2} r_n cosr_n + \frac{1+\nu}{2} sinr_n \right] + \frac{\eta}{2r_n^3} [r_n\eta cosr_n - sinr_n\eta]$$
$$\times \left[cosr_n - \frac{1-\nu}{2} r_n sinr_n \right],$$

and the characteristic equation for finding r_n

$$L(r_n) = -\frac{(1-\nu)^2 r_n^2}{4} + cos^2 r_n + \frac{(1+\nu)^2}{2} sin^2 r_n = 0.$$
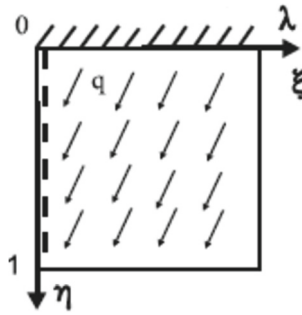
Fig. 1. Calculation scheme.

Arbitrary constants A_n and B_n from the boundary conditions on the transverse sides of the plate were founded.

The correctness of the obtained particular solution is confirmed by the satisfaction of the boundary conditions on the longitudinal sides of the plate:

$$\eta = 0, \ W^*_{(\eta=0)} = \frac{Ph}{24}\left(\eta^4 - 4\eta^3 + 6\eta^2\right) = 0, \ \varphi_y = \frac{P}{24}\left(4\eta^3 - 12\eta^2 + 12\eta\right) = 0;$$
$$\eta = 1, \ M_y^* = \frac{-PD}{24h}\left(12\eta^2 - 24\eta + 12\right) = 0, \ Q_y = \frac{-PD}{24h^2}(24\eta - 24) = 0$$

and the differential equation:

$$\frac{\partial^4 W}{\partial \eta^4} + 2\frac{\partial^2 W}{\partial \eta^2 \partial \xi^2} + \frac{\partial^4 W}{\partial \xi^4} = \frac{qh^4}{D} = \frac{Ph}{24}.$$

Thus, in determining the general solution, the problem is reduced to finding unknown coefficients A_n and B_n from satisfying the boundary conditions on the transverse sides of the plate.

Next, it was necessary to reveal the boundary conditions at the transverse edges of the plate.

For the edge $\xi = 0$ write (4):

$$W_{(\eta,0)} = W^*_{(\eta)}, \tag{4}$$

$$M_x(\eta, 0) = M^*_{x(\eta)}. \tag{5}$$

Next, it is necessary to determine the boundary conditions at the transverse edge of the plate $\xi = \lambda$:

$$2Re \sum_{n=1}^{\infty} (A_n shr_n\lambda + B_n chr_n\lambda)F_n(\eta) = -W^*_{(\eta)} = f_1(\eta); \tag{6}$$

$$2Re \sum_{n=1}^{\infty} (A_n shr_n\lambda + B_n chr_n\lambda)\left(r_n^2 F_n(\eta) + \nu F_n''(\eta)\right) = -\nu \frac{\partial^2 W^*_{(\eta)}}{\partial \eta^2}|_{\xi=\lambda}. \tag{7}$$

The designations were assigned: $C_n = A_n shr_n\lambda + B_n chr_n\lambda$. Further, the generalized orthogonality property was applied

$$\int_0^1 (F_n''(\eta)F_k''(\eta) - r_n^2 r_k^2 F_n(\eta)F_k(\eta))d\eta = \begin{cases} 0, & n \neq k \\ J_n, & n = k' \end{cases},$$

where $J_n = \int_0^1 \left(F_n''^2(\eta) - r_n^4 F_n^2(\eta)\right)d\eta$,

thus, freed up the opportunity to write a formula for determining the coefficient C_n:

$$C_n = \frac{1}{J_n}\left[\int_0^1 f_1''(\eta)F_n''(\eta)d\eta\right]. \tag{8}$$

Note that the eigenfunctions $F_n(\eta)$ has the form (9):

$$F_n(\eta) = \frac{\eta}{2r_n^2} sinr_n\eta\left(\frac{1-\nu}{2}r_n cosr_n + \frac{1+\nu}{2}sinr_n\right) + \frac{1}{2r_n^3}(r_n\eta cosr_n - sinr_n\eta)$$
$$\times \left(cosr_n - \frac{1-\nu}{2}r_n sinr_n\right). \tag{9}$$

4 Results

For numerical experiments, a typical turbine blade was chosen [23]. Input parameters: blade with variable stiffness distribution, blade length –125 mm, chord –60 mm, pressure side length –68 mm, external profile length –94 mm, radius of curvature −630 mm, total contour perimeter –108 mm, maximum blade thickness –19 mm, center of mass X = −2.3 mm, Y = −1.3 mm, Z = −23.6 mm, area –840 mm², material - alloy steel. SolidWorks software was used for research to create the 3D model, and SolidWorks Simulation was used for frequency and strain analysis. The analytical model was analyzed in the mathematical package Mathcad.

At the first stage, following the requirements of the technology, numerical computer experiments were carried out to determine the natural vibration frequencies of the blade in working condition, fixed in the turbine disk. The results obtained were compared with free vibrations of the blade when it was fixed in the clamping device (jaw plate) along its flat surface adjacent to the dovetail.

The studies were carried out in the range of natural frequencies of the blade oscillations up to 50 modes. The study showed that the main part of free vibrations lies in the region of up to 18 modes.

In Fig. 2 shows the frequency distribution of free vibrations of a blade fixed by the blade root in the turbine disk. In Fig. 3 shows the distribution of the total effective mass, which characterizes the amplitude of the oscillations. The calculation results show that the greatest amplitude of oscillations along the Y-axis with a cumulative mass is in the region of critical frequencies 735.1 Hz (0.232 mm), 3273.9 Hz (0.178 mm), along the X-axis at frequencies of 1535.7 Hz (0.230 mm), 4941,1 Hz (0.130 mm), 6301.9 Hz (0.125 mm).
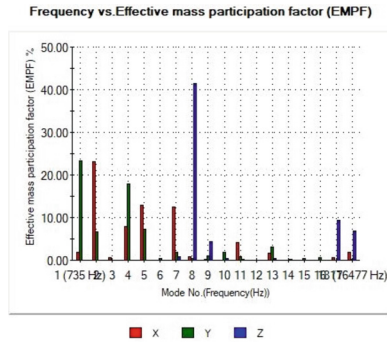
Fig. 2. The frequency distribution of free vibrations of a blade fixed with a blade shank in the turbine disk.
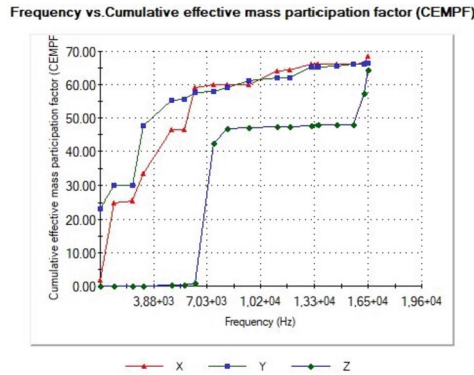
Fig. 3. The distribution of the cumulative effective mass of a blade fixed with a blade shank in the turbine disk.

The Z-axis directed along the blade axis has one higher frequency of manifestation of natural oscillations at 8 modes 7441.4 Hz (0.415 mm). A similar analysis of the natural frequencies of vibrations and the cumulative effective mass when machining a blade fixed in a device (jaw plate) along the lateral surface is shown in Figs. 4 and 5. It should

be noted that in this case, the most dangerous vibrations in the direction of the Y-axis are 924.65 Hz (0.137 mm), 3126.9 Hz (0.122 mm), and along with the X-axis 2247.3 Hz (0.128 mm), 7767.2 Hz (0.158 mm), Z-axis 9440.1 Hz (0.192 mm), 16877 Hz (0.235 mm).
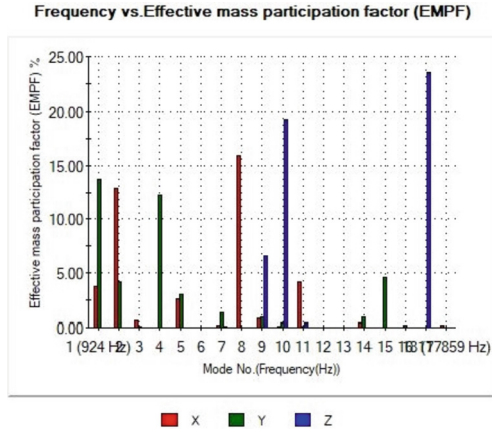
Fig. 4. The frequency distribution of free vibrations of a blade fixed with a blade shank in the jaw plate.
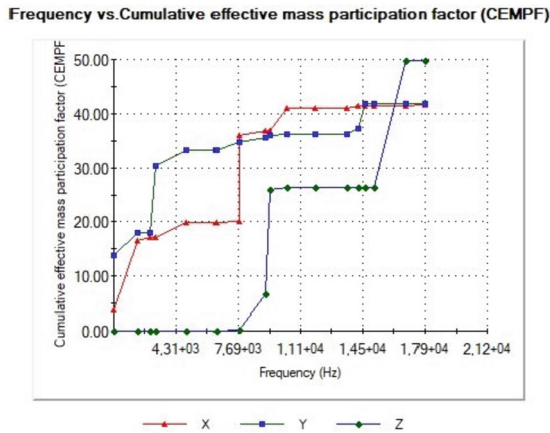
Fig. 5. The distribution of the cumulative effective mass of a blade fixed with a blade shank in the jaw plate.

When the blade is fastened in a jaw plate, the natural vibration frequencies are shifted to the region of higher frequencies and have a lower amplitude along the X and Y axes. It should be noted that, despite the different conditions of fastening, a specific correlation is observed in the number of coinciding modes in both cases (all axes have 2 modes oscillations), and by the numbers of the coinciding modes (Y is number 1, X is number 2, Z is mode 17).

Higher vibration modes (More than 18) and the effective mass distribution are equally probable in all directions X, Y, Z. Thus, it has been established that the conditions for fixing the blade blank during its machining affect the distribution of the natural vibration frequency and vibration amplitude, his hesitation, and qualitatively different from the values of natural frequencies when the blade is fixed in the turbine disk. Since the natural vibration frequencies can shift depending on the attachment conditions in the fixture, this must be considered when developing a technological process for machining the blade profile.
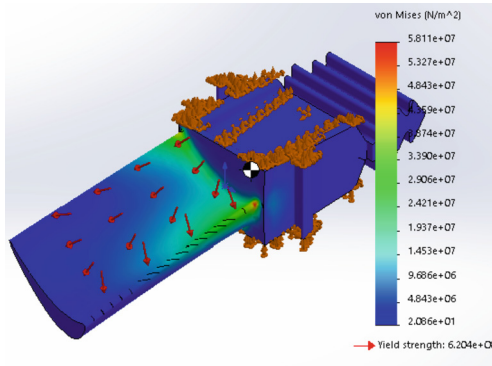
Fig. 6. Simulation of stress changes with a distributed load on the blade airfoil.
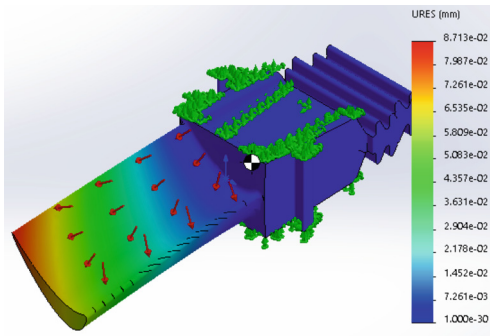
Fig. 7. Simulation of displacement changes with a distributed load on the blade airfoil.

To study the amplitude of the deflection of the blade profile during machining, the change in stresses and deformations was simulated with a distributed load on the blade surface in the range from 0.01 MPa to 0.2 MPa [10]. In Fig. 6 shows the distribution of stresses, and Fig. 7 shows the distribution of deflections of the blade airfoil at a load of 0.15 MPa. That is, in the range of loads close to the maximum permissible.

To identify the patterns of change in the behavior of the characteristics of the blade under the influence of a variable distributed load on its feather, the graphs of the behavior of the simulated parameters were constructed (Fig. 8).
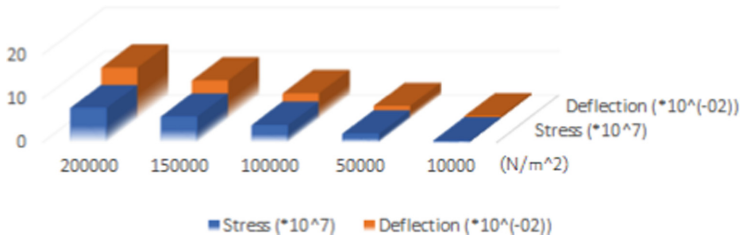
Fig. 8. Behavior graphs of simulated parameters.

From these graphs, it is possible to select the value of the displacement of the blade depending on the load experienced by the blade from the tool.

The solution for analytical models was carried out in the mathematical software complex MathCAD. The data obtained were compared with numerical modeling results using a 3D model.

5   Conclusions

The critical natural frequencies of the transverse vibrations of the blade with the maximum amplitude are predominantly in the low-frequency region of the spectrum. They are mainly found in the area of sound vibrations perceived by humans. Fixing the blade in a place as close as possible to the base of the blade airfoil allows shifting the vibration processes to a higher frequency region and almost halving the vibration amplitude, which can ensure a higher quality of machining and low levels of noise in the future during the operation of the aircraft engine. The results obtained made it possible to establish that numerical simulation by the finite element method of the technological process conditions allows one to find the critical deviations of the blade from the equilibrium position. If the deflection of the blade is comparable in size to the size of the allowance, then the clamping force should be reduced to avoid a scrap of the part. It is important to consider this when creating technological machining processes and with a preliminary assessment of the unit's noise level with such blades.

Comparison of the results obtained using the analytical model and the numerical method gave a discrepancy of (12–15)%. The proposed model can be applied to assess the deviations of the plate with the specified accuracy. This accuracy can be explained by the simplified representation of the deformable plate in analytical calculations. However, such a calculation can be used as an express method when conducting a preliminary assessment of the deformation of the blade profile during finishing.

The results of this work are most applicable, for example, for the development of technological processes for polishing blades. In this case, the load tends to a distributed shape to the large contact area of the polishing wheel and the workpiece surface.

The established fact of the correlation of low-frequency vibration modes under different fixing conditions may indicate the existence of technological heredity in the distribution of natural vibration frequencies at various stages of its manufacture. The final distribution of natural frequencies of finished products depends on the distributions of natural vibration frequencies at all intermediate stages. This factor can reduce the spread

of natural vibrations in a batch of manufactured blades. However, this issue and taking into account the exact distribution of cutting forces, taking into account the temperature requires further research.

This is planned to be done in subsequent studies.

References

1. European Commission. https://ec.europa.eu/info/funding-tenders_en. Accessed 05 Oct 2021
2. Zheng, T., Gao, C., Huang, W.: Modelling and performance analysis of a recuperated gas turbine with low-Btu fuel. Appl. Therm. Eng. **199**, 117514 (2021)
3. Huete, J., Nalianda, D., Pilidis, P.: Propulsion system integration for a first-generation hydrogen civil airliner? Aeronaut. J. **125**(1291), 1654–1665 (2021)
4. Fu, J., Xia, C.: Microstructure evolution and mechanical properties of x6crnimovnb11-2 stainless steel after heat treatment. Materials **14**(18), 5243 (2021)
5. Murzin, S.P., Kazanskiy, N.L., Stiglbrunner, C.: Analysis of the advantages of laser processing of aerospace materials using diffractive optics. Metals **11**(6), 963 (2021)
6. Avdieieva, O., Usatyi, O., Mykhailova, I.: Optimization of the flowing part of the turbine K-310-240 based on the object-oriented approach. In: Machado, J., Soares, F., Trojanowska, J., Ottaviano, E. (eds.) icieng 2021. LNME, pp. 201–213. Springer, Cham (2022). https://doi.org/10.1007/978-3-030-79165-0_20
7. The National Academies PRESS. Assessment of Research Needs for Wind Turbine Rotor Materials Technology (1991). https://www.nap.edu/read/1824/chapter/7. Accessed 05 Oct 2021
8. Novikov, V.A.: Technology of Production and Installation of Steam and Gas Turbines. 2nd edn. GOU VPO USTU-UPI, Ekaterinburg (2009)
9. Poletaev, V.A.: Technology of Automated Production of Gas Turbine Engine Blades, 1st edn. Mechanical engineering, Moscow (2006)
10. Nosmachov, I.G., Dugin, V.N., Nemtsev, B.A.: Finishing operations in mechanical engineering. For young workers. 1st ed. Lenizdat, St. Peterburg (1985)
11. Yuriev, V.L.: Manufacturing Technology of Blades for gas Turbine Engines, 1st edn. Mechanical engineering, Moscow (2011)
12. Krylov, V.N., Poletaev, V.A.: Mechanical treatment of the flow path of monowheels of gas turbine engines (GTE). Ref. B. Eng. J. **6**, 10–12 (2004)
13. Takegami, M., Okuda, K., Kodama, H., Sato, S.: Fundamental cutting properties in end-milling of tial alloy. In: 20th International Symposium on Advances in Abrasive Technology, ISAAT 2017, pp. 285–292. Okinawa (2017)
14. Katta, S.K., Chaitanya, G.: Prediction of process parameters in turning of titanium alloys using response surface methodology. Int. J. Mech. Prod. Eng. Res. Dev. **8**(1), 541–550 (2018)
15. Cao, M., Zhou, C., Li, K.: Research on the relationship between workpiece surface machining quality and turning tool wear. J. Phys: Conf. Ser. **2029**(1), 012071 (2021)
16. Min, C., Yang, X., Xue, M.: Micromachining porous alumina ceramic for high quality trimming of turbine blade cores via double femtosecond laser scanning. Ceram. Int. **47**(1), 461–469 (2021)

17. Dobrotvorskiy, S., Kononenko, S., Basova, Y., Dobrovolska, L., Edl, M.: Development of optimum thin-walled parts milling parameters calculation technique. In: Ivanov, V., Trojanowska, J., Pavlenko, I., Zajac, J., Peraković, D. (eds.) DSMIE 2021. LNME, pp. 343–352. Springer, Cham (2021). https://doi.org/10.1007/978-3-030-77719-7_34

18. Plankovskyy, S., Teodorczyk, A., Shypul, O., Tryfonov, O., Brega, D.: Determination of detonable gas mixture heat fluxes at thermal deburring. Acta Polytechnica **59**(2), 162–169 (2019). https://doi.org/10.14311/AP.2019.59.0162

19. Sokolov, V., Krol, O., Baturin, Y.: Dynamics research and automatic control of technological equipment with electrohydraulic drive. In: 2019 International Russian Automation Conference (RusAutoCon), p. 8867652. IEEE. Sochi, Russia (2019)

20. Krol, O., Sokolov, V.: Modeling carrier system dynamics for metal-cutting machines. In: International Russian Automation Conference (RusAutoCon) 2018, Sochi, pp. 1–5. IEEE (2018)

21. Ivanov, V., Dehtiarov, I., Denysenko, Y., et al.: Experimental diagnostic research of fixture. Diagnostyka **19**(3), 3–9 (2018). https://doi.org/10.29354/diag/92293

22. Ivanov, V., Pavlenko, I., Kuric, I., Kosov, M.: Mathematical modeling and numerical simulation of fixtures for fork-type parts manufacturing. In: Knapčíková, L., Balog, M. (eds.) Industry 4.0: Trends in Management of Intelligent Manufacturing Systems. EICC, pp. 133–142. Springer, Cham (2019). https://doi.org/10.1007/978-3-030-14011-3_12

23. Dobrotvorskiy, S., Basova, Y., Kononenko, S., Dobrovolska, L., Ivanova, M.: Numerical deflections analysis of variable low stiffness of thin-walled parts during milling. In: Ivanov, V., et al. (eds.) DSMIE 2019. LNME, pp. 43–53. Springer, Cham (2020). https://doi.org/10.1007/978-3-030-22365-6_5

24. Pérez-Ruiz, J.D., de Lacalle, L.N.L., Urbikain, G., et al.: On the relationship between cutting forces and anisotropy features in the milling of LPBF Inconel 718 for near net shape parts. Int. J. Mach. Tools Manuf. **170**, 103801 (2021)

25. Kostyk, K., et al.: Simulation of diffusion processes in chemical and thermal processing of machine parts. Processes **9**(4), 698 (2021). https://doi.org/10.3390/pr9040698

26. Ivanov, V., Dehtiarov, I., Pavlenko, I., Kosov, M., Hatala, M.: Technological assurance and features of fork-type parts machining. In: Ivanov, V., et al. (eds.) DSMIE 2019. LNME, pp. 114–125. Springer, Cham (2020). https://doi.org/10.1007/978-3-030-22365-6_12

27. Kombarov, V., Sorokin, V., Tsegelnyk, Y., et al.: Numerical control of machining parts from aluminum alloys with sticking minimization. Int. J. Mechatron. Appl. Mech. **1**(9), 209–216 (2021). https://doi.org/10.17683/IJOMAM/ISSUE9.30

28. Lyengar, K.T.S., Pandya, S.K.: Application of the method of initial functions for the analysis of composite laminated plates. Ingenieur-Archiv **56**, 407–416 (1986)

29. Galileev, S.M., Tabakov, P.Y.: Mathematical foundations of the method of initial functions for the application to anisotropic plates. In: 2nd International Conference on Mechanical, Nanotechnology and Cryogenics Engineering (ICMNC'2013), pp. 59–63. Phnom Penh, Cambodia (2013)

Ensuring the Quality of Conical Mating Surfaces Processing by Diamond Honing

Eshreb Dzhemilov[1]([envelope]) [iD], Alper Uysal[2] [iD], Chingiz Yakubov[1] [iD], and Ruslan Dzhemalyadinov[1] [iD]

[1] Crimean Engineering and Pedagogical University named after Fevzi Yakubov, 8, Uchebniy side St., Simferopol 29501, Republic of Crimea, Ukraine
`eshrebdzhemilov@gmail.com`
[2] Yildiz Technical University, Besiktas, 34349 Istanbul, Turkey

Abstract. Diamond honing is the dimensional treatment of various surfaces using honing heads that rotate and reciprocate while simultaneously feeding stones in a radial direction. The high durability of diamond stones, low temperatures in the cutting zone, and low cutting forces can improve the accuracy and productivity of processing, reduce the roughness of the machined surface, apply active control, automate the honing process and increase the durability of the machine parts and mechanisms. In contrast to the processing of cylindrical surfaces, honing of tapered holes takes place with a constant change in the contact area of the tool with the machined surface, which leads to uneven removal of the allowance. This work aims to ensure the quality of tapered surface processing by honing. The experiments were carried out on industrial equipment. Considering the influence of contact pressures on the surface quality, the correction factor of the generatrix of the conical hole was experimentally determined, and the dependences of the change in the depth of penetration of the cutting grains were obtained.

Keywords: Honing · Conical hole · Contact pressures · Correction factor · Roundness deviation · Process innovation

1 Introduction

The need for the development and improvement of technological methods of machining parts arises due to the high requirements for the quality of products of mechanical engineering production. The use of synthetic diamonds as elements of cutting tools in finishing operations, one of which is honing, allows, with the least material removal, to most intensively influence the surface to be treated and control the microgeometry and physical state of the surface layers.

The processing technology of internal and external precision mating cylindrical surfaces does not cause problems. At the same time, the connection of precise conical surfaces is difficult due to processing errors of conical holes.

2 Literature Review

The research of many authors of the diamond honing process is mainly devoted to processing cylindrical surfaces. Ogorodov [1] researched preventing burring is considered by honing. The authors of the study [2] studied the effect of ceramic and diamond honing on the surface quality of the liner of an internal combustion engine. Zou et al. [3] were engaged in obtaining a certain geometry during the diamond honing of cylinders. Sabri and Mansory [4] achieved cylinder surface quality when honing a vitrified bonded tool. Zhang et al., in their work, investigated the parameters affecting the quality of cast iron sleeves during diamond honing [5]. In the research [6], the authors also corrected the surface of the cylinder liner of an internal combustion engine after honing. The authors solved a similar problem [7] but achieved using honing rods with variable geometry. The research study [8] presents the effect of selected parameters of the honing process on cylinder liner surface topography.

At the same time, considering the quality parameters of the surfaces obtained after diamond honing, the emphasis is mainly on controlling the parameters of cutting conditions. Thus, the authors in the study [9] propose an optimization scheme for improving the surface quality of carburized holes based on the GRA-RSM method to study the law of influence of the honing head rotation speed, axial reciprocating motion speed, grain size, and single grinding depth on the surface roughness. The studies [10, 11] propose up-to-date approaches in designing machine tools.

The authors in the research [12] showed that the abrasive grain size and, to a lesser extent, the tangential velocity and linear velocity have the greatest influence on the surface roughness. In the article [13], the authors propose a new concept of the shape of a honing tool. In the studies [14, 15], the authors developed a model for rational design and optimization of complex shape parts.

The pressing of the honing bars is carried out by piezo-hydraulic force transmission. The authors claim that this design leads to a significant increase in the productivity of the process and allows you to control the normal expansion force of the bars.

Moos et al. [16] propose to use an analytical model of a honing tool that considers the geometry of the abrasive bars and the technological loads of the honing unit. This model will allow you to evaluate the contact surface and the resulting forces in the process of metal removal without the use of sensors.

3 Research Methodology

The kinematics of conical honing differs from the kinematics of cylindrical honing in that, due to a change in the diameter along the generatrix of the cone, the stones perform an additional movement - radial reciprocating, which is a prerequisite for ensuring the position of the surface of the stone from the machined surface. In this case, the variable width of the contact of the working surface of the tool with the part leads to uneven material removal and unevenness of the roughness parameters of the machined surface [17].

The quality of conical connections is affected by errors in angles and deviations in the shape of the mating surfaces. To improve centering accuracy, load capacity, wear

resistance, and tightness of joints, it is necessary to ensure uniform contact along the mating surfaces obtained by lapping the tapered surfaces. However, this is a laborious operation and does not preserve the interchangeability of the paired cones.

The conducted studies of the influence of contact pressures on the honing process of tapered holes [18] made it possible to create a design of block that differs from the industrial design. The contact pressures were recorded using strain gauges glued along the generatrix of the workpiece. Additional supports are introduced into the design of the proposed block (Fig. 1). The position of these supports can change the nature of the contact load depending on the taper angle of the hole being machined.
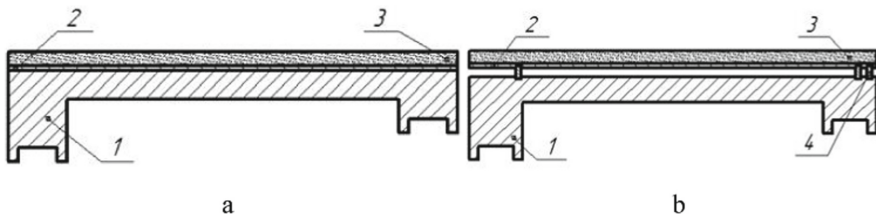
Fig. 1. Honing blocks: a – industrial, b – proposed; 1 - frame; 2 – substrate; 3 – diamond bar; 4 - support bar.

The results of experiments using an industrial block (Fig. 2) showed that the change in contact pressure along the length of the stone is within $1.04 \div 0.07$ MPa (Fig. 3).

Fig. 2. Industrial block.

The proposed construction of the block (Fig. 4) made it possible to reduce the contact pressure along the length of the stone, which was distributed in the range of $0.52 \div 0.05$ MPa (Fig. 5).
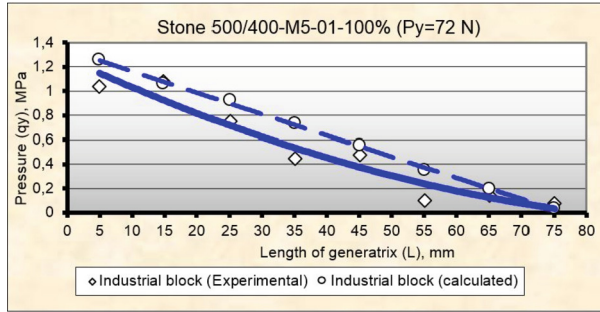
Fig. 3. Distribution of contact pressure q_y along the stone using an industrial block.

Fig. 4. Proposed construction of the block.
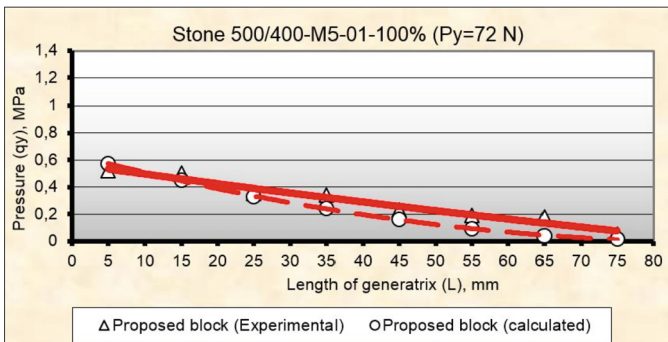
Fig. 5. Distribution of contact pressure q_y along the stone using a proposed block.

The parameter of the depth of penetration of the cutting grains is also important, taking into account the change in the contact area of the stone during conical honing.

To take this parameter into account, a 1 mm thick plexiglass was installed between the stone and the treated surface over the entire length of the contact. A load of 480 N was applied to the stone. At the same time, the plexiglass sagged, assuming the shape of a conical hole in the part. By moving the plexiglass along the bar by 3–5 mm, scratches

were obtained that characterize the depth of penetration of the cutting grains. A synthetic diamond stone 500/400-M5-01-100% was used during the experiments.

AISI 5135 H steel with a hardness of HRC 48 was used as a material for research.

The depth of the resulting scratches was measured in 5 cross-sections along the generatrix of the conical hole on a TR 200 portable roughness tester.

4   Results

Investigations of the influence of the tool's design (honing tool) on the accuracy and quality of the machined surface have been carried out.

Measurements of deviations from roundness after finishing boring, honing with industrial and offered tools have been carried out. The results are shown in Fig. 6. Comparative analysis of the data showed that the alignment of contact loads when using the proposed tool significantly reduces the deviation from roundness.
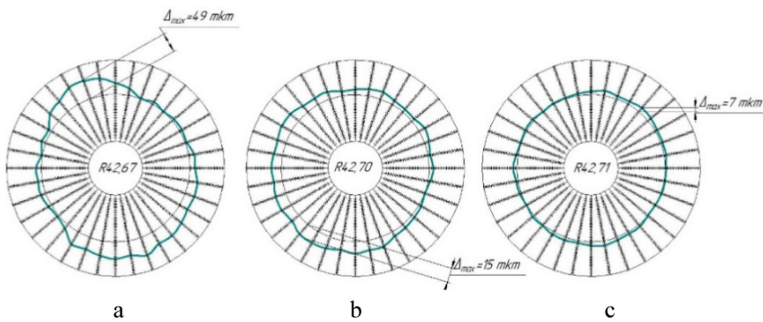
Fig. 6. Roundness deviation of the tapered bore: a - after boring; b - after honing with an industrial block with diamond stones 500/400-M5-01-100% (t_{mach} = 4 min); c - after honing with the proposed block with diamond stones 500/400-M5-01 - 100% (t_{mach} = 4 min).

The straightness of the generatrix of the conical hole was determined in two mutually perpendicular longitudinal sections after processing with industrial and proposed blocks using diamond stones 500/400-M5-01-100% and 125/100-M5-01-100%. The data obtained showed that after honing with stone 500/400-M5-01-100% straightness deviation was $0.028 \div 0.103$ mm with an industrial block and $0.011 \div 0.058$ mm with the proposed block (Fig. 7), and with stone 125/100-M5-01-100% - respectively $0.032 \div 0.095$ mm and $0.006 \div 0.052$ mm, that is, on average, a two-fold straightness correction was obtained.

The intensity of the correction of the deviation of the angle of the taper of the hole was estimated by the correction factor a_i:

$$a_i = \frac{\Delta\alpha_{i.c.} - \Delta\alpha_{a.c.}}{\Delta D} \tag{1}$$

where $\Delta\alpha_{i.c.}$ - initial deviation of the angle of the cone, min;

$\Delta\alpha_{a.c.}$ - deviation of the taper angle after honing, min;
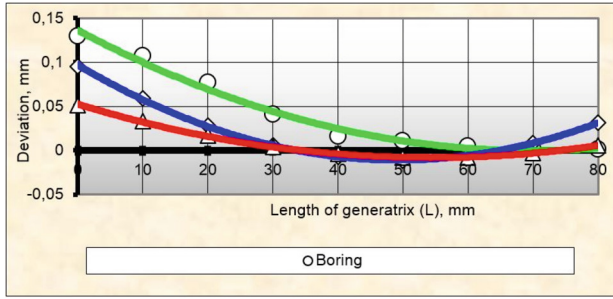
Fig. 7. Straightness deviation of the generatrix of the tapered hole after honing with stone 500/400-M5-01-100%.

ΔD - diametral allowance for honing, μm.

Table 1 shows the experimental values of the correction factor a_i and the generatrix of the conical hole, obtained by processing the results of the straightness deviations shown in Fig. 7.

According to the results of the given data in Table 1, the dependence of the correction factor a_i along the length of the generatrix of the conical hole after 1 min of honing is plotted (Fig. 8). The correction factor a_i depends on the initial shape of the tapered hole obtained during the preliminary operation. From Fig. 8, we can conclude that negative values of a_i are associated with the fact that the machine honing time was $t_{mach} = 1$ min.

Table 1. Experimental values of the correction factor a_i and along the length the generatrix of the tapered hole when honing with a diamond stone 500/400-M5-01-100% and $t_{mach} = 1$ min.

Length of generatrix (L), mm	Correction factor a_i	
	Industrial block	Proposed block
5	0,26	0,22
15	0,29	0,31
25	0,36	0,51
35	0,29	0,54
45	0,27	0,59
55	0,30	0,64
65	0,51	1,07
75	$-0,42$	$-1,34$

This time is not enough to correct the errors of the preliminary operation, the maximum values of which took place in the area of the small hole of the cone.

Table 2 shows the values of the correction factor k and after honing $t_{mach} = 4$ min.
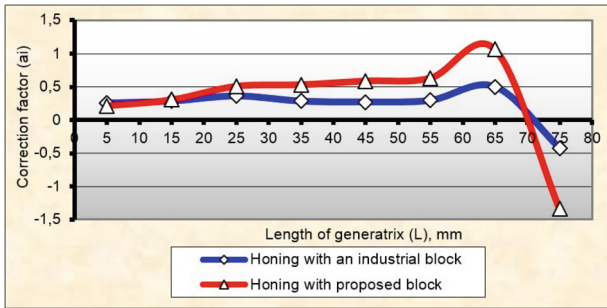
Fig. 8. The value of the correction factor a_i from the length generatrix of the tapered bore ($t_{mach} = 1$ min).

Table 2. Experimental values of the correction factor a_i and along the length the generatrix of the tapered hole when honing with a diamond stone 500/400-M5-1-100% and $t_{mach} = 4$ min.

Length of generatrix (L), mm	Correction factor a_i	
	Industrial block	Proposed block
5	0,52	1,04
15	0,48	1,05
25	0,47	1,05
35	0,44	1,05
45	0,45	1,07
55	0,47	1,08
65	0,51	1,09
75	0,52	1,10

The nature of the graphs (Fig. 9) shows the equivalence of the correction factor along the generatrix of the tapered hole when using the proposed block, which depends on the distribution of contact pressures.

In the process of honing tapered holes, as the tool moves from a small to large bore of the taper, the width of the contact of the bar with the machined surface decreases. At the same time, the number of cutting grains also decreases, which leads to their deeper penetration into the work surface. Therefore, the study of the depth of penetration of cutting grains is of great importance in improving the quality of processing.

Therefore, experiments were carried out, and measurements of the processed surface were carried out using the industrial and proposed pads in the honing tool.
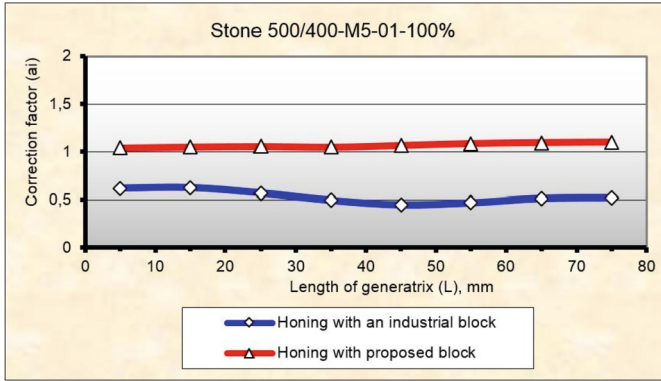
Fig. 9. The value of the correction factor a_i from the length generatrix of the tapered bore (t_{mach} = 4 min).

The results of measurements after experiments with a batch of 20 parts are shown in Table 3.

Table 3. The depth of penetration of cutting grains.

Force (Py), N	Block	Depth of penetration of cutting grains (δ), μm Section				
		I-I	II-II	III-III	IV-IV	V-V
480	Industrial	9,70	7,98	5,73	2,27	1,18
	Proposed	5,70	4,01	2,83	1,26	0,97

Based on the data obtained, graphical dependences of the depth of penetration of cutting grains along the length of the generatrix of the conical hole were plotted (Fig. 10).
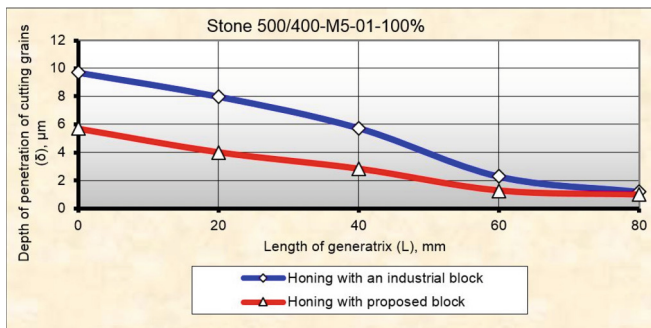
Fig. 10. Depth of penetration cutting grains along the generatrix of a tapered hole.

The graph shows the depth of penetration of the cutting grains of the diamond bar into the work surface.

It should be noted that when using an industrial block, the depth of grain penetration is in the range of $1.2 \div 9.7 \, \mu m$, and with the proposed block $-1.0 \div 5.7 \, \mu m$.

The decrease in the penetration depth of the grains at the larger hole is because the introduction of additional supports, the optimal location of which was determined experimentally, leveled the contact pressures (they increase in the direction from the larger to the smaller radius of the conical hole).

To carry out a comparative analysis of the experimentally obtained curves (Fig. 9), it is necessary to calculate the slope angles of the approximation lines.

The regression equation, which has a value of reliability $R^2 = 09792$, for the depth of grain penetration during honing with an industrial shoe has the form:

$$y = -2.2749x + 12.198, \tag{2}$$

here: $\tan \alpha_1 = 2.2749$; $\alpha_1 = 66°16'15''$.

The regression equation, which has a value of reliability $R^2 = 09628$, for the depth of grain penetration when honing with the proposed block has the form:

$$y = -1.2206x + 6.6146, \tag{3}$$

here: $\tan \alpha_2 = 1.2206$; $\alpha_2 = 50°40'24''$.

The ratio of the slope angles of the approximation lines shows the degree of uniformity of the depth of penetration of diamond grains along the length of the hole.

$$\frac{\alpha_1}{\alpha_2} = 1.31. \tag{4}$$

Thus, from the calculations performed, it can be concluded that with the proposed block, the depth of grain penetration in each section of the conical hole was leveled, regardless of the width of the contact. It is undoubtedly due to the uniform distribution of the load over the entire surface of the bar.

5   Conclusions

Analysis of the industrial block's honing process showed that the processing proceeds with uneven material removal. It is due to a change in the load acting on the working surface of the bar when moving along the generatrix of the conical hole. It leads to a deviation in shaping and a decrease in the surface quality of the tapered bore. Based on the analysis of the distribution of contact loads when using an industrial block, an experimental block was designed, which makes it possible to equalize the contact loads on the working surface of the bar when it interacts with the conical hole.

The studies carried out characterizing the surface quality during honing of tapered holes showed that: the deviation from roundness decreased by 1.7 times; the straightness deviation decreased by 1.8 times; taper angle deviation decreased 1.6 times; the penetration depth of cutting grains along the generatrix of the conical hole was $\delta = 0.97 \div 5.7 \, \mu m$.

Experimental studies have made it possible to establish the effect of contact pressures on the working surface of the tool on the quality of machining tapered holes by diamond honing.

References

1. Ogorodov, V.A.: Prevention of burring in diamond honing. Russ. Eng. Res. **35**(3), 221–226 (2015). https://doi.org/10.3103/S1068798X15030132

2. Hurpekli, M., Yilmaz, R., Kondakci, E., Solak, N.: Effects of ceramic and diamond honing on bore/liner surface in view of oil retention. SAE Techn. Pap. **1**, 199–207 (2014)

3. Zou, W., et al.: Study on performances of special diamond honing stone for producing steppedreticulated patterns on cylinder linear. Diam. Abras. Eng. **30**(1), 29–33 (2010)

4. Sabri, L., Mansori, M.: Process variability in honing of cylinder liner with vitrified bonded diamond tools. Surf. Coat. Technol. **204**(6), 1046–1050 (2009)

5. Zhang, Z., Dong, P.M., Dong, Z.: The honing process for precision holes. Appl. Mech. Mater. **419**, 269–272 (2013)

6. Anderberg, C., Cabanettes, F., Dimkovski, Z., Ohlsson, R., Rosén, B.-G.: Cylinder liners and consequences of improved honing. In: 12th Nordic Symposium on Tribology, pp. 1–13. Helsingör, Danmark (2008)

7. Shcherbyna, K., Hrechka, A., Mazhara, V., Diachenko, T.: Kinematics of cutting process while honing holes with a hone with variable geometry of sticks. Des. Prod. Exploit. Agric. Mach. **50**, 159–164 (2020)

8. Pawlus, P., Dzierwa, A., Michalski, J., Reizer, R., Wieczorowski, M., Majchrowski, R.: The effect of selected parameters of the honing process on cylinder liner surface topography. Surf. Topogr. Metrol. Prop. **2**(2), 025004 (2014)

9. Tang, T., Liu, C., Wang, R.: Optimization of honing surface roughness of carburized holes based on GRA-RSM. Machines **9**(11), 291 (2021)

10. Panchuk, V., Onysko, O., Kotwica, K., Barz, C., Borushchak, L.: Prediction of the accuracy of the tapered thread profile. J. Eng. Sci. **8**(2), B1–B6 (2021). https://doi.org/10.21272/jes.2021.8(2).b1

11. Shvets, S.V., Machado, J.: Numerical model of cutting tool blade wear. J. Eng. Sci. **8**(2), A1–A5 (2021). https://doi.org/10.21272/jes.2021.8(2).a1

12. Nguyen, T.-T., Vu, T.-C., Duong, Q.-D.: Multi-responses optimization of finishing honing process for surface quality and production rate. J. Braz. Soc. Mech. Sci. Eng. **42**(11), 1–17 (2020). https://doi.org/10.1007/s40430-020-02690-y

13. Droeder, K., Hoffmeister, H.-W., Grosse, T.: Force-controlled form honing using a piezohydraulic form honing system. CIRP Ann. Manuf. Technol. **66**(1), 317–320 (2017)

14. Ivanov, V., Pavlenko, I., Kuric, I., Kosov, M.: Mathematical modeling and numerical simulation of fixtures for fork-type parts manufacturing. In: Knapčíková, L., Balog, M. (eds.) Industry 4.0: Trends in Management of Intelligent Manufacturing Systems. EICC, pp. 133–142. Springer, Cham (2019). https://doi.org/10.1007/978-3-030-14011-3_12

15. Ivanov, V., Dehtiarov, I., Pavlenko, I., Kosov, M., Hatala, M.: Technological assurance and features of fork-type parts machining. In: Ivanov, V., et al. (eds.) DSMIE 2019. LNME, pp. 114–125. Springer, Cham (2020). https://doi.org/10.1007/978-3-030-22365-6_12

16. Moos, U., Bähre, D.: Analysis of process forces for the precision honing of small bores. Procedia CIRP **31**, 387–392 (2015)

17. Muratov, K.R., Ablyaz, T.R., Gashev, E.A.: Contact pressure in honing. Russ. Eng. Res. **40**(10), 859–861 (2020). https://doi.org/10.3103/S1068798X20100160

18. Dzhemilov, E., Dzhemalyadinov, R.: Measurement of contact pressure for conical honing. In: Ivanov, V., Trojanowska, J., Pavlenko, I., Zajac, J., Peraković, D. (eds.) DSMIE 2021. LNME, pp. 353–362. Springer, Cham (2021). https://doi.org/10.1007/978-3-030-77719-7_35

Prediction of Remaining Lifetime of the Mold for the Composite Manufacturing

Andrii Kondratiev[1(✉)] , Svitlana Purhina[2] , Anton Tsaritsynskyi[2] ,
Maryna Shevtsova[2] , and Tetyana Nabokina[2]

[1] O.M. Beketov National University of Urban Economy in Kharkiv, 17 Marshal Bazhanov St.,
Kharkiv 61002, Ukraine
`andrii.kondratiev@kname.edu.ua`

[2] National Aerospace University "Kharkiv Aviation Institute", 17, Chkalova St., Kharkiv 61070,
Ukraine

Abstract. Performance capabilities of the structures made of polymeric composite materials depend on the manufacturing accuracy of the part contour. To give the specified contour to the part, it is necessary to ensure the constancy of the shape and dimensions of the tools throughout their operation, considering the peculiarity of accumulation of residual stresses by shaping surface during service. The refined model of the temperature stress-strain behavior of the tools in the process of composite products' molding to determine the equipment lifetime was developed, with the determination of the impact of properties of the material, dimensions, and shape of the shape-generating molding tools on their life. Composites provide a longer equipment lifetime at equal dimensions of the shape-generating molding tools made of different materials. A twofold increase in the thickness of the shaping surface ensures higher stiffness and, as a result, four times and three times the longer lifetime of molding tools for the metallic shaping surfaces and composites, accordingly. It was found that the physical and mechanical characteristics of the molded composite package may have a significant effect on the stiffness of the shaping surface and reduce the lifetime of extensive tools by more than three times. Based on the obtained results, the methods for increasing the lifetime can be developed for composite manufacturing.

Keywords: Life-cycle analysis · Manufacturing innovation · Molding cycles · Shaping surface · Residual stress-strain behavior

1 Introduction

Polymeric composite materials (PCM) are currently used in many industries, including aircraft construction, airspace applications, shipbuilding, automotive industry, and others [1, 2]. These materials provide high structural strength at low weight [3, 4]. PCM is used for manufacturing gear wheels [5, 6] and thread joints [7, 8]. It is necessary to manufacture the molding tools which ensure the structure of regulated quality throughout its lifetime to obtain a predetermined contour and geometry of the composite structure [9, 10]. The choice of optimal parameters of the molding tools at the stage of their design

to obtain high-quality parts at minimal cost requires an integrated approach [11]. This is because designing and manufacturing the molding tools in terms of labor intensity takes 80%, and by duration, it takes 90% of the entire cycle of preproduction engineering [12, 13]. At present, works on the development of methods predicting the behavior of tools at the stage of the molding of composite structures and research of effect of the expiring tool lifetime on a part being manufactured are in progress.

2   Literature Review

In manufacturing the structure of PCM, it is necessary to ensure the required physical and mechanical characteristics, unity of the structure, and shape and geometry of the part [14]. The first two conditions are achieved by choosing the molding process parameters (temperature, pressure, heating, and cooling rates) and their interaction with the PCM [15, 16]. Therefore, an essential role in the drawing up of the technology of PCM structures' manufacturing process belongs to the development of interrelated physical-chemical, thermomechanical and mathematical models which allow to give the timely assessment of any change in the physical and mechanical characteristics of PCM and to establish the critical value of the main technological parameters of the molding to obtain a defect-free structure of the material [17, 18]. Solving problems of this kind, for example, is dealt with in [19, 20]. Analysis of the presented methods allows assessing the changes during the binder curing process, taking into account the exothermic effect, level of residual stresses in the molded composite product, correctly constructing the process of its molding, and identifying the factors affecting the quality of the resulting part. In the calculations of parameters of the molding tools, the level of permissible residual stresses in the manufactured part serves as a limiting factor. However, this rule applies only to smooth metal tooling designed for an infinite lifetime. In this case, because of the large thickness of the shaping surface of the tool, during the molding process, elastic deformation occurs without distortion of the working surface [21]. Thin-sheet tools have the shaping surface of small thickness, and at a certain point in the operation, it features plastic deformations, leaving the small but cumulative effect after removing the load. The mechanism of lifetime reduction in the composite shaping surface of the tool is different from that in the metal one [22]. In repeated temperature loads, the stability of the physical and mechanical characteristics of the PCM is lost. It affects both the bearing capacity of the material and the durability of the tool itself. With each subsequent molding, residual stresses are accumulated, leading to the gradual loss of the shape of the tool shaping surface. This, in turn, can significantly change the operational and dimensional characteristics of the part [23]. However, despite severe developments in this area, the short lifetime of metal and composite molding tools is recorded in the production practice [12, 24]. This is because in searching for more convenient, lightweight, and uniformly heated structures of molding tools, thin-walled frames and composite solutions are usually developed, the optimal parameters border on critical ones. Besides, in most cases, when the molding tools are designed, they meet the individual operational requirements only [14]. The methods for increasing the lifetime of the molding tools are considered in detail in [25, 26]. However, a common drawback of these methods is considering a uniform heat supply from the side of the shaping surface of the tools when solving the heat conduction problems.

Consequently, the improvement of the existing methods for determination of the lifetime of the molding tools will allow to assess the individual residual lifetime and, whenever necessary, to consider various options for its extension. These methods also allow designing the molding tools with the required lifetime, considering the omissions in solving heat conduction problems. So, it will be possible to obtain high-quality products in the specified number of molding procedures. In this regard, the purpose of this work is to develop a methodology for determining the main parameters of the shape-generating molding tool from the condition of ensuring its stiffness in the molding process at given service life.

3   Research Methodology

Autoclave molding technologies take the central place in the production of critical composites since they allow obtaining high-strength materials and are the most reliable for creating high-quality products of PCM. As commonly known [6], the technological process of PCM product molding con-sists in giving it a non-reversible shape using shape-generating molding tools through polymerization of the binder at a specific temperature and pressure, varying in time. When the temperature in the autoclave rises, the tool's PCM package and shaping surface begin to deform according to their linear thermal expansion coefficients [27]. Due to the difference in these coefficients, PCM tends to move relative to the shaping surface. However, it is prevented by the friction force arising between the shaping surface of the tool and PCM because of applied excessive molding pressure. We assume that the friction force is sufficient to ensure that PCM does not slip relative to the shaping surface. As a result, thermal stresses only will appear in the PCM and the shaping surface of the tool. We consider the "PCM + shaping surface" system to determine these stresses as a layered shell obtaining a temperature increment. Since this shell is asymmetric relative to its median plane, thermal stresses are accompanied by its bending. After cooling, the "PCM+" system will not return to its original (undeformed) state. The shaping surface or residual deflection will have some waviness in one molding cycle w_r^0. With each subsequent molding, the shaping surface will receive a similar deflection. Then the lifetime (number of molding cycles) of the tool shaping surface can be found as follows $N = [w_r]/w_r^0$, where $[w_r]$ – allowable deflection of the shaping surface specified under the requirements to the composite structure.

We assume that the lifetime of the molding tool or the number of high-quality products extracted from it will be exhausted when the residual deflection exceeds the allowable deflection of the composite part being molded.

The residual deflection of the shaping surface is determined by the difference between its maximum deflection w_{max} and elastic deflection w_e: $w_r = w_{max} - w_e$.

The reinforcing elements of the tool are assumed stiff. The unreinforced cell of the shaping surface with the PCM package on it is considered a multilayer shallow shell, freely supported along the contour, with the principal curvatures – k_1, k_2. In this case, the lower layer of the shell is the shaping surface of the tool. The origin of coordinates is taken at the midpoint of the lower surface of the cell. Dimensions of the longitudinal (parallel to the x-axis) and transverse sides of the cell are equal to a and b (Fig. 1), respectively.
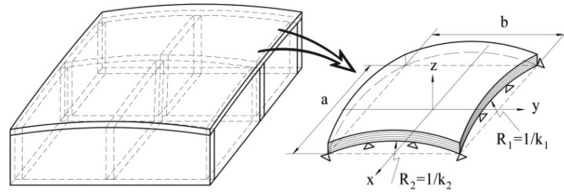
Fig. 1. Computational model.

Deflection of the unsupported part of the molding tool is determined by solving the thermoelasticity problem of a multilayer shallow shell with the lower layer being the shaping surface. The thermoelasticity problem was solved with the use of the Ritz-Timoshenko variational approach. Displacements of the points of the shaping surface were presented as functions of the variables x and y, satisfying the adopted boundary conditions at the edges of the cell of the shaping surface:

$$
\begin{aligned}
u &= (y^2 - b^2)(A_1 + A_2x + A_3y + A_4x^2 + A_5y^2 + A_6x^3 + A_7y^3); \\
v &= (x^2 - a^2)(B_1 + B_2x + B_3y + B_4x^2 + B_5y^2 + B_6x^3 + B_7y^3); \\
w &= (x^2 - a^2)(y^2 - b^2)(C_1 + C_2x + C_3y + C_4x^2 + C_5y^2 + C_6x^3 + C_7y^3); \quad (1)
\end{aligned}
$$

where a, b – dimensions of cell of the shaping surface of the tool, A_i, B_i, C_i – unknown coefficients determined from the condition of the minimum total potential energy of the system [28, 29]:

$$
U = \iint_S (N_x - B_{T1})\varepsilon_x + (N_y - B_{T2})\varepsilon_y + N_{xy}\gamma_{xy} + (M_x - D_{T1})\chi_x
$$
$$
+ (M_y - D_{T2})\chi_y + (M_{xy}\chi_{xy})ds \to \min, \quad (2)
$$

where M_x, M_y, M_{xy}, N_x, N_y, and N_{xy} – moments and forces acting in the system, ε_x, ε_y, γ_{xy} and χ_x, χ_y, χ_{xy} – deformations and curvatures of the initial surface of the shell ($z = 0$) associated with displacements by the following dependencies:

$$
\varepsilon_x = \frac{\partial u}{\partial x} + k_1 w; \ \varepsilon_y = \frac{\partial v}{\partial y} + k_2 w; \ \gamma_{xy} = \frac{\partial u}{\partial y} + \frac{\partial v}{\partial x}; \ \chi_x = \frac{\partial^2 w}{\partial x^2}; \ \chi_y = \frac{\partial^2 w}{\partial y^2}; \ \chi_{xy} = -2\frac{\partial^2 w}{\partial x \partial y}, \quad (3)
$$

B_{mn}, C_{mn}, D_{mn} – membrane, mixed, bending stiffnesses, B_{Tn}, D_{Tn} – membrane, and bending temperature coefficients [28, 29].

After equal transformations, the deformation energy can be represented as a function of unknown coefficients A_i, B_i, C_i: $U = U(A_i, B_i, C_i)$.

Condition for the minimum of the potential deformation energy will be realized by the setting to zero of all derivatives of the total energy with respect to the coefficients of the polynomials (1). That is, the resolving system of equations will be as follows:

$$
\frac{\partial U}{\partial A_i} = 0; \quad \frac{\partial U}{\partial B_i} = 0; \quad \frac{\partial U}{\partial C_i} = 0, \ (i = 1 \dots 7). \quad (4)
$$

This system is a system of linear algebraic equations; the number of these equations will always be equal to the number of terms (coefficients) entered in the series. Therefore,

the system will be complete. When we find the coefficients resulting from solving this system, the displacements can be further determined using formulas (1). As a result, we obtain a complete solution to the problem. After finding the displacements and corresponding deformations (3), stresses in the shaping surface are determined as:

$$\sigma_x = \overline{E}(\varepsilon_x + \mu\varepsilon_y - \alpha(1 + \mu)\Delta T); \quad \sigma_y = \overline{E}(\varepsilon_y + \mu\varepsilon_x - \alpha(1 + \mu)\Delta T); \quad \tau_{xy} = \frac{1}{2}\overline{E}(1 - \mu)\gamma_{xy}.$$

Based on the obtained computational dependencies, it is possible to estimate the degree of impact of the geometric parameters and physical and mechanical characteristics of the molding tool and molded composite package on its lifetime.

4   Results

We consider the tool with the shaping surface of thickness δ and dimensions of sides a and b, the shape of which is determined by the curvature coefficients k_1, k_2. Physical and mechanical characteristics of the considered materials of the molding tool are presented in Table 1. The composite molding tool's reinforcement structure is $[0°;90°]_{2n}$. The composite panel being molded is made by symmetrical laying $[\pm45°]_{20}$ of unidirectional carbon no 1 (Table 1). Here and below, the figure corresponds to the number of the material given in Table 1 [30].

Figure 2 shows the dependences of the lifetime of molding tool N on the thickness of its shaping surface δ. Dimensions of sides of the molding tool were taken equal to $a = b = 1000$ mm. Woven glass fiber reinforced plastic (GFRP) and carbon fiber reinforced plastic (CFRP) (no 5 and no 4 in Table 1) with the reinforcement structure of $[0°, 90°]$, as well as metals: aluminum and steel (no 6 and no 7 in Table 1) were used as the materials of the shaping surface.

Figure 2 a shows that thickening of the shaping surface leads to the increase in value of the lifetime for any material; steel has the most extended lifetime of the presented dependences, and woven GFRP features the shortest lifetime. Figure 2 b presents the dependencies of the values of the lifetime of the square molding tool on its dimensions at the thickness of shaping surface equal to 1 mm. With small dimensions of the sides of the shaping surface of the tool, the high value of the lifetime for the composite shaping surface is observed compared to the metal one. However, when dimensions of the molding tool are increased while maintaining the thickness of the shaping surface at the same physical and mechanical characteristics of the material of the shaping surface, its lifetime decreases rapidly. It indicates the need to enhance the stiffness of the molding tool by increasing its thickness.

The value of the lifetime of the molding tools depends significantly on the spatial shape of the shaping surface. Figure 3 a shows that with the increase in the radius of curvature R of the composite product, and, accordingly, the shaping surface (to $\delta = 1$ mm) at least on one side, a significant increase in the lifetime for all presented materials is observed.

For example, for the ratio $H/a = 0.3$, the lifetime of molding tools increases: for CFRP – approximately 11 times, for GFRP – 7 times, for steel – four times, and for aluminium – three times. Figure 3, b shows the dependences of the lifetime for the

Table 1. Mechanical characteristics of the considered materials of molding tools [30].

Material/Properties	No 1	No 2	No 3	No 4	No 5	No 6	No 7
	Unidirectional PCM			Women PCM		Metals	
	CFRP	GFRP	Organic plastic	CFRP	GFRP	Aluminium	Steel
Elastic modulus along the fibers E_1, GPa	100	45	80	77	30	72	200
Elastic modulus across the fibers E_2, GPa	10	10	5.5	75	30	72	200
Shear modulus G_{12}, GPa	6	5	2	7	5	27	80
Poisson's ratio μ_{12}	0.35	0.30	0.31	0.06	0,17	0.32	0.25
Thermal linear expansion coefficient along the fibers α_1, 10^{-6} K^{-1}	0	8	-4	3.4	10	23	11
Thermal linear expansion coefficient across the fibers α_2, 10^{-6} K^{-1}	30	25	60	3.7	10	23	11
Monolayer thickness δ_0, mm	0.10	0.15	0.12	0.10	0.25	1	1
Density ρ, kg/m^3	1500	1700	1350	1600	2200	2780	7830
Heat conduction coefficient λ, W/(m·K)	4.1	0.3	0.15	4.1	0.3	169	50
Specific heat capacity c, J/(kg·K)	4100	300	150	4000	270	915	494
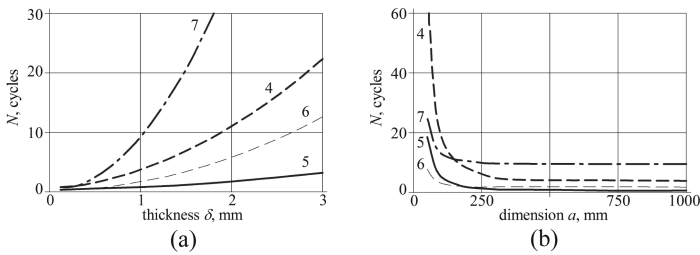
Fig. 2. Dependence of value of the lifetime on thickness (a) and dimensions (b) of shaping the surface of the tools: 4, 5 – woven CFRP and GFRP; 5, 7 – aluminum, steel.
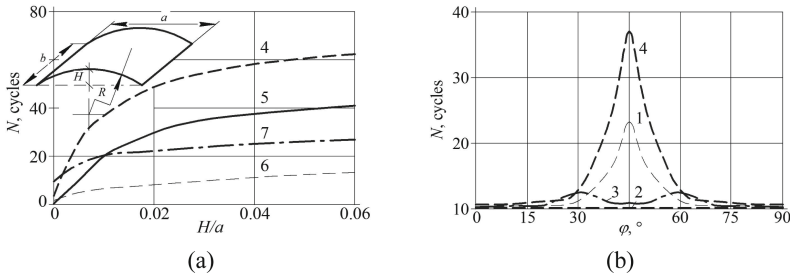
Fig. 3. The lifetime upon changing the curvature (a) and angle of reinforcement (b) of the shaping surface of the tool.

composite shaping surfaces of the tool (while maintaining its thickness) at various angles of symmetrical laying of the shaping surface. For carbon fiber composites no 1 and no 4 (Table 1), the most rational angles of the shaping surface are values of $\pm45°$. The lifetime of molding tools increases 10 times for unidirectional carbon and 25 times for woven CFRP compared to similar material of the shaping surface at an angle of reinforcement of $0°$ or $90°$. For the organic plastic, the rational angles of laying of the shaping surface are $\pm30°$ and $\pm60°$. For the GFRP under consideration (no 5 in Table 1), the reinforcement angle does not affect the lifetime.

Figure 4–5 shows the change in the molding tool's lifetime after changing the angle of reinforcement of the manufactured composite part. Analysis of the presented figures shows that parameters of the molding tools calculated for the angles of the initial laying of the molded package are acceptable for the rest of the layings of the molded package (however, for square-type molding tool only).
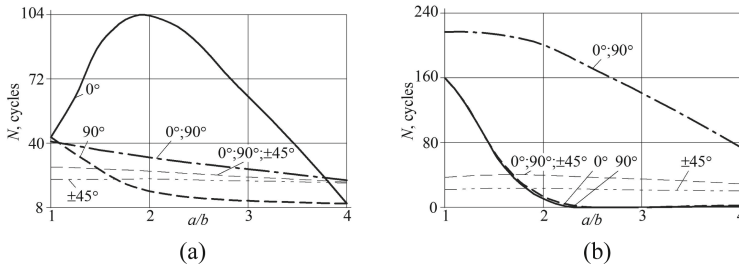
Fig. 4. Dependence of the value of the lifetime of the molding tools made of woven GFRP (a) and CFRP (b) on the angle of reinforcement of the molded package of unidirectional carbon.

Elongation of the molding tool made of any material reduces the initial value of the lifetime by several units at the molding of composite structures with laying angles of $90°$, and for CFRP molding tools with angles of $0°$. For the GFRP molding tools, unidirectional layings of the molded package have the same limiting points. However, the nature of the change in the dependence of the lifetime is practically the opposite. At the ratio of dimensions of 2/1, laying the molded package at $0°$ gives the lifetime advantage of more than 5 times. At the same time, with the dimensions increase to 4/1,
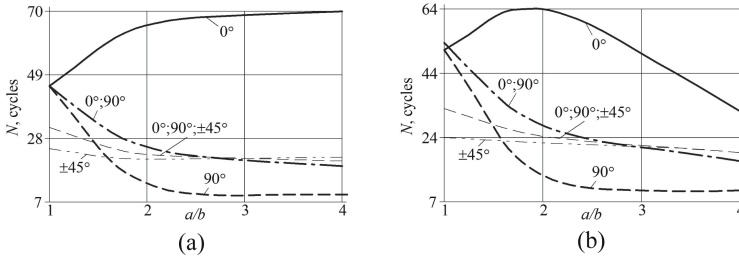
Fig. 5. Dependence of the value of the lifetime of aluminium (a) and steel (b) molding tools on the angle of reinforcement of the molded package of unidirectional carbon.

the lifetime drops to 9 units. For orthotropic layings of the package, there is a constant decrease of the lifetime of the molding tool at the increase of the ratio of dimensions with the clear advantage of the laying of [0°, 90°]. This exceeds the original value on the square molding tool two times, with a ratio of 4/1 – by 6% only. For square CFRP molding tool, the lifetime advantage over the initial laying of the molded package is: for unidirectional composite parts – 8 times, for laying at [0°,90°] – 10 times, for laying at [0°, 90°, ±45°] – almost two times. For the long molding tools, unidirectional layings of the package lose their advantage over the original one, and the lifetime is reduced to three units. The lifetime of the molding tool at the molding of orthotropic layings of the PCM package decreases as well, but not lower than the specified one.

The replacement of the CFRP molded package by GFRP one with the same thermal linear expansion coefficient in mutually perpendicular directions provided a significant increase in the lifetime of all molding tools except the CFRP tool. The maximum value of the lifetime exceeds the specified value: for the GFRP – 65 times, for aluminium – 7.5 times, for steel – 36.5 times. For the CFRP molding tool, none of the layings gives the specified lifetime value; while for the square shape-generating molding tools, the lifetime is about ten cycles, then for long ones – not more than two.

5   Conclusions

The refined model of the temperature stress-strain behavior of the tools in the process of composite products' molding to determine the equipment lifetime has been developed, with the determination of the impact of properties of the material, dimensions, and shape of the shape-generating molding tools on their life.

The research allows concluding below:

– main ways to enhance the lifetime of shape-generating molding tool is to increase the thickness of its shaping surface and reduce the cell size by the introduction of the reinforcing ribs;
– shaping surface of the shell-type tools has a long lifetime compared to molding tools with the flat shaping surface of equal dimensions;
– changing the material or structure of the molded product requires checking for conformity of the lifetime of the molding tools already designed.

Based on the obtained results, the methods for increasing the lifetime can be developed for composite manufacturing.

References

1. Rodichev, Y.M., Smetankina, N.V., Shupikov, O.M., Ugrimov, S.V.: Stress-strain assessment for laminated aircraft cockpit windows at static and dynamic loads. Strength Mater. **50**(6), 868–873 (2019). https://doi.org/10.1007/s11223-019-00033-4
2. Fomin, O., Logvinenko, O., Burlutsky, O., Rybin A.: Scientific substantiation of thermal leveling for deformations in the car structure. Int. J. Eng. Technol. **7**(4.3), 125–129 (2018). https://doi.org/10.14419/ijet.v7i4.3.19721
3. Hsissou, R., Seghiri, R., Benzekri, Z., Hilali, M., Rafik, M., Elharfi, A.: Polymer composite materials: a comprehensive review. Compos. Struct. **262**, 113640 (2021). https://doi.org/10.1016/j.compstruct.2021.113640
4. Kondratiev, A.: Improving the mass efficiency of a composite launch vehicle head fairing with a sandwich structure. East.-Eur. J. Enterp. Technol. **6**(7(102)), 6–18 (2019). https://doi.org/10.15587/1729-4061.2019.184551
5. Wang, J., Li, J., Wang, H., E, J.: Research on gearbox composite fault diagnosis based on improved local mean decomposition. Int. J. Dyn. Control **9**(4), 1411–1422 (2021). https://doi.org/10.1007/s40435-020-00744-6
6. Zorko, D., Tavčar, J., Bizjak, M., Šturm, R., Bergant, Z.: High cycle fatigue behaviour of autoclave-cured woven carbon fibre-reinforced polymer composite gears. Polym. Test. **102**, 107339 (2021). https://doi.org/10.1016/j.polymertesting.2021.107339
7. Nekrasov, S., Zhyhylii, D., Dovhopolov, A., Karatas, M.A.: Research on the manufacture and strength of the innovative joint of FRP machine parts. J. Manuf. Process. **72**, 338–349 (2021). https://doi.org/10.1016/j.jmapro.2021.10.025
8. Kombarov, V., Kryzhyvets, Y., Biletskyi, I., Tsegelnyk, Y., Aksonov, Y., Piddubna, L.: Numerical control of fiberglass pipe bends manufacturing. In: 2021 IEEE 2nd KhPI Week on Advanced Technology (KhPIWeek), pp. 357–362 (2021). https://doi.org/10.1109/KhPIWeek53812.2021.9570068
9. Gonzalez, C., Vilatela, J.J., Molina-Aldareguia, J.M., Lopes, C.S., Llorca, J.: Structural composites for multifunctional applications: current challenges and future trends. Prog. Mater Sci. **89**, 194–251 (2017). https://doi.org/10.1016/j.pmatsci.2017.04.005
10. Otrosh, Y., Kovalov, A., Semkiv, O., Rudeshko, I., Diven, V.: Methodology remaining lifetime determination of the building structures. MATEC Web Conf. **230**, 02023 (2018). https://doi.org/10.1051/matecconf/201823002023
11. Deng, B., Shi, Y.Y., Yu, T., Zhao, P.: Influence mechanism and optimization analysis of technological parameters for the composite prepreg tape winding process. Polymers **12**(8), 1843 (2020). https://doi.org/10.3390/polym12081843
12. Baran, I., Cinar, K., Ersoy, N., Akkerman, R., Hattel, J.H.: A review on the mechanical modeling of composite manufacturing processes. Arch. Comput. Methods Eng. **24**(2), 365–395 (2016). https://doi.org/10.1007/s11831-016-9167-2
13. Kondratiev, A., Píštěk, V., Purhina, S., Shevtsova, M., Fomina, A., Kučera, P.: Self-heating mould for composite manufacturing. Polymers **13**(18), 3074 (2021). https://doi.org/10.3390/polym13183074
14. Boitsov, B.V., Gavva, L.M., Pugachev, Y.N.: The stress-strain state of structurally anisotropic panels from composite materials under force and process temperature exposure. Polym. Sci. Ser. D **12**(1), 85–90 (2019). https://doi.org/10.1134/S1995421219010039

15. Budelmann, D., Schmidt, C., Meiners, D.: Prepreg tack: a review of mechanisms, measurement, and manufacturing implication. Polym. Compos. **41**(9), 3440–3458 (2020). https://doi.org/10.1002/pc.25642

16. Kostyk, K., Hatala, M., Kostyk, V., Ivanov, V., Pavlenko, I., Duplakova, D.: Simulation of diffusion processes in chemical and thermal processing of machine parts. Processes **9**(4), 698 (2021). https://doi.org/10.3390/pr9040698

17. Shah, P.H., Halls, V.A., Zheng, J.Q., Batra, R.C.: Optimal cure cycle parameters for minimizing residual stresses in fiber-reinforced polymer composite laminates. J. Compos. Mater. **52**(6), 773–792 (2018). https://doi.org/10.1177/0021998317714317

18. Kondratiev, A., Gaidachuk, V., Nabokina, T., Kovalenko, V.: Determination of the influence of deflections in the thickness of a composite material on its physical and mechanical properties with a local damage to its wholeness. East.-Eur. J. Enterp. Technol. **4**(1(100)), 6–13 (2019). https://doi.org/10.15587/1729-4061.2019.174025

19. Fleischer, J., Teti, R., Lanza, G., Mativenga, P., Mohring, H.C., Caggiano, A.: Composite materials parts manufacturing. CIRP Ann. Manuf. Technol. **67**(2), 603–626 (2018). https://doi.org/10.1016/j.cirp.2018.05.005

20. Gavva, L.M., Firsanov, V.V.: Mathematical models and methods for calculating the stress-strain state of aircraft panels from composite materials taking into account the production technology. Mech. Solids **55**(3), 403–412 (2020). https://doi.org/10.3103/s002565442003005x

21. Bruschi, S., Cao, J., Merklein, M., Yanagimoto, J.: Forming of metal-based composite parts. CIRP Ann. **70**(2), 567–588 (2021). https://doi.org/10.1016/j.cirp.2021.05.009

22. Shirvanimoghaddam, K., et al.: Carbon fiber reinforced metal matrix composites: fabrication processes and properties. Compos. A Appl. Sci. Manuf. **92**, 70–96 (2017). https://doi.org/10.1016/j.compositesa.2016.10.032

23. Rodionov, V.V.: Optimization of molding the polymeric composite material with improved characteristics. Plast. Massy **3–4**, 55–58 (2019). https://doi.org/10.35164/0554-2901-2019-3-4-55-58

24. Weber, T.A., Arent, J.C., Steffens, L., Balvers, J.M., Duhovic, M.: Thermal optimization of composite autoclave molds using the shift factor approach for boundary condition estimation. J. Compos. Mater. **51**(12), 1753–1767 (2017). https://doi.org/10.1177/0021998317699868

25. Wang, Q., Wang, L.Y., Zhu, W.D., Xu, Q., Ke, Y.L.: Design optimization of molds for autoclave process of composite manufacturing. J. Reinf. Plast. Compos. **36**(21), 1564–1576 (2017). https://doi.org/10.1177/0731684417718265

26. Jayasree, N., Omairey, S., Kazilas, M.: Novel multi-zone self-heated composites tool for out-of-autoclave aerospace components manufacturing. Sci. Eng. Compos. Mater. **27**(1), 325–334 (2020). https://doi.org/10.1515/secm-2020-0033

27. Chen, Y.-X., Wang, L.-C., Chu, P.-C.: A recipe parameter recommendation system for an autoclave process and an empirical study. Procedia Manuf. **51**, 1046–1053 (2020). https://doi.org/10.1016/j.promfg.2020.10.147

28. Vasiliev, V.V., Morozov, E.V.: Chapter 11–circular cylindrical shells. In: Vasiliev, V.V., Morozov, E.V. (eds.) Advanced Mechanics of Composite Materials (3rd edn), pp. 685–743 (2013). DOI: https://doi.org/10.1016/B978-0-08-098231-1.00011-X

29. Grigorenko, A.Y., Grigorenko, Y.M., Müller, W.H., Vlaikov, G.G.: Recent Developments in Anisotropic Heterogeneous Shell Theory: General Theory and Applications of Classical Theory, vol. 1, 1st edn. Springer, Singapore (2016). https://doi.org/10.1007/978-981-10-0353-0

30. Dveirin, O.Z., Andreev, O.V., Kondrat'ev, A.V., Haidachuk, V.Y.: Stressed state in the vicinity of a hole in mechanical joint of composite parts. Int. Appl. Mech. **57**(2), 234–247 (2021). https://doi.org/10.1007/s10778-021-01076-4

Finite Element Simulation of Diamond Grinding

Janos Kundrak[1] , Vladimir Fedorovich[2] , Dmitriy Fedorenko[2] ,
Yevheniy Ostroverkh[2] , and Larisa Pupan[2(✉)]

[1] Institute of Manufacturing Science, University of Miskolc, C/1 108 Miskolc-Egyetemváros,
Miskolc 3515, Hungary
[2] National Technical University "Kharkiv Polytechnic Institute",
2, Kyrpychova St., Kharkiv 61002, Ukraine
`Larysa.Pupan@khpi.edu.ua`

Abstract. The paper focused on the static and dynamic modeling of difficult-to-machine materials' multi-parameter diamond grinding process. The simulation was carried out using SolidWorks Simulation, ANSYS, and LS-DYNA software packages. The influence of diamond wheels' qualitative and quantitative indicators on the stress-strain state in the cutting zone of the "bond – metal phase – grain – processed material" system was studied. The simulation considered the diamond grains' characteristics (concentration, size, depth in a bond, wear area, composition, shape, and size of metal inclusions) and the wheels bond (composition and porosity). The equivalent stresses σ_{eq} were determined depending on the total thermal and force loading. The propagation volumes of destruction stresses in the grain and the bond were analyzed according to the selected criteria. Simulation of the diamond grinding process allowed determining the optimal combinations of physical and mechanical properties of the bond, as well as the required characteristics of diamond grains. The conditions for rational grinding modes ensuring the self-sharpening of the wheel grains were determined. The concentration of diamond grains C_g in the diamond-bearing layer was identified as one of the most influencing factors. The C_g value should be limited to 50% to improve the process stability and reduce the cost of diamond abrasive tools.

Keywords: Grinding wheel · 3D modeling · Diamond grains · Ceramic bond · Self-sharpening · Manufacturing innovation

1 Introduction

In the manufacturing industry, diamond grinding is mainly used as a finishing process to obtain high-quality products for critical industries. The efficiency of diamond grinding of difficult-to-machine materials is determined by complex and interrelated processes of micro-destruction in the contact zone. The micro-destruction intensity of the elements of the "diamond wheel – processed material" system largely depends on the stress-strain state of the contact area.

Optimization of the stress level in the local cutting zone should consider the properties of the diamond wheel's structural elements (bond, grains, metal phase) and the processed

materials. The influence of technological factors of grinding should also be considered. Using experimental methods to solve this multi-parameter problem is laborious and expensive.

In this regard, an urgent task is to develop a methodology for calculating the predicted level of equivalent stresses in the "diamond wheel – processed material" system to prevent the critical stage of micro-destruction in the contact zone and ensure self-sharpening of the diamond wheel.

2   Literature Review

Many works offer a solution to this problem using 3D modeling. The use of software packages based on the finite element method (FDM) for objects of complex geometry and loading conditions, including machining with a diamond abrasive tool, is described in articles [1–4].

The work [5] shows the principles of multiscale simulation in studying phenomena in the interaction zone of contact surfaces. The dimensions of the initial flat computational domains of the 3D finite element model were reduced to micron sizes to study the processes in local areas. The proposed downscaling method improves the geometric and positioning accuracy of the studied objects. The possibility of expanding the proposed multilevel modeling technique for various types of interaction is shown.

In a study [6], based on the use of FDM to simulate the cutting process, a three-zone friction modeling is proposed to assess the distribution of normal and shear stresses and to predict the location of critical regions during machining.

In [7], finite element modeling was provided to analyze distortions caused by residual stresses in a local variable grinding contact area. The developed three-dimensional model makes it possible to identify the thermo-metallurgical effects arising during grinding in the "diamond wheel – processed material" system, considering the physical and mechanical properties of the modeled objects.

In [8, 9], the modeling technique for the stress-strain state of the sintering area of the diamond abrasive tools and the grinding zone (including sharpening and finishing of precision diamond blade tools) is given. Based on the finite element method, the simulation allows determining the rational composition of the diamond-bearing layer of the wheel and the physical and mechanical properties of its components without lengthy, laborious, and expensive experimental studies. The rational design of the wheel is proposed for ultra-high-speed grinding.

The methodology, proposed in [10], includes the following stages of the diamond grinding modeling: 1) 3D computer simulation of stress-strain state in the process of sintering the diamond-bearing layer to determine the conditions for preserving the integrity of diamond grains; 2) 3D computer simulation of the stress-strain state of the grinding zone to determine the rational machining conditions; 3) 3D computer simulation of stress-strain state in the process of dressing the abrasive wheels with a diamond tool; 4) 3D study of the topography parameters of the wheel working surface and the processed surface by the method of laser scanning. Thus, the ideology of full computer automation of all the processes modeling, including manufacture, machining, and operation of precision diamond tools, is proposed [11].

Based on the simulation experiments results, dependencies can be obtained that describe the behavior of structural elements of the wheel working surface, considering its qualitative and quantitative characteristics [12], which, in turn, provides operational control of processing and an increase in the efficiency of the tool as a whole [13].

One of the topical areas of research in FEM modeling is the effect of processes in the contact zone of the grinding wheel with the machined material on the quality of finished products. A correlation was revealed between the characteristics of the surface quality of the processed material (hardness and residual stress [14]) and the heat-and-power effects of grinding [15–17]. Also, comprehensive approaches for numerical modeling are developed in [18, 19].

Notably, the practical implementation of the simulation methodology of diamond grinding, proposed in a number of works, requires additional research. In particular, the developed methodology does not allow calculating the rational characteristics of diamond wheels, for example, the concentration of diamond grains. There is no information on the methodology for dynamic modeling of the grinding process. There is practically no data on modeling the processing of difficult-to-machine materials.

This paper aims to calculate the critical volumes of the destruction of the "diamond grain – metal phase – bond – processed material" system to predict the output indicators of diamond grinding of difficult-to-machine materials in the wheel self-sharpening mode.

3   Research Methodology

The software packages SIMULIA Abaqus, SolidWorks Simulation, ANSYS, and LS-DYNA, were used to computer model diamond grinding.

To determine the parameters that ensure the operation of diamond grains in the self-sharpening mode, the static 3D modeling of the diamond grinding was carried out using a particular software package (SolidWorks Simulation). An example of a 3D model of the "bond – metal phase – grain –processed material (PM)" system, developed to study the grinding process with a diamond wheel of a given porosity of the diamond-bearing layer, is shown in Fig. 1.

The models were loaded by a normal pressure, simulating the radial force P_y (1 MPa, 2 MPa, and 3 MPa for specific processed material) and the tangential force P_z, which was 0.6…0.7 P_y. The temperature in the contact area between the grain and the processed material during dry grinding was set according to the works [20, 21].
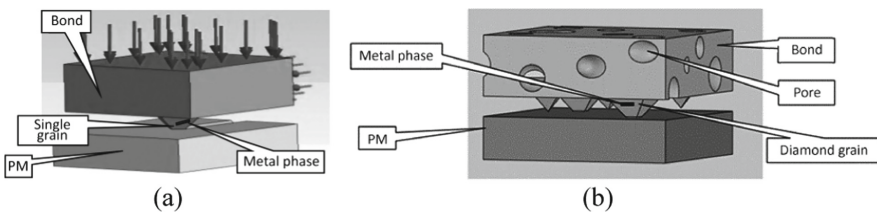
Fig. 1. 3D models for a diamond grinding system analysis: a – model with a single grain; b – model with a given concentration of grains and porosity of the diamond layer.

The considered system is exposed to both force and temperature factors in the actual grinding process. The value of equivalent stresses σ_{eq} was determined in the elements of the "metal phase – grain – bond – processed material" system depending on the total thermal and force loading. As a criterion for the grain destruction, the relative volume of grains V_d was estimated, where the equivalent stresses exceed the ultimate strength (σ_v) for diamond grains, considering their grade and size. A wheel bond was considered destroyed if the equivalent stresses (σ_{eq}) exceeded the corresponding ultimate strength value, and the volume of their propagation V_d exceeded 20%. Such conditions are adopted by analogy with the determination of the resistance of ultra-high temperature ceramics to temperature fluctuations, considering that a constant temperature change occurs in the grinding area [22].

The physical and mechanical properties of the processed materials and the diamond wheel were used (Table 1).

Table 1. Physical and mechanical properties of the studied materials.

Material	Property				
	Young's modulus E_{pm}, GPa	Poisson's ratio μ	Mass density ρ, kg/m^3	Coefficient of thermal expansion α, 10^{-6}/K	Thermal conductivity q, W/(m·K)
Sitall AC-418 (pyroceram AS-418)	85	0.29	2600	2.85	1.95
WC-Co cemented carbide type DIN HG30	590	0.21	14800	5.1	50.2
Diamond grains	1060	0.3	3512	0.95	2400
Ceramic bond K1–01	63	0.243	2390	3.7	0.797
Research grade of bond RM	47	0.310	2770	10.11	0.393

Theoretical studies of the diamond grinding process included the analysis of the stress-strain state of the "metal phase – grain – bond – pore – processed material" system. The following parameters were used as the main influencing factors in the modeling process: the grain size of the diamond powder; the size of the wear areas of the grains; the depth of the grains in the bond; composition, size, and shape of the metal phase in the grain; porosity of the bond.

4   Results

4.1   Effect of Grains Concentration on Stress-Strain State in Grinding Zone

The models were developed to study the effect of the diamond grains concentration on the level of stresses arising during the grinding of materials of different hardness. The concentration of diamond grains C_g was 25%, 50%, and 100% (Fig. 2).

The simulation considered the case of using the diamond grains AC6 125/100 containing a metal phase of the $Fe_{44}Co_{44}(Cr_3C_2)_{12}$ composition, and ceramic bond of wheels: serial grade K1–01 and grade RM developed at NTU "KhPI" (Table 1). Diagrams of the stress-strain state of the "metal phase – grain – bond – processed material" system for sitall AC-418 are given in Fig. 3.

(a)   (b)   (c)
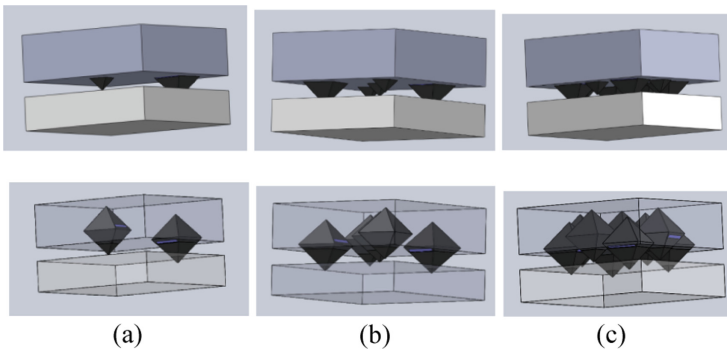
Fig. 2. 3D-models of the diamond-bearing layer fragment: a – $C_g = 25\%$; b – $C_g = 50\%$; c – $C_g = 100\%$.

Analysis of the data received made it possible to reveal the stresses distribution's nature, assess their level, and determine the volumes of the destruction stress propagation in the system elements during diamond grinding of various materials. Calculations showed the maximum equivalent stresses σ_{eq} in the contact zones of diamond grains with a bond and the processed material. For all the studied cases, the internal stresses in grains are localized around the inclusions of the metal phase. However, their value does not reach the critical level for grain material when using the metal phase $Fe_{44}Co_{44}(Cr_3C_2)_{12}$ with a relatively low value of the coefficient of thermal expansion CTE ($\alpha = 9.2 \cdot 10^{-6}$ 1/K).

An increase in the diamond grains concentration of the diamond-bearing layer leads to the stresses increase in the bond, while the stress level in the diamond grain–processed material contact decreases. A decrease in the diamond grains concentration is accompanied by a stress decrease in the bond and an increase in the stress level in the grain–processed material contacts for all the studied materials. This can be explained by increasing the load on a single grain.

The following was established as a result of the analysis of the failure criteria for the diamond grains and the bond (Fig. 3, Fig. 4).

When using the K1–01 bond ($\sigma_v = 31.06$ MPa), an increase in the diamond grains concentration in the range from 25% to 100% causes destructive stresses in the bond, the
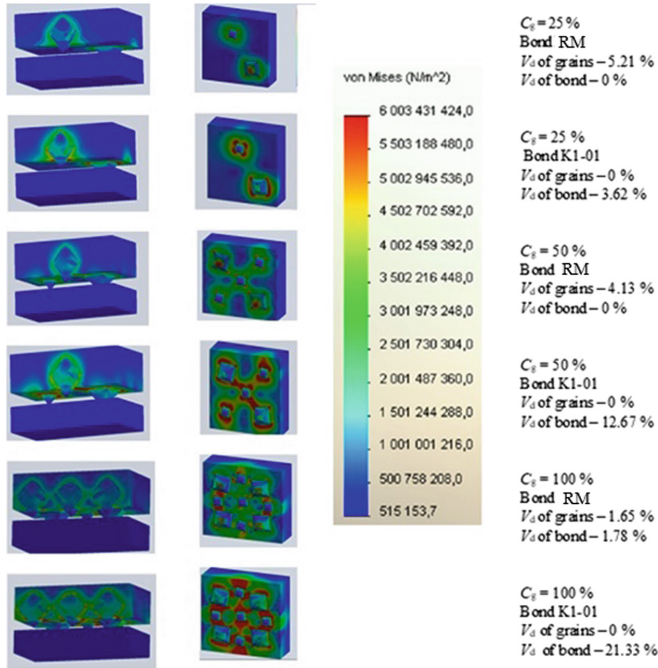
Fig. 3. Visualization of the stress state in the "metal phase – grain – bond – processed material" system during diamond grinding of sitall AC-418.
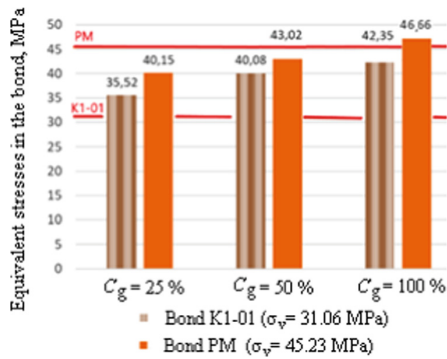
Fig. 4. Dependence of the bond equivalent stresses σ_{eq} on the grain concentration in the diamond-bearing layer.

volume of which (V_d) increases from 3.62% to 21.33%. The diamond grain stresses do not reach the level of their destruction ($\sigma_{eq} < 0.2$ GPa), which excludes the possibility of the grains self-sharpening. An increase in the concentration of the grains over 25% causes bond destruction (Fig. 3), leading to the premature removal of diamond grains with potentially high cutting properties from the wheel working surface and, consequently, to an increase in their specific consumption.

When using an RM bond ($\sigma_v = 45.23$ MPa) at a 25% diamond grains concentration, the destructive stresses arise in a grain (Fig. 3), which is explained by an increase in the load on a single grain. Destruction of the bond does not occur due to its increased strength (Fig. 4). At a 50% concentration of diamond grains, the stresses nature in the grains and the bond remain the same. However, with an increase in the concentration of the grains to 100%, the partial micro-destruction of both system elements occurs. This fact creates the preconditions for renewal of the cutting surfaces of the diamond grains and the removal of grains that completely lost their cutting ability due to the destruction of the surrounding bond.

A comparative analysis of the simulation results showed that the level of equivalent stresses σ_{eq} of the "grain – processed material" contact increases with an increase in the elastic modulus of the bond. With an increase in the hardness of the processed materials, the stress increases while maintaining their distribution.

4.2 Dynamic Micro-level Modeling of the Grinding Process

Dynamic 3D modeling of the grinding process was carried out using the ANSIS and LS-DYNA software packages. The study included the following stages.

1. Design of a 3D model "grain – metal phase – bond – processed material" using the SolidWorks software package (Fig. 5). A workpiece was created in a rectangular parallelepiped with dimensions of $500 \times 600 \times 100\ \mu m$. The bond was modeled in the form of a rectangular parallelepiped with dimensions of $500 \times 500 \times 250\ \mu m$, on one of the sides of which three seating surfaces for the diamond grain were arbitrarily placed. Pores of complex shape were made to reproduce the porous structure of the diamond-bearing layer in the bond's body. Diamond grains were adopted with the geometry of an octahedron; their sizes correspond to a grit size of $125 \times 100\ \mu m$. When modeling the diamond grain, it was filled with inclusions of the metal phase, which was 6% of the grain volume, corresponding to the AC6 125/100 grade. The concentration of grains ($C_g = 50\%$) was set, considering the ratio of the bond volume to the total volume of the grains.
2. Assembling the system model and exporting it from the SolidWorks module to the ANSYS computational complex. In the ANSYS program, the type of finite elements was selected for each system component (for the workpiece – elements of the Hex-dominant type of rectangular shape, for other elements –the Tetrahedron type).
3. Design of a finite element mesh and its selective thickening in the grains embedding in a bond and the contact places of the grains with the workpiece and the metal phase inclusions.
4. Fixing the model (setting of zero or other displacements) was carried out using the attributes of the geometric model (points, lines, surfaces).
5. Exporting the model to the LS-DYNA calculator module.
6. Assigning the properties for each element of the model: diamond grains AC6 125/100; WC-Co cemented carbide type DIN HG30; RM bond; metal phase composition $Fe_{44}Co_{44}(Cr_3C_2)_{12}$.

7. Setting the loading parameters of the model was carried out, considering the forces ensuring the wheel pressing during grinding. The model was loaded with normal pressure P_n, simulating forces of $P_y = 1$–3 MPa and $P_z = (0.6$–$0.7)P_y$. The wheel's speed was also set ($V_w = 30$ m/s).

8. Calculations for the created model were carried out in the corresponding module of the calculator, depending on the task given. The results were displayed on a PC screen. The dynamic changes in the stress values σ_{eq} were determined.

(a)   (b)
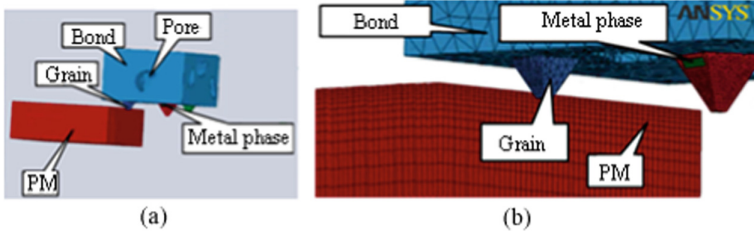
Fig. 5. Models for the grinding process dynamics study: a – 3D model of the "bond – grain – metal phase – processed material (PM)" system; b – finite element mesh model.

As a result of the experiment, the dynamic stress distribution diagrams were obtained during grinding by a group of grains. The volumes of the destroyed material of the workpiece and grains were calculated. A step-by-step visualization of the stress distribution and the nature and destruction volume of diamond grains and the processed material is shown in Fig. 6.
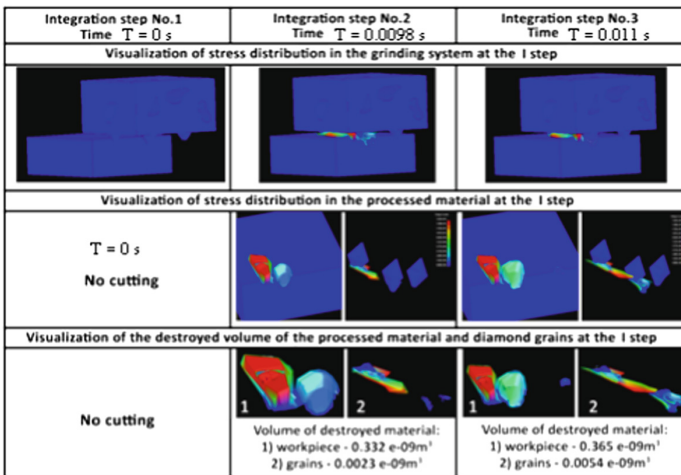
Fig. 6. Stress distribution, destruction of grains, and processed material at the *i*-th step.

Thus, the methodology makes it possible to estimate the specific consumption of diamond grains and the productivity of grinding as the ratio of the removed material volume and the volume of grain destruction for the given parameters of the diamond layer and the specific processed material.

5   Conclusions

The grinding process simulation allows to determine the optimal combinations of the physical and mechanical properties of the bond (elastic modulus, coefficient of thermal expansion, and porosity), the required characteristics of diamond grains (concentration, positioning relative to the processed material, wear state, deepening in the bond), as well as the processing modes for the implementation of rational self-sharpening of the grinding wheel.

The factors determining the intensity of mutual destruction of the diamond wheel elements during grinding were identified.

A high concentration of grains with low-strength grades harmfully impacts the stress in grains and a bond. Limiting the concentration of diamond grains in the diamond-bearing layer to 50% increases the stability of the machining and reduces the cost of the diamond grinding wheels.

It was shown that an excessive concentration of grains (more than 50%) creates a high probability of a decrease in the diamond retention capacity, which leads to the removal of grains with potentially high cutting properties (irrational self-sharpening), and rapid wear of the diamond abrasive tool.

Based on the research performed, recommendations can be given for optimizing the technological parameters of grinding, the characteristics of diamond powders, and the ceramic bond's properties, which ensure the effective grinding in the self-sharpening mode with minimal loss of grains.

The data obtained can be further taken into account in developing the compositions of the diamond-containing ceramic-matrix composite.

References

1. Zhou, T., Wang, Y., Ruan, B., Liang, Z., Wang, X.: Modeling of the minimum cutting thickness in micro cutting with consideration of the friction around the cutting zone. Front. Mech. Eng. **15**(1), 81–88 (2019). https://doi.org/10.1007/s11465-019-0561-y
2. Samuel, R., Asadi, M., Tarda, A., Simbotin, G., Markopoulos, A.P.: Validating dynamic crush response of unidirectional carbon fibre tube via finite element analysis method using LS-DYNA. IOP Conference Series: Materials Science Engineering, p. 1037 (2021). https://doi.org/10.1088/1757-899X/1037/1/012027
3. Krol, O., Sokolov, V.: Research of modified gear drive for multioperational machine with increased load capacity. Diagnostyka **21**(3), 87–93 (2020). https://doi.org/10.29354/diag/126026
4. Atroshenko, O., et al.: The study of multicomponent loading effect on thin-walled structures with bolted connections. Eastern-European J. Enterp. Technol. **1**(7–97), 15–25 (2019). https://doi.org/10.15587/1729-4061.2019.154378

5. Kaselouris, E., et al.: Downscaled finite element modeling of metal targets for surface roughness level under pulsed laser irradiation. Appl. Sci. **11**(3), 1253 (2021). https://doi.org/10.3390/app11031253

6. Wang, Y., Zhou, T., Riemer, O., Heidhoff, J., Karpuschewski, B.: FEM simulation of tribological performance with structured surface. In: Proceedings of the 21st International Conference of the European Society for Precision Engineering and Nanotechnology (EUSPEN), pp. 383–384. Copenhagen, Denmark (2021)

7. Schieber, C., Hettig, M., Zaeh, M.F., Heinzel, C.: 3D modeling and simulation of thermal effects during profile grinding. Prod. Eng. Res. Devel. **14**(5–6), 655–665 (2020). https://doi.org/10.1007/s11740-020-00983-8

8. Jamal, M., Morgan, M.N.: Characterization of material properties based on inverse finite element modelling. Inventions **4**(3), 40 (2019). https://doi.org/10.20944/preprints201907.0070.v1

9. Kundrák, J., Mitsyk, A.V., Fedorovich, V.A., Morgan, M., Markopoulos, A.P.: The use of the kinetic theory of gases to simulate the physical situations on the surface of autonomously moving parts during multi-energy vibration processing. Materials **12**(19), 3054 (2019). https://doi.org/10.3390/ma12193054

10. Kyratsis, P., Tzotzis, A., Markopoulos, A., Tapoglou, N.: CAD-based 3D-FE modelling of AISI-D3 turning with ceramic tooling. Machines **9**(1), 4 (2021). https://doi.org/10.3390/machines9010004

11. Skondras-Giousios, D., Karkalos, N.E., Markopoulos, A.P.: Finite element simulation of friction and adhesion attributed contact of bio-inspired gecko-mimetic PDMS micro-flaps with SiO2 spherical surface. Bioinspiration Biomimetics, **15**(6), 066004 (2020). https://doi.org/10.1088/1748-3190/ab983e

12. Lucca, D.A., Klopfstein, M.J., Riemer, O.: Ultra-precision machining: cutting with diamond tools. J. Manuf. Sci. Eng. **142**(11), 110818 (2020). https://doi.org/10.1115/1.4048194

13. Denysenko, Y., Ivanov, V., Luscinski, S., Zaloga, V.: An integrated approach for improving tool provisioning efficiency. Manage. Prod. Eng. Rev. (MPER) **11**(4), 4–12 (2020). https://doi.org/10.24425/mper.2020.136115

14. Kalisz, J., Żak, K., Wojciechowski, S., Gupta, M.K., Krolczyk, G.M.: Technological and tribological aspects of milling-burnishing process of complex surfaces. Tribol. Int. **155**, 106770 (2021). https://doi.org/10.1016/j.triboint.2020.106770

15. Kohls, E., Heinzel., C., Eich., M.: Evaluation of hardness and residual stress changes of AISI 4140 steel due to thermal load during surface grinding. J. Manuf. Mater. Process. **5**(3), 73 (2021). https://doi.org/10.3390/jmmp5030073

16. Lishchenko, N.V., Larshin, V.P., Krachunov, H.: Simplified grinding temperature model study. J. Eng. Sci. **6**(2), A1–A7 (2019). https://doi.org/10.21272/jes.2019.6(2).a1/

17. Borchers, F., Meyer, H., Heinzel, C., Meyer, D., Epp, J.: Development of surface residual stress and surface state of 42CrMo4 in multistage grinding. Procedia CIRP **87**, 198–203 (2020). https://doi.org/10.1016/j.procir.2020.02.095

18. Pavlenko, I., Trojanowska, J., Ivanov, V., Liaposhchenko, O.: Scientific and methodological approach for the identification of mathematical models of mechanical systems by using artificial neural networks. In: Machado, J., Soares, F., Veiga, G. (eds.) HELIX 2018. LNEE, vol. 505, pp. 299–306. Springer, Cham (2019). https://doi.org/10.1007/978-3-319-91334-6_41

19. Pavlenko, I., et al.: Parameter identification of cutting forces in crankshaft grinding using artificial neural networks. Materials **13**(23), 5357 (2020). https://doi.org/10.3390/ma13235357

20. Patil, P., Patil, C.: FEM simulation and analysis of temperature field of environmental friendly MQL grinding. In: Proceedings of the International Conference on Communication and Signal Processing 2016 (ICCASP), vol. 137, pp. 182–186. Atlantis Press (2017)

21. Holesovsky, F., Pan, B., Morgan, M.N., Czan, A.: Evaluation of diamond dressing effect on workpiece surface roughness by way of analysis of variance. Tehnički Vjesnik **25**(1), 165–169 (2018). https://doi.org/10.17559/TV-20160411122230

22. Ni, D., et al.: Advances in ultra-high temperature ceramics, composites, and coatings. J. Adv. Ceramics **11**(1), 1–56 (2021). https://doi.org/10.1007/s40145-021-0550-6

Discontinuous Generating Gear Grinding Optimization

Vasily Larshin[1]([✉]) [ID], Olga Babiychuk[1] [ID], Oleksandr Lysyi[2] [ID],
and Sergey Uminsky[3] [ID]

[1] Odessa Polytechnic National University, 1, Shevchenko Avenue, Odessa 65044, Ukraine
vasilylarshin@gmail.com
[2] Odessa Military Academy, 10, Fontanskaya doroga Street, Odessa 65009, Ukraine
[3] Odessa State Agrarian University, 13, Panteleymonovskaya Street, Odessa 65012, Ukraine

Abstract. Gear grinding on the MAAG machines allows obtaining a high degree of accuracy of gears but is characterized by a considerable investment of time. In contrast to the copying method, with MAAG discontinuous generating gear grinding, the contact zone of a grinding wheel with a flank of a tooth has a small area. As a consequence, a large number of gear grinding strokes are required to remove the unevenly spaced gear grinding stock allowance. Any the operation is forcing increases the possibility of grinding burns. In this regard, there is a need to optimize the gear grinding parameters, i.e., to increase these parameters so that the resulting burn layer does not exceed the remaining stock allowance for gear grinding. An optimization model is created and studied for two successive stages of the life cycle of gear: at the pre-production stage (gear grinding operation designing) and at the stage of production itself, i.e., at the gear grinding with optimal parameters - both mode parameters (grinding depths) and gear grinding power ones. The primary attention is paid to the pre-production stage, where optimization is a method of operation design. The MAAG machine is equipped with an automatic gear grinding power control system at the production stage. As the input of this system, the specified gear grinding power setpoints were found at the pre-production stage. Automatic robust gear grinding power control allows "continuing optimization" at the production stage to consider random factors that cannot be considered at the pre-production stage. Therefore, such optimization continuing at the production stage is a control method.

Keywords: Smart manufacturing · Hierarchical control · Optimization model · Objective function · Machine time · Grinding depth · Control system · Process innovation

1 Introduction

The paper considers a two-level optimization system corresponding to the traditional product development and production concept. This concept includes the stages of pre-production and production itself. At the first stage (the upper hierarchy level), a model for optimizing the gear grinding operation was developed. At the second stage (the

lower level of hierarchy), the optimal parameters of the gear grinding operation are automatically maintained by regulating the longitudinal feed while stabilizing the gear grinding power utilizing a robust control system.

In modern turbojet aircraft engines, gear wheels (hereinafter gears) in power mechanical transmissions operate at circumferential speeds of up to 100 m/s at exceptionally permissible contact and bending stresses in the gear teeth. Such gears must be manufactured with high accuracy to reduce dynamic loads and ensure smooth transmission operation. The gears' high accuracy (up to quality 2 according to DIN 3961) made of high-strength steels with a surface hardness of 60–62 HRC is known to be achieved by gear grinding. Gear grinding is one of the main methods of finishing hardened gears and is carried out either by the discontinuous generating method or by the copying one (profile grinding). It is known that a unique feature of machines operating by the generating method with two dish-shaped (or disc-shaped) grinding wheels (MAAG SD-32-X, HSS10S, HSS30BC, HSS30X machines, as well as domestic 5851, 5851M machines, etc.) is high grinding accuracy mentioned above. The gear grinding high accuracy here is due to the fact that the conical-concave cutting surface of the grinding dish-shaped wheels occupies a constant axial position during grinding. For this purpose, a unique adjustment mechanism is used, which automatically compensates for the wear of the grinding wheels. However, unlike other methods of gear grinding, the generating method is characterized by low productivity and, in addition, high thermal stress, which is aggravated by the lack of cooling because the grinding is carried out without grinding fluid. The appearance of grinding burns on the working surface of the teeth dramatically reduces the performance (operational properties) of the gears, and in some cases (for example, in the aviation industry), grinding defects (burns and microcracks) are generally unacceptable. Therefore, improving the efficiency of defect-free gear grinding on MAAG machines is an urgent task in mechanical engineering technology.

2   Literature Review

There are two main discontinuous toothed surface grinding methods: discontinuous flank grinding (tooth copying method) and discontinuous generating gear grinding (with two dish-shaped grinding wheels). Each of them has its pros and cons. The first method is based on the fact that the gear cavity's shape repeats the grinding wheel's profile that is being ground. The second method is carried out on the MAAG machines in which the tools are two dish-shaped grinding wheels which are either inclined at 15°–20° with each other or parallel to each other. The wheels are working with periodic interruption to rotate the gear to be ground by one tooth. This method is more accurate (up to quality 2 according to DIN 3961 [1]) but less productive than the gear grinding continuous generating method with a worm grinding wheel. A distinctive feature of the MAAG method is the absence of forced cooling with a grinding fluid since the workpiece heating with this method is less due to theoretical point-contact between the workpiece (gear) and the grinding wheel. However, the possibility of forming thermal defects (grinding burns and cracks) remains. Besides, according to F. Klocke, there are two types of process models to optimize the grinding process: the empiric and physical ones. The empiric process model is based on regression analysis or artificial neural

networks, while the physical process model results from analytic or numeric modeling. These models can be used at the pre-production stage, which is most important in the "product development and launching into manufacture" system. In this sense, the pre-production stage should be considered the top level of the management hierarchy to prioritize the process. At this level, fundamental decisions are made, and tolerances (permissive limits of deviations) are set for the recommended parameters for the lower-level control system [2]. This is the so-called forecasting control strategy [2]. Physical limitations on cutting conditions due to the characteristics of the machine tool-workpiece system should be identified from previous experience and considered in the optimization process. Many deterministic constraints exist, such as allowable maximum cutting force, cutting temperature, depth of cut, speed, feed, machine power, vibration and chatter limits, and constraints on part quality. Some constraints, such as speed, feed, etc., are simple boundary constraints, while others must be computed from linear or non-linear equations. The following general equation can be used [2]

$$G_{ij}(s) = B_{ij} \prod_{k=1}^{p} s_{ij}^{b_{kij}},\tag{1}$$

where b_{kij}, B_{ij} are empirical constants for the i-th operation and j-th constraint.

The objective function in the form of the so-called posynomial has the following similar structure [3]

$$f(X) = \sum_{j=1}^{N}\left(c_i \prod_{i=1}^{n} x_i^{a_{ij}}\right) = \sum_{j=1}^{N}\left(c_i\, x_1^{a_{1j}} x_2^{a_{2j}}\, \dots\, x_n^{a_{nj}}\right),\tag{2}$$

where $c_j > 0$, $x_i > 0$ and a_{ij} are real constants.

For this structure, it is necessary to find the components of the vector X, i.e., $x_1, x_2, \dots, x_n$.

Moreover, in the production stage, the process optimization continues through online process monitoring to provide helpful information for optimizing the grinding process in terms of total grinding time or total grinding cost [4]. Optimization of the process can possibly be achieved if the monitoring system can track the degradation of the process behavior. The information obtained with a sensor system can also be used to establish databases as part of an intelligent system [4]. However, nothing is said about the gear grinding operations and related monitoring systems.

A similar optimization of the grinding operation at the pre-production stage (according to the process model) and the production stage (due to adaptive and/or intelligent systems) is considered in relation to the surface and cylindrical grinding operations [5, 6]. Ideally, it is required to continually optimize feed cycles to maintain accuracy while maintaining short cycle times and set-up times. But there are no specific developments on the gear grinding, on the one hand, and the use of thermal models for adaptive control is still in the early stages on the other hand.

The holistic-type approach, based on integrating the planning and scheduling processes, defines new performance indicators adapted to current market requirements [7]. The approach covers two pre-production levels (stages): planning and scheduling the manufacturing process. But nothing is said about the production level (stage) itself. However, the idea of equivalence of the process levels and the product life cycle stages

can be helpful for hierarchical management at different stages of production. But this idea has not been developed.

Hierarchical two-step finite-element model for process optimization [8] and the thermal structure design optimization and temperature control for worm gear grinding machine [9] also relate to the issues discussed above. However, auxiliary optimization issues are considered here, which can be attributed to a lower level of the hierarchy of the grinding process control. Optimization through the regression equation can be applied when the objective function is the roughness parameter of the surface to be ground [10]. Finally, a hierarchical control system approach [11] can cover both pre-production and production stages within the framework of a unified information system [12]. Today, there are appropriate technical means [13, 14] for the development of automatic measurement systems and models [15] for evaluating grinding performance.

The purpose of the paper is to develop a hierarchical two-level control system and appropriate interaction between these levels when the first (higher or upper) control level is at the stage of pre-production (development and optimization of the operation, preparation of the control program). The second (lower) level is a robust automatic deviation control system that stabilizes the optimal conditions for the operation.

3   Research Methodology

The gear grinding power regression equation can be obtained experimentally using the empirical equation, which is a particular case of Eq. (1). Moreover, it corresponds to Eq. (2). This empirical equation has the following form

$$P = ct^x V_f^{-y} n_0^z k_m k_w k_\rho, \tag{3}$$

where: c, x, y, z are the coefficients that depend on the angle of dish-shaped grinding wheels inclination (at $15°$–$20°$ with each other or parallel to each other); t, V_f and n_0 are the depth of cut (mm), longitudinal feed (mm/min), and gear swings frequency (roll rate in $\min^{-1}$); k_m, k_w and k_ρ are the coefficients that consider the influence of the material to be grinding, abrasive wheel, and tooth profile curvature radius, respectively.

From Eq. (3), we determine the time spent on the k-th working stroke, i.e.

$$\tau_k = \frac{L}{V} = \frac{L(ct_k^x n_0^z k_m k_t k_\rho)^{1/y}}{P_k^{1/y}}. \tag{4}$$

Let us introduce the following designations:

$$\alpha = \frac{x}{y}; \quad \varepsilon = \frac{1}{y}; \quad M = L(cn_o^z k_m k_t k_\rho)^{1/y}.$$

Hence, we have

$$\tau_k = M \frac{t_k^\alpha}{P_k^\varepsilon} \tag{5}$$

The total machine grinding time spent on n working strokes will be

$$\tau_M = M \sum_{k=1}^{n} \frac{t_k^{\alpha}}{P_k^{\varepsilon}} \tag{6}$$

One of the main factors limiting the gear grinding productivity is the temperature defect in the kind of grinding burn. For any k-th working stroke, the defect layer depth (the depth of the grinding burn) h_{dk} formed during gear grinding can be represented by the following experimental dependence:

$$h_{dk} = a(P_k - P_0), \tag{7}$$

where h_{dk} and P_k are respectively the defective layer depth (in μm) and the grinding power (in W) on the k-th working stroke; P_0 is the defectless grinding power (in W) level.

Since for any k-th ($1 \leq k \leq n$) working stroke, the depth of the defective layer formed during gear grinding should not exceed the gear grinding stock allowance remaining for grinding, then

$$h_{dk} = \sum_{i=k+1}^{n} t_i = Z - \sum_{i=1}^{k} t_i. \tag{8}$$

Considering Eqs. (7) and (8), we get

$$P_k = \left[(Z - \sum_{i=1}^{k} t_i)/a \right] + P_0. \tag{9}$$

After substituting this expression into Eq. (6), we get a general mathematical expression for gear grinding machine time when removing the grinding stock allowance for n working strokes. The corresponding equation has the following form:

$$\tau_M = M \left[\frac{1}{P_0^{\varepsilon}} \left(Z - \sum_{i=1}^{n-1} t_i \right)^{\alpha} + \sum_{k=1}^{n-1} \frac{t_k^{\alpha}}{\left[\left(Z - \sum_{i=1}^{k} t_i \right)/a + P_0 \right]^{\varepsilon}} \right]. \tag{10}$$

Optimal grinding depths can be found by sequentially differentiating Eq. (10) $(n-1)$ times by the following variables: $t_1, t_2, \ldots, t_{n-1}$. Further, each of the $(n-1)$ equations (for the derivatives) is equated to zero and we obtain a system of $(n-1)$ equations with $(n-1)$ unknowns.

The equation finds the grinding depth for the last n-th working stroke:

$$t_n = Z - \sum_{i-1}^{n-1} t_i. \tag{11}$$

The analysis of the regularity of the formation of recurrent relations allows obtaining a generalized equation for composing a system of s equations, where $1 \leq s \leq n-1$. To do this, we will write Eq. (10), singling out separately s-th term of this equation (determines the influence of depth t_s), according to which differentiation is performed. We will get the following equation:

$$\tau_M = M \left[f_1 + f_2 + f_3 + f_4 \right]. \tag{12}$$

The following notations are used in Eq. (12):

$$f_1 = \frac{1}{P_0^\varepsilon}\left(Z - \sum_{i=1}^{n-1} t_i\right)^\alpha;$$

$$f_2 = \sum_{k=1}^{s-1} \frac{t_k^\alpha}{\left[\left(Z - \sum_{i=1}^{k} t_i\right)/a + P_0\right]^\varepsilon};$$

$$f_3 = \frac{t_s^\alpha}{\left[\left(Z - \sum_{i=1}^{s} t_i\right)/a + P_0\right]^\varepsilon};$$

$$f_4 = \sum_{k=s+1}^{n-1} \frac{t_k^\alpha}{\left[\left(Z - \sum_{i=1}^{k} t_i\right)/a + P_0\right]^\varepsilon}.$$

Now we find the optimal values of the grinding depths along with the working strokes from the following system of $(n-1)$ equations, i.e.

$$\frac{\partial \tau_M}{\partial t_s} = 0; \text{ for all } s = 1 \div (n-1). \tag{13}$$

This system of $(n-1)$ equations allow finding the optimal grinding depths: $t_1, t_2, \ldots, t_{n-1}$; i.e., a total of $(n-1)$ depths. The grinding depth for the last n-th working stroke is found by Eq. (11).

So, the system of $(n-1)$ equations for finding optimal gear grinding depths $t_1, t_2, \ldots, t_{n-1}$ for all $s = 1 \div (n-1)$ can be represented as

$$\frac{\partial \tau_M}{\partial t_s} = M\left[\frac{\partial f_1}{\partial t_s} + \frac{\partial f_2}{\partial t_s} + \frac{\partial f_3}{\partial t_s} + \frac{\partial f_4}{\partial t_s}\right] = 0. \tag{14}$$

Since the component f_2 in Eq. (12) contains gear grinding depths $t_1, t_2, \ldots, t_{s-1}$ with numbers less than s, then.

$$\frac{\partial f_2}{\partial t_s} = 0; \text{ for all } s = 1 \div (n-1); \tag{15}$$

Hence, Eq. (14) will take the following form

$$\frac{\partial \tau_M}{\partial t_s} = M\left[\frac{\partial f_1}{\partial t_s} + \frac{\partial f_3}{\partial t_s} + \frac{\partial f_4}{\partial t_s}\right] = 0. \tag{16}$$

Now, taking into account Eqs. (10) and (14), we obtain the following system of s (where $1 \leq s \leq n-1$) recurrent equations:

$$-\frac{\alpha(Z - t_1)^{\alpha-1}}{P_0^\varepsilon} + \frac{\alpha t_s^{\alpha-1}}{\left[(Z - \sum_{i=1}^{s} t_i)/a + P_0\right]^\varepsilon} + \sum_{k=s}^{n-1} \frac{\varepsilon t_k^\alpha}{a\left[(Z - \sum_{i=1}^{k} t_i)/a + P_0\right]^{\varepsilon+1}} = 0. \tag{17}$$

The first equation of the system of $(n-1)$ equations is obtained by writing the Eq. (17) for $s = 1$; the second – for $s = 2$; $(n-1) - th$ equation is obtained by writing the Eq. (15) for $s = (n-1)$.

4   Results

To understand the essence of the objective function (10), let consider the case $n = 2$. For this case, Eq. (10) takes the following form:

$$\tau_2(t_1) = M \left\{ \frac{(Z - t_1)^{\alpha}}{P_0^{\varepsilon}} + \frac{t_1^{\alpha}}{\left[\frac{(Z - t_1)}{a} + P_0 \right]^{\varepsilon}} \right\}. \tag{18}$$

For the $0°$ angle of the dish wheels inclination and for the $n_0 = 150$ min^{-1} the following parameters values in equations mentioned above are received: $\alpha = 0.79$, $\varepsilon = 1.05$, $M = 3.04$, and $P_0 = 126$ W.

To more accurately determine the extremum point for the dependence (18), let's use the classical method of finding the function extremum, i.e., determine the partial derivative of the function $\tau_2(t_1)$ on the variable t_1 and equate the derivative to zero. For this case, the system (17) for Eq. (18) degenerates into a single equation (with one unknown) which is written as follows:

$$\frac{\partial \tau_2}{\partial t_1} = -\frac{\alpha (Z - t_1)^{\alpha - 1}}{P_0^{\varepsilon}} + \frac{\alpha t_1^{\alpha - 1}}{[(Z - t_1)/a + P_0]^{\varepsilon}} + \frac{\varepsilon t_1^{\alpha}}{a[(Z - t_1)/a + P_0]^{\varepsilon + 1}} = 0. \tag{19}$$

For example, for $Z = 400$ μm, $Z = 300$ μm, and $Z = 200$ μm, we have the following results (Table 1).

Table 1. Optimal grinding depths for $n = 2$.

Z, μm	400	300	200
t_{1opt}, μm	306.3	218.8	140.0
t_{2opt}, μm	93.7	81.2	84.4
τ_{2min}, min	37.7	32.7	26.9

It can be seen that the objective function $\tau_2(t_1)$ is unimodal and has a global minimum. The study of this function has shown that the values of the cutting depth t_1, at which the physically realized cutting capacities are obtained, i.e., $0 \leq P_1 \leq 600$ W, and the physically realized longitudinal feeds V_f ($50 < V_f < 900$ mm/min) are in the vicinity of the optimal points (Table 2).

It is established that working strokes can remove the same grinding stock allowance Z in two, three, four, etc. For example, the allowance $Z = 325$ μm when grinding in two, three and four working strokes can be removed, respectively, in 34.4, 30.8 and 29.8 min, i.e., when removing the grinding stock allowance $Z = 325$ μm in four working strokes, the machine time of gear grinding is less than when removing the same grinding stock allowance in two passes. This is so because with an increase in the number of strokes n, the longitudinal feeds V_f on each of these strokes increases, leading to a decrease in the total machine time.

Table 2. Changing the grinding parameters.

$\tau_2(t_1)$, min	t_2,μm	t_1,μm	P_1 W	V_{f2} mm/min	V_{f1} mm/min
60.6	380	20	992.4	21.8	1945.8
56.7	340	60	901.2	23.8	738.2
52.7	300	100	810.0	26.2	440.9
48.8	260	140	719.0	29.4	298.1
41.7	180	220	536.4	39.3	153.4
39.0	140	260	445.2	47.9	110.5
37.7	**100**	**300**	**354.0**	**62.5**	**77.6**
39.3	60	340	262.8	93.6	51.4
49.2	20	380	171.6	222.8	30.1

Note: $P_2 = P_0 = 126$ W; $Z = 400$ μm

In other words, a decrease in time on each of the working strokes with an increase in their number in the total amount prevails over a simultaneous increase in time due to an increase in the number of working strokes. In this regard, the problem arises of determining the optimal number of gear grinding working strokes, i.e., the general optimization problem consists of two stages:

– for a specific amount of grinding stock allowance Z, it is necessary to determine the optimal number of gear grinding working strokes (structural optimization);
– knowing the optimal number of working strokes, determine the optimal grinding depths for each of these strokes (parametric optimization). Figure 1 shows a solution to the first-mentioned problem.
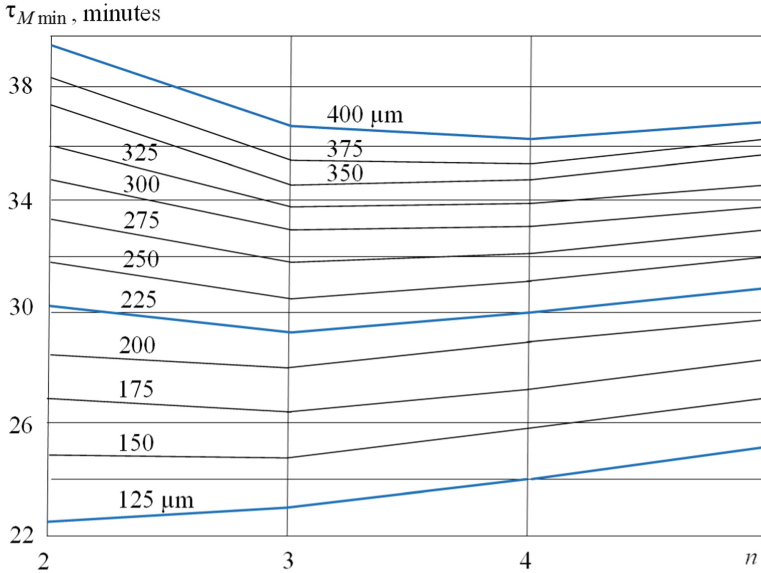
Fig. 1. The dependence of the machine time of gear grinding τ_{Mmin} on the number of strokes n at different values of the gear grinding stock allowance Z

5   Conclusions

The developed optimization model for the grinding stock allowance distribution along the gear grinding strokes (or passes) for MAAG gear grinding machines operating according to the discontinuous generating gear grinding method with two dish-shaped grinding wheels made it possible to control the gear grinding operation at the upper level of the control hierarchy, i.e., at the pre-production stage (technological preparation of production).

The optimal gear grinding parameters found by optimization – the distribution of the gear grinding depth and power along with the working strokes – can be used as input data for controlling the gear grinding operation at the production stage, including using a robust system of automatic control of gear grinding power during the grinding stock allowance is removing.

The paper shows that the procedure for optimizing gear grinding at the pre-production stage is a method of designing a gear grinding operation. In contrast, it is a method of controlling this operation at the production stage. This approach to the development and control of the gear grinding process corresponds to the concept of a single integrated design and production automation system in the development of smart technologies in the framework of the "Industry 4.0" concept.

References

1. Klocke, F.: Manufacturing Processes 2: Grinding, Honing, Lapping. Springer, Heidelberg (2009). https://doi.org/10.1007/978-3-540-92259-9
2. Stephenson, D.A., Agapiou, J.S.: Metal Cutting Theory and Practice. Marcel Dekker Inc, New York (1997)
3. Rao, S.S.: Engineering Optimization: Theory and Practice, 4th edn. Wiley, Hoboken (2009)
4. Marinescu, I.D., et al.: Handbook of Machining with Grinding Wheels. CRC Press/Taylor & Francis, Boca Raton (2007)
5. Malkin, S., Guo, C.: Grinding Technology: Theory and Applications of Machining with Abrasives, 2nd edn. Industrial press, New York (2008)
6. Rowe, W.B.: Principles of Modern Grinding Technology. Elsevier Inc., Oxford (2009)
7. Cezarina, A., Frumuşanu, G.: A review on optimization of manufacturing process performance. Int. J. Model. Optim. **7**(3), 139–144 (2017). https://doi.org/10.7763/IJMO.2017.V7.573
8. Guerrini, G., Lutey, A.H.A., Melkote, S.N., Ascari, A., Fortunato, A.: Dry generating gear grinding: hierarchical two-step finite element model for process optimization. J. Manuf. Sci. Eng. **141**(6), 061005 (2019). https://doi.org/10.1115/1.4043309
9. Shi, X., Yang, X., Chen, G., Wang, W.: Thermal structure design optimization and temperature control for worm gear grinding machine using flood cooling technology. Int. J. Adv. Manuf. Technol. **108**(7–8), 2419–2431 (2020). https://doi.org/10.1007/s00170-020-05600-7
10. Son, N.H., Trung, D.D.: Optimization the cutting parameters when grinding SKD11 steel using CBN grinding wheel. American J. Eng. Res. **8**(10), 77–80 (2019)
11. Mitrishkin, Y., Haber, R.: Hierarchical control system for complex dynamical plants. In: Proceedings of the 6th International Conference on Informatics in Control. Automation and Robotics, Intelligent Control Systems and Optimization, pp. 56–65. Milan, Italy (2009)
12. Larshin, V.P., Lishchenko, N.V., Babiychuk, O.B., Piteľ, J.: Computer-aided design and production information support. Herald of Adv. Inf. Technol. **4**(2), 111–122 (2021). https://doi.org/10.15276/hait.02.2021.1
13. Horst, J., Hedberg, T., Feeney A.B.: On-machine measurement use cases and information for machining operations. National Institute of Standards and Technology, Gaithersburg, Maryland, United States (2019). https://doi.org/10.6028/NIST.AMS.400-1
14. Liu, C.-S., Ou, Y.-J.: Grinding wheel loading evaluation by using acoustic emission signals and digital image processing. Sensors **20**(15), 4092 (2020)
15. Alberro, N.A., Rojas, H.A.G., Egea, A.J.S., Hameed, S., Aguilar, R.M.P.: Model based on an effective material-removal rate to evaluate specific energy consumption in grinding. Materials **12**(6), 939 (2019)

An Analytical and Experimental Study of the Grinding Process of Thermal Barrier Coatings with Highly Porous Wheels of Cubic Boron Nitride

Vladimir Lebedev[1] , Olga Frolenkova[1] , Tatiana Chumachenko[1(✉)] ,
Alla Bespalova[2] , and Olha Dashkovska[2]

[1] Odessa Polytechnic National University, 1, Shevchenko Ave., Odessa 65044, Ukraine
`chumachenko-1981.28@ukr.net`
[2] Odessa State Academy of Civil Engineering and Architecture,
4, Didriksona St., Odessa 65029, Ukraine

Abstract. Thermal barrier coatings are widely used to protect heat-resistant alloys from high-temperature oxidation. Under the requirements arising during operation, practical application found a coating of ZrO_2. Zirconia-based ceramics are highly durable and crack resistant. In the grinding process, high contact temperatures arise, which are comparable to operating temperatures or slightly higher than these temperatures. The task in the design of the grinding process is primarily to control the thermal treatment mode to maintain it within such limits when the residual stresses have values that do not pose a danger to the durability of the sprayed layer. In addition, if the contact temperature of grinding reaches 1200 °C, the sintering of the sprayed layer begins, leading to the loss of thermal barrier properties. The main results of this work are – when grinding with highly porous CBN wheels with a structure 26 and 40, the unit cutting forces are 15–20% higher, the total cutting forces are 7–10% lower, contact temperatures are 10–15% lower. The residual stresses arising under the action of contact temperatures on the surface during grinding of pure zirconium oxide and stabilized with yttrium oxide reach values of the order of 60 MPa. However, these values are much lower than the tensile strength of the thermal barrier layer and do not lead to cracks, an increase in roughness by 1 category can be expected, grinding modes can be increased by 20–25%.

Keywords: Manufacturing innovation · Highly porous wheels · Unit force · Total force · Unit temperature · Contact temperature · Temporary stresses · Residual stresses

1   Introduction

Thermal barrier coatings are widely used to protect heat-resistant alloys from high-temperature oxidation. Three basic requirements are imposed on thermal barrier coatings: low thermal diffusivity, resistance to cracking at high temperatures, and increased

service life. Most fully meets these requirements, thermal barrier coating of ZrO_2. Zirconia-based ceramics are highly durable and crack resistant.

In grinding thermal barrier coatings, high contact temperatures arise, the values of which are comparable to operating temperatures or slightly higher than these [1].

At present, CBN grinding with highly porous grinding wheels has become quite widespread [2].

When grinding with such wheels, it should be borne in mind that initially, the content of CBN grains in a unit volume of the CBN layer is much lower than that of wheels of the N6 structure, which corresponds to ordinary CBN wheels.

2 Literature Review

It should be noted that there is no clear data on the thermodynamics of this grinding in the modern literature. It is noted that the contact temperature of grinding is usually lower than when grinding with ordinary wheels. There is little information on cutting forces during grinding, and they are contradictory.

In [1], new CBN wheels are considered, and some application questions are considered. However, the issues of grinding thermal barrier coatings or tiles of ZrO_2 are not considered. The issues of determining contact grinding temperatures are also not considered. In [2], the grinding process with porous wheels from CBN is considered in detail. However, grinding ceramics is not considered, and data on contact grinding temperatures are not given; there is no data on the values of unit cutting forces. The work [3] deals with the grinding of highly plastic alloys with CBN wheels from CBN. However, this work does not address the issues of grinding ceramics. In [4], grinding by highly porous wheels of aluminum alloys is considered. Ceramic grinding not investigated The work [5] deals with grinding without cooling various alloys. However, the issue of grinding ceramics ZrO_2 is not considered. In addition, the authors measure not the grinding temperature but the average temperature of the part before and after grinding, which gives little information and the process. In [6], grinding issues with highly porous CBN wheels are considered; however, ceramic grinding and contact grinding temperature are not considered. In [7], the grinding process is considered by highly porous CBN wheels from the point of view of minimizing the number of edits, and high porosity is considered as a means of delivering coolant to the cutting zone. Ceramic grinding issues are not considered. The work [8] considers the grinding of hard-to-work materials - titanium and nickel alloys, as well as the determination of the most advantageous porosity of a wheel from the point of view of preserving grain holding forces by a binder. It was shown that the porosity of 30% showed the best results. The issue of grinding ceramics is not considered. In [9], the process of profile gear grinding by highly porous abrasive wheels is studied – recorded data on reducing cutting power and improving the accuracy of polished gears. However, only abrasive wheels are considered in this work, and there is no information about grinding ceramics.

In [6], highly porous wheels of improved design are considered, but the issue of grinding thermal barrier coatings is not considered. In [10], improved conditions for dressing highly porous wheels are considered, but the issue of grinding thermal barrier coatings is not considered. In [11], the advantages of grinding with highly porous wheels

are considered, but the issue of grinding thermal barrier coatings is not considered. In [12], the competitive advantages of highly porous wheels are considered, but the issue of grinding thermal barrier coatings is not considered. In [13], the technological advantages of grinding with highly porous wheels are considered. However, the issue of grinding thermal barrier coatings is not considered.

It can be concluded that despite the large number of works carried out to study the grinding process with CBN highly porous wheels, many questions have not been fully clarified. So, the characteristics related to the working conditions of the grain of the highly porous CBN wheel have not been clarified (e.g., the cutting force of the grain and the temperature of the cutting of grain). Little data is available on the total grinding forces, contact grinding temperatures, and residual thermal stresses in the surface layer. The issue of grinding ceramics is almost not considered.

It can be argued that at present, there is no database on the grinding regimes of high-porous CBN wheels for ceramic thermal barrier coatings that would ensure the properties of the thermal barrier layer after processing are unchanged.

Based on this, in the present work, mathematical modeling of the grinding process with CBN wheels was carried out with a point experimental verification of the results.

The developed mathematical model [14] adequately reflects the performance of the grinding process with CBN wheels and can show the main trends in the cutting process.

3   Research Methodology

The research aimed primarily at studying the grinding forces, grinding temperatures, and establishing patterns of heat field propagation in the thermal barrier layer. The methods of modeling and measuring the grinding process parameters with high-pore wheels correspond to the methodology described in the sources [14]. Immediate attention was paid to obtaining the dependences of the change in the temperature field on the most significant possible number of factors of the grinding process.

So, varied processing modes, grain of wheels, and the supplied coolant effect.

3.1   The Study of Power Dependencies When Grinding with CBN Wheels AEROBOR

Features of grinding with highly porous wheels are that the ratio per unit volume of grains and pores is significantly increased in favor of pores. This means that the number of active cutting grains per unit surface of the CBN wheel is significantly reduced. From this, it follows that the allowance is removed with a smaller number of grains compared to the wheels of porosity 6. Therefore, each grain removes a larger chip, and higher unit cutting forces can be expected during processing. (Table 1–2).

The total cutting forces are formed by summing the unit forces from the grains in the wheel's contact patch with the part, i.e., a smaller number of grains developing a greater unit force is added up. Theoretically, the total force can be greater or less than the cutting forces when grinding with ordinary wheels. Our mathematical modeling shows that the total forces are somewhat reduced.

It should be noted that the relatively large unit forces P_Y to cause large values of temporary stresses. In some cases, the magnitude of these stresses is higher than the compressive strength of the sprayed layer. This may cause cracking. These cracks do not develop since the sprayed layer is porous, and a crack can develop for the time being. Examination of the grinded surface does not show the presence of cracks from temporary stresses.

Table 1. Values of unit P_{Zun} and total P_{Zt} forces when grinding with wheels LO 250/160C10 100% structure 6 and AEROBOR structure 26 and 40.

$t*10^{-5}$, m	P_{Zun}, N			P_{Zt}, N		
	The structure of the CBN wheel and the AEROBOR wheel; Nst					
	6	26	40	6	26	40
0.5	0.31	0.37	0.39	1.50	1.42	1.40
1.0	0.52	0.63	0.66	3.12	2.94	2.89
1.5	0.70	0.85	0.89	4.80	4.55	4.47
2.0	0.88	1.05	1.11	6.60	6.24	6.13
2.5	1.04	1.24	1.31	8.50	8.00	7.85
3.0	1.19	1.42	1.50	10.40	9.81	9.63

Table 2. Values of unit P_{Yun} and total P_{Yt} forces when grinding with wheels LO 250/160C10 100% structure 6 and AEROBOR structure 26 and 40.

$t*10^{-5}$, m	P_{Yun}, N			P_{Yt}, N		
	The structure of the CBN wheel and the AEROBOR wheel; Nst					
	6	26	40	6	26	40
0.5	0.15	0.20	0.21	2.75	2.59	2.54
1.0	0.31	0.39	0.42	5.68	5.34	5.25
1.5	0.46	0.59	0.63	8.79	8.27	8.13
2.0	0.61	0.78	0.84	12.06	11.35	11.15
2.5	0.76	0.97	1.05	15.45	14.54	14.28
3.0	0.92	1.17	1.26	18.95	17.83	17.52

The total cutting forces P_{Zt} are slightly reduced. This is because the number of cutting grains in the contact patch is reduced. Even though unit forces are slightly higher, an increase in unit forces from each grain cannot compensate for a decrease in the number of cutting grains in the contact spot.

An increase in unit cutting forces P_{Yun} causes an increase in temporary stresses. So, under the above grinding conditions, temporary stresses for 6 are 6244 MPa, for structure 26–6635 MPa, and structure 40–6755 MPa. Thus, temporary stresses increase.

The values of temporary stresses are significantly higher than the compressive strength of ZrO_2. Such stresses should cause cracks in the sanding layer, but, as indicated in [19], cracks do not develop due to the porosity of the sprayed layer (Table 3).

Table 3. Values of temporary stresses during grinding by wheels LO 250/160 C10 100% structure 6 and AEROBOR structure 26 and 40.

$t*10^{-5}$, m	$\Sigma_{temp}*10^6$, Pa		
	The structure of the CBN wheel and the AEROBOR wheel; Nst		
	6	26	40
0.5	1537	1736	1799
1.0	2174	2455	2544
1.5	2662	3007	3116
2.0	3074	3472	3598
2.5	3437	3881	4023
3.0	3765	4252	4407

3.2 Single Grain Cutting Temperatures

Unit cutting forces are slightly greater when grinding with highly porous wheels. This suggests that the cutting temperatures of single grains will be slightly higher compared to the temperatures that occur when grinding with wheels of structure 6.

Considering that practically all thermal barrier coatings are non-conductive, the method of artificial thermocouple is applied. One electrode is a steel foil, and a constant foil is used as the second electrode. The foil sheets' thickness is from 6–20 microns, and the distance between them is of the order of 40 microns or less, depending on the thickness of the capacitor paper, which insulates them from each other. For a stable formation of a thermal junction, the thermoelectrodes are annealed at a temperature of 1000–1100 ℃ for 30 min. The ends are brought to the surface and welded together during grinding. As a result, a thermal spike with a thickness of 2–3 microns appears and, therefore, a thermocouple of the "iron-constantan" type is formed, which has very low inertia. The thermal pulse is shown in [14].

Mathematical modeling has confirmed this assumption. The results are shown in Table 4 and Fig. 1.

Analyzing the results, we can conclude that the unit temperature of cutting grain during grinding with highly porous wheels is slightly high.

3.3 Contact Temperatures and Residual Stresses

Simulation of the thermal process during grinding with highly porous wheels shows that since the total cutting forces are slightly reduced, the power of the heat source Pz

Table 4. Comparison of temperatures from single grains during grinding with wheels (LO 250/160 C10 100%) of structures 6 and 40.

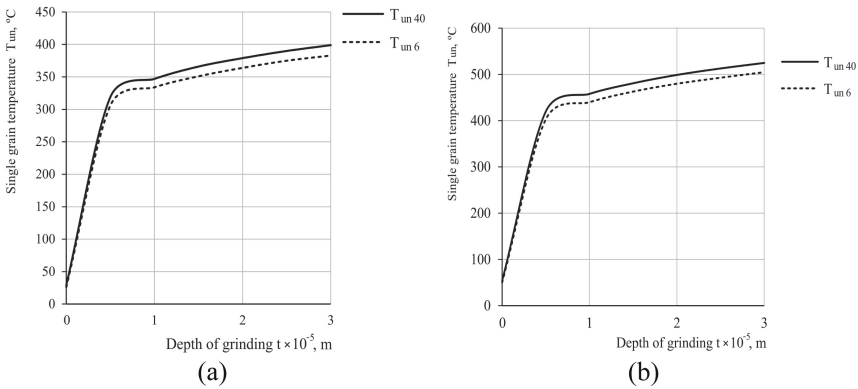| t, m^{-5}	125/100		160/125		250/100	
	Tun 6	Tun 40	Tun 6	Tun 40	Tun 6	Tun 40
0.0	26	29	34	38	50	54
0.5	306	319	341	355	403	420
1.0	334	347	372	387	440	458
1.5	351	366	391	407	463	481
2.0	364	379	406	422	480	499
2.5	375	390	417	434	493	513
3.0	383	399	427	444	505	525

Fig. 1. Unit temperatures of grain cutting during grinding by wheels. (LO250/160 C10 100%) of structure and 40. Modes Vw = 30 m/s; Vsp = 0.166 m/s; S = 0.002 m/v.

* Vw also decreases, which causes a corresponding decrease in temperature. Figure 2. The thermal process was simulated without considering the thermodynamics of cooling the surface with air through the wheel's pores. The total decrease in temperature can be no more than 5–10%. When considering the thermodynamics of cooling, it should be borne in mind that the cooling effect of air is about 10 times less than when cooling with a water-based coolant, so it is impossible to expect large heat transfer from the surface heated by grinding. As shown by thermodynamic calculations], the heat transfer coefficient when blowing the zone of contact of the wheel with the part through the pores of the wheel is not more than 200 W/(m^2 K). Considering the insignificant contact spot area of the wheel, the heat transfer is insignificant. Approximate calculations show that the temperature decrease can be no more than 8–10%. Consequently, given the decrease in the power of the heat source and the cooling effect of air, we can expect a decrease in the contact temperature by 15–20%. Contact temperature measurements using microthermocouples confirm this assumption.

Contact temperatures substantiate residual stresses. In the case of grinding with highly porous wheels, all the laws governing the formation of residual stresses are the same as when grinding with ordinary wheels. Since the contact temperature is lower, the stresses are also lower than grinding with ordinary wheels.

Generally, grinding with highly porous CBN wheels can increase the limiting processing conditions by 15–20%.

The most effective contact grinding temperature can be reduced by feeding mineral oil or water-based coolant to the contact zone.

Modeling of such grinding conditions showed that a decrease in temperature could reach up to 35–40%, which naturally makes it possible to tighten grinding modes, in particular significantly, it is possible to switch to high-speed grinding without fear of causing defects on the thermal barrier layer (Fig. 2).
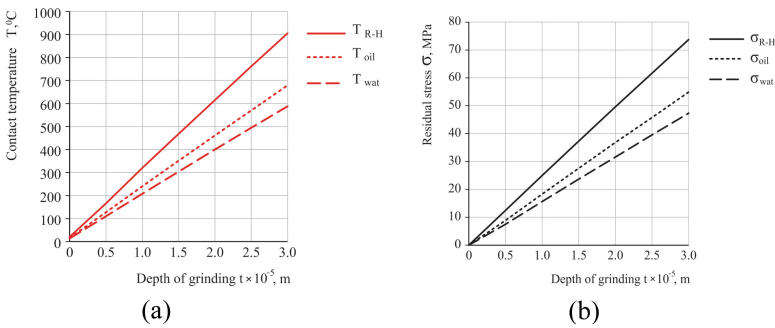

Fig. 2. Contact temperatures (a) and residual stresses (b) when grinding CBN with wheels of structure 40 when cooling with air (using a Ranque-Hillsch tube), when cooling with oil and water-based coolant. Modes Vcr = 30 m/s; Vdet = 0.166 m/s; S = 0.002 m/v (LO 250/160 C10 100%).

It is rather difficult to simulate the roughness value; therefore, the roughness state was estimated indirectly by the magnitude of the grain deepening in the material and by direct measuring [15]. The results of the comparative analysis are shown in Fig. 3.

As can be seen from the above graphs, the magnitude of the deepening of the grain in the material for highly porous wheels is 10–13% more, so we can expect an increase in roughness by about 1 category.
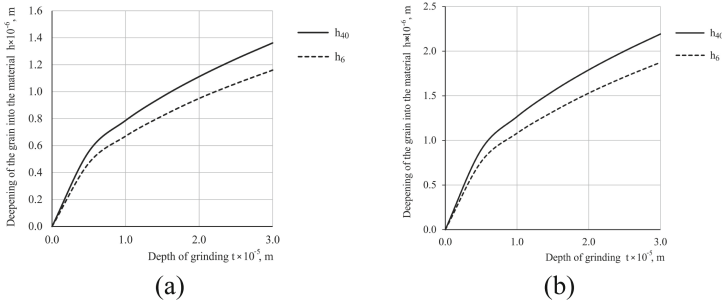
Fig. 3. The magnitude of the deepening of grain into material l when grinding CBN with wheels (LO 250/160 100%) of structure 6 and structure 40. Modes Vw = 30 m/s; Vsp = 0.166 m/s; S = 0.002 m/rev. Grain: a) 120/100; b) 250/160.

4   Results

It was found as a result of mathematical modeling of the CBN grinding of thermal barrier coatings of ZrO_2 and $ZrO_2 + Y_2O_3$.

Depending on the processing conditions, the values of the cutting force component PY can reach values of the order of 20 N. The values of the component of the cutting force P_Z can reach values of 10 N. Cutting forces do not cause temporary stresses that could lead to cracks in the sprayed ZrO_2 layer.

When grinding with highly porous CBN 26 and 40 wheels, the unit cutting forces are 15–20% higher, and the total cutting forces are 7–10% lower.

Contact temperatures are 10–15% lower when grinding with highly porous wheels. Calculations carried out according to the developed mathematical model show that under sufficiently intense grinding conditions with highly porous CNB wheels, the grinding temperature is in the range below 1100 °C. This temperature value excludes the surface sprayed layer sintering and a decrease in its thermal barrier properties.

The temporary stresses during grinding of pure zirconium oxide and stabilized with yttrium oxide by ordinary CBN wheels and highly porous are 3700–4400 MPa. In some cases, the stress exceeds the compressive strength. However, due to the porosity of the sprayed layer, the crack does not develop by depth.

Residual stresses arising under the influence of contact temperatures on the surface during grinding of pure zirconium oxide, stabilized zirconium oxide with yttrium oxide, with wheels of ordinary porosity, and highly porous wheels reach significant values of the order of 60 MPa. However, these values are much lower than the tensile strength of the thermal barrier layer and do not lead to cracks, naturally within the framework of the studied processing regimes.

When grinding with highly porous wheels, an increase in roughness by 1 category can be expected.

When grinding with highly porous CBN wheels, grinding conditions can be increased by 20–25%.

All experimental data were obtained under a careful dressing of the CBN wheel. Therefore it is recommended to avoid salting during operation. It can cause thermal defects on the grinded surface.

5 Conclusions

The purpose of the work to determine the optimal conditions for grinding thermal barrier coatings with highly porous CBN wheels has been mainly achieved.

Grinding with highly porous CBN wheels of ZrO_2 thermal barrier coatings makes it possible to obtain good results when grinding without cooling since the surface, although slightly cooled by blowing air through the pores of the wheel under fairly intense processing conditions.

Since the surface roughness increases somewhat, it is necessary to provide nursing passes when constructing the operation, when unit forces are minimal, and the roughness can be reduced.

When designing the process of grinding the thermal barrier coating, it is recommended to use the data in Tables 1, 2, 3, 4 and Figs. 1, 2, 3.

References

1. Analytical considerations of highly porous bond systems for precision grinding. https://www.nortonabrasives.com/en-gb/resources/expertise/analytical-considerations-highly-porous-bond-systems. Accessed 16 Oct 2021
2. Webster, J., Tricard, M.: Innovations in abrasive products for precision grinding. CIRP Ann. Manuf. Technol. **53**(2), 597–617 (2004)
3. Zhang, W.: Experimental and Computational Analysis of Random Cylinder Packings with Applications. LSU Doctoral Dissertations (2006)
4. Hou, Y.-G., Qiao, G.-Y., Shang, Y., Zou, W.-J., Xiao, F.-R., Liao, B.: Effect of porosity on the grinding performance of vitrified bond diamond wheels for grinding PCD blades. Ceramics Int. **38**(8), 6215–6220 (2012). https://doi.org/10.1016/j.ceramint.2012.04.074
5. High porosity grinding wheels increase productivity and avoid burning. Aircraft Engineering and Aerospace Technology **77**(2) (2005). https://doi.org/10.1108/aeat.2005.12777baf.003
6. Hudson, R.: Taking Wheel Porosity to Another Level, (2004) https://meister-abrasives-toolbox.com/2014/06/19/taking-wheel-porosity-to-another-level-3/. Accessed 16 Oct 2021
7. Cai, R., Rowe, W.B., Morgan, M.N.: The effect of porosity on the grinding performance of vitrified CBN wheels. KEM **238–239**, 295–300 (2003). https://doi.org/10.4028/www.scientific.net/kem.238-239.295
8. Zhenzhen, C., Jiuhua, X., Wenfeng, D., Changyu, M.: Grinding performance evaluation of porous composite-bonded CBN wheels for Inconel 718. Chin. J. Aeronaut. **27**(4), 1022–1029 (2014). https://doi.org/10.1016/j.cja.2014.03.015
9. Beyer, I.P., Elias, N.: High-Porosity Dressing Tools with Extreme Edge Stability – a Contradiction in Terms? (2014). https://www.meister-abrasives.com/pdfdocs/High-Porosity_Dressing_Tools_EN_2014.pdf. Accessed 16 Oct 2021
10. Beyer, P.: The Grinding Journal Explores hDD Technology (2012). https://meister-abrasives-toolbox.com/2012/08/28/the-grinding-journal-explores-hdd-technology/. Accessed 16 Oct 2021
11. Cappadona, T.: Finding Treasure In Your Grinding Process (2012). https://meister-abrasives-toolbox.com/2012/03/03/toms-trouble-shooting-tips-1-4/. Accessed 16 Oct 2021
12. Reed, C.: How Precision Grinding Solutions uses Meister Superabrasive grinding wheels for a competitive advantage (2011). https://meister-abrasives-toolbox.com/2011/01/21/application-specific/. Accessed 16 Oct 2021

13. Northrup, B.: New Advances In Vitrified Diamond Grinding Technology (2009). https://meister-abrasives-toolbox.com/2009/10/16/new-advances-in-vitrified-diamond-grinding-technology/. Accessed 16 Oct 2021

14. Lebedev, V., Klimenko, N., Uryadnikova, I., Chumachenko, T., Ovcharenko, A.: Definition of the amount of heat released during metal cutting by abrasive grain and the contact temperature of the ground surface. Eastern-European J. Enterprise Technol. **5**(7), 43–50 (2016). https://doi.org/10.15587/1729-4061.2016.81207

15. Profilograf-profilometr «Abris-PM7» internet resurs. https://ncontrol.ru/catalog/vizualno_izmeritelnyy_kontrol/profilometry_izmeriteli_sherokhovatosti/profilograf_profilometr_abr is_pm7. Accessed 16 Oct 2021

Preliminary Abrasive Blasting Surface Layer and Quality Assurance of Detonation Coatings of Aircraft Engine Parts

Tetiana Loza[(✉)] , Serhii Nyshnyk , Anatolii Dolmatov ,
and Oleksandr Skachkov

National Aerospace University «Kharkiv Aviation Institute»,
17, Chkalova Street, Kharkiv 61070, Ukraine
`t.loza@khai.edu`

Abstract. Analysis shows that one of the most rational methods of cleanings and strengthening is abrasive blasting because, in this case, a comprehensive solution to the problem occurs: developed surface relief is created, and the density of active centers increases. The urgent problem determining solid particle velocity in the Laval nozzle and beyond is solved by analytical methods in the theoretical part of the work. Expressions are obtained that make it possible to calculate velocity and particle energies when it collides with a substrate based on the kinematics of theoretical investigation studies particle propelled by a gas flow in a nozzle. The simulation of the interaction process of a particle with a substrate is carried out. Influence of energy parameters abrasive processing on the surface quality of titanium alloys parts was held in the experimental part of the work. It can be concluded that the gas flow rate and the processing time significantly affect the value of microhardness and roughness surface. Recommendations have been developed for expanding the technological capabilities of the titanium alloys' gas detonation processing.

Keywords: Process innovation · Coating deposition · Abrasive blasting · Abrasive particle velocity · Strain hardening · Dislocation densities

1 Introduction

Ensuring the reliability and individual life parts and components of modern aircraft engines is a priority for aircraft engine construction [1]. The functional properties of the main parts largely depend on the formation of homogeneous structures [2, 3] and the physical and mechanical properties of the surface layer [4]. Technological support of high erosion resistance of aircraft engine parts strengthening and increasing contact surface wear resistance is achieved by creating highly efficient materials and coatings with special properties [5, 6]. The phase composition, structure, and properties of the functional coating parts of aircraft gas turbine engines are the central area of research in surface engineering [7].

Gas-thermal spraying is one of the most effective ways to protect against wear, high-temperature corrosion, stress, and erosion, increasing parts' service life. The main advantages of gas-thermal spraying are a wide range of sprayed materials, a high degree of deposition of a covering that allows saving material, the possibility of drawing thick coverings (more than 100 microns) on the big area with high speed of drawing, and equipment mobility. This type of surface treatment can be used to meet many requirements: repair of worn areas on damaged parts, restoring the size of uncoordinated parts, increasing the service life of parts by optimizing the physical properties of the surface. One of the methods of gas-thermal spraying is detonation spraying, which is used to obtain rigid, wear-resistant, and dense microstructured coatings. It avoids unwanted thermal stress and distortion of thin-walled parts of complex design.

The work goal is to solve the urgent problem of increasing efficiency coating products process from titanium alloys using an integrated approach to rational choice parameters for preliminary surface parts preparation and coating modes.

2   Literature Review

One of the cleanings methods [8] and strengthening surface [9] complex spatial forms of gas turbine engine parts is abrasive blasting. Emphasizes factors the usefulness of such processing are high productivity [10], simplicity of equipment, versatility [11], the ability to process complex contour parts, cheap consumables, as well as accumulated extensive theoretical and experimental experience in applying this type of finishing [12, 13]. Traditionally, the main theoretical provisions of free abrasive treatment are considered from the calculations of machine parts for friction and wear [14]. However, this does not reflect laws of processing formation quality parameters. It requires the application of new approaches based primarily on provisions of metal cutting theory, which determine the physical nature of the material removal process and justify conditions for significant improvement of abrasive finishing quality and productivity. It is essential to have theoretical solutions to reduce the energy consumption of processing as a significant factor in improving quality and productivity. It is also essential to assess the dynamics of abrasive grains' interaction role with the workpiece in the formation parameters of the quality and to improve the possibility of the efficiency of processing. Effective control of the above processes is possible under conditions of forecasting obtained characteristics of materials depending on processing parameters [15, 16], which necessitated a set of theoretical studies.

One of the most critical efficiency criteria is the kinetic energy of the particle and the quality [17]. It characterizes any technological process based on the contact of a high-speed particle with a target.

This necessitates further theoretical and experimental investigations of the formation laws of the gas-abrasive jet.

3   Research Methodology

We have considered a mathematical model for the process of the gas-abrasive jet. Accelerating by the gas flow solid particle kinematics in the supersonic nozzle has been

investigated. Also, the theoretical research of the deformed condition was carried out with a single contact of the particle with the target.

The dependence of the particle velocity in the channel of the Laval nozzle on the gas flow parameters and the particle (density and diameter) was received [18]:

$$
\left.
\begin{aligned}
\xi_i &= \frac{3C_i \rho_i}{4\rho_u d}; \\
C_1 &= \frac{V_0 {\xi_0}^2 + \xi_0 \sqrt{a\xi_0} - U_0 {\xi_0}^2}{V_0 \xi_0 - \sqrt{a\xi_0} - U_0 \xi_0}; \\
V_{1i} &= a(t_i - t_0) + \frac{\sqrt{a\xi_i} + U_0 \xi_i}{\xi_i} + \frac{2\sqrt{a\xi_i}}{C_1 e^{-2\sqrt{a\xi_i}(t_i - t_0)} - \xi_i},
\end{aligned}
\right\}
\tag{1}
$$

where U_0, V_0 are the flow rate, the particle velocity and flux versus time function t_0; C_i is drag coefficient; ρ_i is flow density of the working medium in the i-th section; ρ_p is particle density; d is particle diameter; a is accelerating flow between the respective sections of the nozzle.

The particle velocity field of metal flow in the deformation zone is obtained:

$$
\begin{aligned}
\vartheta_z &= \vartheta_0 \frac{\sqrt{2R\vartheta_0 t}}{\pi r} \sin \frac{\pi r}{\sqrt{2R\vartheta_0 t}} \left(1 - \frac{z}{k\sqrt{2R\vartheta_0 t}}\right)^2; \\
\vartheta_r &= 2\vartheta_0 \frac{\sqrt{2R\vartheta_0 t}}{\pi^2 kr} \left(1 - \frac{z}{k\sqrt{2R\vartheta_0 t}}\right)\left(1 - \cos \frac{\pi r}{\sqrt{2R\vartheta_0 t}}\right); \quad \vartheta_\theta = 0,
\end{aligned}
\tag{2}
$$

where ϑ_0 is particle velocity; R is particle radius; t is deformation time; k is hardening factor.

It is more clear to analyze the obtained dependencies presented graphically. We have built graphs at specific values of the processing mode parameters to assess the adequacy of the mathematical model.

The graphs of velocity components are plotted for the following parameter values: $V_0 = 400$ м/c, $R = 2 \cdot 10^{-5}$ м, $t = 7{,}5 \cdot 10^{-9}$ c, $k = 3$. (Figs. 1, 2).

As can be seen from Figs. 1 and 2, the given dependencies form is in good agreement with the physical model of the processing process and the actual picture of the material flow, observed experimentally.
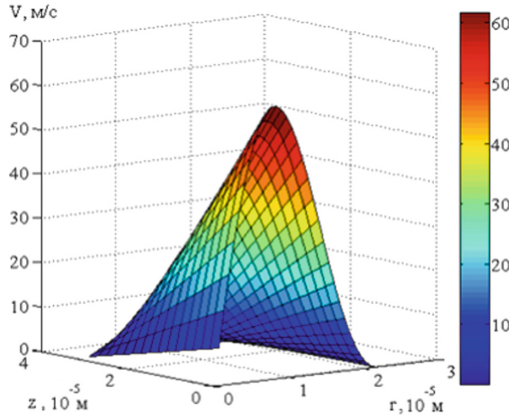
Fig. 1. Radial component of the displacement velocity field.
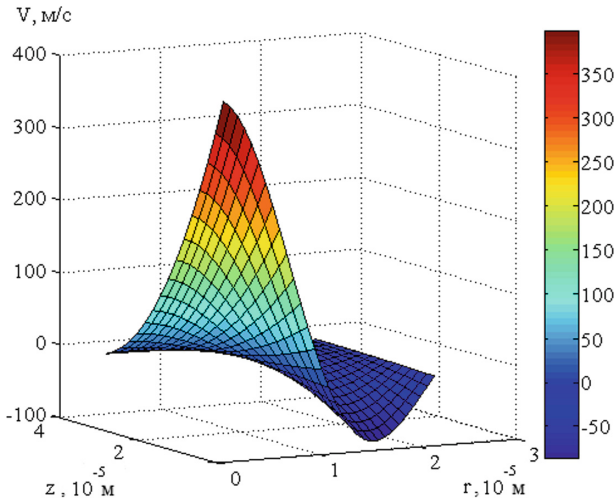
Fig. 2. The axial component of the displacement velocity field.

4 Results

We have determined the fields of strain intensity (Fig. 3) and dislocation density (Fig. 4) by the method presented in the works [19, 20] based on the above analysis of the distribution of strain rates in contact zone particles with a metal surface. The graphs in Figs. 3 and 4 have been built for the same processing parameters as velocity fields.

We chose the following parameters of the BT22 titanium alloy: modulus of elasticity of the second kind (shear modulus) $G = 3.92 \times 10^{10}$ Pa, yield point $530 \cdot 10^6$ Pa, strain hardening index $n = 0.034$, modulus of Burgers vector $b = 2.9 \cdot 10^{-10}$ m.

An experimental investigation is devoted to influencing the energy parameters of abrasive processing on surface quality titanium alloys BT1-0, BT22, BT3-1. Corundum

Fig. 3. Strain intensity fields.

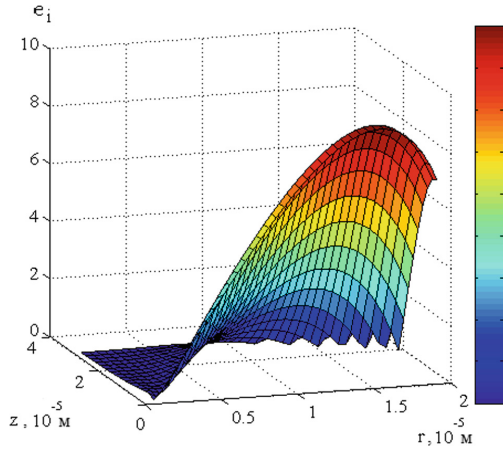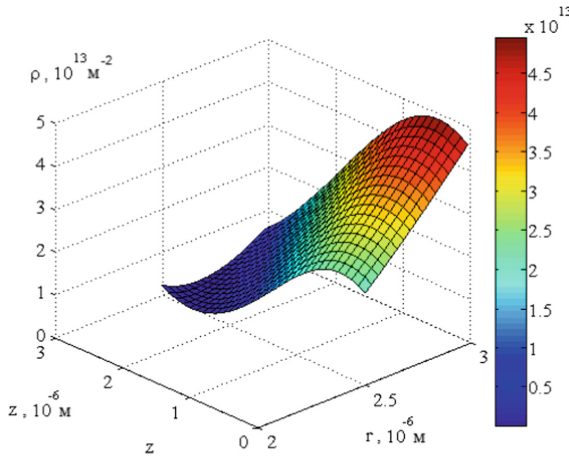**Fig. 4.** Dislocation density fields.

has been used as an abrasive. Recommendations for preliminary machining of the surface and process of complex multi-operation technology have been developed.

The simulation of flow rate and particle velocity and the process particle interaction process with the target has been performed in the Ansys software package. Modeling the distribution of gas flow and particle velocities during abrasive blasting was carried out using the following algorithm: creation three-dimensional (parametric) model of the Laval nozzle and designations of regions describing boundary conditions of calculation; creation computational mesh of finite elements with an indication of boundary conditions for specified regions direct calculation of gas flow and particle velocities. The number of design nozzle sections determines the error of the developed method calculating particle velocity, and it is limited only by the number of calculations. The researcher can correct

the calculation error depending on the required accuracy of the final objective function (velocity upon collision with the surface, kinetic energy, depth, and degree of work hardening) if necessary.

For the physical experiment, six substrates of BT1-0 alloy, 12 substrates of BT3-1 alloy, and 12 substrates of BT22 (Fig. 5) with a size of 40 x 15 mm were prepared, which are widely used in aircraft engine building and aircraft aggregate construction in the production of compressor rotor blades of I and II degrees (Fig. 6).
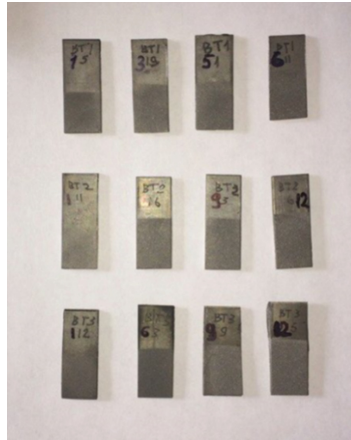
Fig. 5. Titanium alloy substrates BT22.

Fig. 6. General form compressor blades of a gas turbine engine model TB3-117.

Mechanical tests were carried out to determine the microhardness and roughness of the treated surface. Microhardness tester PMT-3M was used to investigate the microhardness of the samples with a load on the indenter of 150 gm. The results obtained were averaged, and a graph of change in microhardness depending on processing parameters was plotted using a particular average value. According to the standard method, the roughness value was determined on profilometers. The output roughness of the samples is Ra 0.6… 0.9 μm. A developed topography is formed as a result of jet-abrasive processing. It consists of many craters left by corundum particles after hitting the surface.

The sample surface roughness is leveled (Ra 4.42 µm) with repeated exposure of the abrasive particles due to the splitting off of the primary microprotrusions and the overlap of craters. The resulting relief has a jagged structure with a protrusion height of up to 36 microns. With an increased exposure time, the Ra value for the BT22 alloy first increases but then decreases due to repeated exposure to the abrasive on the substrate surface. During processing, the microprotrusions break off, and a new surface is formed with a lower roughness and a plastically deformed layer. At the same time, there is a continuous roughness increase in surface depending on the processing time for substrates made of BT1-0 alloy. There is a roughness increase of the treated surface depending on the pressure value at the inlet to the nozzle. Thus, taking into account processing parameters' influence on the surface roughness of titanium alloys allows us to conclude that the value of roughness is in range Ra1.63…4.25 µm. The processing time at which the maximum surface roughness has achieved is about 30 s for BT3-1 and BT22 alloys and 60s BT1-0 for alloy.

Transverse thin sections have been prepared to investigate the effect of coating parameters from a nickel self-fluxing tungsten carbide powder mixture of ПС-12НВК-01 grade on the coating microstructure and the "coating-metal-substrate" interface. The mixture of ПС-12НВК-01 grade is used for restoration, protection against wear and shock loads, corrosion and oxidation at normal and elevated temperatures up to 650 °C, and also as an undercoat before applying the primary coating.

The preparation of thin sections was carried out as follows: the samples were clamped into a metal clamp with a parallel plane. Rough grinding of the surface was carried out with sanding paper of different grain sizes, and the final finishing was held using polishing pastes such as АСН and АСМ under GOST 25593–83 with a fineness is included in the composition of diamond chips from 6 to 0.1 µm.

The structure of the original sample (see Fig. 7) is an alpha alloy with the surface after abrasive blasting. The thin section clearly shows the boundary between substrate and coating. The substrate surface was pretreated by abrasive blasting in order to form a developed relief for better coating adhesion. The roughness of the substrates before spraying corresponded to Ra 4.42 µm, clearly seen (Fig. 7 (a)) that the relief is smoothed during gas detonation spraying due to severe plastic deformations. The sprayed coating is granular eutectic consisting of WC grains embedded in a nickel matrix. Tungsten carbide has a more pronounced dark color in secondary electrons. The coating turned out to be relatively homogeneous, with a granular structure, without clearly defined boundaries due to the wide range of WC phase sizes. The "coating-material" separation boundary is clear the porosity is insignificant.

The average pore size is about 6µm, the maximum pore size is 13 µm, and the minimum pore size is 2.8 µm. The pores are closed and localized in the coating. The average coating thickness is 167 µm.

The coating in Fig. 7 (b) differs from the coating in Fig. 7 (a) in the mode of preliminary preparation and gas detonation spraying and thickness of 245 microns versus 167 microns. The absence of large pores and cavities should also be noted. The coating is homogeneous, porosity at the surface has a more layered structure as the number of pores per unit of a given area is much greater than at the interface. It should also be noted a change in concentration of pores not only by depth but also in geometry - a change
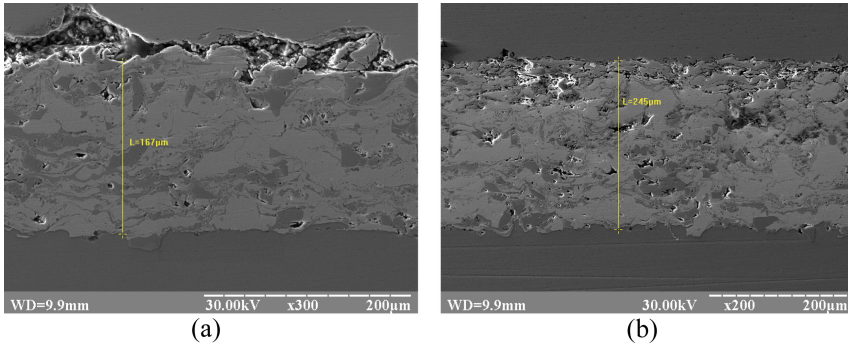
Fig. 7. – General view of the coating on the thin sections of alloy BT22.

in shape and size. Thus, the pore shape is closer to the correct one, with an average increase in a described circle around them diameter from 2 µm at the surface to 5 µm at the interface between the target and coating metal.

5   Conclusions

The analysis of gas-thermal spraying methods was carried out. It was found that the detonation spraying process provides high adhesive strength, low porosity, insignificant thermal effect on the processed material and the surface with residual compressive stresses. The problem of choosing the optimal method of preliminary abrasive-hardening treatment is formulated. An analysis of the abrasive-strengthening treatment surfaces of gas turbine engine parts with a free abrasive is carried out. It is concluded that an abrasive blasting method using is promising. Theoretical investigation of target deformed state at a single contact particle with a substrate has been held to describe the general integral picture of the stress-strain state of the processing. The field of particle velocity, deformation rate, deformation field, and dislocation density has been determined in the deformation zone. The equations have been submitted graphically for specific processing modes to assess the adequacy of the model representations. The investigation of influence energy parameters jet-abrasive machining has been received on the surface quality of titanium alloys parts made.

It has installed:

– air pressure and duration have a significant effect on the microhardness and surface roughness of BT1–0, BT3–1, BT22 titanium alloy specimens;
– mode parameters of preliminary abrasive-strengthening processing to obtain optimal roughness (Ra 1.63…4.25 µm) and microhardness (4.8…5.1 GPa) of surface layer provide high-quality nickel-tungsten carbide coatings.

Complex experimental investigation has established that maintenance of technological recommendations at abrasive-strengthening and gas-detonation spraying leads to a qualitative and quantitative change of coverings quality:

– uniform coatings are formed with a granular structure, without clearly defined boundaries, the "coating-material" interface is straightforward, porosity is insignificant;
– the average pore size decreases from 10 to 6 μm, and the maximum pore size is 40 microns to 13 μm. The pores are closed and localized in the coating.

The recommendations have been developed to implement integrated technology for spraying tungsten carbide coatings on titanium alloys by detonation methods.

The directions for further work are the behavior of pores under load and determining their influence on the formation of cracks.

References

1. Fedele, L., Di Vito, L., Ramundo, F.: Increasing efficiency in an aeronautical engine through maintenance evaluation and upgrades: Analysis of the reliability and performance improvements under financial issues. Energies **13**(12), 3059–3075 (2020). https://doi.org/10.3390/en13123059

2. Krukovich, M.: Technology to improve the performance properties of heterogeneous boronized layers. Mater. Perform. Characterization **3**, 329–338 (2020). https://doi.org/10.1520/MPC20190091

3. Jiang, P.F., Zhang, C.H., Zhang, S., Zhang, J.B., Chen, J., Liu, Y.: Fabrication and wear behavior of TiC reinforced FeCoCrAlCu-based high entropy alloy coatings by laser surface alloying. Mater. Chem. Phys. **255**(5), 123571 (2020)

4. Kombarov, V., Sorokin, V., Tsegelnyk, Y., Aksonov, Y., Fojtů, O.: Numerical control of machining parts from aluminum alloys with sticking minimization International. J. Mechatronics Appl. Mech. **1**(9), 209–216 (2021)

5. Garfias Bulnes, A., Albaladejo Fuentes, V., Garcia Cano, I., Dosta, S.: Understanding the influence of high velocity thermal spray techniques on the properties of different anti-wear WC-based coatings. Coatings **10**(12), 1157–1173 (2020). https://doi.org/10.3390/coatings10121157

6. Pezzato, L., Settimi, A.G., Cerchier, P., Gennari, C., Dabalà, M., Brunelli, K.: Microstructural and corrosion properties of PEO coated zinc-aluminized (ZA) steel. Coatings **10**(5), 448–459 (2020). https://doi.org/10.3390/coatings10050448

7. González, H., Calleja, A., Pereira, O., Ortega, N., López de Lacalle, L. N., Barton, M.: Super abrasive machining of integral rotary components using grinding flank tools. Metals **8**, 24 (2018). https://doi.org/10.3390/met8010024

8. Meng, J., Dong, X., Zhou, H., Liu, W., Yin, Z.: Investigation of adhesive resistance of aluminum alloy by sandblasting and electrochemical machining. Micromachines **8**(3), 91 (2017). https://doi.org/10.3390/mi8030091

9. Cyril, T.A., Baskar, K.: Testing and evaluation of bond surface profile influencing the CFRP strengthening of steel members. J. Test. Eval. **46**(6), 20170195 (2018). https://doi.org/10.1520/JTE20170195

10. Settles, G.S., Garg, S.: A scientific view of the productivity of abrasive blasting nozzles. JTST **5**, 35–41 (1996). https://doi.org/10.1007/BF02647515

11. Bouledroua, O., Hadj Meliani, M., Azari, Z., Sorour, A., Merah, N., Pluvinage, G.: Effect of sandblasting on tensile properties, hardness and fracture resistance of a line pipe steel used in algeria for oil transport. J. Fail. Anal. Prev. **17**(5), 890–904 (2017). https://doi.org/10.1007/s11668-017-0313-4

12. Rudawska, A., Danczak, I., Müller, M., Valasek, P.: The effect of sandblasting on surface properties for adhesion **70**, 176–190 (2016). https://doi.org/10.1016/j.ijadhadh.2016.06.010

13. Jackson, M.J.: Recent advances in ultraprecision abrasive machining processes. SN Appl. Sci. **2**(7), 1–26 (2020). https://doi.org/10.1007/s42452-020-2982-y

14. Li, D., et al.: Enhancement of wear resistance by sand blasting-assisted rapid plasma nitriding for 304 austenitic stainless steel. Surf. Eng. **5**(36), 524–530 (2020). https://doi.org/10.1080/02670844.2019.1641953

15. Kurin, M.O.: Determination of the boundaries of plastic zone of metal deformation during the cutting. Progress Phys. Metals **21**(2), 249–273 (2020). https://doi.org/10.15407/ufm.21.02.249

16. Dolmatov, A.I., Kabatov, A.A., Kurin, M.A.: Investigation and optimization of diamond smoothing technology as applied to stainless steel details for aircraft engines and aggregates. Metallofiz. Noveishie Tekhnol. **10**(35), 1407–1423 (2013)

17. Parajuli, S.P., Zobeck, T.M., Kocurek, G., Yang, Z.L., Stenchikov, G.L.: New insights into the wind-dust relationship in sandblasting and direct aerodynamic entrainment from wind tunnel experiments. JGR Atmos. **4**(121), 1776–1792 (2016). https://doi.org/10.1002/2015JD024424

18. Dolmatov, A.I., Sergeev, S.V., Kurin, M.O., Voronko, V.V., Loza, T.V.: Kinematics of the solid particle accelerated by a flow of gas in a supersonic nozzle and work hardening of the processed surface. Metallofiz. Noveishie Tekhnol. **7**(37), 871–885 (2015). https://doi.org/10.15407/mfint.37.07.0871

19. Kurin, M.O.: Hyperbolae method analysis of a wedge flow at free cutting. Metallofiz. Noveishie Tekhnol. **7**(40), 859–876 (2018). https://doi.org/10.15407/mfint.40.07.0859

20. Kurin, M.O.: Analysis the process of plastic deformation metal chip at non-free cutting. Metallofiz. Noveishie Tekhnol. **42**(3), 433–449 (2020). https://doi.org/10.15407/mfint.42.03.0433

Improvement of the Milling Effectiveness by Application of Composite Milling Heads

Pavlo Kushnirov [ID], Yuliia Denysenko[✉] [ID], Bohdan Ostapenko [ID],
Dmytro Zhyhylii [ID], and Borys Stupin [ID]

Sumy State University, 2, Rymskogo-Korsakova St., Sumy 40007, Ukraine
`uapogor@gmail.com`

Abstract. The problem of providing the possibility of processing flat surfaces of large-sized workpieces with different widths was considered. An alternative option for multi-pass milling is the use of composite milling heads. They were designed with three face-milling cutters with intersecting blade paths. The spindle block of composite milling heads with face face-milling cutters has the ability to rotate to any angle, so it is possible to change and set the required milling width. The authors proposed a scheme for obtaining a symmetrical milling width. The rotation of the spindle unit was carried out around the central face-milling cutter, so the milling width changes symmetrically, which simplifies the preparation of the machining process. The article provides an example of a dependency of the milling width on the angle of indexing (0°–360°) of the spindle carrier of composite milling heads containing three face mills with a diameter of Dmill = 315 mm. The use of the proposed composite milling head makes it possible to increase the effectiveness of the milling process based on the same cutting modes.

Keywords: Process innovation · Industrial growth · Face-milling cutter · Flat surface · Milling width · Spindle carrier rotation · Symmetrical adjustment

1 Introduction

The processing of flat surfaces of large-sized workpieces can be carried out by various methods, for example, planning. However, the effectiveness of this processing method is low. Face milling is one of the most productive methods for machining workpiece planes. However, specific difficulties arise when it is necessary to mill large flat surfaces. For example, if the width of the flat surface of the workpiece is more significant than the diameter of the face-milling cutter, then multi-pass milling is required. This can lead to machining errors in steps between adjacent milling passes. It is possible to use special composite milling heads (CMH) installed on milling machines to perform face milling. These CMHs allow providing the required high cutting speeds of the tool (for example, equipped with superhard materials) due to the use of an individual drive.

In this case, the machine's spindle will not wear out, working at the maximum rotational speeds.

The research aims to increase the effectiveness of milling large-sized workpieces by developing a composite milling head containing three end mills and providing symmetric regulation of the milling width.

2 Literature Review

Much work has been done devoted to improving the process of milling flat surfaces. For example, surface flatness studies are considered in [1]. The authors suggest two approaches based on 3-D holographic laser measurement. In [2], the distinction between Free-step Face Milling Cutter and Normal-Step Face Milling Cutter was analyzed, and the optimum milling layouts were proposed. The dependence of the end mill length on the part size and diameter of the face-milling cutter is studied in the paper [3]. In [4], a model of the geometry and positioning of face-milling cutters under planes milling is proposed. Also, technological assurance and features of fork-type parts machining is considered in [5]. Though, all these approaches do not consider the peculiarities of large-sized workpieces processing and do not reduce the processing time in general.

Problems provoked by flat surfaces milling with a width over 300 mm are considered in papers [6]. In particular, it is challenging to operate large-sized mills (e.g., with a diameter of 400 or 630 mm), which is associated with significant tools masses and the need to use expensive large-scaled equipment.

The use of special CMHs allows milling in one pass. The end mills used in CMH can be installed at the cutting blades' trajectories [6]. Such CMHs allow obtaining a continuous width of the machined surface with relative workpiece and machine table movement in the feed direction. The disadvantage of these CMH designs is the incapability of processing width adjusting, making it difficult to mill surfaces with sidewalls.

The CMH design is a more complex option, which contains two face mills in an indexable spindle carrier [7]. Due to the indexing mechanism, it becomes possible to adjust the processing width (the minimum cutting width is equal to the diameter of the mill, the maximum width is approximately equal to the sum of the diameters of the two mills). One of these technical solution drawbacks is the asymmetrical change in the processing width under spindle indexing. This leads to the need for additional CMH movements in perpendicular to the feed direction.

In a number of works, the problems of the quality and processing accuracy insurance of flat surfaces are investigated, including technology for complex parts machining in multiproduct manufacturing [8], machining of connecting rods [9], in particular, by the loading simulation of the end mill cutting edges [10], with high-speed milling [11, 12] and during finishing [13]. The solution to the problems of ensuring the processing quality indicators is proposed by using flexible specialized devices [14, 15]. Due to ensuring the reliability and high durability of the tool in [16], it is proposed to use correctly selected trajectories of the mill movement.

3 Research Methodology

To ensure a symmetrical change in the working width with the adjusted rotation of the indexed spindle carrier, a CMH has been supposed to contain three end mills with intersecting paths of cutting blades. In this case, the spindle carrier rotation axis coincides with the central end mill axis (Fig. 1).
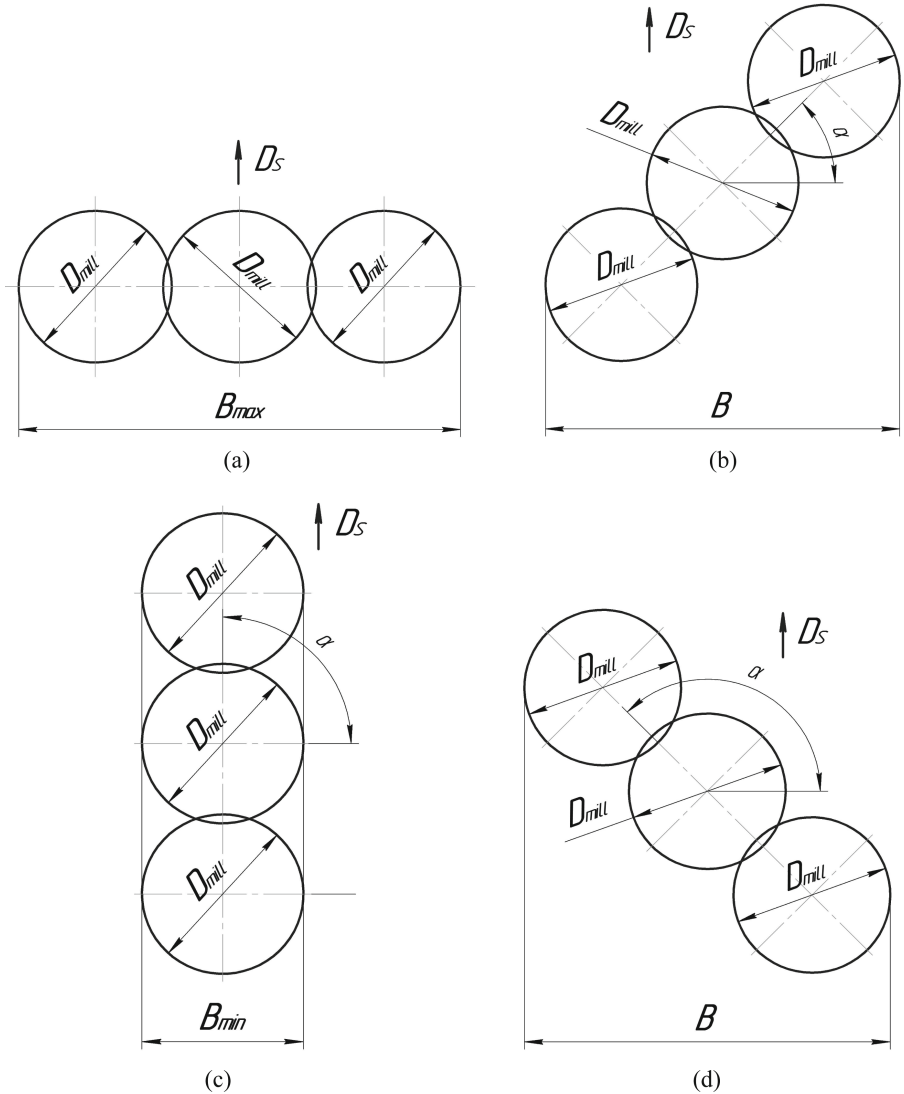

Fig. 1. The scheme of a flat surface machining with width B using a CMH containing three mills of D_{mill} diameter, with spindle carrier rotation on α, °, with cutter feed speed D_s: $\alpha = 0°$ and $\alpha = 180°$ (a), $\alpha = 45°$ (b), $\alpha = 90°$ (c), $\alpha = 135°$ (d).

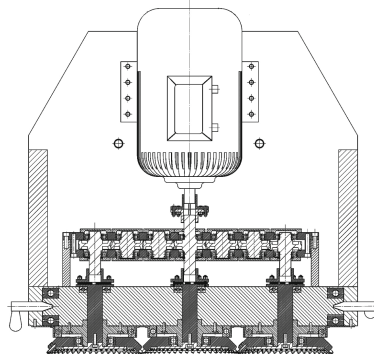Figure 2 shows the proposed CMH design with three face mills.

Fig. 2. CMH design with three face mills.

Face milling of a surface of width B is performed in the feed direction Ds. The spindle carrier CMH contains three mills of diameter D_{mill}. Indexing of the spindle carrier by the angle α can be carried out in the range of 0°–360°. The change in the milling width B occurs with a preliminary (before the milling start) indexing of the spindle carrier with the subsequent fixation of this angular position of the three mills. This rotation changes the possible machining width B of the workpiece plane. The B value varies from a maximum value (equal to approximately the sum of the diameters of three mills, $B_{max} \approx 3D$) to a minimum value (equal to one mill diameter, $B_{min} = D$).

The milling width B symmetry is achieved by indexing the spindle carrier with three end mills about the center end mill axis (Fig. 3). This figure shows a diagram of a symmetrical milling width B obtained by indexing the CMH spindle carrier with three face mills (Mill_1, Mill_2, Mill_3) by an angle α. The direction of rotation of the spindle carrier, which is carried out before starting milling, is shown on the right (counterclockwise).

The maximum value of the operational width B corresponds to the angle of the spindle carrier indexing α = 0°. The same maximum value of the operational width is at α = 180°.

However, a smaller value of the width B is often required under machining workpieces. For example, this requirement arises when milling the groove bottom plane, where the groove sidewalls limit the cutting tool width (the overall dimension along the tool width exceeds the groove width size). Therefore, before milling starts to change the width value B, it is necessary to index the spindle carrier by an angle α. The decrease in the value of width B occurs when an angle α indexes the spindle carrier from 0° to 90°. At an angle α = 90°, the width B is to be minimal. It is equal to the diameter of the mills (Mill_1, Mill_2, Mill_3).

Indexing the spindle carrier by an angle α from 90° to 180° has the effect of increasing the width value B from its minimum value to its maximum. Thus, it is possible to adjust the width value B by changing the value of the angle α. Further indexing the spindle

carrier by the angle α more than 180° is to give a cyclically repeated change in the width value B similar to that discussed above.
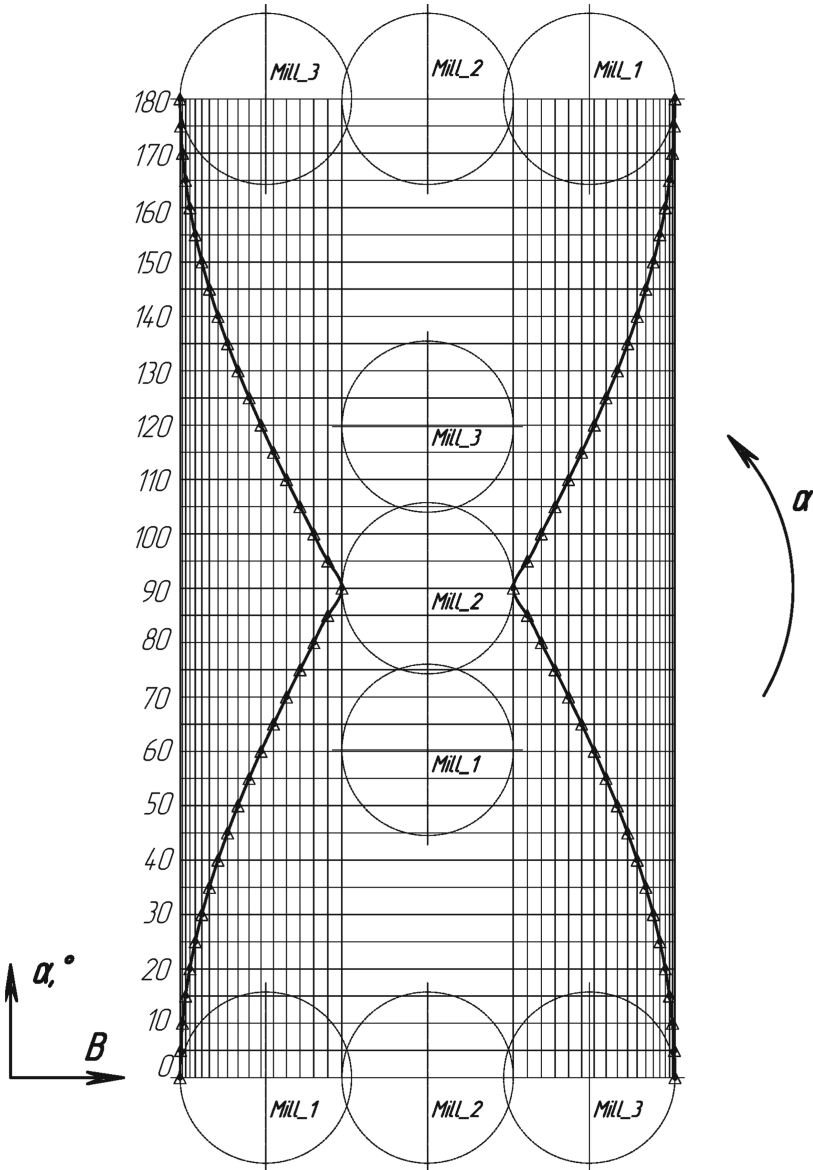
Fig. 3. Scheme of obtaining symmetric milling width B by indexing the spindle carrier CMH with three face mills (Mill_1, Mill_2, Mill_3) by an angle α. The direction of rotation of the spindle carrier is shown on the right (counterclockwise).

4 Results

Figure 4 shows one of the possible variants of the proposed CMH design with three face mills.

(a)　　　　　　　　　　　　　　(b)

(c)　　　　　　　　　　　　　　(d)
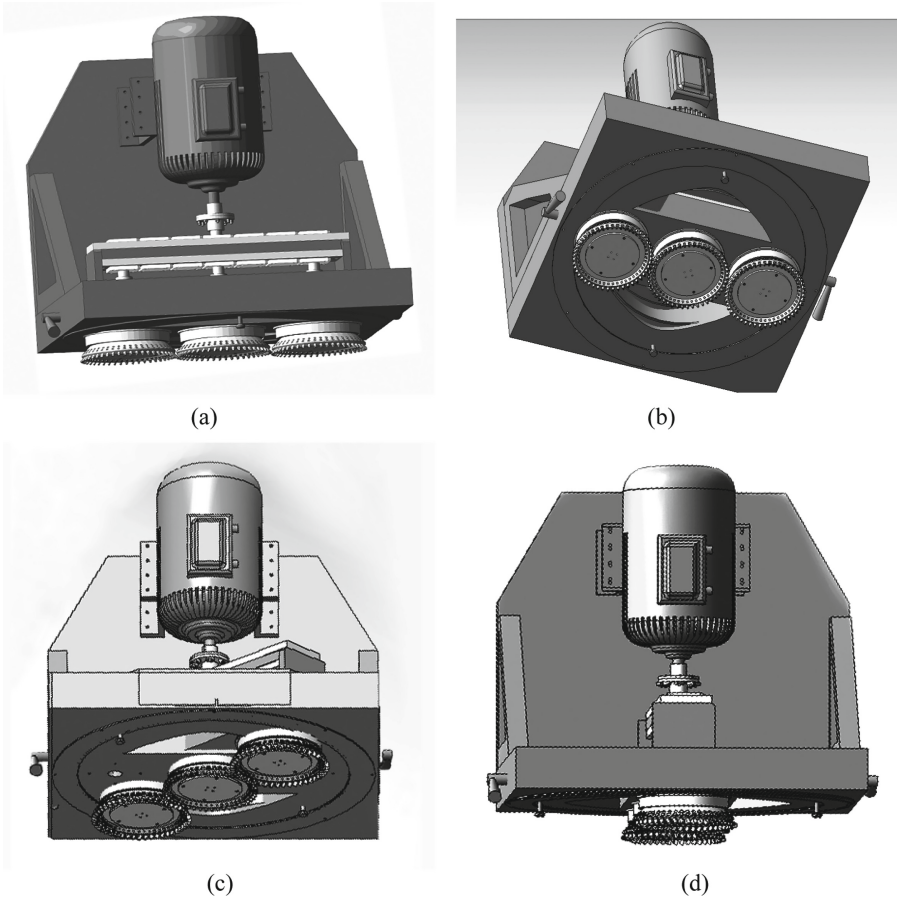
Fig. 4. CMH design with spindle carrier indexing on $\alpha = 0°$ (a) and (b), $\alpha = 45°$ (c), $\alpha = 90°$ (d).

Figure 5 shows the dependence of the milling width B on the angle of indexing α (0°–360°) using the example of a CMH spindle carrier containing three face mills with a diameter of $D_{mill} = 315$ mm.

The effectiveness of the suggested CMH is proposed to be calculated by the formula:

$$E = \frac{T_{mill}}{T_{CMH}}$$

where T_{mill} - the cutting time when using a face-milling cutter;

T_{CMH} - the cutting time when using a composite milling head.
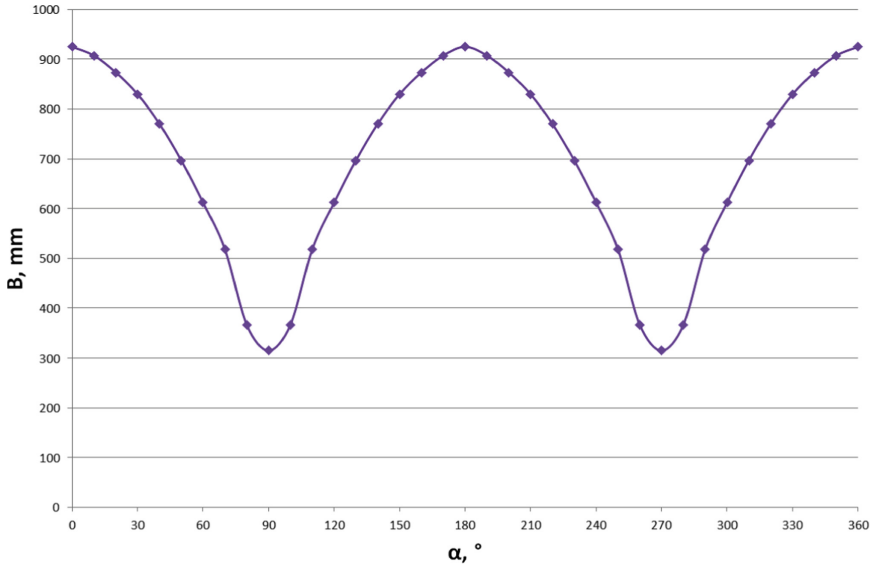
Fig. 5. Dependence of the milling width B on the angle of indexing α (0°–360°) of the spindle carrier CMH containing three face mills with a diameter of $D_{mill} = 315$ mm.

It is known that cutting time depends on cutting length *L*, the number of cuts, feed, and rotations number. Considering that in the two considered cases, the feed and rotation number are the same, the cutting lengths differ in the amount of penetration and overrun, and also considering that CMH is to replace three passes of the face-milling cutter, the formula for calculating the efficiency takes the form:

$$E = \frac{L_{mill} \cdot 3}{L_{CMH}}$$

where L_{mill} и L_{CMH} – cutting lengths with face-milling cutter and CMH.

Depending upon the mills' diameters and indexing angle in the CMH, the milling efficiency increases 2.7–2.9 times.

5   Conclusions

The paper proposes a new approach for processing flat surfaces of wide workpieces using aggregate milling heads containing three end mills with intersecting trajectories of cutting blades. The milling width *B* is adjusted by indexing the spindle carrier CMH by an angle α (0°–360°). The specified width B depends on the diameter D_{mill} of the face mills used in CMH. The milling width *B* has been calculated for the diameter of the end mill $D_{mill} = 315$ mm, which varies in the range of approximately (315–935) mm. Since the indexed spindle carrier rotates around the center end mill, the milling width B changes symmetrically.

The proposed method simplifies the adjustment of the workpiece's and the CMH mills' relative position by rejecting additional adjustment movements perpendicular to

the working feed direction D_s and can increase the efficiency of the face milling process up to 2.7–2.9 times.

It is planned to carry out computer modeling and research of the dynamic characteristics of the proposed design in the future.

References

1. Tai, B., Stephenson, D., Shih, A.: Improvement of surface flatness in face milling based on 3-D holographic laser metrology. Int. J. Mach. Tools Manuf **51**(6), 483–490 (2011). https://doi.org/10.1016/j.ijmachtools.2011.02.006
2. Wu, W.G., Yu, Q.X., Chang, X., Pang, S.Q.: Design theory and experiment of the step face milling cutter based on free cutting. Adv. Grinding Abrasive Process. **259–2**, 132–136 (2004). https://doi.org/10.4028/www.scientific.net/KEM.259-260.132
3. Ramakrishnan, S., Wysk, R.: Optimization of the length of travel in face milling operations for flat surfaces. Trans. North American Manufact. Res. Inst. SME XXX, 431–438 (2002)
4. Hadad, M., Ramezani, M.: Modeling and analysis of a novel approach in machining and structuring of flat surfaces using face milling process. Int. J. Mach. Tools Manuf **05**, 32–44 (2016). https://doi.org/10.1016/j.ijmachtools.2016.03.005
5. Ivanov, V., Dehtiarov, I., Pavlenko, I., Kosov, M., Hatala, M.: Technological assurance and features of fork-type parts machining. In: Ivanov, V., et al. (eds.) DSMIE 2019. LNME, pp. 114–125. Springer, Cham (2020). https://doi.org/10.1007/978-3-030-22365-6_12
6. Taurit, G.E.: Machining Large Parts. Tekhnika, Kyiv (1981)
7. Kushnirov, P., Zhyhylii, D., Ivchenko, O., Yevtukhov, A., Dynnyk, O.: Investigation of the dynamic state of adjustable milling heads. In: Ivanov, V., et al. (eds.) DSMIE 2019. LNME, pp. 169–179. Springer, Cham (2020). https://doi.org/10.1007/978-3-030-22365-6_17
8. Ivanov, V., Dehtiarov, I., Pavlenko, I., Kosov, I., Kosov, M.: Technology for complex parts machining in multiproduct manufacturing. Manage. Prod. Eng. Rev. **10**(2), 25–36 (2019). https://doi.org/10.24425/mper.2019.129566
9. Ivanov, V., Dehtiarov, I., Zaloga, V., Kosov, I., Savchuk, V.: Increasing productivity of connecting rods machining. In: Ivanov, V., Trojanowska, J., Pavlenko, I., Zajac, J., Peraković, D. (eds.) DSMIE 2020. LNME, pp. 264–275. Springer, Cham (2020). https://doi.org/10.1007/978-3-030-50794-7_26
10. Hlembotska, L., Melnychuk, P., Balytska, N., Melnyk, O.: Modelling the loading of the nose-free cutting edges of face mill with a spiral–stepped arrangement of inserts. Eastern Eur. J. Enterp. Technol **1**(91), 46–54 (2018)
11. Lishchenko, N.V., Larshin, V.P., Pitel, J.: Vibrational impact on milled surface irregularities. J. Eng. Sci. **7**(1), A8–A16 (2020). https://doi.org/10.21272/jes.2020.7(1).a2

12. Permyakov, A., Dobrotvorskiy, S., Dobrovolska, L., Basova, Y., Ivanova, M.: Computer modeling application for predicting of the passing of the high-speed milling machining hardened steel. In: Ivanov, V., et al. (eds.) DSMIE 2018. LNME, pp. 135–145. Springer, Cham (2019). https://doi.org/10.1007/978-3-319-93587-4_15
13. Klimenko, S.: Improvement of performance of finishing of details with a cutting tool. J. Zhytomyr State Technol. Univ **2**(88), 56–66 (2017)
14. Ivanov, V., Pavlenko, I.: Comprehensive analysis of the mechanical system system "fixture–workpiece." J. Eng. Sci. **4**(1), A1–A10 (2017)
15. Ivanov, V.: Process-oriented approach to fixture design. In: Ivanov, V., et al. (eds.) DSMIE 2018. LNME, pp. 42–50. Springer, Cham (2019). https://doi.org/10.1007/978-3-319-93587-4_5
16. Coromant, S.: Cutter Path and Chip Formation in Milling. https://www.sandvik.coromant.com/en-gb/knowledge/milling/pages/cutter-path-and-chip-formation.aspx. Accessed 15 May 2021

Deformation Zone Scheme Clarification During Deforming Broaching

Ihor Shepelenko[✉] , Yakiv Nemyrovskyi , Mykhailo Chernovol ,
Andrii Kyrychenko , and Ivan Vasylenko

Central Ukrainian National Technical University, 7, Universytetskyi Ave., Kropyvnytskyi 25006,
Ukraine
`kntucpfzk@gmail.com`

Abstract. The deformation zone scheme during deforming broaching is considered and clarified. It is shown that the theoretical model of the deformation zone makes it possible to reliably calculate the area dimensions of the deformation zone only for a workpiece with a wall thickness less than the critical one. It is proved that in the presence of critical contact pressures in the contact zone, zones of local plastic deformation appear at the joints of non-contact zones, considering the contact. Moreover, the front zone is an influx that increases the length of the contact area, and the rear – a step of the processed material flowing from the contact zone under the action of critical contact pressures. Experimental confirmations of these zones' presence are presented. It was found that in the presence of pressures in the contact zone less than critical, the deformation zone scheme corresponds to the scheme, which includes a contact area and two non-contact zones adjacent to it. It is shown that the local zones formation of plastic deformation has a negative effect on such parameters of processed products quality as the accuracy of the processed product, especially on the axis bending when processing parts of increased length, as well as on the resource of residual plasticity, which is especially important when processing products from low-plastic materials.

Keywords: Process innovation · Deforming broaching · Deformation zone · Contact area · Non-contact zone · Local zone · Modeling · Theoretical model

1 Introduction

Deforming broaching is a technological process of processing holes by the method of stepwise plastic deformation. The tool moves along the generatrix of the hole according to the kinematic sliding pattern. Deforming broaching is used as a finishing and roughing operation, combining the processes of shaping and deformation hardening [1].

The deformation zone scheme is one of the main questions in the study of this process. The kinematic, geometric, and energy parameters of the deformation zone determine the energy consumption for the process and affect the quality of the processed products. Therefore, a number of works have been devoted to studying the deformation zone scheme, but their data are somewhat different from each other [2].

2   Literature Review

The analysis of the available literary sources showed that the most accurate deformation zone scheme is the scheme [1]. The deformation zone consists of a contact area II and two non-contact zones I and III, adjacent to it (Fig. 1). It should be noted that deformation in different areas of the deformation zone is a single process of workpiece plastic shaping. Simultaneously, in all three areas, it determines the stress-deformed state of the workpiece and parameters depending on it.

In works [3], a theoretical model of the deformation zone for the shell-type workpieces expansion ($t_0/r_0 \leq 0, 1$), is proposed, where t_0 and r_0 are the wall thickness and the workpiece hole radius, respectively. This model, built using variational principles [4], made it possible to determine its geometric parameters, namely: the length of areas I, II, and III (Fig. 1).
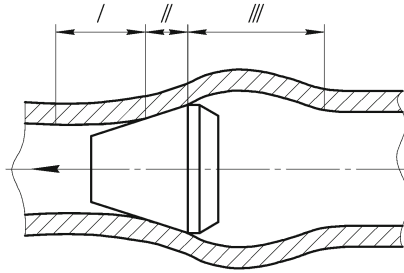
Fig. 1.   Deformation zone scheme: I, III – non-contact zone; II – contact area [1].

As shown by the results of the calculated and experimental data (Fig. 2), the axial dimensions of the non-contact zones, calculated by the model, increase monotonically with an increase in the wall thickness and agree well with the experimental data [5]. Moreover, this coincidence is observed even with significant wall thicknesses ($t_0/r_0 > 0, 5$).

The dependence of the length change of the contact zone and the height of the non-contact zones, depending on the thickness of the workpiece, has a somewhat different character (Fig. 3).

Experiments to determine the contact zone length and the non-contact zone height behind the contact area (Fig. 3) have shown that good agreement between the calculated and experimental results is observed only for the case of processing thin-walled workpieces [6]. With an increase in the wall thickness, the experimental results are fundamentally different from the calculated ones. The model gives reliable results up to a specific wall thickness. The authors [2] call this wall thickness the critical wall thickness. It ensures the appearance of critical contact pressures in the contact zone.

According to the authors [2], critical contact pressures are the physical constant of the processed material. In this case, according to the data [1], the value of this critical wall thickness changes depending on the value of factors affecting the contact pressures, namely, the angle of the generatrix inclination of the working element α and the tension on the element.
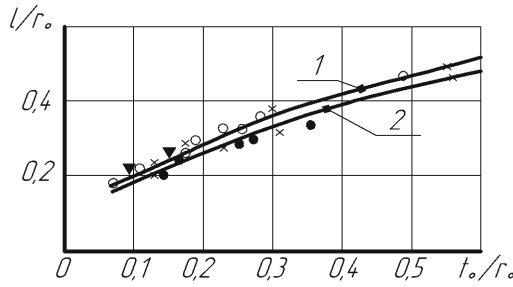
Fig. 2. Dependence of the non-contact zones length of the deformation zone on the workpiece thickness when using the inclination angles of the generatrix $\alpha = 2°–12°$; tension on the element $a/d_0 = 0.0125–0.0375$; 1 – non-contact area behind the tool; 2 – non-contact zone in front of the tool experimental data [2]: $\circ$ – AK6 alloy; Δ – steel 10; $\blacktriangledown$ – St3; $\bullet$ – steel 30HNMA; $\times$ – steel 20.
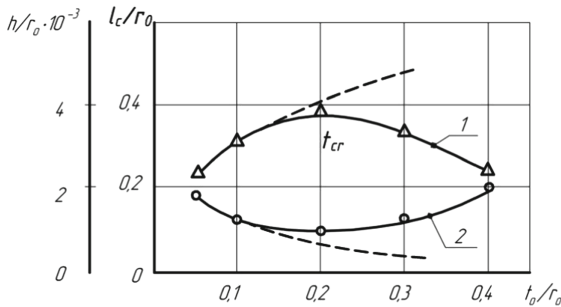
Fig. 3. Dependence of the non-contact zone height contact h/r_0, the contact length l_c/r_0 on the wall thickness of the workpiece t_0/r_0 when processing workpieces made of steel 20, HB 125 with a deforming element with an angle $\alpha = 4°$ and tension $a/r_0 = 0.05$: 1 – the height of the non-contact zones; 2 – the length of the contact zone.

The authors [7] associate the inflection of the contact length function from the wall thickness (Fig. 3, curve 2) of the workpiece with the appearance of critical contact pressures in the contact zone, which lead to the zone formation of local plastic deformation in the form of an influx, which is located at the conjugation point of the non-contact area in front of the contact area and the area of contact itself.

As for the height of the non-contact zone behind the contact area, experiments have shown [5] that it also has an extreme character (Fig. 3, curve 1), which also appears when critical contact pressures are reached in the contact zone.

The presence of such discrepancies between the calculated and experimental data does not allow using the developed theoretical model of the deformation zone when calculating the geometric characteristics of the deformation zone in a wide range of changes in the wall thickness of the workpiece [7–9]. Therefore, it is necessary to carry out additional studies that will allow determining the use areas of the deformation zone theoretical model and develop a calculation method for determining the geometric characteristics of the deformation zone [10].

In this case, a process requires an additional study concerning deformation in the conditions of critical pressures. At deformation in the conditions of critical pressures and the presence of a zone of local flowage at the beginning and end of the zone, clarification of the chart of the hearth of deformation is needed at the deforming reaching [3].

Thus, the performed analysis showed that the developed theoretical model only calculates the deformation zone parameters for thin-walled workpieces. However, the axial dimensions of the non-contact zones can be calculated according to the developed model for thick-walled workpieces [11]. Relatively to the deformation of parts with a greater wall thickness, that is, in the presence of critical contact pressures in the contact zone, the process requires additional study [12, 13].

The purpose of this study is to clarify the existing scheme of the tool interaction with the product during deforming broaching and to develop recommendations for determining the dimensions of each of the deformation zone areas [14].

3   Research Methodology

For an in-depth study of the deformation zone shape, modeling the change in the generatrix (its shape) in the deformation zone was performed using the Deform software package following the scheme shown in Fig. 4.
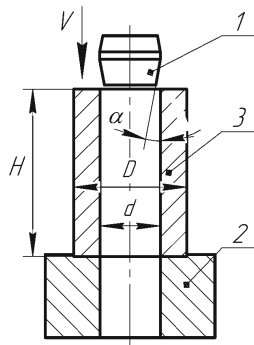
Fig. 4. Processing scheme: 1 – deforming element; 2 – base; 3 – test sample.

The working motion of the deforming element 2 was set by its monotonic longitudinal movement along the processed hole of sleeve 3, which leans on a fixed base 2 (Fig. 4). The speed of the deforming element $V = 0.5$ mm/s. The working cone angle of the deforming element α was 4°, respectively. Nominal tension on the deforming element was $a = 0.05$ mm per side.

A fragment of the Deform-3D preprocessor window is shown in Fig. 5.

The length of the contact area was determined by the original method [15], which consists in measuring the marks on the tool working cone left by diamond-containing pastes applied to the inner surface of the workpiece.

The height of the non-contact zone behind the contact area was measured using a special device.
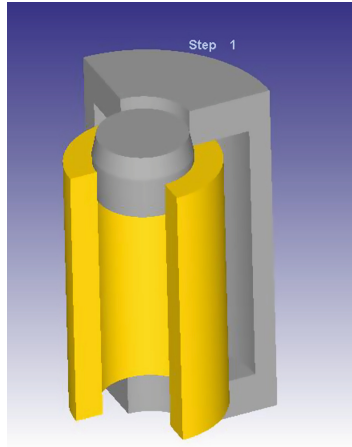
Fig. 5. A fragment of the Deform-3D preprocessor window.

4   Results

The modeling results (Fig. 6) convincingly indicate that the contact zone has two areas of local plastic deformation.
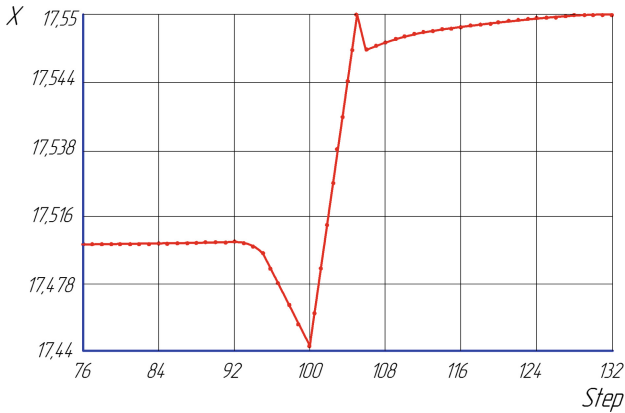
Fig. 6. Changing the X coordinate of the deformation zone surface generatrix (its shape) depending on the step *Step*.

The first area is located at the beginning of the contact zone, the second – at its end, at the point of transition of the contact zone to the non-contact zone.

Since the conditions for the interaction of the conical tool with the workpiece at the entrance and exit from the contact zone are significantly different, we will consider modeling the contact interaction as the expansion of the pipe by a conical punch (Fig. 7) during its radial movement.

(a)

(b)
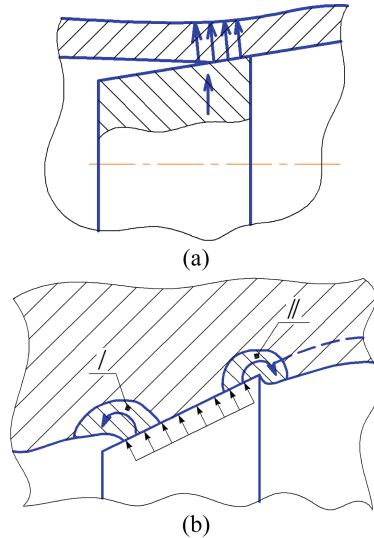
Fig. 7. Expansion of a pipe by a rigid punch with its radial movement: a) expansion of a thin-walled workpiece $q < q_{cr}$; b) expansion of a thick-walled workpiece $q > q_{cr}$; I, II – zones of local plastic deformation.

When expanding the pipe under conditions when $q < q_{cr}$ (Fig. 7, a), hole generatrix is a smooth line, without kinks, which are typical in the presence of local plastic zones.

When expanding the pipe, when $q > q_{cr}$ (Fig. 7, b), under the action of high contact pressures, there is a local outflow of material from under the tool with the formation of local plastic zones I and II. Note that zone I is an influx, zone II is a local extrusion of the workpiece material from under the edge of the punch due to the presence of critical contact pressures.

In this case, zone I leads to an increase in the contact length, and zone II to a decrease in the height of the non-contact zone.

Comparison of the hole generatrix profilogram in these zones (Fig. 6), obtained by simulation by the finite element method of deforming broaching under the condition ($q > q_{cr}$), is in good agreement with the scheme in Fig. 7 (b), that is, for $q > q_{cr}$.

Figure 8 (b) shows the formation of zones of local plastic deformation during deformation in the area of contact pressures critical for a given material.

Leakage (shown by arrows in Fig. 8) in the zone I leads to the formation of an "influx", and outflow in zone II leads to the formation of a step and a decrease in the height of the non-contact deformation wave. As mentioned above, these zones of local plastic deformation change the scheme of the tool interaction with the part, which additionally leads to the appearance of inflections in the function $l_c = f\left(\frac{t_0}{r_0}\right)$ and $h_{n.z} = f\left(\frac{t_0}{r_0}\right)$, which were previously obtained experimentally (Fig. 3).

Considering the modeling results, let us consider the interaction scheme during deforming broaching. When the contact pressures are less than the critical one, the interaction scheme of the workpiece inner surface is described according to Fig. 8 (a).
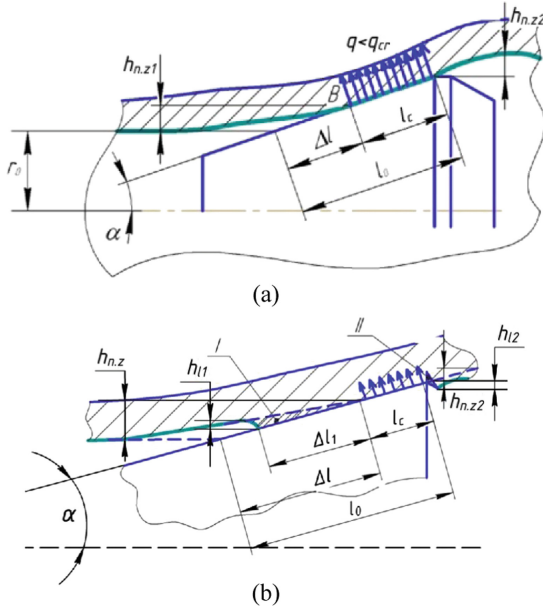
Fig. 8. Deforming broaching of the workpiece: a – thin-walled $q < q_{cr}$; b – thick-walled $q \geq q_{cr}$; I, II – zones of local plastic deformation; I – influx in front of the contact area; II – step behind the contact area.

In this case, the contact length is:

$$l_c = l_0 - \Delta l = \frac{a}{2sin\alpha} - \frac{5l_1}{8cos\alpha}, \tag{1}$$

a – tension on the element;

l_1 – length of the non-contact zone.

As noted earlier, the contact pressure increases with an increase in the angle α, the wall thickness of the workpiece and a decrease in the tension on the element. When it reaches a critical value, the contact length begins to increase due to the formation of an influx, which increases the contact length (Fig. 8, b). For this case, the contact length is:

$$l_c = l_0 - \Delta l = \frac{a}{2sin\alpha} - \frac{h_{n.z.}}{sin\alpha} + \frac{h_l}{sin\alpha}, \tag{2}$$

where h_l – an additional component that considers the height of the local plastic zone (influx).

The height of the non-contact zone behind the contact area also changes, starting to decrease due to the local zone formation of plastic deformation in the form of a step, which is formed when the workpiece material flows out at the end of the contact zone.

With an increase in the contact pressure, for example, due to the wall thickness of the workpiece, the value of this step increases, and the actual height of the non-contact zone decreases:

$$h^d_{n.z.2} = h_{n.z.2} - h_{l2}, \tag{3}$$

where h_{l2} – an additional component that considers the height of the step.

This explains the change in the nature of the dependencies $l_c = f\left(\frac{t_0}{r_0}\right)$ and $h_{n.z} = f\left(\frac{t_0}{r_0}\right)$.

Our studies have shown that zones of local plastic deformation arise even during deforming broaching of workpieces made of low-plastic materials, for example, cast iron SCh20, which are processed exclusively with low tensions [1], which explains the presence of critical contact pressures in the contact zone.

For a more detailed confirmation of this fact, special experiments were carried out, which made it possible to fix the contact zone of the tool with the part in the process of its steady motion, that is, without preliminary installation of the deforming element. For this, conditions were created for the instantaneous stop of deformation in the process of tool movement. We have developed an original technique [16], which considers the low plasticity of cast iron. Also, according to the authors [7], there is a very rigid stress state on the outer surface of the workpiece $\eta = +2$ which corresponds to the stress state of biaxial tension. When the deformation process was stopped immediately due to the destruction of the workpiece, an imprint of the contact zone was obtained. The study of the resulting imprint shape was carried out using special profilograms (Fig. 9).
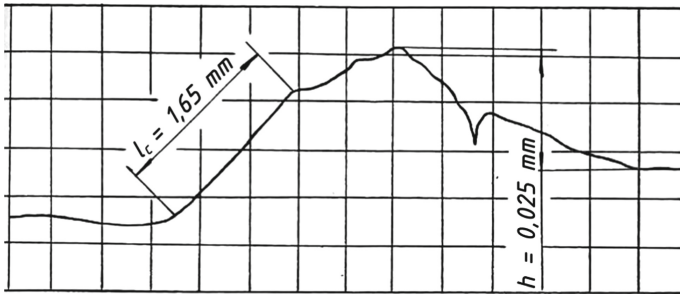
Fig. 9. Profilogram of the contact zone when processing a workpiece made of SCh20 cast iron with dimensions $t_0/d_0 = 0.7$ with a tension $a/d_0 = 0.0004$, $\Sigma a/d_0 = 0.39$ mm, angle $\alpha = 4°$ (vertical increase × 1000, horizontal – × 20).

In Fig. 9, the contact area is clearly visible, the length of which is 1.65 mm, and the profile of the local plastic deformation zone with a height $h = 0.025$ mm. The existence of a non-contact zone in front of the contact area is evidenced by the fact that $l_c/l_0 = 0.8$, where l_0 – geometric length of the contact.

Thus, the performed studies made it possible to establish that if there are pressures less than critical in the contact zone, the deformation zone scheme corresponds to the scheme shown in Fig. 8 (a), which includes a contact area and two non-contact zones adjacent to it.

In the presence of critical contact pressures in the contact zone at the point of conjugation of non-contact with the contact area, zones of local plastic deformation appear, and the interaction scheme corresponds to Fig. 8 (b). According to this figure, the front zone is an influx that increases the length of the contact zone, and the back one is a

step from the material of the part, flowing out of the contact zone under the influence of critical contact pressures.

The appearance of zones of local plastic deformation changes the scheme of tool interaction with the part, as well as its geometric parameters, and leads to the appearance of inflections of the function $l_c = f\left(\frac{t_0}{r_0}\right)$ and $h_{n.z} = f\left(\frac{t_0}{r_0}\right)$.

Determination of the non-contact zones dimensions and the contact area is extremely important in the development of a technological process using deforming broaching, as well as in the designing of working elements of deforming broaches. Local zones formation of plastic deformation negatively affects such parameters of processed products quality as the accuracy of the processed product, especially on the axis curvature when processing parts of increased length, as well as on the resource of residual plasticity, which is especially important when processing products from low-plastic materials.

5   Conclusions

The performed analysis of the deformation zone model made it possible to establish the following provisions:

– it was found that when critical contact pressures are reached in the contact zone in points of conjugation of the contact area with the non-contact zones, local plastic deformation zones are formed, which must be taken into account when calculating the size of the deformation zone and designing the tool;
– at a contact pressure less than the critical one, the geometric dimensions of the deformation zone can be calculated using the theoretical model of the deformation zone without taking into account the influence of local zones of plastic deformation;
– when the contact pressure is greater than the critical one, the calculation of the contact zone length and the non-contact zones height must be performed according to a model that considers the effect of the influxes height arising at the points of conjugation of the non-contact zones with the contact area.

References

1. Dvirna, O.: Analysis of technologies of surface treatment locks grape compressor and turbine. Scientific of Rzeszow University of Technology, Mechanics, 433–440 (2018)
2. Kobets, A., Aulin, V., Derkach, Ol., Makarenko, D., Hrynkiv, A., Krutous, D., Muranov, E.: Design of Mated Parts Using Polymeric Materials with Enhanced Tribotechnical Characteristics. Eastern-European Journal of Enterprise Technologies 5(12(107)), 49–57 (2020). DOI: https://doi.org/10.15587/1729-4061.2020.214547
3. Dobrotvorskiy, S., Balog, M., Basova, Y., Dobrovolska, L., Zinchenko, A.: Concept of the Software for Materials Selection Using .NET Technologies. In: Tonkonogyi, V., et al. (eds.) InterPartner 2019. LNME, pp. 32–43. Springer, Cham (2020). https://doi.org/10.1007/978-3-030-40724-7_4
4. Studenets', S.F., Eryomin, P.M., Chernyavs'kyi, O.V.: The influence of deformation conditions on the structure and hardening of cast iron surface layer in machining with combined carbide broaches. J. Superhard Mater. **37**(4), 282–288 (2015). https://doi.org/10.3103/S1063457615040085

5. Sheykin, S.Y., et al.: Improving the Performance of Hard-Alloy Deforming Broaches Using Modified Technological Lubricants. J. Superhard Mater. **42**(4), 276–282 (2020). https://doi.org/10.3103/S1063457620040085

6. Sheykin, S.Y., et al.: On the Contact Interaction between Hard-Alloy Deforming Broaches and a Workpiece during the Shaping of Grooves in the Holes of Tubular Products. J. Superhard Mater. **43**(3), 222–230 (2021). https://doi.org/10.3103/S1063457621030096

7. Hosseini, A., Kishawy, H.A., Moetakef-Imani, B.: Effects of Broaching Operations on the Integrity of Machined Surface. Procedia CIRP **45**, 163–166 (2016). https://doi.org/10.1016/j.procir.2016.02.352

8. Tkachuk, M.M., Grabovskiy, A., Tkachuk, M.A., Hrechka, I., Ishchenko, O., Domina, N.: Investigation of multiple contact interaction of elements of shearing dies. Eastern-European Journal of Enterprise Technologies **4**(7–100), 6–15 (2019). https://doi.org/10.15587/1729-4061.2019.174086

9. Ivanov, V., Pavlenko, I., Liaposhchenko, O., Gusak, O., Pavlenko, V.: Determination of contact points between workpiece and fixture elements as a tool for augmented reality in fixture design. Wireless Netw. **27**(3), 1657–1664 (2019). https://doi.org/10.1007/s11276-019-02026-2

10. Sheikin, S.E., Pogrelyuk, I.M., Sergach, D.A.: Modification of working surface of titanium components of friction units. J. Superhard Mater. **37**(5), 351–356 (2015). https://doi.org/10.3103/S1063457615050093

11. Kukhar, V.V., Grushko, A.V., Vishtak, I.V.: Shape indexes for dieless forming of elongated forgings with sharpened end by tensile drawing with rupture. SPP **284**, 408–415 (2018)

12. Sheykin, S.E., Pashchenko, E.A., Rostotsky, I.: Process lubricant for deforming drawing of pieces made of titanium. Metallurgy and Mining **4**, 38–43 (2017)

13. Prydalnyi, B.I., Sulym, H.T.: Mathematical model of the tensioning in the collet clamping mechanism with the rotary movable input link on spindle units. Journal of Engineering Sciences **8**(1), E23–E28 (2021). https://doi.org/10.21272/jes.2021.8(1).e4

14. Zanger, F., Boev, N., Schulze, V.: Surface Quality after Broaching with Variable Cutting Thickness. Procedia CIRP **13**, 114–119 (2014)

15. Protosenya, A., Karasev, M., Ochkurov, V.: Introduction of the method of finite-discrete elements into the Abaqus/Explicit software complex for modeling deformation and fracture of rocks. Eastern-European Journal of Enterprise Technologies, 6(7(90)), 11–18 (2017)

16. Shepelenko, I., Tsekhanov, Y., Nemyrovskyi, Y., Gutsul, V., Mahopets, S.: Compression Mechanics of Cylindrical Samples with Radial Deformation Limitation. In: Ivanov, V., Pavlenko, I., Liaposhchenko, O., Machado, J., Edl, M. (eds.) DSMIE 2021. LNME, pp. 53–62. Springer, Cham (2021). https://doi.org/10.1007/978-3-030-77823-1_6

Impact of the Tool's Flank Clearance Angle
on the Pitch Diameter Accuracy
of the Tool-Joint Tapered Thread

Oleh Onysko[1]([✉]) [iD], Vitalii Panchuk[1] [iD], Yaroslav Kusyi[2] [iD], Zenovii Odosii[1] [iD],
and Tetiana Lukan[1] [iD]

[1] Ivano-Frankivsk National Technical University of Oil and Gas, 15, Karpatska Street,
Ivano-Frankivsk 76019, Ukraine
o.onysko@nung.edu.ua
[2] Lviv Polytechnic National University, 12, Bandera Street, Lviv 79013, Ukraine

Abstract. The profiling of high-precision tool-joint tapered threads is inextricably linked with technological aspects of their turning. It includes the geometric parameters of the turning cutting tool. Among these parameters, there is one that depends on the design of the thread. This parameter is called the cutting-edge inclination angle, and it corresponds to the helix angle of inclination of the thread. The accuracy of the threads is mainly regulated by three parameters: the accuracy of the profile, the accuracy, the pitch's accuracy, of the pitch diameter. The precision of the pitch diameter is investigated in this article in its functional dependence on the geometric parameter of the cutting tool – the cutting-edge inclination angle. Studies have shown that the magnitude of the change in the pitch diameter increases with an increasing parameter of the cutter and the helix angle of inclination. In turn, the helix angle of the inclination of the thread depends on its diameter, which means that for tool-joint tapered threads of small sizes, the change in the pitch diameter is more apparent. Theoretical research and predictive algorithms based on them have shown that for lock threads of small diameters, the deviation from the value of the pitch diameter can reach 8% of its tolerance. For the largest drilling tool-joint, this deviation is zero.

Keywords: Pitch · Threading lathe tool · Geometric modeling · Convolute screw · Process innovation

1 Introduction

Today the urgent problem of the global energy industry is the development of classical and development of new, including environmentally friendly and energy-saving mining technologies to increase the productivity of oil and gas wells [1]. Successful implementation of such technologies requires improving mining equipment and tools [2], which is characterized by the presence of many threaded cylindrical and tapered connections [3, 4]. Within the technological support of high-performance and high-precision manufacturing of tapered thread between the design of the threads and the geometry of the

cutting part of the cutting tool, the correlation between the angle of the rise of the thread and identical to it the value of the clearance angle of the cutting edge is used. Simultaneously, one of the most significant indicators of the obtained thread's accuracy is its average diameter. Therefore, the influence of technological, design and operational factors on the quality and accuracy of threads in general and their average diameter should be investigated.

2 Literature Review

The influence of the clearance angle of the cutting edge of the cutter on the productivity of turning is investigated in the article [5]. However, it applies to the gears, not the thread. To improve the performance of drilling tools, the following methods are used: design, technological and operational. During the design of the drilling tool, special attention is paid to the rational choice of materials and coatings [6, 7], to the study of temperature distribution [8] and stresses in layered bodies with coatings [9–11], theoretical and experimental studies of mechanical [12] and wear processes [13–15] and corrosion testing of materials [16, 17], as well as take measures to prevent self-unscrewing of threaded joints [18]. Technological methods ensure a given accuracy [19, 20] and roughness of manufacturing parts of threaded joints [21], as errors in their manufacture lead to an increase in stress levels. In addition, make a rational choice of modern metal-cutting equipment [22].

Operational methods include regular washing of machine tools [23, 24] and fixtures [25], the use of vibration protection devices to improve the working conditions of threaded joints [26], and the choice of rational modes of emergency response [27, 28]. The research of the influence of geometrical and technological parameters of turning on the accuracy of the made cuts from stainless steel is carried out in work [29]. The paper [30] investigates the influence of the infeed method on thread turning of AISI 304L austenitic stainless steel considering tool life, the microhardness of the threaded surfaces, and the temperature during the process measured by infrared thermography. The results showed that the temperature significantly increases as the tool wear progresses.

However, the known methods of improving the performance of drilling tools do not fully meet modern requirements for the performance of threaded joints. Therefore, considering the helix inclination angle of tapered thread, and hence the possible influence of the flank clearance angle of the cutter on the accuracy of the pitch diameter is relevant.

3 Research Methodology

Installation of the cutting edge of the lathe cutter at the flank clearance angle of λ leads to the need to use the algorithm for the predictive calculation of changes in the shape of the profile of the obtained thread [29]. It is possible to receive the profile of the specified thread using a technique of application of cylindrical coordinates (Fig. 1). It is assumed that the top of the cutting edge is placed on the axial plane of the thread - *ZOX*. All other points from *A* to *B* and *D* are placed in the plane of rake face, which does not coincide with the axial plane of the thread. The straight line *AC* belonging to the front plane is placed on the *OX* axis.
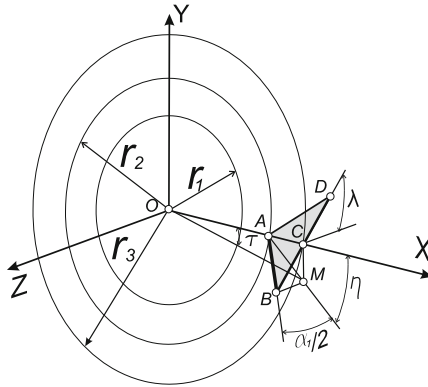
Fig. 1. The scheme to calculate the value of the deviation of the obtained profile of the convolute surface from the specified due to standard profile of the thread; thread parameters: r1– the radius of the main cone; r2 – the radius of the roots; r3 – radius of crests.

In the *XZ* plane, the axial section of the thread ($Y = 0$) is realized in an analytical way as a convoluted helical surface [29], but considering the influence of the flank clearance angle λ:

$$Z(x) = tg\left(\frac{\alpha_1}{2}\right)x\frac{\sin \tau}{\sin \eta} - \frac{P}{2\pi}\tau, \tag{1}$$

where: τ– one of the curvilinear coordinates determined by the formula

$$\tau = \eta - \arcsin\left(\frac{r_2 \sin \eta}{x}\right), \tag{2}$$

P– thread pitch;

$$tg\frac{\alpha_1}{2} = \frac{P\cos \lambda \cos \eta}{2H} = \frac{P\cos \lambda}{2H}\cos\left[arctg\frac{P\sin \lambda}{2H}\right], \tag{3}$$

where: *H* – the height of the fundamental triangle.

Based on the API 7 standard, the scheme of the threaded tool-joint connection of the pin-box in the *ZX* coordinate system with the indicated pitch diameter is made (Fig. 2, Fig. 3).
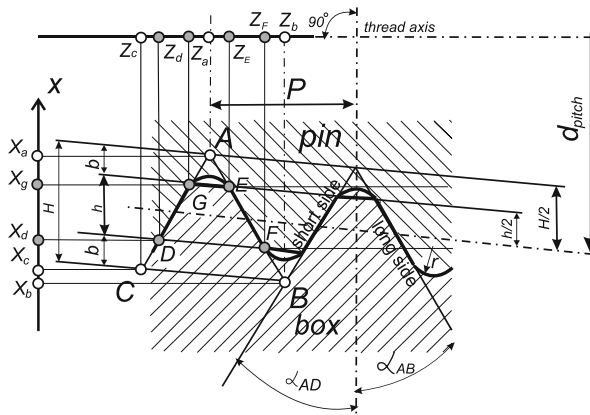
Fig. 2. The scheme of the standard tool-joint tapered thread with the Cartesian coordinate system. H – height of fundamental triangle, h – thread work height, P – thread pitch, dpitch – pitch diameter, αAD, αAB – thread profile angle.

The thread's profile is made using a cutter whose profile is identical to the standard profile *DGEF* of the corresponding size of the thread (Fig. 2). However, the $D_2G_2E_2F_2$ profile of the obtained thread differs from the standard *DGEF* profile, as shown by formulas (1)–(3), which is schematically shown in Fig. 3.
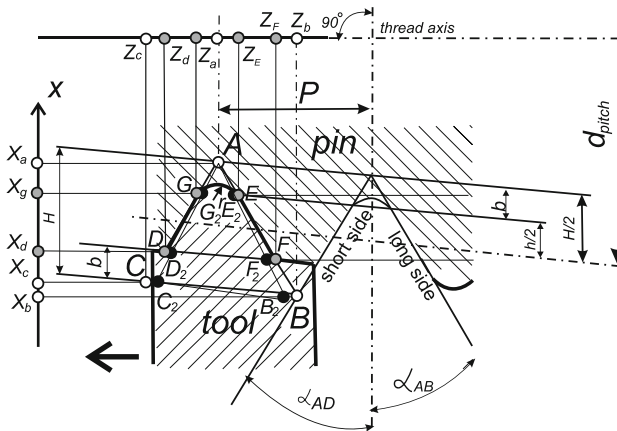
Fig. 3. Scheme of the standard tool-joint tapered thread and cutter tool model with the Cartesian coordinate system.

The curvilinear profile $D_2G_2E_2F_2$ is in reality very close to the straight line one, but its location is such that the vertex points of the standard and obtained profiles coincide, and the farther from it, the more distant, for example, point C is distant from point C_2 by the maximum distance Δc (Fig. 4).

There are also no coincidences in the two profiles at the points, which are located on the average diameter, but they are less apparent. Lathe machining of the inner and outer
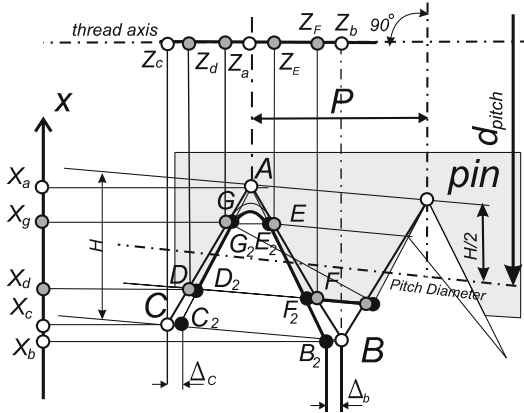
Fig. 4. The displacement scheme of the obtained thread profile is relatively similar to the standard tool-joint tapered thread profile.

tapered thread leads to identical profiles that coincide with the standard in the vicinity of the thread root and are very different in its other points. Therefore, it is essential to combine the obtained models of the threads of the pin and the box to analyze the possible deviations in the value of the pitch diameter. Figure 5 shows a geometric model of the axial section of the pin-box connection. The profiles are obtained by the algorithm of formulas 1–3.
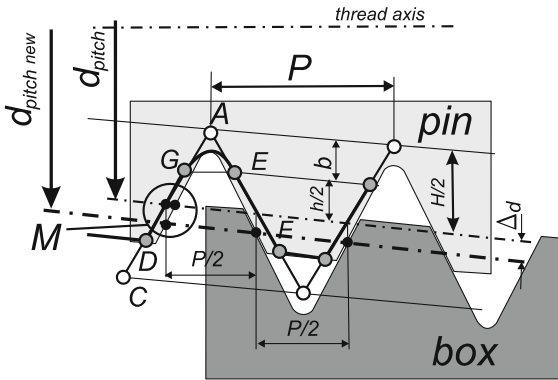
Fig. 5. Comparison of the pin and box threads, considering the offset of their profiles relative to the standard.

From Fig. 5 and 6, it is clear that the method of modeling the pitch diameter of the tapered thread, based on the definition of PITCH DIAMETER: The primary thread pitch diameter is the diameter where the thread thickness is equal to the space between the threads. If the flats at the top and bottom of the thread are the same, the pitch diameter will coincide with the middle of the sloping side of the thread.

As a result of the simulation, the pitch diameter has shifted (bold dashed line) to a value that can be determined using the increase of the area marked by the letter M (from Fig. 5). This area is shown in Fig. 6.

$$\Delta_d = 2 \cdot \Delta_z \cdot ctg30° \tag{4}$$
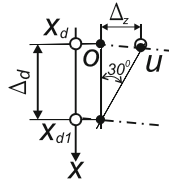
Fig. 6. The scheme for calculating the deviation of the tapered thread pitch diameter.

4 Results

The program calculations are shown in the form of tables. In the left column, the coordinates X are indicated, and in the columns $Z1$, $Z2$, the corresponding coordinates of the standard profile and the profile obtained by the cutter with the corresponding flank clearance angle are indicated (Fig. 7). Column $Z2$-$Z1$ shows the point by point mutual deviation of the profiles. The next fragments (Fig. 7, Fig. 8, Fig. 9, Fig. 10) show the results of program calculation of the profile points and $\Delta Z = Z_2 - Z_1$ of the different sizes of drilling string tapered thread from smallest NC10, throw middle NC23 and NC50 to biggest NC77. The deviation of ΔZ at the place near point M is determined by frame.

X	Z	Z1	Z2	Z-Z1	Z2-Z1
10,290	0,000	0,000	0,000	0,000	0,000
10,590	0,173	0,173	0,172	-0,001	-0,001
10,890	0,345	0,346	0,344	-0,001	-0,002
11,190	0,518	0,520	0,517	-0,002	-0,003
11,490	0,690	0,693	0,689	-0,003	-0,004
11,790	0,863	0,866	0,861	-0,003	-0,005
12,090	1,040	1,040	1,030	-0,004	-0,006
12,390	1,210	1,210	1,210	-0,004	-0,007
12,690	1,380	1,390	1,380	-0,005	-0,008
12,990	1,550	1,560	1,550	-0,005	-0,009
13,290	1,730	1,730	1,720	-0,006	-0,010
13,590	1,900	1,910	1,890	-0,006	-0,010
13,890	2,070	2,080	2,070	-0,006	-0,011
14,190	2,240	2,250	2,240	-0,007	-0,012

Fig. 7. Calculation of the profile of the thread NC10 at the following values of the flank clearance angle of the cutting edge: $\lambda = 3{,}740°$. *Diameter of the smaller conical base:* $d_1 = 25{,}48$ mm, P $= 4{,}23$mm, $H = 3{,}66$ mm, deviations in the value of the pitch diameter: $\Delta d = 0{,}006·1{,}73·2 = 0{,}02$ mm. Calculating step along axis of X is 0,3 mm.

Based on the obtained data, a table of dependence of the change of the tool-joint tapered thread pitch diameter Δ_d depending on their sizes, which are represented by the

X	Z	Z1	Z2	Z-Z1	Z2-Z1
22,160	0,000	0,000	0,000	0,000	0,000
22,450	0,173	0,173	0,173	0,000	0,000
22,750	0,346	0,346	0,346	-0,001	-0,001
23,050	0,519	0,520	0,519	-0,001	-0,001
23,350	0,692	0,693	0,692	-0,001	-0,001
23,650	0,864	0,866	0,864	-0,002	-0,002
23,950	1,040	1,040	1,040	-0,002	-0,002
24,250	1,210	1,210	1,210	-0,002	-0,002
24,550	1,380	1,390	1,380	-0,003	-0,003
24,850	1,560	1,560	1,560	-0,003	-0,003
25,150	1,730	1,730	1,730	-0,003	-0,003
25,450	1,900	1,910	1,900	-0,003	-0,003
25,750	2,070	2,080	2,070	-0,004	-0,004
26,050	2,250	2,250	2,250	-0,004	-0,004
26,350	2,420	2,420	2,420	-0,004	-0,004
26,650	2,590	2,600	2,590	-0,005	-0,005
26,950	2,770	2,770	2,770	-0,005	-0,005
27,250	2,940	2,940	2,940	-0,005	-0,005
27,550	3,110	3,120	3,110	-0,006	-0,006
27,850	3,290	3,290	3,290	-0,006	-0,006

Fig. 8. Calculation of the profile of the thread NC23 at the following values of the flank clearance angle of the cutting edge $\lambda = 2{,}610°$. *Diameter of the smaller conical base: $d_1 = 52{,}43$ mm, P = 6,35 mm, H = 5,49 mm, deviations in the value of the pitch diameter: $\Delta d = 0{,}003 \cdot 1{,}73 \cdot 2 = 0{,}01$ mm. Calculating step along the axis of X is 0,3 mm.*

X	Z	Z1	Z2	Z-Z1	Z2-Z1
53,110	0,000	0,000	0,000	0,000	0,000
53,510	0,231	0,231	0,231	0,000	0,000
53,910	0,462	0,462	0,462	0,000	0,000
54,310	0,693	0,693	0,692	0,000	0,000
54,710	0,923	0,924	0,923	0,000	0,000
55,110	1,150	1,150	1,150	0,000	-0,001
55,510	1,390	1,390	1,380	0,000	-0,001
55,910	1,620	1,620	1,620	-0,001	-0,001
56,310	1,850	1,850	1,850	-0,001	-0,001
56,710	2,080	2,080	2,080	-0,001	-0,001
57,110	2,310	2,310	2,310	-0,001	-0,001
57,510	2,540	2,540	2,540	-0,001	-0,001
57,910	2,770	2,770	2,770	-0,001	-0,001
58,310	3,000	3,000	3,000	-0,001	-0,001
58,710	3,230	3,230	3,230	-0,001	-0,002
59,110	3,460	3,460	3,460	-0,001	-0,002

Fig. 9. Calculation of the profile of the thread NC50 at the following values of the flank clearance angle of the cutting edge $\lambda = 1{,}090°$. *Diameter of the smaller conical base: $d_1 = 128{,}05$ mm, P = 4,23 mm, H = 3,66 mm, deviations in the value of the pitch diameter: $\Delta d = 0{,}001 \cdot 1{,}73 \cdot 2 = 0{,}004$ mm. Calculating step along the axis of X is 0,3 mm.*

X	Z	Z1	Z2	Z-Z1	Z2-Z1
76,940	0,000	0,000	0,000	0,000	0,000
77,340	0,231	0,231	0,231	0,000	0,000
77,740	0,462	0,462	0,462	0,000	0,000
78,140	0,693	0,693	0,693	0,000	0,000
78,540	0,924	0,924	0,924	0,000	0,000
78,940	1,150	1,150	1,150	0,000	0,000
79,340	1,390	1,390	1,390	0,000	0,000
79,740	1,620	1,620	1,620	0,000	0,000
80,140	1,850	1,850	1,850	0,000	0,000
80,540	2,080	2,080	2,080	0,000	0,000
80,940	2,310	2,310	2,310	0,000	0,000
81,340	2,540	2,540	2,540	0,000	0,000
81,740	2,770	2,770	2,770	0,000	0,000
82,140	3,000	3,000	3,000	0,000	0,000
82,540	3,230	3,230	3,230	0,000	0,000
82,940	3,460	3,460	3,460	0,000	0,000

Fig. 10. Calculation of the profile of the thread NC77 at the following values of the flank clearance angle of the cutting edge $\lambda = 0{,}501°$. *Diameter of the smaller conical base: $d_1 = 161{,}87$ mm, P = 4,23 mm, H = 5,47 mm, deviations in the value of the pitch diameter: $\Delta d = 0{,}000 \cdot 1{,}73 \cdot 2 = 0{,}000$ mm. Calculating step along axis of X is 0,4 mm.*

parameters: pitch P, the height of fundamental triangle H, the diameter of the smaller base of the cone d_1. According to the API 7 standard, the accuracy of the pitch diameter for the pin is $+$ 0.25 mm, and for the box, it is -0.25 mm. This figure is placed in a separate column of table 1.

Table 1. The magnitude of the change in the pitch diameter of the tool-joint tapered thread depends on their size, including the following parameters: the diameter of the smaller base d1, the pitch P, and the height of fundamental triangle H.

Size	d_1 diameter of the smaller base, mm	P mm	H mm	Coordinate x of Pitch diameter, mm	Δz, mm	Change of Pitch diameter Δ_d, mm	Percent of Pitch Diameter Tolerance $\pm$ 0,25 mm, %
NC10	25,48	4,23	3,66	12,09	0,006	0,02	8
NC23	52,43	6,35	5,47	25,15	0,003	0,01	4
NC50	114,34	6,35	5,49	55,91	0,001	0,004	1,6
NC77	161,87	4,23	5,47	80,14	0,000	0,0	0

The analysis of the obtained results shows that the functional dependence of the change in the pitch diameter on the step size or the height of the fundamental triangle is not detected. But it is evident that with the increasing diameter of the thread cone smaller base, the magnitude of the change in its pitch diameter decreases from 0.2 to 0.0 (mm).

5   Conclusions

Theoretical research and algorithmic prediction calculations of the accuracy of the process of threading on their basis have shown the following.

The main tool factor that affects the change in the pitch diameter of the tapered thread is the value of the flank clearance angle of the cutter because, with its increasing, the pitch diameter increases too.

The increase in the pitch diameter of the tapered thread functionally depends on the diameter of the conical base, i.e., an increase in this diameter leads to a decrease of the magnitude of the change in the pitch diameter deviation and vice versa.

Among the tool-joint tapered threads of all sizes, the most affected by the change in the pitch diameter are the threads of size NC10 in which the predicted calculation indicates that the deviation of the pitch diameter at the flank clearance angle of $\lambda =$ 3,740° will be only near 8% of the tolerance for the pitch diameter.

The values of the average diameter of the tapered threads of the largest sizes do not depend at all on the value of clearance angle of the cutting edge of the cutter.

In further studies, it is planned to identify the average diameter's functional dependences on the cutter rake angle value.

References

1. Bazaluk, O., Slabyi, O., Vekeryk, V., Velychkovych, A., Ropyak, L., Lozynskyi, V.: A Technology of hydrocarbon fluid production intensification by productive stratum drainage zone reaming. Energies **14**(12), 3514 (2021). https://doi.org/10.3390/en14123514

2. Bazaluk, O., Velychkovych, A., Ropyak, L., Pashechko, M., Pryhorovska, T., Lozynskyi, V.: Influence of heavy weight drill pipe material and drill bit manufacturing errors on stress state of steel blades. Energies **14**(14), 4198 (2021). https://doi.org/10.3390/en14144198

3. Panchuk, V., Onysko, O., Kotwica, K., Barz, C., Borushchak, L.: Prediction of the accuracy of the tapered thread profile. J. Eng. Sci. **8**(2), B1–B6 (2021). https://doi.org/10.21272/jes.2021.8(2).b1

4. Dehtiarov, I.M., Neshta, A.O., Samardak, M.P., Antosz, K., Avramenko, S.E.: Contact of working surfaces for spherical washers and recommendations for determining the gap in the joint. J. Eng. Sci. **7**(2), B1–B7 (2020). https://doi.org/10.21272/jes.2020.7(2).b1

5. Kuhn, F., Lopenhaus, C., Klocke, F.: Analysis of the influence of the Working Angles on the Tool Wear in Gear Hobbing. Gear Technogy January/February, 56–66 (2018)

6. Ropyak, L.Y., Pryhorovska, T.O., Levchuk, K.H.: Analysis of materials and modern technologies for PDC drill bit manufacturing. Prog. Phys. Met. **21**(2), 274–301 (2020)

7. Kostyk, K., et al.: Simulation of diffusion processes in chemical and thermal processing of machine parts. Processes **9**(4), 698 (2021). https://doi.org/10.3390/pr9040698

8. Tatsiy, R.M., Pazen, O.Y., Vovk, S.Y., Ropyak, L.Y., Pryhorovska, T.O.: Numerical study on heat transfer in multilayered structures of main geometric forms made of different materials. J. Serbian Society Comput. Mech. **13**, 36–55 (2019). https://doi.org/10.24874/JSSCM.2019.13.02.04

9. Bedzir, A.A., Shatskii, I.P., Shopa, V.M.: Nonideal contact in a composite shell structure with a deformable filler. Int. Appl. Mech. **31**(5), 351–354 (1995)

10. Bulbuk, O., Velychkovych, A., Mazurenko, V., Ropyak, L., Pryhorovska, T.: Analytical estimation of tooth strength, restored by direct or indirect restorations. Eng. Solid Mech. **7**, 193–204 (2019). https://doi.org/10.5267/j.esm.2019.5.004

11. Ropyak, L.Y., Makoviichuk, M.V., Shatskyi, I.P., Pritula, I.M., Gryn, L.O., Belyakovskyi, V.O.: Stressed state of laminated interference-absorption filter under local loading. Functional Materials **27**(3), 638–642 (2020). https://doi.org/10.15407/fm27.03.638

12. Ivanov, V., Pavlenko, I., Kuric, I., Kosov, M.: Mathematical modeling and numerical simulation of fixtures for fork-type parts manufacturing. In: Knapčíková, L., Balog, M. (eds.) Industry 4.0: Trends in Management of Intelligent Manufacturing Systems. EICC, pp. 133–142. Springer, Cham (2019). https://doi.org/10.1007/978-3-030-14011-3_12

13. Pryhorovska, T.O., Chaplinskyy, S.S.: Probabilistic estimate of pdc drill bit wear rate. Naukovyi Visnyk Natsionalnoho Hirnychoho Universytetu **2014**(5), 39–45 (2014)

14. Ivanov, O., Prysiazhnyuk, P., Lutsak, D., Matviienkiv, O., Aulin, V.: Improvement of abrasion resistance of production equipment wear parts by hardfacing with flux-cored wires containing boron carbide/metal powder reaction mixtures. Manag. Syst. Prod. Eng. **28**, 178–183 (2020). https://doi.org/10.2478/mspe-2020-0026

15. Saakiyan, L.S., Efremov, A.P., Ropyak, L.Y., Gorbatskii, A.V.: A method of microelectrochemical investigations. Soviet Mater. Sci. **23**(3), 267–269 (1987). https://doi.org/10.1007/BF00720884

16. Pashechko, M.I., Shyrokov, V.V., Duryahina, Z.A., Vasyliv, K.: Structure and corrosion-mechanical properties of the surface layers of steels after laser alloying. Mater. Sci. **39**, 108–117 (2003). https://doi.org/10.1023/A:1026134714719

17. Shatskyi, I., Ropyak, L., Velychkovych, A.: Model of contact interaction in threaded joint equipped with spring-loaded collet. Eng. Solid Mech. **8**(4), 301–312 (2020). https://doi.org/10.5267/j.esm.2020.4.002

18. Pryhorovska, T., Ropyak, L.: Machining error influence on stress state of conical thread joint details. In: Proceedings of the International Conference on Advanced Optoelectronics and Lasers, CAOL, 9019544, pp. 493–497 (2019). DOI: https://doi.org/10.1109/CAOL46282.2019.9019544

19. Onysko, O., Kopei, V., Panchuk, V., Medvid, I., Lukan, T.: Analytical study of kinematic rake angles of cutting edge of lathe tool for tapered thread manufacturing. In: Tonkonogyi, V., et al. (eds.) InterPartner 2019. LNME, pp. 236–245. Springer, Cham (2020). https://doi.org/10.1007/978-3-030-40724-7_24

20. Ropyak, L.Y., Vytvytskyi, V.S., Velychkovych, A.S., Pryhorovska, T.O., Shovkoplias, M.V.: Study on grinding mode effect on external conical thread quality. In: IOP Conference Series: Materials Science and Engineering vol. 1018(1), pp. 012014 (2021). https://doi.org/10.1088/1757-899x/1018/1/012014

21. Yakovenko, I., Permyakov, A., Prihodko, O., Basova, Y., Ivanova, M.: Structural optimization of technological layout of modular machine tools. In: Tonkonogyi, V., et al. (eds.) InterPartner 2019. LNME, pp. 352–363. Springer, Cham (2020). https://doi.org/10.1007/978-3-030-40724-7_36

22. Panevnik, D.A., Velichkovich, A.S.: Assessment of the stressed state of the casing of the above-bit hydroelevator. Neftyanoe Khozyaystvo – Oil Industry **1**, 70–73 (2017)

23. Velichkovich, A.S., Dalyak, T.M.: Assessment of stressed state and performance characteristics of jacketed spring with a cut for drill shock absorber. Chem. Pet. Eng. **51**(3–4), 188–193 (2015). https://doi.org/10.1007/s10556-015-0022-3

24. Wojciechowski, S., Twardowski, P.: Tool Life and process dynamics in high speed ball end milling of hardened steel. Procedia CIRP **1**, 289–294 (2012). https://doi.org/10.1016/j.procir.2012.04.052

25. Ivanov, V., Dehtiarov, I., Pavlenko, I., Kosov, M., Hatala, M.: Technological assurance and features of fork-type parts machining. In: Ivanov, V., et al. (eds.) DSMIE 2019. LNME, pp. 114–125. Springer, Cham (2020). https://doi.org/10.1007/978-3-030-22365-6_12

26. Moisyshyn, V., Levchuk, K.: The impact of vibration mechanism' installation place on the process of retrieving stuck drill pipe. Mining of Mineral Deposits **10**, 65–76 (2016). https://doi.org/10.15407/mining10.03.065

27. Onysko, O., Medvid, I., Panchuk, V., Rodic, V., Barz, C.: Geometric modeling of lathe cutters for turning high-precision stainless steel tapered threads. In: Ivanov, V., Trojanowska, J., Pavlenko, I., Zajac, J., Peraković, D. (eds.) DSMIE 2021. LNME, pp. 472–480. Springer, Cham (2021). https://doi.org/10.1007/978-3-030-77719-7_47

28. Krol, O., Porkuian, O., Sokolov, V., Tsankov, P.: Vibration stability of spindle nodes in the zone of tool equipment optimal parameters. Comptes rendus de l'Acade'mie bulgare des Sciences **72**(11), 1546–1556 (2019). https://doi.org/10.7546/CRABS.2019.11.12

29. Costa, C.E., Polli, M.L.: Effects of the infeed method on thread turning of AISI 304L stainless steel. J. Braz. Soc. Mech. Sci. Eng. **43**(5), 1–9 (2021). https://doi.org/10.1007/s40430-021-02978-7

30. An, Q.L., Guo, G.G., Zheng, X.H., Chen, M., Liu, G., Zhang, Y.S.: Experimental study on cutting characteristics for buttress thread turning of 13% Cr stainless steel. In: Advances in Materials Processing IX in Key Engineering Materials, vol. 443, pp. 262–267 (2010)

Improvement of the Efficiency of Fine Boring for Stepped Holes with a Large Diameter Range

Alexandr Orgiyan[1] 🅳, Gennadii Oborskyi[1] 🅳, Vitalii Ivanov[2(✉)] 🅳,
Anna Balaniuk[1] 🅳, and Vasyl Kolesnik[1] 🅳

[1] Odessa Polytechnic National University, 1, Shevchenko Ave., Odessa 65044, Ukraine
[2] Sumy State University, 2, Rymskogo-Korsakova St., Sumy 40007, Ukraine
ivanov@tmvi.sumdu.edu.ua

Abstract. The results of experimental studies of the efficiency of boring two-step holes with a large difference in diameters are described in this paper. Boring was carried out with unique cantilever boring bars, ensuring recommended cutting speed at different steps. These machining conditions increase the boring efficiency due to the same wear rate of cutters with the recommended geometry. The unique boring bar has steps of the same length, which results in an average value of the influence coefficients between the cutters. The results of studies of conventional and stepped boring bars are compared. The paper is devoted to the possibility of fine boring of stepped holes with a large difference in step diameters and unique boring bars providing the same recommended cutting speed. Due to such boring, the wear of the cutters is practically the same, which leads to an increase in boring accuracy, the stability of the roughness values and deviations from roundness, as well as boring at one setup, which makes it possible to reduce the time for adjusting the cutters.

Keywords: Process innovation · Industrial growth · Wear resistance · Two-stepped boring bar · Boring cutter · Roughness · Accuracy · Roundness deviations

1 Introduction

Researchers focus on studying oscillations of cantilever boring bars mounted on the spindle heads [1]. The relative movements of the cutter and the workpiece (static and dynamic) determine the vibrations that occur in the closed dynamic system of the machine and negatively affect the achievable accuracy [2]. An analysis of the round-hole patterns of bored holes shows that vibrations are a factor that determines the errors in cross-sectional shape and machining accuracy [3, 4].

Cantilever boring bars are widely used, providing high productivity when boring smooth holes by unique bore finishing machines. However, it should be noted that it is often necessary to bore stepped holes. Thus, according to our estimates, 21% of fine boring machines are equipped with two-stepped boring bars and more than 10% with three-stepped boring bars. We consider that the insufficient use of multistep cantilever boring bars is due to the lack of the necessary substantiation of the methodology

for designing unique designs of boring bars and multi-cutter heads. One of the main limitations of cantilever boring bars is the increased bending compliance of the cutter (technological compliance), which leads to a decrease in their vibration resistance. At the same time, cantilever boring bars also exhibit significant variability of technological compliance during rotation due to changes in contact conditions in the bearings of the spindle support devices.

2 Literature Review

The main regularities in the development of forced vibrations during multi-cutter fine boring have been studied in a number of works, for example, in [5]. In particular, the mutual influence of the cutters, the sources of vibration excitation depending on the parameters of the elastic system of the machine tool and the cutting process, as well as the dependence of the vibration amplitudes on the ratio of the lengths and diameters of the steps, etc., have been investigated [6].

One of the unsolved problems affecting the efficiency and accuracy of multi-cutter boring is the need to stabilize the cutting conditions when machining stepped holes with a significant difference in diameters, 2–3 times. To ensure that the cutters work in the same conditions, you must set the same cutting speed at different steps. This work shows the results of experiments that have been carried out to study and compare parameters of fine boring during the operation of conventional two-step bars and unique boring bars that ensure the same cutting speed at different steps.

Multi-cut boring bars are used for boring stepped holes following the principle of concentration and combination of operations. Stepped cantilever boring bars equipped with vibration dampers for long overhangs are used to increase productivity and machining accuracy in these cases [7, 8]. Difficulties in predicting machining accuracy are due to the need to consider the mutual influence of disturbances from cutting blades at different steps [9]. The dependences of the amplitudes of forced vibrations were studied when changing the geometric parameters of boring bars, on the ratio of the lengths and diameters of the steps, as well as on the cutting conditions [10].

Studies of oscillations of cantilever boring bars are described in many works devoted to the dynamics of machine tools [11, 12]. A feature of cantilever boring bars using is their limited bending stiffness, characterized by the l/d ratio, where l is the length of the boring bar d is the diameter. At l/d < 3, cutting has steady vibration amplitude, without undermining the cutter, with high vibration resistance of the cutting process. Thus, to increase the accuracy and productivity of finishing fine boring, the characteristics of rigidity and vibration resistance [13] are intensively studied.

Let's consider the content of some investigated problems of the dynamics of the fine boring process:

1. Increasing the stiffness of long cantilever boring bars (l / d > 4 - 10) [14].
2. Development of the theory of precision in fine boring and machining errors Identification and reliable control in internal boring [15].
3. Improving vibration resistance of fine boring by increasing the material removal rate. Maximum machining accuracy is ensured due to the optimal setting of the system parameters [16].

4. Influence of lubrication on cutting force reduction during machining in a cryogenic environment [17].

Due to the design of unique cantilever two- and three-stepped boring bars with a difference in diameters of 2–3 steps that ensure boring with cutters at the same cutting speed, output, and machining accuracy show increase. However, studies of the quality of boring with such machining are practically not reflected in the technical literature.

3   Research Methodology

In metalworking practice, it is often necessary to bore stepped holes (for example, two or three steps) with a significant difference in diameter. In this case, the optimal cutting speed is determined based on the material and diameter of the workpiece, the material of the cutter, the depth of cut, feed, etc. For example, when boring holes Ø 100 mm and Ø 50 mm in peace of medium-carbon steel when cutting with two simultaneously operating cutters, the recommended speed cutting equals 200–250 m/min for carbide tools.

A photo and a diagram of a stand with measuring equipment for studying the vibrations of a unique boring bar are shown in Fig. 1 for steps with different diameters.
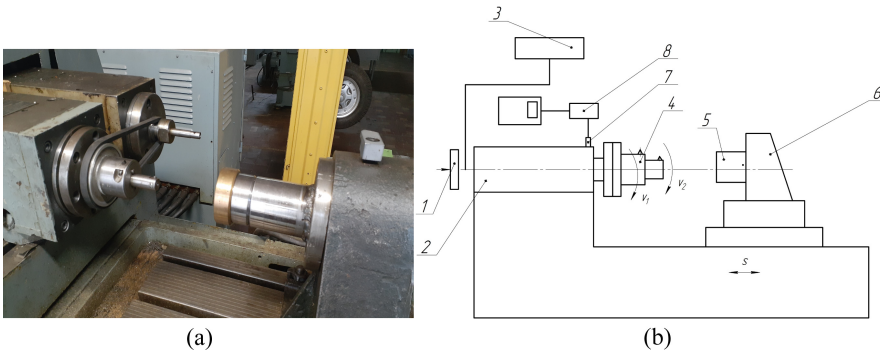
Fig. 1. Photo (a) and a diagram of test stand (b) for boring stepped holes at the same cutting speed: 1 – tachometer; 2 – spindle head; 3 – frequency converter; 4 – unique boring bar; 5 – workpiece; 6 – fixture; 7 – piezoelectric sensor; 8 – vibration spectrum analyzer.

To ensure the same recommended cutting speed for steps with different diameters, the speed of each step should be different. For example, the rotational speed of the step with large diameter should be half of the frequency of a step with a smaller diameter when boring two-step holes with a diameter of Ø85 mm and Ø45 mm.

The task was implemented when boring with a unique boring bar (Fig. 2) mounted on the spindle head. A step with a smaller diameter 1, fitted with a cutter 5 and fixed in the spindle 3 of the boring head 15 using a tapered shank 16, as well as a step with a large diameter 2, equipped with a cutter 6. A step with a larger diameter 2 has the form of a hollow cylinder mounted on a step with a smaller diameter 1 using two duplexed

bearings 4, and step with a larger diameter 2 has angular-shaped grooves 7 for the belt drive. Duplexing of the bearings in order to increase the accuracy of rotation of the boring bar is carried out using spacer sleeves 8, 9 and a clamping nut 11 through the ring 10. The bearings are fixed by the cover 12 using screws 14. A shaft (not shown in the drawing) fitted with pulleys 18 of different diameter is installed in the housing 17 to meet the specified gear ratios.

The fundamental difference between the design of a unique boring bar and all known designs is that a step with a smaller diameter 1 is the base one, on which a step with a large diameter 2 is fixed and has grooves 7 for the belt drive.

This solution ensures the same optimum cutting speed in both steps. During operation, a step with a larger diameter 2 rotates in the same direction as a step with a smaller diameter 1.

A diagram of the design of a unique boring bar is shown in Fig. 2.

The principle of operation of a unique boring bar is that cutters 5 and 6 work simultaneously upon cutting, while the lengths of steps 1 and 2 correspond to the lengths of the holes to be machined. A step with a smaller diameter 1 rotates at a speed that is equal to the rotational speed of the spindle 3 and is equal to the optimal cutting speed for specific machining conditions. To ensure the same operating conditions for cutters 5 and 6, the step with a large diameter 2 is rotated by additional drive, while the ratio of rotation speed of a step with a smaller diameter 1 and a step with a large diameter 2 is inversely proportional to the ratio of their diameters. The required gear ratio is set using pulleys 13 and 18.
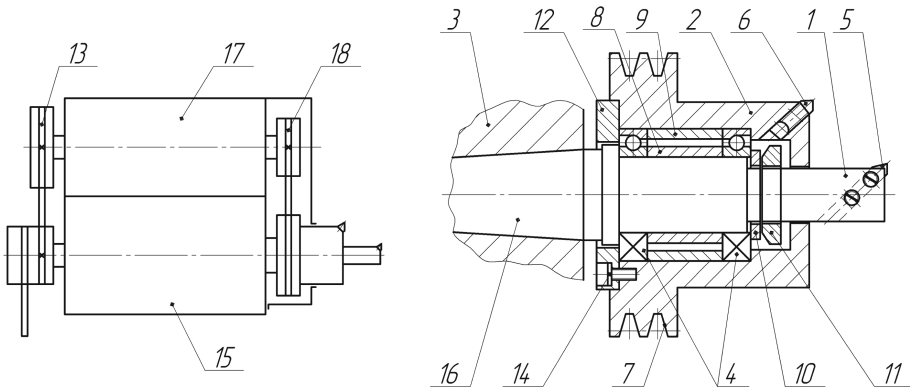
Fig. 2. Drive diagram and design of a unique boring bar for boring stepped holes at the same cutting speed.

Billets of steel 45 and cast iron СЧ 40 were bored. The workpieces were cylindrical bushings with step diameters of 45 and 85 mm. The total length of the unique boring bar is 160 mm. Boring was carried out at a depth of 0.1 and 0.2 mm. Cutting mode: v = 250 m/min in 2 steps; s = 0.06 mm/revolution.

In the experiments, we used cutters made of hard alloy T30K4 (for steel) and ВК3 (for cast iron) with the following geometry:

for steel - = 45°; = 15°; $\alpha = \alpha 1 = 10°$; $\gamma = -10°$; r = 0.2 mm;
for cast iron - with the same geometry, except for $\gamma = -5$; $\lambda = 0$ [18].
Figure 3 shows the numbering of cutters and their location on the steps.
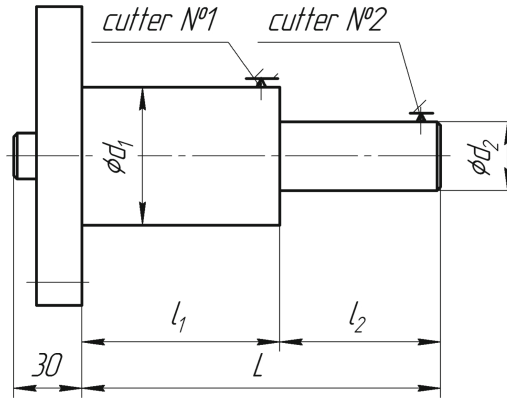
Fig. 3. Design parameters of boring bars used in experiments.

Boring was carried out with a unique stepped boring bar that has steps of the same length equal to 90 mm. Cutters came into operation at the same time. The vibration amplitudes of the cutters, the deviations from the roundness ΔR, the surface roughness Ra, and the wear of the cutters (radial and relative) were determined. The natural frequency of a unique boring bar was determined based on oscillograms of damped oscillations excited by the impact in the section at the second cutter. The rotation frequency was changed sleeplessly using a frequency converter. Each experiment was carried out on 10 samples with six cutters with the same geometry. The criterion for resetting the cutters was the roughness value Ra > 2 μm.

4   Results

Figure 4a shows oscillograms of vibrations of a unique boring bar when 2 cutters operate simultaneously. The vibration amplitudes were determined from the oscillograms and compared with the vibration amplitudes of a conventional two-step boring bar in Fig. 4b.

The vibration amplitudes differ insignificantly, although in Fig. 4b clearly shows oscillations associated with the proximity of the step frequencies. In both cases, the values are expressed in microns.

(a) $v_1 = v_2 = 200$ m/min

(b) $v_2 = 200$ m/min
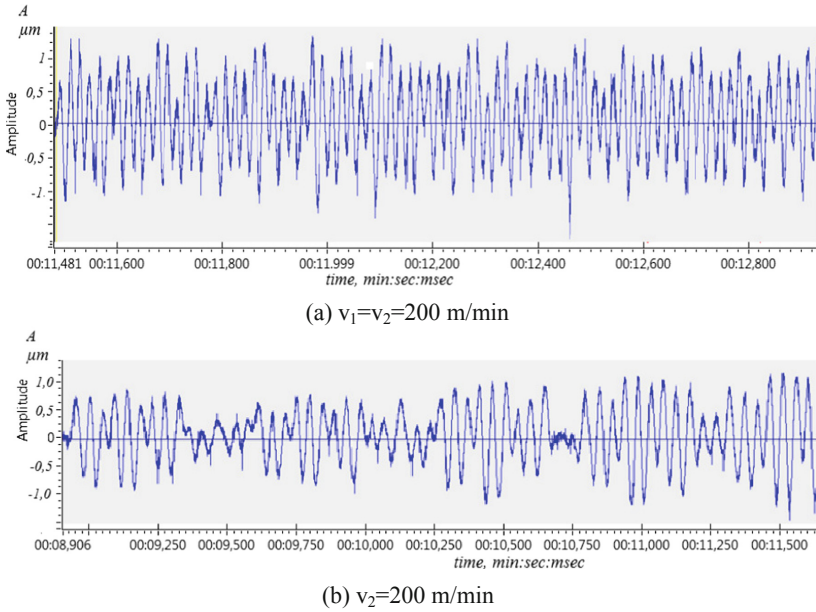
Fig. 4. Oscillograms of vibrations: a) with a unique boring bar A = 2.4 µm; b) a conventional boring bar A = 2.1 µm; processed material steel 45; cuting cinditions: $t_1 = t_2 = 0.1$ mm, s = 0.06 mm/rotation.

Figure 5 shows round diagrams of bored two-step holes with conventional and unique boring bars. Cutting conditions are shown in the figure. Roundness deviation measurements were performed on a TALIROUND measuring machine (Japan).

Conventional boring bar
$v_1 = 400$ m/min; $v_2 = 200$ m/min

Unique boring bar
$v_1 = v_2 = 200$ m / min
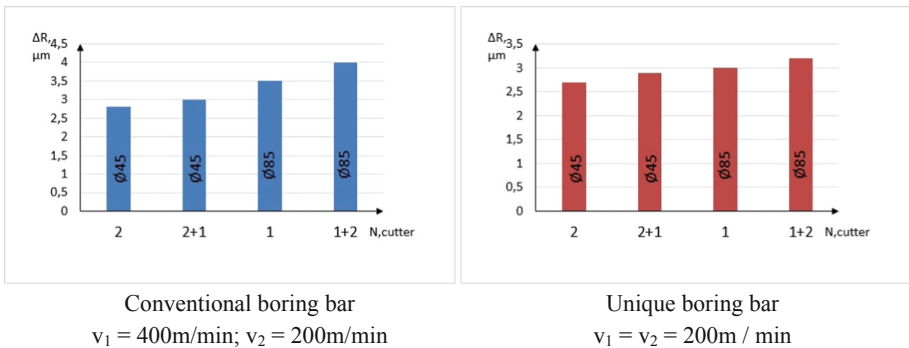
Fig. 5. Diagrams of the dependence of deviations of holes from the circularity on change in the number and sequence of cutters: the processed material is steel 45; $t_1 = t_2 = 0.1$ mm, s = 0.06 mm/revolution; $l_1 = l_2 = 100$ mm.

Based on the machining of roundness charts of bored holes, Fig. 6 shows diagrams of the average values of deviations from the roundness of the holes when changing the number and sequence of cutters (after 10 boring).

Conventional boring bar
$v_1 = 400$m/min; $v_2 = 200$m/min

Unique boring bar
$v_1 = v_2 = 200$m/min
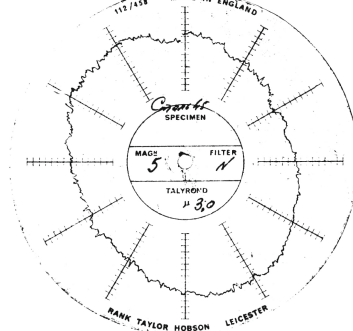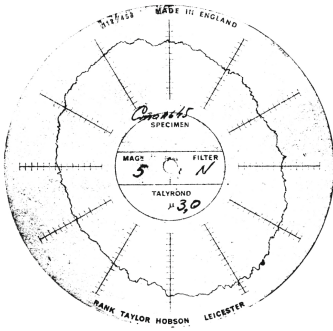
(a) two cutters operate simultaneously, measurements on Ø45 mm;

(c) two cutters operate simultaneously measurements on Ø45 mm
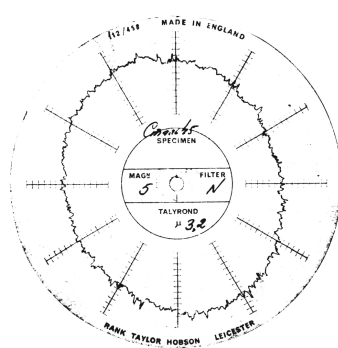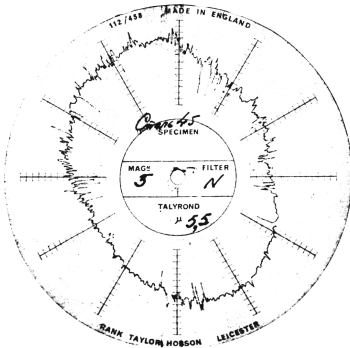
(b) two cutters operate simultaneously, measurements on Ø85 mm;

(d) two cutters operate simultaneously measurements on Ø85 mm

Fig. 6. Examples of roundness charts of bored holes: $t_1 = t_2 = 0.1$ mm, $s = 0.06$ mm/rotation.

It can be seen that the value of deviations from circularity during the operation of the second cutter does not differ significantly. However, in the case of the operation of the first cutter mounted on a conventional boring bar after 10 boring operations, these deviations increase significantly due to wear of the cutting blades. In this case, deviations from circularity when boring with a unique boring bar change slightly.

Figure 7 shows the dependences of the average values of the surface roughness of the holes on the number and sequence of the cutters (the operating conditions of the cutters, as in Fig. 6).
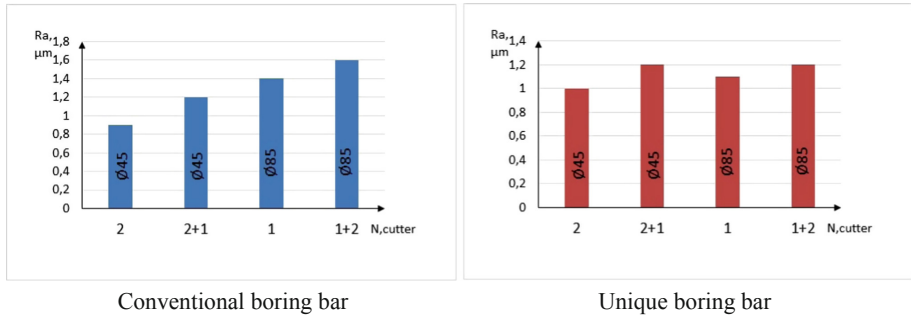
Fig. 7. Diagrams of the dependence of the surface roughness of the holes on the number and sequence of cutters.

5   Conclusions

The experiments show results that characterize vibrations, surface roughness, deviations from roundness and wear of cutting blades. The results obtained during boring with a conventional boring bar and a unique boring bar that ensures same linear speed of the cutting blades at different steps were compared. In the first case, the cutting speeds on the cutters differ by a factor of 2, and the recommended cutting speed is set on the second cutter, which is farthest from the spindle head. Stepped holes with the same step lengths were machines. This ensured the average values of the influence coefficients that determine the transfer of disturbances between cutters during their joint operation.

It should be noted that the comparison of the results is characterized by insignificant changes in the vibration amplitudes. The wear values of the cutting blades during the transition from boring with a solid boring bar to boring with a unique boring bar on the second cutter are practically the same and are within the range of 7–8 μm/103 m. The lower wear value corresponds to a conventional boring bar. The wear values on the first cutter (a step with a large diameter) for such boring bars are different: the relative wear is 13–18 μm/10^3 for conventional boring bar and 8–9 μm/10^3 for a unique boring bar, wear measurement error is 0.5 μm.

The paper devotes to possibility of fine boring of stepped holes with a large difference in step diameters with unique boring bars providing the same recommended cutting speed. Due to such boring, the wear of the cutters is practically the same, which leads to an increase in boring accuracy, the stability of the roughness values and deviations from roundness, as well as boring at one setup, which makes it possible to reduce the time for adjusting the cutters.

Boring of hole steps at the same cutting speed is ensured when designing unique boring bars, taking into account the geometric characteristics of the part, i.e. lengths and diameters of the steps, the material of the workpieces, as well as cuting cinditions.

The study of dynamic interactions upon boring with two- and three-stepped boring bars will be described in the next publication.

References

1. Hayati, S., Shahrokhi, M., Hedayati, A.: Development of a frictionally damped boring bar for chatter suppression in boring process. The International Journal of Advanced Manufacturing Technology **113**(9–10), 2761–2778 (2021). https://doi.org/10.1007/s00170-021-06791-3

2. Suyama, D.I., Diniz, A.E., Pederiva, R.: The use of carbide and particle-damped bars to increase tool overhang in the internal turning of hardened steel. The International Journal of Advanced Manufacturing Technology **86**(5–8), 2083–2092 (2016). https://doi.org/10.1007/s00170-015-8328-z

3. Ivanov, V., Dehtiarov, I., Pavlenko, I., Kosov, M., Hatala, M.: Technological Assurance and Features of Fork-Type Parts Machining. In: Ivanov, V., et al. (eds.) DSMIE 2019. LNME, pp. 114–125. Springer, Cham (2020). https://doi.org/10.1007/978-3-030-22365-6_12

4. Ivanov, V., Pavlenko, I., Kuric, I., Kosov, M.: Mathematical Modeling and Numerical Simulation of Fixtures for Fork-Type Parts Manufacturing. In: Knapčíková, L., Balog, M. (eds.) Industry 4.0: Trends in Management of Intelligent Manufacturing Systems. EICC, pp. 133–142. Springer, Cham (2019). https://doi.org/10.1007/978-3-030-14011-3_12

5. Kaliński, K.J., Galewski, M.A., Mazur, M.R., Stawicka-Morawska, N.: An improved method of minimizing tool vibration during boring holes in large-size structures. Mater. **14**(16) (2021). DOI: https://doi.org/10.3390/ma14164491

6. Oborskyi, G., Orgiyan, A., Tonkonogyi, V., Balaniuk, A., Muraviova, I.: Dynamics of Fine Boring with Multicutting Console Drilling Rods. In: Tonkonogyi, V., et al. (eds.) InterPartner 2020. LNME, pp. 577–587. Springer, Cham (2021). https://doi.org/10.1007/978-3-030-68014-5_56

7. Kiyak, M., Kaner, B., Sahin, I., Aldemir, B., Cakir, O.: The dependence of tool overhang on surface quality and tool wear in the turning process. Int. J. Adv. Manuf. Technol. **51**(5–8), 431–438 (2010). https://doi.org/10.1007/s00170-010-2654-y

8. Shvets, S.V., Machado, J.: Numerical model of cutting tool blade wear. J. Eng. Sci. **8**(2), A1–A5 (2021). https://doi.org/10.21272/jes.2021.8(2).a1

9. Hessainia, Z., Belbah, A., Yallese, M.A., Mabrouki, T., Rigal, J.-F.: On the prediction of surface roughness in the hard turning based on cutting parameters and tool vibrations. Measurement: J. Int. Meas. Confederation **46**(5) (2013). DOI: https://doi.org/10.1016/j.measurement.2012.12.016

10. Krol, O., Porkuian, O., Sokolov, V., Tsankov, P.: Vibration stability of spindle nodes in the zone of tool equipment optimal parameters. Comptes Rendus de L'Academie Bulgare des Sciences **72**(11), 1546–1556 (2019). https://doi.org/10.7546/CRABS.2019.11.12

11. Alammari, Y., Sanati, M., Freiheit, T., Park, S.S.: Investigation of boring bar dynamics for chatter suppression. Procedia Manuf. **1**, 768–778 (2015). https://doi.org/10.1016/j.promfg.2015.09.059

12. Wojciechowski, S., Twardowski, P., Pelic, M.: Cutting forces and vibrations during ball end milling of inclined surfaces. Procedia CIRP **14**, 113–118 (2014). https://doi.org/10.1016/j.procir.2014.03.102

13. Fallah, M., Moetakef-Imani, B.: Investigation on nonlinear dynamics and active control of boring bar chatter. J. Braz. Soc. Mech. Sci. Eng. **43**(3), 1–27 (2021). https://doi.org/10.1007/s40430-021-02808-w
14. Song, Q., Shi, J., Liu, Z., Wan, Y., Xia, F.: Boring bar with constrained layer damper for improving process stability. The International Journal of Advanced Manufacturing Technology **83**(9–12), 1951–1966 (2015). https://doi.org/10.1007/s00170-015-7670-5
15. Basovich, S., Arogeti, S.: Identification and robust control for regenerative chatter in internal turning with simultaneous compensation of machining error. Mech. Syst. Signal Process. **149**(2021). DOI: https://doi.org/10.1016/j.ymssp.2020.107208
16. Reith, M.J., Bachrathy, D., Stepan, G.: Improving the stability of multi-cutter turning with detuned dynamics. Mach. Sci. Technol. **20**(3), 440–459 (2016). https://doi.org/10.1080/10910344.2016.1191029
17. Sastry, C.C., Hariharan, P., Pradeep Kumar, M., Muthu Manickam, M.A.: Experimental investigation on boring of HSLA ASTM A36 steel under dry, wet, and cryogenic environments. Mater. Manuf. Processes **34**(12), 1352–1379 (2019). https://doi.org/10.1080/10426914.2019.1643477
18. Suslov, A.G., Dalsky, A.G.: Scientific Foundations of Engineering Technology. Machine Building, Moscow (2002)

Simulation Studies of High-Speed Machining

Vadym Stupnytskyy , Oleh Prodanchuk , and Nataliya Stupnytska(✉)

Lviv Polytechnic National University, 12, Bandera St., Lviv 79000, Ukraine
`stupn@i.ua`

Abstract. The research described in the article aims to analyze high-speed machining processes by carrying out cutting simulations in DEFORM 2D software using the finite-element method. The simulation of high-speed cutting processes is very complex because the dimensionality of the modelling problem increases ten-fold compared to medium-speed cutting processes! Therefore, the solution of this problem is characterized primarily by methodological novelty. The proposed app-roach enables a comprehensive analysis of force and thermodynamic processes occurring in the tool and chip formation zone during high-speed cutting. The results of cutting force dynamics and thermal loads at different machining speeds are described in the article. The analysis of tool wear rate for different geometrical designs of a cutting edge is carried out. The correct geometry of the cutting edge reduces friction load on the tool rake face and thus reduces cutting force and tool wear. The phenomenon of excessive growth of cutting force with the increase of machining speed is explained. Guidelines for selecting cutting parameters are described.

Keywords: High-speed machining · Cutting force · Simulation study · Finite element analysis · Cutting parameters · Manufacturing innovation · Industrial growth

1 Introduction

High-speed machining (HSM) is the way to a significant increase in productivity and an additional toolset to improve the machined surface quality and reduce cutting strength. It is because the contact time of the tool with the machined material is so short and the rate of chip formation is so high that the chip removes most of the heat released in the cutting zone, and the workpiece and tool do not have time to heat up [1–3], which is effective for the cutting process. In comparison with machining at medium speeds, the main effect of HSM is not the reduction of machine time due to intensification of cutting parameters but the improvement of machining quality and the possibility of effective use of modern CNC machines [1]. However, high-speed machining also has significant drawbacks, including the proper selection of all process components - power rate, complex CNC system, high accuracy cutting tool, utility with a device clamping system, complicated programming system, and high CNC operator software qualifications. All of these factors add significantly to the cost and ignoring one of these components can completely undo the positive achievements of this cutting method.

The purpose of this study is to analyze high-speed machining processes by creating a finite-element simulation in DEFORM 2D by creating a model as close to actual metalworking conditions as possible. Analysis of the results of such research allows a comprehensive study of the reasons and consequences of using various parameters of high-speed cutting. It is crucial for studying complex rheological processes realized in the chip formation zone.

The simulation of high-speed cutting is a complex study due to the rapid deformation, thermodynamic and stress-strain processes. Adequacy of simulation results largely depends on the correctness of the problem statement, the use of reliable models of frictional and force interaction between the tool, chip, and workpiece, consideration of specific features of form, and the right choice of mathematical apparatus for research. This study is devoted to the description of these factors. The study results entirely correlate with the experimental results given in [4].

2   Literature Review

The German researcher Carl Solomon proposed the first concept of High-Speed Machining (HSM) in 1931, who drew an important conclusion: "At certain cutting speeds, heat extraction begins to decrease, accompanied by a reduction in cutting load" (Fig. 1) [5]. The HSM effect is expressed by structural changes in the material (due to plastic deformation carried out at high speed) at the point of separation of the chip. As the rate of deformation increases, the cutting force initially increases and then, at a specific temperature reached in the forming zone, begins to decrease significantly. The chip-tool contact time is so short, and the cutting speed is so high that most of the heat generated in the cutting zone is removed with the chip, and the workpiece and tool cannot heat [3]. It has a beneficial effect on both the force and stress-strain processes in the chip formation zone.
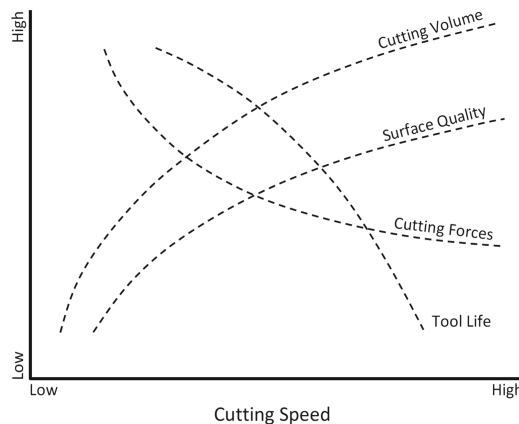
Fig. 1. General properties of high-speed machining [5].

Generally, blade machining of plastic materials produces drain chips, plastic deformation occurs, and it contributes to the efficient cutting of the material. It's observed the

friction process between the chip and the tool's rake face and between the workpiece and the relief face of the tool. In high-speed machining, the coefficient of friction decreases as the speed increases. This is due to softening of the machined material in the cutting zone, in some cases with the appearance of a liquid layer [6].

Many studies [1, 2, 7] have shown that 80% of heat is generated in the formation zone of plastic chips during processing on normal cutting parameters, 18% - on the tool's rake face, and only 2% in the friction tool-workpiece contact zone. However, in [1], it was proved that the chip absorbs 75% heat during HSM, 20% by tool, and 5% by a machined layer of the workpiece.

It is the fundamental principle of the HSM method: the most significant amount of heat produced is removed from the cutting zone along with chips. Like other modern machining methods, high-speed processing has its equipment requirements. Let's analyze these features.

1. High cutting speeds require high spindle speeds (over 20,000 rpm). The high-speed spindle (HSS) design uses a compromise between forces and cutting speeds. As the speed of the spindle increases, its power decreases, e.g., 22 kW (up to 12000 rpm), 12 kW (up to 24000 rpm), 4.5 kW (up to 40,000 rpm). The most critical factor in limiting spindle speeds is the essential bearings' durability. The HSM is characterized by the number DN and is calculated by multiplying the bearing diameter D (mm) by the maximum spindle speed N (rpm). For applications with $DN < 2 \cdot 10^6$, hybrid ball bearings with steel guide bushes and ceramic balls are used, which provide more excellent thermal stability at high speeds. Ceramic balls are durable, stiffer, and much lighter than steel balls. So, they have less centrifugal force. Non-contact bearings (hydrostatic, aerostatic, electrostatic) must be used for applications where the $DN > 2 \cdot 10^6$ [4].

2. The need for a high-speed CNC. HPCC (High Precision Contour Control), where an additional processor is used to increase the speed of feedback signal processing, is compelling. High-speed information processing by powerful processors provides the ability to combine sufficiently precise movements with large working feeds [8].

3. Non-Uniform Rational B-Spline (NURBS) type interpolation is effectively used for HSM [9]. The standard preparation of the CNC program in the CAD/CAM system produces a tool path that is a sequence of short linear movements that approximate the surface of the mathematical model. In this case, the volume of move data in the control program can reach tens of megabytes in the finishing operations. Modern CNC systems can interpolate axis movements smoothly on their own with B-type mathematical splines [10]. Using the built-in NURBS interpolation allows to replace up to 10 frames describing spline interpolation with chords in one frame of the program while maintaining high accuracy of tool movement. Curve interpolation allows the direction to be changed gradually, and the control system maintains a higher average working feed rate than when moving along a polygonal path.

4. The moving part of the tool machine should be less than 10 μm to meet the requirements of dimensional accuracy, surface shape, the accuracy of surface positioning [11]. Significant frame stiffness with good vibration absorption capacity is critical. This condition must be ensured because even relatively small vibrations cause the

carbide tool to break out at high cutting speeds. It is also advisable to provide systems for compensating temperature gaps in the machine's moving parts since high spindle speeds, and high power inputs inevitably lead to temperature inaccuracies.

3 Research Methodology

The primary tool of the described study is the Deform 2D software. The functionality of this software allows us to create a simulation model of high-speed machining. Such basic research parameters as speed and tool design significantly influence the elastic-deformed state and thermodynamic parameters in the cutting zone and allow the creation adequate simulation model of the high-speed cutting process. The advantage of this study is the relative cheapness and rapidity of obtaining the resulting array of results, which can be transformed into a graphical format for further analysis. The accuracy and consistency of the practical verification have been repeatedly verified by experimental studies and provided by the software package's highly efficient mathematical apparatus [12].

At the current stage of science and technology development, modelling of various deformation processes in machining plays an important role, which is facilitated by several factors: modelling allows the researcher to look into the process, estimate the arising stresses and strains, provide for the occurrence of defects; modelling allows to determine the optimal parameters of tool and workpiece to improve process efficiency; modern software modelling complexes provide ample work opportunities. DEFORM-2D is a simulation system designed for analyzing two-dimensional (2D) metal model behaviour in various machining processes. This program uses the most advanced advances in the mathematical (FEA) description of the metal forming processes [13].

The used research method is to analyze simulation results in the rheological modelling system Deform 2D. This system is a multipurpose FEM-analysis program intended to solve two- and three-dimensional dynamic nonlinear problems of solid-state deformation mechanics and problems associated with this process. They implement the explicit and implicit finite element method with the possibility of constructing Lagrangian, Eulerian and hybrid meshes, multi-component fluid dynamics, and the smoothed lattice method based on the Galerkin method. This software included automatic adjustment and smoothing of conventional meshing in degenerate elements, highly efficient algorithms for solving contact problems, a wide range of problem-oriented material specifications, and user programming capabilities. The initial conditions for the DEFORM preprocessor when simulating a machining operation (cutting) are the 2D model of the part (surface) to be machined; cutting parameters; cutting edge geometry, tool material and coating; mechanical and thermophysical characteristics of the machined material (AISI 1020); Usui tool wear model; the total criterion of the repair kit (calculated as the sum of the reduced modelling errors by force vector, velocity vector, and permissible geometric error); deformation modelling type (Lagrange Incremental); iteration method (direct iteration), strain and temperature solver type (Skyline method).

A comparison was made of the most critical parameters of steel AISI 1020 at various speeds and geometry of the cutting tool. The parameters of the stress-strain and thermodynamic state of the workpiece and the tool are analyzed under conditions for modelling with the following cutting speed: 100 m/min; 800 m/min; 1600 m/min. In

addition, imitation studies of the wear of the tool of various designs under high-speed cut conditions were carried out. For the convenience and visibility of the analysis of the obtained data, the entire result array was shown in a graphical format.

4   Results

The simulation study results of the high-speed cutting power parameters are shown in Fig. 2 and Fig. 3.
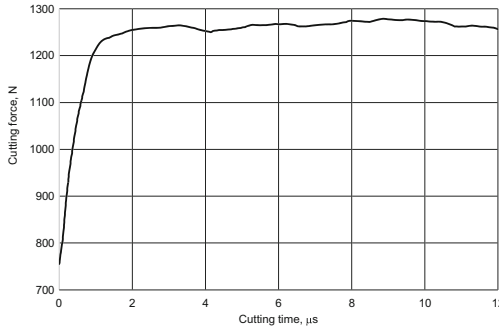
Fig. 2. Cutting force at $V = 100$ m/min

As can be seen on the graph, the steady (permanent) time at $V = 100$ m/min varies between 2–3 µs.
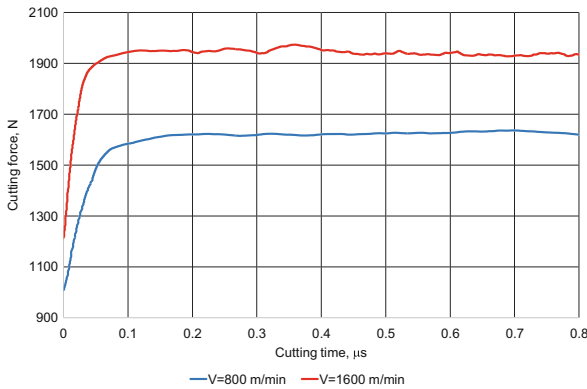
Fig. 3. Cutting forces at $V = 800$ m/min and $V = 1600$ m/min.

As in the previous graph, cutting force depends on machining time. If in Fig. 2 contains only one curve (for $V = 100$ m/min), then in Fig. 3 the results are compared for $V = 800$ m/min (blue curve) and $V = 1600$ m/min (red curve). Illustration of graphs for $V = 100$ m/min separately from graphs for $V = 800$ m/min and $V = 1600$ m/min caused

by a significant difference at the time of output on the established value of cutting. Thus, for V = 800 m/min and V = 1600 m/min, this value is approximately the same and varies between values of 0.06–0.1 μs, and for V = 100 m/min this parameter is approximately 3 μs (which is 30–40 times more).

As in the previous graph, cutting force depends on machining time. If in Fig. 2 contains only one curve (for V = 100 m/min), then in Fig. 3 the results are compared for V = 800 m/min (blue curve) and V = 1600 m/min (red curve). Illustration of graphs for V = 100 m/min separately from graphs for V = 800 m/min and V = 1600 m/min caused by a significant difference at the time of output on the established value of cutting. Thus, for V = 800 m/min and V = 1600 m/min, this value is approximately the same and varies between values of 0.06–0.1 ms, and for V = 100 m/min this parameter is approximately 3 ms (which is 30–40 times more)/

The analysis of graph dependencies showed that at speed V = 1600 m/min, the cutting force is approximately 17% higher than the magnitude obtained by simulating the cutting process at a speed V = 800 m/min. If comparing these values with values obtained at v = 100 m/min, the difference is over 23% and 30%, respectively.

It can be concluded that there is an increase in cutting force when using high-speed machining, but it is not proportional to the increase in cutting speed (in this case, 8 versus 16 times). The cutting force increases rapidly due to the counteracting frictional forces and the periodic formation of ridges on the tool surface. However, why is growth not proportional? The phenomenon of excessive growth of cutting force can be explained by the fact that the machined material at high speeds is subjected to considerable heating, which reduces the strength of the machined material and the coefficient of internal friction. In addition, an increase in cutting speed also reduces the size of the deformation zone.

4.1 Investigation of Temperature Dependence in the Cutting Zone at Various Output Cutting Speeds

One of the main characteristics of the cutting process is temperature. The functionality of the Deform 2D software made it possible to investigate this value, which is shown in Fig. 4. and Fig. 5.
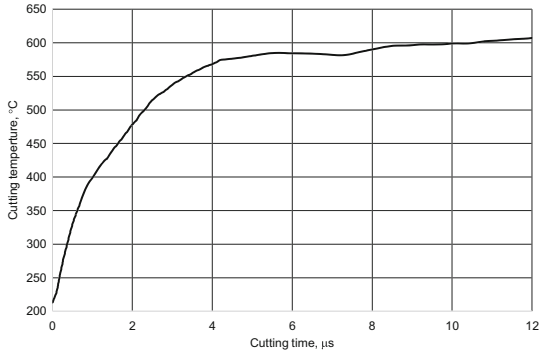
Fig. 4. Graph of cutting temperature changes during machining time with cutting speed V = 100 m/min.

When cutting steel AISI 1020 at normal cutting speeds, the average cutting temperature is approximately 600 °C. Also critical is the chip formation and separation process analysis. With high-speed machining, it is generally one of the critical elements of the cutting process. As can be seen in Fig. 5, most of the heat is removed from the cutting zone by the chips, which reduces the negative impact on tool wear and contributes to better control of machining accuracy.
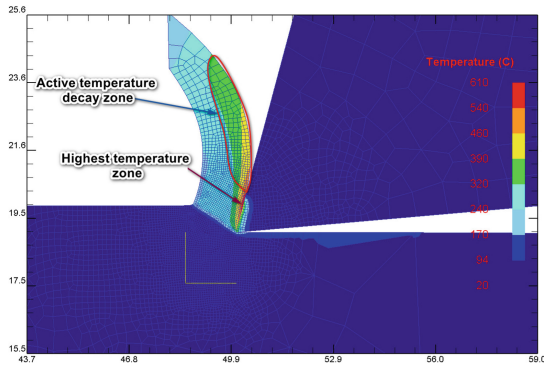
Fig. 5. Temperature indicators in the cutting zone.

Figure 6 illustrates the tool temperature dependence at HSM. At V = 800 m/min and V = 1600 m/min, these values will be 1150 °C and 1400 °C, respectively (that is 550 and 800 degrees higher than at V = 100 m/min). Thus, special requirements for the thermal resistance of the tool must be ensured. It is possible to explain the obtained results of temperature growth by such heat sources in the cutting zone as:

– internal friction between the particles of the material layer being sheared as a result of its deformation during chip formation;
– the friction of the chip against the rake face of the tool;

– the friction of the cutting surface and the machined surface on the relief face of the tool.
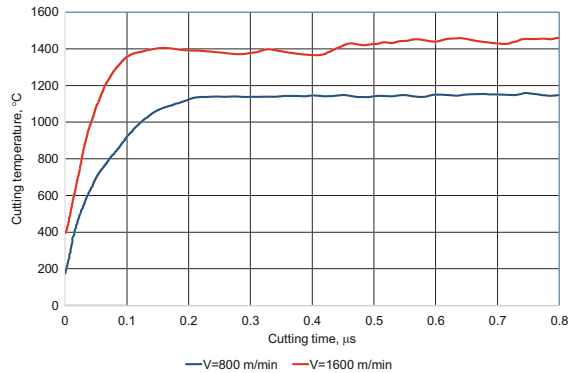
Fig. 6. Comparison of temperature at high cutting speeds.

We would get even more heat with increasing speed if it were not for one of the critical phenomena of HSM, namely heat removal from the cutting zone along with the chips where the heat is quickly removed before it has time to transfer the temperature to the tool.

4.2   Investigation of Cutting Force and Temperature Dependences on Tool Design

Figures 8 and 9 show a comparison of cutting force magnitudes, and this time not as a function of speed but as a function of the geometric configuration of the tool rake face. For this study, two tool designs were analyzed (Fig. 7), which will allow analyzing the influence of cutting edge geometry on the efficiency of high-speed machining most clearly. The rake angle for both tools is 20°, and the relief tool angle is 10°.
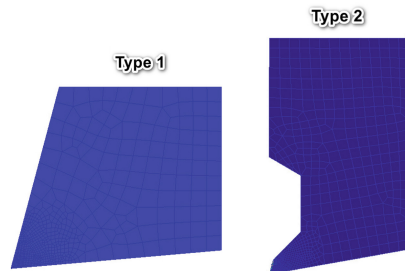
Fig. 7. Investigated designs of the tool.
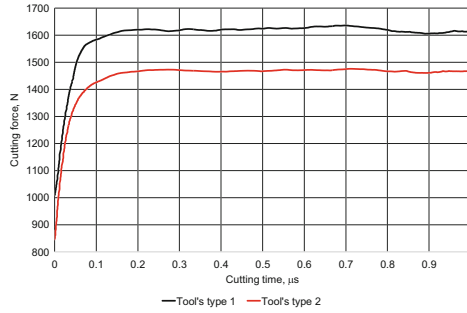
Fig. 8. Comparison of cutting forces with different tool designs at V = 800 m/min.
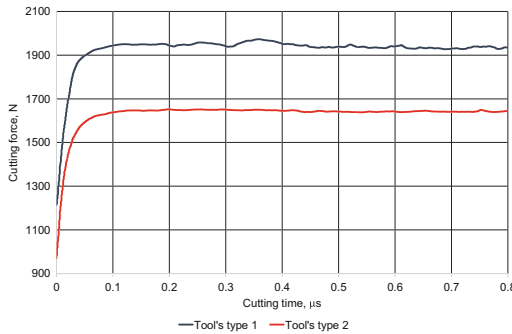
Fig. 9. Comparison of cutting forces with different tool designs at V = 1600 m/min.

The graph shows the tools used: tool type 1 (black curve) and type 2 (red curve). There is a clear difference of 8–9% in cutting load, from which it can be concluded that the required cutting forces for the tool with improved design (type 2) are reduced.

Similar to Fig. 3.8, this graph compares cutting forces depending on the tool design. It is essential that in the preliminary graph, the values of cutting forces for different designs of cutting edge at speed V = 800 m/min are analyzed. In comparison, this graph allows seeing the same dependences already at more high-speed machining - V = 1600 m/min. The resulting curves show a distinct cutting force difference for the different designs of almost 15%, which is significantly greater than machining with different tools at average cutting speed.

Therefore, we can conclude that the tool's design, more precisely its rake face, has a significant influence on the cutting force. It is explained by the fact that during machining, chips are produced, and before their removal from the cutting zone, they can interact with the cutting face, causing abrasion. The friction force distribution is not homogeneous, thus creating high and low tension zones. The design has been modified to eliminate the highest friction force intensity zone and thus reduce the required cutting force. The zone of most significant interaction between cutter and chip has been reduced by changing the tool design.

Not only the machining speed, but also the tool design influences the cutting temperature. Figure 10 shows the temperature values for different tool designs at a V = 800 m/min machining speed.
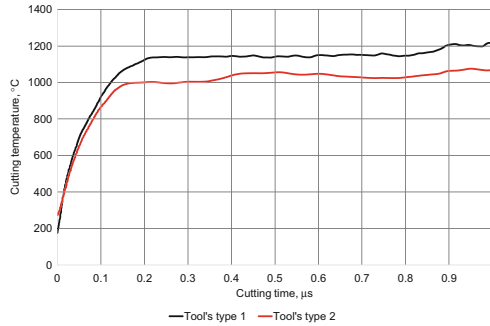
Fig. 10. Comparison of cutting temperature when using tools of various structures at cutting speed V = 800 m/min.

The difference in value between the temperatures of the two different types of tools is 12%, which leads to increased efficiency in using the upgraded tool.

Comparing the average values of the temperature received when simulating machining at speeds of V = 1600 m/min by different types of tools results in a difference of values in size approximately equal to the difference of the previous graph, 10–11%. The average temperature in the cutting zone for a tool type 1 will be about 1420 °C, and for a tool type 2, this temperature is reduced to 1280 °C.

4.3 Investigation of the Influence of the Tool Wear on the Design

The previous part clearly showed the difference in the tool design's impact on the temperature in the cutting zone. A factor such as temperature affects the wear rate of the tool. Nevertheless, to obtain a comprehensive pattern of wear, it is necessary to conduct a separate study, the result of which is shown in Fig. 11.
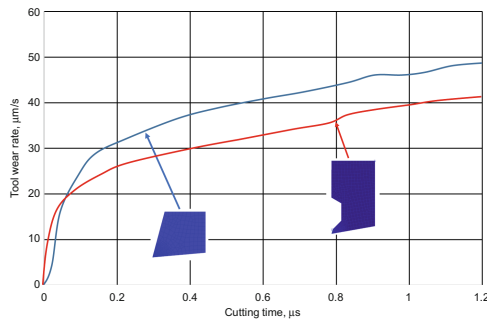
Fig. 11. Dependence of tool wear rate on design.

As shown in Fig. 11, improved design (Type 2) initially has higher values of wear rates, and eventually still wear-resistant improved compared to the standard (Type 1) design of the tool. It should be noted that DEFORM 2D allowed getting accurate data to analyze wear, which has theoretical and practical applications. A more detailed survey of the surface of the cutting edge of the standard tool demonstrates the zone of the most significant wear Fig. 12.
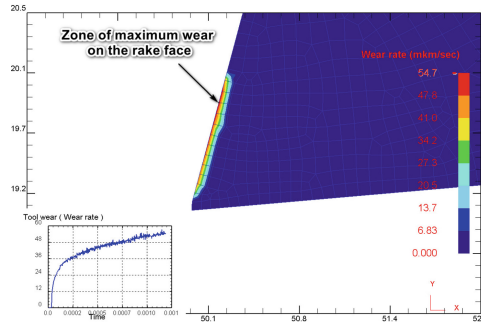
Fig. 12. Zone of maximum wear on the rake face of the standard tool.

For a complete understanding of the nature and extent of the influence of design features on wear rate and magnitude, an optimal variant was found - to create and examine a tool model with a corrected contour of the rake face, thus eliminating the zone of intensive wear Fig. 13.
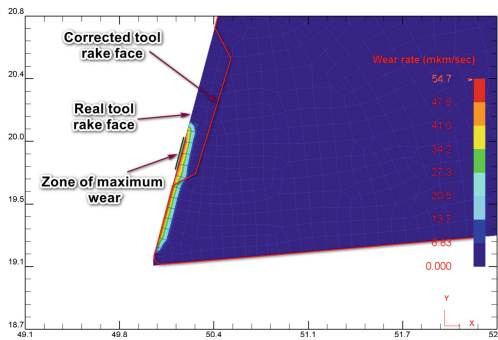
Fig. 13. Zoning the tool's rake face.

By reducing the tool's rake face, which concentrates the zone of most incredible abrasion and thus temperature, we have eliminated the point of maximum concentration, significantly reducing the impact on the rake face and the tool as a whole. The research results of the dependence of the tool wear depth on its design are presented in Fig. 14, where Type 1 is a standard design, and Type 2 is a modified design. The difference in wear values is about 12%, which indicates that the tool is very effective when used with a smaller contact surface.
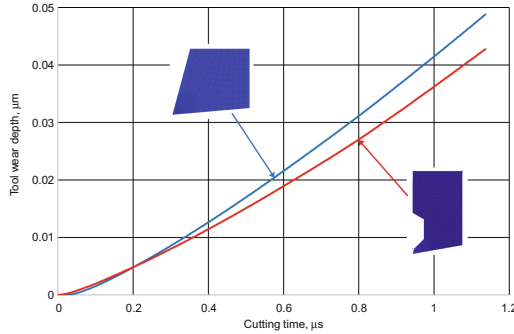
Fig. 14. Dependence of the tool's wear rate on its design.

The reduction in wear rate and depth of wear in the modified tool design can be explained by considering the previous studies that showed a reduction in temperature and cutting force in the modified tool. These parameters have a crucial influence on the wear process, and since both the thermal and cutting forces are higher with the standard tool, it is pretty logical that the wear rate will also be higher. The main reason for this is the size of the abrasion, which makes the tool material rough and removes metal from the surface by forming micro-scratches. Adhesion and diffusion wear also have an effect, especially in high-speed machining.

5   Conclusions

It was analyzed the parameters of the stress-strain and thermodynamic state of the workpiece and tool under simulation conditions at the following cutting speeds: 100 m/s; 800 m/s; 1600 m/s, where 100 m/s is a standard treatment for the comparison with the following investigated high-speed speeds of 800 m/s; 1600 m/s. Simulation studies on the tool-wear capacity of various shapes and form tools in conventional machining and high-speed cutting conditions were also carried out.

When studying the force parameters, analysis of the graphical dependencies showed that at a speed of V = 1600 m/min, the cutting force is 17% higher than the figure obtained when modelling the cutting process at V = 800 m/min. However, by comparing these values to the ones achieved at V = 100 m/min speeds, the difference is about 23% and 30%, respectively.

When investigating the temperature indices at a V = 800 m/min speed, the tool temperature is 1150 °C, at V = 1600 m/min-1400 °C, i.e., 550 and 800 degrees higher at V = 100 m/min (600 °C). Approximately 20% is the difference between treatment at V = 800 m/min and V = 1600 m/min.

The analysis of the cutting force dependence on the tool's design for conventional machining shows a difference in cutting force of 8–9%, making it possible to conclude the reduction of the required cutting force for a tool with an improved design. Even for high-speed machining, the resulting curves show a difference in cutting force for the various designs of up to 15%, which is considerably more significant than machining with different tools at average speed. Analyzing the research results of the effect of

tool design on wear, the noted difference in wear values between the standard and the modified design is over 12%, indicating that a tool with a smaller contact surface is justifiably efficient.

References

1. Gupta, K., Davim, P.: High-Speed Machining. Academic Press, Cambridge (2020)
2. King, R.: Handbook of High-Speed Machining Technology. Springer, NY (1985)
3. Erdel, B.P.: High-Speed Machining. SME Drive, Dearborn (2003)
4. de Lacalle, N.L., Mentxaka, A.L.: Machine Tools for High-Performance Machining. Springer Science & Business Media, London (2008)
5. Schulz, H.: The History of high-speed machining. Rev. Cienc. Tecnol. **1**(5), 9–18 (1999)
6. Schulz, H., Moriwaki, T.: High-speed machining. CIRP Ann. **41**(2), 637–643 (1992)
7. Smith, S., Tlusty, J.: Current trends in high-speed machining. J. Manuf. Sci. Eng. **119**(4B), 664–666 (1997)
8. Huo, F., Poo, A.N.: Precision contouring control of machine tools. Int. J. Adv. Manuf. Technol. **64**, 319–333 (2013)
9. Taheri, A.H., Abolghasemi, S., Suresh, K.: Generalizations of non-uniform rational B-splines via decoupling of the weights: Theory, software and applications. Eng. Comput. **36**, 1831–1848 (2020)
10. Piegl, L., Tiller, W.: The NURBS, 2nd edn. Springer, Berlin (1997)
11. Juan, H., Yu, S.F., Lee, B.Y.: The optimal cutting-parameter selection of production cost in HSM for SKD61 tool steels. Int. J. Mach. Tools Manuf. **43**(7), 679–686 (2003)
12. Davim, J.P.: Surface Integrity in Machining. Springer Science & Business Media, London (2010)
13. Stupnytskyy, V., Hrytsay, I.: Simulation Study of Cutting-Induced Residual Stress. In: Ivanov, V., et al. (eds.) Advances in Design, Simulation and Manufacturing II. LNME, pp. 341–350. Springer, Cham (2020). https://doi.org/10.1007/978-3-030-22365-6_34

Influence of Turning Operations on Waviness Characteristics of Working Surfaces of Rolling Bearings

Valentyn Zablotskyi[1] , Anatolii Tkachuk[1]([✉]) , Serhii Prozorovskyi[1] ,
Valentyna Tkachuk[1] , and Marek Waszkowiak[2]

[1] Lutsk National Technical University, 75, Lvivska St., Lutsk 43018, Ukraine
`a.tkachuk@lntu.edu.ua`

[2] Wyższa Szkoła Kadr Menedżerskich, 3a, Zagórowska St., 62-500 Konin, Poland

Abstract. The formation of micro and macro geometric parameters of conjugate cylindrical surfaces of parts is technological movements of equipment that provide the specified quality characteristics of parts. The waviness of the part's surface is one of the critical geometric characteristics, which provides the functional features of the unit as a whole, as it affects the vibration processes that occur during operation. The ripple is formed under the influence of dynamic processes of processing of details which are characteristic of metalworking machines, depending on changes in system machine-tool (cutting)-part (MTP). Mechanical perturbations during cutting occur due to forced oscillations, self-oscillations, deformation of the rings due to the action of cutting forces. Self-oscillations occur due to the loss of properties of a given motion during cutting and forced oscillations due to external factors. The undulation of the surface is formed due to forced oscillations of the metal-cutting system due to periodic perturbations that occur due to disbalances of the MTP system's parts. The ratio of the oscillation frequency for relative motions of the tool and the part can change the law of oscillating motion and the shape of the surface. The decisive factor influencing the formation of geometric errors of the part is the ratio of the frequency of harmonic oscillations of the tool and the workpiece to the frequency of rotation of the machine tool's spindle.

Keywords: Formation · Harmonic · Heredity · Roller bearing · Spectral analysis · Workpiece · Process innovation · Industrial growth

1 Introduction

Machining of parts takes place using machining operations, which provide the initial and final (finishing) processing, to varying degrees affect the final formation of the geometric characteristics of the functional surface [1].

If the ratio χ/n is an integer (χ – the ratio of the frequency of harmonic oscillations of the tool and the workpiece; n – frequency of rotation of the spindle), the harmonic oscillation does not affect the shape of the longitudinal section of the part [2]. In order to prove the technological heredity of the waviness, it is necessary to establish the

relationship between the processing modes and the microgeometry of the functional surfaces of the bearing rings. Moreover, heredity is manifested not only in the finishing operations. It also occurs during the operation of the bearing in the product because of external factors and operating conditions [3, 4].

The formation of the waviness of the functional surface begins in the provision operations, as the macrogeometric parameters of the surface are formed, and its appearance can be observed in the finishing operations (Fig. 1).

a)   b)
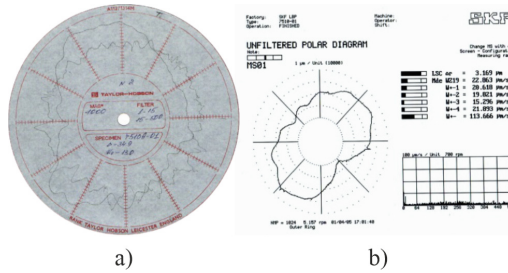
Fig. 1. Hereditary nature of the origin of the waviness: a – round diagram of the ring's raceway after turning; b – polar diagram of the ring's raceway after grinding.

In the technological cycle, the influence of initial operations and transitions on the formation of geometric parameters of the treated surface is less than the finish, but ignoring it will be erroneous. There are irregularities with different pitches and amplitude deviations on actual rolling surfaces.

2 Literature Review

During the rotation of the inner ring of the bearing, the simultaneous interaction of deviations on the rolling surfaces of both rings and the rolling elements causes oscillations of the outer ring of the bearing, i.e., its vibrations [5–7]. A complex periodic function describes the displacement of the outer ring in the form of a Fourier series, which consists of simple harmonic oscillations with frequencies multiples of the fundamental [8]:

$$R(\phi) = \frac{a_0}{2} + \sum_{k=1}^{\infty} A_k \sin(k\phi + \psi_{0k}) \tag{1}$$

a_0 – the constant value of the radius vector; k – is the harmonic number; A_k – is the amplitude of the k-th harmonic; ψ_{0k} – is the initial phase of the harmonic.

If the amplitude of the harmonics $a_0 = 0$, then the zero harmonics of the schedule is a constant component of the series:

$$R(\phi) = \frac{a_0}{2} = R_0 = \frac{d_0}{2} = const \tag{2}$$

For the first harmonic of the schedule ($k = 1$) the deviation of the contour L from the base circle corresponds to the dependence:

$$\delta_1(\phi) = A_1 \sin(\phi + \psi_{01}) \tag{3}$$

As the harmonics' amplitude decreases, the contour's shape approaches the base circle, and deviations are detected in the cut of the contour by the number of faces corresponding to the number of the harmonic (Fig. 2) [9, 10].
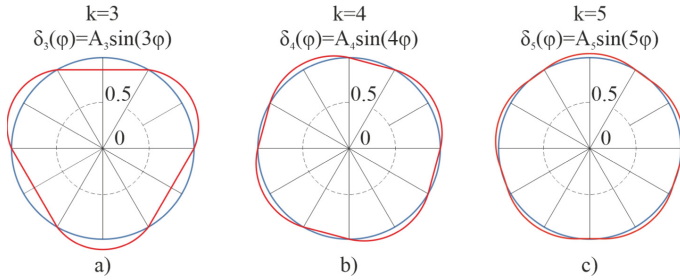
Fig. 2. Contour shapes corresponding to the third (a), fourth (b), and fifth (c) harmonics of a periodic function with period 2π Fourier series for zero initial phases and small amplitudes.

Vibroacoustic characteristics of the bearing deteriorate when the number of waves of the k-th harmonic on the track of the inner or outer rings with the number of bodies of rotation in the bearing, $f_k = qz$, where f_k is the number of waves of the main harmonic on the track [11].

Spectral analysis methods were used to diagnose the causes of technological defects of bearings [12]. The spectrum allows us to identify the predominant harmonics, which are present in the schedule of the series and depend on the number of rolling elements (Fig. 3) [13].
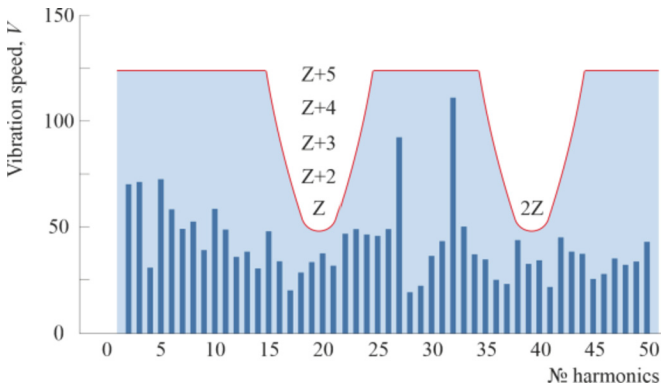
Fig. 3. Tolerances for the harmonics of the spectrum of the bearing ring with the number of rolling elements $Z = 20$.

This mechanism of modeling the vibroactivity of the surface allows solving applied problems of development and optimization of the technology of forming microgeometric parameters of the surfaces of rotating bodies [14].

3   Research Methodology

The modeling of topography parameters is based on the principle of multi-coordinate formation because of the relative movements of the system MTP [15]. The microrelief shape height depends on the disturbances in the MTP system and the movement of the cutting tool relative to the workpiece [16]. The microrelief step parameters depend on the ratio between the longitudinal and transverse feeds and the workpiece's rotation speed [17, 18]. Therefore the formation of vibroacoustic characteristics of the functional surfaces of friction pairs largely depends on the functional features of the technological equipment [19, 20].

The dynamic mathematical model of the turning process is shown in Fig. 4.
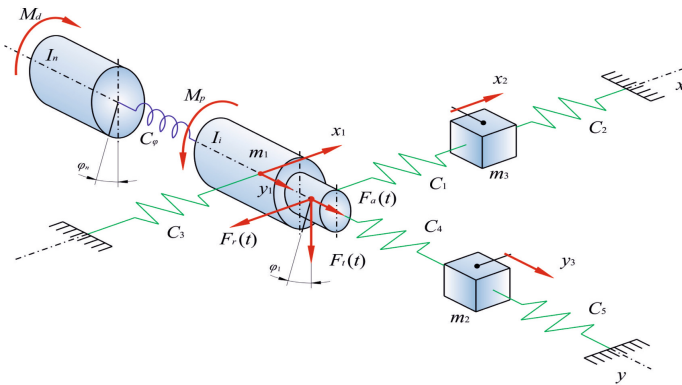
Fig. 4. The calculated scheme of the spindle.

The dynamic calculation scheme includes the masses of the spindle with the part, m_1, m_2, m_3 of transverse and longitudinal supports, the mass of the machine's drive, connected by elastic links C_1–C_5 (Table 1).

Table 1. Designations used for mathematical modeling [1].

Designation	Value
C_φ	Stiffness of the drive machine tool (angular)
M_d, M_p	Moments of cutting force
x_1, x_2	Coordinates of displacements of masses m_1 and m_2 along the x-axis
y_1, y_3	Coordinates of displacements of masses m_1 and m_3 along the y-axis
φ_1, φ_n	Coordinates of angular displacements of rotating masses machine tool
$F_t(t)$, $F_r(t)$, $F_a(t)$	Components of cutting forces

The oscillations of the support masses that take place along the perpendicular axes are connected through the workpiece, so it is necessary to consider the mutual damping of oscillations.

Formulas can describe the equation of oscillation of the masses of a dynamic spindle system in the corresponding directions of rotation:

– in the direction of movement of the transverse support along the x-axis:

$$m_1\ddot{x}_1 + \alpha\,\dot{x}_1 + c_1(x_1 - x_2) + c_3 x_1 = F_r(t)\ ;$$
$$m_2\ddot{x}_2 - c_1(x_1 - x_2) + c_2 x_1 = 0 \tag{4}$$

– in the direction of movement of the longitudinal support along the axis in:

$$m_1\ddot{y}_1 + \beta\,\dot{y}_1 + c_4(y_1 - y_3) = F_a(t)\ ;$$
$$m_3\ddot{y}_3 - c_4(y_1 - y_3) + c_5 y_5 = 0 \tag{5}$$

– spindle oscillations:

$$I_1\ddot{\phi}_1 + c_\phi(\phi_1 - \phi_n) = M_p(t);$$
$$I_n\ddot{\phi}_n - c_\phi(\phi_1 - \phi_n) = 0 \tag{6}$$

In (4) and (5), α and β are the damping coefficients of the transverse and longitudinal support, respectively, and $F_\alpha(t)$, $F_r(t)$, $F_t(t)$ are the forces acting on the respective links.

4   Results

In the course of research works, dependencies of waviness on processing parameters at various frequencies of rotation of a spindle were established (Table 2). Theoretical studies have been confirmed experimentally with 15–20% error.

Table 2. Dependence of spindle oscillation amplitudes on speed rotation.

Spindle speed, rpm	The amplitude of oscillations along the X-axis, μm		The amplitude of oscillations along the Y-axis, μm	
	Theory	Experiment	Theory	Experiment
1800	1,453	1,336	1,115	0,924
1200	2,863	2,376	1,862	1,645
800	5,121	5,349	3,241	3,702
560	1,125	1,093	0,907	0,756
280	3,985	4,366	2,912	3,023

Graphs of dependence of the amplitude of oscillations of the cutting tool during the processing of rings of bearings on the spindle speed are built (Fig. 5, Fig. 6).

These figures show the formation of the waviness of functional surfaces of parts such as "body of rotation" considering theoretical calculations (theory) and their approximation with experimental studies (experiment) to confirm the oscillations of the forming system of the machine, which significantly affects the formation of operational of the waviness roller bearings.
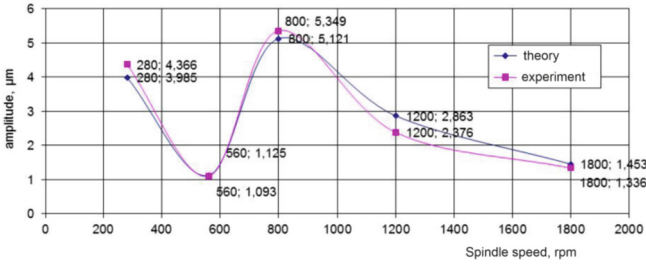
Fig. 5. Dependence of the amplitude of transverse oscillations on the machine's spindle speed.
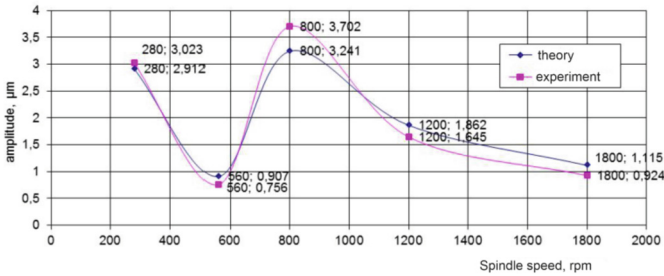
Fig. 6. Dependence of the amplitude of longitudinal oscillations on the machine's spindle speed.

To interpret the influence of technological factors on the formation of microgeometry of functional surfaces, the complex Talyskan was used (Fig. 7).
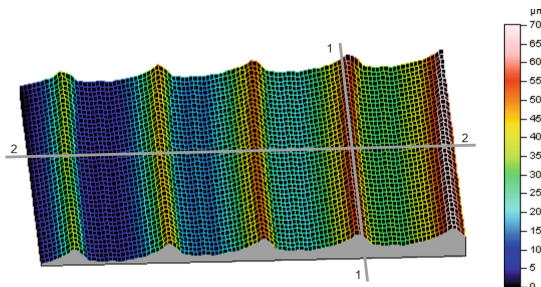
Fig. 7. The working surface of the roller-bearing ring after turning.

The waviness of the functional surface changes during its operation and takes the form obtained during processing in the initial operations, including turning.

Thus, the change in surface geometry at finishing operations leads to the formation of "technological" geometry, which is erroneous in its macrogeometric parameters. After running-in, the surface takes the form of "operational" geometry, which reflects the geometry of the initial machining operations. Forming the necessary geometric parameters of functional surfaces in the initial (rough) machining operations is an essential task to ensure the quality of operation of machine parts.
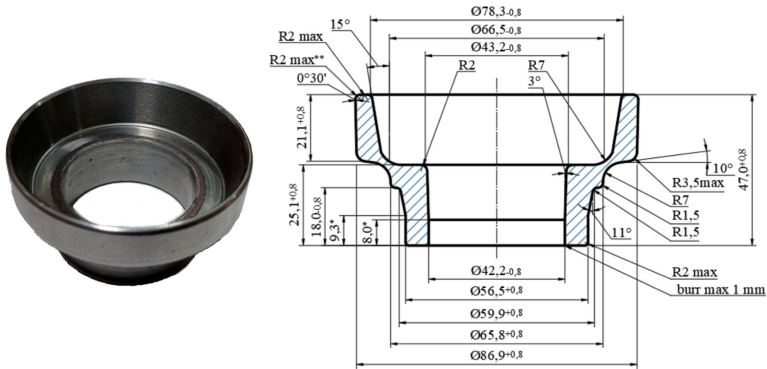
Fig. 8. The prototype and design of the blank set of rings on a roller bearing 7509.

The research results are realized in the form of engineering methods of designing tool adjustments of lathes with a subroutine of adjustment waviness at the stage of determining the forming modes. The design of a continuous billet of a set of 2 rings of a roller bearing (Fig. 8) is offered. The structure of the technological process of manufacturing rings is changed.
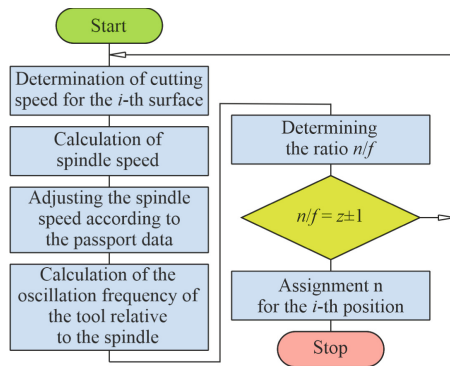
Fig. 9. Algorithm for correcting the waviness of the ring machining process on automatic turning operations: n/f – the ratio of the rotational frequencies of the workpiece n and the oscillation frequency of the tool f.

Due to the introduction of the proposed design of the workpiece, it was possible to avoid systematic defects in the turning of the outer rings associated with the deformation

of the clamping elements of the spindle chucks [21–24]. Technological requirements: diameter inconsistency – up to 0.6 mm; width inconsistency – up to 0.6 mm; cracks are not allowed; *dimensions for references; burr is allowed in the axial direction - max 1 mm with a maximum thickness of 1 mm; hardness of forging HB 179…207. Surface defects: protrusions from wear and chipping of the tool - up to 0.5 mm.

The engineering technique of adjusting lathes in the conditions of multi-nomenclature bearing production allowed the machine to optimize the machine's productivity due to the change of structure of the technological process of manufacturing rings of roller bearings (Fig. 9).

This allowed us to offer optimal cutting modes for tools with different values of the predicted stability. An algorithm for automated design of structures and parameters of tool adjustments of lathes was developed, which allowed predicting the optimal parameters of waviness at the stage of technological design. To do this, a procedure for adjusting the waviness of the working surface of the bearing ring, which allowed to stabilize the performance of roller bearings.

5   Conclusions

To assess the impact of geometric parameters of the surfaces of rotation of bearing parts on its performance, a complex functional-parametric indicator – vibroactivity of the surface allowed during the technological design of molding operations to predict vibroacoustic characteristics of annular surfaces and bearing performance. The waviness and deviations of the shape of the working surfaces of the rings are hereditary. They begin with procurement (10…15%), transformation into mold (40…55%), heat treatment (10…15%), and operation, finally formed on the final operations of roughing and finishing (20…25%). The control of the waviness and accuracy of the working surfaces of the bearing rings must be carried out throughout the life cycle of the rings, starting from the workpiece, turning, shaping operations, and ending with the final grinding.

The leading causes of waviness and deviations of the shape of the functional surfaces of bearing rings are the imperfection of the workpieces and forming processes, the presence of residual deformations from the clamping elements of machines, dynamic oscillations of forming elements of machines, devices, and tools (self-oscillations). The step parameters of the critical harmonic ripple are related to the ratio between the workpiece's rotational frequencies and the oscillations of the forming instruments, and the amplitude parameters – with the amplitude of their oscillating motions. Thus, at the ratio 1/2 of the workpiece's rotational frequencies n and the tool's oscillation frequency k, the shape deviation is close to the oval one. At the ratio of 1/6, the shape deviation is close to the hexagonal one. The waviness of the 12th harmonic results from the frequency ratio of 1/12.

For preventing technological defects during the formation of the rings' working surfaces, it is necessary to avoid exceeding the specified tolerances on waviness for harmonics equal to or multiples of the number of bodies of rotation in the bearing. The harmonics of the waviness should dominant be considered by $h_1 = z \pm 2$ $h_2 = z \pm 3$; $h_3 = z \pm 4$; $h_4 = z \pm 5$ where z is the number of bodies of rotation in the bearing.

It is planned to offer a field of tolerances for the dynamic waviness of rings' working surfaces (wavy spectrogram) for the spectrum of harmonics from 0 to 500 depending on

the ratios of bodies of bearing's rotation and the waviness (number of critical harmonics). This will make it possible to optimize the limit of economically feasible values of vibration velocities of critical harmonics and, hence, the ripple's amplitudes within the specified spectrum.

References

1. Zablotskyi, V., Tkachuk, A., Senyshyn, A., Trokhymchuk, I., Svirzhevskyi, K.: Impact of turning operations on the formation of rolling bearing's functional surfaces. In: Tonkonogyi, V., Ivanov, V., Trojanowska, J., Oborskyi, G., Pavlenko, I. (eds.) InterPartner 2021. LNME, pp. 229–238. Springer, Cham (2022). https://doi.org/10.1007/978-3-030-91327-4_23

2. Berntsen, J., Brandt, A.: Periodogram ratio based automatic detection and removal of harmonics in time or angle domain. Mech. Syst.Signal Processing **165** (2022). https://doi.org/10.1016/j.ymssp.2021.108310

3. Zablotskyi, V., Tkachuk, A., Moroz, S., Prystupa, S., Svirzhevskyi, K.: Influence of technological methods of processing on wear resistance of conjugated cylindrical surfaces. In: Tonkonogyi, V., et al. (eds.) InterPartner 2020. LNME, pp. 477–487. Springer, Cham (2021). https://doi.org/10.1007/978-3-030-68014-5_47

4. Pavlenko, I., Ivanov, V., Kuric, I., Gusak, O., Liaposhchenko, O.: Ensuring vibration reliability of turbopump units using artificial neural networks. In: Trojanowska, J., Ciszak, O., Machado, J.M., Pavlenko, I. (eds.) MANUFACTURING 2019. LNME, pp. 165–175. Springer, Cham (2019). https://doi.org/10.1007/978-3-030-18715-6_14

5. Prydalnyi, B.I., Sulym, H.T.: Mathematical model of the tensioning in the collet clamping mechanism with the rotary movable input link on spindle units. J. Eng. Sci. **8**(1), E23–E28 (2021). https://doi.org/10.21272/jes.2021.8(1).e4

6. Adamczak, S., Zmarzły, P.: Influence of raceway waviness on the level of vibration in rolling-element bearings. Bull. Polish Acad. Sci. Tech. Sci. **65**(4), 541–551 (2017). https://doi.org/10.1515/bpasts-2017-0059

7. Chelabi, M.A., Basova, Y., Hamidou, M.K., Dobrotvorskiy, S.: Analysis of the three-dimensional accelerating flow in a mixed turbine rotor. J. Eng. Sci. **8**(2), D1–D7 (2021). https://doi.org/10.21272/jes.2021.8(2).d2

8. Zhang, C., Liu, Y.: A two-step denoising strategy for early-stage fault diagnosis of rolling bearings. IEEE Trans. Instrum. Meas. **69**(9), 6250–6261 (2020). https://doi.org/10.1109/TIM.2020.2969092

9. Jablonski, A.: Vibration components generated by rotary machinery. In: Condition Monitoring Algorithms in MATLAB®. Springer Tracts in Mechanical Engineering. Springer, Cham (2021).https://doi.org/10.1007/978-3-030-62749-2_3

10. Calabrese, F., Regattieri, A., Bortolini, M., Galizia, F.G.: Fault diagnosis in industries: how to improve the health assessment of rotating machinery. In: Scholz, S.G., Howlett, R.J., Setchi, R. (eds.) KES-SDM 2021. SIST, vol. 262, pp. 257–266. Springer, Singapore (2022). https://doi.org/10.1007/978-981-16-6128-0_25

11. Lü, M., Liu, S., Su, X., Chen, C.: Early degradation detection of rolling bearing based on adaptive variational mode decomposition and envelope harmonic to noise ratio. J. Vibrat. Shock **40**(13), 271–280 (2021). https://doi.org/10.13465/j.cnki.jvs.2021.13.034

12. Wang, G., Zhao, B., Xiang, L., Li, W., Zhu, C.: Information interval spectrum: A novel methodology for rolling-element bearing diagnosis. Measurement: Journal of the International Measurement Confederation 183, 109899 (2021). DOI: https://doi.org/10.1016/j.measurement.2021.109899

13. Ahmad, M.S., Tiwari, R., Mandawat, T.: Multi-objective robust optimization of deep groove ball bearings considering manufacturing tolerances based on fatigue and wear considerations. J. Tribol. **144**(2), 022301 (2022). https://doi.org/10.1115/1.4050883

14. Patil, A.P., Mishra, B.K., Harsha, S.P.: Fault diagnosis of rolling element bearing using autonomous harmonic product spectrum method. Proc. Instit. Mech. Engineers Part K J. Multi-Body Dyn. **235**(3), 396–411 (2021). https://doi.org/10.1177/1464419321994986

15. Stanceková, D., Joch, R., Tavodová, M., Turian, F.: Streamlining the production technology of bearing components by cold rolling. In: 29th International Conference on Metallurgy and Materials, pp. 252–257. Brno, Czech Republic (2020). https://doi.org/10.37904/metal.2020.3463

16. Pape, F., Coors, T., Poll, G.: Studies on the influence of residual stresses on the fatigue life of rolling bearings in dependence on the production processes. Front. Mech. Eng. **6** (2020). https://doi.org/10.3389/fmech.2020.00056

17. Pape, F., Neubauer, T., Maiß, O., Denkena, B., Poll, G.: Influence of residual stresses introduced by manufacturing processes on bearing endurance time. Tribol. Lett. **65**(2), 1–8 (2017). https://doi.org/10.1007/s11249-017-0855-3

18. Benchea, M., Crețu, S.: An investigation regarding the impact of running-in on rolling contacts lives. In: Machado, J., Soares, F., Trojanowska, J., Ottaviano, E. (eds.) icieng 2021. LNME, pp. 459–471. Springer, Cham (2022). https://doi.org/10.1007/978-3-030-79165-0_43

19. Pandey, S., Amarnath, M.: Applications of vibro-acoustic measurement and analysis in conjunction with tribological parameters to assess surface fatigue wear developed in the roller-bearing system. Proc. Inst. Mech. Eng. Part J J. Eng. Trib. **235**(10), 2034–2055 (2021). https://doi.org/10.1177/1350650120982465

20. Redko, R., Zabolotnyi, O., Redko, O., Savchuk, S., Kovalchuk, V.: Improvement of manufacturing technology and recovery of clamping collets for lathe automats. In: Ivanov, V., et al. (eds.) DSMIE 2019. LNME, pp. 290–301. Springer, Cham (2020). https://doi.org/10.1007/978-3-030-22365-6_29

21. Ivanov, V., Dehtiarov, I., Pavlenko, I., Kosov, M., Hatala, M.: Technological assurance and features of fork-type parts machining. In: Ivanov, V., et al. (eds.) DSMIE 2019. LNME, pp. 114–125. Springer, Cham (2020). https://doi.org/10.1007/978-3-030-22365-6_12

22. Prydalnyi, B., Kuznetsov, Y., Lyshuk, V.: methodology and tools for computer-aided calculation of characteristics of electromechanical clamping drive actuated by induction motor. In: Radionov, A.A., Gasiyarov, V.R. (eds.) ICIE 2021. LNME, pp. 256–266. Springer, Cham (2021). https://doi.org/10.1007/978-3-030-54817-9_30

23. Fesenko, A., Basova, Y., Ivanov, V., Ivanova, M., Yevsiukova, F., Gasanov, M.: Increasing of equipment efficiency by intensification of technological processes. Periodica Polytechnica Mech. Eng. **63**(1), 67–73 (2019). https://doi.org/10.3311/PPme.13198

24. Ivanov, V., Pavlenko, I., Liaposhchenko, O., Gusak, O., Pavlenko, V.: Determination of contact points between workpiece and fixture elements as a tool for augmented reality in fixture design. Wireless Netw. **27**(3), 1657–1664 (2019). https://doi.org/10.1007/s11276-019-02026-2

Investigation of the Surface Layer Hardness When Grinding Sintered Porous Workpieces

Oleg Zabolotnyi[1](✉) , Tetiana Bozhko[1] , Tetiana Halchuk[1] , Olha Zaleta[1] ,
and Dagmar Cagáňová[2]

[1] Lutsk National Technical University, 75, Lvivska St., Lutsk 43018, Ukraine
`volynasi@gmail.com`

[2] Slovak University of Technology in Bratislava, Bratislava, Slovak Republic

Abstract. The essential properties of sintered powder materials are porosity and hardness. It is established that a part made through powder metallurgy methods is exposed to external factors during the finishing stages. It leads to changes in the surface layer's characteristics of the part. The experimental research program provided definitions of the influence of transverse feed, cutting speed, and porosity on the hardness of a surface layer and its consolidation. The optimal modes of grinding porous workpieces acquired by isostatic pressing of powder materials with further sintering were obtained. Their surface layers are compacted mainly due to the grinding of porous workpieces. The treatment of porous iron parts by grinding increases the microhardness of the surface layer, yet increasing the transverse feed reduces it. Also, it was found that increasing the hardness of the surface layer of the porous workpiece after grinding is possible because of additional movements of the tool without transverse feed.

Keywords: Isostatic pressing · Sintered powder material · Porosity · Cutting modes · Microhardness · Surface characteristics · Processing quality · Manufacturing innovation · Process innovation

1 Introduction

The rapid development of technology and powder metallurgy has made the geometric shapes of workpieces more complicated [1]. The accuracy of the executive dimensions of machine parts has also increased [2]. It has led to the need to use machining of sintered porous workpieces from metal powders [3, 4]. One of the types of mechanical processing of sintered powder materials is abrasive processing, which provides the highest accuracy and purity class of machined parts [5]. Physical and chemical phenomena differ from the usual processing of metals by cutting [6].

Abrasive machining has become one of the leading methods of extremely fine machining. Without its use, it is impossible to produce friction and brake pads for lifting and transport machines, certain types of plain bearings, parts of complex configuration based on iron powders, such as brackets, handles, holders of metalwork, and assembly tools, etc. [7].

Sintering is one of the essential industrial techniques for optimizing the capabilities of different materials. The porosity is set at the design stage and is used to manufacture the part [8].

The processing of sintered materials differs from compact materials due to the heterogeneous microstructure and porosity [9, 10]. Therefore, the main task in grinding parts of porous sintered materials is to form the necessary properties of the surface layer [11]. The processing of such materials should be reduced not only to obtain a given geometric shape and size of the part, but also to improve or, as a last resort, to preserve the structural features of the material which were formed in the process of the manufacture of the workpieces [12].

The main task of finishing sintered porous materials is to study the influence of feed, cutting speed, and porosity on the hardness of the surface layer and its compaction, which affect the operational parameters of the part.

2   Literature Review

The machinability of powder metallurgy (PM) steels is described in [13]. It has been proved that the porosity and the amount and shape of carbides of the PM steels are essential in the wear mechanism during the machining process. Besides, the addition of MnS leads to a decrease in cutting forces and allows for higher tool life. It is noted that the surface roughness significantly depends on the cutting speed and feed.

In [14], the authors suggest operating PM machining before sintering. It is claimed that direct cutting is a tool-saving and cost-effective manufacturing technique. The research results show that the machined surface roughness decreases with increased cutting thickness and rounded cutting-edge radius. The proposed model shows that the material removal in PM results from particle shearing deformation, peeling, and ploughing/extruding.

The effect of the material composition changes on the secondary machining properties of powder metallurgy steels (PMS) was determined in [15]. It was found that by adding about 4% of copper, the mechanical properties of materials increase, and machinability improves. Above this limit, the properties are not significantly improved. Adding more than 1% carbon reduces machinability but improves the hardness. It is noted that it is preferable to increase the amount of copper in the composition of PM rather than increase the amount of carbon.

The research [16] is aimed to investigate the drilling capabilities of the sintered powder metallurgy parts. In the framework of the experiments, cutting force, drilling torque, and tool wear was measured. Also, the diameter accuracy and circularity were checked. According to the results, the cutting force and the tool wear have had the most significant effect.

In [17], the influence of wear resistance and strength of abrasive grains on the quality of grinding of sintered materials was investigated. The results proved that large solid grains enhance wear resistance [18]. The inclusion of high-strength abrasive grains has improved the stability of the cutting edge when machining parts [19].

As shown in [20], extensive cutting tests have been run to study and model the basic cutting action of a particular sintered metallic material. The chip formation and cutting

modes for the sintered metallic material are like those for ordinary metallic materials. However, the cutting quantities used in the predictive force models are different and must be established for each material [21].

3   Research Methodology

Samples for the study were obtained by pressing on hydrostatic equipment. An elastic shell made of oil-resistant rubber was used as a matrix. The experiments were performed on samples that were made of iron powders.

The chemical composition of the material is shown in [22]. The workpieces were made by pressing and sintering. The iron powder was pressed using a rubber mold in a high-pressure chamber.

Specific pressure force in the range of 600…800 MPa was applied to obtain the porosity θ of the workpiece of 24%, 28%, 32%. Sintering temperatures were between 1100…1200 °C. For the method of mechanical processing of samples, dry grinding was chosen.

The surface grinding machine 3G71 was used for the equipment, and for the tool, a grinding wheel of the brand 1A1 250 × 25 × 75 24A 20 CM2 K6 was used (1A1– circle type (the straight profile); 250 × 25 × 75 – the dimensions of the circle; 24A – electrocorundum white; 20 – granularity; CM2 – the hardness of a circle (average softness the second); К – the ceramic bundle; 6 – the structure).

The following modes of grinding were adopted: depth $t = 0.01…0.05$ mm, the speed of the workpiece $V_{wp} = 5…15$ m/min, cutting speed (speed of rotation of a grinding wheel) $V_w = 35$ m/s, transverse feed $S_t = 0.1…0.5$ mm/stroke, grinding width $B = 15$ mm.

To determine the effect of cutting depth for different cutting modes on the compaction of the workpiece surface layer, the metallographic method was used [23]. Hardness (HB) was determined via the 2109 TB hardness tester.

4   Results

As for the results of these experiments ($V_{wp} = 5$ m/min and $S_t = 0.2$ mm/stroke), it was established that the compaction of the porous sample decreases in the case of increasing the depth of the surface layer (Fig. 1). At the same time, however, porosity increases (Fig. 2).
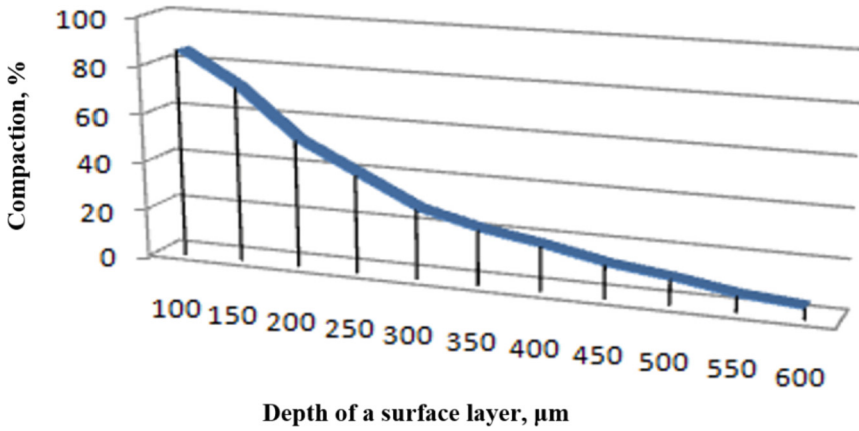
Fig. 1. The dependence of the compaction on the depth of the surface layer.
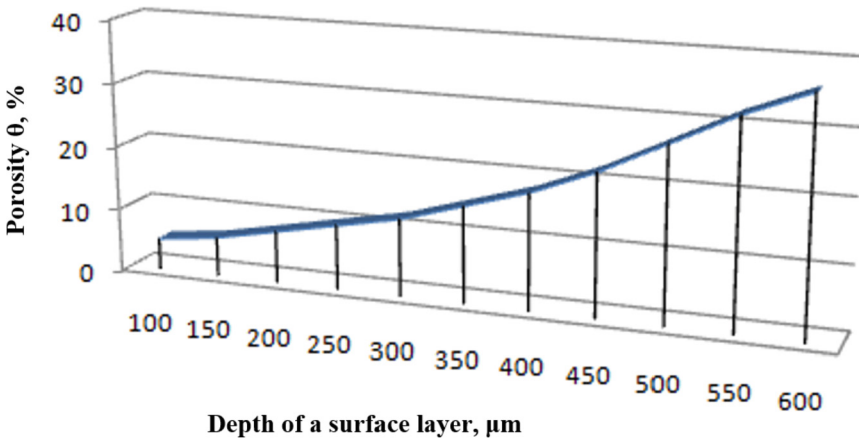
Fig. 2. The dependence of the porosity on the depth of the surface layer.

For the results of experiments on samples with initial porosity of 32%, samples with residual porosity of 5% at a depth of 100 μm were obtained.

It was observed that in the case of a decrease in the transverse feed S_t and cutting speed V_w, the thickness of the compacted layer increased (Fig. 3). For samples with a porosity of 32% (Fig. 3, a), the thickness of the compacted layer is 100 μm greater than for the samples with a porosity of 24% (Fig. 3, b) for the same processing modes ($t = 0.02$ mm, $S = 0.2$ mm / stroke, $V_w = 5$ m/min).

As a result of increasing the speed of the workpiece, the grinding wheel is in less contact with the treated surface, so the area of plastic deformation and the thickness of the compacted layer is also reduced. The increase in the thickness of the compacted layer is due to the expansion of the deformation zone in the case of a decrease in the transverse feed and the layer's depth of the workpiece being cut.
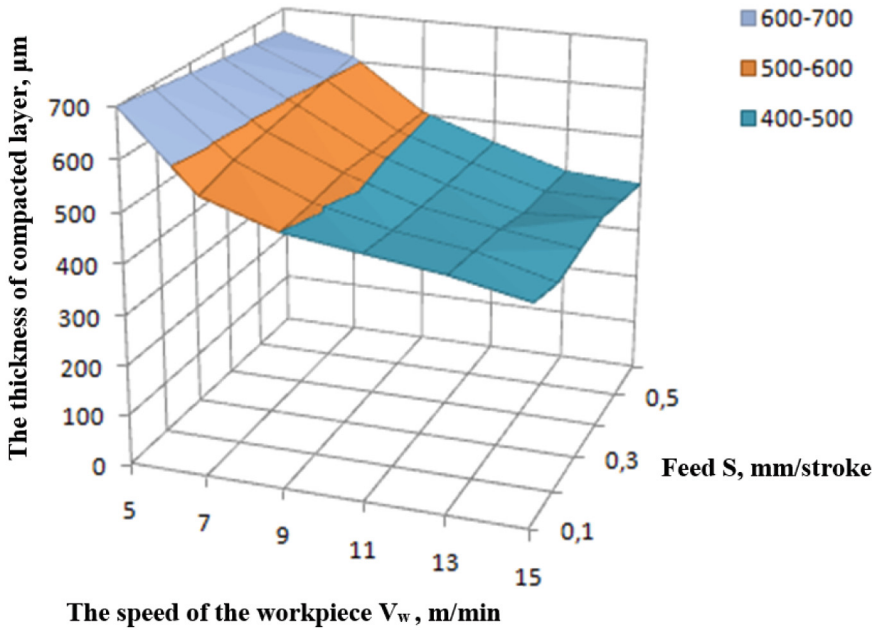
a)
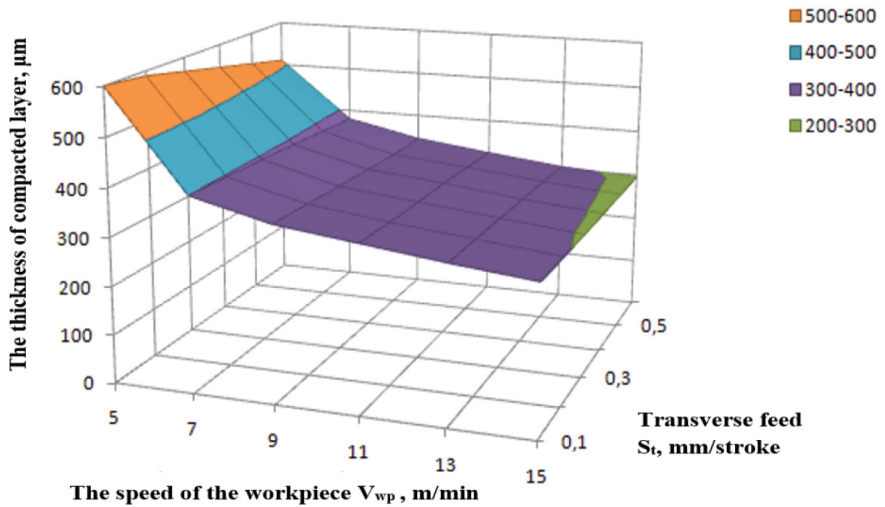
b)

Fig. 3. The thickness of the compacted layer on the speed of the workpiece and the transverse feed: a) $\theta = 32\%$ and b) $\theta = 24\%$.

Under optimal modes of the grinding process $S_t = 0.1$ mm/stroke, $V_{wp} = 5$ m/min, $V_w = 35$ m/s for samples with $\theta = 24\%$, the plastic deformation of the surface layer of the outer surface is 400 μm [23].

Experimental studies have shown that the grinding of workpieces with a large transverse feed reduces the quality of the surface. Thus, the surfaces treated with a transverse feed $S_t = 0.5$ mm/stroke will have microcracks. The application for processing at $S_t = 0,1...0,3$ mm/stroke gives the chance to yield processed surfaces of porous workpieces with a condensed layer of high deformation.

To study the effect of processing speeds of workpiece speed and transverse feed on surface hardness, the authors have chosen an initial workpiece with porosity $\theta = 24\%$ and microhardness HB 46. The obtained results show that the surface hardness of the sample after processing with $V_{wp} = 4$ m/min increased almost twofold. Further increase in speed gradually reduces the surface hardness. In particular, for $V_{wp} = 10...12$ m/min, the hardness is HB 54...40, which is 1.5...2 times less than the surface hardness for processing with $V_{wp} = 4$ m/min (Fig. 4).
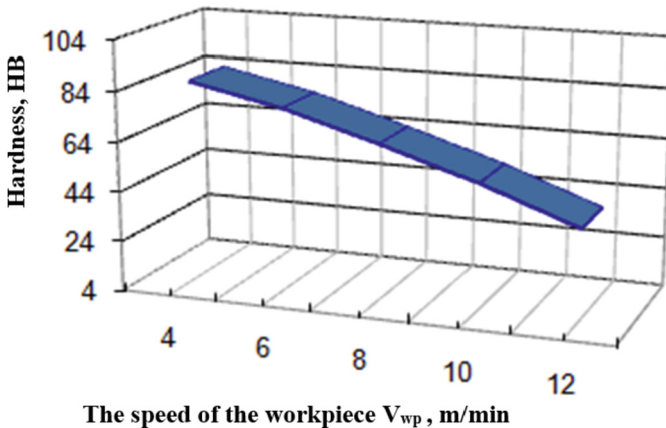
Fig. 4. The influence of the workpiece speed on the hardness of the surface layer.

The hardness of the surface layer is significantly affected by temperature deformations, which directly depend on the transverse feed of the treatment. Increasing the transverse feed raises the temperature in the grinding zone and reduces the hardness of the workpiece surface (Fig. 5).

Feed and speed affect the thickness of the compacted layer. Reducing these processing parameters will increase the compacted layer of the workpiece. Based on a series of experiments with $S_t = 0.1$ mm/stroke; 0.3 mm/stroke; 0.5 mm/stroke obtained dependences of hardness on the depth of the defective layer (Fig. 6).

These data show that with increasing the depth of the defective layer, the hardness gradually decreases and acquires the value of the surface hardness of the initial workpiece. The study shows that to ensure the high hardness of the surface layer, it is necessary to use minimum transverse feed values. Any increase in the value of the transverse feed reduces the hardness of the surface and, as a consequence, reduces its wear resistance.
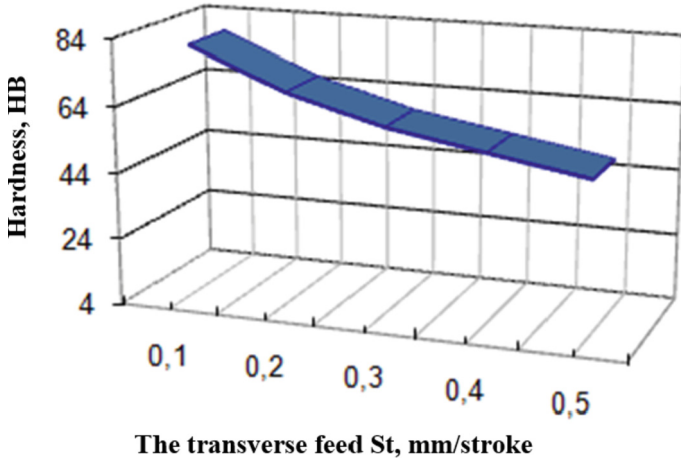
Fig. 5. The effect of transverse feed on the surface layer hardness.
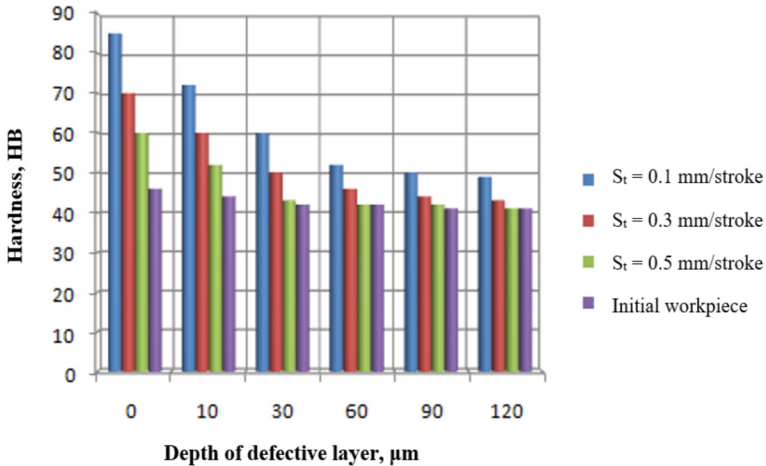
Fig. 6. Dependence of hardness on the depth of the defective layer.

One way to increase the hardness of the surface layer of the porous workpiece after grinding is by the finishing tool in several passes without transverse feed (curing). Studies have shown that the surface hardness of the sample with porosity $\theta = 24\%$ after curing increases by 5…10% depending on the transverse feed of grinding (Fig. 7).
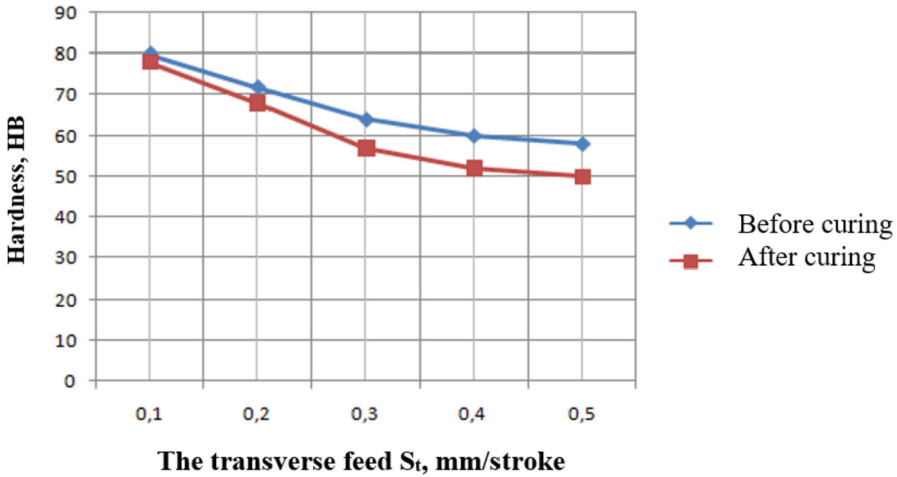
Fig. 7. The dependence of the surface hardness of the sample on the transverse feed.

5   Conclusions

During the study, it was found that grinding sintered powder workpieces is the compaction of their surface layers. The thickness of the compacted layer of such products decreases due to the following factors: the increase in the speed of movement of the workpiece; reducing the time of action of the grinding wheel on the machining surface; the narrowing of the zone of plastic deformation. The increase in the thickness of the compacted layer occurs due to the decrease in the transverse feed and the depth of the cut layer as the deformation zone expands.

They are testing the hardness of the surface layer of the porous iron workpiece by grinding, indicating that this treatment increases the microhardness of the surface layer twofold. It was established that treatments with minimum allowable transverse feed increase the hardness of the surface layer. A decrease in surface hardness is observed during the increase of the transverse feed, which causes an increase in temperature in the cutting zone. To increase the hardness of the surface layer of the porous workpiece after grinding to 10%, the curing process should be applied.

The optimal modes of grinding processing of porous workpieces are $S_t = 0.1...0.3$ mm/stroke; $V_{wp} = 4...5$ m/min to obtain products with HB 82...76. To ensure optimal porosity and degree of density of the workpiece, the plastic deformation of the surface layer of the outer surface should be 400 μm, and the depth of the defective layer should be within 300...400 μm.

The obtained results encourage studying the plastic deformation of the surface layer and residual stresses of the 1st kind, which are the critical factors influencing the surface quality, fatigue strength, and wear resistance of parts.

References

1. Povstyanoi, O.Y., Rud', V.D., Samchuk, L.M., Zubovets'ka, N.T.: Production of porous materials with the use of energy-saving technologies. Mater. Sci. **51**(6), 847–853 (2016). https://doi.org/10.1007/s11003-016-9912-6

2. Boginsky, L., Reut, O., Piatsiushyk, Y., et al.: The development of processes of pressing of articles from powders on the bases of metals. Ceramics and graphite. In: 15 International Plansee Seminar, Reutte, Austria, vol. 3, pp. 197–209 (2001)

3. Zablotskyi, V., Tkachuk, A., Moroz, S., Prystupa, S., Svirzhevskyi, K.: Influence of technological methods of processing on wear resistance of conjugated cylindrical surfaces. In: Tonkonogyi, V., et al. (eds.) Advanced Manufacturing Processes II. Lecture Notes in Mechanical Engineering, pp. 477–487. Springer, Cham (2021). https://doi.org/10.1007/978-3-030-68014-5_47

4. Povstyanoy, O., MacMillan, A.: Mechatronic system's permeable materials with controlled porosity. J. Eng. Sci. **8**(1), C45–C49 (2021). https://doi.org/10.21272/jes.2021.8(1).c6

5. Tkachuk, A., Zablotskyi, V., Kononenko, A., Moroz, S., Prystupa, S.: Directed formation of quality, as a way of improving the durability of conjugated parts of friction Pairs. In: Ivanov, V., et al. (eds.) Advances in Design, Simulation and Manufacturing II. Lecture Notes in Mechanical Engineering, pp. 370–377. Springer, Cham (2020). https://doi.org/10.1007/978-3-030-22365-6_37

6. Redko, R., Zabolotnyi, O., Redko, O., Savchuk, S., Kovalchuk, V.: Improvement of manufacturing technology and recovery of clamping collets for lathe automats. In: Ivanov, V., et al. (eds.) Advances in Design, Simulation and Manufacturing II. Lecture Notes in Mechanical Engineering, pp. 290–301. Springer, Cham (2020). https://doi.org/10.1007/978-3-030-22365-6_29

7. Jackson, M.J., Toward, M.J.: Grinding and abrasive machining of composite materials. In: Shyha, I., Huo, D. (eds.) Advances in Machining of Composite Materials. Engineering Materials, pp. 459–483. Springer, Cham (2021). https://doi.org/10.1007/978-3-030-71438-3_17

8. Mel'nik, V.M., Rud', V.D., Mel'nik, Y.A.: Mathematical formalism of pore stereology of powder materials. Powder Metall. Met. Ceram. **53**(1–2), 107–112 (2014). https://doi.org/10.1007/s11106-014-9592-4

9. Zablotskyi, V., Moroz, S., Tkachuk, A., Prystupa, S., Zabolotnyi, O.: Influence of diamond smoothering treatment power parameters on microgeometry of working surfaces of conjugated parts. In: Tonkonogyi, V., et al. (eds.) Advanced Manufacturing Processes. Lecture Notes in Mechanical Engineering, pp. 372–381. Springer, Cham (2020). https://doi.org/10.1007/978-3-030-40724-7_38

10. Chernobrovchenko, V.S., Dyadyura, K.O., Balynskyi, M., Panda, A.: Influence of technological manufacturing conditions on the porosity of calcium-phosphate scaffolds. J. Eng. Sci. **8**(1), C18–C28 (2021). https://doi.org/10.21272/jes.2021.8(1).c3

11. Zabolotnyi, O., Pasternak, V., Andrushchak, I., Ilchuk, N., Svirzhevskyi, K.: Numerical simulation of the microstructure of structural-inhomogeneous materials. In: Ivanov, V., Trojanowska, J., Pavlenko, I., Zajac, J., Peraković, D. (eds.) Advances in Design, Simulation and Manufacturing III. Lecture Notes in Mechanical Engineering, pp. 562–571. Springer, Cham (2020). https://doi.org/10.1007/978-3-030-50794-7_55

12. Causton, R., Schade, C.: Machinability: a material property or process response. In: Lawcock, R., Wright, M. (eds) Advances in Powder Metallurgy & Particulate Materials Metal Powder Industries Federation, part 7, Princeton, NJ, pp. 154–69 (2003)

13. M'Saoubi, R., Czotscher, T., Andersson, O., Meyer, D.: Machinability of powder metallurgy steels using PcBN inserts. Proc. CIRP **14**, 83–88 (2014). https://doi.org/10.1016/j.procir.2014.03.094

14. Dayong, Y., Longsheng, L., Zhenping, W.: Material removal mechanism of green machining on powder metallurgy parts during orthogonal cutting. Adv. Mater. Sci. Eng. **2020**, 1962602 (2020). https://doi.org/10.1155/2020/1962602

15. Czampa, M., Farkas, B., Szalay, T.: Machinability improvement of powder metallurgy steels. Tehnički vjesnik **23**(3), 809–817 (2016). https://doi.org/10.17559/TV-20150429100430

16. Czampa, M., Markos, S., Szalay, T.: Improvement of drilling possibilities for machining powder metallurgy materials. Proc. CIRP **7**, 288–293 (2013). https://doi.org/10.1016/j.procir.2013.05.049

17. Tanaka, M., Yoshimoto, A., Ohshita, H., Hashimoto, T.: Grinding Mechanism and Case Study on Double-Disc Grinding of Ferrous Sintered Material. Powder Metal. 877–878 (2006)

18. Povstyanoi, O.Y., Sychuk, V.A., McMillan, A., Rud', V.D., Zabolotnyi, O.V.: Metallographic analysis and microstructural image processing of sandblasting nozzles produced by powder metallurgy methods. Powder Metall. Met. Ceram. **54**(3–4), 234–240 (2015). https://doi.org/10.1007/s11106-015-9705-8

19. Ivanov, V., Dehtiarov, I., Pavlenko, I., Kosov, M., Hatala, M.: Technological assurance and features of fork-type parts machining. In: Ivanov, V., et al. (eds.) Advances in Design, Simulation and Manufacturing II. Lecture Notes in Mechanical Engineering, pp. 114–125. Springer, Cham (2020). https://doi.org/10.1007/978-3-030-22365-6_12

20. Armarego, E.J.A., Shi, G., Verezub, S.: Modelling the basic cutting action and machining performance of sintered metallic materials. Mach. Sci. Technol. **5**(3), 353–373 (2001). https://doi.org/10.1081/MST-100108620

21. Zaichuk, N., Shymchuk, S., Tkachuk, A., Feshchuk, Y., Szczot, J.: Structure and properties of surface bandage shelves for the gas turbine engine's blades. In: Ivanov, V., Trojanowska, J., Pavlenko, I., Zajac, J., Peraković, D. (eds.) Advances in Design, Simulation and Manufacturing IV. Lecture Notes in Mechanical Engineering, pp. 602–612. Springer, Cham (2021). https://doi.org/10.1007/978-3-030-77719-7_60

22. Zablotskyi, V., Tkachuk, A., Senyshyn, A., Trokhymchuk, I., Svirzhevskyi, K.: Impact of turning operations on the formation of rolling bearing's functional surfaces. In: Tonkonogyi, V., Ivanov, V., Trojanowska, J., Oborskyi, G., Pavlenko, I. (eds.) Advanced Manufacturing Processes III. Lecture Notes in Mechanical Engineering, pp. 229–238. Springer, Cham (2022). https://doi.org/10.1007/978-3-030-91327-4_23

23. Privezentsev, D., Zhiznyakov, A., Kulkov, Y.: Analysis of the microhardness of metals using digital metallographic images. Mater. Today Proc. **11**(1), 325–329 (2019). https://doi.org/10.1016/j.matpr.2018.12.152

Advanced Materials

Control of the Physical and Mechanical Properties of Mixtures Based on Liquid Glass with Various Fillers

Tetiana Berlizieva[1]([✉]) [iD], Olga Ponomarenko[1] [iD], Igor Grimzin[2] [iD],
Nataliia Yevtushenko[1] [iD], and Oleg Khoroshylov[3] [iD]

[1] National Technical University "Kharkiv Polytechnic Institute", 2,
Kyrpychova Street, Kharkiv 61002, Ukraine
berlizeva.tatyana@gmail.com
[2] Research and Production Center "European Engineering Technologies",
101, Big Panasovskaya Street, Kharkov 61017, Ukraine
[3] Ukrainian Engineering and Pedagogical Academy, 16, Universitetska Street, Kharkiv 61003,
Ukraine

Abstract. The paper presents the results of a study of the main properties of mixtures with liquid glass (LG) and furfuryl oxypropyl cyclocarbonate (FOPCC) for mixtures based on various fillers (chromite compounds, mixtures of quartz sand with chromite and quartz sands). The parameters such as gas generation ability, compressive strength, gas permeability, friability, and residual strength were studied and determined by standard methods. The optimum content of the FOPCC multi-purpose additive in a mixture based on chromite and quartz sands was evaluated. The experimental results showed that the chromite sand-based mixture's compressive strength and gas generation ability is higher than those of the quartz sand-based mixture. The friability and gas permeability is higher with respect to quartz sand-based mixtures. It was found that the breakdown ability of chromite sand-based mixtures is better than that of quartz sand-based mixtures. According to the mixture process sample, the compressive strength value is 2,1 MPa; the gas generation ability of the mixture is about 11,7 cm^3/g; the friability of the mixtures is in 0,045%; the gas permeability is more than 400 units; the residual strength is 0,47 MPa for chromite-based mixtures. For mixtures based on quartz sands, the compressive strength is 2,074 MPa; the gas generation ability of the mixture is about 10,5 cm^3/g; the friability of the mixtures is 0,045%; the gas permeability is 500 units, and the residual strength is 0,97 MPa. A technological process for preparing cold hardening mixtures (CHM) based on chromite and quartz sands was developed. As a result, the surface quality of the molds was improved, and burn marks on the castings were reduced.

Keywords: Cold-solidifying mixture · Soluble glass · Furfuryl oxypropyl cyclocarbonates · Chromite sand · Quartz sand · Product innovation

1 Introduction

The properties of molding sands, which depend on the starting materials, strongly influence the quality of the castings [2]. The amount of fillers in the mixture is on average from 90% to 98%. Fillers should be inactive to molten metal, have relatively high thermal stability, mechanical strength, refractory properties, lower coefficient of thermal expansion, minimum cost, and uniform grain composition [3].

Currently, quartz foundry sands are the most widely used; more than 90% of all foundry's sand is consumed by the foundry [4]. Quartz sand has a number of advantages: it has a high hardness, high melting point; chemical inactivity at ordinary temperatures; good wettability with water and with almost all binders used; in addition, it is used in the manufacture of castings from various alloys; and also mixes well with various components of mixtures [5].

Chromite sand is also used as a filler from facing and core mixtures for steel castings [6]. Highly refractory and chemically inactive chromite sands have also become more commonly used for turbomachinery needs [7].

Chromite sand has a high thermal shock strength and does not have any allotropic transformations at 575 °C. It is inert to iron oxides at high temperatures and is poorly wetted by liquid metal, preventing the formation of burn marks and improving the conditions for metal crystallization [8]. In addition, it has a high thermal storage capacity and thermal conductivity [9].

Therefore, the development and use of new mixtures based on quartz and chromite sands is an urgent task of the foundry.

2 Literature Review

There are a considerable number of ways to make molds [10] and cores [11] using numerous compositions of mixtures [12]. One of the most frequently used methods is obtaining molds and cores on liquid glass (LG). Liquid glass is an available, cheap, and non-toxic binder binding material. The use of liquid glass as a binder for the manufacture of core and molding sands makes it possible to obtain stronger molds, reducing the metal consumption of castings owing to the production of thinner-walled products [13, 14].

One of the main disadvantages of using mixtures on liquid glass that are cured with carbon dioxide is the formation of fusible silicates at temperatures 700 °C, leading to sintering of mixtures, an increase in residual strength, and consequently, to a deterioration in a knockout [15, 16]. Esters are used together with LG to improve the knock-out of molding and core sands.

The dependences of the increase in the compressive strength of mixtures with water glass for casting molds and cores on the composition and amount of ether hardeners were investigated and studied. The difference is in the composition and amount of technological additives with ether hardeners. This makes it possible to increase the compressive strength of mixtures on various fillers with water glass for casting molds and cores. A large number of on-air compositions were tested, based on which the most optimal for use were selected [17].

In this paper, it is proposed to use a multi-purpose additive of furfuryl oxypropyl cyclocarbonate (FOPCC) as an ether hardener in order to produce cores and molds based

on liquid glass. When metal is poured into a mold, furfuryl oxypropyl cyclocarbonate, as a result of thermochemical destruction, releases carbon dioxide and water vapor in the volume of the resulting composition. That is why furfuryl oxypropyl cyclocarbonate is a cleaner material from an environmental point of view [18].

All cyclocarbonates in an alkaline environment are unstable and decompose while releasing carbon dioxide. In turn, carbon dioxide reacts with liquid glass and forms polysilicates in the volume of the composition formed.

The systems that have formed are classified as nanostructured composite materials because the processes of interaction between liquid glass and FOPCC occur in monomolecular layers on the sand surface.

When used as a binder, the Gel time or the sol-gel transition time is an important characteristic of a silica system. The main stage in gel formation is the collision of two silica particles with a reasonably low charge on the surface. During the interaction of such particles between them, siloxane bonds are formed that irreversibly hold the particles together.

Mathematical models were developed that serve to control the strength parameters of mixtures based on a chromite filler, the result of which is the ability to compare the properties of the mixture based on liquid glass with chromite sand, quartz sand, and a mixture of quartz and chromite sands [19, 20].

The study aims to analyze the properties of mixtures based on liquid glass with triethanolamine and FOPCC multi-purpose additive based on chromite sand, quartz sand, and a mixture of quartz and chromite sands to obtain high-quality molds and cores for foundry purposes.

3 Research Methodology

FOPCC is a clear, light yellow liquid. The mixture was obtained as follows: per 100 wt % of sand and 4 wt % of liquid glass.

Liquid hardener was added to the sand and stirred for 180 s, after which liquid glass modified with triethanolamine was added and stirred for another 120 s. The liquid glass was modified with triethanolamine. Triethanolamine was used from the total weight of furfuryl propyl cyclocarbonate. The mixture was made in a 9-seat mold. FOPCC was introduced in the amount from 0.4 to 0.6 wt %, liquid glass – from 4,5 to 5,5 wt%, and triethanolamine – from 2 to 10 wt % of the mass of furfuryl propyl cyclocarbonate.

Grade 2K1O102 GOST 2138-91 quartz sand and Grade AFS45-50 TU U 13.2-35202765-001: 011 chromite grains of sand were used as filler for the molding mixtures.

The paper investigated gas permeability, compressive strength, gas generation ability, and friability properties.

Molding materials must have a number of properties that correspond to a particular molding or core mixture. These include the conditions for the interaction of the mold with the liquid metal during the casting of the mold, cooling, and solidification of the casting.

The strength of the casting mold when it is made, filling it with an alloy, and solidifying the casting determines the mechanical properties. Compressive strength tests of

the mixtures were carried out according to standards. For this purpose, to evaluate the ultimate strength of molding and core mixtures, a Model 04116U facility was used.

Technological properties determine the conditions under which high-quality molds and cores are obtained and castings with the lowest labor intensity and high surface quality (without cracks and surface contamination).

The friability rate of molding and core mixtures according to GOST standards was determined using standard cylinder samples. The samples were tested in a dry state. The crumbling was expressed as a percentage and was determined as follows. The sample was placed in a mesh ram rotating and was determined by the mass loss of the sample.

One of the most accessible methods for quantifying the breakdown ability was determining the residual strength of heated and cooled standard samples. Samples of standard sizes are made and kept for a day. After this time, they are calcined for 1 h in a muffle furnace at a temperature of 800 °C. After they have cooled, they are tested for strength. This is the essence of the method.

The conditions for gas formation mainly determine the hydraulic properties.

Gas permeability is an essential property of molding and core mixtures and is characterized by transmitting gases. With poor gas permeability, it becomes more challenging to remove gaseous products from the casting mold cavity during its pouring. The gas permeability of the core and molding mixtures was carried as follows. Air was blown through a standard sample made from the core or molding mixture.

4   Results

The paper conducts a comparative assessment of the properties of mixtures based on liquid glass with triethanolamine and FOPCC multi-purpose additive based on chromite sand, quartz sand, and a mixture of quartz and chromite sand [21, 22].
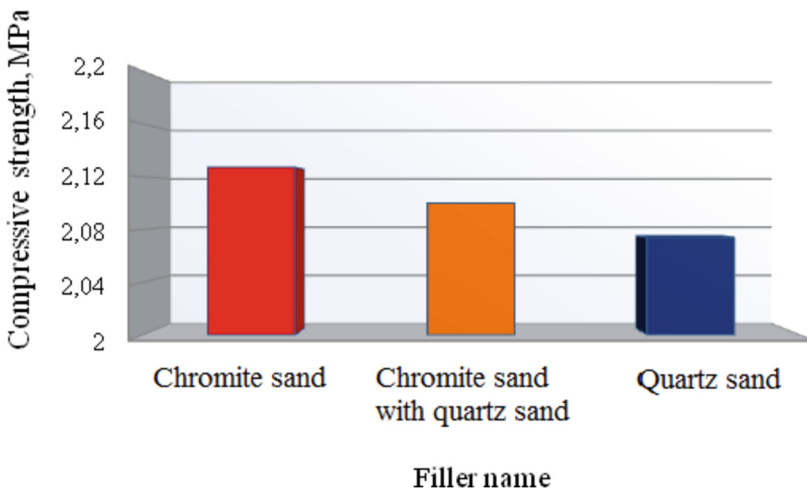
Fig. 1. Compressive strength of mixtures with various fillers.

The main mechanical, technological, and hydraulic properties of mixtures based on liquid glass and FOPCC additives were investigated by standard methods.

According to the mixture process sample, the compressive strength values are on average 2,127 MPa for chromite sands and 2,074 MPa for quartz sands. The gas generation ability of the mixture is on average 11,7 cm^3/g; the friability of the mixtures is in the area of 0,045%; the gas permeability is more than 400 units; the residual strength is 0,47 MPa for chromite-based mixtures.

For mixtures based on quartz sands, the gas generation ability of the mixture is 10,5 cm^3/g; the friability of the mixtures is in the area of 0,045%; the gas permeability is more than 500 units, and the residual strength is 0,97 MPa.

For clarity, the compressive strength, friability, gas permeability, and gas generation ability of mixtures with various fillers are shown in the form of histograms in Fig. 1, 2, 3 and 4, respectively.
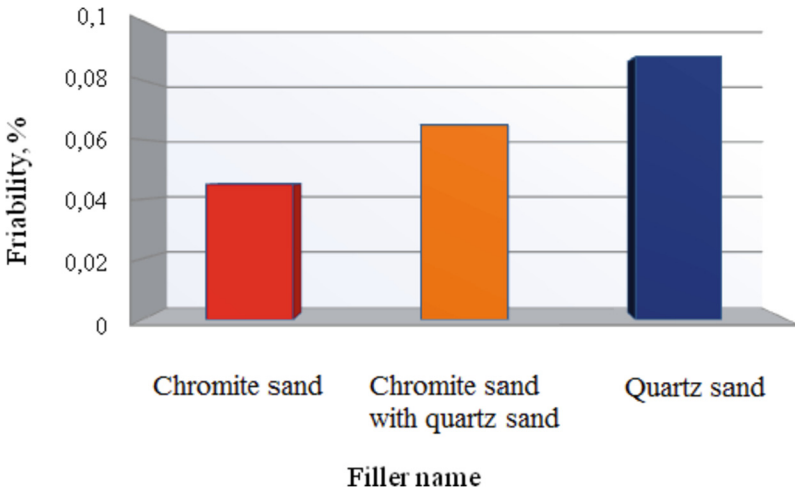
Fig. 2. Friability of mixtures with various fillers.

The review of the histograms shown in Fig. 1, 2, 3 and 4 showed that the compressive strength and gas generation ability of mixtures based on quartz sand are lower than those of the mixtures based on other fillers. The friability and gas permeability is higher in mixtures based on quartz sand.

Additionally, an experiment was carried out to determine the residual strength of mixtures on quartz sand, chromite sand, and a mixture of quartz and chromite sands. The findings of the experiment are shown in Table 1.

The review of the histogram data shows that the residual strength of mixtures based on chromite sand is lower than that of the mixtures based on other fillers.

The comparison of the main properties of mixtures based on chromite filler, on chromite and quartz sands, on quartz sand is reviewed. The investigations have shown the possibility of using chromite sands for cold-hardening mixtures based on LG with a multi-purpose additive of furfuryl oxypropyl cyclocarbonates in the foundry industry.
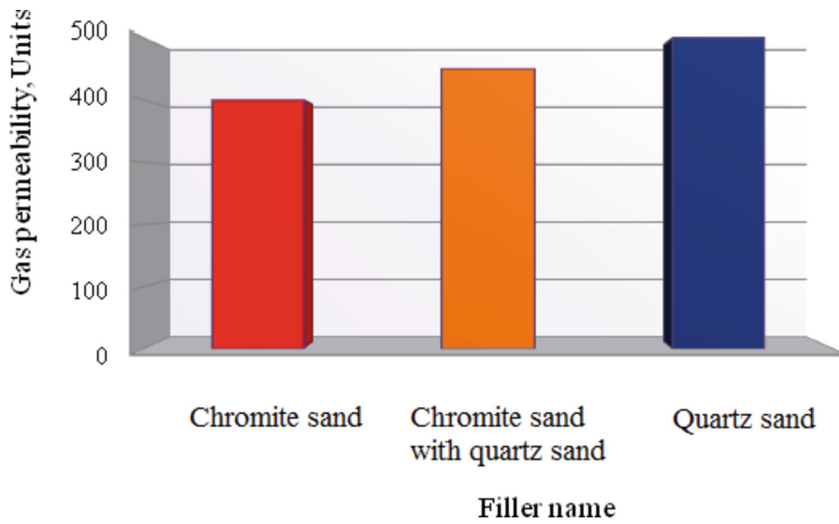
Fig. 3. Gas permeability of mixtures with various fillers.
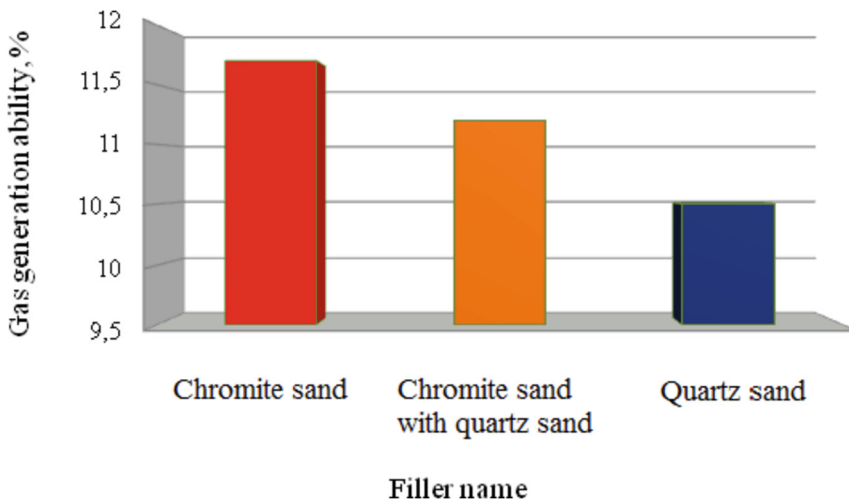
Fig. 4. Gas generation ability of mixtures with various fillers.

Table 1. Residual strength of mixtures with various fillers.

Item No.	Mixture name	Residual strength, MPA
1	Chromite sand	0,47
2	Chromite sand (10%) with quartz sand (90%)	0,53
3	Quartz sand	0,97

5   Conclusions

Technological processes for preparing core and molding CHM based on LG with FOPCC using quartz and chromite sands were developed to obtain high-quality castings from iron-carbon and non-ferrous alloys.

The main properties of CHM based on LG using a multi-purpose additive FOPCC based on quartz and chromite sands were determined, such as compressive strength, gas generation ability, gas permeability, friability, and residual strength. The quality of castings in sand casting depends on these properties.

According to the mixture process sample, the compressive strength values are on average 2,127 MPa for chromite sands and 2,074 MPa for quartz sands. The gas generation ability of the mixture is on average 11,7 cm^3/g; the friability of the mixtures is in the area of 0,045%; the gas permeability is more than 400 units; the residual strength is 0,47 MPa for chromite-based mixtures.

For mixtures based on quartz sands, the gas generation ability of the mixture is 10,5 cm^3/g; the friability of the mixtures is in the area of 0,045%; the gas permeability is more than 500 units, and the residual strength is 0,97 MPa.

The optimum content of the FOPCC multi-purpose additive the mixture based on chromite sand was evaluated. The experimental results showed that the values of the mechanical properties of the mixture based on chromite sand are higher than those of the mixtures based on quartz sand. The breakdown ability of mixtures based on chromite sand is better than that of quartz sand.

The studies have shown the possibility of using chromite and quartz sands for cold-hardening mixtures based on liquid glass with FOPCC in the foundry.

A technological process for obtaining CHM with FOPCC on chromite and quartz sands was developed. CHM with FOPCC based on chromite and quartz sands. As a result, the surface quality of the molds was improved, and burn marks on the castings were reduced.

It is planned to create new ethereal compositions for use in global production and test existing compositions as an opportunity to use with various fillers. The prospect is the organization of the production of essential compositions for widespread use in the foundry industry.

References

1. Lysenko, T.V., Yasyukov, V.V., Prokopovich, I.V.: Casting Shaping Control Concept. Ecology, Odessa (2019)
2. Lyuty, R.V., Houri, I.M.: Molding materials. KPI them. Sikorsky, Kyiv (2020)
3. Berladir, K., Gusak, O.: Influence of mechanically activated fillers of different chemical nature on tribotechnical properties of PTFE-composites. In: Tonkonogyi, V., et al. (eds.) InterPartner 2019. LNME, pp. 395–404. Springer, Cham (2020). https://doi.org/10.1007/978-3-030-40724-7_40
4. Nurjaman, F., Shofi, A., Herlina, U., Suharno, B., Faradila, A.R., Laurensia, Subandrio, S.: Reduction process of low-grade chromite sand using calcium carbonate and calcium sulfate as additives and coal as reductant. In: AIP Conference Proceedings, vol. 2232, p. 040007. AIP Publishing LLC (2020). https://doi.org/10.1063/5.0001853

5. Kabasele, J.K., Nyembwe, K.D.: Assessment of local chromite sand as 'green' refractory raw materials for sand casting applications in a post-pandemic world. S. Afr. J. Ind. Eng. **32**(3), 65–74 (2021). https://doi.org/10.7166/32-3-2615

6. Nurjaman, F., Subandrio, S., Ferdian, D., Suharno, B.: Effect of basicity on beneficiated chromite sand smelting process using submerged arc furnace. In: AIP Conference Proceedings, vol. 1964, p. 020009. AIP Publishing LLC (2018). https://doi.org/10.1063/1.5038291

7. Subandrio, S., Dahani, W., Alghifar, M., Purwiyono, T.T.: Enrichment chromite sand grade using magnetic separator. In: IOP Conference Series: Materials Science and Engineering, vol. 588, p. 012033. IOP Publishing (2019). https://doi.org/10.1088/1757-899X/588/1/012033

8. Dobosz, M.D., Grabarczyk, A., Major-Gabryś, K., Jakubski, J.: Influence of quartz sand quality on bending strength and thermal deformation of moulding sands with synthetic binders. Arch. Foundry Eng. **15**(2), 9–12 (2015). https://doi.org/10.1515/afe-2015-0028

9. Huminski, Y., Rovin, S.L.: Environmentally friendly superfine modified ultrafine liquid glass binder. Cast. Metall. **3**, 41–45 (2019)

10. Thu, A.H., Zakharov, A.I.: Preparation of inorganic binder for cold-hardening mixtures. Refract. Ind. Ceram. **59**(3), 313–317 (2018). Springer

11. Al-Saraireh, F.M., Svinoroev, Y.: Assessment of casting binding materials based on modified technical lignosulfonates. Int. J. Mech. Prod. Eng. Res. Dev. **10**(2), 335–346 (2020)

12. Berladir, K., Hovorun, T., Gusak, O., Reshetniak, Y., Khudaybergenov, D.: Influence of modifiers-ligatures on the properties of cast aluminum alloy AK5M2 for the automotive industry. In: Ivanov, V., Trojanowska, J., Pavlenko, I., Zajac, J., Peraković, D. (eds.) DSMIE 2020. LNME, pp. 473–482. Springer, Cham (2020). https://doi.org/10.1007/978-3-030-50794-7_46

13. Al-Saraireh, F.M.: An assessment of the efficiency of utilizing complex modifiers for softening the liquid-glass mixtures to improve iron and steel casting. ARPN J. Eng. Appl. Sci. **13**(9), 3231–3235 (2018)

14. Saikaew, C., Wiengwiset, S.: Optimization of molding sand composition for quality improvement of iron castings. Appl. Clay Sci. **67**, 2–31 (2012). https://doi.org/10.1016/j.clay.2012.07.005

15. Ingebrigtsen, T.S., Dyre, J.C., Schrøder, T.B., Royall, C.P.: Crystallization instability in glass-forming mixtures. Phys. Rev. X **9**(3), 031016 (2019)

16. Karateev, A.M., Ponomarenko, O.I., Litvinov, D.A., Kalkamanova, O.S., Berlizeva, T.V.: A method of obtaining cold-hardening mixtures. Utility model patent UA No. 95138 Ukraine (2014)

17. Zinchenko, P.S., Aksenenko, M.P., Yovbak, A.V., Orendarchuk, Y.V.: Application of liquid glass mixtures with a low content of liquid glass as a factor in improving the quality of castings for engineering purposes. ScienceRise **5/2**(22), 6–9 (2016)

18. Huminski, Y., Rovin, S.L.: Application of a liquid glass binder modified by ultra-dispersed materials. Foundry **11**, 17–20 (2019)

19. Ponomarenko, O., Berlizeva, T., Grimzin, I., Yevtushenko, N., Lysenko, T.: Strength properties control of mixtures based on soluble glass with ethereos solidifiers. In: Ivanov, V., Trojanowska, J., Pavlenko, I., Zajac, J., Peraković, D. (eds.) DSMIE 2020. LNME, pp. 511–521. Springer, Cham (2020). https://doi.org/10.1007/978-3-030-50794-7_50

20. Karpenko, V.M., Karpenko, V.M., Marukovich, E.I.: Artistic Casting: Materials, Technologies, Equipment. Belarus Science, Minsk (2019)

21. Schetinin, A.A., Ammer, V.A., Turischev, Y.Y.: Advantages and prospects of using cold-hardening mixtures in the manufacture of critical and highly loaded castings for the aviation industry. Bull. Voronezh State Tech. Univ. **3**(13), 68–70 (2017)

22. Al-Saraireh, F.M., Svinoroev, Y.: Production of high quality casting binders from materials containing lignin. Int. J. Mech. Prod. Eng. Res. Dev. **3**(10), 14575–14584 (2020)

Catalytic Growth of Carbon Nanostructures in Glow Discharge

Andrii Breus , Sergey Abashin , Ivan Lukashov, Oleksii Serdiuk,
and Oleg Baranov$^{(\boxtimes)}$

National Aerospace University, 17, Chkalova Street, Kharkiv 61070, Ukraine
o.baranov@khai.edu

Abstract. Glow discharge ignited between a graphite cathode and a copper anode was applied to conduct a process of carbon nanostructure growth in an argon atmosphere. During the first stage of the experiment, the samples mounted on the cathode were heated up till turning red, which significantly increased the thermionic emission and caused the formation of cathode arc spots on the sample surface. The arcing with a period of 3 to 5 s was maintained for 5 more minutes. As a result, a number of craters were observed on the samples, which were investigated using the SEM technique. Carbon nanotubes and bundles of them were found along the whole surface of the samples, and the tips of the nano- and microsized structures were capped by the copper particles, which states in favor of the catalytic growth. The yield of the carbon structures was richer in the craters and the regions at the proximity to them. In addition, a carbon deposit was taken from the anode and studied by use of TEM. In this case, typical nanostructures resemble the branches of spruce trees or balls of rolled nanotubes with a diameter of about 15 to 30 nm; at that, the anode nanostructures do not show any traces of the copper catalyst. Thus, the proposed setup is suitable to grow various carbon nanostructures in a catalytic process in the presence of copper.

Keywords: Industrial growth · Carbon · Nanostructures · Plasma growth · Glow discharge

1 Introduction

Made of the chemically stable element, carbon materials are emerged as promising candidates for neural electrodes due to the significant matching with the surrounding tissues in mechanical and biological properties [1]. Various carbon nanostructures have demonstrated attractive characteristics for field emission devices [2] or as carriers for drug delivery into the brain [3]. It is proven that diamond-like carbon, carbon nanofibers, and nanotubes are inherently interesting for neurotransmitter detection because of their excellent biocompatibility [4]. Carbon-based nanomaterials, including fullerene, carbon nanotubes, graphene, and diamond-like coatings, have exhibited prominent antibacterial properties that can be tailored by changing the nanostructure dimensional factors such as diameter, length for 1D nanostructures, and a number of layers for nanosheets [5]. When

developing the gas sensors, multi-walled carbon nanotubes obtained core-shell carbon nanoparticles covered by functional groups after functionalization conducted using oxygen plasma combined with O-polymerization of maleic anhydride and acetylene, which resulted in an extremely high response of about 32% at 500 ppm of NH_3 [6]. At the same time, carbon nanotube composite treated in an NH_3 plasma environment was successfully applied as an electrode for high-performance supercapacitors by providing an efficient transport pathway for both electrons and ions [7], while graphene is very attractive as an electrode material due to its high specific surface area [8]. A comprehensive review conducted by Hatakeyama provides an extensive list of nanoscale materials of carbon allotropes applications called nanohorns, nanowalls, and nanodiamonds [9].

2   Literature Review

Among a large variety of methods of carbon nanostructure growth, plasma-enhanced techniques are considered the most perspective with respect to the cost-efficiency, productivity, and controllability. For the last decade, all kinds of plasma discharges have been successfully applied to synthesize the 'nanocarbones'. Indeed, Khataee et al. have developed a one-step preparation method of a graphite electrode for the heterogeneous electro-Fenton-like process using glow discharge plasma [10]. Sobczyk and Jaworek carried out the synthesis of carbon microstructures in atmospheric pressure microdischarges [11]. At the same time, spark plasma sintering was employed by Kamal et al. to synthesize iron carbide nanostructures [12]. Capacitively coupled radiofrequency discharge ignited in CH_4/H_2 plasma allowed to obtain the density control of carbon nanowalls with the outstanding electrical properties in the research conducted by Cho et al. [13]. At the same time, the inductively coupled RF plasma was also successful in the growth of graphene and its oxide, as was shown by Ye et al. [14] and Zhou et al. [15]. Bundaleska, Tatarova et al. implemented the microwave plasma at the frequency of 2.45 GHz to conduct the free-standing carbon nanostructures at atmospheric pressure conditions [16, 17]. Electron-cyclotron resonance (ECR) plasma was engaged to study the effect of the key process parameters to substrate on the catalyst-free growth of vertical graphene [18] and to perform its functionalization in oxygen to enhance the performance of electrochemical capacitors [19].

However, considering the number of reports, the arc discharge is the most applied for the plasma synthesis of the carbon nanostructures. This fact can be explained by the extremal conditions created in the arc spots, complex arc interactions with the electric and magnetic fields [20], and highly-developed methods of the distribution control of the arc plasma density [21, 22]. Synthesis of graphene flakes in the magnetically stabilized gliding arc discharge was carried out by Li et al. [23], while Zhang et al. performed the controllable synthesis of carbon nanomaterials in DC arc from the inner wall of the reactor chamber [24]. "Synthesis-on" and "synthesis-off" modes of carbon arc operation were studied by Yatom et al. for a configuration with hollow anode filled with a mixture of powdered metal catalyst and graphite [25]. It was concluded that synthesis-on mode duration is rare compared to the total arc run-time, which explained the poor selectivity and an inevitable inadequacy of arc synthesis. When studying the structure variations of the cathode deposit in the carbon arc, Yeh et al. reported that for an all-carbon system, the

deposit shows spatially distinct structural variations with a strong correlation between the arc current and the area of the nanotube formation [26]. Research conducted by Fang et al. was also dedicated to determining the synthesis region of the single-wall carbon nanotubes [27]. The investigation of the formation of carbon nanowalls, nanotubes, and nanotips on the samples immersed into the plasma fluxes up to four magnitude orders larger than in conventional PECVD was carried out by Bystrov et al. [28]. At the same time, spherical carbon nanoparticles, graphene nanoflakes, and nitrogen-doped carbon nanoparticles were obtained in a magnetically stabilized gliding arc discharge developed by Wang et al. [29]. A comprehensive review of carbon nanomaterials syntheses, such as nanotubes and graphene, on surfaces exposed to arc discharge hot plasma, was made by Su and Zhang [30]. In contrast, Levchenko et al. reported the growth of graphene flakes in the volume of the arc discharge [31].

In this paper, we report the growth of carbon nanostructures using the most cost-effective and straightforward way, namely in a glow discharge.

3   Research Methodology

After the literature analysis, it was concluded about the possibility of the carbon nanostructures catalytic growth on a graphite cathode at the presence of atomic fluxes of copper extracted from the anode or auxiliary fixtures of the setup design. To conduct the synthesis of carbon nanostructures, a plasma set up with an inner diameter of 300 mm and a length of 350 mm was engaged. A schematic of the setup is shown in Fig. 1.
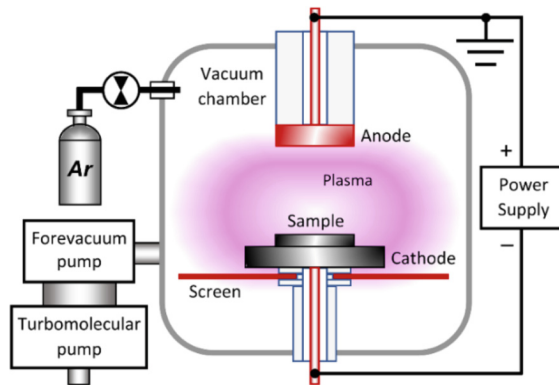
Fig. 1. Schematic of the experimental setup.

In the discharge configuration typical for glow discharges, two electrodes were separated by a gap of 15 mm; one electrode (an anode, 15 mm in diameter) was made of copper, while the other (a cathode, 35 mm in diameter) was made of graphite. The samples of a diameter of 8 mm and height of 5 mm were put on the cathode, and the chamber was pumped out to the pressure of 10^{-3} Pa using the forevacuum and turbomolecular pumps. A screen made of copper was used to protect the cathode from fluxes of material that could be sputtered from the ceramic parts of the cathode fixture and possibly could

serve as a source of the copper atoms to be deposited as the catalyst on the graphite cath-
ode. The chamber was filled with argon, and the pressure was maintained at 620 Pa. The
glow plasma discharge was obtained when applying the potential drop of minus 420 V
to the cathode with respect to the grounded anode and walls of the vacuum chamber;
the discharge current reached a value of 0.4 A. Photograph of the plasma discharge is
shown in Fig. 2.
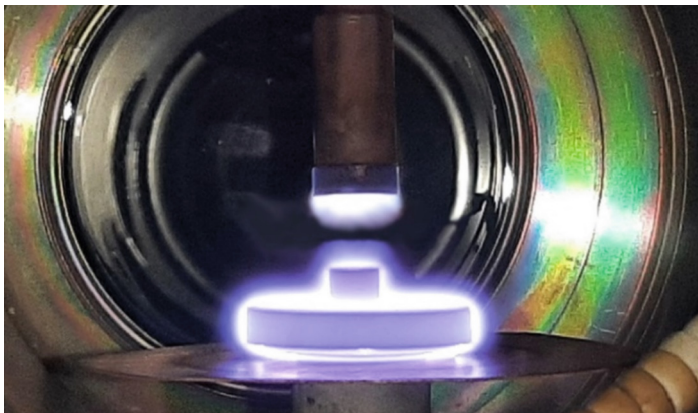
Fig. 2. Photograph of the discharge.

Plasma appeared as a bright glow separated from the cathode by the dark sheath. In
addition, an anodic glow was also observed. Under these conditions, the samples were
heated to a red color. During the last 5 min of each experiment, spots of the arc discharge
were observed on the sample, and the time interval between their appearance was about
3 to 5 s. The full set of experiments included 10 samples with 30 min spent for each
experimental run.

4 Results

After the experiment, all samples exhibited evidence of plasma treatment with a matted
black surface opposite to the glossy layer found after the preliminary mechanical polish-
ing carried out before the plasma exposure. This change in appearance was associated
with the growth of the nanostructures on the surfaces and the arc spots' action that was
confirmed by the scanning electron microscopy (SEM) technique.

SEM images of the samples are shown in Fig. 3.

Many nanostructures were observed in the regions near the craters left after the
cathodic spots of the arc discharge, while the rest of the structures were found on the
part of the surface that was not damaged by the arcs. The general view of the structures
shown in Fig. 3a exhibits nanotubes with the balls on their tips. A magnified view of the
nanotubes shown in Fig. 3b reveals their diameter of about 26 nm, usually associated with
the multi-walled nanotubes (MWNTs). Moreover, the diversity of the nanostructures is
not limited by the nanotubes.

Occasionally, hollow spheric nanostructures of copper partially covered by the carbon net structure can be found on the samples, as shown in Fig. 3c, or the bundles of carbon structures as shown in Fig. 3d. The role of the copper balls as the catalyst for
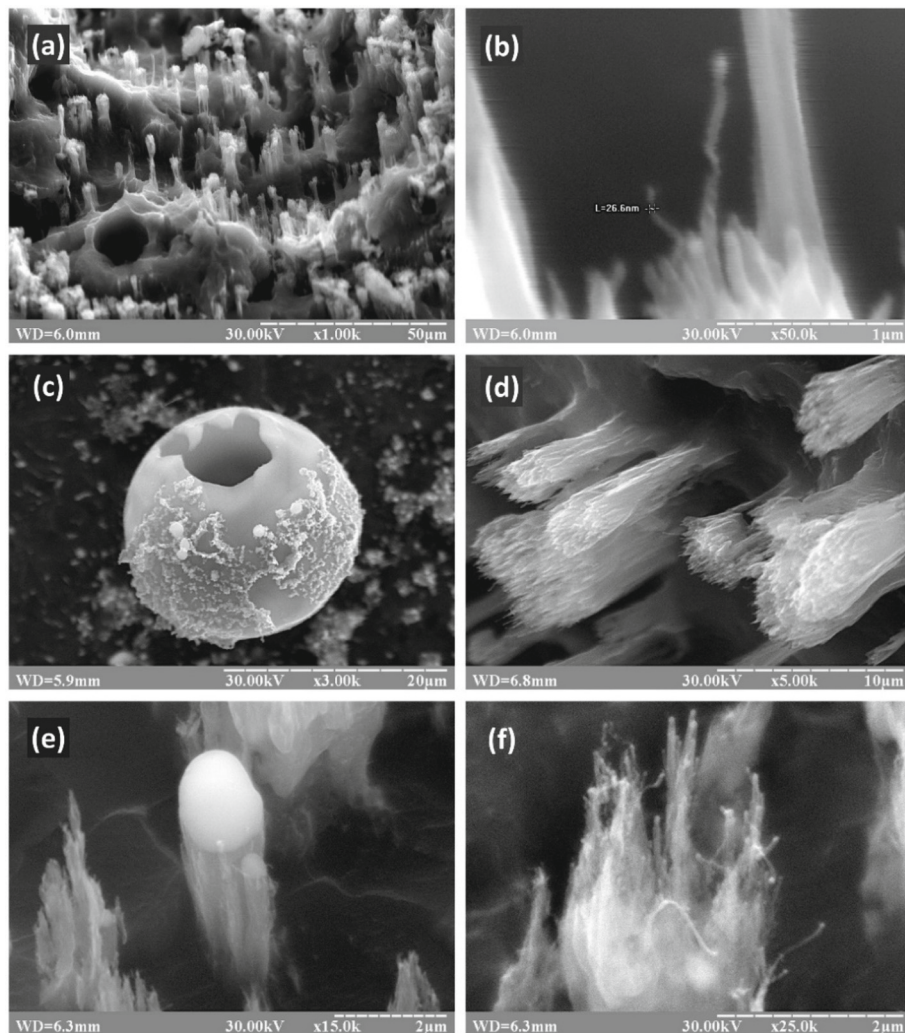
Fig. 3. Carbon nanostructures synthesized on the graphite cathode: a – nanotubes with copper particles on their tips; b – a magnified view of the nanotubes revealing their diameter of about 26 nm that is usually associated with the multi-walled nanotubes (MWNTs); c – a hollow spheric nanostructure of copper partially covered by the carbon net structure; d – bundles of carbon structures; e, f – copper particles of micro-and nanometer size, respectively, on the tips of the carbon structures are assumed to be the seeds for the growth the carbon structures; the copper material that supposedly was deposited from the material sputtered from the copper anode and screen (Fig. 1).

the growth of the carbon nanostructures can be evaluated from the SEM images shown in Fig. 3e and Fig. 3f. The first one illustrates how a copper microparticle with a diameter of about 1 μm serves as a seed for the growth of the whole bundle of the carbon nanostructures; it is noteworthy that the presence of the copper catalyst is not mandatory for such structures, Ref. Fig. 3d. In contrast, the second image confirms that almost all nanotubes are capped with copper catalyst nanoparticles.

The unambiguous association of carbon nanostructures with copper particles can significantly simplify the problem solution of the origin of the nuclei of carbon nanostructures – they are copper particles, the concentration of which determines the concentration of carbon nanostructures on the graphite surface.

In addition to the carbon nanostructures grown on the surfaces of the samples installed on the cathode, an anodic deposit was also studied, an anodic deposit was also studied. For that, carbon powder mechanically removed from the anode surface was exposed to the transmission electron microscopy (TEM) technique; TEM images are shown in Fig. 4. As can be seen, the appearance of the nanostructures changes drastically in the case of anodic growth. The typical nanostructures resemble the branches of spruce trees, as shown in Fig. 4a and Fig. 4b, or balls of rolled 1D nanostructures shown in Fig. 4c and Fig. 4d. The measured thickness of these nanostructures does not exceed the value of 15 nm. Unlike the cathode deposit, the anode structures do not show any traces of the copper catalyst. This fact does not deny the possibility of catalytic growth; however, the mechanisms can be different for the nanostructures. In the case of the nanowires found on the cathode, the copper nanoparticles are possibly grown from the copper material sputtered from the anode or copper screen placed under the cathode. These particles adsorb the carbon adatoms, thus serving as the seeds in the growth process. The carbon
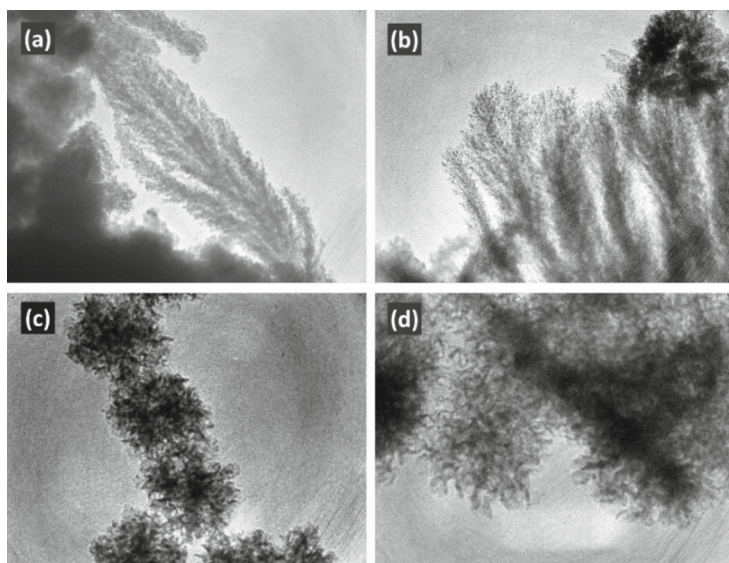
Fig. 4. Carbon nanostructures synthesized on the copper anode: a, b – "branches of spruce trees"; c, d – 1D nanostructures rolled into the balls.

material is concentrated between the copper particle and the carbon cathode, arranged by the growth mechanisms, and lifts the copper particle during the nanowire growth. At the same time, the nanostructures on the anode may use microprotrusions of the copper surface of the anode to concentrate on them under the action of the relatively weak electric field generated in the anode sheath. This field, coupled with the local fields along the anode surface, can serve as the driving force of the growth process. The spruce tree appearance may be conditioned by the number of defects caused on the surface of the growing nanostructure at its bombardment by the ions extracted from plasma.

5 Conclusions

The simple plasma glow setup described in this paper has confirmed its ability to be a powerful development tool for the robust, reliable, and productive synthesis of carbon nanostructures. It was experimentally confirmed that catalytic growth at the presence of copper material is possible both on the cathode and on anode surfaces. At that, the structures obtained on these surfaces are quite different. Cathode structures are a mixture of nano- and microstructures with the catalytic copper particles also ranging from the nanometers to micrometers in diameter and found on the tips of the carbon structures. Opposite to that, anode structures have nanometer sizes and are included in the microsize objects like balls of nanotubes. The typical diameter of nanotubes was observed using SEM and TEM techniqrangesnged from 15 to 30 nm. At the same time, the controllability of the process should be improved concerning its selectivity of the growth mode suitable for the formation of the selected type of nanostructures, as well as application of the proposed carbon materials to the carbonization and generation of nanostructures in surface layers of tool and construction materials [32–34]. For this purpose, further research should involve an application of the magnetic field in the discharge gap.

References

1. Chen, N., et al.: Neural interfaces engineered via micro- and nanostructured coatings. Nano Today **14**, 59–83 (2017)
2. Giubileo, F., Di Bartolomeo, A., Iemmo, L., Luongo, G., Urban, F.: Field emission from carbon nanostructures. Appl. Sci. **8**(4), 526 (2018)
3. Henna, T.K., Raphey, V.R., Sankar, R., Ameena Shirin, V.K., Gangadharappa, H.V., Pramod, K.: Carbon nanostructures: the drug and the delivery system for brain disorders. Int. J. Pharm. **587**, 119701 (2020)
4. Sainio, S., et al.: Integrated carbon nanostructures for detection of neurotransmitters. Mol. Neurobiol. **52**(2), 859–866 (2015). https://doi.org/10.1007/s12035-015-9233-z

5. Al-Jumaili, A., Alancherry, S., Bazaka, K., Jacob, M.V.: Review on the antimicrobial properties of carbon nanostructures. Materials **10**(9), 1066 (2017)
6. Bannov, A.G., Jasek, O., Manakhov, A., Marik, M., Necas, D., Zajickova, L.: High-performance ammonia gas sensors based on plasma treated carbon nanostructures. IEEE Sens. J. **17**(7), 1964–1970 (2017)
7. Malik, R., et al.: Three-dimensional, free-standing polyaniline/carbon nanotube composite-based electrode for high-performance supercapacitors. Carbon **116**, 579–590 (2017)
8. Jiang, J., et al.: Progress of nanostructured electrode materials for supercapacitors. Adv. Sustain. Syst. **2**(1), 1700110 (2017)
9. Hatakeyama, R.: Nanocarbon materials fabricated using plasmas. Rev. Mod. Plasma Phys. **1**(1), 1–110 (2017). https://doi.org/10.1007/s41614-017-0009-y
10. Khataee, A., Sajjadi, S., Hasanzadeh, A., Vahid, B., Joo, S.W.: One-step preparation of nanostructured martite catalyst and graphite electrode by glow discharge plasma for heterogeneous electro-Fenton like process. J. Environ. Manage. **199**, 31–45 (2017)
11. Sobczyk, A.T., Jaworek, A.: Carbon microstructures synthesis in low temperature plasma generated by microdischarges. Appl. Sci. **11**(13), 5845 (2021)
12. Kalyan Kamal, S.S., et al.: A novel Approach for the synthesis of iron carbide nanostructures using spark plasma sintering. J. Magn. Magn. Mater. **510**, 166935 (2020)
13. Cho, H.J., Kondo, H., Ishikawa, K., Sekine, M., Hiramatsu, M., Hori, M.: Density control of carbon nanowalls grown by CH4/H2 plasma and their electrical properties. Carbon **68**, 380–388 (2014)
14. Ye, X., Zhou, H., Levchenko, I., Bazaka, K., Xu, S., Xiao, S.: Low-temperature synthesis of graphene by ICP-assisted amorphous carbon sputtering. Chem. Sel. **3**(30), 8779–8785 (2018)
15. Zhou, H., et al.: Wearable, flexible, disposable plasma-reduced graphene oxide stress sensors for monitoring activities in austere environments. ACS Appl. Mater. Interfaces **11**, 15122–15132 (2019)
16. Bundaleska, N., et al.: Microwave plasma enabled synthesis of free standing carbon nanostructures at atmospheric pressure conditions. Phys. Chem. Chem. Phys. **20**(20), 13810–13824 (2018)
17. Tatarova, E., et al.: Microwave plasmas applied for the synthesis of free standing graphene sheets. J. Phys. D Appl. Phys. **47**(38), 385501 (2014)
18. Ghosh, S., Polaki, S.R., Kumar, N., Amirthapandian, S., Kamruddin, M., Ostrikov, K.: Process-specific mechanisms of vertically oriented graphene growth in plasmas. Beilstein J. Nanotechnol. **8**, 1658–1670 (2017)
19. Sahoo, G., Polaki, S.R., Ghosh, S., Krishna, N.G., Kamruddin, M., Ostrikov, K.: Plasma-tuneable oxygen functionalization of vertical graphenes enhance electrochemical capacitor performance. Energy Storage Materials **14**, 297–305 (2018)
20. Levchenko, I., Romanov, M., Baranov, O., Keidar, M.: Ion deposition in a crossed E×B field system with vacuum arc plasma sources. Vacuum **72**(3), 335–344 (2003)
21. Baranov, O.O., Fang, J., Rider, A.E., Kumar, S., Ostrikov, K.: Effect of ion current density on the properties of vacuum arc-deposited TiN coatings. IEEE Trans. Plasma Sci. **41**(12), 3640–3644 (2013)
22. Baranov, O., Romanov, M.: Current distribution on the substrate in a vacuum arc deposition setup. Plasma Process. Polym. **5**(3), 256–262 (2008)
23. Li, D., Wang, C., Lu, Z., Song, M., Xia, W., Xia, W.: Synthesis of graphene flakes using a non-thermal plasma based on magnetically stabilized gliding arc discharge. Fullerenes, Nanotubes, Carbon Nanostruct. **28**(10), 846–856 (2020)
24. Zhang, D., et al.: Controllable synthesis of carbon nanomaterials by direct current arc discharge from the inner wall of the chamber. Carbon **142**, 278–284 (2018)
25. Yatom, S., Selinsky, R.S., Koel, B.E., Raitses, Y.: Synthesis-on and synthesis-off modes of carbon arc operation during synthesis of carbon nanotubes. Carbon **125**, 336–343 (2017)

26. Yeh, Y.-W., Raitses, Y., Yao, N.: Structural variations of the cathode deposit in the carbon arc. Carbon **105**, 490–495 (2016)
27. Fang, X., Shashurin, A., Teel, G., Keidar, M.: Determining synthesis region of the single wall carbon nanotubes in arc plasma volume. Carbon **107**, 273–280 (2016)
28. Bystrov, K., et al.: Spontaneous synthesis of carbon nanowalls, nanotubes and nanotips using high flux density plasmas. Carbon **68**, 695–707 (2014)
29. Wang, C., Li, D., Lu, Z., Song, M., Xia, W.: Synthesis of carbon nanoparticles in a non-thermal plasma process. Chem. Eng. Sci. **227**, 115921 (2020)
30. Su, Y., Zhang, Y.: Carbon nanomaterials synthesized by arc discharge hot plasma. Carbon **83**, 90–99 (2015)
31. Levchenko, I., Cvelbar, U., Keidar, M.: Graphene sswth. Graphene **5**, 81–89 (2016)
32. Kostyuk, G., Popov, V., Shyrokyi, Y., Yevsieienkova, H.: Efficiency and performance of milling using cutting tools with plates of a new class. In: Tonkonogyi, V. (ed.) Inter-Partner 2020. LNME, pp. 598–608. Springer, Cham (2021). https://doi.org/10.1007/978-3-030-68014-5_58
33. Kostyk, K., Kostyk, V., Akimov, O., Kamchatna-Stepanova, K., Shyrokyi, Y.: Ensuring the high strength characteristics of the surface layers of steel products. In: Tonkonogyi, V. (ed.) Inter-Partner 2021. LNME, pp. 292–301. Springer, Cham (2022). https://doi.org/10.1007/978-3-030-91327-4_29
34. Shyrokyi, Y., Kostyuk, G.: Investigation of the influence of crystallization energy on the size of nanostructures during copper ion-plasma treatment. In: Nechyporuk, M. (ed.) ICTM 2021. LNNS, pp. 57–66. Springer, Cham (2022). https://doi.org/10.1007/978-3-030-94259-5_6

Metallographic Determination of the Number and Sizes of Grains Depending on Structural and Phase Changes in the Metal of Welded Steam Pipe Joints

Olena Harashchenko[1]([✉]) [ID], Vitaly Dmytryk[1] [ID], Viacheslav Berezutskyi[1] [ID], and Tetiana Syrenko[2] [ID]

[1] National Technical University "Kharkiv Polytechnic Institute", 2, Kyrpychova Street, Kharkiv 61002, Ukraine
garashchenko.helena@gmail.com

[2] Kharkiv National Automobile and Highway University, 25, Yaroslava Mudrogo Street, Kharkiv 61002, Ukraine

Abstract. Research results of the number and size of structural components grains in a metallographic analysis of metal samples of welded steam pipe joints considering the operating life are presented. The number of grains and their sizes were determined based on a statistical analysis of their boundaries intersections with given measured lines (cutting lines method according to ISO 643:2019) on metallographic images. Software implementation of the statistical analysis of features obtained due to the intersection of conditional boundaries of structural components in the images of microsections by straight lines is carried out. The computer system was tested for a number of samples cut from sections of steam pipes with different operating times under creep and low-cycle fatigue conditions. Required number of measured lines was found to obtain the statistical characteristics necessary for comparative analysis of metallographic images of various samples. Comparative analysis of features for images of microsections of various metal sections with different operating times of steam pipes is carried out. The research was carried out for the heat-affected zone areas, base metal, weld, and substrate. As a result, an influence of operating life on the changes in boundaries of structural components in the metal of welded steam pipe joints was confirmed. This is based on analyzing statistical characteristics of research features distribution obtained by cutting lines.

Keywords: Sustainable manufacturing · Steam pipes metal · Welds · Metallographic analysis · Structural boundaries · Number of grains · Heat-affected zone · Industrial innovation

1 Introduction

Long-term operation in creep and low-cycle fatigue conditions of welded steam pipe joints leads to structural changes [1]. This leads to poor physical and mechanical properties and a decrease in the service life [2]. During the long-term operating time (280,000 h)

under creep conditions, the initial metal structure recommended by the normative documentation [3] changes, and in the process of degradation, creep pores and fatigue cracks are formed [4]. Identification of premature degradation processes in the metal of welds by forming defects based on the metallographic analysis of structural changes makes it possible to create conditions for trouble-free operation of steam pipelines [5].

One of the approaches to quantifying metallographic images is to determine the number of grains and their sizes using the method of cutting straight lines and circles according to the standard ISO 643:2019 [6]. It is known that the grain size of structural elements can be used as one of the main characteristics that determine the mechanical properties of metals [7]. Grain sizes of structural components of the metal are enough informative quantitative characteristics of the material structure. These characteristics depend both on the original structure of the material and the duration of cyclic loads during fatigue failure processes [8].

2 Literature Review

Progress of methods for assessing the structure of materials thanks to computer technologies has brought to a new level their perform. Many authors have studied the interactions of the parameters of metals' structure and the complexity of their physical and mechanical properties [9, 10]. Significant subjectivity in assessing the metal structure arises from the presence of many elements that, due to the complexity of their geometric description, are difficult to quantify analysis [1]. This circumstance creates obstacles for studying structure-property dependence. Quantitative assessment of metals' structures usually consists of determining statistical characteristics for grain sizes, grain boundaries, etc. [11].

In the known interactions model of mechanical properties of steel after thermomechanical treatment with the geometry of structural elements, grain sizes of austenite and ferrite are taken into account [7].

An integral mathematical model was developed to predict the microstructure and mechanical properties of steels processed by specified modes of hot deformation and accelerated cooling [12]. This model predicts the evolution of austenite microstructure upon hot deformation and its transformation upon cooling, taking into account the formation of ferrite, pearlite, bainite, and martensite. The effect of ultrafast heating on the microstructure of steel was also researched [13]. This work [14] presents research on the long-term operation effect of bridges (over a hundred years old) on the microstructural and mechanical properties of steel components. Based on the chemical composition analysis, possibilities of extending the structure's service life are discussed.

Computational modeling to predict the evolution of steels' microstructure and mechanical properties in thermo-mechanical-metallurgical processes is also implemented by integrating finite element modeling, cellular automaton modeling, and phase transformation kinetics [15].

The problem of geometric characteristics determining structural metal elements of steam pipes for assessing residual resource is present despite many works due to constant increase in their operating time.

This work proves the hypothesis that statistical analysis of the distribution of grains numbers and their sizes makes it possible to evaluate the boundaries features of structure

components selection and consider when assessing the effect of material structure on a residual resource.

Purpose – to substantiate the possibility of a quantitative assessment of the features of structural components of welded steam pipe joints, the number of grains, and their sizes based on metallographic analysis, taking into account operating life.

3   Research Methodology

The solution to analyzing metallographic images of steam pipes metal samples was carried out using the system of statistical analysis of images developed at NTU "Kharkiv Polytechnic Institute" (Ukraine). This system allows quantitative assessment of metal structure based on analysis of image consisting of pixels array using RGB and HSV color models. To solve this problem, the subsystem is shown in Fig. 1.
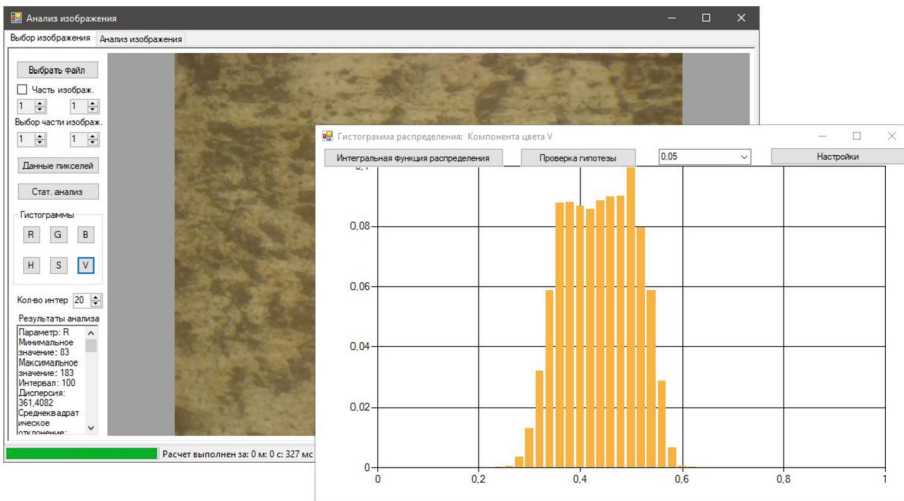
Fig. 1. Screenshot of the screen form of a statistical image analysis system.

The developed system (Fig. 1) gives the following basic capabilities:

- formation of an array of pixels with a definition of color components according to *RGB* and *HSV* models;
- image visualization;
- determination of the main statistical characteristics of color components distribution;
- determination of fractal dimension for a given range of scales to measure the structural components boundaries;
- statistical analysis of the distribution of research features (selected pixels along the width and length of image, the number of grains and their sizes along the measured straight lines);
- the output of analysis results in the form of density or integral probability function.

Definition of the components of *RGB* and *HSV* color models for an array of image pixels is performed by defining their built-in properties: Red, Green, Blue, Hue, Saturation, Brightness (Value).

Estimation of grains number and their sizes along the measured lines by boundary pixels was carried out using the example of metallographic images of microsections obtained at 500 times magnification. For the experiment, four samples of welds were used. They were cut out of existing steam pipes with different operating times. One sample was taken as the initial (basic) version, with no operating time. The rest samples have operating times of 120 and 150 thousand hours, respectively. Two samples with the greatest operating time were taken: one with an external weld and the other with an internal weld. The main material for all samples is heat-resistant pearlitic steel of 12Cr1MoV (analog of 14MoV6-3 steel, 1.7715 EN 10216-2:2020).

In this research, areas for the heat-affected zone, base metal, weld, and substrate were studied. Of most significant interest is the heat-affected zone (HAZ). Metallographic images were taken for the fine-grained subzone of HAZ. These images showed fine metal grains (9 points of grain size according to GOST 5639-82).

4   Results

The first task was to determine image pixels belonging to the researched component of metal structure. Areas of selection of metal structure elements (individual pixels were selected from the total pixels set of microsection image, Fig. 2) are formed by setting a filter (range of values) for selected color components (one or more) based on RGB or HSV model. As a result, closed selection areas are formed, consisting of an array of pixels related to the researched structural element. Such areas obtain when the values of pixel color components fall within a certain range. In most cases, selection areas are created based on the need to consider the main component of the structure. We take the selected boundary pixels as an outline of selected areas. Defining conditions for them is the location of unselected pixels next to them. The task was simplified by considering the structure of a metal as two-phase. In this case, the standard task of estimating grains numbers and their sizes is solved by the number of boundary pixels crossed by the measured line. Grains sizes and distances between them determine the distances between boundary pixels.

Visualization of metallographic analysis was carried out by highlighting pearlite areas in the microsection image. The original color (Fig. 2a) was replaced with the selected one (Fig. 2b shows the selection in white).

Separate research was made to substantiate the visually determined value of lightness threshold V_{max} (brightness component V for *HSV* color model) for selected structural element area of microsection in work [16]. $V_{max} = 0.46$ was chosen as the threshold value of color brightness, as it makes it possible to distinguish perlite in the image of a metal microsection. This value is also seen in the distribution density of V (brightness) component values for the *HSV* color model.

In the microsection image shown in Fig. 2a, pearlite can be attributed to the main structural element, which has the highest relative content in the metal. Figure 2b shows superimposed measurement lines (in this example, 3 horizontal and vertical lines are specified) on the image with selected pixels belonging to ferrite.

a   *b*
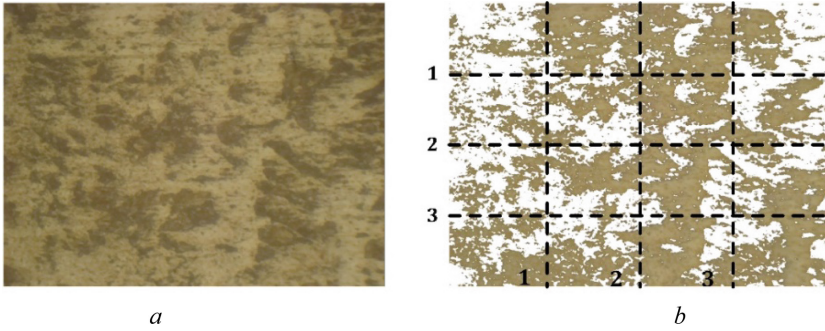
Fig. 2. Image of the original microsection (a) and after selecting pixels with a brightness of 0 ÷ 0.44 and setting of three vertical and horizontal measuring lines (b) for the weld of a sample without operating time.

In practice, there will necessarily be restrictions on the minimum and the maximum number of measuring lines sufficient for a statistically justified determination of grains number and their sizes. In this research, the minimum image size and condition for determining the boundary pixel were constraints for choosing the number of measurement lines. If we consider the need for statistical analysis of the features under research, then a condition appears for the minimum number of lines $N_i > 3$. Researched images of microsections have the same dimensions - 1536×1152 px. Accordingly, the following list of number of the measured lines $N_i = \{3, 5, 7, 9, 20, 30, 40, 60\}$ pixels is formed.

Using a constant number of measuring lines N (horizontal and vertical) for all images made it possible to obtain the relative values of the features that can be compared. This circumstance makes it possible to carry out a comparative analysis of the number of grains and their sizes for all samples.

Figure 3 shows the capabilities of the developed system for displaying image analysis results. First of all, these are the main statistical characteristics of the features (Fig. 3a). Presented histograms of distribution density (Fig. 3b-d) make it possible to visually assess the distributions of the features.

Histograms of the density distribution of grain sizes and the distances between them are presented in image pixels. For further analysis, we considered the relative values of the features in comparison to the width of the image. This approach allows comparative analysis regardless of the resolution of the original image. Further transition to absolute values is possible, taking into account the actual size of the site.

The main characteristic is an arithmetic mean grain size according to ASTM E112–13 [17]. In our research, in addition to the arithmetic mean, the standard deviation of values of the signs (on an example of work [18]) was also considered.

The initial task of our research was to identify the influence of specified lines number for measurements on the features. This problem was solved for all obtained images of microsections of welded steam pipes samples.

Examples of calculation results for determining the number of grains, their sizes, and distances between them in one of the weld sections of a test sample without operating time are shown in Fig. 4.

Minimum value: 17
Maximum value: 50
Interval (range): 33
Dispersion: 65.999
Standard deviation: 8.123
Arithmetic mean: 31.333
Asymmetry coefficient: 0.1067
Kurtosis coefficient: -0.5173
Coefficient of variation: 0.2593

a)

b)

c)

d)
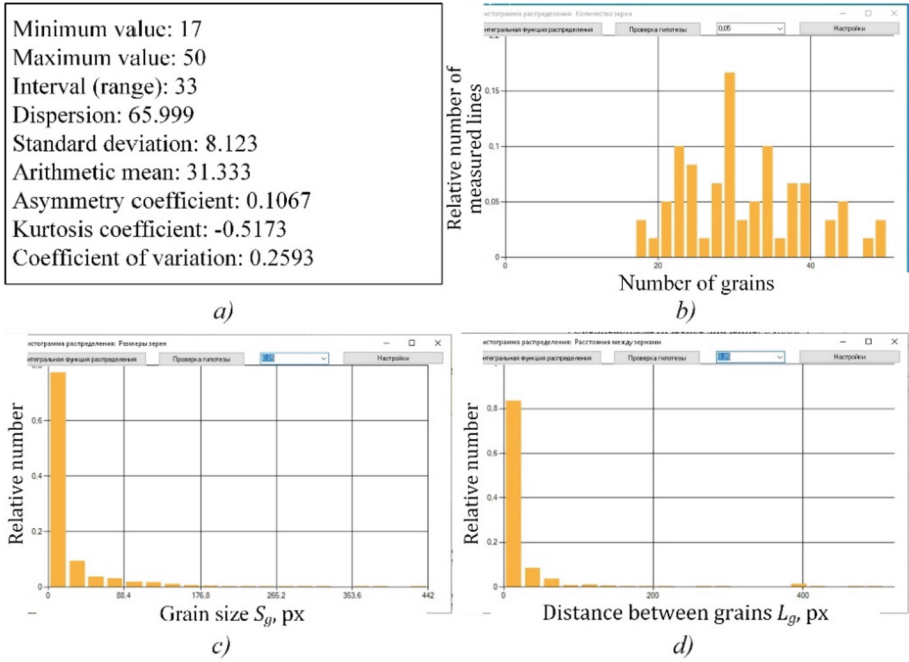
Fig. 3. Statistical characteristics for a number of grains (a) and histograms of the distribution of the features (b - number of grains, c - grain size, d - the distance between grains) for welds of the sample without operating time.

a)

b)

c)

d)
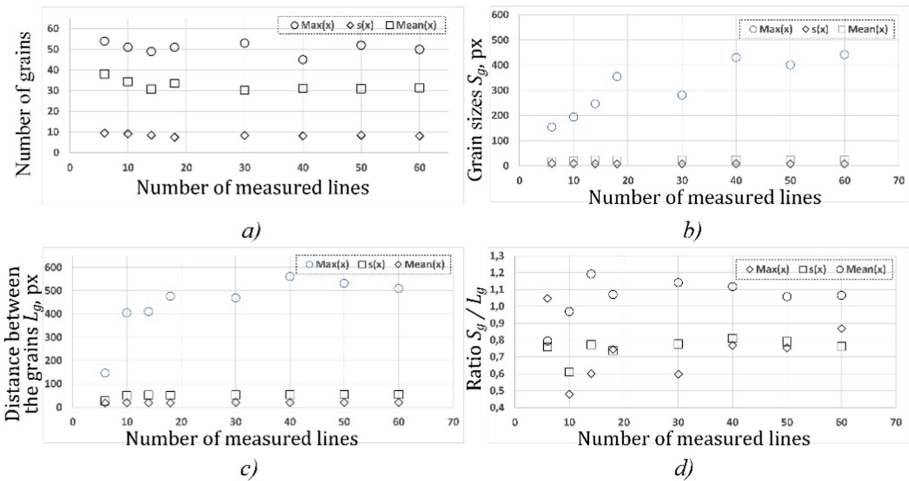
Fig. 4. Dependence of the statistical characteristics of the features (a - number of grains, b - grain sizes, c - the distance between the grains, d - the ratio of characteristics for grain sizes to distances between them) on the number of measured lines for the samples weld without operating time.

Presented graphs allow a selection of a sufficient number of measured lines to obtain statistically stable values of the features. The number of lines in the range of $9 \div 40$ makes it possible to get fairly stable values of statistical characteristics of the research features.

There are characteristic tendencies applicable to all tested images of microsections for all dependencies. This circumstance was considered by means of putting the research results into uniform graphs (Fig. 5) for comparative analysis. Analysis was carried out according to two statistical characteristics: arithmetic means and standard deviation.

Graph of the statistical characteristics of grains number distribution (in Fig. 5a) revealed some trends and distinctive features. The influence of operating time T_R for the base metal of samples was revealed in terms of the standard deviation $\sigma\{N_i\}$. An increase in T_R leads to a downward trend in $\sigma\{N_i\}$. For a weld, an increase in T_R leads to an increase in the arithmetic mean and standard deviation $\sigma\{N_i\}$ after 120 thousand hours of operation. If T_R increases, then for the sections of the heat-affected zone, the characteristics of N_i and $\sigma\{N_i\}$ slightly decrease to 83.3% and 69.3% of initial values, respectively. The samples base metal of pipes differs from weld metal and heat-affected zone, which does not depend on the operating time. The result is a relatively large value of the standard deviation $\sigma\{N_i\}$. The smallest values of N_i and $\sigma\{N_i\}$ can be seen in the heat-affected zone of the sample with external weld and highest operating time.
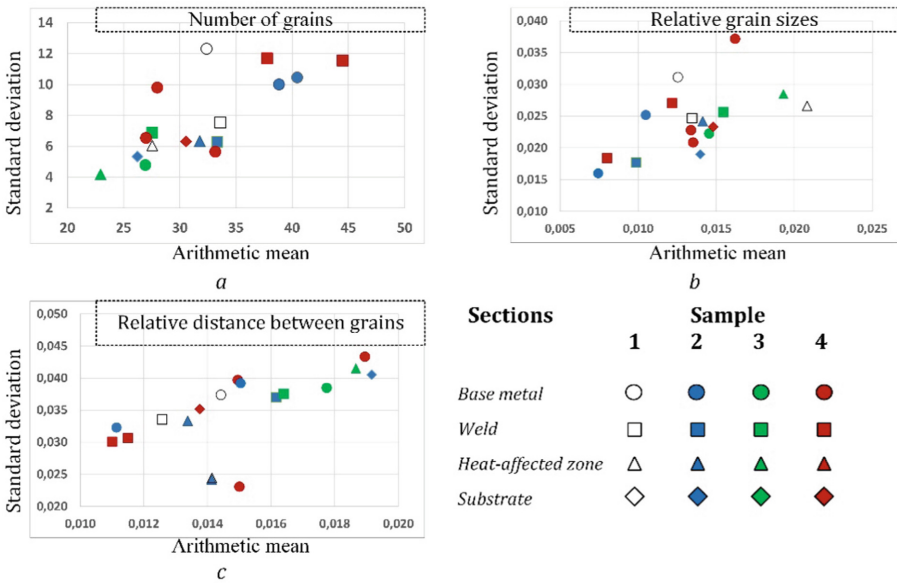
Samples (operating time): 1st, 2nd, 4th - internal weld (the initial version, 120 and 150 thousand hours, respectively); 3rd – external weld (150 thousand hours)

Fig. 5. Comparative analysis of the main statistical characteristics of the features (a - number of grains, b - grain sizes, c - the distance between grains).

Figure 5b shows the statistical analysis results of grain sizes relative to the image width. For the base metal, samples with lifetime T_R have smaller values of the standard deviation $\sigma\{S_i\}$ relative to the original sample. For S_i, there are no regularities of the influence of resource time T_R. For a weld, an increase in T_R leads to a decrease in S_i and $\sigma\{S_i\}$. In this case, S_i decreases to 59.6%, and $\sigma\{S_i\}$ to 74.4% of the original sample value. For the heat-affected zone, arithmetic mean value S_i decreases for samples with operating time up to 67.9% of the initial value.

For both investigated features of the sizes of S_i and the distances between the grains of L_i, there is a fairly wide range of changes in the arithmetic mean values of $0.0074 \div 0.0208$ and $0.0110 \div 0.0192$, respectively. Standard deviations $\sigma\{S_i\}$ and $\sigma\{L_i\}$ have the following ranges of $0.0160 \div 0.0372$ and $0.0231 \div 0.0433$, respectively.

Most informative for assessing the actual operating time and residual life of welded steam pipe joints can be considered the number of grains of metal structural components and their sizes.

5   Conclusions

Statistical analysis of the results of assessing the number of structural components grains and their sizes for microsections of steam pipes metal, obtained by the method of cutting straight lines, makes it possible to create a scientifically grounded basis for studying structural changes.

Root-mean-square deviations from the average number of grains and their sizes are most interesting for assessing the degree of influence of service life of steam pipes on structural changes.

Revealed some tendencies can be attributed to the necessity for creating methodological foundations for assessing the structural changes that occur during steam pipes operation. But they are not sufficient due to some exceptions and a wide range of statistical characteristics of the studied features. In the future, it is necessary to determine the additional investigated features that allow identifying the features of structural changes leading to a decrease in a steam pipe's residual resource.

Our further research aims to identify the relationship between the obtained data and the mechanical properties of metal. This will expand the possibility of identifying structure parameters based on metallographic analysis to predict the residual life of the steam pipes.

Considering standard ISO 643:2019, in the future, it is planned to continue this research through a comparative analysis of studied features obtained by measuring secant lines and circles.

References

1. Zielinski, A., Golanski, G., Sroka, M.: Evolution of the microstructure and mechanical properties of HR3C austenitic stainless steel after aging for up to 30,000 h at 650–750 °C. Mater. Sci. Eng. A, 139944 (2020). DOI: https://doi.org/10.1016/j.msea.2020.139944
2. Golański, G., Zieliński, A., Sroka, M., Słania, J.: The effect of service on microstructure and mechanical properties of HR3C heat-resistant austenitic stainless steel. Materials **13**(6), 1297 (2020). https://doi.org/10.3390/ma13061297

3. SOU-N MPE 40.1.17.401:2004. Control of metal and extension of service life of the main elements of boilers, turbines and pipelines of thermal power plants. Typical instructions (2004) [in Ukrainian]

4. Golański, G., et al.: Microstructure and mechanical properties of HR3C austenitic steel after service. Archives of Materials Science and Engineering **81**(2), 62–67 (2016). https://doi.org/10.5604/01.3001.0009.7100

5. Thong-On, A., Boonruang, C.: Design of boiler welding for improvement of lifetime and cost control. Materials **9**(11), 891(2016). https://doi.org/10.3390/ma9110891

6. Flipon, B., et al.: Grain size characterization in metallic alloys using different microscopy and post-processing techniques. Mater. Charact. **174**, 110977 (2021). https://doi.org/10.1016/j.matchar.2021.110977

7. Kusiak, J., Kuziak, R.: Modelling of microstructure and mechanical properties of steel using the artificial neural network. J. Mater. Process. Technol. **127**(1), 115–121 (2002). https://doi.org/10.1016/s0924-0136(02)00278-9

8. Naimark, O.B., Bayandin, Y.V., Zocher, M.A.: Collective properties of defects, multiscale plasticity, and shock induced phenomena in solids. Phys. Mesomech. **20**, 10–30 (2017). https://doi.org/10.1134/S1029959917010027

9. DeHoff, R.T.: Microstructology: the realistic and quantitative description of micro-structural evolution. Metall. Microstruct. Anal. **1**, 244–258 (2012). https://doi.org/10.1007/s13632-012-0042-8

10. Dadé, M., et al.: Influence of microstructural parameters on the mechanical properties of oxide dispersion strengthened Fe-14Cr steels. Acta Mater. **127**, 165–177 (2017). https://doi.org/10.1016/j.actamat.2017.01.026

11. Miletić, I., Ilić, A., Nikolić, R.R., Ulewicz, R., Ivanović, L., Sczygiol, N.: Analysis of selected properties of welded joints of the HSLA steels. Materials **13**(6), 1301 (2020). https://doi.org/10.3390/ma13061301

12. Sokolov, D.F., Ogoltcov, A.A., Vasilyev, A.A., Kolbasnikov, N.G., Sokolov, S.F.: Modeling of microstructure and mechanical properties of hot rolled steels. Mater. Sci. Forum **762**, 116–121 (2013). https://doi.org/10.4028/www.scientific.net/msf.762.116

13. Banis, A., Hernandez Duran, E., Bliznuk, V., Sabirov, I., Petrov, R.H., Pa-paefthymiou, S.: The effect of ultra-fast heating on the microstructure, grain size and texture evolution of a commercial low-c. Medium-Mn DP Steel. Metals **9**(8), 877 (2019). https://doi.org/10.3390/met9080877

14. Kowal, M., Szala, M.: Diagnosis of the microstructural and mechanical properties of over century-old steel railway bridge components. Eng. Fail. Anal. **110**, 104447 (2020). https://doi.org/10.1016/j.engfailanal.2020.104447

15. Chen, S.-F., et al.: Predictive integrated numerical approach for modeling spatio-temporal microstructure evolutions and grain size dependent phase transformations in steels. Int. J. Plast. **139**, 102952 (2021). https://doi.org/10.1016/j.ijplas.2021.102952

16. Garashchenko, Y., Glushko, A., Kobets, O., Harashchenko, O.: Fractal analysis of structural and phase changes in the metal of welded steam pipe joints. In: Ivanov, V., Trojanowska, J., Pavlenko, I., Zajac, J., Peraković, D. (eds.) DSMIE 2021. LNME, pp. 31–40. Springer, Cham (2021). https://doi.org/10.1007/978-3-030-77719-7_4

17. Gajalakshmi, K., Palanivel, S., Nalini, N.J., Saravanan, S., Raghukandan, K.: Grain size measurement in optical microstructure using support vector regression. Optik – Int. J. Light Electron **138**, 320–327 (2017). https://doi.org/10.1016/j.ijleo.2017.03.052

18. Peregrina-Barreto, H., Terol-Villalobos, I.R., Rangel-Magdaleno, J.J., Herrera-Navarro, A.M., Morales-Hernández, L.A., Manríquez-Guerrero, F.: Automatic grain size determination in microstructures using image processing. Measurement **46**(1), 249–258 (2013). https://doi.org/10.1016/j.measurement.2012.06.012

Influence of Additives Processed by Physical Fields on Tribotechnical Properties of Polymer Composites

Vitalii Kashytskyi(✉) , Oksana Sadova , Mykola Melnychuk , Petro Savchuk ,
and Oleksandr Liushuk

Lutsk National Technical University, 75, Lvivska Street, Lutsk 43018, Ukraine
`v.kashytskyi@lntu.edu.ua`

Abstract. The influence of specific load on the intensity of weight and linear wear is determined in the article. The coefficient of friction and temperature in the zone of tribocontact of polymer composites, the components of which were processed in physical fields, were studied. The study of polymer composites with different content of components carried out at a constant sliding speed of 0.5 m/s. Epoxy resin and polyethylene polyamine hardener were used as a matrix to form polymer composites. To ensure increased heat resistance of the polymer matrix, a modifying additive (organosilicon varnish) was used. For the first time, the processing of organosilicon varnish in an electromagnetic field was applied, which allowed removing part of the solvent. Discrete aramid and glass fibers were used as reinforcing additives. For the first time, ultrasonic treatment of fibers in acetone was used, which allowed cleaning the surface of the fibers from contaminants and lubrications. Because of the use of the modifying additive and treated discrete fibers, the wear resistance of polymer composites increased by 30% due to the improvement of the adhesive interaction between the components of the system and the reduction of structural defects of the material. Removal of lubrication from the surface of the fibers and the solvent from the modifying additive increased by 0.1–0.15 the coefficient of friction of the polymer composites and will improve their service life. Friction polymer composite materials with high density and improved tribotechnical properties are designed for manufacturing brake systems of scooters.

Keywords: Epoxy composite material · Friction · Wear intensity · Coefficient of friction · Sliding speed · Friction load · Product innovation · Industrial growth

1 Introduction

The area of application of polymer-based composite materials in various industries is expanding rapidly, which is associated with high manufacturability of product processes, low energy, and relatively low material costs. Therefore, developing new friction composite materials on a polymer matrix can significantly reduce the cost of expensive non-ferrous metals and reduce energy costs. Significant progress has been made in creating new friction polymer composites based on phenol-formaldehyde and phenolic resins

containing mineral and glass fibers. However, the developed materials have limitations in use due to the high toxicity of the polymer matrix components during manufacturing, insufficient adhesive strength at the interface, and low mechanical properties, which reduces the performance characteristics of polymer composite systems. Replacement of phenol-formaldehyde matrix with high-tech and low-toxic epoxy resins solves a number of problems. However, epoxy composites require a modification of the structure that will increase the heat resistance of the epoxy polymer matrix due to the introduction of organosilicon compounds and improve the interaction between the polymeric binder and fibrous fillers.

2   Literature Review

The increase in the production of friction polymer composites is limited due to the ban in most countries on using asbestos, which is carcinogenic. One of the ways to solve the problem is the development of new friction material compositions using mineral fibers instead of asbestos and the development of new technologies for their production [1]. Promising fibrous fillers are basalt, aramid, and glass fibers, which provide frictional properties of the developed polymer composites [2].

The functional purpose of fillers is to increase the physical and mechanical characteristics of polymer composites [3], which is achieved by the introduction of fibrous reinforcing fillers [4] and fine powders [5].

The advantages of polymer composites are high corrosion resistance, satisfactory thermal protection, cushioning, and antifriction or friction properties [6, 7]. Modern research aims to develop materials with a set of controlled properties [8], which is achieved by introducing organic and mineral fillers [9]. The main factor that can significantly improve polymer composites' physical, mechanical, and tribotechnical characteristics is the polymer matrix's structural and physical modification [10].

It is known that the performance characteristics of epoxy polymer composites depend on the physical nature, filler content, and dispersion [11]. The authors proved that the critical content of filler in the matrix depends on its dispersion. The decrease in particle size causes an increase in its specific surface area [12]. This affects physicochemical processes at the phases interface of "polymer-filler". As a result, outer surface layers with a heterogeneous structure are formed around the particles.

The introduction of fine organic and mineral fillers precludes the structuring of the epoxy polymer [13], which is due to the specifics of the interfacial interaction of polymers with fillers. During structuring on the surfaces of filler particles, isolated polymer molecules, molecular aggregates, and other supramolecular formations are adsorbed. Therefore, when using fillers of different chemicals, there is selective adsorption of binder components at the interface. It reduces the reactivity of the matrix due to the transition of the epoxy polymer on the surface of the filler particles in the state of boundary layers, in which there is a decrease in the mobility of macromolecules [14]. As a result, defects, structural inhomogeneity are formed [15], the mechanical properties of composites are reduced.

The authors of [16] investigated the structure and properties of the polymer composite material reinforced with chaotically placed discrete fibers and gravel produced by

Junkers. Composite sheets made by pressing. Sensitivity to crack propagation studied in composites. It proved that reinforcement of polymer composites with fillers increases fracture toughness. The viscosity of the composite increased compared to the matrix due to the appearance of gravel at the end of the basalt fibers, confirmed by electron microscopic structures. The model of research of the influence of the change of technological parameters on the production of basalt fiber presented.

The physical modification of the binder by the action of ultrasonic waves on the composition increases the penetration of the binder into the interfiber space of the filler [17]. When modified, the liquid binder intensively fills the micropores of the fibrous material, and impregnation time is reduced by tens of times. The advantage of the ultrasonic treatment is degassing the filler and reducing the binder's viscosity repeatedly. This facilitates the penetration of the binder into the interfiber space.

The use of mechanically activated basalt fiber increases polymer composites' physical and mechanical characteristics and wear resistance [18]. The elasticity of the polymer composite material remains minimal, and the strength increases by 39–42%.

Modifying composites with organosilicon resins increases polymer composites' physical, mechanical, and technical performance characteristics, improving the insulating and anti-corrosion properties. This allows the use of modified materials in difficult operating conditions, where mechanical and thermal loads are combined with the influence of aggressive environments [19].

The use of multifunctional fillers provides high wear resistance of epoxy composites operated in conditions in dry friction at high sliding speeds and loads [20, 21]. The developed composition of epoxy composite tribomaterials allows realizing selective transfer effect during frictional interaction. As a result of establishing the impact of the selective transfer on tribosurfaces, a copper protective film is formed. This copper film reduces the coefficient of friction and wear intensity. This will control the friction process, reduce material and economic costs during maintenance and repair of equipment.

Wear intensity [22] of developed polymer composite materials based on the epoxy binder, which contains a modifying additive of 2,4-diaminotoluene and a mixture of nanopowder fillers (Si_3N_4, Al_2O_3, AlN, TiN) with a particle size of 20–80 nm and discrete fibers, viscose, polyamide, silk, rong, and cashmere), is less than 50% compared to the epoxy matrix without modifying additives.

In most works, the analysis of results of researches of influence of modifying additives on the structure of antifriction polymeric composites. Discrete fibrous fillers give friction properties to polymer composites. It is problematic to provide high adhesive strength between the polymeric binder and the surface of the reinforcing additive. This problem can be solved by physically modifying the surface layer of fibrous fillers with ultrasonic waves, which allows you to clean the surface of the fibers and activate reactive groups on the surface of the fibers. The content of a solvent complicates the introduction of heat-resistant organosilicon varnish into polymer composites. The content of the solvent in organosilicon varnish decreases after its treatment in an electromagnetic field. This provides high thermodynamic compatibility of components and increases polymer composites' physical and mechanical characteristics.

3   Research Methodology

The epoxy-dian resin of the ED-20 brand (DSTU 2093-92) was used as a polymer matrix. For curing epoxy compositions used polyethylene polyamine - PEPA (TU 6-02-594-85). Organosilicon varnish KO-915B (TU 2311-429-05763441-2004)was used as a modifying additive, a solution of polymethylphenylsiloxane resin modified with polyester in toluene. The content of the modifying additive (organosilicon varnish KO-915B) is 20 wt. parts. Discrete glass fibers (6–10 wt. Parts) and discrete aramid fibers (1–2 wt. Parts) 3–4 mm long, as well as a highly dispersed aluminum powder (7 wt. parts) were used to form polymer composites.

Aramid fibers have high strength and low weight, are less brittle than carbon and glass fibers, resistant to fire, high temperatures, organic solvents, petroleum products.

The main mechanical characteristics of glass fibers are high tensile strength and modulus of elasticity, which depend on the composition, temperature, and humidity of the environment and the degree of defect of the fibers, limiting their use compared to aramid fibers. The particles of highly dispersed aluminum powder preferably have the form of thin plates with a thickness of 0.2–0.5 μm, and the average linear size does not exceed 30 μm.

The counterbody (Fig. 1) is a disk from steel 45 (ISO 7148-2) with a diameter of 50 mm with a surface roughness $R_a = 3,2$. The samples were made of monolithic material with a square cross-section of 10×10 mm and a height of 15 mm. The friction path was 3000 m, sliding speed - 0.5 m/s, the specific load varied in the range from 0.5 MPa to 1.5 MPa.
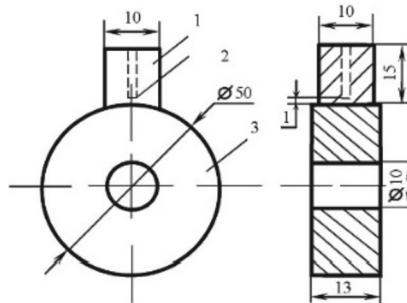
Fig. 1. The scheme of friction and the dimensions of the elements of the tribopair: 1 – sample; 2 – socket for thermocouple; 3 – counterbody.

The mass of the samples was determined on analytical laboratory scales type VLA – 200 with an accuracy of 0.0001 g. The linear dimensions of the polymer composite samples were measured with a DIP-2 device with an accuracy of 0.001 mm. The temperature in the friction zone was measured by introducing a thermocouple "chromel-kopel" into the sample at a distance of 0.5–1 mm from the friction surface.

The composition containing epoxy resin and organosilicon modifier was treated physically, followed by cooling the composition to room temperature. The hardener and fillers were then added to the composition. The fillers were processed in a solvent

by ultrasonic waves. Forming and curing polymer samples for tribotechnical studies was performed in a mold under pressure. Curing of epoxy composites under normal conditions lasted 24 h. Additional heat treatment was carried out in an oven at 160 °C for 4 h, the temperature deviation of which did not exceed ±2 K.

4   Results

The optimal composition and technology of forming polymer composite samples (Table 1) for tribotechnical studies were established from the analysis of research results of physical and mechanical properties and mathematical planning of a multifactor experiment.

Table 1. Composition and processing technology of additives for polymer composites.

Composition №	Composition of material			Processing of fibers	Processing of modifying additive
	Polymer matrix	Modifying additive	Content of reinforcing additive		
1	Epoxy resin ED-20 (100 wt. parts) + PEPA (12 wt. parts)	КО-915B (20 wt. parts)	1) discrete glass fibers (10 wt. parts) 2) discrete aramid fibers (1 wt. parts) 3) aluminum powder (7 wt. parts)	–	–
2				+	–
3				–	+
4				+	+
5			1) discrete glass fibers (6 wt. parts) 2) discrete aramid fibers (2 wt. parts) 3) aluminum powder (7 wt. parts)	+	+

NOTE 1. Ultrasonic waves process discrete fibers in acetone solution for 5 min.
NOTE 2. Modifying additive KO-915B processed in an electromagnetic field (120 W) for 10 min.

It was experimentally established that at low sliding speed (0.5 m/s) and specific load (0.5 MPa), the intensity of weight wear of the polymer composite of composition № 1 is 2.3 mg/km, polymer composite of composition № 2 – 1.1 mg/km, polymer composites of composition № 3 and № 5 – 2.0 mg/km, and polymer composites of composition № 4 – 1.8 mg/km. It is established that with an increase in the specific load from 0.5 MPa

to 1.5 MPa at a constant sliding speed V = 0.5 m/s in the intensity of weight wear for polymer composites increase for compositions № 1–3 (Fig. 2) in 1, 4–3.7 times, which is 8.5 mg/km, 1.9 mg/km, 2.8 mg/km, respectively. When the specific load is increased to 1.5 MPa, the intensity of weight wear is reduced by 1.1–1.2 times for polymer composites of composition № 4 (1.5 mg/km) and № 5 (1.7 mg/km). The higher wear resistance of these polymer composites is due to the ultrasonic processing of aramid and glass fibers and electromagnetic processing of the modifying additive (KO-915B), which increases the cohesive strength and wear resistance of polymer composites.
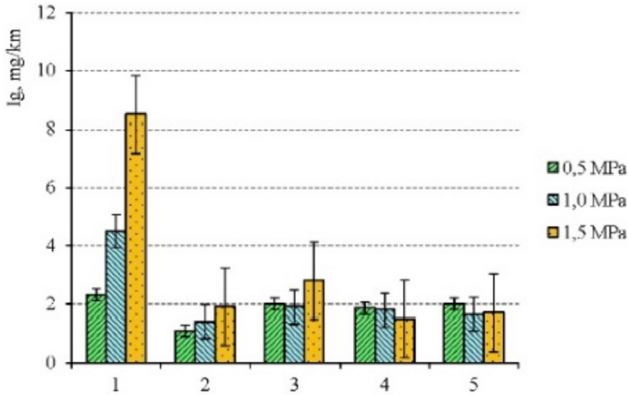
Fig. 2. The intensity of weight wear of polymer composites depending on the composition and type of processing of components.

The highest intensity of weight wear (8.5 mg/km) has a polymer composite of composition № 1 at a sliding speed V = 0.5 m/s and a specific load P = 1.5 MPa. The lowest intensity of weight wear (1.1 mg/km) has a polymer composite № 2, containing discrete fibers, processed by ultrasonic waves, with minimum values of friction parameters (V = 0.5 m/s, P = 0.5 MPa).

It is investigated that the highest intensity of linear wear has a polymer composite of composition № 1 (Fig. 3), which is 17.5–70.5 µm/km. This is due to the introduction into the composition of the unprocessed fibers and modifiers. The intensity of linear wear for the polymer composite of composition № 2 and the polymer composite of composition № 3 is lower by 52.6–70.8% than the polymer composite of composition № 1. The lower intensity of linear wear of these materials is explained by the content of fibers, processed by ultrasonic waves (polymer composite composition № 2) and organosilicon varnish, processed by an electromagnetic field (polymer composite composition № 3). With increasing specific load from P = 0.5 MPa to P = 1.5 MPa at a constant sliding speed V = 0.5 m/s for polymer composites of compositions № 1–3 increases the intensity of linear wear.

For polymer composites of compositions № 4 and № 5, the intensity of linear wear decreases by 14.9–18.3% with increasing specific load from P = 0.5 MPa (14.2 µm/km for polymer composites of composition № 4 and 15.9 µm/km for polymer composites
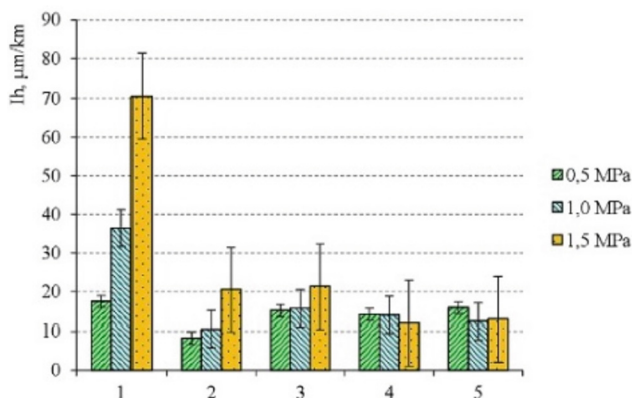
Fig. 3. The intensity of linear wear of polymer composites depending on the composition and type of processing of components.

of composition № 5) to P = 1.5 MPa (12.0 µm/km for polymer composites of composition № 4 and 13.0 µm/km for polymer composites of composition № 5) at a constant sliding speed V = 0.5 m/s. These polymer composites contain processed fibers and modifiers, which significantly reduces the intensity of linear wear compared to the polymer composite of composition № 1.

It is established that the temperature in the zone of tribocontact (Fig. 4) of the polymer composite-counterbody increases with increasing frictional load. As a result of increasing the specific load at a constant sliding speed V = 0.5 m/s, the temperature increases for the polymer composites of compositions: № 1 – from 62 °C to 90 °C; № 2 – from 58 °C to 135 °C; № 3 – from 58 °C to 125 °C; № 4 – from 74 °C to 152 °C; № 5 – from 58 °C to 100 °C.

The lowest temperature (58–74 °C) in the zone of tribocontact was recorded for polymer composites at low sliding speed (V = 0.5 m/s) and specific load P = 0.5 MPa.

This is due to the content of toluene in organosilicon varnish and the presence of lubricants on the surface of the fibers, which perform a lubricating function and prevent adhesion. The highest temperature (90–152 °C) in the zone of tribocontact of friction pair is observed at a specific load of 1.5 MPa, which causes plastic deformation of local ledges, resulting in the increased contact area between the tribosurfaces.

With increasing specific load from P = 0.5 MPa to P = 1.5 MPa at a constant sliding speed V = 0.5 m/s for polymer composites of compositions № 1 and № 4 there is a decrease in the coefficient of friction (Fig. 5) by 31, 8–47.5%, which is f = 0.21 and f = 0.30, respectively.

For the polymer composite of composition № 3, which contains unprocessed fibers, as well as the polymer composite of composition № 1, the values of the friction coefficients (0.27–0.32), are lower compared to the polymer composites of composition № 2 (f = 0.32–0.36), № 4 (f = 0.30–0.44) and № 5 (f = 0.40–0.46), containing discrete fibers, processed by ultrasonic waves. The lower values of the coefficients of friction can be explained by the presence on the surface of glass and aramid fibers of the lubricant used in their manufacture. The lubricant increases the strength of the fibers by 20–30%
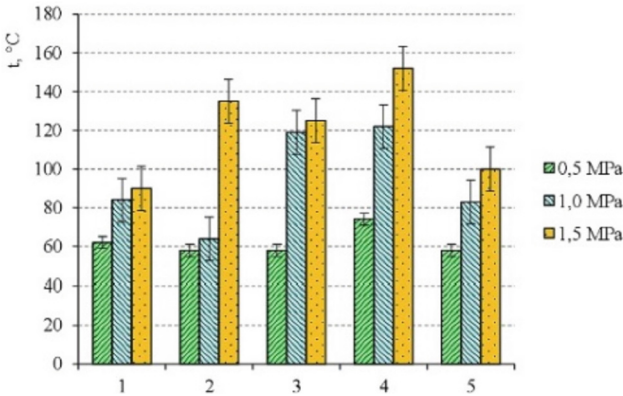
Fig. 4. Temperature in the zone of tribocontact "polymer composite-counterbody" depending on the composition and type of processing of components.
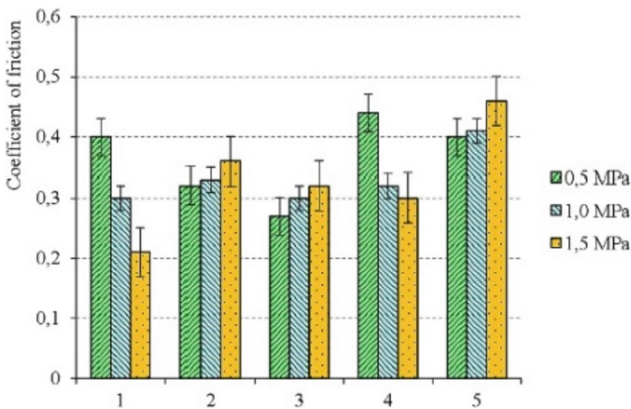
Fig. 5. Coefficient of friction of polymer composites depending on the composition and type of processing of components.

and reduces the coefficient of friction. The polymer composite of composition № 3 also contains organosilicon varnish KO-915B, processed by an electromagnetic field, which reduces the friction coefficient. Ultrasonic treatment was performed in acetone solution. For the purpose of removal of lubricant from the surface of the aramid and glass fibers. This will improve the interfacial interaction of the fiber surface with the modified by organosilicon varnish epoxy matrix and increase the coefficient of friction. This is confirmed by the experimental results of determining the coefficient of friction of polymer composites of compositions № 4 and № 5, which have increased values of this characteristic (0.30–0.46) compared with the polymer composite of composition № 3, which contained unprocessed fibers.

Higher values of the coefficient of friction of the polymer composite composition № 5 ($f = 0.46$ at V = 0.5 m/s, P = 1.5 MPa) compared with the polymer composite № 4 ($f = 0.3$ at V = 0.5 m/s, P = 1.5 MPa) due to the higher content of aramid fibers (2 wt.

parts for the sample № 5 and 1 wt. parts for the sample № 4) and lower content of glass fibers (6 wt. parts for the sample № 5 and 10 wt. parts for the sample № 4). Aramid fibers provide a higher coefficient of friction ($f = 0.70$) compared to glass fiber ($f = 0.85$).

5   Conclusions

Polymer composites containing unprocessed modifying additive (organosilicon varnish) and discrete aramid and glass fibers, processed by ultrasonic waves in the solvent, have 30% lower values of weight wear compared to polymer composites containing organosilicon varnish, processed by an electromagnetic field, and unprocessed discrete fibers. This indicates the dominant effect of the lubricant on the surface of discrete fibers on the structuring processes because the formation of chemical bonds between the reactive groups of epoxy binder and discrete fibers is complicated. Therefore, the fibers are detached from the polymer matrix, which causes intense destruction of the polymer composite during friction. The intensity of weight wear is reduced and stabilized in the case of introduction into the composition of the components, processed by physical fields (polymer composites of composition № 4 and № 5), which form a highly structured polymer composite system with a low content of volatile compounds.

The results of studies of the intensity of linear and weight wear are correlated. This confirms the positive effect of modified by physical fields of modifying and reinforcing additives on the structuring of polymer composites.

Low-temperature values (60–90 °C) in the tribocontact zone are provided by lubricants on the surface of discrete fibers and toluene as a part of organosilicon varnish. Toluene cools the surface, which prevents the formation of adhesive bonds between the tribosurfaces. Polymer composites of composition № 5 have temperatures lower by 10–50 °C compared with polymer composites of composition № 4, which is due to the lower total content of discrete high-modulus fibers for polymer composites of composition №5. Polymer composites of composition № 4 have a higher content of discrete glass fibers, characterized by a higher density than aramid fibers, which leads to the generation of more thermal energy.

It first established that removing the solvent from the modifying additive provides an increase of 0.1–0.15 coefficient of friction of polymer composites, as there is the formation of a dense structure without voids and pores. The occurrence of structural defects is caused by the removal of the solvent during the thermal structuring of polymer composites. Removal of lubricant from the surface of discrete fibers also increases the coefficient of friction. This is important when developing materials for friction products.

In the future, it is planned to conduct microscopic studies of the developed tribotechnical epoxy composites to determine the transformation of the surface layer structure. It will also be necessary to determine the wear intensity under a stricter triboload regime to establish the limit of more difficult operating conditions.

References

1. Sumithra, H., Sidda Reddy, B.: A review on tribological behaviour of natural reinforced composites. J. Reinf. Plast. Compos. **37**(5), 349–353 (2018). https://doi.org/10.1177/0731684417747742

2. Klepner, D., Sperling, H., Utracki, L.: Interpenetrating polymer networks. In: Advances in Chemistry Series, vol. 239. American Chemical Society, Washington (2009)

3. Bauer, B.J., Briber, M., Klepner, D.: Advances in Interpenetrating Polymer Networks. Lancaster, Tehnomic (2008)

4. Peijs, T., Rijsdijk, H.A., Lemstra, P.J.: Role of interface and fibre anisotropy in controlling the performance of polyethy-fibra-reinforced composites. Compos. Sci. Technol. **52**, 449–466 (2010)

5. Smedskajer, M.M., Solvang, N., Yue, Y.: Crystallisation behavior and high-temperature stability of stone wool fibres. J. Eu. Ceram. So **30**, 1287–1295 (2010)

6. Parikh, H.H., Gohil, P.P.: Tribology of fiber reinforced polymer matrix composites – A review. J. Reinf. Plast. Compos. **34**(16), 1340–1346 (2015). https://doi.org/10.1177/0731684415591199

7. Hurey, I., Gurey, V., Bartoszuk, M., Hurey, T.: Formation of residual stresses during discontinuous friction treatment. J. Eng. Sci. **8**(1), C38–C44 (2021). https://doi.org/10.21272/jes.2021.8(1).c5

8. Berladir, K.V., Sviderskiy, V.A.: Designing and examining polytetrafluoroethylene composites for tribotechnical purposes with activated ingredients. East. Eur. J. Enter. Technol. **6**(84), 14–21 (2016). https://doi.org/10.15587/1729-4061.2016.85095

9. Marshall, D.V., Cos, B.N., Evans, A.G.: The mechanics of matrix in brittle-matrix fiber composites. Acta Metallurg. **12**(22), 201 (2013)

10. Berladir, K.V., Hovorun, T.P., Sviderskiy, V.A., Rudenko, P.V., Vyshehorodtseva, M.E.: Nanostructural modification of polytetrafluoroethylene and its composition by energy influence. J. Nano- Electron. Phys. **8**(1), 01033-1–01033-5 (2016). https://doi.org/10.21272/jnep.8(1).01033

11. Hutchinson, J.V., Jensen, H.M.: Models of fiber debonding and pullout in brittle composites with friction. Mech. Mater. **15**(112), 139–163 (2011). https://doi.org/10.1016/0167-6636(90)90037-G

12. Mostovoy, A., Bekeshev, A., Tastanova, L., Akhmetova, M., Bredihin, P., Kadykova, Yu.: The effect of dispersed filler on mechanical and physicochemical properties of polymer composites. Polym. Polym. Compos. **29**(6), 583–590 (2020). https://doi.org/10.1177/0967391120929040

13. Dhand, V., Mittal, G., Yop Rhee, K., Park, S.-J., Hui, D.: A short review on basalt fiber reinforced polymer composites. Compos. B Eng. **73**, 166–180 (2015). https://doi.org/10.1016/j.compositesb.2014.12.011

14. Buketov, A., Stukhlyak, P., Maruschak, P., Panin, S., Menou, A.: Key: Physical and chemical aspects of formation of epoxy composite material with microfilling agent. Eng. Mater. **712**, 143–148 (2016)

15. Peijs, T., Rijsdijk, H.A., Lemstra, P.J.: Role of interface and fibre anisotropy in controlling the performance of polyethylene-fibra-reinforced composites. Compos. Sci. Technol. **52**, 449–466 (2010). https://doi.org/10.1016/0266-3538(94)90180-5

16. Czigány, T., Vad, J., Pölöskei, K.: Basalt fiber as a reinforcement of polymer composites. Periodica Polytech. Mech. Eng. **49**(1), 3–14 (2005)

17. Fuller, G.G.: Optical Rheometry of Complex Liquids. Oxford University Press, New York (2005)

18. Vasilev, A.P., Struchkova, T.S., Okhlopkova, A.A., Dyakonov, A.A., Alekseev, A.G.: Effect of carbon and basalt fibers with ultrafine PTFE on the mechanical and tribological properties of polytetrafluoroethylene. AIP Conf. Proc. **2315**, 050026 (2020). https://doi.org/10.1063/5.0036648

19. Mutlu, D., Eidogan, I., Findik, O.: Production of ceramic additive automotive brake pad and investigation of its braking characteristics. Int. J. Tribol. **57**, 84–92 (2005)

20. Savchuk, P.P., Kashytsky, V.P., Sadova, O.L., Lyushuk, O.M.: Structural transformations on the surfaces of epoxy composite–steel tribological pair. Powder Metall. Met. Ceram. **56**(7–8), 448–455 (2017). https://doi.org/10.1007/s11106-017-9915-3
21. Berladir, K., Gusak, O., Demianenko, M., Zajac, J., Ruban, A.: Functional properties of PTFE-composites produced by mechanical activation. In: Ivanov, V., et al. (eds.) DSMIE 2019. LNME, pp. 391–401. Springer, Cham (2020). https://doi.org/10.1007/978-3-030-22365-6_39
22. Buketov, A., Sapronov, O., Brailo, M., Sapronova, A., Sotsenko, V.: The use of complex additives for the formation of corrosion- and wear-resistant epoxy composites. Adv. Mater. Sci. Eng. **2019**, 8183761 (2019). https://doi.org/10.1155/2019/8183761

Impact of Thermomechanical Phenomena in the Surface Layer of Functional-Gradient Materials on Quality Considering Hereditary Defects

Maksym Kunitsyn(✉) , Anatoly Usov , and Yulia Sikirash

Odessa Polytechnic National University, 1, Shevchenko Ave., Odessa 65044, Ukraine
m.v.kunitsyn@op.edu.ua

Abstract. When studying the mechanical properties of wear-resistant coatings, it was assumed that during dimensional processing with a technological tool, the occurrence of defects of technological origins, such as chips and cracks, occurs directly in the localized area of processing with the tool under the influence of thermomechanical stresses. In this regard, a mathematical model was proposed to determine the separation conditions for the exfoliated coating depending on the properties of materials and considering previous types of processing. In this case, hereditary inhomogeneities were formed that affected the crack resistance of the treated surfaces and were based on a quantitative analysis of the thermal and stress state. The dependences obtained in the article allowed us to simulate the process of machining parts with a wear-resistant coating, considering the requirements for the quality of the treated surfaces. As a result, criteria relations were obtained that link the grinding temperature, the intensity of the heat flow, the stress-strain state of the processed surface of the products with technological parameters that allow controlling the quality of processing to prevent peeling of the coating from the main matrix. The results can be used to process materials containing structural inhomogeneities and having low crack resistance characteristics. The prospects of using the model are associated with expanding the scope of application. For example, the models constructed in this article can be used to analyze the development of defects in welded joints and not only.

Keywords: Industrial growth · Coating · Stresses · Temperature · Material · Grinding · Cracks · Defect

1 Introduction

Further increasing machining efficiency, cutting speed, and toughening of reliability requirements associated with increasing level of production automation leads to the need to create new tool materials with improved performance characteristics. One of the ways to improve the performance characteristics of tool materials is to improve their surface properties by applying modified coatings [1]. In turn, the properties of modified coatings continue to improve, and their architecture and element composition

is becoming more complex. Multilayer composite coatings, nanostructured and graded coatings, and coatings with a multi-component element composition have been widely used in recent years [2, 3]. The use of multilayer coating architecture and the application of nanostructured technology can significantly improve the performance characteristics of the new generation of coatings. However, along with such coatings, new problems arose that did not arise with monolithic coatings of the first generation. In particular, problems related to interlayer delamination and specific longitudinal cracks in the coating structure have arisen.

2   Literature Review

A great deal of research has been done on the cracking problems. The general assumption is that microcrack formation is associated with dislocation [3, 4]. Many mechanisms of dislocation microcrack formation are well known. In principle, these mechanisms block dislocation progression by obstacles (e.g., a grain boundary, a nanolayer boundary, or an inclusion). If dislocations stop in front of a sufficiently robust obstacle in any sliding plane, a cluster of dislocations is formed. This effect causes a high concentration of stress on the obstacle. Such a concentration of stresses leads to the formation of a dislocation microcrack [4, 5].

Various coating defects (mainly interspersed micro drops and vapors) [6] can become essential in forming longitudinal cracks and delamination. Figure 1 shows how the crack reaches the macro droplet and forms branches. In this case, one of the crack branches passes through the macro drop, and the second branch of the crack crosses it along the contour. This micrograph shows the separation of the processed material from the coating; this separation indicates a low adhesive bond between the materials. At the same time, there is no separation of the coating from the tool material due to the strong adhesive bond between them.
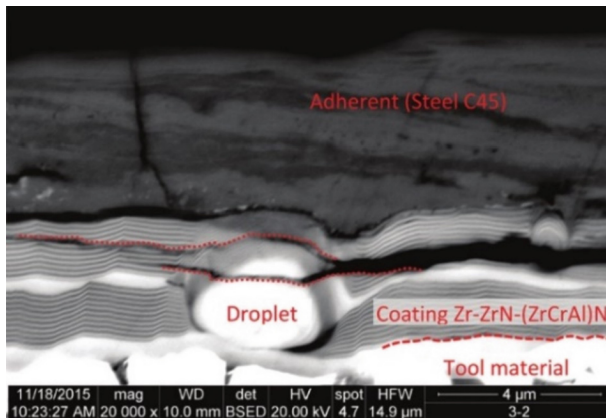
Fig. 1. An example of longitudinal crack development in the NMCC Zr-ZrN-(Zr, Cr, Al) N [6].

One of the directions of modern repair technologies to restore geometric dimensions and functional properties of worn parts is the use of various technological methods,

the basics of which are based on the formation of a coating of wear-resistant materials [7, 8]. For choosing the type of coating for the specified purpose and the method of application, it is necessary to justify the requirements for their wear resistance and physical and mechanical properties, considering the specifics of the operating conditions and the material properties of the part being restored itself. Based on the above, it can be concluded that the problem under consideration, which consists in substantiating the effectiveness of restoring the functional properties of worn parts, assemblies, and mechanisms of machines, is an urgent scientific problem.

The primary purpose of the study is to simulate thermomechanical phenomena that are formed in products at finishing operations and affect the quality of the surface layer, considering the types as mentioned earlier of processing, in which hereditary inhomogeneities are formed that affect the fracture toughness of the treated surfaces based on a quantitative analysis of the thermal and stress state.

3   Research Methodology

Dimensional machining of parts after application of wear-resistant coatings to their working surfaces is associated with the appearance of defects such as cracks and chips [9, 10]. Therefore, when studying the mechanical properties of coatings, it is assumed [11, 12] that their destruction occurs directly in the processing zone of the tool and the part under the influence of thermomechanical stresses formed in the localized zone.

The strength of the coating is determined by the stresses of chipping, shear, and separation arising in them, and the bases – by the maximum contact stresses [13, 14].

Consider the following model of a $2n$ coated product loaded with normal $q_n(x, y)$, and tangent $q_\tau(x, y)$ loads. The O_Z axis is directed inside the product and the O_X and O_Y axes are in the median plane of the coating (in the area of contact of the tool with the treated surface). Here and in the future, the lower indices $m = 1, 2, 3$ denote the changes in O_X, O_y, and O_Z axes, respectively. Between the coating and the primary material of the product, there are areas of partial non-adhesion (defects such as microcracks). Denoting $p_m(x, y)$ contact stresses between the coating and the base material, $U_M(x, y)$ – the displacement of the coating under the action of thermomechanical processes accompanying the machining of the surface layer of the product ($m = 1, 2, 3$), we write the following equations [14, 15]:

$$
\begin{aligned}
&\left[\bar{U}_1\right]''_{xx} + v_2[U_2]''_{xy} + v_1\left[\bar{U}_1\right]''_{yy} = \theta^{-1}[p_1 - q_1]; \; 2v_2 = 1 + v; \\
&2v_1 = 1 - v; \; \left[\bar{U}_1\right]''_{yy} + v_2[U_2]''_{xy} + v_1\left[\bar{U}_1\right]''_{xx} = \theta^{-1}[p_2 - q_2]; \\
&\theta = 2Eh/(1 - v^2); \\
&D\Delta^2\bar{U}_3 = q_3 - p_3 + h[q_1 + p_1]'_x + h[q_2 + p_2]'_y; \\
&\Delta = \partial^2/\partial x^2 + \partial^2/\partial y^2; \\
&D = \theta h^2/3; \; \left[\bar{U}_m, q_m, p_m\right] = \left[\bar{U}_m(x, y), q_m(x, y), p_m(x, y)\right], (|x|, |y| < \infty).
\end{aligned}
\tag{1}
$$

The displacement $U_m(x, y)$ of the surface points of the elastic layer is determined by the formulas [16, 17]:

$$U_m(x, y) = \theta_0 \sum_{j=1}^{3} \iint_{-\infty}^{\infty} K_{mj}(x - s, y - \eta)p_j(s, \eta)ds\,d\eta;$$

$$K_{mj}(x, y) = \frac{1}{4\pi^2} \iint_{-\infty}^{\infty} H_{mj}(\alpha, \beta)e^{-ix\alpha - iy\beta}d\alpha\,d\beta - \text{transformation core};$$

$$H_{11} = \bar{\alpha} + \zeta_0\beta^2\bar{\alpha}^3; H_{22} = \bar{\alpha} + \zeta_0\alpha^2\bar{\alpha}^3; H_{33} = \bar{\alpha}; \tag{2}$$

$$H_{12} = H_{21} = -\zeta_0\alpha\beta\bar{\alpha}^3;$$

$$H_{31} = -H_{13} = \alpha_0 i\alpha\bar{\alpha}^2; H_{32} = -H_{23} = \alpha_0 i\beta\bar{\alpha}^2; \bar{\alpha} = 1/\sqrt{\alpha^2 + \beta^2};$$

$$\theta_0 = 2\left(1 - v_0^2\right)/E_0; \zeta_0 = v_0/(1 - v_0); \alpha_0 = (1 - 2v_0)/(2 - 2v_0),$$

where E_n, E_0 – elastic modulus of the coating and the main product; v_n, v_0 – Poisson coefficients of the coating materials and the primary product material.

The movements of the coating and surface points of the product material in the contact zone "tool – surface to be treated" must meet the conditions:

$$\overline{U}_1 - h[\overline{U}_3]'_x = V_1; U_2 - h[U_3]'_y = V_3;$$
$$U_3 = V_3; \left(x \notin (\alpha_i, \beta_i), i = \overline{1, N}\right), |y| < \infty. \tag{3}$$

When processing coated bodies, the question arises about the possible development of areas of detachment (crack-type defects), i.e., when a state of mobile equilibrium occurs at the points $x = a_i - 0$, $x = b_i + 0$, $(a_i, b_i, i = 1, 2, \ldots, N$ – areas of partial detachment), determined by the condition [14]:

$$K_{m,i}^{\mp}(y) = K_{mc}/\pi, m = \overline{1, 3}; i = \overline{1, N}, |y| < \infty, \tag{4}$$

where K_{mc} – the coefficients of adhesion of the coating to the matrix product of the shear $(m = 1)$, shear $(m = 2)$ and margin $(m = 3)$ coating, which is determined experimentally; $K_{m,i}^{\mp}(y)$ - the coefficients of the intensity of the contact stresses for the i-th delamination at the points b_i the end and the beginning of the a_i plot clutch obtained based on the linear theory of elasticity, determined by the formula [14]:

$$K_{m,i}^{-}(y) = \lim_{x \to a_i - 0}\sqrt{a_i - x}p_m(x, y), K_{m,i}^{+}(y) \lim_{x \to b_i + 0}\sqrt{x - b_i}p_m(x, y), \tag{5}$$

where $p_m(x, y)$ – stress between the coating and the base material.

Following the work [17, 18], we introduce functions that determine the growth values of crack-like delaminations (a_j, b_j):

$$\chi_1 = U_1 - h[U_3]'_x, \chi_2 = U_2 - h[U_3]'_y - V_2, \chi_3 = U_3 - V_3, |x, y| < \infty. \tag{6}$$

Applying the Fourier transform on the variables x, y with the parameters α, β to formulas (1)–(6), solving these equations concerning $p_m^{\alpha\beta}$ and applying the inverse Fourier

transform on the variable α, we obtain such integrodifferential equalities [19]:

$$\begin{pmatrix} p_1^\beta(x) \\ p_2^\beta(x) \\ p_3^\beta(x) \end{pmatrix}_{x\notin(a_i,b_i)} = -\left(\frac{d^2}{dx^2} - \beta^2\right)$$

$$\times \sum_{j=1}^N \int_{a_j}^{b_j} \begin{pmatrix} K_{11}^{\beta,1}(x-s) K_{12}^{\beta,1}(x-s) K_{13}^{\beta,1}(x-s) \\ K_{21}^{\beta,1}(x-s) K_{22}^{\beta,1}(x-s) K_{23}^{\beta,1}(x-s) \\ K_{31}^{\beta,1}(x-s) K_{32}^{\beta,1}(x-s) K_{33}^{\beta,1}(x-s) \end{pmatrix} \begin{pmatrix} \chi_{1,j}^\beta(x) \\ \chi_{2,j}^\beta(x) \\ \chi_{3,j}^\beta(x) \end{pmatrix} ds$$

$$+ \sum_{j=1}^N \int_{-\infty}^{\infty} \begin{pmatrix} K_{11}^{\beta,0}(x-s) K_{12}^{\beta,0}(x-s) K_{13}^{\beta,0}(x-s) \\ K_{21}^{\beta,0}(x-s) K_{22}^{\beta,0}(x-s) K_{23}^{\beta,0}(x-s) \\ K_{31}^{\beta,0}(x-s) K_{32}^{\beta,0}(x-s) K_{33}^{\beta,0}(x-s) \end{pmatrix} \begin{pmatrix} q_{1,j}^\beta(x) \\ q_{2,j}^\beta(x) \\ q_{3,j}^\beta(x) \end{pmatrix}_{x\in(a_j,b_j)} ds = \begin{pmatrix} 0 \\ 0 \\ 0 \end{pmatrix}$$

$$K_{pm}^{\beta,r}(z) = \frac{1}{2\pi}\int_{-\infty}^{\infty}\alpha^{2r}e^{-iz\alpha}L_{p,m}^\beta(\alpha)d\alpha; \ p,m=\overline{1,3}; \ i=\overline{1,N}, \ r=0,1...$$

$$(7)$$

Here $L_{j,m}^\beta(\alpha)$ – elements of the inverse matrix for the matrix $\overline{L}^\beta(\alpha)$:

$$\overline{L}^\beta(\alpha) = \begin{pmatrix} \beta^2 + H_{11}^{\alpha\beta}\alpha\beta + H_{12}^{\alpha\beta}i\alpha h + H_{13}^{\alpha\beta} \\ \alpha\beta + H_{21}^{\alpha\beta}\alpha^2 + 2\nu_1\beta^2 + H_{22}^{\alpha\beta}i\beta h + H_{23}^{\alpha\beta} \\ -i\alpha h + H_{31}^{\alpha\beta}i\beta h + H_{32}^{\alpha\beta}1 + H_{33}^{\alpha\beta} \end{pmatrix} \tag{8}$$

The second equality in (7) is a matrix system of integrodifferential equations for determining the Fourier transformants of the disclosure of *j*-x delaminations, and the first equality in (7) defines the Fourier transformants of the contact stresses between the delaminations.

From the representation for $K_{jj}^{\beta,1}(x)$ it follows that these functions have a logarithmic singularity at $x = 0$. Therefore, solutions of a system of integrodifferential equations from (7) for $x \in (a_j, b_j)$ is sought as a series over Chebyshev polynomials of the second kind $U_m(x)(j = \overline{1,3}, i = \overline{1,N})$ [13, 20]:

$$\chi_{j,i}(s) = l_i^{-2}\sqrt{(b_j - s)(s - a_j)}\sum_{m=0}^{\infty}\varphi_{m,j}^{(i)}U_m((s-\zeta_i)/l_i);$$
$$2l_j = b_j - a_j; \ 2\zeta_j = b_j + a_j \tag{9}$$

To determine the coefficients $\varphi_{m,j}^{(i)}$, a system of linear algebraic equations is obtained:

$$\sum_{i=1}^N \sum_{m=0}^{\infty} \varphi_{m,j}^{(i)} I_{m,i,j}^{(i,r)} = f_{j,k}^{(r)}, \ \left(j=\overline{1,3}, r=\overline{1,N}, k=\overline{0,\infty}\right) \tag{10}$$

The coefficients of the system (10) depend on the loads on the coating and the product's material.

The Fourier transformants of the coefficients $K_{0,j,i}^{\mp}$ will be calculated using the formulas:

$$K_{\beta,j,i}^- = \sum_{m=0}^{\infty}(m+1)(-1)^{m+1}\varphi_{m,j}^{(i)},$$
$$K_{\beta,j,i}^+ = \sum_{m=0}^{\infty}(m+1)\varphi_{m,j}^{(i)}, \ \left(i=\overline{1,N}, j=\overline{1,3}\right) \tag{11}$$

The solution is significantly simplified for one partial separation, and with increasing separation width, the convergence of the proposed approximate solution worsens. Therefore, we indicate another solution for one separation, the convergence of which will improve with increasing the width of the separation. We assume that the detachment occupies the area:

$$-a \leq x \leq a, |y| < \infty$$

By representing the Fourier transformants of the given loads in the variable y with the parameter β in the form of an even $q_{m,\beta}^+(x)$ and odd $q_{m,\beta}^-(x)$ components, we get a system of integral equations with the difference and summable kernels ($\alpha_0 = \beta a$):

$$\sum_{j=1}^{3} \int_0^\infty \left[l_{m,j}^\beta(|t - \tau|) \mp K_{m,j}^\beta(t + \tau + 2\alpha_0) \right] p_{j,\beta}^\pm(\tau + \alpha_0) d\tau = f_{m,\beta}^\pm(t), \, m = \overline{1,3} \tag{12}$$

We are looking for solutions to this system in the form of [19]:

$$p_{j,\beta}^\pm(\tau + \alpha_0) = 2(2t)^{-1/2} e^{-t} \sum_{n=0}^\infty \mu_n \varphi_{n,j}^\pm(\beta) L_n^{-1/2}(2t), \, \beta > 0, \, t \geq 0 \tag{13}$$

where $\mu_n = 2\sqrt{2n!}/\Gamma(n + 0.5)$, $l_n^\alpha(z)$ – Chebyshev-Laguerre polynomials; $\Gamma(z)$ – Euler's gamma function [13, 21]. Coefficients $\varphi_{n,j}^\pm(\beta)$ are determined from the system of equations:

$$\sum_{j=1}^{3} \sum_{n=0}^\infty \left(I_{m-n}^{r,j} \mp k_{m+n}^{r,j} \right) \varphi_{n,j}^\pm(\beta) = f_{m,j}^\pm, \, r = \overline{1,3}, \, m = \overline{0, \infty} \tag{14}$$

The intensity coefficients at $x = a$ are equal to:

$$K_{\beta,j} = \sqrt{2} \sum_{n=0}^\infty = \mu_n \left(\varphi_{n,j}^+(\beta) + \varphi_{n,j}^-(\beta) \right), \, j = \overline{1, 3} \tag{15}$$

If the coating loads $q_j(x, y) = \overline{q}_j(x)$, then the contact stresses $\overline{p}_j(x)$, ($x \geq 0$) can be determined from the integrodifferential equations [14]:

$$\overline{p}_j(x) + D_j \int_0^\infty \overline{K}_j(x - s) \overline{p}_j(s) ds = \overline{q}_j(x), \, \overline{K}_j(x) = \frac{1}{2\pi} \int_{-\infty}^\infty |t|^{-1} e^{-ixt} dt, \, x > 0 \\ D_1 = D_2 = -d^2/dx^2, \, D_3 = d^4/dx^4 \tag{16}$$

The exact solutions of these equations are constructed by the factorization method [22, 23].

The following mathematical model is proposed to establish the calculated dependencies between the technological parameters of processing and the phenomenon of separation of coatings, provided their insufficiently strong adhesion.

The system of equations determining the thermal and stress-strain state of a coated product during machining contains the equation of non-stationary thermal conductivity [24] $k = 1, -h \leq z \leq h$ and $k = 2, h \leq z < \infty$:

$$a_k^2 \overline{\Delta} T_k = \partial T_k/\partial \tau, \, \overline{\Delta} = \partial^2/\partial x^2 + \partial^2/\partial z^2 \tag{17}$$

and the Lame elasticity equation in displacements:

$$
\begin{aligned}
&\overline{\theta}_k \partial\theta_k/\partial z + \overline{\Delta}_k \overline{U}_k = b_k^T \partial T_k/\partial z, \ \overline{\theta}_k \partial\theta_k/\partial x + \overline{\Delta}_k \overline{V}_k = b_k^T \partial T_k/\partial x \\
&\overline{\theta}_k = 1/(1-2v_k), \ b_k^T = 2\overline{\theta}_k G_k(1+v_k)\alpha_t^{(k)}, \ \theta_k = \partial\overline{U}_k/\partial z + \partial\overline{V}_k/\partial x
\end{aligned}
\tag{18}
$$

where $T_k(x, z, \tau)$ is the contact temperature at a point with coordinates (x, z) and at any time τ (for $k = 1$ – in the coating, for $k = 2$ – in the product material); a_k – thermal diffusivity of coating materials ($k = 1$) and product ($k = 2$); $\alpha_t^{(k)}$ – temperature coefficients of linear expansion; v_k, G_k – Lamé constants; U_k, V_k – components of the vector of displacements of the point (x, y) of the surface layer of the product during machining.

The initial conditions for this task can be zero. Boundary conditions for temperature and stress fields, considering heat transfer from the surface outside the contact zone of the tool with the part and intense heat release in the processing zone, have the form [25] ($|x| < l$):

$$
\begin{aligned}
&\lambda_1 \partial T_1/\partial z|_{z=-h} = -q_1(z, x, \tau), \ \lambda_1 \frac{\partial T_1}{\partial z}|_{z=-h} = q_1(x, z, \tau)[H(x) - H(x - 2l)] \\
&-\lambda_1 \frac{\partial T_1}{\partial x} + \gamma(T_1 - T_0) = 0, \ |x| > l, \ \sigma_z^1(x, 0, \tau) = \sigma_z^2(x, 0, \tau)
\end{aligned}
\tag{19}
$$

where $q(x, z, \tau)$ – the intensity of the heat flux released in the contact zone of the tool with the machined surface; λ_1 is the thermal conductivity of the coating; $2l$ – length of the contact zone of the tool with the machined surface; γ – coefficient of thermal conductivity with the environment; σ_x^1, σ_x^2 – normal stresses in the coating and in the matrix, respectively; $H(x)$ – Heaviside unit function; T_0 – ambient temperature.

Conditions of coupling of the coating with the material of the part:

for temperature fields:

$$
\begin{aligned}
&T_1(x, h-0, \tau) = T_2(x, h+0, \tau), \\
&\lambda_1 \frac{\partial T_1}{\partial x}(x, h-0, \tau) = \lambda_2 \frac{\partial T_2}{\partial x}(x, h+0, \tau)
\end{aligned}
\tag{20}
$$

for deformation and stress fields:

$$
\begin{aligned}
&U_1(x, h-0) = U_2(x, h+0), \ V_1(x, h-0) = V_2(x, h+0), \\
&\sigma_x^1(x, h-0) - \sigma_x^2(x, h+0) = [\sigma_x], \ |x| < a
\end{aligned}
\tag{21}
$$

The solution of Eqs. (17)–(18) with conditions (19)–(21) allowed us to obtain explicit expressions for calculating the temperature both in the coating and in the base material in the form of [20]; assuming that $q(x, z, \tau) = \frac{cV_1^*}{2\pi\lambda_1 l\sqrt{V_2^* S}}$:

$$
\begin{aligned}
T_1(x, z, \tau) &= \frac{cV_1^*}{2\pi\lambda_1 l\sqrt{V_2^* S}} \int_{-l}^{l} \frac{e^{\frac{(x-\eta)^2+(z-\eta)^2}{4a_1^2(\tau-t)^2}}}{2\sqrt{\pi(\tau-t)}} \\
&- \left\{ \frac{1}{\sqrt{\pi(\tau-t)}} + \gamma e^{\gamma^2(\tau-t)} \left[1 + \Phi\left(\gamma\sqrt{\tau-t}\right)\right] \right\} d\eta dt, \ -h < z < 0; \\
T_2(x, z, \tau) &= \frac{cV_2^*}{2\pi\lambda_2 l\sqrt{V_2^* S}} \int_{-l}^{l} \frac{\sqrt{z^2+(x-\eta)^2} e^{\frac{V_2(y-\eta)^2}{2a_2}}}{2\sqrt{\pi(\tau-t)}} \\
&\times K_{1/2}\left(\frac{V_2}{2a_2}\sqrt{(x-\eta)^2+z^2}\right) d\eta dt, \ z > 0
\end{aligned}
\tag{22}
$$

where $K_{1/2}(x)$ – Bessel function; c, V_1, V_2, S – technological parameters of processing coated products; $T_{1,2}(x, z)$ – contact temperatures in the coating and product material.

The formulas determine the temperature stresses:

$$\sigma_x^{(1)} = \sigma_y^{(1)} = -\bar{\alpha}_t^{(1)} T_1(x, z, \tau) + b_1^* x/h + b_0^*; \ \bar{\alpha}_t^{(k)} = \alpha_t^k E_k/(1 - \nu_k)$$

$$\sigma_x^{(2)} = \sigma_y^{(2)} = -\bar{\alpha}_t^{(2)} T_2(x, z, \tau) + m_1^{-1} \left(m_h b_1^* x/h + b_0^* \right)$$

$$N_0^* b_0^* = 2m_1 | 2 \left(m_1 + m_h^3 \right) N_1^* - 3 \left(m_h^2 - m_1 \right) N_2^*$$

$$N_0^* b_1^* = 6m_1 | 2 \left(m_1 + m_h \right) N_2^* - \left(m_h^2 - m_1 \right) N_1^*$$

$$hN_1^* = \left[\bar{\alpha}_t^{(1)} \int_0^{+h} T_1(x, z, \tau) dx + \bar{\alpha}_t^{(2)} \int_0^{\delta} T_2(x, z, \tau) dx \right] \quad (23)$$

$$h^3 N_2^* = \left[\bar{\alpha}_t^{(1)} \int_0^{+h} T_1(x, z, \tau) dx \right] + \bar{\alpha}_t^{(2)} \int_0^{\delta} T_2(x, z, \tau) dx$$

$$N_0^* = 4(m_1 + m_h) \left(m_1 + m_h^3 \right) - 3 \left(m_h^2 - m_1 \right)^2$$

$$m_1(1 - \mu_1)E_2 = (1 - \mu_2 E_1), \ m_h = \delta/h$$

where V_1, V_2 – technological parameters: λ_1, λ_2, a_1, a_2, $\alpha_t^{(1)}$, $\alpha_t^{(2)}$ – thermal properties of the coating materials and the main material; E_k – the elastic modulus of the coating (1) and material goods (2).

The dependencies (22)–(23) allow us to simulate the machining process of parts coated with the processed surfaces' quality requirements.

4   Results

The adequacy of the constructed model was tested experimentally on samples of steel C45, on the surface of which a wear-resistant coating based on NMCC Zr-ZrN-(Zr, Cr, Al) N. To calculate the parameters of defect-free processing, the following physical-mechanical characteristics were used: $K_c = 2.0$ MPa $\cdot$ m$^{1/2}$, $\alpha = 8.58$; K^{-1}; $G = 168$ GPa.

Considering the randomness of the size and distribution of defects in the body, it is necessary to establish the law of probabilistic distribution of these defects. According to the results of micro-grinding analyses of the working surfaces of the samples under study (before the grinding operation) there is a defect size distribution function that determines for each value the relative frequency n/m of the appearance of this size in the contact zone of the circle with the part (n_i – the sum of the frequencies of the sizes l_i that fall into the i-th interval, m – the length of the partial interval).

To confirm the analytical model, tribocorosion studies of composite materials based on NMCC Zr-ZrN-(Zr, Cr, Al) N. As a result, the limiting values of the contact temperature gradients of grinding and the permissible values of the heat flux are established. It depends on the size of structural defects and delamination located at the boundary

"wear-resistant coating – cylinder material" will not lead to the formation of cracks and chips on the treated surfaces, which have the form [24]:

$$q^*(h) = \frac{cP_z V_1 d_n}{\sqrt{SI}} \leq \frac{\sqrt{3}\lambda_n K_{1c}}{Hl\sqrt{\pi l}\sigma_y^{(1)}} \tag{24}$$

where c, Pz, V_1, S – technological parameters of the working surface treatment; K_{1c} – crack resistance coefficient of the coating; I – mechanical coefficient of heat entering the coated product; $2l$ – length of the detachment section (a_1, b_1); H – parameter characterizing the properties of the coating.

Therefore, to ensure the quality of the treated surfaces, it is necessary, according to the established functional relationships between the physical and mechanical properties of materials and the parameters of the grinding process, to select such processing modes and tool characteristics that the current values of the grinding temperature $T(x, y, \tau)$ and heat flux $q(y, \tau)$, stresses σ_{pmax} and grinding forces P_Y, P_Z, intensity coefficient K_I $(S, \alpha, \sigma_{pmax})$ do not exceed their limit values, which guarantee the necessary quality of the surface layer.

5 Conclusions

A mathematical model has been developed to determine the separation conditions for the exfoliated coating depending on the properties of the materials. The criterion relations linking the grinding temperature, the intensity of the heat flow, the stress-deformed state of the processed surface of the products with technological parameters are obtained, which allow controlling the quality of processing to prevent defects in the peeling of the coating from the main matrix.

The work results can be applied in machining materials containing structural inhomogeneities and having low crack resistance characteristics.

References

1. Nee, J.G., Dufraine, W., Evans, J.W.: Fundamentals of Tool Design, 6th edn. Society of Manufacturing Engineers, Michigan (2010)
2. Slepyan, L.I.: Models and Phenomena in Fracture Mechanics. Springer, Berlin (2012)
3. Sun, C.T., Jin, Z.: Fracture Mechanics. Academic Press, (2011)
4. Recho, N.: Fracture Mechanics and Crack Growth. Wiley, New York (2012)
5. Anderson, T.L.: Fracture Mechanics: Fundamentals and Applications, 4th edn. CRC Press, New York (2017)
6. Vereschaka, A., Grigoriev, S., Sitnikov, N., Batako, A.: Delamination and longitudinal cracking in multilayered composite nanostructured coatings and their influence on cutting tool wear mechanism and tool life. Wear **390**, 209–219 (2017)
7. Truhanska, O.O.: Technological methods of increasing wear resistance and durability of details. Machinery, energy, transport of agro-industrial complex **4**, 111 (2020)
8. Ruberti, A.: Distributed Parameter Systems: Modelling and Identification. Springer (2014)
9. Sierikova, O., Koloskov, V., Degtyarev, K., Strelnikova, O.: The deformable and strength characteristics of nanocomposites improving. Mater. Sci. Forum **1038**, 144–153 (2021)

10. Mekhtiev, M.F.: Asymptotic Analysis of Spatial Problems in Elasticity. Springer (2018)
11. Lamon, J.: Brittle Fracture and Damage of Brittle Materials and Composites: Statistical-Probabilistic Approaches. Elsevier (2016)
12. Mkhitaryan, S.M., Grigoryan, M.S., Kanetsyan, E.G., Mkrtchyan, M.S.: On Contact Interaction Between Edges of Circular Crack in Elastic Semi-Space and Absolutely Rigid Inclusion. Contemporary Problems of Architecture and Construction. CRC Press (2021)
13. Gradstein, N.S., Ryzhik, I.M.: Tables of Integrals, Sums, Series and Products. Fizmatgiz, Moscow (1971). [in Russian]
14. Kunitsyn, M., Usov, A., Sikirash, Y.: Impact of the heterogeneous structure of magnetic hard alloys on the quality characteristics of the surface layer during grinding processing. In: Tonkonogyi, V., Ivanov, V., Trojanowska, J., Oborskyi, G., Pavlenko, I. (eds.) Advanced Manufacturing Processes III. InterPartner 2021. Lecture Notes in Mechanical Engineering, pp. 405–414. Springer, Cham (2022). https://doi.org/10.1007/978-3-030-91327-4_40
15. Altenbach, H., Altenbach, J., Kissing, W.: Mechanics of Composite Structural Elements. Springer, Singapore (2018)
16. Chawla, K.K.: Composite Materials: Science and Engineering. Materials Research and Engineering. Materials Research and Engineering. Springer, New York (2013)
17. Christensen, R.M.: Mechanics of Composite Materials. Dover Civil and Mechanical Engineering. Dover Publications, New York (2012)
18. Baruchel, J., Peix, G., Buffiere, J.Y. et al.: X-ray Tomography in Material Science. Hermes Science (2000)
19. Bader, M.G.: Handbook of composite reinforcements. Int. Mater. Rev. **39**(3), 123–124 (2012)
20. Daniel, G.: Composite Materials: Design and Applications, 3rd edn. CRC Press, Boca Raton (2014)
21. Weinert, K., Blum, H., Jansen, T., Rademacher, A.: Simulation based optimization of the NC-shape grinding process with toroid grinding wheels. Prod. Eng. Res. Devel. **1**(3), 245–252 (2007)
22. Rafieian, F., Hazel, B., Liu, Z.: Regenerative instability of impact-cutting material removal in the grinding process performed by a flexible robot arm. Procedia CIRP **14**, 406–411 (2014)
23. Nayfeh, A.H., Pai, P.F.: Linear and Nonlinear Structural Mechanics. Wiley (2008)
24. Oborskiy, G.A., Daschenko, A.F., Usov, A.V., Dmitrishin, D.V.: System Modeling. Astroprint, Odessa (2013). [in Russian]
25. Carslaw, H.S.: Introduction to the Mathematical Theory of the Conduction of Heat in Solids (Classic Reprint). Fb&c Limited, London (2017)

Mechanisms of the Structure Formation of Soldered Seams When Using Composite Solders

Vladimir Lebedev[1] , Ivan Vegera[1] , Eshreb Dzhemilov[2(✉)] ,
and Ruslan Dzhemalyadinov[2]

[1] Physical and Technical Institute of the National Academy of Sciences of Belarus, 10, Kuprevicha Street, 220141 Minsk, Belarus
[2] Crimean Engineering and Pedagogical University named after Fevzi Yakubov, 8, Uchebniy Side Street, Simferopol 29501, Republic of Crimea, Ukraine
eshrebdzhemilov@gmail.com

Abstract. This study shows the results of experimental studies of the mechanism of formation of the structure of soldered joints during high-frequency heating (49 kHz). The magnetic-dynamic effect of a high-frequency electromagnetic field on iron-nickel particles can lead to a redistribution of iron particles in suspensions flux - phosphorous copper, copper - iron, flux - copper-phosphorus melt - iron due to the movement of iron particles to the surface of the holder. The heating of iron particles under a high-frequency electromagnetic field changes the mechanism of dissolving particles in a copper-zinc melt. An increase in the particle temperature increases the solubility of iron in the melt of the diffuse boundary layer and, at the same time, the solubility of copper and zinc in iron. A diffusion boundary layer with an iron concentration exceeding the value of iron solubility in the surrounding melt is formed around the particles. It is shown that the main factors affecting the structure of a brazed joint are the heating rate of the composite solder and the solubility of more refractory components.

Keywords: Process innovation · Brazing alloys · Soldering · Flux · Hard alloys · Solders · Brazed tool

1 Introduction

In modern metalworking production, cutting tools with replaceable inserts made of hard alloys and superhard materials are often used. However, this did not lead to a complete replacement of the brazed tool. Brazed tools are most widely and effectively used in small-scale production. The ability to change the tool's geometry, considering specific processing conditions, allows you to effectively assign processing modes and achieve the required accuracy and quality parameters. At the same time, the geometry of the cutting blade is the most versatile adjustable parameter, which allows the use of one tool material for processing a wide range of processed materials.

The toughening of cutting conditions the use of new structural materials require an increase in the enduringness of the tool system the strength and dependability of fastening the plates of tool materials to the tool body. Ensuring these requirements allows the brazed tool to compete with the tool in certain areas of metalworking industries [1].

For brazing plates of hard alloys to the holder body, the most widely used brazing alloys on a copper-zinc base with a temperature brazing of 1225–1275 °K. However, at such temperatures there is intense oxidation of the surface of the plates, a decrease in their hardness, as well as a decrease in the strength of the soldered seam and, accordingly, the attachment of the plates to the holder. One of the ways to reduce the soldering temperature and increase the physicomechanical characteristics of the solder in the seam is the use of multicomponent composite solders. Such solders contain low-melting and refractory components, and the solder joint is formed in the process of heating the solder and interacting with the components.

2 Literature Review

For brazing carbide plates to steel holders, brazing alloys based on copper-zinc, copper-zinc-nickel, copper-zinc-nickel-manganese alloys of various grades are used (CrxBy, Ni3Si, Ni3B, D Bronze, Braze 252, etc.).

An increase in the strength of the connection of the plates with the tool body is achieved by using solders with sufficiently high physical and mechanical characteristics. On the other hand, for reducing the oxidation of the plates of tool materials, it is necessary to reduce the temperature and duration of the soldering process [2]. Chiu et al. are investigating the process of vacuum brazing parts made from tool steel. Thin foil was used as solder. The authors found that the applied compression force exerts the greatest influence on the process of vacuum soldering and the properties of the formed joint [3]. In [4, 5], technological features of complex shape parts machining were proposed.

For brazing plates of hard alloys to the holder body, the most widely used brazing alloys on a copper-zinc base with a temperature brazing of 1225–1275 K [6]. Sometimes Cu-Sn solder is used for soldering the plates. In [7], the effect of Sn content in the filler metals on the properties of brazed joints was investigated. The experimental results show that the maximum shear strength is 341 ± 15 MPa for the joints brazed at 1080 °C for 10 min using Cu-9Sn filler. However, at such temperatures, there is intense oxidation of the surface of the plates, a decrease in their hardness, and a decrease in the strength of the soldered seam and, accordingly, the attachment of the plates to the holder. One of the ways to reduce the soldering temperature and increase the physicomechanical characteristics of the solder in the seam is the use of multicomponent composite solders. Such solders contain low-melting and refractory components, and the solder joint is formed in the process of heating the solder and interacting with the components.

Vinardi et al., considering the process of soldering a hard alloy plate onto a holder made of structural steel, studied the effect of filler and heat treatment on the physical and mechanical properties of a brazed joint [8].

The formation of the structure of the brazing alloys was discussed in the article [9]. When brazing cermet plates, the reaction layer of the Cu-Ni-Ti solid solution between the cermet and the filler metal was difficult to form during brazing at 870 °C, which led

to very low shear strength. joints. During brazing at 910 °C, a Cu-Ni-Ti solid solution was formed between the cermet and the filler metal, which became thick with increasing holding time.

In [10], researchers evaluated the effect of heating temperature and holding time during soldering on the evolution and hardening effect of α-Cu.

Johari Miab and Hadian [11] also evaluated the obtained microstructure and properties of the diffusion layer when soldering cubic boron nitride (cBN) crystals on a steel holder (CK45) using Cusil-ABA as solder as a function of process time. Bonding is due to the formation of a reactive layer between cBN and solder and a diffusion layer between steel and solder. In work [12], the problem of brazing hard-alloy plates for rock cutting tools is considered. The types of used solders and their shape were considered in this case.

The authors in [13] calculate the binding energy and interaction parameters between WC and other elements (for example, Co, Fe, Cr, Mo, and V). The authors in [14] investigated the influence of the thickness and structure of the solder from the foil on the residual stresses in the solder joint. Analytical calculations comparing the resulting residual stresses in joints formed with conventional solders and solders with the addition of pure copper foil have shown that the thickness of the solder is the dominant factor. In [15], the dependences of the plate fastening strength on the applied modes of the soldering process and directly on the type of solder were studied. Mechanical behaviors of polymer composites and reinforced hybrid composites were studied in [16, 17].

3 Research Methodology

The formation processes of solders investigated during the melting of the charge - a low-melting component - a refractory component - a flux on the surface of steel holders. Holders in the form of a rod with a diameter of 10 mm have a hole at the end into which a solder charge is placed (a mixture of powders with a flux). Heating was carried out using a high-frequency generator with a power of 80 kW. The operating frequency of the generator during soldering was 49 kHz. The heating rates of holders and tools were 40 and 50 K/s. The holder (and plate) temperature during soldering was controlled with an Optris-ST2MN optical pyrometer. The soldering temperature varied in the range of 660–1775 °K. The solders used were mixtures of powders of a copper-zinc alloy (BCuZn-1 grade solder), nickel, and iron. The fractional composition of the powders in the solder charge was 80/63 μm. The concentration of nickel and iron in the charge was 15 wt.%. Powder of copper-phosphorous alloy with 8 wt.% phosphorus was also used as a low-melting component of the solder. The eutectic alloy KBF_4-$Na_2B_4O_7$ was used as a flux. The concentration of the flux in the solder-flux charge was 15 vol.%.

The microstructure of the solders was identified by etching in a 30 wt.% solution of "aqua regia" (3 wt. part hydrochloric and 1 wt. part nitric acid). The morphology of the brazed joints' fracture surface, the solders' microstructure, and the holder's surface were investigated using scanning electron and optical microscopy using a VEGA TESCAN microscope and a MICRO hardware complex.

4 Results

The beginning of the formation of a liquid phase when heating a mixture of composite solder (CuP-Ni) with flux is noted after 8 s of heating at a heating rate of 40 K/s. The process begins with the melting of the flux. The formation of a metal melt is noted after 14 s of heating. After 20 s of heating, a copper-nickel-phosphorus alloy with a heterogeneous structure and composition is formed. The structure contains regions enriched with nickel (Fig. 1). Such regions of inhomogeneous composition in the round and shapeless particles are present in the alloy even after 23 s of heating.

a   b

c   d
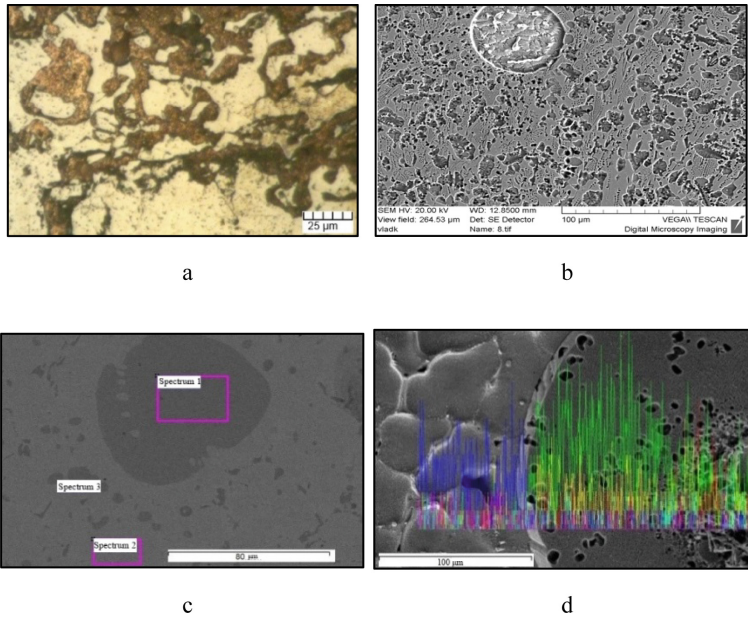
Fig. 1. Microstructure of Cu-Ni-P-based solder. Heating speed: a – 40; b, c, d – 50, К/s. Heating duration: a – 23; b, c, d – 18, s.

Increasing the heating rate of the charge (Cu-P)-Ni-flux up to 50 K/s leads to the formation of solder with a different structure and composition than at a heating rate of 40 K/s. After 18 s of exposure, an interlayer of an iron-copper-phosphorus alloy is formed at the holder-solder interface, in which particles of a copper-nickel-phosphorus alloy of various shapes, enriched with iron, are located (Fig. 1b, c, d). These round and shapeless particles are located at a distance of 400–600 μm from the holder surface and represent an iron-nickel-phosphorus alloy (Fig. 1b, d).

The phosphorus concentration in these particles exceeds its concentration in the copper-phosphorous alloy.

The formation of solder when heating the charge (Cu-P)-Fe-flux proceeds in the same way as when heating the charge (Cu-P)-Ni-flux. At the first stage, at temperatures of 675–825 °K, a flux melt is formed, and a copper-phosphorous alloy melts. With

heating durations of 18–20 s, a suspension is formed from a copper-phosphorous melt, iron particles, flux drops, and flux melt. In this heating time interval, the suspension is stratified into two "phases": the flux melt and the copper-phosphorous melt suspension - iron particles.

After 18 s of heating at the holder-solder interface, the layer with dimensions of 100–200 µm contains particles from the iron - phosphorus alloy. The phosphorus concentration (16–19 wt%) is higher than the surrounding alloy (Fig. 2a). These particles are surrounded by shells of a copper-based alloy (Cu-89.81; Fe-8.34; P-1.85 wt%). Particles with a similar structure and composition are present in the solder at a distance of 400 - 600 µm from the holder (Fig. 2a).

After 20 s of heating, the structure of the solder also contains particles with a higher concentration of iron (77–83 wt.%) And phosphorus (19 wt.%) Than in the surrounding alloy.

A decrease in the heating rate of the charge (Cu-P)-Fe to 40 K/s does not lead to the appearance of solder with a homogeneous distribution of iron. The solder structure contains shapeless particles that differ in composition from the surrounding alloy (Fig. 2, Table 1).

| a | b | c |
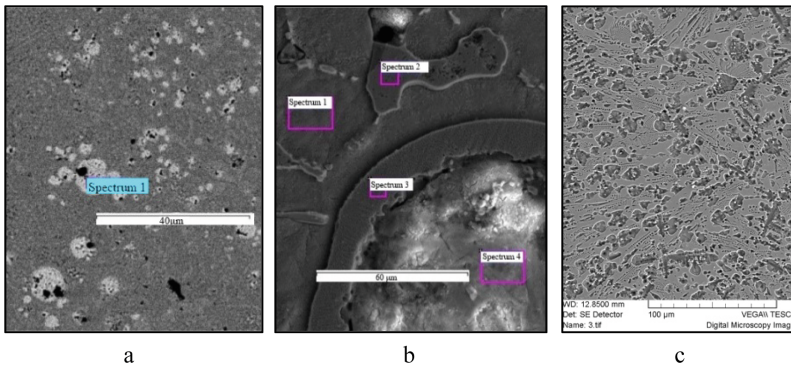
Fig. 2. Microstructure of Cu-Fe-P solder. Heating speed: a – 50; b, c – 40, К/s. Heating duration: a – 18, b – 20 c – 23, s.

Table 1. Elemental composition of the Cu-Fe-P solder section. The heating speed is 40 K/s. Heating duration - 23 s.

Element	S_1, wt.%	S_2, wt.%	S_3, wt.%	S_4, wt.%
P		15,65	13,93	16,58
Cr	0,07	0,71	0,75	0,86
Mn	0,87	0,24	0,29	0,30
Fe	99,06	80,30	81,34	79,68
Cu		3,09	3,69	2,58

The microstructure of the solder formed during heating of the charge is an alloy of the copper-phosphorus-iron system, in which shapeless particles are located based on an alloy of the iron-phosphorus-copper system of a different composition (Fig. 2b, c).

Heating the charge alloy Cu-Zn (Cu - 36.5–39.5 wt.%; Zn - the rest) - Ni with a higher melting point (low-melting component) than the alloy (Cu - 8 wt.% P), to temperatures soldering (1225 °K), as in the case of the alloy (Cu - 8 wt.% P), leads to the formation of solders with a heterogeneous structure. Heating the charge (Cu-Zn)-Ni-flux to soldering temperatures at a rate of 50 K/s is accompanied by the formation of a solder layer on the holder surface, which differs in composition and structure from the rest of the solder. At the interface between the holder and the solder, the 50–100 μm layer structure is represented by shapeless particles of iron and an iron-based alloy in a copper-zinc-nickel-iron alloy matrix. These particles are inhomogeneous in composition, and they contain interlayers of an alloy of different compositions, dividing the particles into fragments (Fig. 3a). Particles with a similar structure are also present in the solder layer at a distance of 100–200 microns from the holder surface (Fig. 3a).

a   b
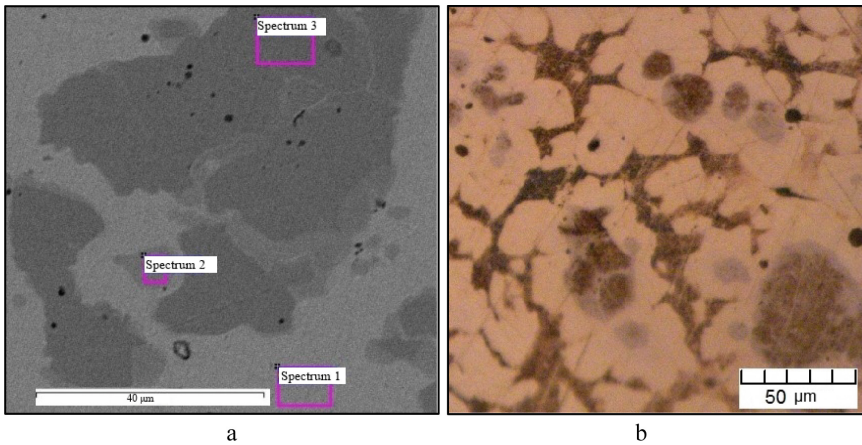
Fig. 3. The microstructure of the (Cu-Zn)-Ni system solder. Heating speed: a - 50; b - 40 K/s. Heating duration: a – 18; b - 23 s. Distance from holder: a – 100; b - 200 μm.

The solder structure formed after heating the charge at a rate of 50 K/s represents grains of an alloy of the copper-zinc-nickel (iron) system, among which there are alloy particles enriched in iron (Fig. 3). After heating the charge to the soldering temperature at a rate of 40 K/s, the structure of the solder is represented by dendrites with an inhomogeneous composition and eutectic interlayers between them. Inhomogeneities in the composition of dendrites are rounded particles that appear with greater contrast than the surrounding alloy.

A decrease in the heating rate of the charge to 40 K/s also does not lead to the appearance of solder with a homogeneous structure: particles of different composition and morphology than the alloy of the Cu-Zn-Ni system are present in the solder after heating the charge for 23 s (Fig. 3b).

Heating the charge (Cu-Zn)-Fe to the soldering temperature at speeds of 50 and 40 K/s, as well as when heating the charge (Cu-Zn)-Ni, does not lead to the appearance of solder from the alloy of the Cu-Zn-Fe system with a homogeneous structure (Fig. 4).

The microstructure of the solder formed after heating the charge to the soldering temperature at a rate of 50 K/s is the grains of the copper-zinc-iron alloy, in which and between which the iron-based alloy particles are located. The concentration of these particles in the layer at the interface of the holder with the solder is greater than in the solder layer (Fig. 4).

a   b
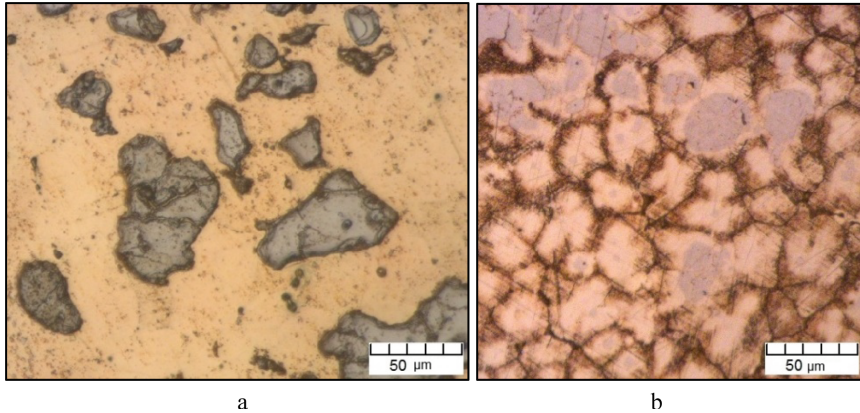
Fig. 4. Microstructure of the solder (Cu-Zn) - Fe at a distance of 300 μm from the holder surface. Heating speed a - 50 K/s, b - 40 K/s. Soldering temperature, K: a - 1155°; b - 1195°.

A decrease in the heating rate of the charge (Cu-Zn) - Fe (40 K/s) to the soldering temperature changes the microstructure of the solder (Fig. 4b). The microstructure of the solder is a copper-zinc-iron alloy grains. Individual grains have a heterogeneous composition: the central part of the grains has an increased iron content (Fig. 4b). A decrease in the soldering temperature to 1155 °K changes the microstructure of the solder. The microstructure of the solder, in this case, is the grains of an alloy based on a copper-zinc system, between which particles of an iron-based alloy are located (Fig. 4a).

The microstructure of the brazing alloys formed in the brazed seams differs from the microstructure of the brazing alloys on the surface of the holder. There are no layers on the surfaces to be joined that differ in structure and composition from the brazing alloy in the central part of the seams (Fig. 5).

The structure of the solders formed in the brazed joints is represented by alloy grains of low-melting and refractory components of the solder, between which and in which there are alloy particles based on the refractory component. In the brazed seam of the (Cu-Zn) - Ni solder, iron is present at 7.25 wt. % (Fig. 5a).

In contrast to brazing alloys made from alloys of the systems Cu-Zn-Ni, Cu-Zn-Ni-Mn, etc., the structure of which does not change during melting and subsequent brazing of parts, the structure of composite brazing alloys largely depends on the brazing modes.

The formation of the solder begins at the time moment following the melting of the low-melting component and the separation of the liquid metal suspended matter and the
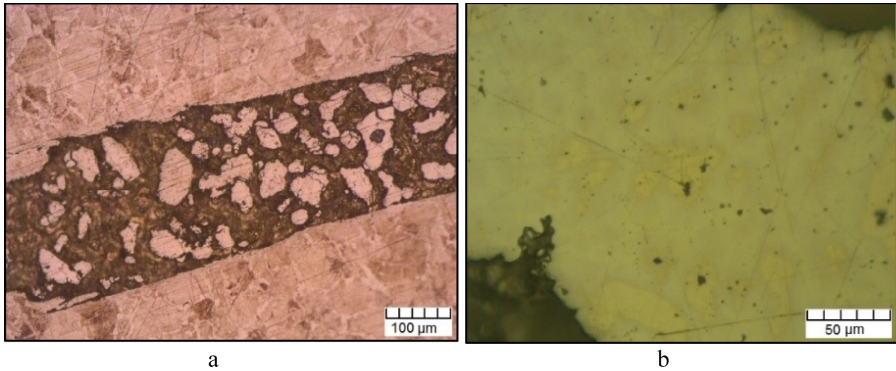
Fig. 5. The microstructure of the brazed seam. Soldering temperature 1175 °K. Heating speed 40 K/s. a - solder (Cu-Zn) - Fe; b - solder (Cu-Zn) – Ni.

flux melt (Fig. 4b). At subsequent moments in time, the interaction of the components of the liquid metal suspension leads to the formation of a melt. The microstructure of the solders of the systems (Cu-P) - Ni (Fe), (Cu-Zn) - Ni (Fe), formed when the charge is heated to soldering temperatures, regardless of the heating rate, shows that homogeneous alloys with a structure characteristic of cast alloys are not formed (Figs. 1b, 2c, 4b). Heating the charge (Cu-P) - Ni to 1075 °K leads to forming a structure, which is a shapeless nickel alloy particles with dimensions larger than the initial nickel particles located in a copper-phosphorous alloy matrix (Fig. 1a). The formation of such a structure is possible with the formation of a structurally inhomogeneous melt, which is a copper-phosphorous melt and shapeless lumps (particles) of a nickel-copper-phosphorus alloy in a viscous-plastic state. The formation of a melt of the Ni-Cu-P system with a liquidus temperature close to 1175 °K is possible at the phosphorus, copper, and nickel concentration in alloy 5–8; 70–90; 5–15 wt.%, respectively.

The nature of the change in the structure of the solder when the charge is heated at a rate of 40 K/s indicates the formation of a suspension of copper-phosphorous melt and nickel particles after melting the copper-phosphorous alloy. The suspension turns into an emulsion consisting of shapeless lumps of nickel alloy in a viscous plastic state (premelting) and copper-phosphorous melt, then into a structurally inhomogeneous melt (Fig. 1).

After forming a copper-phosphorous melt, following the basic concepts of the diffusion kinetics of dissolution of solid metals in liquid metals, the stage of dissolution of nickel in a copper-phosphorous melt should follow and the formation of a ternary melt under the phase diagram of the Cu-Ni-P system. The dissolution rate of nickel in a copper-phosphorous melt is limited by the solubility of nickel in a copper-phosphorous melt and by hydrodynamic conditions at the particle-melt interface.

5   Conclusions

The study of the formation processes of solder melts during induction soldering showed that the contact processes of dissolution of refractory particles in a more low-melting

solution change depending on the effect of an electromagnetic field. This influence manifests itself as a predominant resistive heating of the refractory component particles and a magnetic-dynamic effect on the solder components. Indirectly, the influence of the electromagnetic field on the processes of contact interaction of the components of the solder is manifested in the rapid heating of the composite solder and the non-isothermal mode of melting of the refractory component of the solder in the low-melting one. The consequence of these influences is the formation of brazing alloys with a structure uncharacteristic for cast alloys on the brazed surface and brazing alloys with a structure similar to that of cast dispersion-strengthened composite materials the brazed seams. The main factors influencing the structure of the brazed joint are the heating rate of the composite solder and the value of the solubility of the refractory component in the low-melting one.

References

1. Ma, B., Song, Q., Bu, F., Wang, X., Cao, T.: Self-sharpening of tools with unilateral braze coating fabricated using WC- and Ni-based alloys. J. Test. Eval. **48**(5), 3742–3751 (2020)
2. Tillmann, W., Henning, T., Boretius, M.: Effect of the dwell time on the microstructure and tensile strength of vacuum-brazed tool steels using BNi-2 filler metal. Weld. World **63**, 1477–1488 (2019)
3. Tusek, J., Skumavc, A., Klobcar, D.: Vacuum brazing of tools with a thin foil. Metalurgija **54**(1), 67–70 (2015)
4. Ivanov, V., Dehtiarov, I., Pavlenko, I., Kosov, M., Hatala, M.: Technological assurance and features of fork-type parts machining. In: Ivanov, V., et al. (eds.) DSMIE 2019. LNME, pp. 114–125. Springer, Cham (2020). https://doi.org/10.1007/978-3-030-22365-6_12
5. Ivanov, V., Pavlenko, I., Kuric, I., Kosov, M.: Mathematical modeling and numerical simulation of fixtures for fork-type parts manufacturing. In: Knapčíková, L., Balog, M. (eds.) Industry 4.0: Trends in Management of Intelligent Manufacturing Systems. EICC, pp. 133–142. Springer, Cham (2019). https://doi.org/10.1007/978-3-030-14011-3_12
6. Chiu, L., Liao, H., Lin, S., Pan, Y., Liou, H.: Effect of brazing temperature on the microstructure and property of vacuum brazed WC-Co and carbon steel joint. Advanced Materials Research **47–50**, 682–685 (2008)
7. Wang, H., Chiu, L., Chang, H.: Effect of tin content on the microstructure and property of brazed WC-Co/CrMo alloy steel joints. Adv. Mater. Res. **47–50**, 596–599 (2008)
8. Winardi, Y., Triyono, Wijayanta, A.T.: Effect of filler and heat treatment on the physical and mechanical properties of the brazed joint between carbide tip and steel. In: IOP Conference Series Materials Science and Engineering, vol. 176, no. 1, p. 012026 (2017)
9. Jing, Y., Yang, Q., Xiong, W., Huang, B., Li, B., Zhang, M.: Microstructure and shear strength of brazed joints between Ti(C, N)-based cermet and steel with Cu-Ag-Ti filler metal. J. Alloy. Compd. **682**, 525–530 (2016)
10. Jiang, C., Chen, H., Wang, Q., Li, Y.: Effect of brazing temperature and holding time on joint properties of induction brazed WC-Co/carbon steel using Ag-based alloy. J. Mater. Process. Technol. **229**, 562–569 (2016)
11. Johari Miab, R., Hadian, A.M.: Effect of brazing time on microstructure and mechanical properties of cubic boron nitride/steel joints. Ceram. Int. **40**(6), 8519–8524 (2014)
12. Pashkov, I., Misnikov, V., Morozov, V., Tavolzhanskii, S.: Induction brazing of carbide cutters for a mining tool. The choice of composition and solder form. Weld. Int. **33**(9), 1–7 (2021)

13. Zheng, M.L., Gao, S.Y., Chen, J.G., Zhang, W., Li, J.N., Chen, B.L.: Impacts of element diffusion on bond breakage of cemented carbide cutter. Ann. Chimie – Sci. Matériaux **43**(3), 151–158 (2019)
14. Bobzin, K., Öte, M., Hebing, J.: Approaches and possibilities for reducing residual stresses in induction brazed cemented carbide/steel joints. Weld. World **64**(9), 1579–1587 (2020). https://doi.org/10.1007/s40194-020-00928-w
15. Pashkov, I.N., Misnikov, V.E., Morozov, V.A., Gadzhiev, M., Bazlova, T.A.: Influence of solder and flux composition on thermal stability of brazed PDC cutters. Weld. Int. **35**, 121–126 (2021)
16. Rudenko, S., Berladir, K., Trojanowska, J., Varenyk, S., Shvetsov, D., Kravets, V.: Application of FMEA for assessment of the polymer composite materials quality. J. Eng. Sci. **8**(2), B12–B18 (2021). https://doi.org/10.21272/jes.2021.8(2).b3
17. Harikrishna, V., Kumar, K.V.: Mechanical behaviors of hybrid composites reinforced with epoxy resin. J. Eng. Sci. **8**(2), C24–C29 (2021). https://doi.org/10.21272/jes.2021.8(2).c4

Mathematical Modeling of Processes and Equipment for the Manufacture of Electrode Carbon Graphite Products

Serhii Leleka , Anton Karvatskii[(✉)] , Ihor Mikulionok , Victor Vytvytskyi , and Olena Ivanenko

National Technical University of Ukraine "Igor Sikorsky Kyiv Polytechnic Institute", 37, Peremohy Avenue, Kyiv 03056, Ukraine
`anton@rst.kpi.ua`

Abstract. Production of electrode carbon-graphite products is one of the most energy-intensive chemical and metallurgical industries. One of the ways to reduce the energy intensity of electrode carbon-graphite products is to improve the energy efficiency of the furnace equipment of its main processes. A mathematical model of the combustion process of synthesis gas and natural gas in the working space of a rotary kiln was formulated. Two numerical models were developed. The first one is to study the heat-hydrodynamic state of a rotary kiln during natural or synthetic gas. The second one is to study the thermal parameters of a rotary kiln during the combustion of synthesis gas together with natural gas. Calculations were carried out to determine the synthesis gas consumption as a substitute for natural gas. It was established that at the expense of partial or complete replacement of natural gas by synthesis gas during operation of a calcining rotary kiln, it is possible to decrease natural gas consumption up to 100%. A complete replacement of natural gas with synthetic gas instead of 192 nm^3/h of natural gas, it is necessary to burn 908 nm^3/h of synthetic gas, which is significantly less than the synthetic gas capacity of the rotary kiln cooling drum.

Keywords: Carbonaceous filler · Calcination · Rotary kiln · Physical fields · Natural gas · Synthetic gas · Energy efficiency · Numerical simulation · Product innovation · Process innovation

1 Introduction

The production of electrode carbon graphite products is highly energy-intensive. In particular, the specific electricity consumption during its manufacture is 55800–59400 MJ/t. Therefore, the main trends in improving the production of carbon graphite products are the development of new innovative technological equipment and increasing the energy efficiency of the existing, in particular as energy-intensive as rotary kilns for calcination of carbonaceous bulk materials.

In this case, one of the most effective ways to increase the energy efficiency of the production of electrode carbon graphite products may be using the kiln equipment as

a gaseous fuel synthesis gas formed during the processing of carbon-containing raw carbon materials.

2 Literature Review

Analysis of the current development of world production of graphite electrodes shows that the research and development in this area are mainly aimed at improving the energy efficiency of kiln equipment its major redistributions (calcination of filler, mixing, pressing blanks, firing, and graphitization), and quality of the final product.

In the paper [1], using numerical simulation was developed a vertical electrocalciner which allows obtaining high-quality graphite coke and electroanthracite with a peak temperature of the center of the working space of the kiln 3000 °C, which was implemented in production.

In [2, 3], a method is proposed that provides high accuracy of calculations of active and inductive resistance and reduction of active power according to three-dimensional numerical modeling of complex systems for bus packages of furnace circuits and methods of intensification of electrical parameters and calculation of effective cross-sections of end tires conclusions of graphitization furnaces. However, there is no information about thermal processes in furnace equipment in these articles.

Work [4] is devoted to studying the possibility of using heat recovery of thermal insulation during the cooling of Kastner furnaces. However, the proposed method is complex and requires significant capital investment for industrial implementation.

Work [5] is devoted to studying the influence of contact resistance between electrode blanks on the temperature field of the column during graphitization. It is shown that poor thermoelectric contact between the workpieces in the column can lead to their deformation and even more significant deterioration of the contact between them.

The work [6], as well as [4], is devoted to an indirect method of increasing the energy efficiency of the process of graphitization of electrode blanks, which consists in the use of plates of a heat-insulating carbon material or carbon dust (lamp soot). A significant disadvantage of the proposed method is the high explosiveness of soot and the use of special plates requires additional capital costs and has low energy efficiency.

In articles [7, 8], the lining design and modern refractory materials of the calcination rotary kiln used to produce calcined petroleum coke and mathematical model of technological process for its use in the furnace control system in SimInTech environment are offered.

In [9], the expediency of using the existing equipment of the cooling drum of a rotary kiln for heat treatment of a carbonaceous filler to obtain synthesis gas was evaluated. It is established that given the ratio of $O_2/C = (42.7\ldots 51.6)\%$ the predicted quantitative composition of combustible gases of synthesis gas in molar fractions is: $CO = (32.8\ldots 36.9)\%$, H2 = $(17.1\ldots 18.4)\%$ and CH4 = $(0.03\ldots 0.16)\%$.

In the paper [10], a generalized mathematical model of the physical fields of the main technological redistributions of carbon graphite production was developed, based on a continuous-discrete approach to the description of nonlinear behavior in both solids and liquids and gases, and bulk media. Applying the generalized mathematical model for construction or specification of mathematical and numerical models of separate

redistributions for the performance of the numerical analysis of physical fields and parameters of processes and equipment of electrode manufacture has resulted.

Thus, from the analysis of the current state of development of world production of carbon graphite electrode products, it follows that now, except [10], there is no comprehensive approach to solving the problem of improving the energy efficiency of industrial equipment of this production. There are developments for separate redistributions, but they do not fully consider the features of some processes and equipment.

3   Research Methodology

3.1   Problem Statement

This work aims to determine by numerical modeling of thermal parameters of the rotary kiln for calcination of carbonaceous filler during partial or complete replacement of natural gas with synthesis gas.

It is necessary to solve the following tasks to achieve the stated goal:

– construction based on the generalized model of physical fields of processes and the equipment of redistributions of carbonite production mathematical model of the combustion process of synthesis gas together with natural gas in a rotary kiln;
– development of a numerical model of the combustion process of natural and synthetic gas in a rotary kiln for calcination of a carbonaceous filler;
– performing comparative calculations to determine the consumption of synthesis gas;
– determining the consumption of synthetic gas as a substitute for natural gas.

3.2   Mathematical Model of Physical Fields of the Combustion Process of Synthetic Gas Together with Natural Gas in a Rotary Kiln

Construction of a mathematical model of physical fields of the combustion process of synthetic gas together with natural gas is based on a generalized mathematical model [10] (1)–(13) and includes the first, second, third, and fifth equations of the system of Eqs. (1), physical Eqs. (7), (10) and (12).

The mathematical formulation of the problem of combustion synthesis of gas together with natural one in a rotary kiln, taking into account the turbulent flow regime and thermal radiation, includes a system of equations RANS, which contains: the equation of conservation of mass, conservation of momentum, transfer of components of chemical reactions, conservation of energy and two equations of the k-ε model of turbulence for turbulent kinetic energy and its dissipation and in the tensor form of the record has the

form [9]:

$$
\begin{cases}
\dfrac{\partial \overline{\rho}}{\partial t} + \dfrac{\partial}{\partial x_i}\left(\overline{\rho}\widetilde{v}_i\right) = 0; \\[2mm]
\dfrac{\partial \overline{\rho}\widetilde{v}_i}{\partial t} + \dfrac{\partial}{\partial x_i}\left(\overline{\rho}\widetilde{v}_i\widetilde{v}_j\right) = -\dfrac{\partial \overline{p}}{\partial x_i} + \dfrac{\partial \overline{\overline{\tau}}^{\mathrm{eff}}}{\partial x_i} + \overline{\rho}g_i; \\[2mm]
\dfrac{\partial \overline{\rho}\widetilde{Y}_k}{\partial t} + \dfrac{\partial}{\partial x_i}\left(\overline{\rho}\widetilde{v}_i\widetilde{Y}_k\right) = -\dfrac{\partial \overline{J}_i^{\,k}}{\partial x_i} + \overline{\dot{\omega}_k}, k = \overline{1,N}; \\[2mm]
\dfrac{\partial \overline{\rho}\widetilde{h}}{\partial t} + \dfrac{\partial}{\partial x_i}\left(\overline{\rho}\widetilde{v}_i\widetilde{h}\right) = \overline{\dot{\omega}_T} + \dfrac{\partial \overline{p}}{\partial x_i} + \dfrac{\partial}{\partial x_i}\left(\lambda\dfrac{\partial T}{\partial x_i} + \dfrac{\mu_t}{\mathrm{Sc}_t}\dfrac{\partial h}{\partial x_i}\right) + \\[2mm]
\qquad + \overline{\overline{\tau}}_{ij}^{\mathrm{eff}}\dfrac{\partial v_j}{\partial x_i} - \dfrac{\partial}{\partial x_i}\overline{\left(\rho \sum_{k=1}^{N} J_i^k h_k\right)} + S_{\mathrm{rad}}; \\[2mm]
\dfrac{\partial(\overline{\rho}k)}{\partial t} + \dfrac{\partial}{\partial x_i}\left(\overline{\rho}\widetilde{v}_i k\right) = \dfrac{\partial}{\partial x_i}\left[\left(\mu + \dfrac{\mu_t}{\sigma_k}\right)\dfrac{\partial k}{\partial x_i}\right] + \overline{\overline{\tau}}_{ij}^{\mathrm{eff}}\dfrac{\partial v_j}{\partial x_i} - \overline{\rho}\varepsilon; \\[2mm]
\dfrac{\partial(\overline{\rho}\varepsilon)}{\partial t} + \dfrac{\partial}{\partial x_i}\left(\overline{\rho}\widetilde{v}_i\varepsilon\right) = \dfrac{\partial}{\partial x_i}\left[\left(\mu + \dfrac{\mu_t}{\sigma_\varepsilon}\right)\dfrac{\partial \varepsilon}{\partial x_i}\right] + C_{\varepsilon1}\dfrac{\varepsilon}{k}\left(\overline{\overline{\tau}}_{ij}^{\mathrm{eff}}\dfrac{\partial v_j}{\partial x_i}\right) - C_{\varepsilon2}\overline{\rho}\dfrac{\varepsilon^2}{k}; \\[2mm]
\overline{p} = \overline{\rho}\dfrac{R}{W}\overline{T},
\end{cases}
\tag{1}
$$

where $\overline{}$, $\widetilde{}$ – means that the value is averaged over Reynolds and Favre, respectively; $\overline{\rho}$ – volumetric mass density, kg/m^3; t – time, s; $x_i, i = 1, 2, 3$ – Cartesian coordinate system, m; $\widetilde{v}_i, i = 1, 2, 3$ – components of the velocity vector, m/s; $\overline{p}$ – pressure, Pa;

$$
\overline{\overline{\tau}}_{ij}^{\mathrm{eff}} = (\mu + \mu_t)\left[\dfrac{\partial \widetilde{v}_i}{\partial x_j} + \dfrac{\partial \widetilde{v}_j}{\partial x_i} - \dfrac{2}{3}\dfrac{\partial \widetilde{v}_k}{\partial x_k}\delta_{ij}\right] - \dfrac{2}{3}\overline{\rho}k\delta_{ij} i, j = 1, 2, 3 - \text{components of the}
$$

tensor of effective stresses, Pa; μ – coefficient of dynamic viscosity, Pa·s; $\mu_t = \overline{\rho}C_\mu\frac{k^2}{\varepsilon}$ – coefficient of turbulent viscosity, Pa·s; $\delta_{ij}, i, j = 1, 2, 3$ – Kronecker symbol; k – turbulent kinetic energy, J/kg; ε – dissipation rate of turbulent kinetic energy, J/(kg·s); $g_i, i = 1, 2, 3$ – components of the free-fall acceleration vector, m/s^2; $\widetilde{Y}_k$ – mass fraction of species k of the mixture; N – number of species in the reacting mixture; $\overline{J}_i^{\,k} = -\left(\overline{\rho}D_{m,k} + \frac{\mu_t}{\mathrm{Sc}_t}\right)\frac{\partial \widetilde{Y}_k}{\partial x_i} + D_{T,k}\frac{1}{T}\frac{\partial T}{\partial x_i}$ – components of the vector diffusion turbulent flow of species k of the mixture, kg/(m·s); $D_{m,k}$ – mass diffusion coefficient of species k of the mixture, m^2/s; $\mathrm{Sc}_t = \frac{\mu_t}{\rho D_t}$ – Schmidt number; D_t – turbulent diffusion coefficient, m^2/s; $D_{T,k}$ – coefficient of thermal diffusion of species k of the mixture, kg/s; $\overline{\dot{\omega}_k}$ – source due to the average reaction rate of species k of the mixture $\sum_{k=1}^{N}\overline{\dot{\omega}_k} = 0$, кг/(m^3·s); $\widetilde{h}_k = \int_{T_{\mathrm{ref},k}}^{\widetilde{T}} C_{p,k}dT$ – explicit mass enthalpy of species k of the mixture, J/kg; T – absolute temperature, K; $T_{\mathrm{ref},k}$ – absolute reference temperature, K; C_p – mass isobaric heat capacity, J/(kg·K); $\overline{\dot{\omega}_T} = -\sum_{k=1}^{N} h_k^0\left(T_{\mathrm{ref},k}\right)\dot{\omega}_k$ – volumetric heat source due to combustion, W/m^3; λ – coefficient of thermal conductivity, W/(m·K); S_{rad} – volumetric heat source due to thermal radiation, W/m^3; $C_{\varepsilon1} = 1,44$; $C_{\varepsilon2} = 1,92$; $C_\mu = 0,09$; $\sigma_k = 1,0$; $\sigma_\varepsilon = 1,3$ – coefficients of the standard $k - \varepsilon$ the turbulence model; R – universal gas constant, J/(mol·K); W – molar mass, kg/mol.

Analysis of the combustion of synthetic gas together with methane (natural gas) in a rotary kiln is based on the following equations of global reactions:

$$
H_2 + 0.5O_2 \rightarrow H_2O \tag{2}
$$

$$
CH_4 + 1.5O_2 \rightarrow CO + 2H_2O \tag{3}
$$

$$CO + 0.5O_2 \rightarrow CO_2 \tag{4}$$
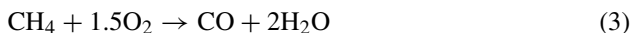
Reactions (2)–(4) are determined by stoichiometric coefficients and instantaneous thermodynamic parameters, on which their speed depends. Turbulent mixing of reagents is a factor limiting the rate of reactions. Turbulent-chemical interaction during combustion, the synthesis of gas and methane is described using two models: the first is a model of limited reaction rate based on the law of Arrhenius [11]; the second is the vortex dissipation model (Magnussen) [12, 13]. As a result, fewer of the obtained values from the reaction rate are used.

Initial conditions for (1):

$$\begin{cases} T(X) = T_0; \\ \mathbf{V}(X) = 0; \\ Y_k(X) = Y_{0k}, k = \overline{1, N}; \\ k(X) = k_0; \\ \varepsilon(X) = \varepsilon_0, \end{cases} \tag{5}$$

where $X(x, y, z) \in \Omega$ – Cartesian coordinates, м; Ω – calculation area.

Boundary conditions for (1):

– at the inlet gas synthesis – (6) at the inlet of natural gas – (7) and oxidizer (air) – (8) and the outlet of the rotary kiln – (9)

$$\begin{cases} G = G_{inlet-syngas}; \\ Y^k_{syngas} = Y^k_{syngas-inlet}, k = \overline{1, N_{syngas}}; \\ T = T_{inlet-syngas} \\ k = k_{inlet-syngas} \\ \varepsilon = \varepsilon_{inlet-syngas} \\ \varepsilon_b = 1, \end{cases} \tag{6}$$

$$\begin{cases} G = G_{inlet-CH4}; \\ Y_{CH4} = Y_{CH4-inlet}; \\ T = T_{inlet-CH4} \\ k = k_{inlet-CH4} \\ \varepsilon = \varepsilon_{inlet-CH4} \\ \varepsilon_b = 1, \end{cases} \tag{7}$$

$$\begin{cases} G = G_{inlet-air}; \\ Y_{O_2} = Y_{O_2-air}; \\ T = T_{inlet-air} \\ k = k_{inlet-air} \\ \varepsilon = \varepsilon_{inlet-air} \\ \varepsilon_b = 1, \end{cases} \tag{8}$$

$$\begin{cases} P_{\text{outlet}} = 0; \\ Y_{O_2} = Y_{O_2-\text{outlet}}; \\ T = T_{\text{outlet}} \\ k = k_{\text{outlet}} \\ \varepsilon = \varepsilon_{\text{outlet}} \\ \varepsilon_b = 1, \end{cases} \tag{9}$$

where G – mass flow rate, kg/s; N_{syngas} – number of components of gas synthesis; ε_b – degree of blackness of the border.

– at the boundaries of the contact of the solid elements of the kiln structure (absolute contact) – (10), the gas path of the kiln – (11), and the protection of the kiln with the environment:

$$\begin{cases} \{T\} = 0; \\ \{n_i q_i\} = 0, i = 1, 2, 3, \end{cases} \tag{10}$$

$$\begin{cases} v_i = 0; \\ \{T\} = 0; \\ \{n_i q_i - q_r\} = 0, i = 1, 2, 3; \\ \varepsilon_b = \varepsilon_{\text{lining}}, \end{cases} \tag{11}$$

$$n_i\left(-\lambda \frac{\partial T}{\partial x_i}\right) = \alpha_{\text{eff}}(T)(T - T_{\text{amb}}), i = 1, 2, 3, \tag{12}$$

where $\{T\} = T^+ - T^-$; $\{n_i q_i\} = n_i^+ q_i^+ - n_i^- q_i^-, i = 1, 2, 3$; $q_i = -\lambda \frac{\partial T}{\partial x_i}, i = 1, 2, 3$ – heat flux density vector components, W/m^2; n_i – components of the vector normal to the contact surface; q_r – radiation heat flux density, W/m; $\varepsilon_{\text{lining}}$ – degree of black of the lining; α_{eff} – effective heat transfer coefficient, W/(m^2·K); T_{amb} – ambient temperature, K.

3.3 Procedures of Numerical Solution

The procedures of numerical solution of the formulated problem (1)–(12) are based on the finite volume method (FVM) [14], considering [11, 15]. The universal procedure of numerical solution of the RANS system equations, transport of chemical components of the combustion reaction, energy, turbulent energy and its dissipation rate in the approximation of $k - \varepsilon$ model taking into account the compressibility of liquid [16] or $k - \omega$ [17] is based on the SIMPLE algorithm (Semi-Implicit Method for Pressure-Linked Equations - semi-implicit method of solving equations binding pressure, first proposed by L. S. Caretto, S. V. Patankar, D. B. Spalding) using unstructured tetrahedral and hexahedral grids. The method of discrete ordinates (MDO), presented in the works of J. C. Chai, H. S. Lee, S. V. Patankar [18], is the closest in its implementation to FVM. That is why this method was used to determine the radiation component of the energy Eq. (1). MDO makes it possible to perform calculations of radiative heat transfer in the radiating and absorbing medium with any optical thickness and at the same time consider the scattering, selectivity, and anisotropy of the optical properties of the system.

3.4   Numerical Models

For the numerical implementation of the combustion process mathematical model of natural and (1)–(12) synthetic gas in a rotary kiln for calcination of carbonaceous filler, the free open-source code OpenFOAM was used [19].

Two numerical models were developed to perform comparative calculations to determine the consumption of synthesis gas as a substitute for natural gas. The first one is to study the heat-hydrodynamic state of the rotary kiln during the combustion of natural or synthetic gas. The second one is to study the thermal parameters of the rotary kiln during the combustion of synthesis gas together with natural.

Numerical models of the gases combustion process in a rotary kiln are built based on axis-symmetric formulation, the schemes of types of boundary conditions (BC) shown in Fig. 1.
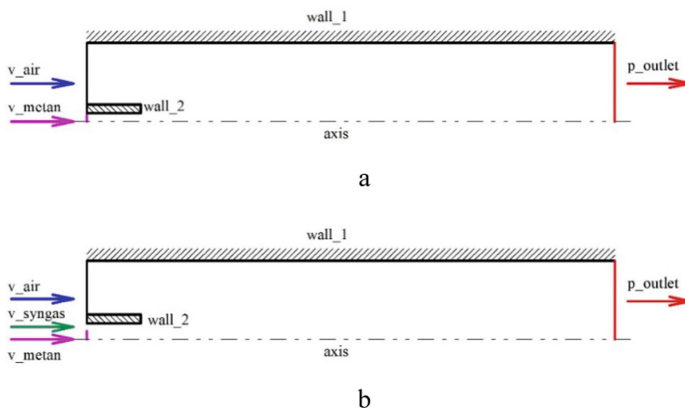
Fig. 1. Scheme of BC types of numerical models of the process of combustion of gases in a rotary kiln in the axisymmetric formulation: a – natural or synthetic gas combustion scheme; b – synthesis gas together with natural combustion scheme; axis – axis of symmetry of the rotary kiln; wall_1, wall_2 – solid walls; v_air, v_metan, v_syngas (velocity inlet) – input streams at a given speed; p_outlet (pressure outlet) – flow output; kiln dimensions: diameters 2500/2000 mm, length 40000 mm.

The parameters of BC numerical models according to the schemes (Fig. 1) were as follows:

- on v_air – air flow with a chemical composition ($O_2 = 0{,}23$ (mass.)) with an axial speed $v_{air} = 0{,}184$ m/s, temperature $T_{air} = 300$ K and the degree of blackness of the boundary $\varepsilon_{air} = 1$;
- on v_metan – the methane flow with a chemical composition ($CH_4 = 1{,}0$ (mass.)) with an axial velocity $v_{metan} = 7{,}96; 15{,}92$ m/s, temperature $T_{metan} = 300$ K the degree of blackness of the boundary $\varepsilon_{metan} = 1$;
- on v_syngas – the flow of synthetic gas with a chemical composition ($CO = 0{,}37; H_2 = 0{,}18; CH_4 = 0{,}002; H_2O = 0{,}01;$ (mol.)) with an axial velocity v_{syngas},

the numerical values of which are determined based on the numerical analysis of the thermal effects of chemical reactions of methane and synthesis gas combustion, temperature $T_{syngas} = 300$ K and the degree of blackness of the boundary $\varepsilon_{syngas} = 1$;

– on p_outlet set the pressure $p_{outlet} = 0$; $-50\,\Pi a$ and temperature $T_{outlet} = 300$ K reverse airflow with chemical composition ($O_2 = 0,23$ (mass.)), the degree of blackness of the boundary $\varepsilon_{outlet} = 1$;

– on wall_1 – adhesion conditions for gas flow, the degree of blackness of the boundary $\varepsilon_{wal\_11} = 0,7$ and BC III kind, taking into account the layer of fireclay refractory thickness 250 mm with ambient temperature $T_{env} = 300$ K and heat transfer coefficient $\alpha_{env} = 15\,W/(m^2 \cdot K)$);

– on wall_2 – adhesion conditions for gas flow, the degree of blackness of the boundary $\varepsilon_{wal\_11} = 0,7$ and BC I kind with temperature $T_{wal\bar{l}2} = 300$ K.

Axial speed $v_{metan} = 15,92$ m/s in the given schemes of types of BC of numerical models corresponds to experimentally defined volumetric expense of natural gas $-192\,nm^3/h$ taking into account the cross-sectional area of the burner nozzle, and speed $v_{air} = 0,184$ m/s– meets the condition $V_{air}/V_{metan} \approx 10$, considering the corresponding cross-sectional area.

The sampling parameters of the numerical models included: according to Fig. 1, a - nodes - 1 612 164 and finite volumes - 1 603 537; according to Fig. 1, b - nodes - 1,596,389 and finite volumes - 1,587,338. The grid convergence of these numerical models was determined by double recalculation. As a result, it was found that the used sampling of numerical models does not exceed 0.5%.

4 Results

Modeling of the combustion process of natural and synthetic gases to the rotary kiln was carried out in three ways:

– the first - combustion of natural gas to maintain the level of operating temperatures in the rotary kiln (Fig. 1, a);

– the second - co-combustion of synthesis gas together with natural one in a calcination rotary kiln (Fig. 1, b, partial replacement of natural gas);

– third - combustion of synthesis gas to maintain the level of operating temperatures in the calcination rotary kiln (Fig. 1, a, complete replacement of natural gas).

According to the first option, the methane supply rate was $15,92$ m/s, which corresponds to a volumetric flow rate of natural gas of $192\,nm^3/h$, taking into account the cross-sectional area of the burner nozzle. According to the second and third variants, the feed rate of the synthesis gas was set from the condition of the ratio of the calorific value of methane to the synthetic gas ($34.05/7.2 = 4.73$). Since the second option replaces half the volume flow of natural gas, so $v_{syngas} = 4.73 v_{metan} = 4.73 \cdot 7.96 = 37.65$ m/s. According to the third option with complete replacement of natural gas - $v_{syngas} = 4.73 \cdot 15.92 = 75.3$ m/s.

Verification of the correctness of the synthetic gas consumption setting was carried out based on the comparison of the calculated by numerical models of the thermal effects

of chemical reactions of combustion of gases, according to options 2 and 3 with option 1.

To visualize the numerical analysis results of gas combustion processes in a rotary kiln, freely open-source code ParaView was used [20]. The results of numerical analysis of the physical fields of the natural gas combustion process in the rotary kiln are shown in Fig. 2.
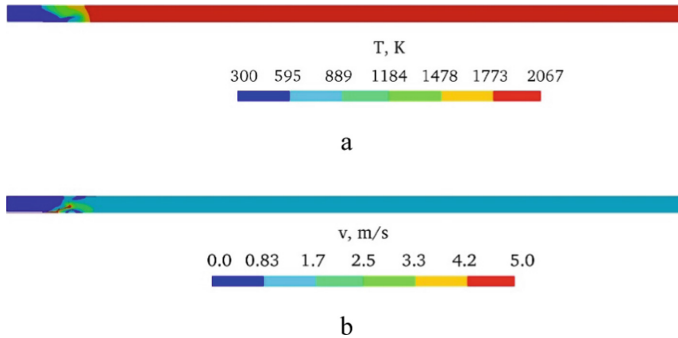
Fig. 2. The results of numerical analysis of the physical fields of the natural gas combustion process in a rotary kiln: a - temperature field; b - velocity field.

By using multivariate calculations according to options 2 and 3, it was found that the consumption of synthesis gas can be determined from the ratio of the calorific value of methane to synthetic gas, which in our case is 4.73.

The second option of replacing natural gas with synthesis gas can decrease the consumption of natural gas in a rotary kiln by 96 nm^3/h, and the third option - to completely abandon the combustion of methane, i.e., to save the consumption of natural gas in the amount of 192 nm^3/h. The consumption of synthetic gas will be 454 nm^3/h, and 908 nm^3/h, respectively, which is much less than the performance of the synthetic gas of the cooling drum of the rotary kiln, which is 1500 nm^3/h.

5   Conclusions

Based on the results of the conducted research analysis, the following conclusions can be drawn.

The mathematical model of the synthesis gas combustion process and natural gas in the working space of a rotary kiln in a continuous formulation has been formulated, which is required to determine the energy efficiency of the gasification process.

Two numerical models have been developed to perform comparative calculations to determine the consumption of synthesis gas as a substitute for natural gas. The first one is to study the heat-hydrodynamic state of the rotary kiln during the combustion of natural or synthetic gas. The second one is to study the thermal parameters of the rotary kiln during the combustion of synthesis gas together with natural.

Under using the developed numerical models of the gas combustion process, it is confirmed that the consumption of synthesis gas to replace natural gas can be determined from the ratio of the calorific value of methane to synthetic gas.

It is established that due to partial or complete replacement of natural gas with synthetic gas, it is possible to save the consumption of natural gas in the amount of up to $192\,\mathrm{nm}^3/\mathrm{h}$. The consumption of synthetic gas will be $454\,\mathrm{nm}^3/\mathrm{h}$, and $908\,\mathrm{nm}^3/\mathrm{h}$, respectively, which is much less than the performance of the synthetic gas of the cooling drum of the rotary kiln [9], which is $1500\,\mathrm{nm}^3/\mathrm{h}$.

References

1. Yang, Y., Gong, S., Ning, Q., Zhou, X., Zhao, H.: Development and application of electrocalciners with increased calcination temperature. In: Martin, O. (ed.) TMS 2018. The Minerals, Metals & Materials Series, pp. 1363–1371. Springer, Cham (2018). https://doi.org/10.1007/978-3-319-72284-9_178
2. Yarymbash, D.S., Kilimnik, I.M., Yarymbash, S.T.: Features of the decomposition of graphitization kiln electric circuit in modeling AC electromagnetic fields. Russ. Electr. Engin. **90**, 54–59 (2019). https://doi.org/10.3103/S1068371219010176
3. Yarymbash, D.S., Oleinikov, A.M.: On specific features of modeling electromagnetic field in the connection area of side busbar packages to graphitization kiln current leads. Russ. Electr. Engin. **86**, 86–92 (2015). https://doi.org/10.3103/S1068371215020121
4. Shen, C., Zhang, M., Li, X.: Numerical study on the heat recovery and cooling effect by built-in pipes in a graphitization kiln. Appl. Therm. Eng. **90**, 1021–1031 (2015). https://doi.org/10.1016/j.applthermaleng.2015.04.036
5. Piekło, J., Maj, M.: Analysis of the state of stress in the connection of graphite electrodes. Arch. Foundry Eng. **15**, 85–88 (2015)
6. Vedin, V., Pirogov, V.: Improving thermal insulation for graphitization kilns. Refract. Ind. Ceram **49**, 416–417 (2008). https://doi.org/10.1007/s11148-009-9115-x
7. Dontsova, T.V., Kozulin, K.G., Piskazhova, T.V., Danykina, G.B.: Simulation of the control system of the coke calcination in tubular rotary kilns. Russ. Metall. **2020**, 1600–1606 (2020). https://doi.org/10.1134/S0036029520130091
8. Lapaev, I.I., Sorokin, V.V., Goloskin, S.E., Orlov, A.V.: Lining of the rotary kilns for petroleum coke calcination. Refract. Ind. Ceram **60**(1), 1–5 (2019). https://doi.org/10.1007/s11148-019-00299-w
9. Karvatskii, A., Lazariev, T., Leleka, S., Mikulionok, I., Ivanenko, O.: Determination of parameters of the carbon-containing materials gasification process in the rotary kiln cooler drum. Eastern-Eur. J. Enterp. Technol. **106**(4/8), 65–76 (2020). https://doi.org/10.15587/1729-4061.2020.210767
10. Leleka, S.V.: Generalized mathematical model of physical fields of technological redistributions of manufacturing electrographite products. Energy Technol. Resour. Saving **2**, 28–43 (2021). https://doi.org/10.33070/etars.2.2021.03. (in Ukrainian)
11. Poinsot, T., Veynante, D.: Theoretical and Numerical Combustion, 2nd edn. Edwards, Philadelphia (2005)
12. Magnussen, B.F., Hjertager B.H.: On mathematical models of turbulent combustion with special emphasis on soot formation and combustion. In: 16th Symposium (International) on Combustion, vol. 16, no. 1, pp. 719–729 (1976). https://doi.org/10.1016/S0082-0784(77)80366-4

13. Henkes, R.A.W.M., van der Flugt, F.F., Hoogendoorn, C.J.: Natural convection flow in a square cavity calculated with low-reynolds-number turbulence models. Int. J. Heat Mass Transf. **34**, 1543–1557 (1991). https://doi.org/10.1016/0017-9310(91)90258-G

14. Patankar, S.V.: Numerical Heat Transfer and Fluid Flow (Hemisphere Series on Computational Methods in Mechanics and Thermal science), 1st edn. McGraw-Hill Book Company, New York (1980). https://doi.org/10.1201/9781482234213

15. Rhie, C.M., Chow, W.L.: A numerical study of the turbulent flow past an isolated airfoil with trailing edge separation. AIAA J. **21**, 1525–1532 (1983). https://doi.org/10.2514/3.8284

16. Shih, T.-H., Liou, W.W., Shabbir, A., Yang, Z., Zhu, J.: A new k-ε eddy-viscosity model for high reynolds number turbulent flows - model development and validation. Comput. Fluids **24**(3), 227–238 (1995). https://doi.org/10.1016/0045-7930(94)00032-T

17. Wilcox, D.C.: Reassessment of the scale-determining equation for advanced turbulence models. AIAA J. **26**(11), 1299–1310 (1988). https://doi.org/10.2514/3.10041

18. Murthy, J.Y., Mathur, S.R.: A finite-volume scheme for radiative heat transfer in semitransparent media. Numer. Heat Transf. Part B **37**, 25–43 (2000). https://doi.org/10.1080/104077900275530

19. OpenFOAM – Open Field Operation and Manipulation. http://www.openfoam.org/. Accessed 24 Oct 2020

20. ParaView. https://www.paraview.org/. Accessed 24 Oct 2020

Influence of Multi-pin Ultrasonic Impact Treatment on Microrelief, Structure, and Residual Stress of AISI O2 Tool Steel

Dmytro Lesyk[1,3,4(✉)] , Walid Alnusirat[2] , Vitaliy Dzhemelinskyi[1] ,
Andrii Burmak[1] , and Bohdan Mordyuk[1,3]

[1] National Technical University of Ukraine "Igor Sikorsky Kyiv Polytechnic Institute", Kyiv
03056, Ukraine
lesyk_d@ukr.net
[2] Al-Balqa Applied University, Al-Salt 19117, Jordan
[3] G.V. Kurdyumov Institute for Metal Physics of the NAS of Ukraine, Kyiv 03142, Ukraine
[4] West Pomeranian University of Technology, 70310 Szczecin, Poland

Abstract. AISI O2 tool steel specimens were hardened by an ultrasonic impact treatment (UIT) technique to increase the surface integrity. This paper focuses on studying the effect of the multi-pin UIT treatment on the surface layer characteristics of the peened surface. The UIT treatment with a seven-pin impact head was performed by varying vibration amplitude of the ultrasonic horn and ultrasonic peening time. Surface roughness/waviness, hardness, and residual stress in the UIT-peened specimens were measured. The effect of vibration amplitude and UIT duration on the 3D surface texture and hardening intensity of tool steel was also examined. The results demonstrated that the multi-pin UIT treatment induced the high-dislocated and fine-grained structure fixed by nanoscale vanadium carbides and compressive residual stress. The multi-pin UIT process formed the wavy microrelief on the surface with average surface waviness *Wa* parameter ~0.7 μm at optimum regimes. The UIT promotes a significant reduction in surface roughness. An increase in the vibration amplitude or UIT duration adversely affected surface roughness.

Keywords: Ultrasonic impact peening · Roughness · Waviness · Structure · Hardening intensity · Macrostress · Process innovation · Industrial growth

1 Introduction

The mechanical surface treatments are widely used to provide the superior surface integrity of metal components. It is well-known that the destruction of the metal parts, including corrosion, wear, and fatigue failure is usually initiated on the surface under dynamic and static loads. The surface modification methods lead to grain refinement and form the required compressive residual stress in the near-surface layers, extending the life of steel parts significantly. Therefore, improving surface peening processes is an urgent task in the mechanical engineering industry.

2 Literature Review

The mechanical surface treatments are effective and low-cost solutions for the surface modification of structural/tool steel parts, improving the corrosion [1], wear [2], and fatigue strength [3]. The type of appropriate surface treatment is selected based on the analysis of the shape and dimensions of the part to be processed [4]. The burnishing [5], conventional shot peening [6] or water jet shot peening [7], hammer peening [8], cavitation peening [9], laser shock peening [4], and ultrasonic peening [1] can be applied to enhance surface integrity of the tool steels which operate in extreme conditions in terms of temperature/loading, friction, wear, and corrosion.

Currently, the compressed air-type shot peening (SP) technique is widely used for the surface modification of large-sized and small-sized metal parts due to the low cost of the technological process. The SP treatment leads to the formation of the nanoscale grain structure in the sub-surface layer, increasing the surface integrity. Harada et al. found that SP using the shot media (from 0.03 to 0.15 mm in diameter) is effective in improving the surface properties of high-speed steels [10] and cold tool steels [11]. Vaxevanidis et al. [12] identified that the surface microrelief is characterized by randomly overlapping craters with dimensions increasing with an increase in the shot size (S230) and air-blast pressure (0.55 MPa). At the same time, the average surface roughness was increased as compared to the unpeened specimen ($R = 0.63\ \mu m$), irrespective of the regime used. The surface damage and surface roughness are usually increased after SP with an increase in the shot size and peening intensity. Sawada et al. [13] reported that the compressive residual stress at the sub-surface layer of cold tool steels induced by the SP treatment works to suppress crack initiation.

Moreover, the shot peening modifies surface structure, extending the fatigue strength limit of tool steels [14]. Bhavar et al. [15] established that the coefficient of friction and wear rate of AISI L6 tool steel was reduced by 19% and 44%, respectively, at the optimum SP parameters (the shot size of 0.4 mm and peening intensity of 0.3 A). Application of the SP treatment combined with nitriding treatment is another effective way to improve the surface characteristics of the AISI D2 tool steel [16], Cr-Mo-V tool steel [17], and AISI H13 tool steel [18]. Generally, despite a significant work hardening effect, the SP-peened surface suffers from excessive roughness and waviness.

An ultrasonic impact treatment (UIT) can provide the low surface roughness, and high surface hardness with the required compressive residual stresses in the sub-surface layer can be provided by an ultrasonic impact treatment (UIT). The ultrasonic peening can significantly improve the wear resistance of tool steels [19]. The microstructure with the refined grains (the hardening depth is about $70\ \mu m$.) and significantly increased dislocation density ($10^{10}\ cm^{-2}$) were observed in the AISI D2 tool steel processed by a multi-pin UIT [20]. At the same time, the study of the effect of the multi-pin UIT treatment on the surface properties of AISI O2 tool steel becomes especially relevant.

This work aims to study the surface texture/microrelief, roughness, waviness, structure, microhardness, and residual stress of AISI O2 tool steel peened by multi-pin ultrasonic impact treatment. Particular attention is paid to comparing the intensity hardening under different UIT parameters.

3   Research Methodology

The plane specimens (300 mm × 60 mm × 20 mm) of AISI O2 tool steel with the annealed condition were subjected to the multi-pin ultrasonic impact treatment (UIT). The nominal chemical composition of the studied steel given in wt% is the following: 0.884% C, 2.03% Mn, 0.35% Cr, 0.28% Si, 0.075% V, ≤0.25% Ni, ≤0.25% Mo, ≤0.25% Cu, 0.017% P, 0.002% S, and balance Fe. The UIT process was performed using the computer numerical control (CNC) milling machine [21].

An ultrasonic tool with a seven-pin impact head was forcedly rotated during processing with a rotation speed of 76 rpm. At the same time, the high-frequency multiple sliding impacts (~2 kHz) were produced by the steel pins of 5 mm in diameter. The UIT treatment was conducted by the vibration frequency of the ultrasonic horn of 21.6 kHz, the vibration amplitude of the ultrasonic horn of 15 μm (UIT1–UIT4) and 18 μm (UIT5–UIT8), and the ultrasonic peening time (UIT duration) of 60…240 s. The applied UIT parameters are listed in Table 1.

Table 1. UIT parameters.

Static loading of ultrasonic tool (N)	Rotation speed of impact head (rpm)	Vibration amplitude of ultrasonic horn (μm)	UIT duration (s)	Impact energy produced by pin (mJ)	Accumulated mechanical energy (mJ/cm^2)	Regime number
50	76	15	60	6.2	26	UIT1
		15	120		53	UIT2
		15	180		77	UIT3
		15	240		105	UIT4
		18	60	8.9	26	UIT5
		18	120		53	UIT6
		18	180		77	UIT7
		18	240		105	UIT8

The surface texture/microrelief observation was carried out using a laser 3D profilometer Leica DCM3D. The arithmetic mean deviation of the surface roughness (*Ra* parameter) and surface waviness (*Wa* parameter) profiles were estimated on both X and Y axes according to the ISO 4287 standard.

The microstructure in the subsurface layer was analyzed using a Polyvar 2 light optical microscope (LOM) and REM-106I scanning electron microscope (SEM). The microhardness in the sub-surface layers was measured using a Leica VMHT tester at a load on an indenter of 0.025 kg. The surface macrohardness was registered using a Computest SC hardness tester at a load on an indenter of 5 kg.

The intensity of surface hardening I_{hard} was estimated by the macrohardness (HRC) values of the initial and peened samples by the following formula:

$$I_{hard} = \frac{I_{HRC}^{peen.} - I_{HRC}^{in.}}{I_{HRC}^{in.}}, \tag{1}$$

The residual macrostresses were measured by analyzing the (310) diffraction maximum using a $\sin^2\psi$ method using CuKα-radiation.

4   Results

4.1   Surface Microrelief

The surface morphology of AISI O2 tool steel in the unpeened and UIT-peened specimens is demonstrated in Fig. 1 and Fig. 2, respectively. Compared to the initial (polished) specimen, the surface texture is completely changed after the multi-pin UIT treatment, forming a wavy surface microrelief. The surface microrelief is flattered due to simultaneous forced rotation of the ultrasonic tool, producing the sliding impact of pins by the specimen surface. Consequently, in contrast to unpeened surface, the area surface roughness Sz parameter is reduced irrespective of the UIT regimes used.

In the initial state, the used samples were characterized by an average surface roughness parameter of 0.6 μm (Fig. 3). It can be seen that the multi-pin UIT process significantly reduced the surface roughness. In particular, the UIT treatment with a minimum of peening intensity (UIT duration) and amplitude of ultrasonic vibrations (UIT1 regime) leads to a decrease in the surface roughness parameter Ra by about 50% in comparison with the unpeened specimen (Fig. 3). Further increase in the UIT duration (UIT2 regime) resulted in lower average surface roughness. It should also be noted that the Ra parameter is slightly increased at higher vibration amplitude (UIT5–UIT8 regimes). The observed average surface roughness magnitudes correlate well with the literature data regarding average surface roughness magnitudes of the UIT-peened tool or carbon steels [21].
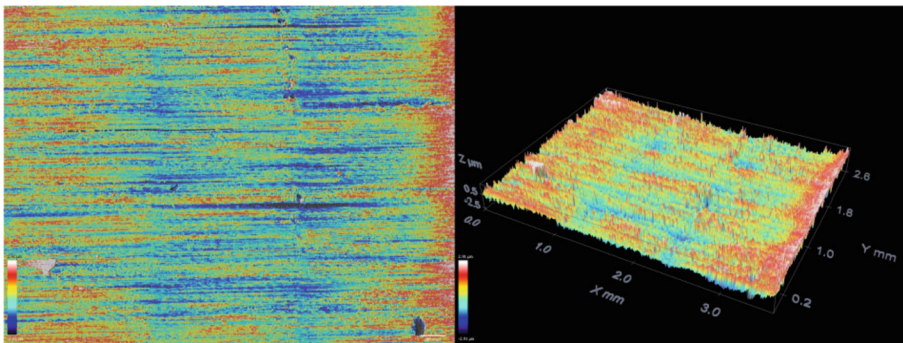
Fig. 1. 2D and 3D surface morphology of the unpeened AISI O2 steel sample.

The average surface waviness magnitudes are presented in Fig. 4. In contrast to the unpeened/polished specimen, using the multi-pin UIT treatment causes a significant increase in the *Wa* parameter, irrespective of the UIT parameters applied. The UIT treatment increased the Wa parameter from 0.09 µm to 1.44 µm (UIT1 regime) and 1.75 µm (UIT5 regime) for studied steel. Further increase in the peening intensity (120…240 s)
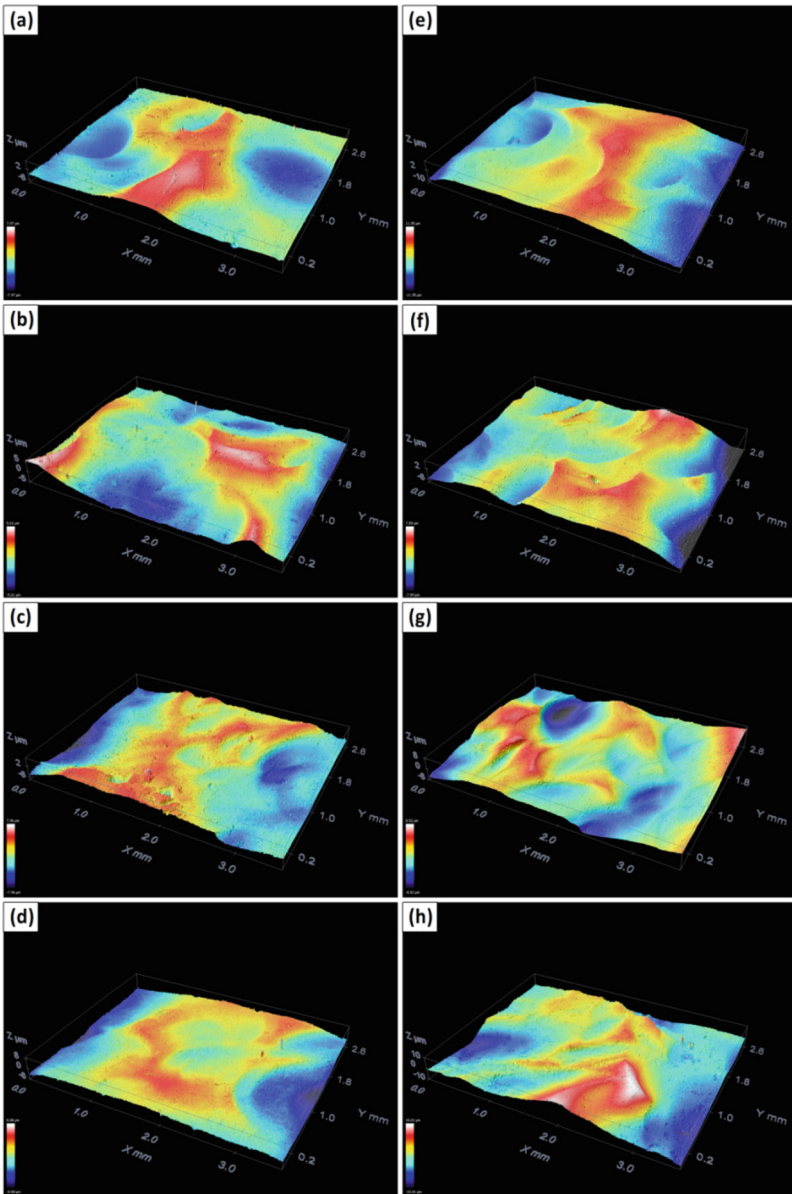
Fig. 2. Surface morphology of the UIT-peened AISI O2 steel samples.

led to a decrease in the lower average surface waviness magnitudes in the range of 0.6…0.82 µm (Fig. 4).
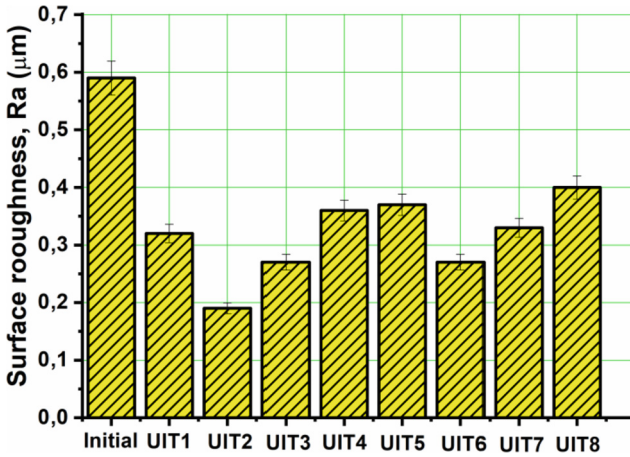
Fig. 3. Surface roughness of the unpeened and UIT-peened AISI O2 steel samples.
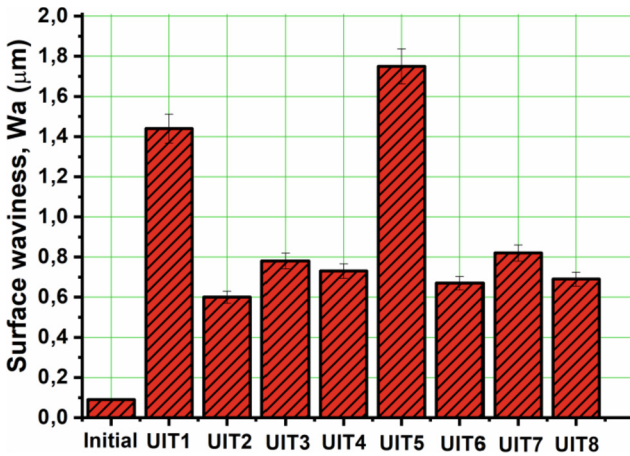
Fig. 4. The surface waviness of the unpeened and UIT-peened AISI O2 steel samples.

4.2   Microstructure and Hardening

The results showed that along with wavy surface microrelief with a low surface roughness formation, the multi-pin UIT treatment also induces a work hardening effect (Fig. 5) and improves surface structure (Fig. 6) which is responsible for significant improvement in the surface properties of the studied tool steel.

The hardening intensity of the UIT-peened specimens is enlarged irrespective of the UIT regimes used (Fig. 5). The most remarkable increase in the I_{hard} magnitudes (~50%) was observed after the UIT6 and UIT7 treatments. The surface macrohardness the ultrasonic peening increased HRC magnitudes from 8.3 HRC_5 to 12.6 HRC_5 (UIT6 regime) and 12.9 HRC_5 (UIT7 regime) due to high-density dislocations, sub-grain boundaries, fixing them by nanoscale vanadium carbides/cementite, and grain refinement (down to crystallite/grain size of ~280 nm). The UIT7 process provides a hardening depth of about 100 μm (Fig. 6). The nanoscale structure formed in the sub-surface layer can significantly improve surface hardness (Fig. 6) and the corrosion/wear performance of AISI O2 tool steel.
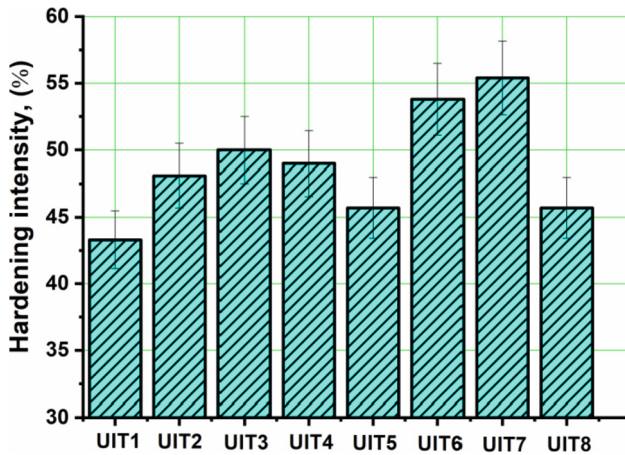
Fig. 5. Hardening intensity of the unpeened and UIT-peened AISI O2 steel samples.

In addition to the relatively large vanadium carbides and/or cementite observed by SEM (top-left image in Fig. 6), fine pearlitic colonies and fine ferritic 'islands' are visible in the TEM observations (middle-left image in Fig. 6). The uniformly dispersed fine (of 20–60 nm) vanadium carbides and/or cementite particles can fix both the dislocations and grain/sub-grain boundaries resulting in additional hardening. Considering the selective area diffraction pattern (down-left image in Fig. 6), it appears that the microstructure comprising fine pearlitic colonies with ferrite interlayers supersaturated with carbon is formed. The diffraction spots related to ferrite appear significantly dispersed in a radial direction and the azimuthal one, indicating many fine misoriented crystallites in the diffracted area.

4.3 Residual Stress

The multi-pin UIT treatment formed the compressive residual macrostresses (σX and σY), irrespective of the UIT regimes applied (Fig. 7). The measurement of surface macrostress values was carried out using the (310) diffraction reflection. The studied specimens were turned by 0°…45°.
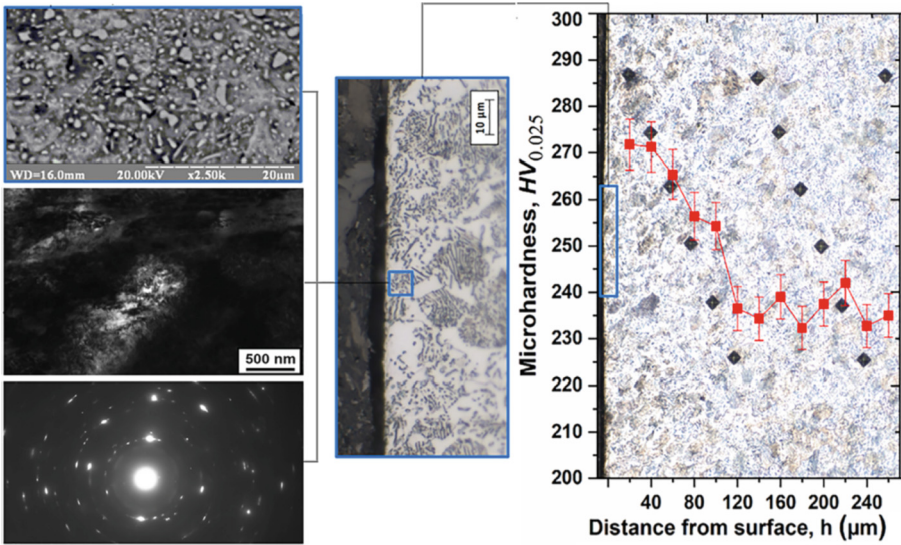
Fig. 6. Microhardness distribution and structure of the UIT7-peened AISI O2 steel sample.

The UIT2 and UIT5 treatments at the peening intensity of 60 s induce the lowest residual macrostresses compared to other cases (Fig. 7). Further increase in the UIT duration (120…150 s) resulted in higher compressive residual macrostress values (–450…–780 MPa). Application of the UIT treatment at the vibration amplitude of 18 μm allows increasing the compressive residual stress values as compared to the UIT with lower vibration amplitude.
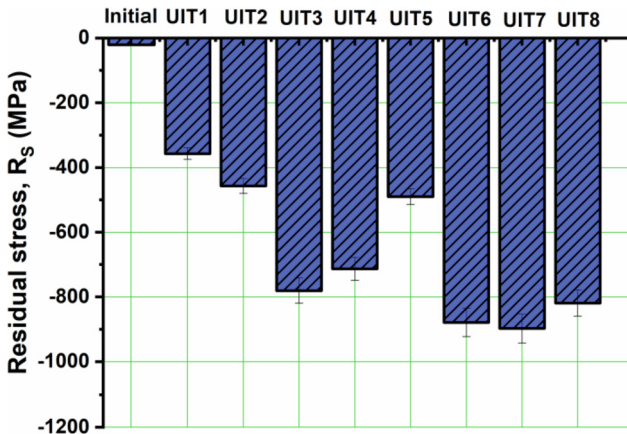
Fig. 7. Residual stress of the unpeened and UIT-peened AISI O2 steel samples.

The results confirmed that the multi-pin UIT treatment generated the fine-grained structure and compressive residual stress are beneficial for the corrosion/wear resistance and prolonged fatigue life of AISI O2 tool steel.

5   Conclusions

The results of this study can be summarized as follows.

The UIT parameters, such as the vibration amplitude of the ultrasonic horn and ultrasonic peening intensity, significantly influence the surface characteristics of the studied steel. The UIT duration of 120…150 s and vibration amplitude of 18 μm are the optimum UIT parameters for surface hardening of AISI O2 tool steel.

The multi-pin UIT process formed the wavy microrelief on the surface with the *Ra* parameter ~0.3 μm and *Wa* parameter ~0.7 μm.

The multi-pin UIT treatment at the optimum regimes provides the formation of high-density dislocations, sub-grain boundaries, and refined grains (~280 nm) with boundaries fixed by nanoscale vanadium carbides and compressive residual stresses (–850 MPa) in the sub-surface layer.

The multi-pin UIT technique can be applied to increase the surface integrity of tool steels, leading to essential hardening.

Further research is planned to study the corrosion and wear behavior of UIT-peened AISI O2 tool steel.

References

1. John, M., et al.: Peening techniques for surface modification: processes, properties, and applications. Mater. **14**, 3841 (2021)
2. Astaraee, A.H., et al.: Evaluating the homogeneity of surface features induced by impact-based surface treatments. Mater. **14**, 3476 (2021)
3. Kumar, D., et al.: Effect of surface mechanical treatments on the microstructure-property-performance of engineering alloys. Mater. **12**, 2503 (2019)
4. Epp, J., et al.: Comparison of alternative peening methods for the improvement of fatigue properties of case-hardened steel parts. J. Heat Treatm. Mat. **71**, 109–116 (2016)
5. Toboła, D.: Impact of mechanical processes as a pre-sulphonitriding treatment on tribology properties of selected P/M tool steels. Mater. **12**, 3431 (2019)
6. Omari, M.A., Mousa, H.M., AL-Oqla, F.M., Aljarrah, M.: Enhancing the surface hardness and roughness of engine blades using the shot peening process. Int. J. Miner. Metall. Mater. **26**(8), 999–1004 (2019). https://doi.org/10.1007/s12613-019-1818-5
7. Soyama, H., et al.: The effect of shot peening on surface integrity and tribological behaviour of tool steels. JSME Int. J. A-Solid M. **46**, 398–402 (2003)

8. Schubnell, J., et al.: The influence of coverage for high frequency mechanical impact treatment of different steel grades. J. Mater. Process. Technol. **277**, 116437 (2020)

9. Soyama, H., et al.: Cavitation shotless peening for surface modification of alloy tool steel. JSME Int. J. Ser. A Solid Mech. Mater. Eng. **46**, 398–402 (2003)

10. Harada, Y., Fukaura, K.: Influence of shot peening on surface characteristics of high-speed steels. Int. J. Mod. Phys. B **22**, 6094–6099 (2008)

11. Harada, Y., et al.: Influence of microshot peening on surface layer characteristics of cold tool steel. Mater. Sci. Forum **561–565**, 897–900 (2017)

12. Vaxevanidis, N.M., et al.: The effect of shot peening on surface integrity and tribological behaviour of tool steels. In: International Conference on Tribology, AITC-AIT 2006, Parma, Italy, pp. 1–8 (2006)

13. Sawada, T., et al.: Properties of cold work tool steel shot peened by 1200 HV-class Fe-Cr-B gas atomized powder as shot peening media. Mater. Trans. **51**, 735–739 (2010)

14. Chang, S.-H., et al.: Enhancement of thermal cracking and mechanical properties of H13 tool steel by shot peening treatment. Surf. Eng. **27**, 581–586 (2011)

15. Bhavar, V., et al.: Influence of shot peening on DIN 1.2714 hot work tool steel. J. Mater. Sci. Chem. Eng. **7**, 81–90 (2017)

16. Nambu, K., et al.: Influence of nitriding and multiple peening on surface characteristic of tool steel AISI D2. HTM – J. Heat Treat. Mater. **75**, 97–104 (2020)

17. Ariati, M., et al.: The effects of double shot peening and nitriding on the die soldering behaviour of H13 and Cr-Mo-V tool steel. Int. J. Technol. **3**, 463–470 (2016)

18. Ren, Z., Wang, X.: Effect of high-energy shot-peening on H13 tool steel ion-nitriding. Adv. Mat. Res. **393–395**, 67–71 (2011)

19. Chen, Z., He, B.: Influence of ultrasonic peening on wear resistance of U70 rails. Adv. Mat. Res. **97–101**, 1471–1474 (2010)

20. Lesyk, D., et al.: Effects of the combined laser-ultrasonic surface hardening induced microstructure and phase state on mechanical properties of AISI D2 tool steel. In: Ivanov, V., et al. (eds.) DSMIE 2019. LNME, pp. 188–198. Springer, Cham (2020). https://doi.org/10.1007/978-3-030-22365-6_19

21. Lesyk, D., et al.: Combined laser-ultrasonic surface hardening process for improving the properties of metallic products. In: Ivanov, V., et al. (eds.) DSMIE 2018. LNME, pp. 97–107. Springer, Cham (2019). https://doi.org/10.1007/978-3-319-93587-4_11

New Technology for Producing Castings from Magnesium Alloys with Increased Corrosion Resistance

Tatiana Lysenko[1] , Kyryll Kreitser[1(✉)] , Evgeny Kozishkurt[1] ,
Vadym Dotsenko[1], and Olga Ponomarenko[2]

[1] Odessa Polytechnic National University, 1, Shevchenko Avenue, Odessa 65044, Ukraine
dakerkir@gmail.com
[2] National Technical University "Kharkiv Polytechnic Institute",
2, Kyrpychova Street, Kharkiv 61002, Ukraine

Abstract. In this work, the schemes of production of magnesium alloy AZ91 using flux-free gas protection of alloys based on sulfur dioxide are investigated. A series of experiments were performed to determine the effect of a mixture of shielding gases on magnesium alloys' oxidation (corrosion resistance). Flux-free smelting of magnesium alloys is not used in the foundries of Ukraine. In Europe, almost all responsible parts of magnesium alloys for aerospace, power tools, electronic devices use flux-free melting. Therefore, the paper compared these two types of protection. Also, this method of protecting magnesium alloys from ignition helped reduce the consumption of protective gases. This has greatly improved the economic efficiency and quality of the metal. The paper presents the results of atmospheric tests on samples of magnesium alloy ML5 with dimensions of $40 \times 40 \times 1$ mm, obtained by two technologies: in a protective environment of a mixture based on protective gases and under a layer of protective flux VI2.

Keywords: Magnesium alloy · Flux-free casting · Metallography · Control system · Gas protection · Manufacturing innovation

1 Introduction

We have developed a new casting technology to obtain complex thin-walled castings from magnesium alloys with high corrosion resistance. This technology is based on the laws, mechanisms, and regression equations of the influence of the main technological factors on the conditions for protecting the surface of the magnesium melt from oxidation. This technology is used in high-pressure casting. The new technology is called an impulse protection system for magnesium alloys. Its creation made it possible to modernize equipment and automated control systems for injection molding systems.

According to the literary analysis on the types of technological processes of melting magnesium alloys in a protective gaseous medium [1], it became expedient to study the regularities of magnesium alloy AZ91 using fluxless gas protection of alloys based on sulfur dioxide SO_2. It was found that the increase in corrosion resistance of magnesium

alloys is significantly influenced by the content of SO_2 in the protective atmosphere of the furnace, as well as the content and ratio of chlorine Cl_2 and hydrogen H_2 in this protective mixture, which requires the optimal ratio of protective gases [2].

Therefore, to optimize the technological parameters of the flux-free melting of magnesium alloys using a 4-component protective gas mixture, a series of experiments was performed to determine the effect of the protective gas mixture on the oxidation (corrosion resistance) of magnesium alloys.

2 Literature Review

Trends in the development of industry and mechanical engineering require light alloy casting technology development. These alloys are crucial for the aerospace, machine-building, and automotive industries.

Significant progress has been made in high-performance cast magnesium alloys and advanced cast technologies [3].

Magnesium alloy has the characteristics of lightweight, robust shock absorption, high casting performance, and good electromagnetic shielding performance, which can meet the demand of lightweight products. This alloy is widely used in aerospace, automobile, motorcycle, computer, communication equipment, and electronic products [4].

In modern technology, the most relevant is the development of magnesium production. Over the past decade, magnesium, a rare material for the space industry, has become the third most used metal after steel and aluminum [5].

The interaction of the workshop atmosphere with molten magnesium can lead to deterioration of the casting quality and an emergency. Therefore, since the development of magnesium melting technologies, its protective equipment has also been developed.

Fluxes that contain at least small amounts of magnesium chloride, which partially decomposes already at 400 °C, have the best protective properties - flux VI2. Fluxes that do not contain magnesium chloride satisfactorily protect the melt at temperatures above 700 °C.

However, fluxes have characteristic drawbacks. The VI2 flux is highly hygroscopic. This leads to an increase in gas contamination and forms additional microcracks. Also, the relatively low viscosity and density greatly complicate the separation of flux from metal [6, 7].

The new technology of flux-free melting of magnesium alloy is based on gas Protection, which allows you to isolate the metal from contact with air better than flux coating. A gas medium can perform its protective function if it chemically interacts with a liquid magnesium alloy and forms a thin, dense film [8].

3 Research Methodology

An experimental stand was created to research and develop the technological process of casting magnesium alloys with gas shielding of liquid metal. The stand was made based on a hot chamber die casting machine (model CP MGH 400).

Gas shielding was carried out based on studying the characteristics of the surface tension of the liquid alloy. Studies have been carried out on the effect of the composition of the protective gas mixture on the oxidizability and mechanical properties of magnesium alloys [9].

The CP MGH 400 machine complies with European safety standards in the metallurgical industry, namely 98/37 EG and EN869, and particular standards for injection molding equipment.

The technological process using the above set of equipment is implemented in the following order.

First, it is necessary to fulfill conditions that the melting furnace was tight to exclude air suction from the atmosphere of the shop. At the same time, the sealed space of the furnace must be with a slight decrease in internal pressure so that the active gases do not enter the atmosphere of the shop. Also, the mixing speed of the liquid metal should be such that the oxide film does not mix with the liquid metal, and the use of SF_6 is possible at a temperature not exceeding 800 °C because at temperatures above 800 °C thermal decompositions of SF_6 and its protective properties are lost.

The authors carried out a series of experimental studies, making it possible to give technological recommendations for melting in a protective atmosphere.

It should be noted that the protective film should not be mixed with technological actions in the melting furnace in the mixing mode, and a quiet oxide film on 60 dm^2 of the area of the metal mirror should be consumed SO_2 - 5 l/h, SF_6 - 2 l/h. The value of the surface tension of the magnesium alloy ML5 at a temperature of 700 °C should be 520–525 dynes/cm.

Dry air must have a moisture content up to the dew point temperature at the dehumidifier outlet to -70 °C and a residual moisture content of 0.0033 g/m^3.

The operating mode of the protective medium based on sulfur dioxide SO_2, which was mixed with dry air, was provided according to the scheme (Fig. 1).

The system provides three protective gas circuits introduced into the mainline to the melting furnace on the melted mirror.

The essence of using an inert gas atmosphere to protect the melt from contact with air is determined by the primary operations and monitoring of indicators [10].

4 Results

To optimize the parameters of the protective gas mixture, the method of a full-factor experiment was used [11], in which the variable factors were:

– content of sulfur dioxide SO_2 in the composition of dried air in a mixture of protective gases;
– the content of chlorine Cl_2 in the mixture of protective gases;
– the content of hydrogen H_2 in the mixture of protective gases.

The limits of variation by variable factors in a series of experiments are determined under the following conditions.

SO_2 content in the gas mixture.
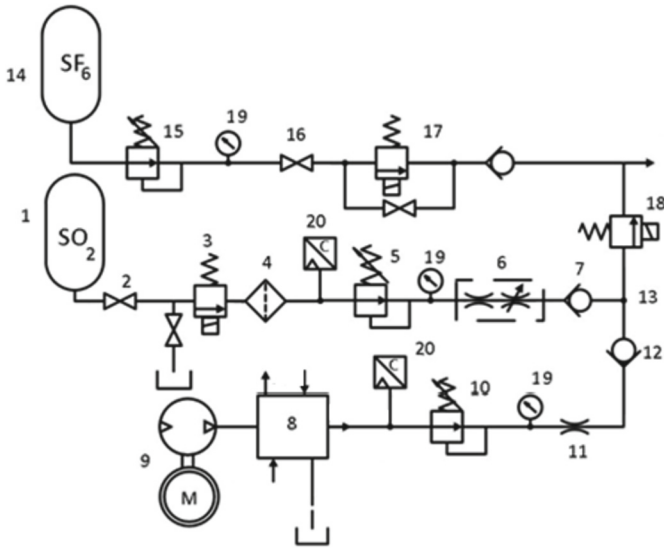
Fig. 1. Installation diagram for Flux-free protection of magnesium alloys: 1 - cylinder with sulfur gas; 2 - needle valves; 3 - solenoid valve; 4 - filter system; 5 - pressure reducer; 6 - rotameter; 7 - check valve; 8 - a device for dehumidification and purification of Air; 9 - compressor; 10 - pressure valve; 11 - calibrated diaphragm; 12 - check valve; 13 - mixing point of air and sulfur dioxide; 14 - cylinder with SF6; 15 - pressure valve; 16 - needle valve; 17, 18 - electrically controlled valves; 19 - pressure gauge; 20 - pressure transmitter.

The upper level of SO_2 content by volume in the mixture of protective gases was limited by the absence of magnesium ignition, which is 0.696 l/min, and the lower level of SO_2 content - 0.116 l/min.

The hydrogen content of H_2 in the gas mixture.

The upper level of H_2 content by specific volume in the mixture of protective gases was $9.0 \cdot 10^{-3}$ m³/kg, and the lower level of H_2 content - $3.0 \cdot 10^{-3}$ m³/kg.

The chlorine content of Cl_2 in the gas mixture.

The upper level of Cl_2 content by specific volume in the mixture of protective gases was $14.0 \cdot 10^{-3}$ m³/kg, and the lower level of Cl_2 content - $2.0 \cdot 10^{-3}$ m³/kg.

The effectiveness of gas protection of magnesium alloys from oxidation during melting was determined by the corrosion resistance of this alloy in castings samples by the mass index of corrosion (g/m²h) according to a well-known method.

A series of full-scale experiments were carried out on existing injection molding equipment while developing the casting bimetallic radiators of convectors made of magnesium alloy AZ91.

The complex includes an injection molding machine with a hot pressing chamber of 400 t.f., which is additionally equipped with a magnesium alloy flux-free protection system with a low cold installation for dehumidification [12].

During a series of experiments, a given volume of SO_2 was added to the dehumidified air within the established Table 1, providing reliable magnesium alloy protection from ignition and oxidation.

Table 1. Limits of variation in research parameters.

Parameter limits	Parameters of the protective gas mixture					
	Instant expenses SO_2		Content value H_2		Content value Cl_2	
	Natural Z_1, l/min SO_2	Encoded, X_1	Natural Z_2, 10^{-3} m^3/kg	Encoded, X_2	Natural Z_3, %	Encoded, X_3
Upper level	0,696	+1	9	+1	0,12	+1
Lower level	0,116	−1	3	−1	0,04	−1
Main (zero level)	0,406	0	6	0	0,08	0
Variation step	0,290	−	3	−	0,04	−

An extended full-factor experiment planning matrix was created for three factors with a fictitious variable. The planning matrix includes 2^3 studies [13].

To determine the technological parameters of the gas protection of the alloy for the corrosion resistance of castings, three series of experiments of the same type were performed using the experiment planning matrix [14].

Following the average values of the data given in the experimental matrix, the coefficients of the regression equation for the complete factor experiment are determined, which determines the dependence of the mass corrosion of samples made of magnesium alloy AZ91 on variations in the parameters of the composition of the gas protective mixture (SO_2 content, H_2 content, Cl_2 content).

In the final form the regression equation for determining the mass corrosion of magnesium alloy AZ91 in code form will take the following form:

$$Y = 48 + 12x_1 + 2x_2 + 9x_3 + 4x_1x_2 + 3x_1x_3 - x_2x_3 + 3x_1x_2x_3, \text{ g/m}^2\text{h} \tag{1}$$

$$12 + 3x_1 + 0{,}5x_2 + 2{,}25x_3 + x_1x_2 + 0{,}75x_1x_3 - 0{,}25x_1x_3 + 0.75x_1x_2x_3, \cdot10^{-3}, \text{ g/m}^2\text{h}.$$

Figure 2 shows a graphical interpretation of Eq. 1.

Analysis of the data obtained by regression Eq. (1) allows us to establish that the composition of protective gas mixtures in the melting unit has the most significant influence on the protection against oxidizability of the alloy in the melting unit, which further increases the corrosion resistance of magnesium alloy castings.

Using the constructed regression model (1) and its graphical interpretation (Fig. 2), it becomes possible not only to analyze the melting process of magnesium alloys but also to optimize and predict the degree of oxidation or corrosion resistance of castings made of magnesium alloys when they are obtained in a protective gas atmosphere in the melting mode of the initial magnesium alloys.

So, according to the analysis of the data shown in Fig. 2, it was found that the lowest oxidizability of the experimental magnesium alloy of the AZ91 type and its mass corrosion resistance in castings are achieved with minimal consumption of sulfur dioxide
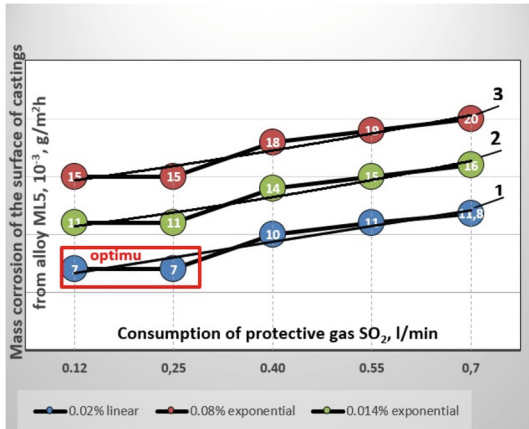
Fig. 2. Influence of the protective mixture of gases in the melting unit in the production of magnesium alloys.

SO2 and chlorine content Cl2 (Fig. 2 curve 1), the values of which are 0.12 l/min and 0.02%, respectively, and the coefficient of mass corrosion rate under these conditions is 0.007 g/m^{2}h In this mixture in a protective gas, which corresponds to the values of oxidizability and corrosion resistance X (Fig. 2 curve 1) and Y (Fig. 2 curve 2). Moreover, when the value of SO2 consumption increases to 0.7 l/min, the coefficient of mass corrosion rate under these conditions increases to 0.012 g/m2h, i.e., by 70%.

The change in the values of the mass corrosion rate is also significantly affected by the content of chlorine Cl_2 in the protective mixture. So when minimizing costs at the level of 0.12 SO_2, but with an increase in the content of Cl_2 in the mixture with 0.002% (Fig. 2 curve 1) up to 0.014% (Fig. 2 curve 3), the value of the mass corrosion coefficient increases from 0.007 (Fig. 2, curve 1) up to 0.015 (Fig. 2 curve 3) g/m^{2}h, i.e., 2.1 times.

It should be noted that the effect of the H_2 hydrogen content in the protective gas mixture within the experiment is not significant and may differ under different conditions of the experiment series only by 10–15% (according to Eq. 2).

The highest values of the mass corrosion coefficient of metal castings made of magnesium alloy ML5 are achieved under conditions when the importance of the main parameters of the protective gas mixture: the consumption of SO_2, the content of hydrogen H_2, and chlorine Cl_2 are in the range of 0.6–0.7 l/min, 0.012–0.014% and 7–9%, respectively (Fig. 2 curve 1, curve 2, curve 3). Under these conditions, the values of the weight corrosion coefficient of castings made of magnesium alloy AZ91 reach values of 0.015–0.020 g/m^{2}h, which is 2.1–2.9 times higher than the optimum composition of the protective gas mixture (Fig. 2 curve 1, curve 2).

According to the analysis of the results of a series of experiments using the regression Eq. (1) to study the effect of the composition of a protective gas mixture on the oxidizability of magnesium alloys during their production in metal-intensive melting aggregates, the optimal composition of the protective mixture should be considered the ratio:

1. the optimal consumption of sulfuric anhydride SO_2 in a mixture of protective gases will be - 0.12–0.25 l/min,
2. the optimal content of hydrogen H_2 in the mixture of protective gases will be 3.0–4.0 $\cdot 10^{-3}$ m³/kg.
3. the optimal content of chlorine Cl_2 in the mixture of protective gases will be 0.002–0.004 l/min, which allows minimizing the oxidizability according to the criterion of the mass corrosion coefficient of castings made of magnesium alloy type AZ91 value of 7–8 $\cdot 10^{-3}$ g/m²h (Fig. 2 curve 1, curve 2).

According to the optimal composition of the gas mixture in the melting unit (SO_2 consumption - 0.12–0.15 l/min, H_2 content - 3,0–3,5 $\cdot 10^{-3}$ m³/kg, chlorine content Cl_2 - 0.002–0.003 l/min) and according to the method given earlier, samples were made to study the corrosion resistance of castings made of magnesium alloy AZ91 in various climatic conditions, which were carried out in a specialized laboratory of climate tests based on the state enterprise "engineering center casting under pressure", which allowed in the future to obtain calculated dependences for determining the resource indicators of corrosion resistance of castings made of magnesium alloys in the following modes:

– ambient temperature 40 °C at 100% relative humidity - 12 h;
– ambient temperature 25 °C at 95% relative humidity - 10 h;
– exposure to air at room temperature - 2 h;
– test duration - 4 cycles;
– the duration of one cycle is 24 h.

Initially, the assessment of the corrosion state was carried out by external inspection after the end of the tests; the area of the sample on the surface of which there are corrosion products was taken as a criterion.

Figure 3 presents data on changes in the surface of samples after accelerated tests obtained by two technological processes of protection of magnesium alloy AZ91, including in the protective medium of a mixture based on SO_2 (a) and under a layer of protective flux VI2 (b).

When visually analyzing the surface of a sample with AZ91 (Fig. 3a), no corrosion was detected during melting in a gas protective medium of the SO_2-based mixture. Visual analysis of the sample's surface with AZ91 (Fig. 3b) was obtained during melting under a layer of protective flux on the surface. There is a loose white coating, which is a product of corrosion of the base metal, the area of corrosion damage is 80%.

At the same time, atmospheric tests of samples with AZ91 for one month were carried out.

Figure 3 shows the results of atmospheric tests on samples made of magnesium alloy AZ91 with dimensions of 40 × 40 × 1 mm, obtained using two technologies: in a protective environment of a mixture based on SO_2 (a) and under a layer of protective flux VI2 (b).

According to the analysis of the surface of a sample made of magnesium alloy AZ91 obtained during melting in a gas protective medium of a mixture based on SO_2 (Fig. 3,a), [15] it was found that its area is affected by corrosion products only by 1.6%, and the corresponding surface of the sample obtained during melting under a layer of protective

a   b
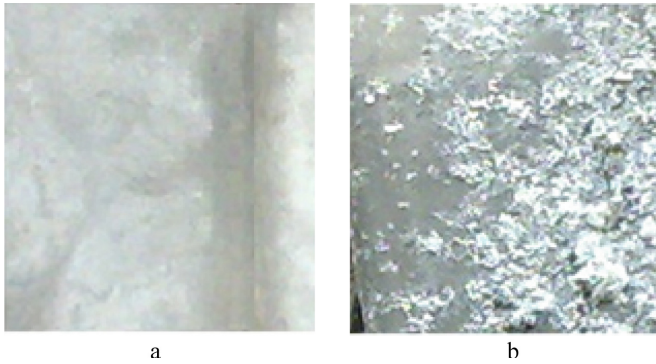
Fig. 3. Surface of samples after climatic tests of castings samples made of magnesium alloy ML5 obtained during melting in a gas protective medium of a mixture based on SO2 (a); melting under a layer of protective flux VI2 (b). Scale 1:2.1

flux VI2 (Fig. 3,b) is significantly affected by corrosion products and is 40%. At the same time, after removing corrosion products from the sample (Fig. 3,b), the defects are crater-type depressions (Fig. 4, 5). The individual spots on this sample were 2.5–3 mm^2, and the average depth was 0.8 mm. Along the perimeter, there is some swelling, the height of which was 0.025 mm.

a   b
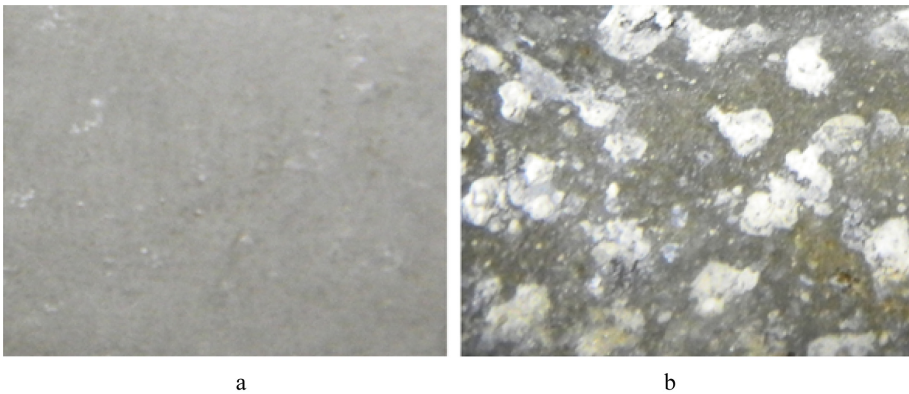
Fig. 4. Surface of samples after atmospheric tests of castings samples made of magnesium alloy AZ91 obtained during melting in a gas protective medium of a mixture based on SO2 (a); during melting under a layer of protective flux VI2 (b). Scale 1:2.1

To quantify the corrosion resistance results based on the data obtained in this series of experiments, two indicators were selected: mass and depth, and the corresponding calculations were performed [16].
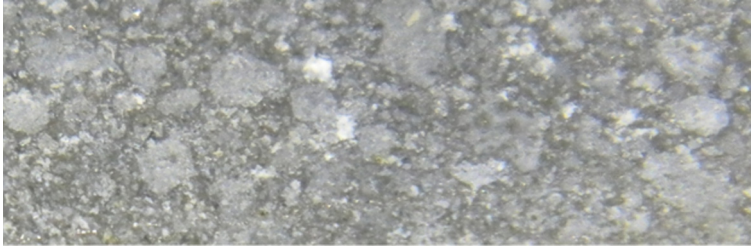
Fig. 5. Defective surface of the sample after atmospheric tests from magnesium alloy AZ91 obtained during melting under a layer of protective flux VI2 (b). Scale 1:2.1

5 Conclusions

For the first time, the regularities of obtaining magnesium alloys (the studied alloy AZ91) using fluxless continuous gas protection of a melt based on sulfur dioxide SO_2 and the ratio of chlorine Cl_2 and hydrogen H_2 in the protective atmosphere of the melting unit was established, the analysis of the obtained results of field and calculation experiments was carried out, and it was determined that the growth of corrosion resistance of these alloys is significantly affected by the content of SO_2 (0.12–0.70 l/min), the value of which changes inversely proportionally from 7 to $12 \cdot 10^{-3}$ g/m^{2}h, that is 1.7 times; optimal consumption of SO_2, H_2, Cl_2 in a mixture of protective gases is also established, which are in the range of 0.12–0.25 l/min, 3.0–$4.0 \cdot 10^{-3}$ m^3/kg and 0.002–0.004 m^3/kg, and this allows minimizing the oxidizability according to the criterion of the mass corrosion coefficient of castings made of magnesium alloy type AZ91 to values of 7–$8 \cdot 10^{-3}$ g/m^{2}h.

The work results will be disseminated at enterprises in Ukraine and Europe for the broader use of magnesium alloys. The results of research on the development of technology and experience in the practical use of cast products from magnesium alloys can be recommended for use by researchers of specialized departments and research institutions, engineers of enterprises engaged in the production of castings from magnesium alloys, as well as in the educational process disciplines.

References

1. Erickson, S.: Magnesium: a proven material for light weight automotive die castings. SAE Technical Paper, 770323 (1977). https://doi.org/10.4271/770323
2. Gratz, E.: Efficiency and stability of solid oxide membrane electrolyzers for magnesium production. Magnes. Technol. 39–42 (2011). https://doi.org/10.1002/9781118062029
3. Jiangfeng, S.: Latest research advances on magnesium and magnesium alloys worldwide. J. Magnes. Alloys **8**(1), 1–41 (2020). https://doi.org/10.1016/j.jma.2020.02.003
4. Hanxue, C.: Research status and prospects of magnesium alloys' melt refining and purification technology. J. Magnes. Alloys **7**(3), 370–380 (2019). https://doi.org/10.1016/j.jma.2019.07.002
5. Brown, R.E.: Magnesium and Its Alloy. In: Kutz, M. (ed.) Mechanical Engineers Handbook: Materials and Mechanical Design (2015). https://doi.org/10.17798/bitlisfen.502290
6. Hwang, I.S.: Inverter DC resistance spot welding of magnesium alloy AZ31. Mater. Manuf. Process. **48**(2), 112–117 (2011). https://doi.org/10.22075/jme.2017.1747

7. Tarelnyk, V., et al.: New sulphiding method for steel and cast iron parts. IOP Conf. Ser.: Mater. Sci. Eng. **233**(1), 012049 (2017). https://doi.org/10.1088/1757-899X/233/1/012049

8. Kim, S.K.: Eco-Mg for magnesium future. In: Proceedings of 66th Annual World Magnesium Conference (2011). https://doi.org/10.5772/13836

9. Beals, R.S.: Magnesium global development: outcomes from the TMS 2007 annual meeting. JOM **59**, 39–42 (2007). https://doi.org/10.1007/s11837-007-0102-8

10. Easton, M.: Magnesium alloy applications in automotive structures. JOM **60**(11), 57–62 (2008). https://doi.org/10.1007/s11837-008-0150-8

11. Lysenko, T., Kreitser, K., Derevianchenko, O., Kozishkurt, E., Vasylyev, D.: Comparison of technologies for the magnesium alloys protection using the quality assessment and quantitative metallography. In: Tonkonogyi, V., et al. (eds.) InterPartner 2020. LNME, pp. 322–329. Springer, Cham (2021). https://doi.org/10.1007/978-3-030-68014-5_32

12. Czerwinski, F.: Welding and Joining of Magnesium Alloys. Magnesium Alloys - Design, Processing and Properties, pp. 469–490 (2010). https://doi.org/10.5772/13947

13. Cao, X.: A review of laser welding techniques for magnesium alloys. J. Mater. Process. Technol. **171**(2), 188–204 (2006). https://doi.org/10.1016/j.jmatprotec.2005.06.068

14. Luo, A.A.: Magnesium casting technology for structural applications. J. Magnes. Alloys 2–20 (2013). https://doi.org/10.1016/j.jma.2013.02.002

15. Cole, G.S.: Summary of "magnesium vision 2020: a north american automotive strategic vision for magnesium." In: Mathaudhu, S.N., Luo, A.A., Neelameggham, N.R., Nyberg, E.A., Sillekens, W.H. (eds.) Essential Readings in Magnesium Technology, pp. 35–40. Springer, Cham (2016). https://doi.org/10.1007/978-3-319-48099-2_5

16. Huang, W., Hou, B., Pang, Y., Zhou, Z.: Fretting wear behavior of AZ91D and AM60B magnesium alloys. Wear **260**(11–12), 1173–1178 (2006). https://doi.org/10.1016/j.wear.2005.07.023

Protection of Paper Surface from Water Wetting by Two-Layer Siloxane (TEOS/PEHS) Coating

Nina Merezhko[1] , Volodymyr Komakha[1] , Olga Komakha[1] ,
Valentyna Tkachuk[2(✉)] , and Oksana Rechun[2]

[1] Kyiv National University of Trade and Economics, 19, Kioto Street, Kyiv 02156, Ukraine
[2] Lutsk National Technical University, 75, Lvivska Street, Lutsk 43018, Ukraine
v.tkachuk@lntu.edu.ua

Abstract. The scheme of forming protective two-layer coatings for paper based on siloxanes containing Si-O groups as an adhesive sublayer and polyethylhydridesiloxane as the primary protective layer is proposed. The mechanism of formation and interaction between the coating components was investigated by the methods of IR spectroscopy and complex thermal analysis. It was found that the presence of a chemical interaction involving the $\equiv Si-H$ bond of PEHS with $-OH$ and $\equiv Si-OC2H5$ groups in the TEOS and the fundamental possibility of regulating the level of completion of these processes. It is shown that the maximum of the main exothermic effect of the thermal oxidation process can be shifted from 350–570 to 630–650 °C. The influence of treatment with two-layer siloxane coatings on the reaction efficiency of paper concerning water is investigated. A quantitative assessment of the application (by the nature of thermal destruction, the edge angle of wetting the surface with water, the degree of shielding) of such coatings for paper protection in wet conditions is provided. The efficiency of using a two-layer organosilicon coating for a paper operated in high humidity conditions has been proven. Two-layer siloxane-based coatings applied to the surface of unbleached cellulose paper have a higher degree of shielding and, as a result, water repellency.

Keywords: Process innovation · Paper protection · Adhesive sublayer · Protective layer · Water repellency · Wetting angle

1 Introduction

The presence of cellulose in the paper necessitates its protection for long-term and reliable operation. This is primarily due to the relatively high chemical activity of the components of cellulose-containing materials and the ability of cellulose to interact with water in various physical states, which is one of the most aggressive environmental factors [1].

The cellulose matrix can be divided into crystalline domains, which are highly stable ordered regions, and amorphous [2], which can be easily destroyed by chemicals (acids, alkalis, oxidizers, polluted air), physical (moisture, light, vibration, electromagnetic radiation, temperature fluctuations) or biological effects (bacteria, mold, fungi) [3].

Existing methods of paper protection include reducing the impact of destructive environmental factors (fluctuations in relative humidity, light, contaminants, and temperature), as well as the use of protective compositions based on epoxy polymers [4], paraffins, and polylactic acid biodegradable plastics [5], compositions of polyamines with polyvinyl alcohol [6], silicones and nanoparticle applications [7].

Given the full range of requirements for paper protection [8] (a wide range of protective action against atmospheric and operational factors with a stable level of mechanical properties, environmental friendliness, fire resistance, inertness to the substrate, economic feasibility), the use of organic silicon compounds with reactive groups, including those synthesized using sol-gel methods, is of considerable interest [9].

Implementing adhesive layers-bases with adjustable reactivity in the composition of two-layer organosilicon coatings is of considerable scientific and practical interest can be carried out using ethyl silicate hydrolyzate, an industrial product containing tetraethoxysilane (TEOS). To increase the effectiveness of paper protection, in particular in moisture-resistant conditions, it is proposed to apply an additional layer of polyethylhydridesiloxane (PEHS).

The use of organic silicon compounds with reactive groups, including those synthesized using sol-gel methods, as part of protective coatings on cellulosic materials allows their formation from solutions at low temperatures. It provides the required level of functional properties by selecting appropriate ingredients.

2 Literature Review

To ensure the most effective protection of the paper, possibly by using thin-layer coatings based on siloxanes containing reactive groups near the silicon atom. This should shield a specific part of the hydroxyl groups in the paper to increase chemical resistance [10].

There are known methods of obtaining unique properties of wood and cellulosic materials by using protective coatings such as adsorption of prehydrolyzed alkoxysilanes onto the surface of cellulosic fibers in ethanol/water mixtures [11], SiO_2 nanoparticles deposition by spraying method [12], pre-treatment by $ZnCl_2$ followed by the use of a SiO_2 sol-gel process and grafting of hydrophobic groups [13], roller application of chitosan nanofibers and cellulose nanocrystals emulsions [14], applying a coating agent containing a water emulsion of triethoxymethylsilane with standard starch solutions [15], dispersion non-porous polymer film coating of polyvinyl alcohol and alkyl ketene dimer [16].

The presence of a significant number of hydroxyl groups in the structure of cellulose potentially allows to implement the process of their condensation with silanols of siloxanes and to ensure a strong bond on the surface [17, 18] of cellulose-containing materials [19].

In turn, the use of TEOS as an adhesive sublayer can provide the required level of interaction with the surface of cellulose-containing substrates and the outer protective layer of the siloxane water repellent. Obtaining this effect is possible by controlled hydrolysis of ethyl silicate. It is well known that the latter consists of four ethoxy groups, which can be cleaved by water in the presence of catalysts of a certain chemical nature according to various schemes.

Silicic acid obtained by complete hydrolysis of TEOS undergoes rapid condensation, forming branched siloxane structures. Siloxane chains grow chaotically with the formation of brittle polymers of spatial structure. They do not have film-forming properties and are not suitable for coatings based on them, e.g., to apply in separation devices [20, 21]. But highly active silicic acid is well sorbed on the surface of many materials and participates in the processes of interaction with organosilicon compounds that contain reactive groups $\equiv Si - OH$, $\equiv Si - H$, etc. A chemical bond is formed between the silica surface and the hydrophobic layer, resulting in the formation of chemisorbed hydrophobic films [17, 22].

Solutions with film-forming properties are obtained by complete hydrolysis of ethyl silicate. However, even with the optimal ratio of TEOS - water, the technological properties of coatings based on the obtained products largely depend on the conditions of hydrolysis of ethyl silicate and the concentration and type of catalysts used.

The most stable solutions are the molar ratio of TEOS: water is in the range of 1:2.0–1:2.5. The structure of xerogels is primarily determined by the number of siloxane bonds in their composition and, consequently, the amount of water taken for the hydrolysis of TEOS. Xerogels obtained using hydrochloric acid as a catalyst are most widely used to obtain coatings [23, 24].

Regarding the outer layer of the protective coating, the most promising may be using polyalkylhydride siloxanes. The combination of active hydrogen and hydrocarbon radicals in them allows to realize at the same time the possibility of chemical bonding according to the scheme $Si - H + HO - Si \rightarrow Si - O - Si + H2 \uparrow$ and to achieve a significant water-repellent effect [25].

3   Research Methodology

The industrial-grade paper used in the electrical engineering industry was used for the study. The composition of the fiber – unbleached sulfate cellulose – 100%. Thickness – 70 $\pm$ 3 microns. Porosity – 55.0%; edge angle of wetting the surface with water – 60°.

Tetraethylorthosilicate (TEOS) was used to form an adhesive sublayer in the form of partial hydrolysis products in aqueous-acetone solution (10 vol.%) (Ratio of TEOS: water – 1.20–1.25, hydrolysis catalyst – hydrochloric acid (2.5 wt.%).

Polymethylhydridosiloxane (PEHS) was applied to the surface by spraying an aqueous emulsion with a basic substance content of 10 vol. %.

The FTIR spectra of the investigated dispersed, and tableted materials with spectrally pure KBr were recorded on a Specord IR-75 spectrometer in the range of 400–4000 cm^{-1}.

The complex thermal analysis method was used to study the coatings formed on substrates containing CO and Si – O bonds to model the course of possible processes of their interaction with cellulose-containing substrates. Comprehensive thermal analysis was performed on OD-102 derivatograph at a 10 deg/min heating rate.

The surface's wettability with water was determined by measuring the wetting edge angles on an instrumental microscope with a refracting prism and an angular measuring head. This device allows direct measurements of the wetting angle of a tenfold magnified image of a drop of water applied to a flat surface. The accuracy of measuring the edge angles is $\pm 1°$.

The wettability of the flat surface of solids that are hydrophobized by organosilicon compounds depends on the degree of its shielding by organic radicals. It is considered that the adhesion work of the wetting fluid Wn $= 100 \cdot$ Wx is the sum of the adhesion work (Wp) on the monomolecular layer of the surface (X,%) and (Ws) on its uncovered area. The degree of shielding or filling is determined by the formula:

$$X = \frac{W_x - W_s}{W_p - W_s} \cdot 100$$

Writing this expression according to Dupre's law for the case of using a specific material coated with a water repellent allows to represent the equation as follows:

$$X = K(1 - \cos\theta_x)$$

where $\cos\theta_x$ – cosine of the wetting angle of the hydrophobized surface.

4 Results

The substrate layers' properties based on TEOS hydrolyzate (composition, structure) and the conditions and completeness of chemisorption of hydrophobizing oligomers on them are essential in creating optimal formulations for coatings.

In view of the above, ethyl silicate partially hydrolyzed in the presence of hydrochloric acid was selected as the adhesive layer for the surface of the cellulose-containing substrates. Ethyl silicate contains a number of reactive groups, in particular –OH in various combinations with silicon atoms to the level of $Si(OH)_4$ and fragments of the type $\equiv Si–OC_2H_5$ at ratios Si: C from 1: 2 to 1: 6.

The amount of water that enters the hydrolysis reaction when used as a catalyst for hydrochloric acid can reach 60%, and its flow scheme has the form:

$$Si(OC_2H_5)_4 + 2{,}5H_2O \rightarrow (C_2H_5O)_{2.5}\,Si(OH)_{1.5} + 1{,}5C_2H_5OH + H_2O$$
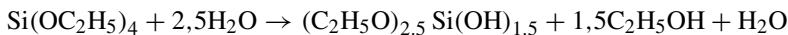
In the system, monomers of different compositions are formed: $(C_2H_5O)_2Si(OH)_2$ and $(C_2H_5O)_3SiOH$. It is not excluded either the formation of $(C_2H_5O)_2Si(OH)_3$ and $Si(OH)_4$. The next stage is characterized by the course of condensation processes with the synthesis of oligomers and the release of up to 29% of the water from the amount taken for hydrolysis:

$$n(C_2H_5O)_{2.5}\,Si(OH)_{1.5} \rightarrow n\big\{(C_2H_5O)_{2.5}[Si-O-Si]_{0,7}(OH)_{1.5}\big\} + 0{,}7\,H_2O$$
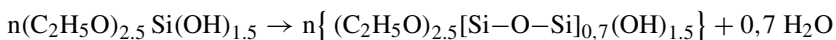
There is an initial formation of the structure of the film-forming polymer, which determines the following properties of the coating – its adhesion to the substrate, porosity, microhardness, elasticity.

After the formation of oligomers of varying degrees of condensation, the process of prehydrolysis of individual ethoxyl groups begins. Subsequently, the hydrolysis in the system slows down, and the growth of polymer chains occurs according to the scheme:

$$\equiv Si-OC_2H_5 + HO-Si \equiv \leftrightarrow Si-O-Si \equiv + C_2H_5OH$$
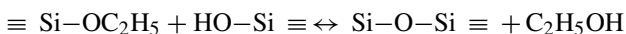
It is established that the process of hydrolysis and condensation does not occur simultaneously but strictly sequentially, one after another, and the limiting stage is the process of condensation, not hydrolysis.

The hydrolysis process prevails at a molar ratio of TEOS: water equal to 1: 1. Its increase from 1: 2 to 1: 4 contributes to its fuller course at the initial stage and intensification the condensation process. Prehydrolysis of residual ethoxyl groups is significantly slowed down.

As a water repellent for the outer layer of the combined coatings, it is advisable to use PEHS, which are almost the only type of siloxanes, which contain a highly reactive group $\equiv$Si – H and are chemically non-aggressive. It is possible to assume that in this variant of the combination will be achieved variant of interaction with the compounds of the adhesive layer according to the scheme:

$$\equiv \text{Si}-\text{H} + \text{HO}-\text{Si} \equiv \rightarrow \equiv \text{Si}-\text{O}-\text{Si} \equiv + \text{H}_2 \uparrow$$
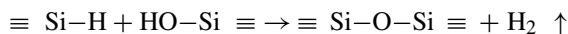
The processes of interaction of PEHS with TEOS hydrolyzate at different ratios of ingredients at the stages of formation of two-layer coatings are investigated. The infrared spectroscopy method was used to study possible interactions when combining PEHS with TEOS in the liquid state, followed by polymerization at elevated temperatures.

It is established that a characteristic feature of the IR spectrum of TEOS is the presence of three groups of absorption bands of different intensities, the minimum ratio for the bands at 2304 and 1636 cm^{-1}. The average intensity is observed for the characteristic absorption bands responsible for the valence vibrations of the bonds O–H (3452 cm^{-1}), C–H (2969 cm^{-1}), Si–O (689 cm^{-1}), Si–C (600 cm^{-1}) and Si–O–R (943 cm^{-1}) (Fig. 1). The maximum intensity for the band is 1072 cm^{-1} (valence bonds Si–O–Si).
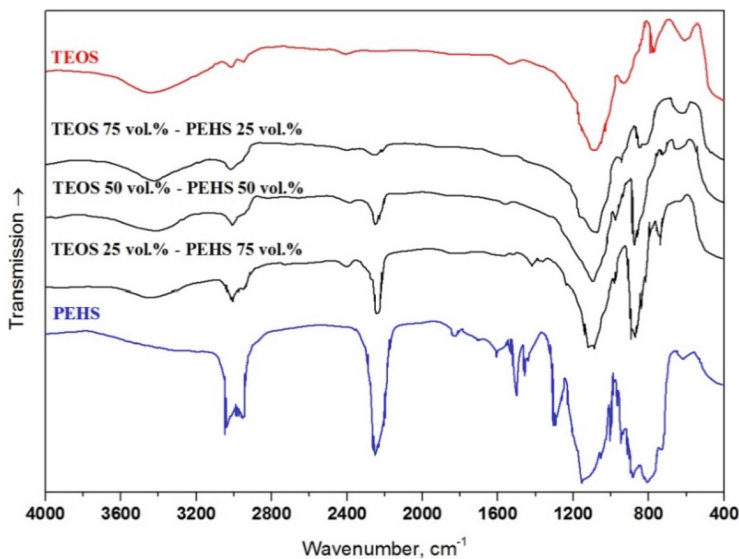
Fig. 1. FTIR spectra of TEOS – PEHS systems.

The spectrum of PEHS is relatively more complex in the absence of absorption bands responsible for the valence vibrations of OH groups. The following characteristic absorption bands can be distinguished by intensity:

– valence oscillations of Si – H bond (776 i 846 cm^{-1});
– valence oscillations of Si–O–Si bond (973, 1000, 1061, 1084 cm^{-1});
– valence oscillations of C–H bond (2873, 2960 cm^{-1});
– deformation oscillations of OH groups (1253, 1413 cm^{-1});
– deformation oscillations of the CH bond (1454 cm^{-1}).

Quantitative analysis of the IR spectra of mixtures of TEOS and PEHS in the range of ratios (% vol.) from 25:75 to 75:25 showed the possibility of chemical interaction between the ingredients. Proof of this is the decrease in the intensity of the bands of valence vibrations of OH groups.

Regarding the valence vibrations of the Si – O – R group in the composition of TEOS, the intensity of its band decreases, and at 1: 1, it is entirely absent. In the part of valence and deformation oscillations of the Si – H bond from the composition of PEHS, the displacement of the corresponding bands up to 7 cm^{-1} at the ratios 1: 3 and 1: 1 and up to 13 cm^{-1} (3:1) was also recorded.

Against the background of changes in the parameters of the absorption bands characteristic of the reactive groups of both components, it should be noted that the intensity of the bands responsible for oscillations of the CH bonds increases at a ratio of 1:1 and their displacement toward lower frequencies reaches 1 cm^{-1}.

Concerning the valence oscillations of the Si – O – Si bond, the combination of components against the background of TEOS simultaneously leads to a shift of their characteristic absorption bands toward higher frequencies up to 51 cm^{-1} (1: 1).

Thus, the fundamental possibility of chemical interaction involving the $\equiv$ Si – H bond of PEHS with OH and $\equiv$Si – OC$_2$H$_5$ groups in TEOS composition is shown by IR spectroscopy. These processes take place against the background of weakening the strength of the Si – O – Si bond.

The method of complex thermal analysis was used to study coatings to model the course of possible processes of their interaction with cellulose-containing substrates.

The heating of the paper with TEOS hydrolyzate applied to the surface is accompanied by the development of an intense exothermic effect, which is characterized by the presence of two areas. The first (up to 205 °C) has a relatively gentle character, and weight loss is 2%. Next, the process of thermal-oxidative degradation proceeds more rapidly with an intermediate exoeffect at 260 °C and ends with a slight exoeffect at 410 °C. The weight reduction in the range of 200–600 °C is 8.4%. The maximum of the specified process at a temperature of 400 °C is fixed on a curve of DTG (Fig. 2).

A similar pattern is observed with the use of PEHS with the difference that the maximum exothermic effect is recorded at 350 °C, and weight loss does not exceed 2.7%. The DTG curve does not contain special extremes.

Replacement of 25% by volume of TEOS with PEHS is accompanied by preservation of the exoeffect at 260 °C, the appearance of the end effect at 305 °C and shift of the maximum of Thermo oxidative destruction to 380 °C. Weight loss in the temperature range up to 600 °C reaches 9.6% with extremes at 260 °C and 345 °C.
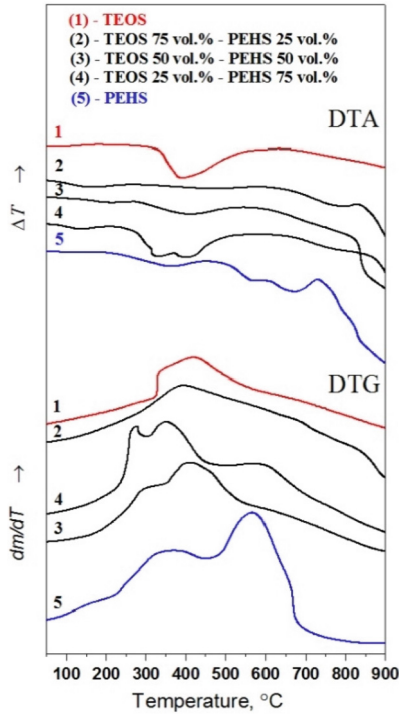
Fig. 2. Thermograms of TEOS – PEHS systems formed on the paper surface.

A further increase in PEHS proportion to 50 vol.% is accompanied by a shift of exothermic maxima following 420 and 640 °C with an intermediate endoeffect at 530 °C. The mass decreases by 2.8% (up to 400 °C) and 9.5% (400–700 °C). The maxima of its extreme change are recorded at 340, 620, and 710 °C.

The system with the maximum content of PEHS is characterized by a relative decrease in thermal stability. Exothermic effects were observed at 215, 350, and 570 °C, with intermediate endoeffects at 260 and 490 °C. Weight loss is up to 6.3% in the 20–600 °C temperature range with an extremum at 345 °C.

It was found that after treatment of the paper surface with TEOS hydrolyzate, the value of the edge angle of wetting its surface with water increases from 60 degrees in the control to 77 (Table 1).

Table 1. Properties of paper with organosilicon thin-layer coatings.

Coating	Contact angle, deg.	The degree of surface shielding, %
–	60	–
TEOS	77	61,2
TEOS/PMHS	94	84,5

A slight increase in the level of water repellency when using the TEOS may be related to the presence of up to four (depending on the degree of hydrolysis) hydroxyl groups in its composition and almost complete absence hydrophobic hydrocarbon radicals.

The use of two-layer coatings based on siloxanes allows forming on the paper's surface from unbleached cellulose coatings with a greater degree of shielding and, consequently, water-repellent ability.

5   Conclusions

The scheme of forming double-layer protective coatings for paper from unbleached cellulose based on siloxanes sol-gel technology containing $\rightarrow$ Si – OEt groups in the functional sublayer and PEHS in the surface layer is proposed. The processes of interaction of these systems in a wide range of ingredient ratios (from 3: 1 to 1: 3 by volume) are studied. The methods of IR spectroscopy and complete thermal analysis showed the presence of a chemical interaction involving the $\equiv$ Si – H bond of PEHS with – OH and $\equiv$Si – OC$_2$H$_5$ groups in the TEOS and the fundamental possibility of regulating the level of completion of these processes. It is shown that the maximum of the main exothermic effect of the thermal oxidation process can be shifted from 350–570 to 630–650 °C, respectively.

The combined use of an adhesive and protective coating allows obtaining a dense hydrophobic film on the paper surface, which allows a waterproof plastic protective layer on the surface of the material.

References

1. Hubbe, M.A.: Paper's resitance to wetting — a review of internal sizing chemicals and their effects. BioResources **2**, 106–145 (2007). https://doi.org/10.15376/biores.2.1.106-145
2. Ciolacu, D., Popa, V.: Cellulose Allomorphs: Structure, Accessibility and Reactivity: Polymer Science and Technology Series. Nova Science Publisher Inc., New York (2010)
3. Dankovich, T.A., Gray, D.G.: Contact angle measurements on smooth nanocrystalline cellulose (I) thin films. J. Adhes. Sci. Technol. **25**, 699–708 (2011). https://doi.org/10.1163/016942410X525885
4. Song, J., Rojas, O.J.: Approaching super-hydrophobicity from cellulosic materials: a review. Nord. Pulp Pap. Res. J. **28**(2), 216–238 (2013). https://doi.org/10.3183/NPPRJ-2013-28-02-p216-238
5. Triantafillopoulos, N., Koukoulas, A.: The future of single-use paper coffee cups: current progress and outlook. BioResources **15**, 7260–7287 (2020). https://doi.org/10.15376/biores.15.3.Triantafillopoulos
6. Osyka, V., Merezhko, N., Koptjukh, L., Komakha, V., Kniaz, S.: Polyamidaminepichlorohydrin application for eco-safe waterfast and waterproof food packaging paper production. Food Sci. Technol. **15**, 2 (2021). https://doi.org/10.15673/fst.v15i2.2102
7. Samyn, P.: Wetting and hydrophobic modification of cellulose surfaces for paper applications. J. Mater. Sci. **48**(19), 6455–6498 (2013). https://doi.org/10.1007/s10853-013-7519-y
8. Pivnenko, K., Eriksson, E., Astrup, T.F.: Waste paper for recycling: overview and identification of potentially critical substances. Waste Manage. **45**, 134–142 (2015). https://doi.org/10.1016/j.wasman.2015.02.028

9. Hubbe, M.A., Gardner, D.J., Shen, W.: Contact angles and wettability of cellulosic surfaces: a review of proposed mechanisms and test strategies. BioResources **10**, 8657–8749 (2015). https://doi.org/10.15376/biores.10.4

10. Abdelmouleh, M., Boufi, S., ben Salah, A., Belgacem, M. N., Gandini, A.: Interaction of silane coupling agents with cellulose. Langmuir **18**(8), 3203–3208 (2002). https://doi.org/10.1021/la011657g

11. Ogihara, H., Xie, J., Okagaki, J., Saji, T.: Simple method for preparing superhydrophobic paper: spray-deposited hydrophobic silica nanoparticle coatings exhibit high water-repellency and transparency. Langmuir **28**, 4605–4608 (2012). https://doi.org/10.1021/la204492q

12. Musikavanhu, B., et al.: Facile method for the preparation of superhydropho-bic cellulosic paper. Appl. Surf. Sci. **496**, 143648 (2019). https://doi.org/10.1016/j.apsusc.2019.143648

13. Amirabad, L.M., Jonoobi, M., Mousavi, N.S., Oksman, K., Kaboorani, A., Yousefi, H.: Improved antifungal activity and stability of chitosan nanofibers using cellulose nanocrystal on banknote papers. Carbohyd. Polym. **189**, 229–237 (2018). https://doi.org/10.1016/j.carbpol.2018.02.041

14. Ganicz, T., Olejnik, K., Rózga-Wijas, K., Kurjata, J.: New method of paper hydrophobization based on starch-cellulose-siloxane interactions. BioResources **15**(2), 4124–4142 (2020)

15. Shen, Z., Kwon, S., Oh, K., Abhari, A.R., Lee, H.L.: Facile fabrication of hydrophobic cellulosic paper with good barrier properties via PVA/AKD dispersion coating. Nord. Pulp Pap. Res. J. **34**, 516–524 (2019). https://doi.org/10.1515/npprj-2019-0040

16. Rutter, T., Hutton-Prager, B.: Investigation of hydrophobic coatings on cellulose-fiber substrates with in-situ polymerization of silane/siloxane mixtures. Int. J. Adhes. Adhes. **86**, 13–21 (2018). https://doi.org/10.1016/j.ijadhadh.2018.07.008

17. Alekseevsky, D.G., Chernysh, Ye.Yu., Shtepa,V.N.: Formalization of the task of creating a mathematical model of combined wastewater treatment Processes. J. Eng. Sci. **8**(2), H1–H7 (2021). https://doi.org/10.21272/jes.2021.8(2).h1

18. Pylypaka, S., Zaharova, T., Zalevska, O., Kozlov, D., Podliniaieva, O.: Determination of the effort for flexible strip pushing on the surface of a horizontal cylinder. In: Tonkonogyi, V., et al. (eds.) InterPartner 2019. LNME, pp. 582–590. Springer, Cham (2020). https://doi.org/10.1007/978-3-030-40724-7_59

19. Yanjun, X., Hill, C.A.S., Xiao, Z., Militz, H., Mai, C.: Silane coupling agents used for natural fiber/polymer composites: A review. Compos. Part A-Appl. Sci. Manuf. **41**, 806–819 (2010). https://doi.org/10.1016/j.ijadhadh.2018.07.008

20. Sklabinskyi, V., Liaposhchenko, O., Pavlenko, I., Lytvynenko, O., Demianenko, M.: Modelling of liquid's distribution and migration in the fibrous filter layer in the process of inertial-filtering separation. In: Ivanov, V., et al. (eds.) DSMIE 2018. LNME, pp. 489–497. Springer, Cham (2019). https://doi.org/10.1007/978-3-319-93587-4_51

21. Pavlenko, I., Liaposhchenko, A., Ochowiak, M., Demyanenko, M.: Solving the stationary hydroaeroelasticity problem for dynamic deflection elements of separation devices. Vibr. Phys. Syst. **29**, 2018026 (2018)

22. Glaser, R.H., Wilkes, G.L.: Structure property behavior of polydimethylsiloxane and poly(tetramethylene oxide) modified TEOS based sol-gel materials. Polym. Bull. **19**, 51–57 (1988). https://doi.org/10.1007/BF00255023

23. Girardi, F., et al.: Hybrid organic-inorganic materials on paper: surface and thermo-mechanical properties. J. Sol-Gel. Sci. Technol. **60**(3), 315–332 (2011). https://doi.org/10.1007/s10971-011-2563-z

24. Cappelletto, E., et al.: Hydrophobic siloxane paper coatings: the effect of increasing methyl substitution. J. Sol-Gel. Sci. Technol. **62**(3), 441–452 (2012). https://doi.org/10.1007/s10971-012-2747-1

25. Lin, W., et al.: Preparation of highly hydrophobic and anti-fouling wood using poly(methylhydrogen)siloxane. Cellulose **25**(12), 7341–7353 (2018). https://doi.org/10.1007/s10570-018-2074-y

Axial and Lateral Buckling Characteristics of Basalt/Carbon Hybrid Composite Laminates

Özkan Özbek[1(✉)] , Ömer Yavuz Bozkurt[2] , and Ahmet Erkliğ[2]

[1] Kilis 7 Aralık University, 79000 Kilis, Turkey
ozkanozbek@kilis.edu.tr
[2] Gaziantep University, 27310 Gaziantep, Turkey

Abstract. The objective of this work was an experimental investigation of the buckling performance of basalt/carbon hybrid composite laminates. To this end, the laminates fabricated via vacuum-assisted resin transfer molding were prepared at five different stacking sequences (B6, B5C1, B3C3, B1C5, and C6). To perform the hybridization process, carbon layers were replaced with basalt ones from inner to outer layers. The samples with twelve layers were subjected to axial and lateral buckling loads, applying fixed-fixed and fixed-free boundary conditions. Furthermore, failure modes were discussed to analyze the damage mechanisms of the samples. The findings demonstrated that the buckling performance of basalt composites was improved with the introduction of carbon layers. B6 samples showed the lowest values in critical loads, while the samples with totally carbon fiber reinforced samples (C6) had the highest values for both buckling experiments. The maximum critical buckling loads in axial and lateral directions were 1560 N and 76.7 N, respectively, which were 358.8% and 200.6% higher than B6 samples. Hybrid configurations exhibited critical loads between the results of the non-hybrid carbon and non-hybrid basalt fiber-reinforced composites. Furthermore, failure modes were observed as matrix fragmentation and delamination from the microscopic views of the samples.

Keywords: Basalt fiber · Carbon fiber · Hybridization · Axial buckling · Lateral buckling

1 Introduction

In the design of thin-walled structures used in engineering applications, ensuring the stability of a system by avoiding buckling has a crucial role. Buckling is a failure mode that suddenly occurs in the materials before yield or fracture strengths [1]. The members suffer from buckling failures under axial or lateral compressive loads like columns and beams. Although the first investigation about the buckling phenomenon was encountered from Euler's study in 1744 [2], today, many scientific studies devoted to buckling performances of materials, especially for thin-walled structures, are seen in the literature [3, 4].

With their superior specific strength and stiffness, composite materials are gained popularity in various engineering applications and are frequently used in several industrial areas such as aviation, automotive, aerospace, civil, electric-electronic [5]. Furthermore, they also exhibit outstanding properties like better fatigue life [6], higher corrosion resistance [7] compared to conventional metal-based monolithic materials. However, they suffer from buckling failures due to their thin-walled structures. Therefore, the buckling performance of fiber-reinforced composites is essential, especially for applications requiring higher structural stability. In this context, new material derivation techniques such as hybridization can reduce the material's negative effects and may have more economical and desired properties.

The current work aims to investigate the carbon fiber hybridization on buckling performances of basalt fiber-reinforced composite laminates. Even though some studies investigated the carbon fiber hybridization on the axial buckling behavior of basalt fiber reinforced composites, examination of lateral buckling behavior is not encountered in the literature. For this purpose, basalt fiber reinforced composites were hybridized with carbon fiber in three different stacking sequences (B5C1, B3C3, and B1C5), and the hybrid and non-hybrid composite samples were fabricated using the technique of vacuum resin transfer molding (VARTM). The buckling test samples were subjected to axial compression and lateral loads to understand axial and lateral buckling characteristics. The bucking performances of hybrid samples were compared with non-hybrid basalt, or non-hybrid carbon fiber reinforced composites.

2 Literature Review

Among the reinforcement materials used in polymer-based composites, basalt, obtained from the extrusion of volcanic basalt rocks formed by molten lava in volcanic regions, is a relatively new and natural fiber. It is of great interest to researchers due to its superior properties such as non-flammable, high insulation, no toxic impurities, and non-hazardous [8]. Furthermore, with their similar mechanical characteristics, basalt fiber seems a potential alternative for glass fiber [9] and is cost-effective compared to several fibers such as carbon fiber. Many studies devoted to the mechanical properties of basalt/epoxy reinforced composites are seen in the literature [10, 11]. Sapuan et al. [12] investigated the mechanical behaviors of basalt and glass fiber reinforced composites. They concluded that basalt samples showed much more tensile and flexural strength, Young's modulus compared to glass ones. Elmahdy and Verleysen et al. [13] performed a comparison study to understand the possibility of basalt usage in aircraft secondary structures. The glass and basalt samples were subjected to tensile loads at high strain rates. They explained that basalt samples exhibiting higher tensile properties than glass might be a promising alternative as a material used in aircraft secondary structures, and improvements in shear characteristics of basalt composites were required.

Although basalt fiber-reinforced composites offer interesting behaviors, their buckling performances are relatively low. Some techniques such as hybridization [14] and micro-or nano-sized additives [15] are widely applied to enhance the mechanical characteristics of basalt/epoxy fiber-reinforced materials. The hybridization with a superior

material providing the opportunity to eliminate material weakness is seen as an attractive way by scientists. The literature has seen numerous studies devoted to hybridization effects on the mechanical behaviors of basalt fiber-reinforced composite materials. Živković et al. [16] investigated the effect of moisture absorption on the low-velocity impact behaviors of basalt/flax hybrid composites. They stated that hybrid samples showed a more stable behavior since the lower moisture uptake of flax layers resulted from outer basalt layer protection. Sajid et al. [17] conducted a study on the axial buckling characteristics of perforated basal/carbon hybrid composites. They reported that the carbon fiber usage in hybridization decreased the influence of holes in samples. Özbek et al. [18] examined the crashworthiness behaviors of basalt/glass hybrid composite tubes. The filament wound samples were loaded in a compression direction with a 70.2% stroke efficiency. They concluded that hybrid samples exhibited a more stable crushing process when compared to pure glass or pure basalt ones.

3   Research Methodology

3.1   Preparation of Samples

The plain-woven basalt fabric with 202 g/m^2 areal density and 0.28 thickness was supplied from Tila Composite Representation Domestic and Foreign Trade. Ltd. Sti., Turkey. For the hybridization process, plain woven carbon fabrics having 204 g/m^2 areal density and 0.25 thickness were procured from Dost Kimya Endustriyel Hammaddeler Sanayi Ve Ticaret Limited Sirketi, Turkey. Additionally, the epoxy resin (MOMENTIVE MGS L285) and hardener (MOMENTIVE MGS H285) were used to prepare the matrix phase of the laminates. The epoxy and hardener were stirred at 100:25 weight ratio, respectively, and were mechanically mixed at 8000 rpm for 5 min. The tensile strength and modulus information of the reinforcement fabrics and neat epoxy were given in Table 1.

Table 1. The tensile properties of the reinforcements and neat epoxy.

Property	Basalt fabric	Carbon fabric	Neat epoxy
Tensile strength (MPa)	2000–2300	2500–3000	70–80
Tensile modulus (GPa)	90–92	200–700	3.2–3.5

Composite laminates fabricated via VARTM (Fig. 1) were prepared at five different configurations. First of all, the twelve numbers of dry fabrics were placed on the bottom mold. Then, peel ply was applied to the fabrics to provide easy extraction after manufacturing. Then, resin distribution media were placed to supply the uniform flow of resin mixture entire the vacuum process. Lastly, vacuum bagging film was used to cover all systems. After creating a closed environment, resin mixture was injected from the vacuum inlet side. When all laminates were wet, the inlet valve was turned off. The system was kept under a 680 mmHg vacuum for 8 h, and the initial curing process was performed at 80 °C. The final curing was carried out on the system at 40 °C for 2 h.
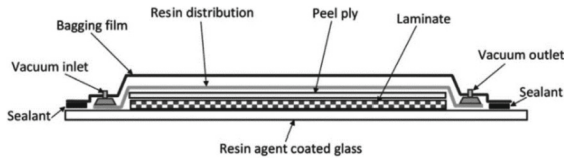
Fig. 1. The VARTM schematic illustration [2].

After the production stage, the laminates were cut on a 3-axis CNC router to prepare the samples with 20 mm wide and 200 mm length for experiments.

As seen in Fig. 2, five different configurations were performed with a sequence from totally basalt fabrics to carbon fabrics. The configurations were started from the total basalt fabrics, and 2, 6, and 10 numbers of basalt layers were replaced with the carbon fabrics from inner layers to outer for hybrid laminates.

	(B6)s	(B5C1)s	(B3C3)s	(B1C5)s	(C6)s
Thickness (mm)	2.18	2.22	2.43	2.63	2.86
Naming	B6	B5C1	B3C3	B1C5	C6
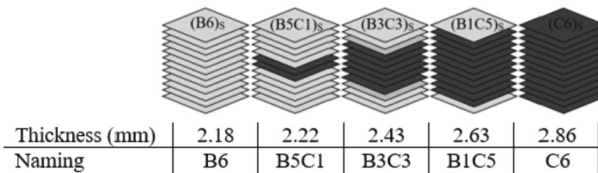
Fig. 2. Configurations of prepared laminates.

3.2 Buckling Experiments

To determine buckling performances of the non-hybrid or hybrid fiber reinforced samples, the axial and lateral buckling experiments were conducted on Shimadzu AG-X Series universal testing machine with a 300 kN capacity (Kyoto/Japan) as given in Fig. 3. The samples were compressively loaded in the axial direction with a crosshead speed of 0.25 mm/min, as seen in Fig. 3(a). Axially compressed samples with a gauge length of 145 mm were fixed on both sides.

(a)   **(b)**
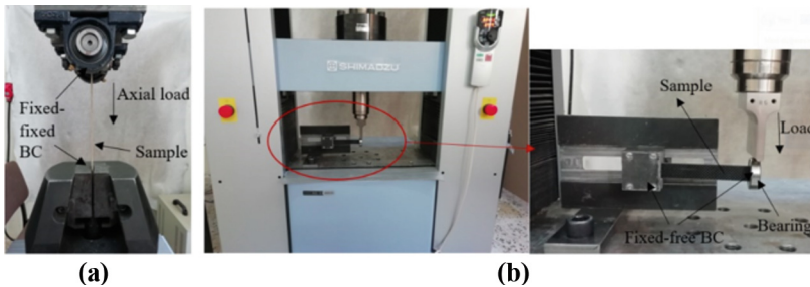
Fig. 3. Buckling experiments in axial (a) and lateral (b) directions.

In lateral buckling tests, the samples having 125 mm gauge length were subjected to transverse loads with 1.0 mm/min speed and were exposed to fixed-free boundaries, as shown in Fig. 3(b). A ball bearing between the sample and loading nose was used in lateral loading to prevent negative impacts of friction that could cause an unreliable buckling process.

4   Results

4.1   Axial Buckling

The axial compressive load versus displacement diagrams obtained from the samples are presented in Fig. 4. The samples showed a linear curve until they buckled where the nonlinear behavior began. Then, stable load curves were seen after the formation of buckling formations on samples. Herein, it can be said that C6 samples exhibiting the highest load-bearing capability had much more resistance against axial loads. The weakest sample group to compression was seen as B6. When carbon fiber amount was increased in hybrid configurations, improvements were seen according to load responses. This can be related to much stiffer characteristics of the carbon fibers compared to basalt fibers [19].
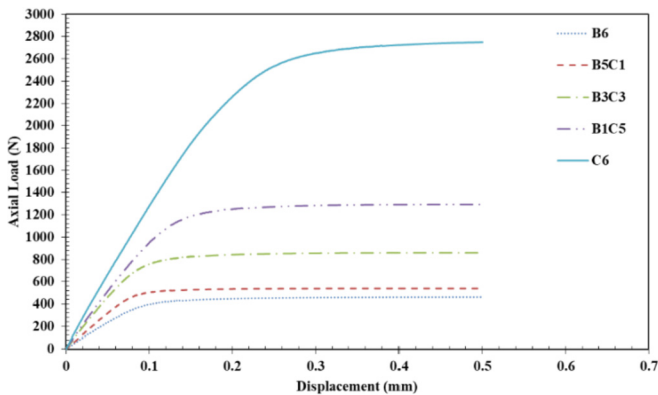
Fig. 4. Axial load vs. displacement diagrams.

The critical buckling load values of the samples exposed to axial compressive loading conditions were given in Fig. 5. The minimum critical buckling load of 340 N was achieved from the B6 samples. The hybrid configurations of B5C1, B3C3, and B5C1 exhibited 19.1%, 62.9%, and 181.3, respectively, more buckling load values than B6 samples. This demonstrated that an increment in carbon fiber content of the hybrid composite samples led to an increase in the buckling performance of basalt fiber-reinforced composites. Similarly, there are research works in the literature that the mechanical behaviors of basalt composites can be enhanced by hybridizing them with carbon fiber. More suitable materials can be derived in terms of costs and mechanical properties rather than fully carbon or carbon basalt fiber reinforcements [20].
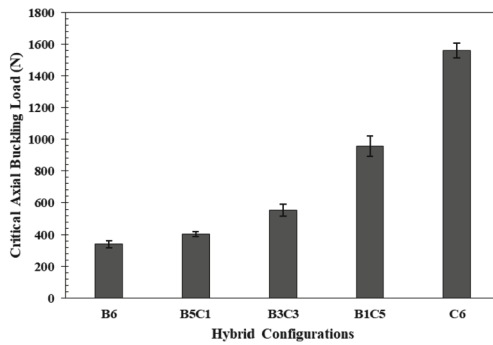
Fig. 5. Critical axial buckling load.

The sample behavior in axial buckling was seen in Fig. 6. All buckled specimens typically showed similar characteristics, exhibiting maximum lateral displacement in mid-region. Moreover, it can be said that bending formation due to axial compression was seen as the primary reason for failures, causing a decrease in the stiffness of composite samples [2].

Fig. 6. The sample behavior in axial compression.

The microscopic views of the axially buckled samples are presented in Fig. 7. For all samples, failures were started with matrix cracking and then separated layers. Thus, it can be concluded that matrix fragmentation and delamination were listed as failure modes of the samples. Herein, delamination growth was seen in one side of the samples exposed to more stress concentration in the convex side when they buckled. Furthermore, the formation of delamination was observed from the point where carbon and basalt fiber interface in hybrid samples. This can be attributed to the weaker interfacial bonding in dissimilar layers [21].

4.2   Lateral Buckling

The lateral load-displacement responses of the samples with non-hybrid or hybrid fiber reinforcements were presented in Fig. 8. A similar trend with axial buckling results was
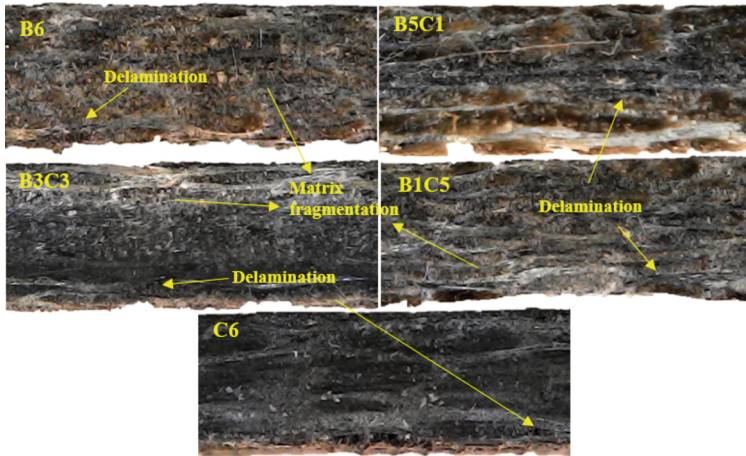
Fig. 7. Failures in axial buckling.

seen in terms of the load-bearing capabilities of the samples. All samples except C6 showed a linear curve until they were buckled, then nonlinear behavior was seen. After the buckling formation, the load characteristics tried to be stable or resulted in a decrease due to the failure of the samples. The presence of basalt fibers exhibited a fracture propagation in a more ductile way than C6 samples due to the less stiff characteristics. However, C6 samples exhibiting the higher ability to resist against lateral load showed a sharp decrease in loads. The higher brittleness of carbon fibers can ascribe this compared to basalt fibers [21].
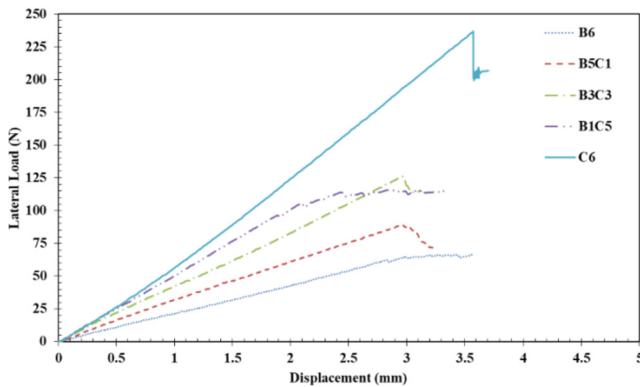
Fig. 8. Lateral load-displacement responses.

The critical lateral buckling loads of the samples are given in Fig. 8. The hybrid samples showed critical load values between non-hybrid basalt (B6) and non-hybrid carbon-fiber-reinforced samples (C6). Hybrid samples' critical buckling load values showed an increasing trend by the increment in carbon fiber content. The hybridization

with carbon fiber increased the buckling load of B6 samples. The B1C5, B3C3, and B5C1 hybrid samples exhibited 19.4%, 55.6%, and 148.4% higher buckling loads than the B6 non-hybrid samples. The maximum critical lateral buckling load was obtained from C6 samples as 76.7 N, while the B6 samples showed the minimum as 25.50 N (Fig. 9).
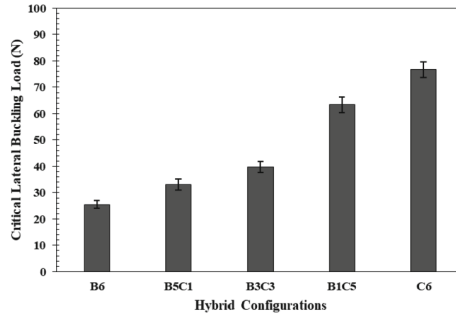
Fig. 9. Critical lateral buckling load.

Typical sample behaviors were observed from the lateral buckling experiments, as shown in Fig. 10. Bending and twisting formations seen in the front and side views, respectively, were observed. Also, the laterally buckled appearance of the samples was detected in the top view. This stated that collapsing of the samples in lateral loading, due to both bending and twisting formations, was responsible for buckling of the samples in lateral direction [2]. C6 samples showed a sudden twisting motion that explains the sharp decrease in loads, while the other samples showed a gradual twisting.
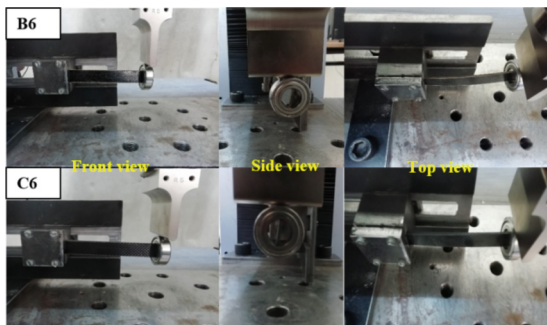
Fig. 10. The samples of B6 and C6, subjected to a lateral buckling experiment.

5 Conclusions

In this study, the effects of carbon fiber hybridization on the buckling performances of basalt fiber-reinforced composite laminates were experimentally examined. Three different hybrid configurations replacing basalt fabrics with carbon ones were prepared, and

the samples were subjected to axial and transverse loads to determine critical buckling loads. The findings achieved from buckling tests can be listed as follows:

- The hybridization noticeably increased the buckling performances of B6 samples with carbon fibers in terms of load-bearing capability and critical loads.
- In hybrid samples, B1C5 configurations exhibited the highest performances. Its buckling loads were seen as 956.25 N and 63.33 N for axial and lateral directions, respectively, 91.9% and 136.1% higher than B5C1 samples.
- The minimum critical buckling loads were obtained from the B6 non-hybrid samples, while the highest ones were achieved from C6 non-hybrid samples.
- The hybridization process showed the critical buckling load values between B6 and C6 non-hybrid samples for axial and lateral loadings.
- Matrix fragmentation and delamination were seen as the main failure modes.

The above implications demonstrated that carbon fiber hybridization improved the buckling performances of basalt fiber-reinforced composites. Thus, it was proved that buckling characteristics of the basalt materials could be tailored by hybridization with carbon fabrics. Additionally, the buckling performance of intraply fiber hybridization or different stacking sequences and various fiber orientations would be studied to explore all aspects of basalt/carbon hybridizations in the future.

References

1. Deng, J., Kanwar, N.S., Pandey, M.D., Xie, W.C.: Dynamic buckling mechanism of pillar rockbursts induced by stress waves. J. Rock Mech. Geotech. Eng. **11**(5), 944–953 (2019). https://doi.org/10.1016/j.jrmge.2019.02.005
2. Özbek, Ö.: Axial and lateral buckling analysis of kevlar/epoxy fiber-reinforced composite laminates incorporating silica nanoparticles. Polym. Compos. **42**(3), 1109–1122 (2021). https://doi.org/10.1002/pc.25886
3. Song, M., Yang, J., Kitipornchai, S.: Bending and buckling analyses of functionally graded polymer composite plates reinforced with graphene nanoplatelets. Compos. B Eng. **134**, 106–113 (2018). https://doi.org/10.1016/j.compositesb.2017.09.043
4. Doğan, N.F.: Buckling analysis of graphene nanoplatelets-doped carbon/aramid hybrid polymer composite plates. Polym. Compos. **42**(11), 5712–5720 (2021). https://doi.org/10.1002/pc.26253
5. Maziz, A., Tarfaoui, M., Rechak, S., Nachtane, M., Gemi, L.: Finite element analysis of impact-induced damage in pressurized hybrid composites pipes. Int. J. Appl. Mech. **13**(7), 2150074 (2021). https://doi.org/10.1142/S1758825121500745
6. Oguz, Z.A., Erklig, A., Bozkurt, Ö.Y.: Degradation of hybrid aramid/glass/epoxy composites hydrothermally aged in distilled water. J. Compos. Mater. **55**(15), 2043–2060 (2021). https://doi.org/10.1177/0021998320984237
7. Bulut, M.: Mechanical characterization of Basalt/epoxy composite laminates containing graphene nanopellets. Compos. B Eng. **122**, 71–78 (2017). https://doi.org/10.1016/j.compositesb.2017.04.013
8. TG, Y.G., Kushvaha, V., MR, S., Siengchin, S.: A new study on flax-basalt-carbon fiber reinforced epoxy/bioepoxy hybrid composites. Polym. Comp. **42**(4), 1891–1900 (2021). https://doi.org/10.1002/pc.25944

9. Asadi, A., Baaij, F., Mainka, H., Rademacher, M., Thompson, J., Kalaitzidou, K.: Basalt fibers as a sustainable and cost-effective alternative to glass fibers in sheet molding compound (SMC). Compos. B Eng. **123**, 210–218 (2017). https://doi.org/10.1016/j.compositesb.2017.05.017

10. Sharma, V., Meena, M.L., Kumar, M., Patnaik, A.: Mechanical and three-body abrasive wear behavior analysis of glass and basalt fiber-reinforced epoxy composites. Polym. Compos. **41**(9), 3717–3731 (2020). https://doi.org/10.1002/pc.25670

11. Wang, L., He, C., Fu, J.: RETRACTED ARTICLE: physical, mechanical, and thermal behavior analyses of basalt fiber-reinforced composites. Int. J. Plast. Technol. **23**(2), 123–131 (2019). https://doi.org/10.1007/s12588-019-09244-5

12. Sapuan, S.M., et al.: Mechanical properties of longitudinal basalt/woven-glass-fiber-reinforced unsaturated polyester-resin hybrid composites. Polymers **12**(10), 2211 (2020). https://doi.org/10.3390/polym12102211

13. Elmahdy, A., Verleysen, P.: Mechanical behavior of basalt and glass textile composites at high strain rates: a comparison. Polym. Testing **81**, 106224 (2020). https://doi.org/10.1016/j.polymertesting.2019.106224

14. Azimpour-Shishevan, F., Akbulut, H., Mohtadi-Bonab, M.A.: Mechanical and thermal properties of carbon/basalt intra-ply hybrid composites. I. effect of intra-ply hybridization. Fibers Polym. **21**(11), 2579–2589 (2020). https://doi.org/10.1007/s12221-020-9843-6

15. Demirci, M.T., Tarakçıoğlu, N., Avcı, A., Akdemir, A., Demirci, I.: Fracture toughness (Mode I) characterization of SiO2 nanoparticle filled basalt/epoxy filament wound composite ring with split-disk test method. Compos. B Eng. **119**, 114–124 (2017). https://doi.org/10.1016/j.compositesb.2017.03.045

16. Živković, I., Fragassa, C., Pavlović, A., Brugo, T.: Influence of moisture absorption on the impact properties of flax, basalt and hybrid flax/basalt fiber reinforced green composites. Compos. B Eng. **111**, 148–164 (2017). https://doi.org/10.1016/j.compositesb.2016.12.018

17. Sajid, Z., Karuppanan, S., Azmi, M.A.A.B.M.: Effect of hybridization on the buckling behavior of perforated CFRP/BFRP laminates. Emerg. Mater. Res. **10**(1), 66–74 (2021). https://doi.org/10.1680/jemmr.19.00164

18. Özbek, Ö., Bozkurt, Ö.Y., Erkliğ, A.: An experimental study on intraply fiber hybridization of filament wound composite pipes subjected to quasi-static compression loading. Polym. Testing **79**, 106082 (2019). https://doi.org/10.1016/j.polymertesting.2019.106082

19. Saba, N., Jawaid, M., Alothman, O.Y., Paridah, M.T.: A review on dynamic mechanical properties of natural fibre reinforced polymer composites. Constr. Build. Mater. **106**, 149–159 (2016). https://doi.org/10.1016/j.conbuildmat.2015.12.075

20. Subagia, I.A., Kim, Y., Tijing, L.D., Kim, C.S., Shon, H.K.: Effect of stacking sequence on the flexural properties of hybrid composites reinforced with carbon and basalt fibers. Compos. B Eng. **58**, 251–258 (2014). https://doi.org/10.1016/j.compositesb.2013.10.027

21. Sun, G., Tong, S., Chen, D., Gong, Z., Li, Q.: Mechanical properties of hybrid composites reinforced by carbon and basalt fibers. Int. J. Mech. Sci. **148**, 636–651 (2018). https://doi.org/10.1016/j.ijmecsci.2018.08.007

The Effect of Deposition Conditions and Irradiation on the Structure, Substructure, Stress-Strain State, and Mechanical Properties of TiN Coatings

Nataliia Pinchuk[(✉)] , Mykola Tkachuk , Mariia Zhadko , Hanna Kniazieva , and Andriy Meilekhov

National Technical University "Kharkiv Polytechnic Institute", 2, Kyrpychova Street, Kharkiv 61002, Ukraine
spiritnata@gmail.com

Abstract. The influence of the displacement potential and the radiation factor on the features of the formation and mechanical properties of titanium nitride coatings obtained by the vacuum-arc method has been established. Important indicators of the process of bombardment by charged ions of the coating surface and the growing surface itself are determined, namely, at the maximum penetration depth of ions reaches (1.5–5 nm) and the number of vacancies (0.45–1.35). The simulation results are compared with actual experiments, and it is established that the above changes do occur. The hardness of TiN coatings was 42–45 GPa. The relaxation process of residual stresses is observed at $U_i = -1200$ V. As a result, the level of microdeformation is reduced to the value of 0.61%, the size of the crystallites reaches 23 nm. The analysis of the reasons for the observed structural changes is carried out based on the mechanism of formation of surface layers of vacuum-arc coverings in the conditions of the implantation processes stimulated by giving negative potential on a substrate. Irradiation with accelerated argon ions leads to a decrease in the physicomechanical characteristics of the coating (a decrease in the hardness (22–29 GPa) and elastic modulus (~410 GPa)). The changes are more pronounced in coatings TiN applied under high-voltage pulsed conditions.

Keywords: Industrial innovation · Modeling · Impulse · Macrostrain · Radiation damage · Hardness · Relaxation

1 Introduction

Nowadays, a lot of attention is focused on obtaining and studying the properties of submicron, nanocrystalline materials due to their application in various fields of technology, such as electronics, catalysis, magnetic data storage, structural components, etc. Submicron and nanocrystalline metal and ceramic materials are widely used at this time as structural elements and functional layers in modern microelectronic devices, aerospace parts, as well as solid wear-resistant coatings in the manufacturing industry

[1–6]. To meet the technological requirements for use in these areas, the size of the structural elements must be reduced to a submicron or nanometer scale. The technological process of producing hard and superhard coatings and their properties, i.e., hardness, wear-resistance, and radiation resistance, are under development. This is primarily determined by the complexity of modeling processes and the small amount of experimental data obtained from the analysis of the influence of production modes on the structure and properties.

Individual elements of the NPP structure are exposed to irradiation with argon, helium, and hydrogen ions with different energies, which leads to their accelerated degradation due to a decrease in the physical and mechanical properties of the materials from which they are made. Various protective coatings are used to improve their performance, including vacuum-arc titanium nitride coatings with high hardness, adhesion, and anti-corrosion properties. This is the reason for the interest in studying the physicomechanical properties of TiN coatings irradiated with argon ions.

2   Literature Review

In recent decades, the deposition of coatings has evolved from a promising development [7] into a technology necessary for industrial development, which is embodied and implemented in all major industries related to coatings (engineering (tool industry)) [8], nuclear energy [9], optoelectronics [10], optics [11], medicine [12, 13], and aerospace equipment [14], as well as all machine tools [15, 16]). Accordingly, there is an excellent variety of coating methods. Physical Vapor Deposition (PVD) is the technology most widely used to obtain coatings with unique specified properties [17] on different substrates [18]. Changing the deposition parameters can result in a wide range to affect the functional properties of the formed coatings.

However, the questions of the features of the formation of nitride coatings under conditions of condensation with ion bombardment remain topical. Such knowledge will allow it to obtain coatings with the necessary technological properties for specific tasks and industries. Simulation of these processes has an economic effect and a reduction in material costs. Therefore, this study is promising and in demand in the modern world.

This work aimed to study the bias potential and irradiation effect on phase-structural state, macrostrain, and hardness of vacuum-arc of titanium nitride coatings and compare them with computer simulations.

3   Research Methodology

The samples were obtained by the vacuum-arc method on a modernized Bulat-6 installation. The pressure of the working (nitrogen) atmosphere during the deposition of nitride layers was $p_N = 0.6$ Pa. The total deposition time of the coating was about 1 h, while the total thickness of the coating was 10–12 μm. In the deposition process, a constant negative potential of the value $U_s = -200$ V was applied to the substrates and a pulsed potential $U_i = -1200$ V (pulse frequency $\tau = 10$ μs). Stainless austenitic steel plates 12Cr18Ni10Ti (analog of stainless steel SS 321) with dimensions $18 \times 18 \times 2$ were used as substrates.

Modeling processes during bombardment with accelerated ions were carried out using the STRIM software package [19].

The phase-structural analysis was carried out by X-ray diffractometry according to the θ-2θ scheme (in reflection [20]) in Cu-k$_\alpha$ radiation on a DRON-4 setup. The coatings were irradiated with argon ions using the Sokol accelerator [21]. Substructural characteristics were determined by the approximation method, and the macrostressed-strain state was studied using the X-ray tensometry method ("a – sin$^2\psi$" method) [22, 23]. Nanoindentation was carried out using a Mikron-Gamma microindentor [24] with a Berkovich pyramid under loading within 20 G with automatic loading and unloading for 30 s.

4 Results

4.1 Modeling of Processes and Structural-Phase State of Nanocomposites of the TiN Coatings

Computer simulation of the processes occurring during ion implantation, sputtering, and ion beam mixing was performed in the mode that best meets the requirements for obtaining actual TiN films. This is the "Monolayer Collision Steps/Surface Sputtering" mode. All cascade damage is taken into account during simulation in this mode. Each atom is observed until its energy falls below the minimum displacement threshold energy of any target atom. Thus, all damage to the target occurred during the collision is analyzed.

The simulations were performed for two cases - a TiN system with nitrogen ions for bombing and a TiN system with titanium ions for the bombing. For each of these two cases, energies of different magnitudes were established, corresponding to the actual conditions in obtaining titanium nitride coatings. This energy was 800, 1200, and 2000 eV (Table 1 and Table 2).

Table 1. Summary table of the obtained parameters of the cascades after 5 iterations.

Parameter	Nitrogen ions → TiN			Titanium ions → TiN		
	Energy, eV			Energy, eV		
	800	1200	2000	800	1200	2000
Depth of penetration of ions, nm	3	10	10	2	3	5
The radius of the obtained coating, nm	1.5	3	4	1.5	2	3
The maximum number of vacancies per ion	0.65	0.9	1.35	1.3	1.1	1.9
Depth of the zone with the largest accumulation of ions, nm	0.1–3	0.1–5	0.1–5	0.1–2	0.1–3	0.1–5

That is, 6 different cases were considered. In each of them, the first five iterations were considered the most informative compared to actual films, and cascades of a thousand iterations were considered to get a general picture of the simulated processes.

Table 2. Summary table of the obtained parameters of the cascades after 1000 iterations.

Parameter	Nitrogen ions → TiN			Titanium ions → TiN		
	Energy, eV			Energy, eV		
	800	1200	2000	800	1200	2000
Depth of penetration of ions, nm	8	9	12	4	5	7
The radius of the obtained coating, nm	4	4.5	7	2.5	3	4
The maximum number of vacancies per ion	0.45	0.6	0.62	1.1	1.1	1.35
Depth of the zone with the largest accumulation of ions, nm	1.5–3	0.5–5	1–7	1.5–3	1–4	1–4.5

The results of X-ray diffraction studies are shown in Fig. 1. It can be seen that the formation of a polycrystalline state of TiN (PDF card JCPDS 38-1420).

Fig. 1. Sections of the diffraction spectra of TiN coatings obtained at $p_N = 0.6$ Pa, $U_s = -200$ V: $1 - U_i = 0$ V; $2 - U_i = -1200$ V, $\tau = 10$ μs.

It has been established that in the coatings obtained at $U_i = 0$ V, the crystallite size (L) is 91 nm, and the supply of a high-voltage pulsed potential leads to a decrease in L to 23 nm. At the same time, in the absence of a pulsed displacement potential, microde-formation $<\varepsilon>$) was 0.7% and 0.61% under high-voltage exposure, which indicates the relaxation of residual stresses, resulting in the formation of displacement cascades.

One of the essential properties of the coating, which determines its durability, is hard-ness. It has been established that during condensation with additional ion bombardment, the hardness increases from 42 GPa to 45 GPa. The same high hardness was obtained in [5, 6]. Such coatings can be classified as superhard. Such an increase in hardness can be

associated with a high value of macrostrain, namely compression, up to -1.95% and -2.05%.

4.2   The Effect of Irradiation on the Structure and Mechanical Properties of Vacuum-Arc Tin Coatings

The next stage of the study was to determine the effect of irradiation with argon ions with energies of 1 meV and 1.8 meV.

Analysis of the diffraction spectra of a series of coatings TiN, obtained at $p_N = 0.6$ Pa, $U_s = -200$ V, before and after Ar irradiation showed that, without fundamentally changing the phase composition of the coating (Fig. 2, a), irradiation leads to a change
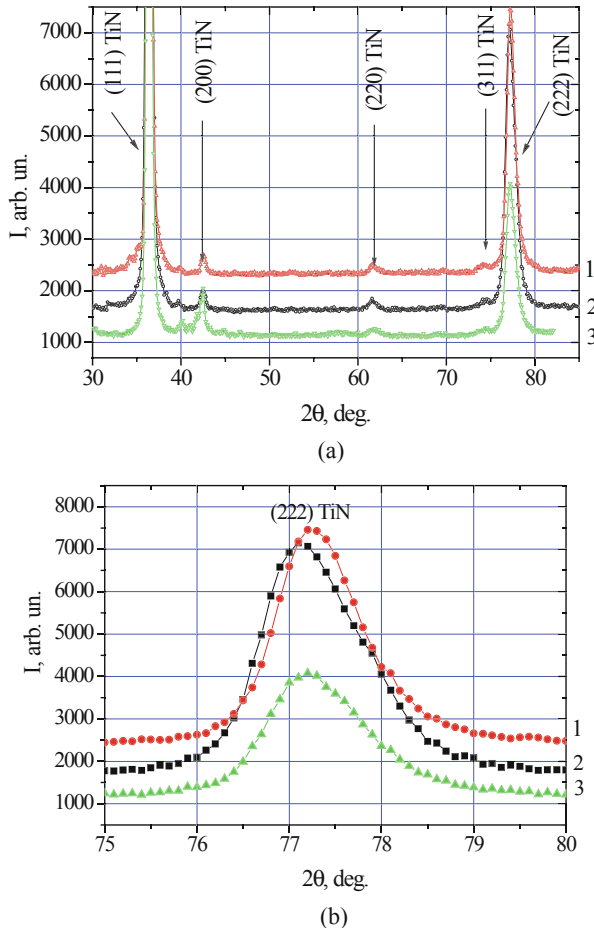
Fig. 2. Sections of diffraction spectra of TiN coatings obtained at $p_N = 0.6$ Pa, $U_s = -200$ V: 1 – unirradiated, 2 – irradiated by argon ions with energies of 1 meV, 3 – irradiated by argon ions with energies of 1.8 meV. a – full diffraction spectrum (30–85) degrees, b – part of the diffraction spectrum, peaks (222) (75–80) degrees.

in the stress state (by the shift of the peaks) and substructural characteristics (widening of the peaks). The displacement of the peaks is well traced by the change in the position of the distant reflex (222) - Fig. 2, b.

The study of the substructural characteristics of the coatings, determined by the method of profile shape approximation by the Cauchy function, showed that irradiation leads to a decrease in the average grain size of crystallites from 91 nm in the initial state to 45 nm and 38 nm, respectively, at different irradiation energies of Ar. Microstrain, balanced in the volume of grains, also changes during irradiation, increasing with the irradiation energy (0.79–0.82)% after irradiation.

Analysis of the diffraction spectra of a series of coatings TiN, obtained at $p_N = 0.6$ Pa, $U_s = -200$ V, $U_i = -1200$ V, $\tau = 10\,\mu s$, before and after irradiation with Ar, showed that
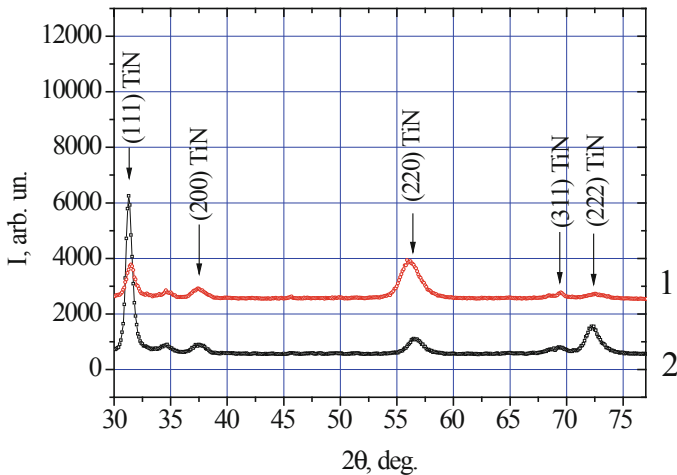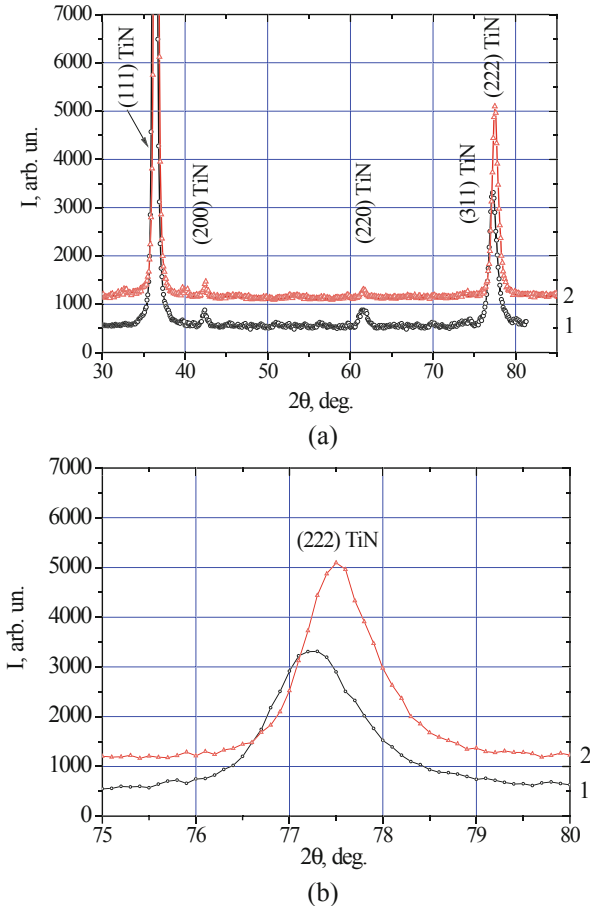

Fig. 3. Sections of diffraction spectra of TiN coatings obtained at $p_N = 0.6$ Pa, $U_s = -200$ V, $U_i = -1200$ V, $\tau = 10\,\mu s$: 1 – unirradiated, 2 – irradiated by argon ions with energies of 1.8 meV. a – full diffraction spectrum (30–85) degrees, b – part of the diffraction spectrum, peaks (222) (75–80) degrees.

the phase composition of the coating remains unchanged even after the impulse exposure (−1200 V) (Fig. 3, a). In this case, a change in the position of distant reflections (Fig. 3, b), namely, its displacement towards large angles, under the assumption of a stress-strain effect on this position, indicates a decrease in the value of condensation compressive stresses in the coating.

The study of the substructural characteristics showed that similarly to the previous case, the average grain size of crystallites decreases from 28 nm to 23 nm under irradiation. At the same time, in contrast to the series of coatings obtained without additional impulse exposure, microstrain decreases from 0.61% to 0.38%.

Investigation of the stress-strain state by the "a-sin$^2 \psi$" method showed that the most significant decrease in mechanical properties upon irradiation (series of coatings with additional impulse exposure) is accompanied by a strong relaxation of the macrostrain state of compression from deformation of −(2.05–2.1)% in the initial state to −1.38% – after irradiation.

The results of measuring the hardness and Young's modulus of TiN coatings exposed to different irradiation values are shown in Table 3.

Table 3. Mechanical characteristics of TiN coatings determined by indentation.

Energies of argon ions, MeV	$p_N = 0.6$ Pa, $U_s = −200$ V			
	$U_i = 0$ V		$U_i = −1200$ V, $\tau = 10$ μs	
	H, GPa	E, GPa	H, GPa	E, GPa
1.0	29	402	25	415
1.8	28	390	22	422

The table shows that irradiation with accelerated argon ions leads to a decrease in the physicomechanical characteristics of the coating (a decrease in the hardness and elastic modulus). The changes are more pronounced in coatings applied under high-voltage pulsed conditions.

Thus, studies of titanium nitride coatings obtained at a constant negative bias potential of −200 V without and under the action of a high-voltage (−1200 V) pulse potential showed that, without fundamentally changing the phase composition of the coating. Irradiation to varying levels changes its stress-strain state, depending on whether the deposition of coatings took place without or with high-voltage pulses. The comparison shows that deposition with high voltage (−1200 V) pulses leads to a higher level of the compressive stress-strain state. Apparently, the reason for this is implantation processes, which is typical when the impact energy already exceeds the critical value for the formation of a relaxing displacement cascade. Hence, the results obtained under irradiation can also be explained. In the case of a high implanting action (with pulses), the formation of a high compressive stress-strain state, on the one hand, leads to an increase in hardness, and on the other hand, makes such a structure unstable to subsequent radiation exposure, leading to a strong relaxation of the compressive stress-strain state and a

drop in hardness. The same instability also affects the substructural level, leading to the relaxation of microstrains.

It is interesting to note that a change in the average crystallite size does not have a decisive effect on the change in hardness compared to the effect of compressive stresses in the coating. Thus, a decrease in the average size of crystallite grains after irradiation against the background of a change in the stress-strain state does not increase hardness. It should follow from the size dependence of the Hall-Petch type's mechanical properties.

5   Conclusions

According to the simulation results, it was found that the average penetration depth of ions, both titanium and nitrogen, is 1.5–5 nm during condensation under ion bombardment conditions. In this case, a change in the distribution of vacancies over the depth of the layer as a result of radiation damage was observed.

Computer simulation made it possible to establish that the change in energy during the formation of TiN coatings changes the processes that affect the formation of vacancies, stress, thickness, and structure of the coatings. The simulation results are compared with natural experiments. It is established that the above changes do occur. To study the surface structure of the coating, it is more important to model cascades with a small number of iterations because large cascades form a loose region through which ions can penetrate deeper into the coating, i.e., they will affect the structure and properties in the middle of the material, to the extent that this occurs in at surface areas.

It is shown that the supply of high-voltage pulse bias potential increases the mobility of particles and leads to relaxation processes. The latter provides a reduction in the growth stresses of compression and disorientation of the crystallite grains at a constant U_s.

The analysis of the reasons for the observed structural changes is carried out based on the mechanism of formation of surface layers of vacuum-arc coverings in the conditions of the implantation processes stimulated by giving off negative potential on a substrate.

It has been established that in these coatings, the values of nano- and microhardness reach the level of 42–45 GPa, which is associated with the stress-strain and phase-structural states.

The influence of argon ion irradiation on the structure and mechanical properties has been studied. It is established that hardness values after irradiation differ almost twice from the initial state and reach a value of 22–29 GPa.

References

1. Gusev, A.I.: Nanomaterials, Nanostructures, Nanotechnology. Fizmalit, Moscow (2005)

2. Shpak, A., Cheremskoy, P., Kunitsky, Yu., Sobol, O.: Cluster and Nanostructured Materials. Vol. 3 Porosity as a Special State of a Self-organized Structure in Solid Materials. Academperiodica, Kyiv (2005). (in Russian)

3. Pinchuk, N., Sobol, O.: Simulation of the influence of high-voltage pulsed potential supplied during the deposition on the structure and properties of the vacuum-arc nitride coatings. In: Ivanov, V., et al. (eds.) DSMIE 2019. LNME, pp. 447–455. Springer, Cham (2020). https://doi.org/10.1007/978-3-030-22365-6_45

4. Golovin, Y.: Introduction to Nanotechnology. Mechanical Engineering, Moscow (2007)

5. Pinchuk, N.V., Sobol', O.V., Subbotina, V.V., Zelenskaya, G.I.: Influence of the bias potential applied in the process of deposition in constant and pulsed form on the structure, substructure, stress-strain state and hardness of TiN vacuum-arc coatings. Funct. Mater. **27**(3), 595–604 (2020). https://doi.org/10.15407/fm27.03.513

6. Andreev, A.A., Sablev, L.P., Shulaev, V.M., Grigoriev, S.N.: Vacuum Arc Devices and Cover. NNTSKHFT, Kharkov (2005)

7. Orhing, M.: Materials science of thin films: deposition and structure, London (2001)

8. Bobzin, K.: High-performance coatings for cutting tools. CIRP J. Manuf. Sci. Technol. **18**, 1–9 (2017). https://doi.org/10.1016/j.cirpj.2016.11.004

9. Marinin, V.G.: Coatings for protection of elements of the heat power equipment. Eastern Eur. J. Adv. Technol. **5/5**(53), 32–37 (2011)

10. Nakamura, S., Fasol, G.: The Blue Laser Diode. Springer, Berlin (1997)

11. Baumeister, P.W.: Optical Coating Technology, Bellingham (2004)

12. Giles, C., Lamont-Friedrich, S.J., et al.: The importance of fungal pathogens and antifungal coatings in medical device infections. Biotechnol. Adv. **36**(1), 264–280 (2018). https://doi.org/10.1016/j.biotechadv.2017.11.010

13. Geyao, L., Yang, D., Wanglin, C., Chengyonga, W.: Development and application of physical vapor deposited coatings for medical devices: a review. Procedia CIRP **89**, 250–262 (2020). https://doi.org/10.1016/j.procir.2020.05.149

14. Gray, J.E., Luan, B.: Protective coatings on magnesium and its alloys - a critical review. J. Alloy Comp. **336**, 88–113 (2002). https://doi.org/10.1016/S0925-8388(01)01899-0

15. Bewilogua, K., Bräuer, G., Dietz, A., et al.: Surface technology for automotive engineering. CIRP Ann. Manuf. Technol. **58**, 608–627 (2009). https://doi.org/10.1016/j.cirp.2009.09.001

16. Bruzzone, A.A.G., Costa, H.L., Lonardo, P.M., Lucca, D.A.: Advances in engineered surfaces for functional performance. CIRP Ann. Manuf. Technol. **57**, 750–769 (2008). https://doi.org/10.1016/j.cirp.2008.09.003

17. Sobol', O.V., Andreev, A.A., Grigoriev, S.N., et al.: Physical characteristics, structure and stress state of vacuum-arc TiN coating, deposition on the substrate when applying high-voltage pulse during the deposition. PAST. Ser. Phys. Radiat. Damage Radiat. Mater. Sci. **4**(98), 174–177 (2011)

18. Schneider, J.M., et al.: Recent developments in plasma assisted physical vapour deposition. J. Phys. D Appl. Phys. **33**, R173–R186 (2000). https://doi.org/10.1088/0022-3727/33/18/201

19. Ziegler, J.F., Ziegler, M.D., Biersack, J.P.: SRIM – the stopping and range of ions in matter. Nucl. Instr. Meth. Phys. Res. B **268**, 1818–1823 (2010). https://doi.org/10.1016/j.nimb.2010.02.091

20. Sobol', O.V., Shovkoplyas, O.A.: On advantages of X-ray schemes with orthogonal diffraction vectors for studying the structural state of ion-plasma coatings. Tech. Phys. Lett. **39**(6), 536–539 (2013). https://doi.org/10.1134/S1063785013060126

21. Vergunov, A.D., Levchenko, Y., et al.: Small-sized electrostatic accelerator at 2 MeV of horizontal type (preliminary tests). VANT. Ser. TFE **1**(22), 26–28 (1985)

22. Noyan, I.C., Cohen, J.B.: Residual Stress Measurement by Diffraction and Interpretation. Springer, New York (1987)

23. Gargaud, P., Labat, S., Thomas, O.: Limits of validity of the crystallite group method in stress determination of thin film structures. Thin Solid Films **319**, 9–15 (1998). https://doi.org/10.1016/S0040-6090(97)01100-0
24. Aznakayev, E.: Micron-gamma for estimation the physico-mechanical properties of micro-materials. In: Proceedings of the International Conference "Small Talk – 2003", San Diego, California, USA, vol. 001, pp. 8–10 (2003)

Calculation of Thermal Stresses in Oxide Layers Synthesized on Cu Substrates

Oleksandr Shorinov[(✉)] [ID]

National Aerospace University "Kharkiv Aviation Institute", 17, Chkalov Street, Kharkiv 61070, Ukraine
o.shorinov@khai.edu

Abstract. The paper presents the results of analyzing the nature and magnitude of residual thermal stresses in the oxide layer of Cu2O synthesized on a substrate of pure copper using a known analytical model for calculating thermal stresses in multilayer and single-layer coatings. The operating temperatures of the formation of thin-film oxide layers are the main technological parameter on which the values of thermal stresses depend. After the synthesis, the coated substrates are cooled to ambient temperature. A significant difference in the coefficients of thermal expansion of the oxide layer materials and the coating leads to compressive residual stresses. The stress-strain state during the cooling of the substrate-coating system free from external forces was investigated. The mathematical model assumed that the resulting deformations do not exceed the elastic limit, i.e., the residual stresses lie in the region of elastic deformations, and the temperature in the thickness of the material does not change. It should also be noted that the values of thermal expansion coefficients, elastic modulus, and Poisson's ratios are constant, i.e., they do not depend on temperature changes. The paper presents the main analytical dependences of thermal stresses on the physical and mechanical properties of coating materials and the substrate and their thicknesses.

Keywords: Oxide layers · Residual stress · Strain · Elastic modulus · Manufacturing innovation

1 Introduction

Currently, thin-film structures and coatings are widely used in various industries. For instance, the use of wear-resistant coatings increases the stability of the cutting tool [1], or thin-film structures are used in the manufacture of electronic products [2]. The development of technologies for the formation of nanostructures offers new opportunities in the design of high-quality and non-standard equipment, semiconductor integrated circuits, etc.

Methods for obtaining thin-film structures and coatings include magnetron sputtering [3], plasma-based methods [4], thermal spray depositions, e.g., plasma [5] and cold gas-dynamic [6], and other spraying methods.

To ensure a particular set of specified physical and mechanical characteristics, it is often necessary to use multilayer coatings and thin-film structures consisting of an

adhesive sublayer and an essential functional coating. Examples of multilayer coatings are thermal barrier coatings to protect aircraft engines' hot gas path parts [7].

Regardless of the method and purpose of coatings and films, the most critical indicator is the adhesive strength, which determines the reliability and performance of the product on which they are obtained. Adhesion is a very complex phenomenon that depends on many technological parameters of their formation. After process completion, the coating and the film are in a tense state, whereas the residual stresses tend to relax. Stress and adhesive strength largely determine the mechanism to be implemented for their relaxation.

Stresses can be compressive and tensile. If specific limit values are exceeded, they can deform and destroy thin-film structures and coatings. Strong coating adhesion on thin and flexible substrates can lead to their bending, and in the case of poor adhesion, edge peeling can occur. Compressive stresses are a source of swelling and corrugation of coatings, whereas tensile stresses may cause fracture [8].

The total stress of the coating-substrate system is determined by three components: structural, thermal, and compound, which consider external factors. The purpose of this paper is to analyze the thermal component and estimate the magnitude of thermal stresses that occur during the formation of oxide structures on the example of Cu_2O synthesized on copper substrates.

2   Literature Review

It is necessary to know the magnitude and distribution of residual thermal stresses in the coating-substrate system to prevent deformation and destruction of thin-film structures and coatings. A number of papers have been published to develop methods for determining residual stresses and studying the nature of their occurrence depending on various factors [9]. However, due to multifactorial processes and causes that affect the formation of residual stresses, no single mathematical model that would consider all factors, or at least try to do so, was proposed. In addition, many aspects of predicting and controlling the nature and sign of stresses remain open, especially in the field of oxide nanostructures [10].

In many methods of obtaining coatings and thin films, the process temperature is one of the main factors influencing the formation of coatings' physical, mechanical, and operational properties. In some cases, the temperature affects the intensification of the growth processes of coatings and thin films [11, 12]. The operating temperatures of the process influence the formation of residual thermal stresses in coatings and substrates that occur when the system is cooled after forming coatings [13].

In terms of analysis of existing methods for determining the residual stresses occurring in thin films and coatings, currently, no direct way for their determination is known. Various computational and experimental approaches are presented in [8]. According to the developed equations, stress determination is performed "indirectly" with recalculation.

Mathematical modeling of coating formation and residual stresses was given impetus with the advent of modern software computational systems based on the finite element method [14]. Different mathematical models of residual stress formation that occur

during other technological processes vary significantly in the construction method and methods of their implementation. The use of computer technology allows the determination of distribution and magnitude of residual thermal and mechanical stresses, analysis of the coating-substrate system's overall stress-strain state, and determination of critical values.

In addition to experimental methods and methods of numerical modeling, the use of analytical models for the calculation of residual stresses takes an important place. Analytical models based on the classical theory of beam bending were developed to calculate residual thermal stresses arising from changes in ambient temperature [15]. For multilayer coatings, the number of assumptions for calculating the stress-strain state due to thermal loads increases, leading to difficulties in developed models describing the process with reliable accuracy. For instance, it is the assumption about the constancy of physical and mechanical properties of materials, which are a function of temperature [16].

The existing models for calculating thermal stresses are united by the fact that they are all based on Stoney's equation [17]. In the study of thin-film structures, when the coating thickness is much less than the substrate thickness, the deformation of the substrate can be neglected, and the equation of thermal stresses connects the curvature of the system with the thermal load on the coating. As the coating thickness ratio to the substrate thickness increases, the stress gradients become more significant, and the question arises of introducing a characteristic criterion into the equation [18].

Models describing the thermal stress state of single-layer, multilayer coatings with a gradient of properties, composite coatings, and multilayer coatings with an intermediate layer with a gradient of properties are presented in [19].

3   Research Methodology

3.1   Thermal Stresses in Multilayer Coatings

aper uses an analytical model that presented below to calculate thermal stresses [19]. The cause of thermal stresses in the formation of coatings is the cooling of the coating system-substrate from the spray temperature T_d or to ambient temperature T_R.

Significant differences in the thermal expansion coefficients (CTE) of thin-film structure materials and the substrate lead to residual thermal stresses.

Deformations occur during the formation of thin-film structures and coatings at the interface with the substrate, or between the coating layers. Deformations associated with the primary cooling of the coating system can be represented as follows:

$$\Delta\varepsilon = \frac{\sigma_q}{E'_c}, \tag{1}$$

where σ_q is the stresses arising during cooling, E'_c is the effective elastic modulus (Young's modulus).

In the case where the width of the coating system-substrate is commensurate with its thickness, E'_c equals the elastic modulus of the coating ($E'_c = E_c$). Provided that E'_c

corresponds to the biaxial module of a flat system, then in this case $E'_c = E_c/(1 - v)$, where v is the Poisson's ratio.

The coating thickness affects the substrate temperature as it rises. If the temperature gradient of the coating is neglected and in the case of obtaining thin-film structures, when the coating thickness is less than the substrate thickness, the substrate temperature is almost equal to the coating temperature after the growth process, which means that

$$T_s \cong T_d \cong T_c. \tag{2}$$

The Eq. 2 can be used to find thermal residual stresses during secondary cooling [20]. During secondary cooling, the deformation $\Delta\varepsilon_q$ that occurs due to differences in the physical properties of the coating materials and the substrate can be determined as follows

$$\Delta\varepsilon_t = \int_{T_s}^{T_R} \alpha_s(T)dT - \int_{T_d}^{T_R} \alpha_c(T)dT, \tag{3}$$

or

$$\Delta\varepsilon_t = (\alpha_s - \alpha_i)\Delta T = \Delta\alpha\Delta T. \tag{4}$$

where $\alpha_s(T)$, $\alpha_c(T)$ are the substrate and coating CTE, respectively, T_R is the ambient temperature.

After finding the deformation, thermal stresses in the coating system-substrate can be calculated. For this purpose, it is necessary to make the equation of force and momentum balance. It should also be noted that the resulting deformations do not exceed calculating, i.e., the residual stresses are in the region of elastic deformations.

Figure 1 shows the coating-substrate system for the calculation of thermal stresses during its cooling after completion of the spraying process. The following value shall be used further: t_s is the substrate thickness; t_c is the coating thickness; t_i is the thickness of the single i-th applied coating layer n. The number of layers ranges from 1 to n, where the 1st layer is on the interface with the substrate surface with the beginning of the frame of reference $z = 0$. The upper coordinate corresponds to the upper layer of the coating, i.e. $z = t_c$, whereas the lower one corresponds to the lower surface of the substrate, i.e. $z = -t_s$. The coordinate of the interface between the layers of the coating i and $i + 1$ is defined as $z = h_i$. Thus, the correlation between h_i and t_i can be defined as

$$h_i = \sum_{j=1}^{i} t_j (1 \leq i \leq n, 1 \leq j \leq n), \tag{5}$$

where index j is the layer number lying within the range from 1 to i.

Since the coating-substrate system is in an unfixed state, the temperature difference ΔT causes temperature deformations of the substrate $\alpha_s\Delta T$ and in i-th coating layer $\alpha_i\Delta T$. Occurrence of thermal stresses is caused by compliance with a compatibility condition of separate interface shift. These thermal stresses eventually lead to the formation of a bend in the coating-substrate system.

The correlation between normal stresses in the coating σ_i and the substrate σ_s and total deformation of the coating ε_i and the substrate ε_s can be expressed with the following equation

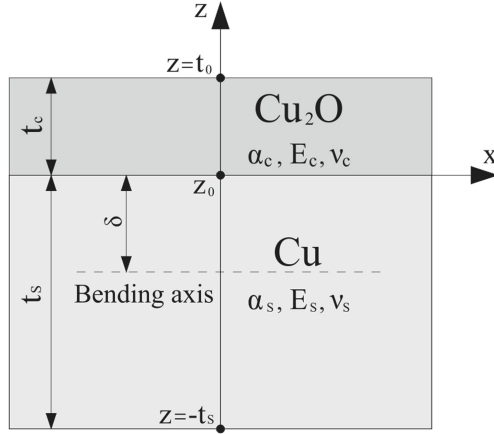$$\sigma_s = E'_s \varepsilon_s, \sigma_i = E'_i \varepsilon_i, \tag{6}$$

Fig. 1. Calculation diagram for determining the thermal stresses of the coating-substrate system.

where $E_s^{'}$ and $E_i^{'}$ is the effective elastic modulus of substrate and coating, respectively.

It is a known fact that the total deformation occurring in the coating layer and the substrate consists of deformation in the corresponding plane (substrate or coating layer) and bending deformation [19].

The deformation leads to the occurrence of forces acting in the substrate plane and i-th coating layer F_s and F_i, respectively. The equilibrium state of the coating-substrate system is that the sum of forces acting on the system must equal zero

$$\sum_{i=1}^{n} F_i + F_s = 0. \tag{7}$$

The second component of complete deformation – bending deformation – occurs due to the bending moment under above forces. The bending deformation of the substrate and the single layers of the coating can be described as follows

$$\varepsilon(K) = K(z + \delta)(-t_s \leq z \leq h_i), \tag{8}$$

where δ is the distance from the axis of bending to the interface between the substrate and the coating ($z = 0$), K is the radius of curvature.

The forces arising from the bending deformation in the substrate and the coating layers lead to the formation of the bending moment M. Compilation of the equation of balance of bending moment relative to the bending axis needs to take into account the forces arising in the substrate planes and the coating F_s and F_i, respectively

$$M + \int_{-t_s}^{0} \frac{F_s}{t_s}(z + \delta)dz + \sum_{i=1}^{n} \int_{h_{i-1}}^{h_i} \frac{F_i}{t_i}(z + \delta)dz = 0. \tag{9}$$

According to the known values of coating deformation ε_s^0, i-th coating layer ε_i^0, radius of curvature K, δ and z, the equation to determine the total deformation in the substrate ε_s and i-th coating layer ε_i can be defined. Substituting the obtained values into Eq. 6, the equation for finding thermal stresses in the substrate σ_s and i-th coating

layer σ_i can be obtained. The same were obtained in the papers of other researchers [21]. In addition, the obtained equations can lead to conclusion that the neutral axis is at a distance of 2/3 of the substrate thickness [19].

3.2 Thermal Stresses in Single-Layer Coatings

In single-l coatings, the Eq. 5 to determine temperses that occur due to different CTE values is used. Zhang et al. [22] introduced criteria to describe the radius of curvature of the coating-substrate system Σ and η. Figure 2 shows an analytical model for calculation
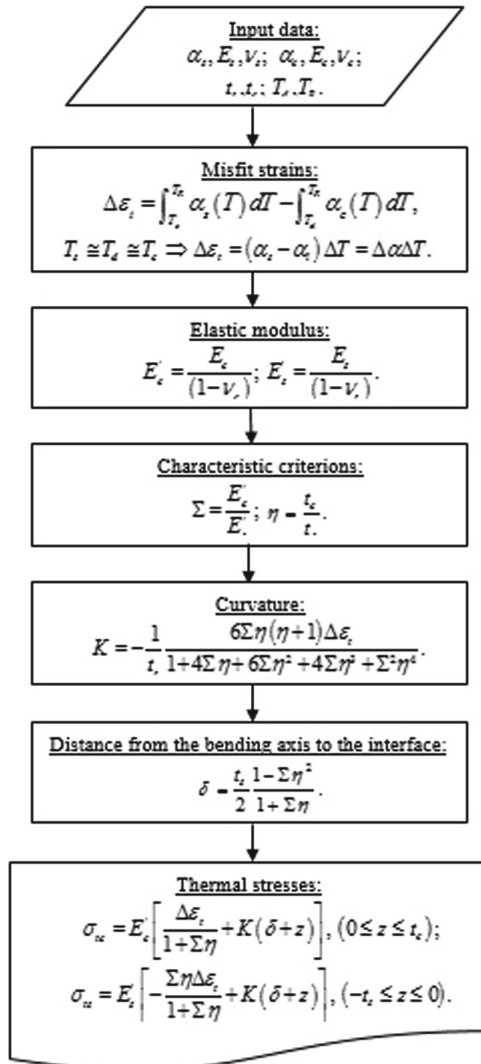
Fig. 2. An analytical model for calculation of thermal stresses in thin films and coatings.

of residual thermal stresses in thin-films and coatings, which was described by Zhang et al. [22].

4   Results

The method of obtaining these structures is following. Cupper substrates were placed in the quartz tube and oxidated in the oxygen atmosphere at controlled pressure (70 Pa, 890 Pa, and atmospheric), temperature (550 °C, 600 °C, 650 °C, and 700 °C.), and oxygen flow rate. To heat samples, an electrical heater was used. Low-pressure conditions in the tube were produced using a rotary pump. After processing, samples were taken out of the chamber and cooled at ambient temperature and pressure [23].

The results of the calculation of the final thermal stresses for oxide structures of Cu_2O synthesized by heating substrates of pure copper in an oxygen environment are presented below.

The following operaresidual thermals of the process were set to calculate thermal residual stresses T_d: 550 °C, 600 °C, 650 °C, and 700 °C. After completion of the formation of oxide layers, the samples were cooled to ambient temperature T_R taken at 20 °C. The thickness of the obtained layer depends on the time in the chamber and is accepted in this study from zero to 0.1 mm. The thickness of copper substrates is 2.0 mm.

The paper considers a coating-substrate system consisting of a copper substrate and an oxide structure of Cu_2O which is cooled at a temperature difference $\Delta T = T_R - T_d$. Stresses in the system occur only due to the temperature difference. The substrate material has a Poisson's ratio E_s, CTE α_s, elastic modulus ν_s, and the coating material is E_c, α_c and ν_c, respectively. The properties of the materials used in the calculations are presented in Table 1.

Table 1. Thicknesses and mechanical-and-physical properties of Cu and Cu_2O [16].

Properties	Layer	
	Cu substrate	Cu2O oxide layer
Layer thickness t, mm	2.0	0.1
CTE α, $\times 10^{-6}$ 1/°C	16.5	0.9
Poisson's ratio E, $\times 10^3$ MPa	123.0	25.0
Elastic modulus ν	0.35	0.462

The results of the residual thermalhermal residual stresses in coating and substrate depending on the temperature difference ΔT are presented in Fig. 3.

As a result of the significant difference in CTE, values, thermal stresses largely depend on the temperature difference, i.e., on the operating temperature of the Cu_2O synthesis process. In the oxide layer, the stresses are always compressive, as the case $\alpha_c < \alpha_s$ is considered. The stress in the substrate varies from tensile to compressive at a distance from the interface of the coating with the substrate. The neutral axis is at a distance $z \approx 1, 3$ mm from the interface, which roughly corresponds to $z = -2t_s/3$. Similar results were obtained in the papers of other authors [22].
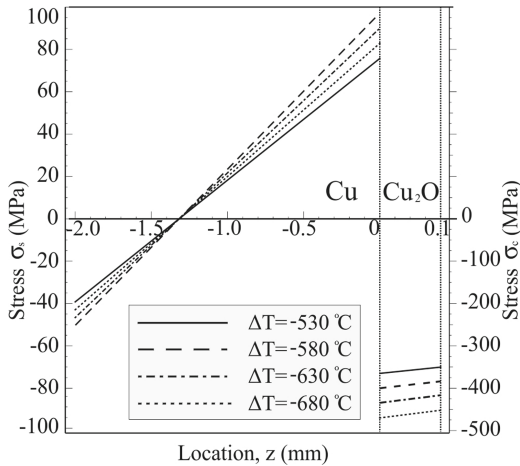
Fig. 3. Calculation results: thermal stress in Cu substrate and Cu$_2$O oxide layer.

5   Conclusions

An analytical model was used to calculate thermal stress in the Cu$_2$O oxide layer obtained on a copper substrate. The obtained results show the thermal stress distribution in a thin film/substrate system that is compressive in the oxide layer and changes the sign within substrate thickness from residual to compressive. According to the calculation results, there is no significant difference in magnitude of residual thermal stress resulting from cooling after the completion of the oxide layer synthesis process from the operating temperature to the ambient temperature. It can be concluded that at higher process temperature, thermal stress in the oxide layer is higher, which can be the reason for crack formation and the initiation of its destruction from the substrate.

References

1. Deng, Y., Chen, W., Li, B., Wang, C., Kuang, T., Li, Y.: Physical vapor deposition technology for coated cutting tools: a review. Ceram. Int. **46**(11), 18373–18390 (2020)
2. Naghdi, S., Rhee, K.Y., Hui, D., Park, S.J.: A review of conductive metal nanomaterials as conductive, transparent, and flexible coatings, thin films, and conductive fillers: different deposition methods and applications. Coatings **8**(8), 278 (2018)
3. Baranov, O., Romanov, M., Wolter, M., Kumar, S., Zhong, X., Ostrikov, K.: Low-pressure planar magnetron discharge for surface deposition and nanofabrication. Phys. Plasmas **17**, 053509 (2010)
4. Levchenko, I., Xu, Sh., Baranov, O., Bazaka, O., Ivanova, E., Bazaka, K.: Plasma and polymers: recent progress and trends. Molecules **26**(13), 4091 (2018)

5. Wang, C.-C., Li, K.-Z., He, D.-Y., Shi, X.-H.: Oxidation behavior and mechanism of MoSi2-Y2O3 composite coating fabricated by supersonic atmospheric plasma spraying. Appl. Surf. Sci. **506**, 144776 (2020)

6. Tan, K., Markovych, S., Hu, W., Wang, Y., Shorinov, O., Wang, Y.: On the characteristics of cold spray technology and its application in aerospace industries. IOP Conf. Ser. Earth Environ. Sci. **719**, 032023 (2021)

7. Krishna Anand, V.G., Parammasivam, K.M.: Thermal barrier coated surface modifications for gas turbine film cooling: a review. J. Therm. Anal. Calorim. **146**(2), 545–580 (2020). https://doi.org/10.1007/s10973-020-10032-2

8. Abadias, G., et al.: Review Article: stress in thin films and coatings: current status, challenges, and prospects. J. Vac. Sci. Technol. A **36**, 020801 (2018)

9. Marzbanrad, B., Jahed, H., Toyserkani, E.: On the evolution of substrate's residual stress during cold spray process: a parametric study. Mater. Des. **138**, 90–102 (2018)

10. Guo, B., et al.: Single-crystalline metal oxide nanostructures synthesized by plasma-enhanced thermal oxidation. Nanomaterials **9**(10), 1405 (2019)

11. Dolmatov, A.I., Polyviany, S.A.: Interaction of solid particles from a gas stream with the surface of a flat nozzle. Metallofizika i Noveishie Tekhnologiithis **43**(3), 319–328 (2021)

12. Canales, H., Cano, I.G., Dosta, S.: Window of deposition description and prediction of deposition efficiency via machine learning techniques in cold spraying. Surf. Coat. Technol. **401**, 126143 (2020)

13. Yang, J., Wang, L., Li, D., Zhong, X., Zhao, H., Tao, S.: Stress analysis and failure mechanisms of plasma-sprayed thermal barrier coatings. J. Therm. Spray Technol. **26**(5), 890–901 (2017). https://doi.org/10.1007/s11666-017-0544-7

14. Zhu, W., Wang, J.W., Yang, L., Zhou, Y.C., Wei, Y.G., Wu, R.T.: Modeling and simulation of the temperature and stress fields in a 3D turbine blade coated with thermal barrier coatings. Surf. Coat. Technol. **315**, 443–453 (2017)

15. Bogdanovich, V., Giorbelidze, M.: Calculation of residual stresses in plasma spray coatings taking into account the build-up process. J. Phys. Conf. Ser. **1368**, 042079 (2019)

16. Liu, N., Sun, J., Wu, D.: Elastic constants and thermodynamic properties of Cu, Cu_2O and CuO from first-principles calculations. Adv. Mater. Res. **335–336**, 328–332 (2011)

17. Wen, J., Wei, Y., Cheng, Y.-T.: Examining the validity of Stoney-equation for in-situ stress measurements in thin film electrodes using a large-deformation finite-element procedure. J. Power Sources **387**, 126–134 (2018)

18. Song, Y., Zhuan, X., Wang, T.J., Chen, X.: Evolution of thermal stress in a coating/substrate system during the cooling process of fabrication. Mech. Mater. **74**, 26–40 (2014)

19. Zhang, X., Wu, Y., Xu, B., Wang, H.: Residual stresses in coating-based systems, part I: mechanisms and analytical modeling. Front. Mech. Eng. China **2**, 1–12 (2007)

20. Zhang, X.C., Xu, B.S., Wang, H.D., Wu, Y.X.: Effects of oxide thickness, Al_2O_3 interlayer and interface asperity on residual stresses in thermal barrier coatings. Mater Design **27**(10), 989–996 (2006)

21. Hsueh, C.H.: Thermal stresses in elastic multilayer systems. Thin Solid Films **418**(2), 182–188 (2002)

22. Zhang, X., Wu, Y., Xu, B., Wang, H.: Residual stresses in coating-based systems, part II: optimal designing methodologies. Front. Mech. Eng. China **2**(2), 125–136 (2007)

23. Baranov, O., Košiček, M., Filipič, G., Cvelbar, U.: A deterministic approach to the thermal synthesis and growth of 1D metal oxide nanostructures. Appl. Surf. Sci. **566**, 150619 (2021)

Erosion Processes on Copper Electrodes Applied to Growth of Nanostructures in Plasma

Yurii Shyrokyi[(✉)] and Gennadiy Kostyuk

National Aerospace University "Kharkiv Aviation Institute", 17, Chkalov Street, Kharkiv 61070, Ukraine
i.shyrokyi@khai.edu

Abstract. The paper describes a theoretical model of erosion processes in electrode spots during vacuum discharge. The proposed model considers the sources and drains of heat in the electrode spots. Temperature fields near the spots and the rate of evaporation of the material during the life of the spot are determined. In turn, this made it possible to determine the erosion coefficient for the electrode spot. To verify the adequacy of the model, calculations were performed for copper electrodes. The dependence of the erosion coefficient on the lifetime of the spot and the current density at the electrodes is obtained. When the current density is more than 10^9 A/m^2, the probability of material emission in the liquid state increases, preventing nanostructures' appearance. For both the stationary and moving spots, the dependences of the erosion coefficient on the lifetime are obtained. The dependencies reveal a significant decrease in the erosion rate with increasing the velocity of the spots. The calculated values of the arc current density coincide in order with the experimental values. The model can be used to find the critical values of technological parameters in obtaining nanostructures for different electrode materials.

Keywords: Industrial innovation · Electrodes · Vacuum arc · Electrode spots · Erosion · Nanostructures

1 Introduction

In modern research, many scientists are studying the issue of obtaining nanostructures in various structural materials. The attention to plasma technologies is based on a wide range of possibilities for their use, for example, for the generation of laser-plasma [1] or deposition of thin metal films [2, 3], as well as a source of energy in space plasma engines [4, 5]. Continuous studies of the processes occurring in the plasma medium [6, 7] and their parameters [8] provide new opportunities for technologies and their application. Issues related to the production of nanostructures in plasma by use of using a vacuum arc in the creation of nanostructured films [9], nanostructured coatings [3], and the cultivation of nanotubes [10] deserve special attention. The processes in a vacuum arc have been considered in detail. Thus, cathodic and anodic processes with both cold and hot electrodes, as well as some processes in the interelectrode plasma, were considered [11, 12]. The loss of material by electrodes in the form of vapor at high values of ionic

current, which contributed to the creation of jets in the cathode spots, was considered. Also, measurements of ion current density in the vacuum arc using refractory anodes of different thicknesses were performed [11, 13]. The evolution of the anode temperature in the vacuum arc using dark solid electrodes was studied [14, 15].

2   Literature Review

Considering the predominant influence of electrode spots on the quality of the arc technologies, many studies of cathode and anode spots in a vacuum arc have been conducted. The behavior of the arc in the transverse magnetic field [16], the grouping of cathode spots, and their reverse motion were considered. The cathode group spots (GSs) were studied during pulse-enhanced vacuum arc evaporation [17]. This study showed the effect of high-pulse current on electron emission, which contributes to a higher expansion rate of GSs. At the same time, studies of the formation and behavior of plasma spots on the surface of titanium films [18, 19] showed that plasma spots with a dense core occur as a result of the interaction of microscopic vortices in the plasma channel and the resulting magnetic field along electrode, which can cause helical plasma spot current. In the study of the discharge of a pulsed vacuum arc with a composite cathode (zirconium deuteride) [8], it was shown that the main supplier of ions in an arc discharge of microsecond length is cathode spots. And consideration of the evolution of a vacuum arc with nanosecond resolution [20] showed that the channel between the electrodes is created in the form of a cathode plasma long before the anode develops significant activity. Theoretical studies were also conducted in [21], where a statistical model of vacuum arc was developed to describe the effect of spontaneous quenching, which shows the cyclic nature of the processes of cathode spots and shows the self-supporting properties of the arc due to explosive emission. Much less attention was paid to the processes on the electrodes of the vacuum arc in the formation of nanostructures in the plasma medium. Thus, studies of the influence of electric and magnetic fields in arc plasma during the synthesis of single-walled carbon nanotubes were performed [22]. Experimental studies of the influence of the nanostructured layer's thickness on the tungsten cathode's physical properties [23] and the erosion rate at the nanostructured copper cathodes [24] were also conducted. Some experiments on arc spots were also carried out [25, 26]. It was shown on the electrodes of nanostructured tungsten that the width of the arc trace increases with the increasing thickness of the nanostructured layer.

Although the processes on the surfaces of the electrodes during the operation of the vacuum arc were studied in detail [11, 14, 16], further studies have shown [27, 28] that some nanostructures in plasma can be obtained in other, rather strict modes. This means that the task of creating a three-dimensional thermal model of erosion processes at the electrodes is urgent, thus allowing more accurately determining the critical regimes and indicating new possibilities for the formation of nanostructures in plasma.

3   Research Methodology

As the analysis of papers [26, 27] showed, the main erosion processes during the discharge in different media are realized mainly in the electrode spots. Therefore, the

development of the model should begin with the consideration of erosion processes in the electrode spots. For the correct theoretical study of erosion processes, we begin work on the consideration of sources and drains of heat in the electrode spots and then analyze the calculation results.

It was shown that the volume and direction of heat transfer from the plasma column of the discharge to the body of the electrode has a decisive influence on the processes and mechanism of erosion of the electrode material [28, 29]. Therefore, we consider possible heat sources and drains in electrodes with fixed spots and spots moving at a certain speed. As shown in experiments, there are both those and other types of spots on the electrodes [29, 30]. First, we consider the source of heat on the surface of the electrodes, which arises due to the transfer of energy by particles. The following expression can represent the heat flux density due to ion bombardment of the cathode surface:

$$q_i = J_k(U_k \cdot \mu_i + U_i)p_k/(1 + p_k), \tag{1}$$

where μ_i is the ion accommodation coefficient in the cathode material; $p_k = J_i/J_e$ is the proportion of ionic current at the cathode; U_k is a cathodic potential drop; j_k is total current density at the cathode; U_i is the ionization potential of the bombardment ion; j_i is the ion current density at the cathode.

The cooling of the cathode spot surface is mainly due to electron emission, as was reported in [27, 29]. The density of the thermal current dissipated by the electrons is determined by the formula:

$$q_e = \left(A_i + \left(e^3 E\right)^{\frac{1}{2}} + 2kT(0, y, z, t)\right)j_e/e, \tag{2}$$

where A_e is electron output work; j_e is electric current density at the cathode.

To determine the heat flux generated by the reverse electric current, we use the following expression:

$$q_{re} = \alpha_e(U_k + 2kT_e)n_e \,\mathcal{V}_e exp\left(-\frac{eU_k}{kT_e}\right)/4e, \tag{3}$$

where α_e is electron accommodation coefficient; T_e is electron temperature; $\mathcal{V}e$ is electron velocity determined by the Maxwell particle velocity distribution; n_e is electron concentration.

Heat generation at the cathode during autoelectron emission (Nottingham heat) can also make a significant contribution to the surface heat source [10, 11] because it is released directly on the simulating surface and adds density to the heat flux:

$$q_N = 9, 3 \cdot 10^{-1} \mu_y E \sqrt{A_e} j_k(0, y, z, t)\left(\frac{1}{\beta_k + 1}\right), \tag{4}$$

where E is the electric field strength near the cathode, V/m; A_e is electron output work, eV; μ_y is the electric field strength gain coefficient.

Considering the emission cooling, reverse electric current, and Nottingham heat, the heat flux density generated by ions for the cathode is defined as:

$$Q_k = q_i - q_e + q_{er} + q_N, \tag{5}$$

At the same time, for the anode, the heat flux generated by the surface heat source with a positive anode potential drop can be described as:

$$Q_a = j_a \mu_a \left(\frac{2kT_e}{3} + U_a + A_e \right), \tag{6}$$

where j_a is current density at the anode; U_a is potential drop near the anode; T_a is electron temperature.

Taking into account the action of ion and electron fluxes on the surface of the anode, the expression for the heat flux density takes the following form for the negative anodic potential drop:

$$Q_a = j_a \left\{ \frac{5k}{2l} (T_e - T(0, y, x, z)) + \frac{j_{af}}{j_0} \left[U_i + |U_a| + \frac{5k}{2l} (T_i - T(0, y, z, t)) \right] + A_e \right\}, \tag{7}$$

where T_e, T_i is the temperature of electrons and ions near the cathode; j_e, j_i is the density of ionic and electric current at the anode; A_e is the work of the electron output from the anode material; j_{af} is a total current density at the anode.

It should be noted that all values in expressions (4)–(7) vary during the life of the spot, depending on the parameters in the area near the electrons.

The heat caused by the action of a volumetric heat source, which acts in the entire volume of the electrode, is found as follows:

$$Q_v = \rho \left[T(x, y, z, t) \right] j^2(x, y, z, t). \tag{8}$$

To solve the thermal problem on the electrodes through the balance equation, heat dissipation must be considered. Thus, in the general case, the heat dissipation due to the shift of the evaporation front can be written in such form:

$$Q_{ev} = C_v \left[T(x, y, z, t) \right] V_{ev.f} \frac{\partial T(x, y, z, t)}{\partial x}, \tag{9}$$

where $C_v \left[T(x, y, z, t) \right]$ is the heat capacity of the electrode material at this point at the appropriate temperature T (x, y, z, t), which is given by the array using experimental values of this value or by linear extrapolation; $V_{ev.f}$ is the value of the shear rate of the evaporation front for the case when the electrode surface does not have a layer of metal superheated above the melting point, i.e., $T(0,y,z,t) < T_{mil}$, (T_{mil} is the effective melting point of the electrode material, taking into account the heat consumption for melting). This shear rate can be defined as follows:

$$V_{ev.f} = \frac{1}{\gamma} \sqrt{\frac{M}{2\pi R T(0, x, y, z, t)}} \left[exp \left(A - \frac{B}{T} \right) - P_{res.} \right], \tag{10}$$

where A and B are tabulated constants [14]; R is a gas constant; γ is the density of the electrode material; M is the atomic weight of the heated electrode material; $P_{res.}$ is residual gas pressure.

When a layer of superheated or molten metal appears on the surface of the electrode, the Frenkel mechanism is realized. The rate of displacement of the evaporation front will be found as follows:

$$V_{ev.f} = V_o exp\left(-\frac{T_s}{T(0, x, y, z, t)}\right), \tag{11}$$

where V_0 and T_s are the shear rate of the evaporation front and the surface temperature of the spot at steady-state evaporation, determined by Eq. (6).

To determine the heat flux removed from the elementary volume of thermal conductivity, we use the expression:

$$Q_{th.c.} = C_v\big[T(x, y, z, t)\big] \cdot \varepsilon\big[T(x, y, z, t)\big]\Delta T(x, y, z, t), \tag{12}$$

where ε is the coefficient of thermal conductivity.

Heat supply to the surface of the spot leads to an increase in heat flux density due to plasma radiation, which we find by the expression:

$$Q_{r.p} = b_p\sigma T_p^4, \tag{13}$$

where b_p is the degree of blackness of the plasma; σ is the Stefan-Boltzmann constant; T_p is the plasma temperature.

Thus, the heat dissipation from the spot due to radiation is calculated by the formula of Stefan-Boltzmann:

$$Q_r = b\sigma\big[T(0, y, x, t)\big]^4, \tag{14}$$

The decrease in the density of the heat flux at the electrode due to the heat dissipation by evaporation is determined by the formula:

$$Q_{ev} = F_{ev}\gamma V_f, \tag{15}$$

where F_{ev} is the latent heat of vaporization; V_f is the shear rate of the evaporation front.

Moreover, if the surface temperature is less than the board temperature, then V_f is found by expression (10).

Heat exchange between the electrodes (filler) and gas background at a sufficient cost of the working fluid can be described as convective:

$$Q_{con} = \alpha_{con}\Delta T_{lg}, \tag{16}$$

where α_{con} is the heat transfer coefficient of conventions; T_{lg} is the average logarithmic heat transfer temperature.

Heat exchange in the spot area also occurs due to the movement of spots. The heat flux removed by the moving spot is defined as follows:

$$Q_{v.sp} = C_v\big[T(x, y, z)\big]V_{sp}\frac{\partial T(x, y, z, t)}{\partial y}, \tag{17}$$

where V_{sp} is the speed of movement of the heat source (speed of electrodynamic displacement or anti-ampere motion for some modes of the electrode spot).

Taking into account the above sources, both heat sources and drains, the energy balance in the elementary volume of the spot (Fig. 1) can be written in the form:

$$Q_{k.a} - Q_{v.sp} = Q_m + Q_{ev.} + Q_v - Q_{th.e},$$ (18)

The boundary conditions for this equation will take into account the surface heat source and the change in the intensity of the surface heat source due to plasma-electrode radiation, as well as heat dissipation with metal evaporation:

- when $t < T_l$: $-\frac{\partial T(x,y,z,t)}{\partial t} = \frac{Q_1}{\lambda} - \frac{Q_{ev}}{\lambda} + \frac{\sigma}{\lambda}\left[b_p \sigma T_p^4 - bT^4(0, y, z, t)\right] - \frac{Q_{can}}{\lambda}$, if the size of the spot will be $\sqrt{z^2 + (y - V_p t)^2} \le R$, then $Q_1 = Q_s$, and $\sqrt{z^2 + (y - V_p t)^2} > R$, then $Q_1 = 0$, where R is the radius of the spot;
- when $t > T_l$: $Q = 0$, the boundary conditions on the surface x_e, y_s, y_e, z_s, z_e can be written as follows: if $t = T_l = t_s$, then $x_e = \sqrt{6at_s}$, $y_s = -R - \sqrt{6at_s}$, $y_s = R + \sqrt{6at_s} + V_p\tau_p$, $z_s = -R - \sqrt{at_s}$, $z_e = R + \sqrt{at_s}$;
- which means: $T(x_e, y, z, t) = T(x, y_s, z, t) = T(x, y_e, z, t) = T(x, y, z_s, t) = T(x, y, z_e, t) = T_s$,

The area of the electrode space with coordinates $x_e = 0$, y_s, y_e, z_s, z_e is shown in Fig. 1.
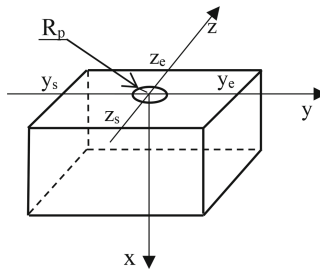

Fig. 1. Scheme of the electrode fraction near the electrode spot.

4   Results

These coordinates limit the area of space in which the problem of thermal conductivity is considered. The initial conditions are: $t = 0$, $T(x, y, z, 0) = T_s$. The solution of the thermal Eq. (18) determines the temperature field near the spot on the electrode, and the integration of the rate of evaporation on the surface of the electrode for twice its lifetime, gives the amount of evaporated mass:

$$M_{ev} = \int\limits_{z_s}^{z_e} \int\limits_{y_s}^{y_e} \int\limits_{0}^{2t_l} V_{ev.f}\left[T(0, y, z, t)\right] dz dy dt,$$ (19)

In experimental studies of the composition of the erosion with an electrode spot, emissions of liquid metal in the form of droplets are observed in almost all modes of discharge [30]. Theoretical works on erosion consider a large number of options for metal emissions [29, 30]. Based on this, the condition of emission of the liquid phase should consider a condition when the pressure created by the forces emitting the metal exceeds the pressure created by the forces holding it, considering their directions. The erosion coefficient for the electrode spot is defined as the ratio of the evaporated mass M_{ev} to the amount of charge transferred in the spot. The magnitude of the charge is defined as:

$$q_{\sum} = \int\limits_{z_s}^{z_e} \int\limits_{y_s}^{y_e} \int\limits_{0}^{2t_l} j(0, y, z, t)dzdydt, \qquad (20)$$

where $j(0, y, z, t) = j_{en}$, when $\sqrt{z^2 + (y - V_p t)^2} > R$.

Then the erosion coefficients are found as: $k_1 = M_{ev}/q_{\sum}$,

Calculations were carried out to check the adequacy of the proposed model for copper electrodes. The cathode potential drops and the ion accommodation coefficient were taken as averages for copper. As a result of theoretical calculations, the dependences of the erosion coefficient on the spot lifetime were obtained for both the anode and the cathode (Figs. 2, 3). The calculations were carried out for different current densities $10^8 \dots 10^{10}$ A/m^2 and for different velocities of movement of spots 1 m/s $\dots 0.5 \cdot 10^2$ m/s.
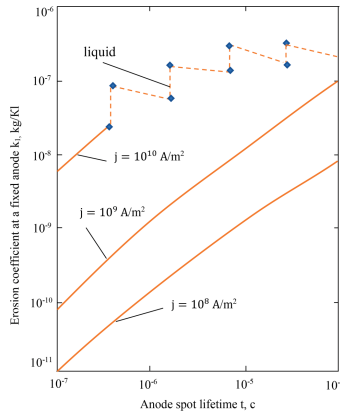

Fig. 2. Dependence of the erosion coefficient on the lifetime of the spot on the anode.

As we can see from the obtained dependences, with an increase in the current density to 10^9 A/m^2, the erosion coefficient also changes by order of magnitude, increasing to 10^{10} A/m^2 by almost two orders of magnitude at the same spot lifetime (Fig. 2). Also, at a current density of 10^{10} A/m^2, discontinuities of the first kind appear, indicating metal ejection in a liquid state. This is confirmed experimentally [11, 25]. All this indicates the excess of the pressure forces that facilitate the removal of liquid metal over the surface

tension forces. All of the above indicates an excess of the pressure forces that facilitate the removal of liquid metal over the surface tension forces. At the same time, the height of these discontinuities decreases with an increase in the lifetime of the spot. This is obviously due to the greater heating of the electrode in the spot area, and the subsequent emissions of metal require large expenditures of energy. The obtained dependences of the erosion coefficient on the lifetime of a moving spot (Fig. 3) show decreasing the erosion coefficient for moving spots.
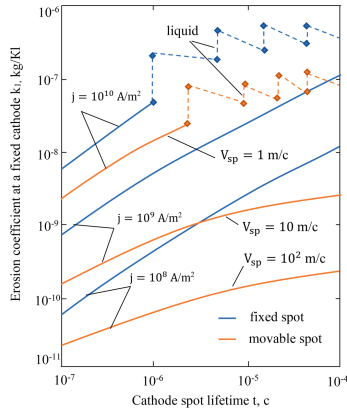

Fig. 3. Dependence of the erosion coefficient on the lifetime of the spot on the cathode.

So, the spot speed of 1 m/s leads to a noticeable decrease in the erosion coefficient, and this is significant at the same current densities and a shorter spot lifetime. At a spot speed of 10 m/s, the erosion coefficient decreases by order of magnitude for all the lifetimes of the spot and the same current densities. We can note that even at low velocities of the spot movement, the range of parameters at which liquid metal is ejected decreases (Fig. 3).

5   Conclusions

A theoretical model that describes erosion processes in electrode spots is developed. The main result of the model is the determination of modes where a high probability of ejection of the electrode material in the liquid phase occurs, which prevents the formation of nanostructures. A system with copper electrodes was chosen as a test model since it is widely used to obtain copper oxide nanostructures. The erosion coefficients were calculated for a moving and stationary spot depending on its lifetime. It was revealed that the ejection of the liquid phase does not occur at a current density of less than 10^{10} A/m^2. During the intense modes (10^{10} A/m^2), the ejection of the liquid phase occurs in spots, the lifetime of which exceeds 1 μs. In this case, for the same spot lifetime ($t > 1$ μs), the probability of the liquid phase ejection for a stationary spot is an order of magnitude higher than for a moving spot. Thus, the speed of motion of the spot is an important factor in the formation of nanostructures. This parameter can be controlled,

for example, by using a magnetic field of a certain configuration. The lifetime of the spot can be influenced by changing the surface roughness. The proposed model is a useful tool for determining the technological parameters of the plasma medium during the production of nanostructures. In the future, the model is planned to be used to determine the modes of formation of one- and two-dimensional copper oxide nanostructures in a glow discharge at elevated oxygen pressures in a chamber (more than 1000 Pa) [31, 32], and formation of nanostructures in undersurface layers [33, 34].

References

1. Wang, D., Namihira, T.: Nanosecond pulsed streamer discharges: II. Physics, discharge characterization and plasma processing. Plasma Sour. Sci. Technol. **29**(2), 023001 (2020)
2. Beilis, I.I., Boxman, R.L.: Thin film deposition by plasma beam of a vacuum arc with refractory anodes. In: Pogrebnjak, A.D., Novosad, V. (eds.) Advances in Thin Films, Nanostructured Materials, and Coatings. LNME, pp. 1–15. Springer, Singapore (2019). https://doi.org/10.1007/978-981-13-6133-3_1
3. Glukhov, O.V., Kolpakov, M.G., et al.: Nanostructured coatings based on amorphous carbon and gold nanoparticles obtained by the pulsed vacuum-arc method. J. Nano- Electron. Phys. **11**(4), 04019 (2019). https://doi.org/10.21272/jnep.11(4).04019
4. Zolotukhin, D., Keidar, M.: Optimization of discharge triggering in micro-cathode vacuum arc thruster for CubeSats. Plasma Sourc. Sci. Technol. **27**(7), 074001 (2018)
5. Levchenko, I., Xu, S., Teel, G., et al.: Recent progress and perspectives of space electric propulsion systems based on smart nanomaterials. Nat. Commun. **9**, 879 (2018)
6. Balanovskiy, A.E.: Digital visualisation of the process of heating and melting of metal in arc discharge with a non-consumable electrode. Weld. Int. **31**(6), 467–476 (2017)
7. Babaeva, N.Y., Zhang, C.J., Hou, Q.X., et al.: The role of fast electrons in diffuse discharge formation: monte Carlo simulation. Plasma Sourc. Sci. Technol. **26**(8), 085008 (2017)
8. Nikolaev, A.G., et al.: Effect of the discharge parameters on the generation of deuterium ions in the plasma of a high-current pulsed vacuum arc with a composite zirconium deuteride cathode. Tech. Phys. **62**(5), 701–707 (2017). https://doi.org/10.1134/S1063784217050218
9. Medhisuwakul, N., Pasaja, S., et al.: Development and application of cathodic vacuum arc plasma for nanostructured and nanocomposite film deposition. Surf. Coat. Technol. **29**, 36–41 (2013)
10. Timerkaev, B.A., Shakirov, B.R., Timerkaeva, D.B.: Creation of silicon nanostructures in electric arc discharge. High Energy Chem. **53**(2), 162–166 (2019). https://doi.org/10.1134/S0018143919020152
11. Beilis, I.: Cathode spot jets. Velocity and ion current. In: Plasma and Spot Phenomena in Electrical Arcs. Springer Series on Atomic, Optical, and Plasma Physics, vol. 113 (2020)
12. Baranov, O., Romanov, M.: Current distribution on the substrate in a vacuum arc deposition setup. Plasma Process. Polym. **5**, 256 (2008)
13. Baranov, O., Romanov, M., Fang, J., Cvelbar, U., Ostrikov, K.: Control of ion density distribution by magnetic traps for plasma electrons. J. Appl. Phys. **112**(7), 073302 (2012)
14. Beilis, I.I., Koulik, Y., et al.: Anode temperature evolution in a vacuum arc with a blackbody electrode configuration. IEEE Trans. Plasma Sci. **45**(8), 2115–2118 (2017)

15. Anders, A.: The evolution of ion charge states in cathodic vacuum arc plasmas: a review. Plasma Sourc. Sci. Technol. **21**(3), 035014 (2012)
16. Beilis, I.I.: Vacuum arc cathode spot grouping and motion in magnetic fields. Trans. Plasma Sci. **30**(6), 2124–2132 (2002)
17. Ma, Y., Gong, C., Tian, X., Chu, P.K.: Imaging and motion of cathode group spots during pulse-enhanced vacuum arc evaporation. Vacuum **139**, 37–43 (2017)
18. Hermanns, P., Kogelheide, F., Bracht, V., Rie, S., et al.: Formation and behaviour of plasma spots on the surface of titanium film. J. Phys. D Appl. Phys. **54**(8), 085203 (2020)
19. Böddeker, S., Bracht, V., Hermanns, P., et al.: Anode spots of low current gliding arc plasmatron. Plasma Sourc. Sci. Technol. **29**(8), 08LT01 (2020)
20. Zhou, Z., Kyritsakis, A., Wang, Z., et al.: Direct observation of vacuum arc evolution with nanosecond resolution. Sci. Rep. **9**, 7814 (2019)
21. Mesyats, G.A.: Ecton mechanism of the cathode spot phenomena in a vacuum arc. IEEE Trans. Plasma Sci. **41**(4), 676–694 (2013)
22. Keidar, M., Shashurin, A., Li, J., Volotskova, O., et al.: Arc plasma synthesis of carbon nanostructures: where is the frontier? J. Phys. D Appl. Phys. **44**(17), 174006 (2011)
23. Barengolts, S.A., Mesyats, V.G., Tsventoukh, M.M., Kajita, S., Hwangbo, D., Ohno, N.: Effect of the nanostructured layer thickness on the dynamics of cathode spots on tungsten. IEEE Trans. Plasma Sci. **46**(11), 4044–4050 (2018)
24. Rao, L., Munz, R.J., Meunier, J.L.: Vacuum arc velocity and erosion rate measurements on nanostructured plasma and HVOF spray coatings. J. Phys. D Appl. Phys. **14**(40), 4192–4201 (2007)
25. Hwangbo, D., Kajita, S., Barengolts, S.A., Tsventoukh, M.M., Ohno, N.: Transition in velocity and grouping of arc spot on different nanostructured tungsten electrodes. Results in Physics **4**, 33–39 (2014). https://doi.org/10.1016/j.rinp.2014.03.001
26. Kajita, S., Ohno, N., Takamura, S., Tsuji, Y.: Direct observation of cathode spot grouping using nanostructured electrode. Phys. Lett. A **373**(46), 4273–4277 (2009)
27. Levchenko, I., Romanov, M., Baranov, O., Keidar, M.: Ion deposition in a crossed E × B field system with vacuum arc plasma sources. Vacuum **72**(3), 335–344 (2003)
28. Kostyuk, G., Popov, V., Shyrokyi, Y., Yevsieienkova, H.: Efficiency and performance of milling using cutting tools with plates of a new class. In: Tonkonogyi, V., et al. (eds.) Inter-Partner 2020. LNME, pp. 598–608. Springer, Cham (2021). https://doi.org/10.1007/978-3-030-68014-5_58
29. Baranov, O.O., Fang, J., Rider, A.E., Kumar, S., Ostrikov, K.: Effect of ion current density on the properties of vacuum arc-deposited TiN coatings. IEEE Trans. Plasma Sci. **41**(12), 3640–3644 (2013)
30. Beilis, I.I.: Cathode spot development on a bulk cathode in a vacuum arc. IEEE Trans. Plasma Sci. **41**(8), 1979–1986 (2013)
31. Breus, A., Abashin, S., Serdiuk, O., Baranov, O.: Linking dynamics of growth of copper oxide nanostructures in air. In: Nechyporuk, M., Pavlikov, V., Kritskiy, D. (eds.) ICTM 2021. LNNS, vol. 367, pp. 555–564. Springer, Cham (2022). https://doi.org/10.1007/978-3-030-94259-5_47
32. Breus, A., Abashin, S., Serdiuk, O.: Carbon nanostructure growth: new application of magnetron discharge. J. Achiev. Mater. Manuf. Eng. **109**(1), 555–564 (2021). https://doi.org/10.5604/01.3001.0015.5856
33. Kostyk, K., Kostyk, V., Akimov, O., Kamchatna-Stepanova, K., Shyrokyi, Y.: Ensuring the high strength characteristics of the surface layers of steel products. In: Tonkonogyi, V., Ivanov, V., Trojanowska, J., Oborskyi, G., Pavlenko, I. (eds.) InterPartner 2021. LNME, pp. 292–301. Springer, Cham (2022). https://doi.org/10.1007/978-3-030-91327-4_29
34. Shyrokyi, Y., Kostyuk, G.: Investigation of the influence of crystallization energy on the size of nanostructures during copper ion-plasma treatment. In: Nechyporuk, M., Pavlikov, V., Kritskiy, D. (eds.) ICTM 2021. LNNS, vol. 367, pp. 57–66. Springer, Cham (2022). https://doi.org/10.1007/978-3-030-94259-5_6

An Increase in Tribocharacteristics for Highly Loaded Friction Units of Modern Equipment

Alexander Stelmakh[1,2] , Ruslan Kostunik[2] , Volodymyr Radzievskyi[2] ,
Sergii Shymchuk[3(✉)] , and Natalia Zaichuk[3]

[1] Beijing Institute of Technology, 5, Zhongguancun Street, Haidian Qu, China
[2] National Aviation University, 1, Liubomyra Huzara Ave, Kyiv 03058, Ukraine
[3] Lutsk National Technical University, 75, Lvivska Street, Lutsk 43018, Ukraine
s.shimchuk@lntu.edu.ua

Abstract. The paper highlights the methodological problem of neglecting the presence of air microbubbles in the oil film during the study of the contact of tribological pairs. This phenomenon is usually explained as hydrodynamic bubbling. To eliminate this effect, special additives are used. An installation for research of a two-phase oil-vapor-gas mixture modified by a diffuser pump-generator has been developed. An express method of testing lubricants is proposed. The device for controlling an aggregate-phase condition of an oil environment is made. Comparative tribological tests of homogeneous liquid oil and its oil-vapor-gas suspension are carried out. The ways of controlling the current aggregate-phase state of lubricating media are revealed. The presence of low-pressure microbubbles in the lubricating medium, which occur in the diffuser areas and are delivered to all friction nodes, leads to their setting and damping of currents in the confusing areas and their easy expansion - in the diffuser areas of tribocontact. The study opens the way for the production of high-performance two-phase lubricants and methods to control their current physical and phase state in circulating lubrication systems, which is still an unresolved and urgent problem of the new field of knowledge about unstable environments such as two-phase oil-vapor mixture.

Keywords: Product innovation · Bubbles · Circulation · Liquid · Lubrication · Mixture · Phase state · Physical state

1 Introduction

Lubricating fluid is traditionally considered a solid-fluid, the tribological properties of which are determined only by the viscosity-temperature characteristics according to known methods in the steady-state of the fluid [1, 2]. In normal atmospheric conditions in lubricants, there are dissolved air gases (about 12%) are usually neglected [3]. It is believed that the formation of gas bubbles in lubricating fluids is a harmful factor and is identified with foams, the formation of which is explained as hydrodynamic bubbling, the capture of air by a fluid moving at the interface [4, 5]. Therefore, use antifoam additives [6]. The formation of bubbles in working hydraulic systems is indeed

an undesirable phenomenon due to the high requirements for hydraulic fluid that should not be compressed [7]. In other systems, for example, in oil and gas, on the contrary, bubbles are used as a transport medium [8, 9].

The study aims to develop a technology for controlling the current physical and phase state of lubricants to optimize the state of their main consumer parameters (viscosity, density, dielectric constant, and current operating temperature) and consider the type of commercial lubricants of different viscosities to improve tribotechnical characteristics and the resource of highly loaded friction units [10, 11].

2   Literature Review

About 70…80% of wear of parts of friction units of engines of equipment occurs at the time of their start, which from the standpoint of the adhesive-hydrodynamic model of friction and wear is because all friction units from the beginning of their movement to the normal mode when the limit friction mode is realized. It is in these transient modes when epitropic liquid crystal boundary layers with dense packing are formed on the friction surfaces after long settling, and the oil is in a homogeneous single-phase state. Under such conditions, the adhesive interaction and wear of the friction surfaces take place [12–14].

The resource and operational characteristics of rolling tribosystems and, consequently, the efficiency of machines and mechanisms, in general, depend on the quality of lubrication of their functional surfaces. As a result of the increase in efficiency of cleaning responsible tribosystems of cars and lubricating working liquids, the resource of mechanisms can be increased by 2…3 times, and in cases with precision knots - to 10 times. Thus, ensuring and controlling the purity of lubricants of tribosystems improves their performance and increases resources [15, 16]. One way to increase the life and enhance the performance of tribosystems is to effectively remove air bubbles from the working lubricant [17].

The elastohydrodynamic theory of friction still adheres to the assumption of continuity of the lubricating film. The presence and presence of nano- and microbubbles in the friction medium are not considered. However, in the diffuse regions of all tribocontacts under conditions of comprehensive stretching, they are formed and generated in volume [18, 19]. Using two-phase oil-vapor-gas lubricants is promising and requires further research and development of criteria and tools to control the current aggregate-phase state of these fluids in circulating lubrication systems to determine and optimize their parameters [20].

3   Research Methodology

Based on the adhesive-hydrodynamic model of friction and wear and the phenomenological model of oil-vapor-gas lubricants formation, a laboratory system for modeling a two-phase oil-vapor-gas mixture with the possibility of regulating its current aggregate-phase state (Fig. 1) was developed and modified pump-generator (TPG) [9, 21]. The main idea of such generator pumps was to use the phenomenon of comprehensive stretching of lubricating layers in the diffuse areas of tribocontacts, which leads to the generation

of vapor-gas microbubbles in the lubricating fluid and injection of this mixture in the confusing areas of tribocontacts [22].

Fig. 1. The scheme of the laboratory system for modeling a two-phase oil-vapor-gas mixture with the possibility of adjusting its current physical-phase state: 1 - crankcase of the power plant; 2 - lubricating medium; 3 - FPS sensor; 4 - control and regulation module; 5 - TPG two-phase oil-vapor-gas mixture.

Therefore, to study the main performance properties of commodity transmission, hydraulic and motor groups of oils with standard additives, the developed express test method with the appropriate modification was used. The technique consists of four or six stages, depending on the operating conditions of the studied group of lubricants. Step-by-step tests make it possible to control the formation of secondary structures (SS) on the working surfaces of samples of the friction test unit and evaluate the antiwear and antifriction properties of commercial fuels with regular additives over time, namely:

– after the selected axial load is carried out in the contact of the friction unit of the laboratory device ASK-01 (Fig. 2a) and the drive shaft drive requires the required sliding friction speed (Table 1), the countdown of the test time to the passage of the counterbody 500 m in the area contact. This stage reflects the beginning of the formation of the aircraft on the working surface of the counter-sample during friction;

Table 1. Correction of express methods depending on the operating conditions of different groups of commercial oils.

Groups of oils	Axial load, N	Sliding speed, m/s	Number of stages
Motor	230	0,4	4
Transmission	300	0,6	6
Hydraulic	230	0,4	4

Table 1. (*continued*)

Groups of oils	Axial load, N	Sliding speed, m/s	Number of stages
Refrigerators	300	0,6	4
Transformer	230	0,4	4

– the second, third, fourth, and fifth (for transmission oils) stages are carried out by the same counterboby on a new surface of the stationary sample within 500 m of a path of friction. These stages determine the completion of the formation of the SS;
– the fourth (or sixth for transmission oils) stage of friction occurs under the same initial conditions as the previous ones, but during 3000 m of the path, simulating longer-term tests developed in the first three (or five) stages of friction of SS and tests their antiwear properties in the tribochemically modified lubricating medium.

As a result of three or five short-term and one long-term friction stages, four or six wear marks are formed on the working surface of the flat sample. The wear criterion is the linear wear of the material and the volume of the worn material, considering the plastic deformation (track friction) and the density [23].

The volume of worn material was measured with a laser profilograph-profilometer LSDFPP (Fig. 2b) and linear wear - on the profilograph-profilometer "Caliber M – 201". Rapid comparative analysis of the working surfaces of the model samples before and after the tests was performed on a scanning electron microscope REM-106I (Fig. 2c).
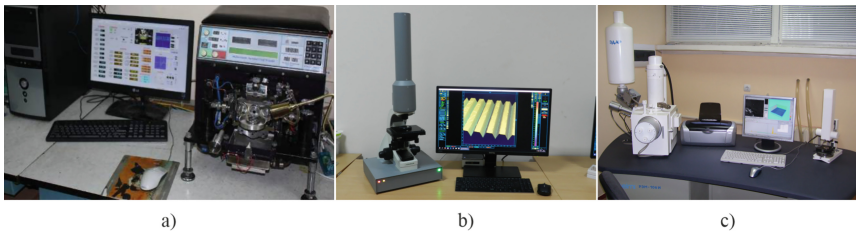

a)   b)   c)

Fig. 2. Laboratory complex: a) laboratory friction device ASK-01; b) laser profilograph-profilometer LSDFMP; c) raster electron microscope REM-106I.

To determine the optimal current aggregate-phase state of commercial lubricants in circulating lubrication systems in laboratory conditions, a device for monitoring the current aggregate-phase state of the working fluid was made and connected to the laboratory friction device ASK-01 (Fig. 3).

Tribological tests on the friction device ASK-01 were performed as follows: sliding is carried out by rotating the roller (counterbody), fixed perpendicular to a stationary flat sample, i.e., contact of the counterbody with the sample occurs on the forming cylinder of the counterbody, which in turn realizes contact. The sample brought to the roughness of $R_a \leq 0.02 \, \mu m$ was placed in a bath filled with the experimental lubricating medium, the

8

Fig. 3. The complex of devices of comparative estimation of tribological characteristics of commodity oils at the optimization of their current aggregate-phase state.

antiwear properties of which need to be determined. The sample, counterbody, bath, and fasteners were thoroughly washed in aviation gas and B-70 gasoline before the tests, then wiped dry with a clean cloth and dried at room temperature. The drive shaft's rotation speed with the counterbody was kept constant in automatic mode and was 0.2 m/s. The axial load occurred with a certain acceleration to the pre-determined experimentally given value given in (Table 1) and was maintained at this level during the tests. Each test sample of the commercial lubricant was tested five times.

When the linear speed of the rotating model shaft of the TPG rotor was increased to 0.2…0.3 m/s, all commercial oils were in a transparent state for a long time during the tests. A further increase in the linear velocity (up to 0.4…0.6 m/s) led to their turbidity, while the accumulation of microbubbles was visually observed (Fig. 4a).
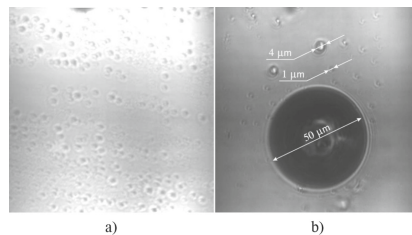

Fig. 4. Oil saturation with microbubbles (diameter $< 1\ \mu m$).

After reaching the calculated speed according to the test method, the oil rapidly became opaque due to the saturation of two types of microbubbles: some of which arose due to bubbling, and others - due to tribocavitation in the diffuse regions of all TPG gaps. Figure 4a shows the appearance of microbubbles, which was obtained by scanning in the differential-phase mode on the LSDFPP in the configuration "on the lumen", the picture (Fig. 4b) - taken in the calibration mode.

According to the results of comparative tribological tests of oils, it is knowing their parameters according to technical conditions and taking into account its current operating parameters (viscosity, density, and dielectric constant), the optimal range of speeds of the main drive TPG for each commercial lubricating medium depending on its type and viscosity (Table 2).

Thus, comparative tribological tests of homogeneous liquid oil and its oil-vapor-gas suspension were performed on a laboratory device ASK-01 under the following conditions: initial contact stresses in surfaces (steel 100Cr6, HRC 58…62, Ra < 20 nm), linear sliding speed - from 0.2 to 0.6 m/s.

The obtained data were automatically processed by the on-board controller of the control unit of the friction device ASK-01, according to which tables and graphs are built according to the appropriate programmed form, which is stored as a library file on a personal computer (Fig. 5).

Table 2. The results of experimental tests of commercial oil of different viscosities.

Test environment	Calculation criterion (K)	Wear of material I, μm	Coefficient of friction, μ_f	Range of speeds of rotation of a rotor of TPG, rpm
Transformer oil T-1500	16,3	1,192	0,09	1550…1650
Hydraulic oil AMG-10	25,5	0,267	0,039	1975…2025
Compressor oil HF 22-24	34,3	0,699	0,078	2350…2450
Turbine oil MS-8P	15,7	0,366	0,058	1300…1400
Turbine oil MS-8RK	16,1	0,343	0,051	1750…1850
MS-20 engine oil	42,1	0,567	0,07	2350…2450
PMS-5 silicone oil	12,9	1,934	0,11	1100…1300
PMS-10 silicone oil	27,0	1,734	0,098	2150…2350

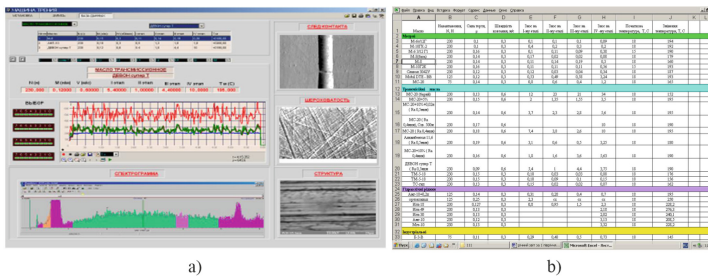a)   b)

Fig. 5. The appearance of the interface of the working panel (a) and the database (b) tribological of lubricants and additives to them.

After that, it is possible to correct and add missing and necessary for further analysis of data, tables, and graphics. The software works according to an algorithm that provides data processing and analysis at all stages of tribotechnical tests. Criteria for test fuel and additives' operation are the maximum, minimum, or average value of their defined tribocharacteristics, namely: friction forces, temperature, wear over time, maximum wear. The control of the current aggregate-phase state of lubricating lubricants in determining the main consumer parameters (viscosity, density, dielectric constant, and current operating temperature) to optimize their condition further and take into account the type of applied commercial lubricants of different viscosities was developed and created layout of the device for monitoring the current physical and phase state of the working fluid.

4   Results

The test results showed a significant (on average 2 times) decrease in wear intensity with a decrease of 20...25% of the average value of friction force and the level of its oscillations under other equal test conditions.

This is explained by the increase in the compression ratio of the lubricating medium due to the presence of steam-gas microbubbles formed in the base oil (Fig. 5). It also explains the 2.5-fold decrease in the level of oscillations of the friction force during tests and wear intensity of working friction surfaces, which occurs in the diffuser contact zone, where the presence of vapor cavities reduces the degree of vacuum, the amount of additional load and desorption of lubricating layers. In this case, the wear intensity during the long testing stage in high-molecular hydrocarbon lubricants (MS-8P, MS-20) is not a constant value but decreases over time. This indicates the formation on the friction surfaces of secondary structures, which further affects the intensity of wear due to their interaction with the tribochemically altered environment. Confirmation of the formation of secondary structures is the painting of the actual friction surfaces, the color and intensity of which are different after work in different environments. The appearance of the moving sample and the wear trace (3D model) on the stationary sample after sliding friction in the lubricant MS-8P are presented in (Fig. 6).
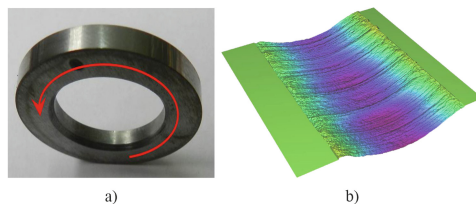

a)   b)

Fig. 6. Type of moving sample (a) and the trace of wear (b) after the tests.

During the tests of commercial oils of different viscosities, there was a change in their physical-phase state (from liquid to optimally saturated with bubbles), which was evaluated both visually and by certain current criteria and parameters of the input FPS sensor at certain values of rotor speed TPG (Table 3). The viscosity, density, and constant

Table 3. The results of comparative tribotechnical tests commercial oils of different viscosities.

Test environment	Liquid state		Two-phase state	
	Wear of material I, µm	Coefficient of friction, μ_f	Wear of material I, µm	Coefficient of friction, μ_f
Transformer oil T-1500	1,739	0,106	1,192	0,09
Hydraulic oil AMG-10	0,623	0,052	0,267	0,039
Compressor oil HF 22-24	1,233	0,098	0,699	0,078
Turbine oil MS-8P	0,776	0,074	0,366	0,058
Turbine oil MS-8RK	0,728	0,066	0,343	0,051
MS-20 engine oil	0,934	0,081	0,567	0,07
PMS-5 silicone oil	2,111	0,135	1,934	0,11
PMS-10 silicone oil	1,997	0,128	1,734	0,098

dielectric product are determined by the most sensitive criterion (K, kg/ms) to the current aggregate-phase state of lubricating liquids. It is known that lubricants have a relative dielectric constant of 2.5…3.5, and in the air, about 1.0 (whereas in water 81). In the process of oil saturation with oil-vapor-gas tribocavitation microbubbles, the dielectric constant naturally decreases to the values of 1.5…1.8, almost 2 times.

As a result, the viscosity and density will decrease, and their product in absolute terms for each oil will tend to a certain value. For example, for MS-20 oil (Fig. 7), the current optimal aggregate-phase state, in which the criterion K = 32, determined by tribological tests, the speed of rotation of the rotor TPG (V = 5700 rpm), accompanied by a decrease in friction to F_f = 0.15, and the minimum linear wear of the material of the stationary sample of the model friction unit (I = 0.01 µm per hour).

The determination method is based on a criterion that includes three physical quantities that characterize electrical permeability, density, and viscosity. The product of these values allows us to estimate the actual presence of microbubbles with reduced pressure. Depending on the nature and physicochemical properties of different working fluids, each parameter included in the criterion is more or less sensitive to the actual physical-phase state. Therefore, a set of test methods for determining this criterion allows us to convincingly state that this method and the proposed criterion are scientifically sound and experimentally proven.
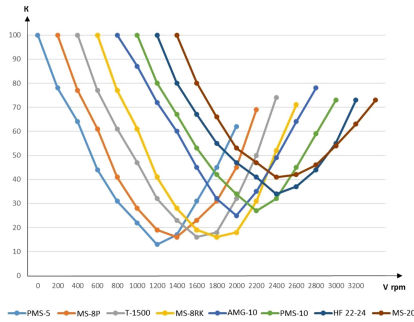
Fig. 7. Comparison of lubricants of different types and viscosities.

The method is based on the provisions of the adhesion-hydrodynamic-deformation theory of friction and wear developed by the authors of this work. In particular, confusing backflows and diffuse all-round stretching of lubricant fragments in the elastic-deformation contact areas contribute the most to the total friction force. Conditions are created for adhesive primary wear due to repeated deformation micro-cutting of friction surfaces and the efficiency of the environmental resource of tribosystems.

The analysis of dependences and the results of comparative tribotechnical tests testify to the positive influence of microbubbles on the efficiency of tribosystems: the friction force decreases, and the wear intensity decreases significantly. These results are consistent with the main provisions of the adhesion-hydrodynamic theory of friction:

– reduction of wear intensity and critical load of friction surfaces is associated with an increase in the compression ratio of two-phase oil compared to its liquid state, which leads to a decrease in the degree of rarefaction of the boundary layers in the diffuser contact area;
– the friction force decreases due to the increase of the compression modulus of the two-phase oil compared to its liquid state, leading to a decrease in the reverse flow velocity in the confusing contact area and a decrease in the diffuse vacuum friction resistance component.

The presence of low-pressure microbubbles in the lubricating medium, which occur in the diffuse areas of TPG and are delivered to all friction nodes, leads to their setting and damping of flows in the confusing areas and their easy expansion in the diffuse areas of each tribocontact.

From the standpoint of the adhesive-hydrodynamic model of friction and wear, the known lubrication methods have a number of significant scientifically sound disadvantages caused by hydrodynamic processes occurring in the characteristic areas of tribocontacts.

In the confusing region of tribocontact sliding and rolling (the region where the relative motion of the friction surfaces narrows the gap where the oil comes into contact in the liquid state in the form of a homogeneous uncompressed Newtonian fluid. In these confusing areas, or narrowing gaps or sliding, the oil is compressed, which causes the secondary reverse movement of the lubricating layers, which realize strong friction with

the molecules of the layers in contact with the friction surface, and in turn, leads to the following negative consequences:

– in the confusing areas of tribocontacts, the temperature before contact rises, caused by the friction of "secondary" and "invading" molecules of the boundary layers. It is confirmed by thermal imaging studies; the primary source of temperature rise in the bearings is the friction of the oncoming and running out molecules before contact;
– the friction force in tribocontacts of high-speed compressed layers of single-phase drip liquid increases;
– in the diffuser region of the tribocontacts of sliding and rolling (the area where the movement of the friction surfaces widens) is the rarefaction of the boundary layers of oil and their vacuum. The oil coming into contact in the liquid state as a homogeneous uncompressed Newtonian fluid and is a continuous medium goes into a two-phase state by generating microbubbles with reduced pressure. The degree of vacuum reaches the values of the for vacuum. In these diffuser contact areas, which are continuously formed in the direction of friction, the lubricating layers are subjected to comprehensive stretching and thinning. This leads to the desorption of the boundary layers and the realization of the quasi-dry friction regime in the elastically deformed diffuse regions of the tribocontacts. This results in a second reversal of the flow of oil fragments from the volume to the contact. At the boundary of the formed vacuum cavity and lubricating fluid, micro-and submicrobubbles with reduced pressure are generated. These processes lead to the following negative consequences:
– in the diffuser areas of contacts, there is tribocavitation (cavitation in the contacts of friction nodes, which can turn into super- and hypercavitation), which leads to adhesive-cavitation-erosion wear of friction surfaces with characteristic signs of the formation of a scaly structure during rolling and adhesive microscatching when sliding;
– in the diffuse areas of the tribocontacts of rolling, the vacuum in the medium of liquid oil reaches high values (less than 100 kPa), which leads to additional resistance to rolling and sliding friction surfaces and additional loading of surfaces in highly diluted oil, which leads to a corresponding increase in friction;
– in all diffuse areas of tribocontacts, there are prerequisites when the friction surfaces can enter into adhesive interaction. In this case, the most probable setting of friction surfaces occurs in elastically deformed diffuser areas, which is unacceptable because it is recognized that the adhesion of friction surfaces even at the micron-scale level in aircraft engines determines their service life, reliability, and safety.

All the above shortcomings are eliminated by arranging lubrication of high-speed and high-load friction surfaces with two-phase air suspension, which non-contact TPG creates to optimal values determined by the developed device for monitoring the current aggregate-phase state of working fluid in circulating lubrication systems. Following the above physical processes occurring in the confusing-diffuse areas of tribocontacts, the authors proposed the following technology for controlling the current aggregate-phase state of lubricating fluids. In the circulation systems of actual installations, it is necessary to install a unique TPG two-phase oil-vapor-air environment by using the effects of micro-and nanovesicles with reduced pressure in the diffuser areas and their injection

through special receiving devices - in the confusing ones. At the entrance to the oil pump, the developed device of control of an aggregate-phase condition of lubricating liquid, which at the achievement of optimum values through the microcontroller gives a control signal on switching off of TPG, is established. If the aggregate-phase state of the lubricating fluid is supersaturated or depleted, then the developed device gives a command to increase or decrease the speed of the rotor.

Laboratory comparative tests with the circulation and injection of TPG two-phase lubricants showed their high efficiency, namely - a decrease in wear intensity by 30%, friction forces by 15%, and an increase in the setting load of surfaces by 20%.

Such TPG has desirable technical characteristics (non-contact surfaces that provide microbubble generation and injection of oil and steam-liquid liquid, low power consumption - less than 20 w), so in the future are considered as oil pumps with an independent drive for use in circulating lubrication systems for various purposes. The necessary completion of the TPG design, materials for manufacturing parts, appropriate sizes, and fasteners. Preliminary analysis of existing circulating systems has shown that in modern machines and mechanisms, it is common to place two filters on the oil line at once - full-flow and part-flow, where the volumes of engine oil passing through them are correlated as 9:1, which satisfies the conditions work of the developed TPG and gives the chance to place the developed prototype of the device in the line parallel to the main oil pipeline. A small amount of lubricating medium, which will run along the parallel circuit repeatedly, will generate microbubbles and injection of oil-vapor liquid at the outlet of the corresponding line, directly directed to the high-load parts of the friction units. Therefore, the prototype of the device (Fig. 8) was designed as a universal auxiliary oil pump-generator with good, operational technology, namely - ease of mounting, external inspection during operation, installation and replacement of oil filter, drain excess oil accumulated during operation mechanical impurities.
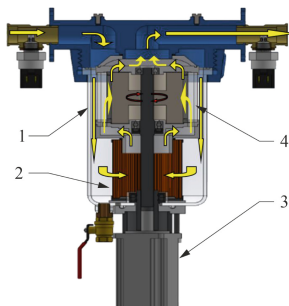

Fig. 8. Circulation of the lubricating medium in the model of the device for monitoring the physical and phase state of the working fluid in the circulating lubrication systems: 1- filter housing; 2 - filter element; 3 - DC motor; 4 - tribomolecular generator.

The body of the product is a transparent flask of the collapsible filter container type FG-100, which allows you to control the degree of contamination of the oil filter element and visualize the main and transient modes of the flow of the working lubricating medium

TPG. In the lower part, a filter element prevents mechanical particles up to 0.001 mm from entering the TPG collector.

It is known that the oil in the crankcase is usually heated to a temperature of about 100 °C, increasing the oil temperature to 120 °C and above, its oxidation processes are accelerated, resulting in increased corrosion of the oil and thermal decomposition products and leads to engine malfunctions increased wear of its critical parts of the friction units. Due to this, plastic materials (polyamides, polypropylenes) were used for the production of TPG body and working parts, which are characterized by high impact strength (up to 80 kgf·cm/cm^2), frost resistance (up to −40 °C), melting point (up to + 190 °C) oil and gasoline resistance, reduced water absorption and chemical resistance. To determine, compare and regulate the current state of the lubricating medium in the central line of the ESU on the prototype of the control device placed unique ports of input and output flow in the form of manufactured tees, taking into account the size and landing dimensions of mounting points with FPS sensors. According to NIST standards, specialized sensors pre-calibrated at the factory have high sensitivity and good correlation with modern laboratory qualification measurement methods and allow simultaneous measurements of parameters such as viscosity, density, and temperature (−60 °C to +150 °C), and dielectric constant of lubricant environment.

Control of the actuator of the prototype device, collection, calculation, and transmission of current data is carried out using a designed and manufactured control unit with a programmable microcontroller Atmel AVR (ATmega 328) and special software on a PC (Fig. 9).

Fig. 9. Control unit: 1 - LSD-indicator of current parameters of FPS sensors; 2 - switch direction of rotation of the drive; 3 - TPG drive driver switch; 4 - switch mode of operation of the drive "manual – automatic"; 5 - speed controller of the drive.

Verification of efficiency with the corresponding complex debugging of the made prototype of the device of control of a current aggregate-phase condition of working liquid in laboratory conditions showed that it realizes circulation of working fluid in a model circulating system of greasing (Fig. 10) with speed up to 4 l/min and creates excess pressure up to 8...9 kPa due to non-contact working zones of TPG injection. The control module performs measurements, performs comparative analysis, and provides regulation of the working fluid's current physical and phase state.

Comparative analysis of laboratory tribotechnical tests results on the ASK-01 friction device showed a positive effect of microbubbles on the efficiency of the model sliding tribosystem, thus reducing the friction force and significantly reducing the wear intensity of wear the model friction unit. These results are consistent with the developed method
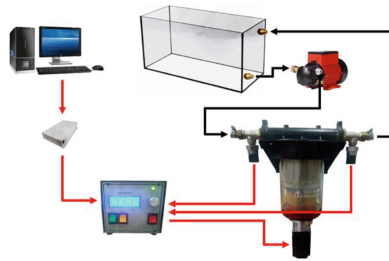
Fig. 10. Wiring diagram of the research device.

for determining the current aggregate-phase state of the working fluid in circulating lubrication systems.

5   Conclusions

The current aggregate-phase control of lubricating fluids for circulating systems can be widely used in an aircraft engine, ground, water, and another engineering of general and unique engineering, where high-voltage tribosystems with circulating lubrication systems are used. In addition, the use of this technology is envisaged in various other sectors of the economy (medicine, food and chemical industry, in the heat-generating and water supply systems, in hydraulic, fuel, and oil systems of engines, in energy heat generators, in engines of oil and gas pumping networks and other energy plants.

It has been experimentally determined that the use of oil-vapor suspensions as a lubricant in the art is promising because it reduces the temperature, friction force, and the probability of desorption of the lubricating layers in the diffuser contact zones.

A number of regularities have been established when comparing experimental data and pressure distribution in lubricating layers in friction dynamics with theoretical calculations of maximum contact stresses in static surfaces:

- during friction, the maximum pressure in the lubricating layers increases with increasing viscosity of the medium, sliding speed, and contact load;
- the minimum pressure in the lubricating layers in the diffuser contact zone decreases with increasing viscosity of the medium, sliding speed, and contact load;
- the values of maximum and minimum pressure in the lubricating layers in the contact change inversely proportionally, at least within the speeds (up to 0.3 m/s) and loads ($\sigma_{max} < 0.6$ MPa), which were set in laboratory studies.

Developed and created technology for controlling the current aggregate-phase state of lubricating fluids for circulating ESU systems with a set of methods and criteria (K) of the current aggregate-phase state of the working fluid in circulating lubrication systems are fundamentally new, theoretically sound and experimentally proven.

The defined criterion of the liquid's current physical and phase state, as the product of viscosity, density, and dielectric constant at the current temperature, is entirely correct and objectively correlates with the saturation of lubricants with oil and gas microbubbles. It is advisable to use in circulating systems of different energy.

The introduction of technology to control the current physical and phase state of lubricants of different viscosities is expected to increase the life of power plants more than 2 times, their more leisurely start at low operating temperatures and under normal conditions, and reduce emissions of combustion products into the atmosphere.

References

1. Myshkin, N. K., Goryacheva, I. G., Grigoriev, A., Kavaliova, I. N., Makhovskaya, Y.: Contact interaction in precision tribosystems. J. Friction Wear **41**(3), 191–197 (2020). https://doi.org/10.3103/S1068366620030113

2. Frene, J., Nicolas, D., Berthe, B., Godet, M.: Hydrodynamic Lubrication. Bearings and Thrust Bearings. Tribology Series. Elsevier (1997)

3. Bulgarevich, S.B., Boiko, M.V., Lebedinskii, K.S.: Adsorption separation of components of liquid lubricant on rubbing surfaces under sliding friction. J. Friction Wear **36**(6), 534–541 (2015)

4. Lyashenko, I.A., Popov, V.L.: Transition between modes of adhesion and sliding friction in contacts of axially symmetric bodies. J Friction Wear **40**(1), 39–45 (2019)

5. Kiriyan, S.V., Altoiz, B.A.: The rheology of motor oils with quasi-liquid crystalline layers in a tribotriad. J. Friction Wear **31**(3), 234–239 (2010)

6. Varenberg, M., Kligerman, Y., Halperin, G., Nakad, S., Kasem, H.: Assessing workability of greased bearings after long-term storage. Friction **7**(5), 489–496 (2018). https://doi.org/10.1007/s40544-018-0255-1

7. Zimmerman, W.B., J, Tesař V.: Bubble Generation for Aeration and Other Purposes. European Patent EP2081666 (2012)

8. Ivanov, V., Dehtiarov, I., Pavlenko, I., Kosov, M., Hatala, M.: Technological assurance and features of fork-type parts machining. In: Ivanov, V., et al. (eds.) DSMIE 2019. LNME, pp. 114–125. Springer, Cham (2020). https://doi.org/10.1007/978-3-030-22365-6_12

9. Berladir, K., Hovorun, T., Gusak, O.: Strengthening of the NKV type centrifugal pump's shaft by chemical-thermocycling treatment. In: Ivanov, V., Trojanowska, J., Pavlenko, I., Zajac, J., Peraković, D. (eds.) DSMIE 2021. LNME, pp. 525–535. Springer, Cham (2021). https://doi.org/10.1007/978-3-030-77719-7_52

10. Stelmakh, A.U., Kostunik, R.E., Radzievskiy, V.A., Maystrenko, A.L., Sokhan, S.V., Kulich, V.G.: Rolling friction of hybrid ceramic-steel pairs under different lubrication conditions. J Friction Wear **41**(5), 432–442 (2020)

11. Kostyk, K., et al.: Simulation of diffusion processes in chemical and thermal processing of machine parts. Processes **9**(4), 698 (2021). https://doi.org/10.3390/pr9040698

12. Krmela, J., Hovorun, T., Berladir, K., Artyukhov, A.: Increasing the structural strength of corrosion-resistant steel for elastic components of diaphragm compressor. Manufac. Technol. **21**(2), 207–213 (2021). https://doi.org/10.21062/mft.2021.034

13. Ivanov, V., Pavlenko, I., Kuric, I., Kosov, M.: Mathematical modeling and numerical simulation of fixtures for fork-type parts manufacturing. In: Knapčíková, L., Balog, M. (eds.) Industry 4.0: Trends in Management of Intelligent Manufacturing Systems. EICC, pp. 133–142. Springer, Cham (2019). https://doi.org/10.1007/978-3-030-14011-3_12

14. Rudenko, S., Berladir, K., Trojanowska, J., Varenyk, S., Shvetsov, D., Kravets, V.: Application of FMEA for assessment of the polymer composite materials quality. J. Eng. Sci. **8**(2), B12–B18 (2021). https://doi.org/10.21272/jes.2021.8(2).b3

15. Svirzhevskyi, K., Zabolotnyi, O., Tkachuk, A., Machado, J., Kononenko, A.: An increase in wear resistance frictional contact of functional surfaces for plunger pairs. In: Ivanov, V., Pavlenko, I., Liaposhchenko, O., Machado, J., Edl, M. (eds.) DSMIE 2021. LNME, pp. 84–94. Springer, Cham (2021). https://doi.org/10.1007/978-3-030-77823-1_9

16. Tkachuk, M.M., Grabovskiy, A., Tkachuk, M.A., Hrechka, I., Ishchenko, O., Domina, N.: Investigation of multiple contact interaction of elements of shearing dies. Eastern-Euro. J. Enterprise Technol. **4**(7–100), 6–15 (2019). https://doi.org/10.15587/1729-4061.2019. 174086

17. Yaroshevich, N., Zabrodets, I., Shymchuk, S., Yaroshevich, T.: Influence of elasticity of unbalance drive in vibration machines in its oscillations. Eastern-Euro. J. Enterprise Technol. **7**(95), 62–69 (2018)

18. Lyashenko, I.A., Khomenko, A.V., Chepulskyi, S.N., Metlov, L.S.: Nonequilibrium kinetics of phase transitions in the boundary friction mode. J. Friction Wear **33**(4), 224–252 (2012)

19. Darovskoy, G. V., Krotov, V. N., Polyakov, V. N., Ezupova, M. N.: Modeling the hydrodynamic friction mode on amsler type friction testing machines. J. Friction Wear **40**(3), 223–228 (2019). https://doi.org/10.3103/S1068366619030036

20. Dmytrychenko, N., Khrutba, V., Savchuk, A., Hlukhonets, A.: Using mathematical, experimental and statistical modeling to predict the lubricant layer thickness in tribosystems. In: Palagin, A., Anisimov, A., Morozov, A., Shkarlet, S. (eds.) MODS 2019. AISC, vol. 1019, pp. 39–49. Springer, Cham (2020). https://doi.org/10.1007/978-3-030-25741-5_5

21. Markova, L.V.: Intelligent method for monitoring the state of lubricating oil. J. Friction Wear **37**(4), 308–314 (2016)

22. Senin, P. V., Ionov, P. A., Stolyarov, A. V., Zemskov, A. M.: Device for tribotechnical tests of friction pairs. J. Friction Wear **41**(2), 141–145 (2020). https://doi.org/10.3103/S10683666 20020130

23. Zablotskyi, V., Tkachuk, A., Moroz, S., Prystupa, S., Svirzhevskyi, K.: Influence of technological methods of processing on wear resistance of conjugated cylindrical surfaces. In: Tonkonogyi, V. et al. (eds.) Advanced Manufacturing Processes II. InterPartner 2020. Lecture Notes in Mechanical Engineering, pp. 477–487. Springer, Cham (2021). 0.1007/978-3-030-68014-5_47

Theoretical and Experimental Studies of the Properties of Porous Permeable Materials Obtained from Industrial Waste

Oleksandr Povstyanoy[1]([✉]) [iD], Nataliya Imbirovich[1] [iD], Valentyna Tkachuk[1] [iD], Rostyslav Redko[1] [iD], and Olga Priadko[2] [iD]

[1] Lutsk National Technical University, 75, Lvivska Street, Lusk 43018, Ukraine
`povstjanoj@ukr.net`
[2] National University of Life and Environmental Sciences of Ukraine, 15, Heroyiv Oborony Street, Kyiv 03041, Ukraine

Abstract. This article theoretically and experimentally investigates the scientific and technical problem of using multilayer porous permeable materials from industrial waste with controlled functional and technological characteristics by predicting the composition, structure, properties using computer information technology. These porous permeable materials (PPM) from industrial waste are suitable for the purification of technical liquids and gases, which has increased the efficiency of using products in various fields of mechanical engineering. The method of computer modeling proposed by the authors will allow not only to determine the porosity distribution of the filter material but also to determine the relationship between technological and structural parameters. The results of this scientific work are used to develop porous permeable products - filters - for the purification of technical, industrial water, lubricants, and fuels from mechanical impurities contaminants. Developed multilayer porous permeable materials have a higher coefficient of permeability, resource, and dirt capacity with similar single-layer.

Keywords: Product innovation · Porosity · Forecasting · Properties · Permeable · Filtering · Industrial growth

1   Introduction

Modern industry needs new structural and functional materials, including composite and nanostructured [1]. The technological equipment introduced to meet these demands, automated and robotic, equipped with nonlinear drives, allows the development of fundamentally new technologies to produce materials with high-performance properties [2]. The instrument base of diagnostics and scientific research provides research of the structure of new materials in any dimensional scale from nano- to macro- [3].

The rapid development of high-performance computer systems and software allows for the computer modeling of new materials and advanced technologies [4, 5].

The study of porous materials in various industries is a current global trend and is realized using computational materials science methods with the use of computer metallographic analysis [6].

The formation and structuring of information about PPM for parallel computer modeling of technologies and loaded structures is a topical issue that scientists can successfully solve.

An important area of research and research is to study the relationship between the structure and properties of porous permeable materials [7]. Metal porous materials are the predominant class of structural materials in mechanical engineering, the main purpose of which is the ability to carry a force load [8]. The internal structure significantly affects the mechanical properties of metallic materials [9].

Therefore, the study, forecasting, and targeted formation of the characteristics of strength, durability, wear-resistance, and other performance properties is necessarily associated with the search for the physical nature of changes in the structure of materials under the influence of technological and operational loads.

2 Literature Review

Studying the properties of porous permeable materials is important both for scientific purposes and in their practical use. Creating new materials with predetermined properties makes new demands on the study and solution of problems that require immediate and effective solutions.

The results of field experiments to study the properties of PPM are taken into account in the development of separate technological instructions, but the widespread introduction is constrained by the high cost of physical experiment and conservative attitude of practicing technologists to this initial operation [10].

In research practice, the process of studying a discrete environment is of constant interest, and recently it has been successfully solved by methods of mathematical and computer modeling [11].

Analysis of the current state of theoretical and experimental research in powder metallurgy indicates a clear trend in the descriptive properties of materials and physical processes in them [12].

In the direction of computer modeling of PPM properties, the works of Kadushnikov R.M. are widely known. On modeling the evolution of the microstructure of polydisperse materials during sintering.

The possibility of application of geometrical modeling [13, 14] of microstructure at the research of polydisperse materials as one of the methods of describing their real structure is resulted in articles [15–17].

Adaptation of the properties of the PPM structure to the intended application is a serious problem for materials scientists, as long as there are no methods of accurate morphological processing.

Quantitative and qualitative relationships between the morphology of porous material its local and global filtering properties are essential in many applications [18–21].

The porosity and its distribution throughout the sample is a feature with a certain effect on the filtering properties of the flow and mass of PPM [22].

Analyzing the current trends in the creation of PPM today, there is a need for comprehensive research and development of scientific and practical principles of forecasting, modeling, development of the structure and properties of PPM from industrial

waste, development of new, based on existing, technology for powder products with high mechanical and functional properties with adjustable porosity for cleaning liquids and gases based on computer information technologies.

3   Researches Methodology

The study of capabilities and evaluation of modern software for computer tools for the study of metallographic images to determine the qualitative and quantitative characteristics of metals or alloys is dictated by scientific and industrial problems in modern materials science.

The main requirement for qualitative analysis of images can be formulated and set as follows: on a photograph obtained under a microscope, it is necessary to identify structural components and then classify them by brightness, size, and shape.

The practical implementation of this includes tasks that have become classic, such as segmentation, filtering defects, selection of objects from the background, defining the boundaries of objects, pattern recognition [23].

The morphology of PPM determines their filtering characteristics and, consequently, their effectiveness in many application areas. Adaptation of the properties of PPM structure to the intended application is a serious problem for materials scientists, as long as there are no methods of accurate morphological processing [24].

The studied PPM sample consists of a solid metal structure (monolithic skeleton; opaque) with a porosity of ~69% (intermediate voids, shaded) (Fig. 1).

The direct dependence of permeability on the structural features of PPM (porosity, pore size distribution, pore shape, and curvature coefficient) will be valid only for certain types of filter materials.
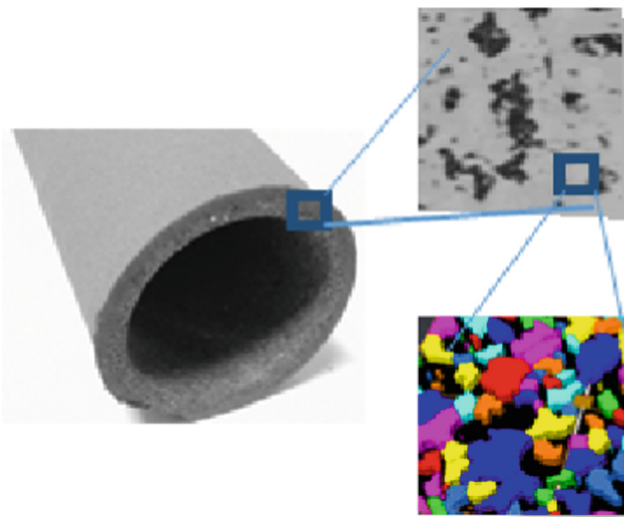

Fig. 1. 3D-image of the reconstructed volume of the cylindrical sample PPM.

Correlations are offered for the estimation of permeability of PPM depending on the size of particles of powder, which determine the reduction of the coefficient to penetrating with the increase of surface of particles (reduction to the factor of the form).

4   Results

4.1   Determination of the Dependence of Permeability on the Structural Features of PPM

To ensure minimal pressure drop losses in the filtered medium, the highest permeability of the PPM should be as high as possible at a given filtration fineness. The permeability increases with increasing porosity, pore size, pressure drop and decreases with increasing thickness of the filter element and viscidity of the filtrate. This is quite clear from Table 1.

Table 1. Correspondence of permeability to porosity.

Curvature coefficient, %	Porosity, %	Permeability, darcy
5,6	46,2	375
10,5	40,8	317
15,0	35,2	243
19,0	32,7	200
22,7	27,4	134

4.2   Study of PPM Permeability Experimentally

Based on previous studies, the particle size of BBS15 steel powder was chosen to be 0.1–0.16 mm, as this fraction makes it possible to produce PPM with an average pore size of 20 µm.

From the point of view of optimal filtration characteristics, PPM with an asymmetric porous structure used for cleaning liquids or gases characterized by the presence of low-concentration polydisperse solid contaminants should have lower porosity and smaller pore sizes in the flow direction.

At the same time, filtration effectively occurs when the first layer, placed on the original surface of the PPM, with zero concentration of pore-forming agent (with minimal porosity and pore size), provides the required filtration fineness; the second layer, placed on the entrance surface of the PPM, with the maximum pore concentration (with maximum porosity and pore size) catch the most significant parts of the pollutant.

The porosity and pore size of the intermediate layers of PPM are easily adjusted by changing the concentration of the pore former.

These experimental studies' results allowed the development of the technology of PPM production by the method of layer formation and became a prerequisite for further filtering studies.

For samples with different porosity, the completeness and fineness of filtration were determined. The results of this study are presented in Table 2.

Table 2. The dependence of the completeness and fineness of the liquid filtration on the properties of the source powders

The average particle size, microns	Porosity material, %	Diameter of pore, µm	Fineness filtrations, microns
0,050–0,100	28	25	7–9
0,100–0,150	30	30	15–18
0,150–0,200	35,5	55	20–25
0,200–0,250	36,5	75	35–45
0,250–0,300	38,5	130	50–65
0,300–0,500	40	160	75–85

4.3   Investigation of PPM Permeability by Modeling Methods

To model the permeability of PPM, we use the following realistic data Table 3.

Table 3. Chemical composition of steel powder BBS15.

Chemical element	Percentage composition, %
Si	0,17–0,37
Cu	0,25
Mn	0,20–0,40
Ni	0,30
P	0,027
Cr	1,30–1,65

Figure 2 shows a 3D model of PPM made of steel powder BBS15 with a given real data (a) and performed internal and external filtering (b).
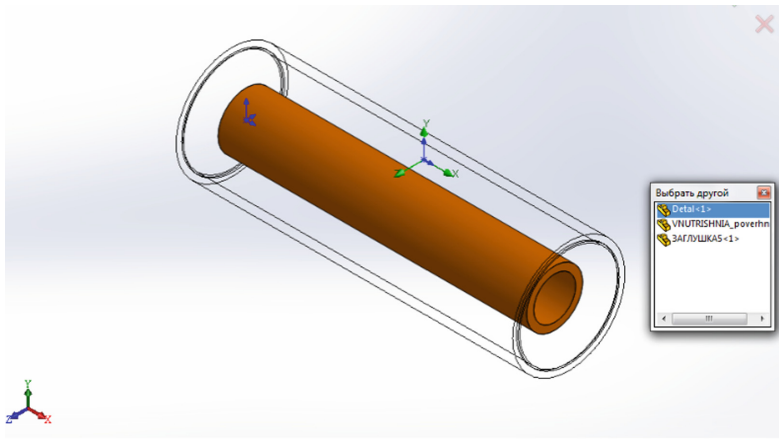
(a)
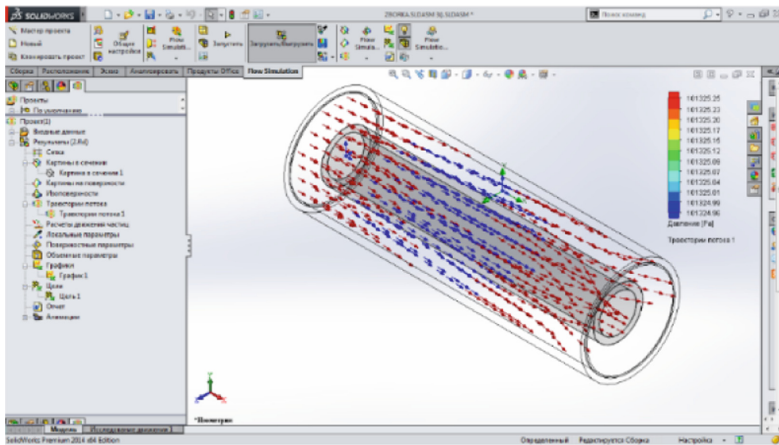
(b)

Fig. 2. 3D model of PPM made of BBS15 steel powder with given real data (a) and internal and external filtering (b).

Figure 3 shows the cross-section of the flask in which the PPM is fixed. Inside the flask, the liquid inside the filter moves into the flask—the speed at which the liquid acts on the PPM is determined. Blue areas indicate the flow areas in which the speed is minimal, and red is the maximum.
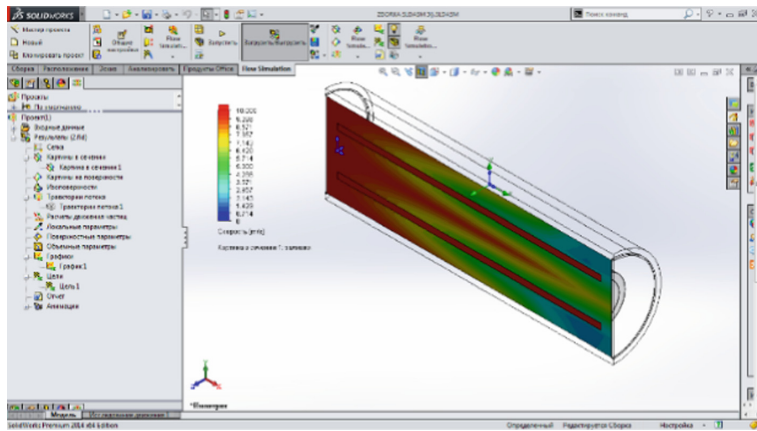
Fig. 3. Display of cross-section of PPM by the parameter of internal filtration rate.

4.4 Systematic Determination of PPM Permeability

The water environment is represented by moving arrows, which in different parts of the PPM are marked with different colors, according to the maximum and minimum values that they receive in the process of movement (Fig. 4).
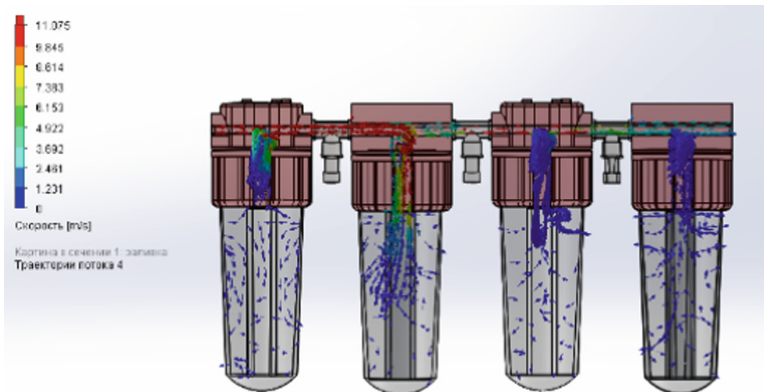
Fig. 4. When determining the speed, directions of water flow in a system of four PPM.

The conclusions of Table 4 are based on previous studies of the authors.

1. Porous permeable materials have a high degree of purification of the liquid medium from solid microparticles and fine impurities;
2. PPM can be used as filters to filter the various technical means;
3. Porous permeable materials can be used in the same way for water purification as drinking water.

Table 4. Characteristics of PPM.

Indexes	Value of indexes
Porosity, %	25–55
Operating temperature	… 100
The filtration efficiency of dispersed micro-impurities with a particle size greater than 0.01 µm,%	… 99,99
Productivity of ultrafiltration of water at a pressure drop in the filter of 0,1 MPas, l/cm^2 × h	… 10
Productivity of ultrafiltration of gases at pressure drop on the filter of 2 kPa, l/cm^2 × h	… 40
Bending strength, MPa	≥0,5
Geometric dimensions of samples, mm: cylinders, pipes, glasses, diameter; length	up to 40 up to 100

5   Conclusions

In addition, the results allow us to conclude the effectiveness of cleaning liquids. The resistance of a porous filter element depends on the pore size and total pore volume, filtration rate, wall thickness, and grittiness of the initial powder.

The fineness of filtration and resistance directly depends on the size of the porosity of the filter element. The higher the porosity - the higher the fineness of filtration and resistance.

As the particle size of the powder increases, the resistance of the filter material decreases, but the filter properties reduce.

The pore diameter directly depends on the particle size of the original impurities.

References

1. Budnik, A.F., Rudenko, P.V., Berladir, KV., Budnik, O.A.: Structured nanoobjects of polytetrafluoroethylene composites. J. Nano- Electron. Phys. **7**(2), 02022 (2015)
2. Berladir, K., Gusak, O.: Influence of mechanically activated fillers of different chemical nature on tribotechnical properties of PTFE-composites. In: Tonkonogyi, V., et al. (eds.) InterPartner 2019. LNME, pp. 395–404. Springer, Cham (2020). https://doi.org/10.1007/978-3-030-40724-7_40
3. Povstyanoy, O., Zabolotnyi, O., Rud, V., Kuzmov, A., Herasymchuk, H.: Modeling of processes for creation new porous permeable materials with adjustable properties. In: Ivanov, V., et al. (eds.) DSMIE 2019. LNME, pp. 456–465. Springer, Cham (2020). https://doi.org/10.1007/978-3-030-22365-6_46
4. Xi, Z.P., Tang, H.P.: Sintered Metal Porous Material. Metallurgical Industry Press, Beijing (2009)
5. Bruno, G., Efremov, A.M., Levandovskyi, A.N.: Connecting the macro- and microstrain responses in technical porous ceramics: Modeling and experimental validations. J. Mater. Sci. **46**(1), 161–173 (2020)

6. Bejan, A., Dincer, I., Lorente, S., Miguel, A.F., Reis, A.H.: Porous and Complex Flow Structures in Modern Technologies, vol. 1, pp. 90–99. Springer, Heidelberg (2014). https://doi.org/10.1007/978-1-4757-4221-3

7. Chern, M., Vaziri, N.: Effect of porous media on hydraulic jump characteristics by using smooth particle hydrodynamics method. Int. J. Civ. Eng. **18**, 367–379 (2020)

8. Hunyadi Murph, S.E., Jacobs, S., Siegfried, M., Hu, T., Serkiz, S., Hudson, J.: Manganese-doped «gold nanoparticles as positive contrast agents for magnetic resonance imaging (MRI)». J. Nanopart. Res. **14**, 658–659 (2012)

9. Jonsson, P., Jonsen, P., Andreasson, P., Lundstrom, T.S., Hellstrom, J.G.: Smoothed particle hydrodynamic modelling of hydraulic jumps: bulk parameters and free surface fluctuations. Engineering **8**, 386–402 (2016)

10. Faisal, A.A.H., Sulaymon, A.H., Khaliefa, Q.M.: A review of permeable reactive barrier as passive sustainable technology for groundwater remediation. Int. J. Environ. Sci. Technol. **15**(5), 1123–1138 (2017). https://doi.org/10.1007/s13762-017-1466-0

11. Lagae, A., Dutré, P.: A Comparison of methods for generating Poisson disk distributions. Comput. Graph. **27**(1), 114–129 (2018)

12. McMillan, A., Jones, R., Peng, D., Chechkin, G.A.: A computational study of the influence of surface roughness on material strength. Meccanica **53**(9), 2411–2436 (2018). https://doi.org/10.1007/s11012-018-0830-6

13. Pylypaka, S., Nesvidomin, V., Volina, T., Sirykh, L., Ivashyna, L.: Movement of the particle on the internal surface of the spherical segment rotating about a vertical axis. INMATEH Agric. Eng. **62**(3), 79–88 (2020). https://doi.org/10.35633/inmateh-62-08

14. Pylypaka, S., Volina, T., Hryshchenko, I., Rybenko, I., Sydorenko, N.: Dynamics of a particle on a movable wavy surface. In: Tonkonogyi, V., et al. (eds.) InterPartner 2020. LNME, pp. 196–206. Springer, Cham (2021). https://doi.org/10.1007/978-3-030-68014-5_20

15. Nurkanov, E.Y., Kadushnikov, R.M., Kamenin, I.G., Alievsky, D.M., Kartashov, V.V.: Study of the density characteristics of three-dimensional stochastic packages of spherical particles using a computer model. Powder Metall. **5**(6) (2001)

16. Rusark, Z., Horvarth, I., Mandorli, F.: Towards multi-domain knowledge transfer in engineering analyses and simulations based on virtual prototypes. Eng. Comput. **29**(3), 247–250 (2013)

17. Pavlenko, I., Liaposhchenko, A., Ochowiak, M., Demyanenko, M.: Solving the stationary hydroaeroelasticity problem for dynamic deflection elements of separation devices. Vibr. Phys. Syst. **29**, 2018026 (2018)

18. Crnkovic, G.D.: Information and Computation nets. Investigations into info-computational world. In: Information and Computation, pp. 91–96. Verlag, Saarbrucken (2019)

19. Povstyanoy, O., Sychuk, V., Makmyllan, A., Rud, V., Zabolotnyy, O.: Metallographic analysis and processing of images of microstructure of nozzles for sandblasting which are made by powder metallurgy. Powder Metall. **3**(4), 234–240 (2015)

20. Pavlenko, I., Ivanov, V., Gusak, O., Liaposhchenko, O., Sklabinskyi, V.: Parameter identification of technological equipment for ensuring the reliability of the vibration separation process. In: Knapcikova, L., Balog, M., Perakovic, D., Perisa, M. (eds.) 4th EAI International Conference on Management of Manufacturing Systems. EICC, pp. 261–272. Springer, Cham (2020). https://doi.org/10.1007/978-3-030-34272-2_24

21. Chernysh, Y., Plyatsuk, L., Roubik, H., Yakhnenko, O., Skvortsova, P., Bataltsev, Y.: Application of technological solutions for bioremediation of soils contaminated with heavy metals. J. Eng. Sci. **8**(2), H8–H16 (2021). https://doi.org/10.21272/jes.2021.8(2).h2

22. Saadatfar, M., et al.: Imaging of metallic foams using X-ray micro-CT. Colloid Surf. Physicochem. Eng. Aspect **344**(1), 107–112 (2009). https://doi.org/10.1016/j.colsurfa.2009.01.008

23. Sidi Practical Extrapolation Methods: Theory and Applications. Cambridge Monographs on Applied and Computational Mathematics. Cambridge (2002)
24. Shyberko, V., Rud, V.: Modelling of structural and inhomogeneous materials based on the finite element method. Actual Prob. Econ. APE, 124–130 (2013)

ICT for Engineering Education

Development of Materials Science Virtual Laboratory Work for the Metal Grains Calculation

Kristina Berladir[1](✉) ⓘ, Tetiana Hovorun[1] ⓘ, Oleksandr Gusak[1] ⓘ, Vita Pavlenko[2], and Anatoliy Ruban[1]

[1] Sumy State University, 2, Rymskogo-Korsakova Street, Sumy 40007, Ukraine
`kr.berladir@pmtkm.sumdu.edu.ua`
[2] Machine Building College of Sumy State University, 17, Sevchenka Avenue, Sumy 40011, Ukraine

Abstract. In a global pandemic, distance learning is becoming increasingly important. In this aspect, virtual laboratory work and simulators in teaching by creating electronic software products make it possible to conduct classes at a higher level in the educational environment. The paper describes developing a virtual laboratory work «Methods for Detection and Determination of Grain Size», used in both classroom and distance education. The methodology for the development and implementation of virtual laboratory work on three methods for determining the grain size in steels is described in detail, following the relevant current standard of Ukraine. The C# programming language is the choice of most developers working with applications of this type. Visual Studio was chosen among the development environments, one of the best among competing analogs used to develop these technology applications. The program designed for materials science students to perform laboratory work to determine the size of the grain of metals was created to calculate the grain score and avoid random errors in mathematical calculations more conveniently and accurately.

Keywords: Industrial growth · Virtual laboratory work · Education quality · Distance education · Steel grain · Counting method · Comparison method

1 Introduction

New educational standards imply a competence-based approach, which means project-based teaching methods, the approbation of various forms of work based on independence and responsibility for the student's learning outcomes [1]. Based on the competence-based approach, the student is developing key competencies, which are an integral part of his activities as a future specialist and one of the leading indicators of his professionalism and a necessary condition for improving the quality of professional education. Implementing a new model of results-oriented education requires improving the management system, methodological work, and approaches to the design of classes,

their content, the development and implementation of competence-oriented tasks. Therefore, one of the most critical tasks is the modernization of the educational process in universities, which is aimed at training a new generation of specialists [2]. The rather drastic changes in living conditions require the addition of new technologies to traditional education.

Modern education is the development of such forms of education as digitalization [3], eLearning [4], Mobile Learning [5, 6], training through Coursera, OCW, and other online institutions, the introduction of virtual reality into engineering practice [7, 8], virtual networks [9, 10], etc.

MOOC-training (Massive Open Online Courses, mass lectures from open sources) is great for transferring ideas, formulas, and other theoretical knowledge in lessons and classes. But for the completeness of mastering many disciplines, practical studies are also needed. Digital learning has felt this evolutionary need and created a new form - virtual laboratory work and simulators, both for school and university learning [11].

Virtual laboratories and simulators are needed for [12]: preparation for real laboratory work; such activities when there are no appropriate conditions, materials, reagents, and equipment; distance learning; independent study of disciplines at the university; scientific work; higher education with a significant practical component.

In this regard, developing and improving training methods using computer technology is a timely and crucial task. In this aspect, virtual laboratory works and simulators in training by creating electronic software products make it possible to conduct classes at a higher level. It has also become vital in the current pandemic when distance learning is gaining importance [13].

Replacing traditional laboratory methods with virtual ones, where a simulated system acts as the object of research, it is possible to simplify laboratory exercises, reduce the classroom load, and reduce the load on laboratory equipment. Simultaneously, while increasing the efficiency and quality of training, due to an individual approach to tasks performed as part of the student's independent work and the use of a remote access system, it becomes possible to conduct laboratory work on computers [14] to realize further the sustainable manufacturing goals [15, 16].

It is also applied to training engineering students, including materials science students. When studying materials, structure, properties, and technology of obtaining, students should receive theoretical knowledge of the discipline and learn practical skills.

2 Literature Review

Studying materials science disciplines is associated with the study of metals, to determine the structure of which use a microscope and photo microstructures in the process of laboratory work, where they must select the size of the metal grain [17]. Many standards for metallurgical products impose microstructure requirements. It is applied to critical products made of high-alloy steel and section and sheet products made of structural steel.

One of the essential characteristics of the microstructure is the grain size or grade [18, 19]. Evaluation of the grain size of metals, like any other study of the microstructure, is an important task. The grain size is one of the metal microstructure parameters, and the microstructure, as is known, determines the properties [20].

Metallographic methods determine [21]:

- the size of the actual grain (grain formed during specific processing). In the study and control of steels, it is often determined not the exact grain size, but the "hereditary" grain, that is, the size of the austenite grain after heating under certain conditions (temperature, holding time, and cooling rate) specified in the relevant standards. "Hereditary" grain characterizes the sensitivity of steel to grain growth when heated for heat treatment and has a significant impact on many properties of steel, on its resistance to fracture;
- the tendency of the grain to grow - by determining the size of the austenite grain after heating at the temperature and holding time established by the normative or technical documentation for the corresponding steels and alloys;
- the kinetics of grain growth - by determining the size of the grain after heating in the temperature range and holding time established by the regulatory or technical documentation for steels and alloys [22].

Simultaneously, it is impossible to create sets of scales for all possible variants of structures. For an adequate description and analysis of the structure of metals, it is necessary to use modern mathematical and computational methods of image processing. Computer analysis, in this case, has no alternatives.

Today, a variety of software products are increasingly used to analyze the structure of the metal grain [23]. But modern image processing programs are a significant challenge for users. Typically, such programs are created for complex processing and contain many modules and functions for analyzing objects of various kinds in biology and medicine. As for metallography, they have a wide range of different structure parameters [24]. Therefore, often the user does not know precisely how to solve a problem by computer methods and what parameters to use. At the same time, errors of the methodical plan, which can be a consequence of the wrong metallurgical conclusion, are possible. It is also essential to have computer equipment reasonably high, which is not always the case, especially in production.

Another problem is that currently, the analysis of the structure of metals and alloys by computer methods is not provided by the state standard. Therefore, the structure analysis by computer methods cannot be considered officially permitted and cannot be used as evidence in resolving controversial issues. There are very few specialized computer programs that would calculate the structure parameters strictly based on algorithms and terms laid down in the state standard of Ukraine.

Therefore, it is relevant to develop a program for materials science students to perform laboratory work to determine the size of the grain for a more convenient calculation of the grain score and avoid accidental errors in mathematical calculations.

The paper aims to develop virtual laboratory work to consolidate students' theoretical knowledge and practice their skills in determining the size of metal grains using an interactive system based on three different methods of calculating the size of metal grains.

3   Research Methodology

The purpose of the developed virtual laboratory work (VLW) is to train the students to determine the grain size or grain score of metal.

The grain size is determined under a microscope by one of the following methods by the current state standard of Ukraine DSTU 8972:2019 «Steels and Alloys. Methods of detection and determination of grain size»:

1. Visual comparison of grains visible under a microscope with reference images of scales by DSTU 8972:2019;
2. Counting the number of grains per unit area of the section;
3. Measuring the average conditional diameter of the grains or the number of grains in 1 mm^2, in the case of non-equiaxed grains.

Until recently, such analysis was carried out manually using photographs obtained by the traditional method when photographing on photographic film or photographic plate. Compared to the last century, the technologies to produce metal materials have advanced, and the current state standards of Ukraine cannot continuously adequately regulate the structure of metal products and semi-finished products. Materials with a high dispersion structure, which cannot be investigated and classified according to the current standards at magnifications of 100 and 200, are widely used.

The interactive system developed in VLW has the following functions:

- determination of the grain size of the metal by counting;
- determination of the grain size of the metal by the method of counting when crossing the grain boundaries;
- determination of metal grain size by comparison with DSTU structures;
- creating a report on laboratory work in the form of a document MS Office Word.

Because there are different methods for studying the metal grain score, and each of them does not give an accurate result, when researching the grain score, various ways are used at the same time to obtain a more precise result.

Choosing a programming language suitable for development using Windows Forms technology was necessary to implement virtual laboratory work. The C# programming language is the choice of most developers working with applications of this type.

Visual Studio was chosen among the development environments, one of the best among competing analogs used to develop these technology applications.

The scenario of the student's work with the program is quite simple to understand. On the home page, the student sees information about laboratory work (Fig. 1), the topic of laboratory work and compilers, and buttons to obtain basic information about the user. The "Start" button is inactive until all three TextBox elements have been filled.

After clicking the "Start" button, the student goes to the page with the calculation method, where he also sees the image of the resulting microstructure. After completing the task using the first method, a student goes to the page with the process of counting at the intersection, after which the page with the practice of comparison. After completing
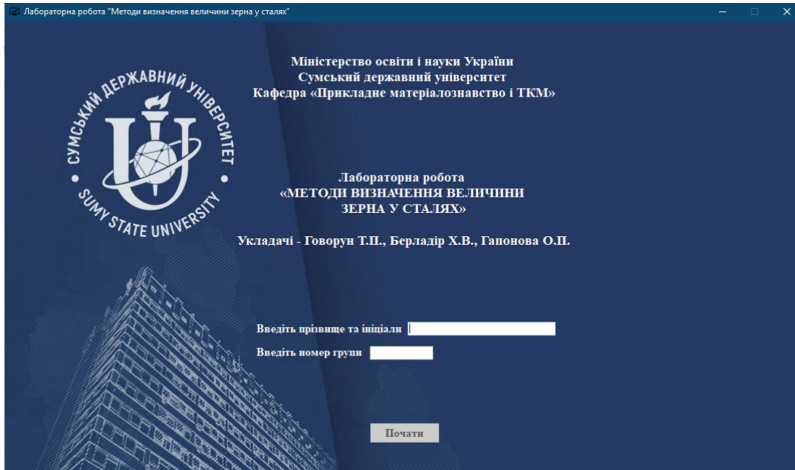
Fig. 1. Screenshot of the initial page of laboratory work.

the task using all three scenarios, the laboratory work can be achieved, saved, and submitted for testing to the trainer.

For making it easier to present the business process, the VLW project is shown in the form of a rectangle using a context diagram of the process of performing virtual laboratory work - IDEF0 notation (Fig. 2). Control arrows are connected to their sides. Each indicator is responsible for a different type of data:

- the left arrow is the input data of the system;
- the right arrow is the source data of the system;
- the upper arrow is the control data: a document that records how the system should work and be implemented;
- the bottom arrow is the data of the mechanism: software or personnel involved in the implementation of the system.

The Use Case diagram used in the development of VLW describes the user's interaction with the system. One actor has been defined for this application: user. Artifacts in an information base and a reporting document were also identified. The Use Case diagram was developed based on these scenarios, presented in Fig. 3.

Before starting work on the virtual simulator, the student must acquire theoretical knowledge under the guidance of a lecturer. In addition, when performing VLW, the student can always view the theory using the button in the lower-left corner of the screen. The button «Read theory» is active for each of the three methods.

Initially, the developed VLW is intended for students of specialty «Materials Science», studying the discipline «Defectoscopy and methods of structural analysis of materials and product», but can also be used by any student to acquire the skills of determining and counting the grain size in the structure of the material.
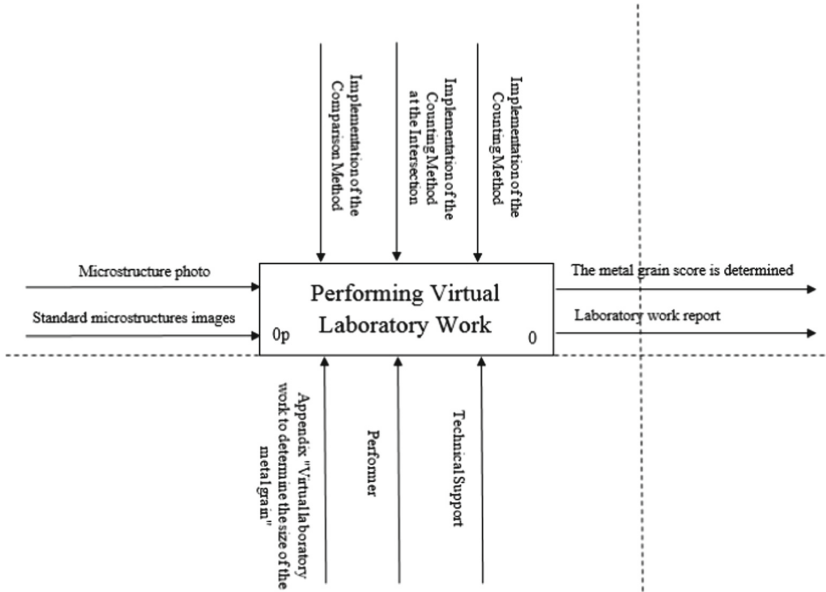
Fig. 2. Context diagram of IDEF0 notation.
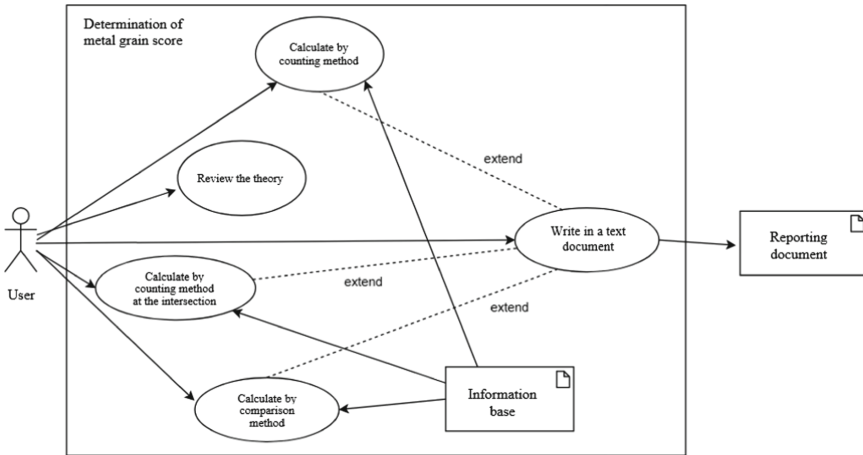
Fig. 3. Use case diagram.

4 Results

The practical implementation of the work is divided into three main stages: the counting method, the counting method at the intersection, and the comparison method. Each method is implemented as a separate UserControl.

4.1 Implementation of the Counting Method

When performing the task by the counting method, the user makes a mark in the form of "plus" symbols on the photo of the microstructure to indicate the grains. This function was implemented using the Drawing library and the public void method OnPictureBoxClicked (object sender, MouseEventArgs e, Func < FirstMethodDrawing, bool > pointSaver), which drew the notation in the coordinates of the user's click on the PictureBox.

The ability to change the size and color of the markings to better display them in the image was implemented using the ComboBox element in the form of a drop-down list and the corresponding event handler. It was called after each change of the selected list item and changed the color value of the text displayed on the structure image. It was also possible to clear the last symbols in case of error. The coordinate values of each notation on the structure were stored in the array, and when you clicked the "Clear last notation" button, the last element of the array was deleted, and all other notations were redrawn. The program independently counts the number of notes made of each type for further use of these values in calculating the grain score. A separate UserControl was created to substitute values into formulas and obtain a grain score. It processes the data entered by the user into the appropriate TextBox elements and uses them to calculate the metal grain score after the user clicks the "Calculate Grain Score" button. Calling the private void countGrainPointButton_Click method (object sender, EventArgs e) checked that all the required values were set in the TextBox elements. The implementation of the first method and filling in the formulas is shown in Fig. 4.
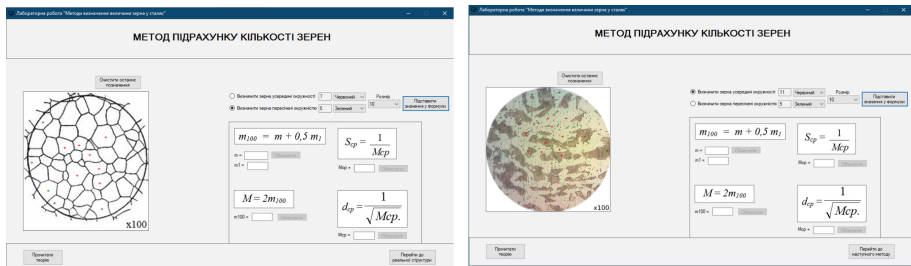
Fig. 4. Implementation of the first method and filling in formulas.

The transition from working with a schematic microstructure to a real one was realized (Fig. 4, right). A new image was installed in the PictureBox, and all labels were cleared using the private void clearMicrostructureDrawingSurface method.

4.2 Implementation of the Counting Method at the Intersection

When performing the task by counting at the intersection, the user marks the photo of the microstructure in the form of segments. It was possible to clear the last symbols in case of error. The program automatically calculates the total length of the segments required to calculate the grain score further and displays the estimated value in the TextBox after

drawing each new element. The implementation of the transition to the image of the real microstructure and the implementation of calculations are implemented similarly to the previous version of the work. This method also implemented the change from working with a schematic microstructure to a real one (Fig. 5).
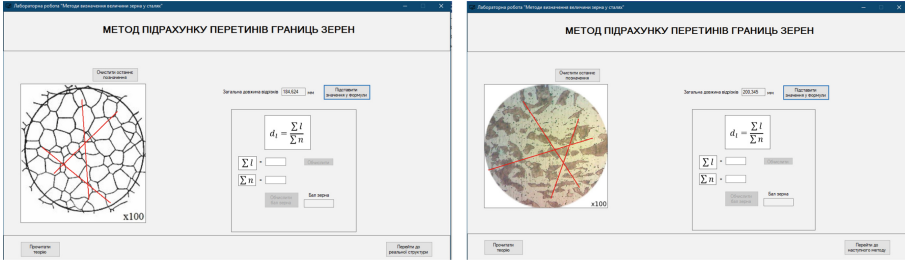

Fig. 5. Implementation of the second method and completion of formulas.

4.3   Implementation of the Comparison Method

When performing the task, the user compares the microstructure with which he worked with the microstructures from DSTU. In this method, the user determines the grain score by entering its value in the appropriate TextBox. The implementation of the third method is shown in Fig. 6.
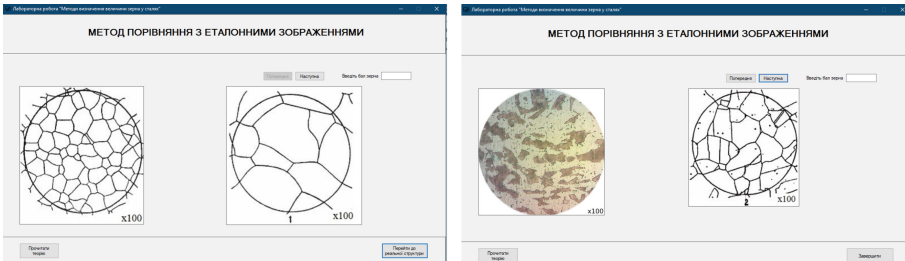
Fig. 6. Implementation of the third method for the schematic and the real structure.

When performing VLW, the student can always view the theory using the button in the lower-left corner of the screen.

It was implemented to save all the obtained values in the Word document of the template of the report on laboratory work, which occurs after clicking on the "Finish" button. A separate ReportDocHelper class was created to create the report, which stores the values of all indexes to be searched in the report template as constants and all replacement values stored in the array after each method completes the calculation. It gets the value of the report file path selected by the user and saves the document in the created additional folder along this path, storing images of microstructures.

To more accurately follow the process of determining the grain size when counting, a pop-up window with a warning appears on the screen before starting work. After reading it and giving consent, the student can proceed to the next step and perform the laboratory work itself.

After implementing the software product, an installer was created to easily download the program to the user's computer. The software product works correctly after downloading.

Both schematic structures and photos of actual structures processed in the Photoshop graphic editor are used for virtual laboratory work. It makes it possible to bring virtual work closer to actual research.

5 Conclusions

Nowadays, studying using laboratory works and materials presented in electronic form is more convenient. It reduces the time to complete tasks and check the task by the trainer. Despite this, students of engineering specialties who study the analysis of the structure of metals, even today, use standard physical equipment to perform the necessary experiments. The developed software can replace the performance of real physical laboratory work during the study of the discipline «Defectoscopy and methods of structural analysis of materials and products» and simplify the organization of the educational process by distance learning.

The developed VLW for students of the specialty «Materials Science» allows you to assess the knowledge and skills of the student, which can be used as a criterion for admitting students to the passage of real laboratory work. It is also possible to use VLW in a distance learning system. Thus, traditional forms of laboratory work can be successfully supplemented with virtual laboratory work.

But still, the approach to the problem of creating VLW and their introduction into the educational process should be differentiated. It is impossible to reduce the training of especially engineering specialists to virtual learning, to a situation where a student does not have the opportunity to touch equipment and materials with his own hands.

The knowledge gained during the performance of VLW can be used to study microstructures when performing tests, course projects, writing qualifying graduate work for bachelor's and master's degrees. It is expected that the developed VLW will be in demand at the departments of metal research in higher education. Using VLW, trainers will reduce the amount of time and human resources spent on studying the metal grain score.

References

1. Shet, S.V., Pereira, V.: Proposed managerial competencies for industry 4.0 – implications for social sustainability. Technol. Forecast. Social Change **173**, 121080 (2021). https://doi.org/10.1016/j.techfore.2021.121080

2. Artyukhov, A., Omelyanenko, V., Prokopenko, O.: University technology transfer network structure development: education and research quality issues. TEM J. **10**(2), 607–619 (2021). https://doi.org/10.18421/TEM102-16

3. Vorontsova, A., Vasylieva, T., Lyeonov, S., Artyukhov, A., Mayboroda, T.: Education expenditures as a factor in bridging the gap at the level of digitalization. In: 2021 11th International Conference on Advanced Computer Information Technologies (ACIT), pp. 242–245 (2021). https://doi.org/10.1109/ACIT52158.2021.9548338

4. Denysenko, Y., Ivanov, V., Ivchenko, O.: Quality assessment of teaching the disciplines in the e-learning environment of sumy state university. In: CEUR Workshop Proceedings. 13th International Conference on ICT in Education, Research and Industrial Applications. Integration, Harmonization and Knowledge Transfer, ICTERI 2017, vol. 1844, pp. 166–175 (2017)

5. Zhylenko, T., Ivanov, V., Pavlenko, I., Martynova, N., Zuban, Y., Samokhvalov, D.: Mobile applications in engineering based on the technology of augmented reality. In: Machado, J., Soares, F., Trojanowska, J., Yildirim, S. (eds.) icieng 2021. LNME, pp. 366–376. Springer, Cham (2022). https://doi.org/10.1007/978-3-030-79168-1_33

6. Švač, V., Cagáňová, D.: Managerial skills for innovation support. Mob. Netw. Appl. **25**(3), 925–931 (2020). https://doi.org/10.1007/s11036-020-01517-3

7. Ivanov, V., Pavlenko, I., Trojanowska, J., Zuban, Y., Samokhvalov, D., Bun, P.: Using the augmented reality for training engineering students. In: Bruzzone, A.G., et al. (eds.) Proceedings of the 4th International Conference of the Virtual and Augmented Reality in Education, VARE 2018, pp. 57–64 (2018)

8. Bun, P., Trojanowska, J., Ivanov, V., Pavlenko, I.: The use of virtual reality training application to increase the effectiveness of workshops in the field of lean manufacturing. In: Bruzzone, A.G., et al. (eds.) Proceedings of the 4th International Conference of the Virtual and Augmented Reality in Education, VARE 2018, pp. 65–71 (2018)

9. Bakhovskyy, P., Yevsiuk, M., Zabolotnyi, O., Cagáňová, D., Tkachuk, A.: Stages of the virtual technical functions concept networks development. In: Cagáňová, Da., Horňáková, N., Pusca, A., Cunha, P.F. (eds.) Advances in Industrial Internet of Things, Engineering and Management. EICC, pp. 119–135. Springer, Cham (2021). https://doi.org/10.1007/978-3-030-69705-1_7

10. Tkachuk, A., Zablotskyi, V., Zabolotnyi, O., Cagáňová, D., Yakymchuk, N.: Basic stations work optimization in cellular communication network. In: Cagáňová, D., Horňáková, N., Pusca, A., Cunha, P.F. (eds.) Advances in Industrial Internet of Things, Engineering and Management, pp. 1–19. Springer International Publishing, Cham (2021). https://doi.org/10.1007/978-3-030-69705-1_1

11. Korotun, M., Denysenko, Y., Malovana, N., Dutchenko, O.: Improvement of the effectiveness of general engineering courses using trainers. In: Ivanov, V., Trojanowska, J., Pavlenko, I., Zajac, J., Peraković, D. (eds.) DSMIE 2020. LNME, pp. 23–34. Springer, Cham (2020). https://doi.org/10.1007/978-3-030-50794-7_3

12. Bilous, O., Hovorun, T., Berladir, K., Dunaeva, M.: Ensuring the quality of training engineers in a virtual environment. In: Tonkonogyi, V., et al. (eds.) InterPartner 2020. LNME, pp. 765–774. Springer, Cham (2021). https://doi.org/10.1007/978-3-030-68014-5_74

13. Núñez-Canal, M., de Obesso, M., Pérez-Rivero, C.A.: New challenges in higher education: a study of the digital competence of educators in Covid times. Technol. Forecast. Soc. Chang. **174**, 121270 (2022). https://doi.org/10.1016/j.techfore.2021.121270

14. Nagayev, V., Danchenko, I., Mitiashkina, T., Kyrepin, V.: Administrative fundamentals of ecological competence forming in agricultural engineering students under conditions of their professional training. In: Tonkonogyi, V., Ivanov, V., Trojanowska, J., Oborskyi, G., Pavlenko, I. (eds.) Advanced Manufacturing Processes III: Selected Papers from the 3rd Grabchenko's International Conference on Advanced Manufacturing Processes (InterPartner-2021), September 7-10, 2021, Odessa, Ukraine, pp. 697–706. Springer International Publishing, Cham (2022). https://doi.org/10.1007/978-3-030-91327-4_67

15. Trojanowska, J., Karwasz, A., Machado, J.M., Varela, M.L.R.: Virtual reality based ecodesign. In: Golinska-Dawson, P., Kolinski, A. (eds.) Efficiency in Sustainable Supply Chain. E, pp. 119–135. Springer, Cham (2017). https://doi.org/10.1007/978-3-319-46451-0_8

16. Karwasz, A., Trojanowska, J.: Using CAD 3D system in ecodesign—case study. In: Golinska-Dawson, P., Kolinski, A. (eds.) Efficiency in Sustainable Supply Chain. E, pp. 137–160. Springer, Cham (2017). https://doi.org/10.1007/978-3-319-46451-0_9

17. Ji, X., Mirkoohi, E., Ning, J., Liang, S.Y.: Analytical modeling of post-printing grain size in metal additive manufacturing. Opt. Lasers Eng. **124**, 105805 (2020). https://doi.org/10.1016/j.optlaseng.2019.105805

18. Ostroverkh, A.S., et al.: Challenges of fuel cell technologies for the needs of the energy transition to a zero-carbon technology. J. Eng. Sci. **8**(2), G1–G10 (2021). https://doi.org/10.21272/jes.2021.8(2).g1

19. Wittwer, M., Gaskey, B., Seita, M.: An automated and unbiased grain segmentation method based on directional reflectance microscopy. Mater. Charact. **174**, 110978 (2021). https://doi.org/10.1016/j.matchar.2021.110978

20. Berladir, K., Hovorun, T., Gusak, O., Reshetniak, Y., Khudaybergenov, D.: Influence of modifiers-ligatures on the properties of cast aluminum alloy AK5M2 for the automotive industry. In: Ivanov, V., Trojanowska, J., Pavlenko, I., Zajac, J., Peraković, D. (eds.) DSMIE 2020. LNME, pp. 473–482. Springer, Cham (2020). https://doi.org/10.1007/978-3-030-50794-7_46

21. Gu, Q., et al.: Microstructure heritance of metallographic feature in the anodization of carbon steels. Mater. Lett. **288**, 129410 (2021). https://doi.org/10.1016/j.matlet.2021.129410

22. Zhang, Y., et al.: Study of the kinetics of austenite grain growth by dynamic Ti-rich and Nb-rich carbonitride dissolution in HSLA steel: In-situ observation and modeling. Mater. Charact. **169**, 110612 (2020). https://doi.org/10.1016/j.matchar.2020.110612

23. Plotkowski, A., et al.: A stochastic scan strategy for grain structure control in complex geometries using electron beam powder bed fusion. Addit. Manuf. **46**, 102092 (2021). https://doi.org/10.1016/j.addma.2021.102092

24. Luengo, J., et al.: A tutorial on the segmentation of metallographic images: taxonomy, new MetalDAM dataset, deep learning-based ensemble model, experimental analysis and challenges. Inf. Fusion **78**, 232–253 (2022). https://doi.org/10.1016/j.inffus.2021.09.018

Integration of End-to-End and Dual Learning as a Guarantee of Quality Professional Training for Future Power Engineers

Karine Gorbunova[1] , Viktor Nagayev[2(✉)] , Svitlana Litvinchuk[1] ,
Kateryna Ulitina[1] , and Tetiana Gannichenko[1]

[1] Mykolayiv National Agrarian University, 9, Georgy Gongadze Street, Mykolaiv 54020,
Ukraine
[2] State Biotechnological University, 44, Alchevskih Street, Kharkiv 61002, Ukraine
nagaevviktor1966@gmail.com

Abstract. This article substantiates the organization of end-to-end learning in combination with dual learning in the professional education of future power engineers to ensure the competence and competitiveness of future specialists in the dynamic labour market. Theoretical and empirical methods (monographic analysis, synthesis, modeling, experiment, observation, forecasting) were used in the research. An applied model of end-to-end professional training in combination with dual education for future specialists of the agricultural sector at master's level is proposed through the example specific topic in which an important role belongs to the research work of higher education learners. In order to more fully assess the depth of such an organization of professional training of future power engineers at Mykolayiv National Agrarian University, based on end-to-end training in combination with dual learning, the established level of readiness of higher education learners for future professional activity is analysed which will provide the labour market with highly qualified and competent specialists for the fuel and energy complex of Ukraine. Research results confirmed the acceptability of the model of the professional competence forming process of power engineering students during their professional training. Implementation of the model of end-to-end training in combination with dual training provides visualization of pedagogical conditions of activating didactic processes, along with organizational and technological procedures and, as a result, improves the quality characteristics of specialists' training.

Keywords: End-to-end training · Dual education · Future power engineers · Job training · Professional training · Model · Instruction quality · Sustainable development education · Educational policies

1 Introduction

Changes in the economic, political, social, cultural, and spiritual spheres of public life (especially in the era of the Covid-19 pandemic) require significant changes in the

education paradigm in improving the organization, content, forms, and methods of the educational process of future power engineers. The main strategic objectives of modern education according to the National strategy of development of education in Ukraine on 2012–2021 are ensuring national and regional needs for qualified personnel, competitive in a dynamic market relationship, bringing professional education in Ukraine to the level of developed countries [1].

Today, higher education institutions face the critical task of professional training of future power engineers, who can adequately respond to changes in the country's social, political, and economic life in modern conditions. Implementing the tasks requires the search for more effective ways and principles of organization of the educational process, which would provide quality training of power engineering specialists, one of which should be considered the introduction of the end-to-end principle in combination with dual learning in the educational process. Research on this issue is of great scientific and practical importance, which consists of possibly improving the system of organization of the educational process by introducing end-to-end learning in combination with dual learning during the teaching of electric power disciplines for future professionals.

Considering the significant experience in the field of training, in particular, in the specialty 141 «Electric power engineering, electrical engineering, and electromechanics», the problem of developing and implementing the integration of end-to-end and dual learning in professional training of future power engineers by the Bologna process, has not been sufficiently considered.

2   Literature Review

Analysis of recent research and publications on the organization of end-to-end training of students allows us to conclude about its importance and relevance. The scientific papers of such scientists as V. Nagayev, I. Danchenko, T. Mitiashkina, V. Kyrepin [2], D. Kostyuk [3], V. Duganets [4] have been devoted to the issue of theoretical and methodological substantiation of the mechanism of end-to-end practical training of future specialists of engineering specialties. They substantiate the expediency of such training for future specialists of technical specialties.

A significant contribution to the development of practical recommendations for the organization of job training of specialties of different qualification levels, the development of practical skills outside the classroom, as well as training in the workplace was made by scientists: N. Nychkalo [5], P. Luzan [6], O. Koshuk [7]. Their works became the basis and example for further development of designing end-to-end practical training issues in broader aspects.

The theoretical and methodological substantiation and experimental verification of the mechanism of end-to-end organization of independent work of future specialists in engineering specialties are studied in the doctoral dissertation of D. Kostyuk [3]. V. Duganets substantiates the expediency of implementing end-to-end practical training in his works [8]. In the papers of N. Nychkalo, a method of designing and adjusting the content of end-to-end training of future specialists based on a competence-oriented approach is proposed [5]. Foreign scientists investigate various aspects of agricultural education and the professional competence of specialists. Thus, J. Kirsten explores

interdisciplinary aspects of training in agricultural economics [9]; M. Newman defines the general philosophy of agricultural education [10]; H. Hassenpflug studies the system of dual agricultural education in Germany and the possibility of its implementation in Ukraine [11].

It is worth noting that the modern educational strategy of national and European universities, that the modern educational strategy of national and European universities, which clearly defines the focus on quality results training of future energy professionals and the use of active teaching methods, and aims at implementing the basic principles of the Bologna Declaration, is directly related to the end-to-end approach [12]. Under these conditions, dual education is essential [13, 14]. The development of dual education, when educational institutions and specialized agricultural enterprises are involved in the training of future highly qualified specialists, improves the quality of education and its compliance with European standards [15] and a competitive dynamic labour market [16].

At the same time, the problems of forming professional qualities of future energy engineers in the context of integration of end-to-end and dual education in higher education in terms of innovative pedagogical activity that will contribute to the implementation of the basic principles of the Bologna Agreements remain insufficiently studied [17, 18]. The analysis results show that the attention to this problem is not yet systematic, and there is almost no scientific research on end-to-end training with dual training of future power engineers in agriculture.

Because of the above considerations, this article aims to substantiate an indicative model that organically combines end-to-end training with dual training of future power engineers in agrarian educational institutions and practical research on the effectiveness of this organization of training.

3   Research Methodology

The research is based on a set of methodological approaches to forming and developing the professional competence of future power engineers. The main approaches are personality-oriented, competency-based, activity, systematic, technological, managerial, and synergistic [19, 20].

To solve the tasks, we use the following research methods: theoretical (aspect and conceptual-terminological analysis of literary sources, comparative analysis, generalization and systematization of research directions and engineering specialists educational programs); empirical (experiment, observation, functional analysis of research results, statistical processing, and data interpretation) [21].

The use of didactic models and innovative technologies of pedagogical process management ensures a high professional level [22]. This article considers implementing an applied model of end-to-end professional training in combination with dual education in professional competence forming in engineering personnel of the energy sector. A variety of methodological and practical approaches allowed to form a didactic management system for the formation of professional competence of future power engineers. This system considers organizational forms and educational technologies to provide educational results and production skills [23].

It should be noted that the development of a model of practical training of future power engineers should be preceded by: analysis of job training internship, determination of qualitative changes in modern production and prospects for the development of the electric power industry; consideration of changes in production and the requirements of the European labour market; determination of current needs for the future power engineers based on the actual job training [24].

4 Results

In agricultural educational institutions, practical training was planned by top lecturers who taught specific disciplines. There was practically no connection between its types both within the discipline itself and at the interdisciplinary level. The topics of practical works were chosen to consider the research activities of lecturers. The topics of diploma projects were determined in senior courses and were practically unrelated to job training content [25].

It is offered to introduce the technology of creating educational process on end-to-end principle at Mykolayiv National Agrarian University on which the theme of the diploma project and course works (projects) is defined at junior courses. Laboratory work, practical work, and work in the workplace are carried out because of their organic inclusion in the training practices included in the production, and those, in turn, in the pre-diploma. In this case, all students' practical work stages are coordinated with an enterprise. It testifies to the organization of dual training combined with end-to-end future power engineers in the Mykolayiv National Agrarian University at Electric Power Engineering, Electrical Engineering, and Electromechanics Department.

Mykolayiv National Agrarian University (MNAU) has always paid considerable attention to improving the practical component of training highly qualified specialists. This is evidenced by the functioning of branches of departments at enterprises, the organization of job practices, the holding of practical classes in enterprises, offsite meetings of the examination board for the defense of master's theses at enterprises. In 2017, the Regulation on the Procedure for Organizing and Implementing Dual Training at MNAU was approved. Thus, in particular, the Faculty of Engineering and Energy has concluded agreements on dual training with 11 companies.

The experience of cooperation of MNAU with public utility «Mykolayivoblteploenergo» is especially interesting. The cooperation begins with coordinating curricula for training specialists in the specialty 141 «Electric Power Engineering, Electrical Engineering, and Electromechanics» with the management of the public utility «Mykolayivoblteploenergo». This makes it possible to adjust curricula to the latest technologies and modern equipment in electric power engineering. First-year students are involved in educational tours, where they have the opportunity to get acquainted with electrical installations, monitoring instrumentation, equipment of heating units, and pumping stations (see Table 1).

After the first and second courses at the enterprise, students undergo internships. For example, last year, ten students, after the internship, expressed a desire to get a job and at the same time continue their studies in a dual form of education. It should be noted that these students, studying according to individual plans, have good academic performance, which allows them to receive salary and academic scholarships.

The Department of «Electrical Power Engineering, Electrical Engineering, and Electromechanics» involved lectures on disciplines of professional and practical training of leading specialists of «Mykolaivoblteploenergo». It should be noted that 10–20% of the master's theses are related to scientific research of heat supply problems, and specialists of public utility «Mykolayivoblteploenergo» review these works. Based on the development of scientists, we substantiated and built an applied model of the organization of end-to-end job training in combination with dual learning for educational level «master» in specialty 141 «Electric Power Engineering, Electrical Engineering, and Electromechanics» (illustrated on an example of a specific topic).

In the model, individual creative tasks are included in course papers (projects), research papers and publications, reports on internships and diploma projects. Course papers (projects) may be included in scientific papers and publications, reports on internships, and diploma projects. Scientific works and publications may be included in course papers (projects), reports on internships, and diploma projects. Internship reports are included in course papers (projects), research papers and publications, and diploma projects. Describing the model of an integrated combination of end-to-end training with dual learning provides various options for including some components in others. Small-scale works can be thematically included in medium-scale ones. They, in turn, are included in qualification work, which is usually agreed with production and corresponds to research topics of the department where the graduate is assigned.
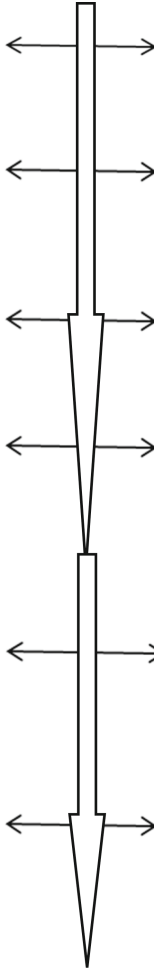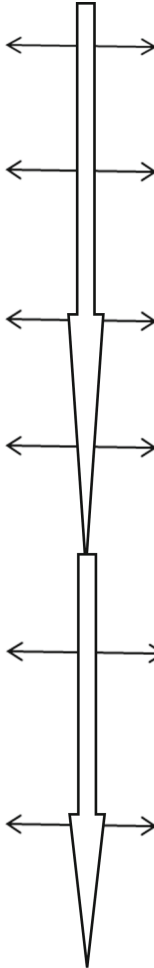
Thus, the essence of end-to-end learning is to perform the maximum number of works on the subject of the future diploma project, the development of which is the final stage of the future power engineer's professional competence formation. Characterizing the model, we consider that end-to-end training combined with dual training of future power engineers starts when higher education learners begin to study a cycle of professionally oriented disciplines, which is the second year of study at the university. This is preceded by an introductory practice, which depends on the motivational component of professional training of future power engineers. It should be carried out at the best production units of public utility «Mykolayivoblteploenergo». Practical bases should demonstrate where the future graduate will be able to work what knowledge and skills he/she will need for future work. At the end of the third and the beginning of the fourth year, there is a job technological training internship, during which students receive internships primarily for full-time positions with a salary.

The close link between the educational process and production also takes place during the pre-graduation internship, where students gain experience in production management. In addition, they collect material for the diploma project.

It should be noted that production workers are involved in preparing tasks for the diploma project of higher education learners to assess the possibility of providing the student with a workplace upon completion of the work. Such an organization of training is more complicated than a traditional one and requires more effective implementation of enterprise resources, as the organization of the educational process will involve equipment and production specialists.

Over the past five years, thanks to the cooperation with public utility «Mykolayivoblteploenergo» curricula have been adjusted. The following changes have been

Table 1. Indicative applied model of the organization of end-to-end professional training with dual training of higher education learners in the educational specialty 141 «Electric power engineering, electrical engineering and electromechanics» based on the public utility «Mykolayivoblteploenergo».

Educational degree	Year of study	Topics of educational and scientific works related to production tasks of public utility «Mykolayivoblteploenergo»	The end-to-end character of professional training of learners of the educational specialty «Electric power engineering and electromechanics»	Individual creative tasks, research works, and scientific articles on the topic of the diploma project «Mykolayivoblteploenergo»
ED «Bachelor» in Energy Engineering	1 year	Final module test, the topic of which is related to professional disciplines Training electromechanical practical training with productive and technical tasks		Scientific Workshop «My scientific debut» on energy issues
	2 year	Course paper on the discipline «Field and electromagnetic calculations» on the proposed topic «Power supply systems» Electrical installation practical training on based of production		Individual creative tasks on the theme of the coursework
	3 year	Course paper on discipline «Theoretical Foundations of Automation» Course paper on discipline «Electrical machines» Technological operational practical training based on «Mykolayivoblteploenergo»		Competition of creative research papers on the subject of tasks of «Mykolayivoblteploenergo»
	4 year	Course paper on discipline «Fundamentals of Electric Power Engineering and Electrical Power Supply» Course project «Theory of electric drive»		Participation in conferences on the subject of tasks
ED «Master» in Energy Engineering	1 year	Course project on discipline «Design of Automatic Electric Drive in Agroindustrial Complex» Course project on discipline «Design of Electric Power Supply Systems of Agroindustrial Complex» Professional Internship: Pre-Graduation Internship (second (master's) level of higher education)		Competition of creative research papers on the subject of the diploma project
	2 year	Course work on discipline «Fundamentals of Relay Protection and Automation Electrical Power Supply» Qualifying Paper at the second (master's) level of higher education «Estimation of the reliability of initial information and calculation models for determining the modes of distributive electric networks		Final conference of graduates-power engineers with leading specialists of public utility «Mykolayivoblteploenergo»

made to the content of the training (disciplines added): 1) Field electromagnetic calculations (2nd year, 4th semester, 120 h (4 credits), Credit, and Course paper); 2) Electrical Engineering (4th year, 8th semester, 150 h (5 credits), Credit); 3) Theory of Electric Drive (4th year, 7th, and 8th semesters; 7th semester - 120 h (4 credits) - Exam; 8th semester - 120 h (4 credits) Exam, and Course Project).

Topics of course work, course projects, and other research papers are coordinated with external stakeholders to bring them closer to production topics. Having received the topic of course work in the second year, higher education learner has the opportunity to continue working on it in the fourth year, and further when completing a diploma project, to consider it more thoroughly and in detail.

During this period, students need to identify the theme of the future diploma project and choose a supervisor. This approach ensures an organic relationship between course projects and diploma topics and determines those aspects that should be paid special attention to during the internship at the public utility "Mykolayivobltteploenergo".

An important place in the indicative applied model of integration of end-to-end and dual training is individual creative tasks, research papers, and scientific articles on the diploma project. The implementation of research works by higher education learners is carried out on the materials of the «Mykolayivobltteploenergo» enterprise, which is the base for job training internship and preparation of diploma projects. The performance of research works by higher education learners on production materials occupies an essential place in the given model because it allows: firstly, to solve problems of deficit of qualitative student's works; secondly, to save much time on the implementation of diploma projects, which will contain scientific novelty; thirdly, to bring training closer to the complex solution of specific production situations. Working in an end-to-end system in combination with dual learning, each student is a «specialist in his/her field» allowing one always to be ready to speak at conferences of different levels.

End-to-end technology of diploma projects, which involves determining the topics of all course papers (projects) and research papers as close as possible to the diploma, will contribute to the fact that education and research activities of students will be productively motivated to perform individual creative tasks. As a result of the study, we propose an applied model of the end-to-end professional training system in combination with a dual system for future power engineers, which integrates education, science, and production. An essential role in this model is given to the research work of higher education learners (see Table 2).

In order to more fully assess the thoroughness of professional training of future power engineers at the Mykolayiv National Agrarian University based on end-to-end training in combination with dual, we will analyze the level of readiness of future professionals for professional activity.

The experiment involved 37 students of the experimental group (end-to-end learning in combination with dual learning) and 39 students of the control groups (traditional learning). In order to determine the levels of formation of the components of readiness for future professional activity, tests, oral and written interviews, self-assessment, modeling of situations, solving productive and technical tasks, practical tasks related to the tasks of «Mykolayivobltteploenergo» were used.

Table 2. Levels of formation of readiness of future power engineers for professional activity.

Component	Need-motivational				Problem-cognitive				Practical-activity orientated			
Levels	High	Sufficient	Average	Low	High	Sufficient	Average	Low	High	Sufficient	Average	Low
EG (experimental groups), %	37,2	43,8	19,0	0	35,8	39,4	21,2	3,6	33,6	35,8	30,6	0
CG (control groups), %	19,0	34,3	45,2	1,5	17,5	31,4	32,9	18,2	15,3	26,3	41,6	16,8

According to the experts' assessments, most students have gained knowledge based on which professional abilities and skills have been formed, which are part of the holistic complex of readiness provision for future professional activity in the fuel and energy complex of Ukraine. Analysis of experimental data showed that in the process of training, there were significant changes in indicators of future power engineers' readiness levels for professional activity in the electric power industry. They are especially noticeable in the experimental groups (see Table 2).

The comparative analysis of the obtained results has given grounds to state that higher education learners in the experimental groups have a higher level of readiness for professional activity, reflected in motivational, cognitive, and practical spheres. The table's data shows that at the end of the experiment, the high level of the motivational sphere of readiness reached the mark: for students of EG – 37.2%; for students of CG – 19.0%.

The analysis of the state of the problem-cognitive sphere resulting from the pedagogical experiment showed that 35.8% of future EG specialists found a high level, 39.4% - a sufficient level of readiness for professional activity. Respectively, 17.5% and 31.4% of CG students have acquired knowledge of electrical engineering disciplines and have reached a high and sufficient level of problem-cognitive component of readiness for professional activity. The average level of readiness remained in 32.9% of higher education students of CG and 21.2% of EG students. This indicates that students have mastered the amount of theoretical knowledge needed to solve problems of professional activity and have developed the ability to analyze technical and scientific literature. A high level of practical activity component of readiness was revealed by 33.6% of students in the EG and 15.3% - of students in the CG. The sufficient level was revealed by 35.8% of EG students and 26.3% of CG students.

The students of experimental groups with a high level of practical-activity orientated component of readiness for professional activity revealed the ability to solve problems of practical content analysis and find solutions to non-standard or problematic production situations. The creative and cognitive activity of EG students has significantly increased, which was manifested in the process of solving productive and technical problems implementation of the course and diploma projects in research work. At the end of the pedagogical experiment, the high level of CG students was recorded only in some indicators, which indicates the imperfection of their professional training. In comparison with the experimental groups in the control groups, there was a significant difference in conducting research work in the professional field.

5 Conclusions

The comparative analysis of the received results has allowed stating that the future power engineers of the experimental groups have a higher level of readiness for professional activity, characterized by the presence of theoretical knowledge, practical abilities, and skills, which are shown in the needed-motivational, problem-cognitive and practically-activity orientated spheres. Most future specialists have mastered practical knowledge, skills, and abilities.

The significant difference in quantitative and qualitative indicators of the levels of practical knowledge, skills, and abilities confirmed the effectiveness of implementing the proposed applied model for the organization of the end-to-end in combination with dual training for future power engineers in an agrarian educational institution.

Such end-to-end cooperation combined with dual training in the practical training of future power engineers guarantees high-quality professional training. It contributes to providing the labour market with highly qualified and competent specialists for the fuel and energy complex of Ukraine.

The obtained results allowed us to determine the ways of further scientific and pedagogical investigation in this direction: the creation of information electronic methodical systems of the educational and methodical provision in a context of future power engineers professional competence forming; implementation of pedagogical technologies of management of educational activity of students during the period of their engineering education.

References

1. Yagupov, V., Kostyuk, D.: Methods of formation of professional competence of future technicians-electricians of agriculture. Coll Sci. Works Natl. Acad. State Border Guard Serv. Ukr. Ser. Pedagogical Psychol. Sci. **1**, 320–332 (2015)
2. Nagayev, V., Danchenko, I., Mitiashkina, T., Kyrepin, V.: Administrative fundamentals of ecological competence forming in agricultural engineering students under conditions of their professional training. In: Tonkonogyi, V., Ivanov, V., Trojanowska, J., Oborskyi, G., Pavlenko, I. (eds.) InterPartner 2021. LNME, pp. 697–706. Springer, Cham (2022). https://doi.org/10.1007/978-3-030-91327-4_67
3. Kostyuk, D.: Pedagogical conditions of formation of professional competence at future technicians-electricians of agriculture. Sci. Bull. Natl. Univ. Life Environ. Sci. Ukr. Pedagogy Psychol. Philos. **199**(2), 344–349 (2014)
4. Duganets, V.: Through practical training of students - the approximation of future professionals to the manufacturing sector. Prob. Eng. Pedagogical Educ. Coll. Sci. Wash Kharkiv UIPA **24**(25), 9–16 (2014)
5. Nychkalo, N., Lazarenko, N., Gurevich, R.: Informatization and digitalization of society in the 21st century: new challenges for institutions of higher education. Mod. Inf. Technol. Innov. Teach. Methods Train. Methodol. Theory Exp. Prob. Coll. Sci. Works **60**, 17–29 (2021). https://doi.org/10.31652/2412-1142-2021-60-17-29
6. Luzan, P., Koshuk, O., Titova, O., Mosia, I.: The technology of the learning outcomes test development. In: Tonkonogyi, V., Ivanov, V., Trojanowska, J., Oborskyi, G., Pavlenko, I. (eds.) InterPartner 2021. LNME, pp. 687–696. Springer, Cham (2022). https://doi.org/10.1007/978-3-030-91327-4_66

7. Koshuk, O.: Perspective directions of modernization to vocational training of future mechanical engineers agricultural industry. Sci. J. Innov. Sol. Mod. Sci. **8**(17), 24–36 (2017)
8. Duganets, V.: End-to-end practical training of students of agricultural and engineering specialties. Vocat. Tech. Educ. **3**, 26–29 (2015)
9. Kirsten, J.: The case for interdisciplinary research and training in Agricultural Economics in Southern Africa. Nat. Sci. Soc. **16**(4), 356–363 (2014)
10. Newman, M., Capital, A., Capital, E.: Ripples in the agricultural education pool. J. Agric. Educ. **58**(1), 4–13 (2017)
11. Hassenpflug, H.: The system of dual agricultural training in Germany – Options for Ukraine. German-Ukrainian agricultural policy dialogue, Kyiv (2017)
12. Hadgraft, R., Kolmos, A.: Emerging learning environments in engineering education. Aust. J. Eng. Educ. **25**(1), 3–16 (2020). https://doi.org/10.1080/22054952.2020.1713522
13. Rychen, D.S., Salganik, L.H.: Defining and Selecting Key Competencies. Hogrefe and Huber Publishers, Göttingen (2001)
14. Lean-Filho, W., Nesbit, S., et al.: New Developments in Engineering Education for Sustainable Development. Springer, Switzerland (2016). https://doi.org/10.1007/978-3-319-32933-8
15. Boon, J., Klink, M.: Competenciec: the triumph of fuzzy concept. In: Proceedings of Academy of Human Resources Development Annual Conference, Honolulu, vol. 1, pp. 327–334 (2002)
16. Hernandez-de-Menendez, M., Morales-Menendez, R.: Technological innovations and practices in engineering education: a review. Int. J. Interact. Design Manuf. (IJIDeM) **13**(2), 713–728 (2019). https://doi.org/10.1007/s12008-019-00550-1
17. Vries, P., Klaassen, R., Kamp, A.: Emerging technologies in engineering education: can we make it work? In: 13th International CDIO Conference Proceedings. University of Calgary (2017)
18. Duganets, V.: Programming of end-to-end practical training of junior specialists in the specialty «Mechanization of Agriculture». Higher School **3**(4), 59–67 (2016)
19. Nagayev, V., Bakum, M., Mityashkina, T., Sementsov, V.: Technological bases of formation of professional and creative competence of future engineers of agro-industrial production. Image Mod. Teach. **1**(190), 16–22 (2020)
20. Sosnytska, N., Titova, O., Symonenko, S., Kravets, O.: Examining the creative potential of engineering students. In: Nadykto, V. (ed.) Modern Development Paths of Agricultural Production, pp. 299–306. Springer, Cham (2019). https://doi.org/10.1007/978-3-030-14918-5_31
21. Cropley, D.H., Cropley, A.J.: Engineering creativity: a systems concept of functional creativity. Creat. Across Domains Faces muse **1**(15), 169–185 (2005)
22. Bilous, O., Hovorun, T., Berladir, K., Dunaeva, M.: Ensuring the quality of training engineers in a virtual environment. In: Tonkonogyi, V., et al. (eds.) InterPartner 2020. LNME, pp. 765–774. Springer, Cham (2021). https://doi.org/10.1007/978-3-030-68014-5_74
23. Lushchyk, Y.: Training future agrarians: specifics of academic programmes of bachelor's degrees in Great Britain. Central Eur. J. Sci. Res. **5**(41), 42–52 (2017)
24. Titova, O., Luzan, P., Sosnytska, N., Kulieshov, S., Suprun, O.: Information and communication technology tools for enhancing engineering students' creativity. In: Ivanov, V., Trojanowska, J., Pavlenko, I., Zajac, J., Peraković, D. (eds.) DSMIE 2021. LNME, pp. 332–340. Springer, Cham (2021). https://doi.org/10.1007/978-3-030-77719-7_33
25. Svyrydiuk, V., Luzan, P., Svyrydiuk, O., Titova, O., Popova, O.: Electronic textbooks as means for developing professional competencies of engineering students. In: Tonkonogyi, V., Ivanov, V., Trojanowska, J., Oborskyi, G., Pavlenko, I. (eds.) InterPartner 2021. LNME, pp. 707–716. Springer, Cham (2022). https://doi.org/10.1007/978-3-030-91327-4_68

The Design of Workplaces with Augmented Reality in Engineering Education

Jozef Husár[(✉)] [iD], Lucia Knapčíková [iD], Stella Hrehova [iD], and Michal Balog [iD]

Technical University of Košice, 1, Bayerova Street, Prešov 080 01, Slovak Republic
`jozef.husar@tuke.sk`

Abstract. The article deals with the possibility of using augmented reality on the principle of marker target for student education. The whole proposed concept consists of the principle of displaying 3D models of machines, equipment, robots, conveyors, and accessories above the markers depicting an actual device. The first part of the article was focused on the 3D model software tools and was presented a step-by-step procedure for creating an AR application. We will describe a specific strategy for building a 3D model, creating a marker in the Vuforia engine interface. Subsequently, the procedure for working in the Unity development interface up to the final export of the final application was presented. The second part of the article was focused on the developed application and the possibilities of its deployment in the educational process. The initial tests were used by university students on the subject "Digitalisation of Production and Services". The gained results show the innovativeness of the proposed solution. In this article, an AR application was implemented in the educational process as a new distance education tool during the COVID-19 pandemic. This new way of presenting 3D models using AR falls under the concept of Industry 4.0, which is becoming a necessity today and brings many benefits in education and practice.

Keywords: Augmented reality · 3D model · Application · Unity · Sustainable manufacturing · Industrial innovation · Educational policies

1 Introduction

The current trend is to discover new technologies. Progress is moving at an unstoppable pace and brings in some directions, even futuristic technologies. Our task is to know how we will deal with this fact; either we will ride the wave of development or close ourselves to it. In any case, man is forced to broaden his horizons because we are surrounded by technology. Because of this fact, it is part of our daily lives, so it cannot be avoided [1].

Virtual reality technology is one of many constantly evolving technologies. This technology has wholly changed one's view of reality as such [2].

It has opened a chapter in technology that literally created a new unknown world. However, this technology has also taken on a new dimension with technical progress. With the emergence of augmented reality, the virtual world merged with the real. By putting virtual elements into the real environment, human perception of the world has

been taken to another level [3]. Despite the knowledge gained so far with this technology, it is impossible to set boundaries. The practical use of augmented reality is still an unexplored area. The essence of this article is to explore the possibilities of augmented reality in terms of practical use in designing the production. The aim is to move standard design technologies to another level or demonstrate the potential that can be achieved today and prepare the way for this technology. The intention is to present the possibilities of software for creating virtual objects in coherence with CAD models through the developed application for augmented reality [4]. The presented application, which is the product of this work, points to the use of augmented reality together with CAD software in the field of education and the manufacturing sector as a tool for product dimension, workplaces, and the entire production company process [5–8].

2 Literature Review

Augmented reality applications are widely used, especially in the entertainment industry. The use of this technology in the industrial sphere is still rising. Since the possibilities of using augmented reality are many and still increasing, it is not possible to include them in one application [9]. The role of the application, which is the subject of this article, is primarily of an educational and presentational nature. In education, it is possible to better present various objects, transfer them with a simple image to a 3D model within augmented reality and thus virtually point out their actual use. In this way, the whole nature of education is changed. It facilitates a practical understanding of the context, which increases the quality of students' professional knowledge [10, 11]. It allows supplementing virtual 3D models with information that complements the standard information of technical drawings (production process, production technologies, physical contexts,…) when technical drawings are projected in augmented reality. In the field of design, it is possible with the help of this application to improve the design of products resp. Products are already at the design stage [12]. With the use of projection of virtual 3D models, it is possible to dimension their parameters, overall design, technical discrepancies with requirements, etc. In this way, it is possible to minimize the cost of prototypes or prevent improper production [13]. When designing production equipment, it is possible to set up a productive workplace with the help of markers before purchasing these devices. The advantage of this method is the ability to dimension production departments, optimize material flows, simulate the production process. The essence of this method is to reduce the acquisition costs of production equipment and optimize production capacity requirements [14].

3 Research Methodology

In this article, we try to design a procedure for creating an AR application that is to be used for product design. A simple principle is to create a more significant number of AR markers to which machine models are assigned, which are then combined into lines. In total, when creating an application, we must focus on three essential components. The first is to define the CAD software to create the 3D model. The second component is the Unity development software, and the last component is the Vuforia tool, in which we define a marker above which the 3D model will be displayed [15].

3.1   Software Support

To demonstrate the possibilities of our application in the augmented reality environment, we chose displaying using 3D models. These models can be created in a whole range of CAD programs depending on the programmed object, resp. The area in which the building fits (engineering, architecture, films, games, etc.). We use Autodesk Inventor software from Autodesk. The advantage of this software is its practicality, availability, experience, and user reviews, but mainly its compatibility with the Unity program [16].

This section describes the principle of creating a simple model in Autodesk Inventor and its subsequent transformation through Unity to an augmented reality application and its presentation in this environment. In addition to the programmed model based on the technical drawing, this section also describes the process of transforming more complex 3D models from various areas and software using Autodesk Inventor and Unity software. These models can be drawn from multiple freely accessible CAD databases available on the Internet [17].

3D Model Creation

After creating a CAD model or importing it into the Autodesk Inventor environment, comes the first step, which is the right format choice. The primary format for Autodesk Inventor is Inventor Part File (IPT). Because Unity does not support this format, saving the created model in OBJ (Object) format is necessary. The OBJ format is primarily for 3D objects in Unity [18].

Click on the "File" button we go to the "Export" link and select the "CAD Format" option. After clicking on this option, a new window will appear. Clicking on the "Save in" box will display a menu of alternative formats into which the created model can be converted. Select the "OBJ files" option and confirm by clicking on the "Save" option. It is possible to continue working with the saved 3D model in the Unity program [19].

Markers Creation

Every 3D model needs its own unique marker. A marker can take several forms (image, quadratic object, conical object, another more complex 3D object), but for the purpose of this article, we will use the form of images. For each 3D model, the 2D format of the model was selected, resp. Its image is in black and white/color. Better readability is the more pronounced color transitions, which results in the image providing more reference points for recognition. It is basically an identification tag that has the task of representing a virtual object. Each virtual object must have its own unique marker so that the final application can recognize and assign the correct object to that marker. The marker can take several forms [20]. The basic forms include a simple image, but it is also possible to use a cubic object, a conical object, and thus also a more complex 3D object. The Vuforia program then uses the "3D Tracking system" to search for object reference points and thus identify the appropriate marker. The Vuforia package contains several basic markers in the form of simple images. Of course, these markers can be used, but there is also the possibility to create your own markers. First of all, you need to activate the "ImageTarget" option from the Vuforia package (path: GameObject > Vuforia > ImageTarget).

The principle of creating new markers is that we upload new markers to this portal, which will create an installation package. We will then download this package and run

it to activate the new markers, which will be automatically added to the Unity program. It is important to note that you must be registered on the Unity website if you want to add new markers. Then all you have to do is log in. Subsequently, we generate a license key for each application separately in the Vuforie environment [21] (Fig. 1).
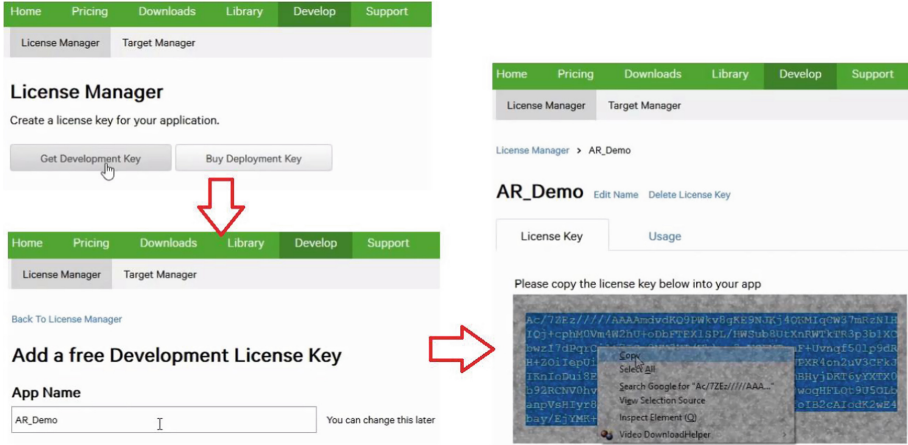
Fig. 1. License key generation.

After activating the license key, we will create a database of markers "Target Manager". As a first step, choosing the type of marker is necessary. There are four options to choose from: image, block, cone, and 3D object. In the next column, we will add the already selected marker format from any folder of the computer's memory. The third part requires the width of the selected marker. The function of this value is the representation of the marker itself in the Unity program on an absolute scale. The basic unit of the Unity program is the meter, so if we choose the dimensions of the marker in centimeters, we must use decimal numbers for this data. The last step is to select a unique marker name. Under this name, it will be identifiable in the Unity program. After completing all the window requirements, it is possible to assign a new marker by clicking on the "Add" button. This procedure must be applied to each marker individually. We can download the database to the development program if the database is complete.

Unity Development Program

The creation of 3D models in itself is slightly different from the creation of virtual 2D objects. Using Autodesk Inventor to modify 3D models to export them to OBJ format, there is no need to create a virtual object for these 3D models. The 3D models themselves, saved in the OBJ format, serve as virtual objects. Importing them into Unity is similar to 2D objects. Before starting the actual creation of virtual objects, it is necessary to set up the Unity program environment. Since we want to create an augmented reality application, we need to define an AR Camera (Fig. 2).

To set up this tool correctly, it is necessary to set its coordinates. The primary setting is its position in the X, Y, and Z axes are zero, and the camera view is parallel to the
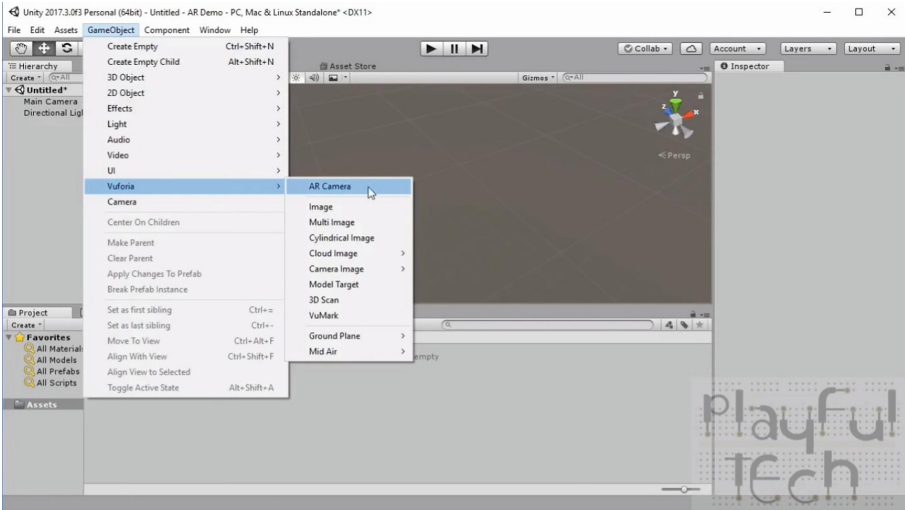
Fig. 2. Unity environment.

virtual surface of the scene. Since the "AR Camera" tool is a reference element, just set the value Y, which represents the height from which the objects will be scanned and presented through the created augmented reality application. Then we set the number of markers, lighting, shading model size. After setting the markers correctly, we can move on to creating virtual 3D models. The primary step is to assign the imported models
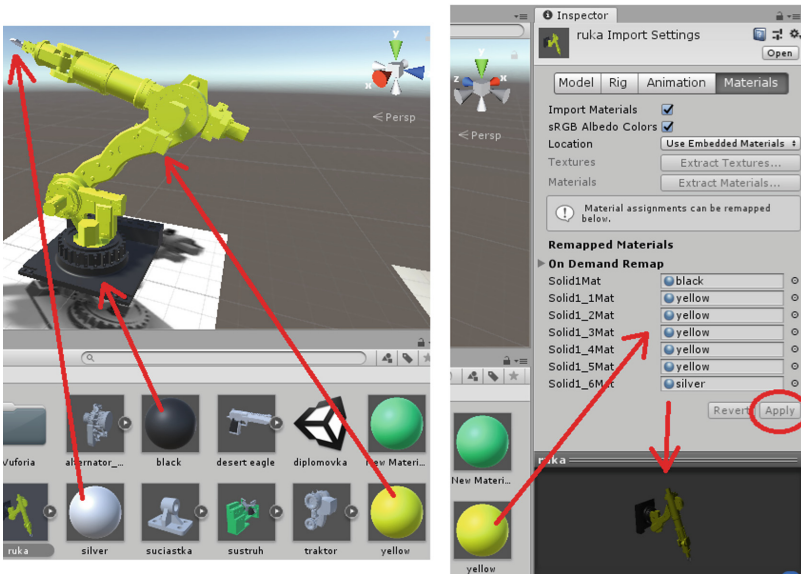
Fig. 3. 3D model editing.

from Autodesk Inventor, which we converted to OBJ format, to the appropriate markers. Then we define the colors and adjust the appearance of the 3D model according to our requirements (Fig. 3).

During the whole creation of the scene, resp. virtual 3D models, we can check the process correctness. Above all, however, it is necessary to make the correct setting of the scanning device or camera (Fig. 4).
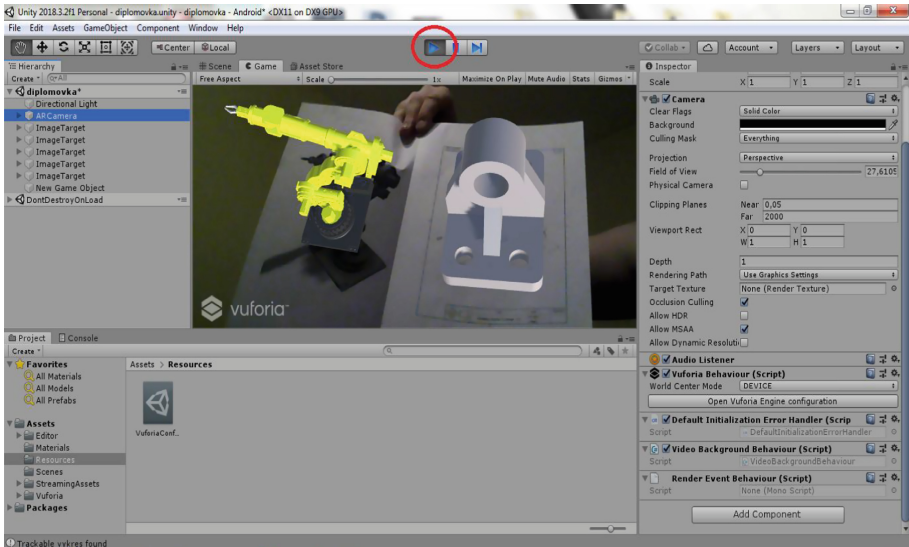
Fig. 4. The principle of created virtual objects control.

After creating virtual 3D models and their successfully checking, we can move on to creating an augmented reality application. In any case, it is necessary to know in advance which device we will use the developed application. If it is a device running on Android, we will adjust the "build Settings" to the required version of Android for its export. As an output, we get the application in.apk format. We will then import it into the mobile display device.
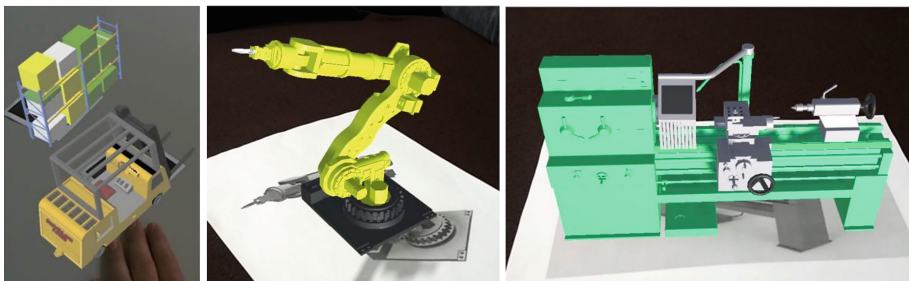
Fig. 5. Examples of 3D models above markers.

4   Results

Chapter 2 described the principle of creating a simple augmented reality application. The idea was to create a database of 3D models displayed in a mobile display device above the markers. Depending on the position of the markers, the position of the virtual 3D models is also changed. This principle can be used in the education of students in such a way that the student receives several 2D printed markers, which will then be distributed in space. When view via a mobile device, a 3D model of the device is loaded from the database above each marker. Its task is to correctly place the individual markers so that the principles for workplace design are maintained. Figure 5 shows 3D models from our application.

With such 3D assembled models, we can build a simple assembly line, production plant, or production firm. Our idea is to use 2D floor plans of production halls above which the markers of machines created by us will be placed. In this way, students will improve in the design of production systems. They will learn to place machines, conveyors, pallets, bins, racks, robots, and pallets. They will improve in the design of transport routes, in the design of supply infrastructure, taking into account elements of ergonomics. Figure 6 shows an example of our proposed concept for education.

Fig. 6. AR-based manufacturing company concept.

Such a new form of education brings many positive results. One is that it increases students' interest, encourages imagination, and introduces interactivity. This principle can also be applied in distance education when students are sent pictures of markers, layout solutions, applications, and checking the correctness of the layout of machines by the teacher is possible after sending a screenshot of a mobile device. After the initial tests of the given application and the overall concept on the Faculty of Production Technologies TUKE premises based in Prešov, there was only a positive response.

5   Conclusions

The result of this article is a presentation of the principle of an application that can change the overall view of reality as we know it so far. Virtual objects embedded in reality can be a credible replica of real objects. In education, this application can significantly benefit and change teaching understanding of new knowledge and context. Augmented reality is being implemented more and more into new industries every day, so this application was only a fractional demonstration of its potential. As this is a relatively new technology, we cannot pinpoint its boundaries.

The goal of augmented reality development is to get as close as possible to the real world. The role of developers is to supplement augmented reality with physical laws, thus strengthening its real character. Over time, using this technology could be a regular part of our lives. In the production sphere, augmented reality could become an integral part of the entire production process, from product development through the organization of workplaces to the actual promotion of production products.

A promising idea for the future could be to improve augmented reality software. Implementing augmented reality creation functions in CAD software would greatly simplify working with this technology. This would open up a till now unknown design sphere for designers. Despite the higher purchase price and the unexplored possibilities of this technology, we think this is the perspective path to the future in innovative technologies.

References

1. Buń, P., Trojanowska, J., Rewers, P.: VR and AR in lean manufacturing classes. In: Trojanowska, J., Ciszak, O., Machado, J.M., Pavlenko, I. (eds.) MANUFACTURING 2019. LNME, pp. 342–351. Springer, Cham (2019). https://doi.org/10.1007/978-3-030-18715-6_29
2. Kascak, J., et al.: Implementation of augmented reality into the training and educational process in order to support spatial perception in technical documentation. In: IEEE 6th International Conference on Industrial Engineering and Applications (ICIEA), pp. 583–587. IEEE, Tokio (2019)
3. Trojanowska, J., Pająk, E.: Using the theory of constraints to production processes improvement. In: Proceedings of the International Conference of DAAAM Baltic "Industrial Engineering" (2010)
4. Husár, J., Knapčíková, L., Hrehová, S.: Augmented reality as a tool of increasing the efficiency of RFID technology. In: Perakovic, D., Knapcikova, L. (eds.) FABULOUS 2021. LNICSSITE, vol. 382, pp. 401–414. Springer, Cham (2021). https://doi.org/10.1007/978-3-030-78459-1_30
5. Ivanov, V., Pavlenko, I., Trojanowska, J., Zuban, Y., Samokhvalov, D., Bun, P.: Using the augmented reality for training engineering students. In: 4th International Conference of the Virtual and Augmented Reality in Education, VARE 2018, pp. 57–64 (2018)

6. Bun, P., Trojanowska, J., Ivanov, V., Pavlenko, I.: The use of virtual reality training application to increase the effectiveness of workshops in the field of lean manufacturing. In: 4th International Conference of the Virtual and Augmented Reality in Education, VARE 2018, pp. 65–71 (2018)

7. Stadler, S., Cornet, H., Mazeas, D., Chardonnet, J.-R., Frenkler, F.: ImPro: immersive prototyping in virtual environments for industrial designers. In: Proceedings of the Design Society: DESIGN Conference, pp. 1375–1384 (2020)

8. Lasinska, N.: Hybrid management methodology for transport projects related to rolling stock. J. Eng. Sci. **8**(2), B7–B11 (2021). https://doi.org/10.21272/jes.2021.8(2).b2

9. Trojanowska, J., Żywicki, K., Varela, M.L.R., Machado, J.: Improving production flexibility in an industrial company by shortening changeover time: a triple helix collaborative project. In: Peris-Ortiz, M., Farinha, L., Ferreira, J.J., Fernandes, N.O. (eds.) Multiple Helix Ecosystems for Sustainable Competitiveness. ITKM, pp. 133–146. Springer, Cham (2016). https://doi.org/10.1007/978-3-319-29677-7_9

10. Trojanowska, J., Kolinski, A., Galusik, D., Varela, M.L.R., Machado, J.: A methodology of improvement of manufacturing productivity through increasing operational efficiency of the production process. In: Hamrol, A., Ciszak, O., Legutko, S., Jurczyk, M. (eds.) Advances in Manufacturing. LNME, pp. 23–32. Springer, Cham (2018). https://doi.org/10.1007/978-3-319-68619-6_3

11. Denysenko, Y., Ivanov, V., Ivchenko, O.: Quality assessment of teaching the disciplines in the e-learning environment of Sumy State University. CEUR Workshop Proc. **1844**, 166–175 (2017)

12. Zywicki, K., Bun, P.: Process of materials picking using augmented reality. IEEE Access **9**, 102966–102974 (2021). https://doi.org/10.1109/ACCESS.2021.3096915

13. Židek, K., Maxim, V., Pitel, J., Hosovsky, A.: Embedded vision equipment of industrial robot for inline detection of product errors by clustering-classification algorithms. Int. J. Adv. Robot. Syst. **13**, 1–10 (2016)

14. Mižáková, J., Piteľ, J., Hošovský, A., Kolarčík, M., Ratnayake, M.: Using special filter with membership function in biomass combustion process control. Appl. Sci. **8**(8), 13 (2018)

15. Geroimenko, V.: Augmented reality technology and art: the analysis and visualization of evolving conceptual models. In: 16th International Conference on Information Visualisation, pp. 445–453 (2012). https://doi.org/10.1109/IV.2012.77

16. Židek, K., et al.: Digital twin of experimental smart manufacturing assembly system for Industry 4.0 concept. Sustainability **12**(9), 3658 (2020)

17. Kujawińska, A., Diering, M.: The impact of the organization of the visual inspection process on its effectiveness. Int. J. Adv. Manuf. Technol. **112**(5–6), 1295–1306 (2021). https://doi.org/10.1007/s00170-020-06543-9

18. Peraković, D., Periša, M., Sente, R.E.: Information and communication technologies within Industry 4.0 concept. In: Ivanov, V., et al. (eds.) DSMIE 2018. LNME, pp. 127–134. Springer, Cham (2019). https://doi.org/10.1007/978-3-319-93587-4_14

19. Tokorova, M., et al.: Augmented reality as a support tool in machining process. TEM J. **9**(1), 407–411 (2020)

20. Trojanowski, P.: Comparative analysis of the impact of road infrastructure development on road safety–a case study. Sci. J. Maritime Univ. Szczecin **63**(135), 23–28 (2020)

21. Gorski, F., Bun, P., Stefanska, K.: Use of virtual mirror in design of individualized orthopedic supplies. In: Machado, J., Soares, F., Trojanowska, J., Ottaviano, E. (eds.) ICIENG 2021. LNME, pp. 388–394. Springer, Cham (2022). https://doi.org/10.1007/978-3-030-79165-0_36

Using Telegram Bots for Personalized Financial Advice for Staff of Manufacturing Engineering Enterprises

Vitaliy Kobets[(✉)] and Serhii Savchenko

Kherson State University, 27 Universitetska Street, Kherson 73003, Ukraine
vkobets@kse.org.ua

Abstract. This paper covers the research on using instant messengers' chatbots to provide automated financial advice to manufacturing engineering enterprises employees in the scope of a chatbot application, which helps to calculate personal savings programs to ensure a constant level of consumption. The paper aims to develop telegram bots for personalized financial advice of manufacturing engineering enterprises staff. The application uses a model of life-cycle hypothesis and generates a customized saving plan based on the information provided by a user. The factors affecting decisions regarding advice include previous satisfaction with decision-making, investors' preferences, perceived difficulty, the relationship between financial literacy, expertise, and confidence. Different approaches to developing messengers' bots have been compared. The paper also gives a brief overview of the life-cycle approach, which suggests that finance managers plan consumption and savings behavior over the whole life cycle of their personnel. The research is focused on the Telegram platform and includes an overview of Telegram Bot API and the process of chatbot development using Java programming language.

Keywords: Instant messenger · Chatbot · Savings plan · Life-cycle analysis

1 Introduction

Manufacturing engineers focus on the design and operation of integrated systems to produce high-quality, economically competitive products as project management for engineers. These systems may include financial aspects of project engineering and contracting. Business engineers of the manufacturing enterprise may decide to invest in optimal investment portfolios develop complex financial models taking into account the risk preferences of enterprises.

Thus, there is a gap in handling the problem in personalized financial advice for staff of manufacturing engineering enterprises and business processes of manufacturing enterprises due to the existence of 2 tasks, such as high-quality product and finance results. As a bridge-builder between business engineers and manufacturing engineers, they can enhance the decision-making process at various enterprise levels, ranging from

operational decisions on the work floor to strategic decisions at the top level of the enterprise.

Business economists are familiar with the enterprise business processes to perform finance calculations. Still, as engineers, they also have a much more comprehensive overview of the firm's technologies and logistic operations to improve using different digital services.

Instant messenger (messenger) is a software tool that allows users to communicate in real-time. Messengers could have centralized architecture when data transfer is carried out through the service servers using a particular protocol or peer-to-peer architecture when data is transferred directly from one client to another. There is no need on the server-side.

Over the last ten years, the total number of users of instant messenger applications raised from 1.6 billion in 2011 up to 7.5 billion in 2021, and the number of unique users using at least one of the messengers is 4.48 billion [1]. The most popular mobile messenger apps chart based on the number of monthly active users is presented in Fig. 1.
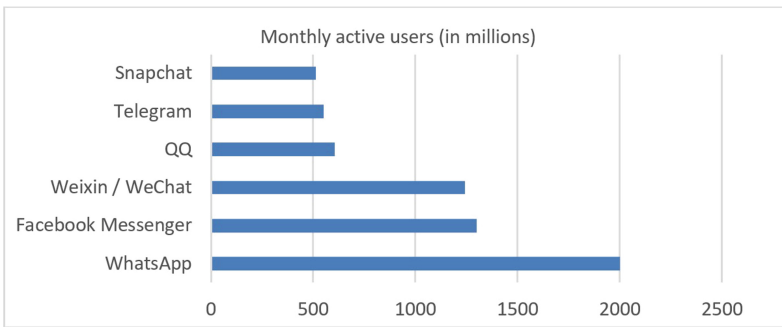
Fig. 1. Most popular mobile messenger apps [1].

The statistic among Android smartphone users in Ukraine shows that the most popular messenger apps are Viber (97%), Telegram (77%), Facebook Messenger (72%), and WhatsApp. Based on publicly available sources, Telegram has the most significant annual growth of active users' number equals 25%, while Facebook Messenger has 7.4% active users' growth, and Viber has only 6.8% [2]. Therefore, when developing a bot for a specific platform, it makes sense to consider Telegram first.

Each of the messengers mentioned before allow to create chatbot applications (chatbots) for business or personal purposes. Bots are special accounts operated by software. They can receive text or media messages from clients and send them responses. The three most popular messengers in Ukraine (Viber, Telegram, and Facebook Messenger) provide accessible application programming interfaces (API) for chatbots development. Simultaneously, WhatsApp requires passing business verification through accessing WhatsApp REST API. Basic features, which could be implemented using chatbots, include informing, communication, and partial or complete implementation of specific engineering business processes for personal and organizational goals.

The paper aims to develop optimal investment schedules in personalized financial advice for staff of manufacturing engineering enterprises using digital service.

The paper has the following structure: Sect. 2 considers literature reviews; Sect. 3 describes the model and architecture of the bot; Sect. 4 examines the practical application of telegram bot for engineering enterprises staff; the conclusion is the last part.

2   Literature Review

The engineering equipment manufacturing industry includes a financial risk evaluation model, which is based on financing channels, enhancing capital strength, increasing cash flow, improving risk prevention [3]. The study [4] points out 'the implementation path of lean digitalization for traditional manufacturing enterprises under different competitive positions' and reveals 'situational factor affecting the implementation of lean digitalization'. Paper [5] considers Enterprise Information Systems functional architecture and reviews AI applications integrated into Inventory and logistics, Production Planning, Finance and accounting, Product Lifecycle Management, with particular attention focused on the manufacturing enterprises. AI-enablement implements improved decision-making or automation using Machine Learning models or logic-based systems.

Authors [6] 'measures the value of Korean ICT manufacturing and service businesses using DEA and regression to evaluate the impact of capital structure on its profitability efficiency' and reveal that 'the liquidity ratio had a positive effect on the profitability efficiency of SME'. One of the problem factors is the flushing of working capital for non-production purposes that should be stopped by fulfilling the tasks of financial rehabilitation of aviation manufacturing companies [7] using a new digital online P2P lending-investment platform. Nowadays, knowledge graphs in finance help better meet users' needs [8].

Digidhan dashboard (http://digipay.gov.in) is an innovative government portal to monitor the growth of digital transactions on a central platform (Fig. 2).

Fig. 2. Home page of Digidhan dashboard.

It is further enhanced by developing a chatbot to address user queries [9]. The Dashboard proposes tracking of total digital payments transactions and bank analysis, target

setting, and monitoring to evaluate the KPI of enterprises and their financial services. This Dashboard is integrated with public and private sectors foreign banks through APIs [9]. Analysis of digital payments is prepared and is offered on the dashboard in the form of BI reports. This data analysis is used to rank the enterprises.

The growth in the volume of finance queries over time demanded a real-time solution, which could eliminate the need for a human advisor to address such repeated queries. A chatbot was developed to handle user queries on a real-time basis. The chatbot was built using NLP processing through Google Dialog Flow and self-learning functions (Fig. 3).

Fig. 3. Chatbot window for the dashboard.

This is problematic to detect the sentiment of an utterance which often depends on the context and timing of the conversation while using chatbots. It is found that chatbots classify positive utterances with high accuracy, but classifying negative utterances is more doubt [10]. It means that chatbots will answer more correctly if questions are described as numeric input data to provide effective and low-cost advice to assist investors in making decisions [11].

Based on studied works, the ways of how bots can be used as a part of other services [12–14] are following:

- Bots could be an entry point for a client to work with some service. The bot has to provide general information about the service and implement certain functionality to encourage potential customers to use the service.
- Using a bot as a means of one-way communication (aggregation and showing information from various sources, user notifications, informing about new offers and news).
- Using a bot as a two-way communication (interactive guide, support service). This use is now widespread in online banking (e.g., manufacturing engineering enterprises).
- Bot as an independent service.

There are two ways of developing a bot for a few messaging platforms. The first is creating a separate application for each platform using its API and software development

kit (SDK). Another option is the use of particular services (such as Pipe, Appy Pie, SnatchBot, etc.) that allow the implementation of bots logic using their instruments and then publish it on a few messaging platforms at once (Chatbot as a Service). Such services enable creating the minimum viable product (MVP) or proof-of-concept (PoC) version of a bot and quickly launching it on different platforms. However, they also have drawbacks. Differences between these approaches are shown in Table 1.

Table 1. Comparison of different approaches to creating bots.

Approach	Advantages	Disadvantages
Custom implementation	Ability to take full advantage of all the unique features each messenger provides Minimize the security risks of users' data	Need to support multiple versions at one time New features and bug fixes should be implemented on each bot separately Data synchronization
Third-party services	Fast prototyping and launching MVP or PoC versions on different platforms No need to support multiple versions of the codebase	Significantly limited functionality compared to the direct use of the APIs Increased risk of leakage of personal data of users

After analysis of some Telegram bots were found subsequent weaknesses, which may negatively affect user's experience and should be avoided during the development of a bot:

– There is complex, overloaded, and confusing work logic in bots with a large number of functions.
– It is necessary to carefully consider and implement the bot's logic in case of incorrect data entry by the user.

Telegram uses its symmetric encryption scheme called MTProto. This protocol is based on 256-bit symmetric AES encryption 2048-bit RSA encryption and uses the Diffie-Hellman critical exchange method [15]. Telegram provides HTTP API that covers all features, so any developer can create their Telegram client with no need to work directly with MTProto protocol.

Telegram Bot API is an add-on over Telegram API, allowing developing bots. There are plenty of software libraries for different programming languages (including PHP, JavaScript, Rust, Python, Java, Go, etc.) generated and maintained by the open-source community [16].

Basic features of bots include receiving and sending text messages and providing pre-defined quick commands. Telegram Bot API also gives access to advanced features, such as receiving and sending extended messages (stickers, images, other types of files) and creating custom buttons, which helps to simplify and improve the user interface [17].

This paper is focused on creating a Telegram bot using Java programming language and Spring Boot framework.

3   Research Methodology

3.1   Model

The research methodology consists of two main parts: data collection through a questionnaire developed as the Telegram chatbot and processing user's input via mathematical framework described further.

Our previous work [18] developed a high-level architecture for a typical Robo-Advisor (RA) application. This research will show how architecture could be extended and how Telegram bots can be used as part of the RA application for temporarily free funds.

A developed Telegram bot will determine how much an institutional investor (enterprise) should invest annually in savings S under the real percentage r to ensure a constant level of consumption for a particular time. Such a bot may be an entry point for new users of the RA service.

The bot uses a model of the Life-cycle approach, which suggests that business engineers plan consumption and savings behavior over the whole life cycle of their personnel. This means that business engineers should save part of the disposable income until the retirement of personnel during the manufacturing process.

Input data should contain information about person's annual income (Y), age when the person will startperiodme savings (t_1), age when the person will end making savings (t_2), age until which the person plans to spend savings (t_3), expected nominal annual interest rate on savings (r), and information on what percentage reduction from the expected average interest rate will be critical in deciding to review (terminate) the savings program.

The first step is calculating the future value of the annuity (1):

$$FVA = S \cdot \frac{(1 + rr)^{N_1} - 1}{rr} \tag{1}$$

where $N_1 = t_2 - t_1$, rr is real interest rate, which could be found by the Fisher Eq. (2):

$$rr = \frac{1 + r}{1 + i} - 1 \tag{2}$$

where r is the nominal interest rate and i is an expected inflation rate.

The expected inflation rate could be taken from official statistics for the previous three years (3):

$$i = \sqrt[3]{i_1 \cdot i_2 \cdot i_3} \tag{3}$$

In our bot implementation, we have used the average inflation rate in Ukraine for 2018, 2019, and 2020 from ukrstat.gov.ua, which gives the expected inflation rate equals 1.063.

The next step is determining the current value of the annuity (4):

$$PVA = C \cdot \frac{1 - (1 + rr)^{-N_2}}{rr} \tag{4}$$

where $N_2 = t_3 - t_2$. To ensure a constant level of consumption, the following Eq. (5) must be met.

$$FVA = PVA \tag{5}$$

Person's income Y is distributed among consumption C and savings S: $Y = C + S$, therefore we can designate S as $Y - C$. After all equations are solved, we can finally find the values of consumption C and savings S.

3.2 Architecture of the Bot

The logic of the bot's workflow is described in Fig. 4. The entry point of this workflow is the moment when a user first opens his dialogue with the bot. The first message contains general information about what this bot can do and a list of available commands. Users can execute/start/help command at any time, which will show this information again.
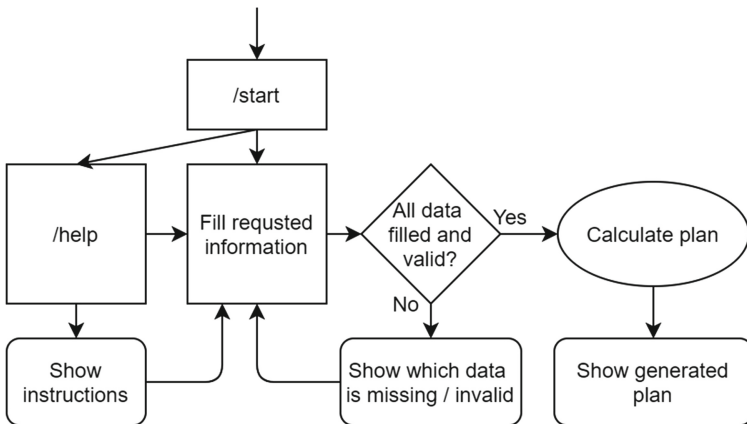
Fig. 4. Bot's workflow.

After the user executes/helps command, they will see what data they need to fill in. After every user input, the data is validated on the server-side. If the data has an invalid format or does not meet set certain restrictions (for example, the age cannot be lower than zero), the corresponding warning message will be shown. The final step is generating a constant consumption plan level, which is based on information provided by the user.

The bot has been developed using the following programming languages, frameworks, and libraries:

– Java – object-oriented, general-purpose programming language.

– Spring Boot – Java framework for creating web applications, which helps implement Model-View-Controller architecture and efficiently run your application inside an embedded Tomcat server.
– Maven – build automation tool used for Java projects.
– TelegramBots-Spring-Boot-Starter is a maven library that includes Telegram API and basic Spring Boot configuration.

After creating Spring Boot basic project, we need to create a new class that will extend the abstract class *TelegramLongPollingBot*. The *TelegramLongPollingBot* class has three methods, which we should override and implement. The primary method, which is called whenever some user sends a message to the bot, is public void *onUpdateReceived(Update update)*. It receives an *Update* object that contains the message and information about its sender.

To send a message to the user, we should create a *SendMessage* object, set chat id, message text, and call *SendMessage.execute()* method. A simple example of *onUpdateReceived* method implementation, which response to any user message, is presented in Fig. 5.

```java
@Override
public void onUpdateReceived(Update update) {
    try {
        SendMessage sendMessage = new SendMessage();
        sendMessage.setChatId(String.valueOf(update.getMessage().getChatId()));
        sendMessage.setText("Hello, " + update.getMessage().getFrom().getUserName() + "!");
        execute(sendMessage);
    } catch (TelegramApiException e) {
        e.printStackTrace();
    }
}
```

Fig. 5. Example of *onUpdateReceived* method implementation.

To indicate that our Spring Boot application should create an instance (Spring bean) of the class that implements Telegram Bot methods, we need to add a @Component annotation. This annotation will initiate the class instance creation during the initialization of the Spring application context.

The chosen technology stack makes it easy to scale and expand the bot's functionality. According to the TIOBE Programming Community index, Java is one of the three most popular programming languages [19]. The developed application could be extended for other messengers using Java Bot libraries or HTTP APIs (e.g., Viber Java Bot API or Viber REST API) [20].

4   Results

The following figures demonstrate the process of working with the bot, which could be found in Telegram by its username @FinAdviceBot (Fig. 6).

Let us try to generate a constant level of a consumption savings plan with the following parameters: person's annual income is UAH 100,000; an age when the person will start making savings is 35; a period when the person will end making savings is 60; age

until which the person plans to spend savings is 80; expected nominal annual interest rate on savings is 10%.
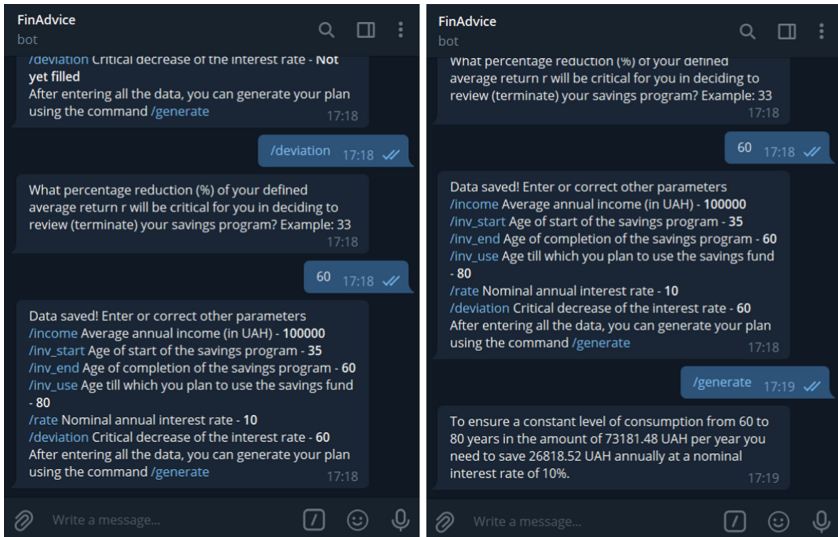
Fig. 6. Example of the generated plan.

As we can see, after executing/generating command, our bot has calculated that to ensure a constant level of consumption from 35 to 80 years in the amount of UAH 73,181, it is necessary to save UAH 26,818 per year at a nominal interest rate of 10% and an average inflation rate of 6.3%.

The chosen approach to creating a chatbot ensures the maximum security of users' data. As mentioned earlier, the security of personal data is a weakness of third-party services that allow developing chatbots for several messaging platforms at once. Based on the bot architecture presented in paragraph Sect. 3.2, it is shown that the bot workflow is clear enough, so the implementation of a separate version for another messaging platform will not be a big challenge.

5 Conclusions

Thus, the paper contains the business analysis of the modern instant messengers market and justification that Telegram is currently the most actively expanding platform with free API for chatbots development. It also describes a methodology behind the planning of a personalized savings program of enterprise for ensuring a constant level of consumption and covers the development process of the Telegram bot. Business engineers of manufacturing enterprises can use the practical results of this work to plan the consumption and savings behavior of their personnel.

The paper does not cover implementing more complex Telegram API features like creating custom keyboards buttons and adding bots to group chats. These topics, along

with the way of integrating the bot with other services (e.g., Robo-advising service), will be explored in further research.

References

1. Global social media stats. https://datareportal.com/social-media-users, Accessed 10 Oct 2021
2. Telegram Revenue and Usage Statistics. https://www.businessofapps.com/data/telegram-statistics/, Accessed 10 Oct 2021
3. Tang, J., Fu, Y.: Analysis and research on financial competitiveness of listed companies in offshore engineering manufacturing. J. Coast. Res. **106**, 45–48 (2020)
4. Jing, S., Feng, Y., Yan, J.: Path selection of lean digitalization for traditional manufacturing industry under heterogeneous competitive position. Comput. Ind. Eng. **161**, 1–18 (2021). https://doi.org/10.1016/j.cie.2021.107631
5. Zdravkovic, M., Panetto, H., Weichhart, G.: AI-enabled enterprise information systems for manufacturing. Enterp. Inf. Syst. **20**, 1–53 (2021). https://doi.org/10.1080/17517575.2021.1941275
6. Kim, Y.J., Kim, C.H.: The impact of capital structure on the profitability efficiency of ICT FIRMS. In: 2021 21ST ACIS International Winter Conf. on Software Engineering, pp. 127–135. AI, NPDC (2021). https://doi.org/10.1109/SNPDWinter52325.2021.00036
7. Kryvokon, O.G., Kryvokon, M.O.: Features of financial management on aviation engineering enterprises of Ukraine. Finan. Credit Act.-Prob. Theory Pract. **4**(27), 159–166 (2018). https://doi.org/10.18371/fcaptp.v4i27.154176
8. Su, L., Wang, Z., Ji, Y., Guo, X.: A survey based on knowledge graph in fault diagnosis, analysis, and prediction: key technologies and challenges. In: 2020 International Conference on AI and Computer Engineering (ICAICE), pp. 458–462 (2020)
9. Misra, D., Sethi, I., Gupta, O., Kapoor, M., Dwivedi, R.: Digidhan dashboard—monitoring and analysis of digital payments. In: Tuba, M., Akashe, S., Joshi, A. (eds.) ICT Systems and Sustainability. AISC, vol. 1077, pp. 91–104. Springer, Singapore (2020). https://doi.org/10.1007/978-981-15-0936-0_8
10. Ireland, D., Hassanzadeh, H., Tran, S.N.: Sentimental analysis for AIML-based e-health conversational agents. In: Cheng, L., Leung, A.C.S., Ozawa, S. (eds.) ICONIP 2018. LNCS, vol. 11302, pp. 41–51. Springer, Cham (2018). https://doi.org/10.1007/978-3-030-04179-3_4
11. Snihovyi, O., Kobets, V., Ivanov, O.: Implementation of robo-advisor services for different risk attitude investment decisions using machine learning techniques. In: Ermolayev, V., Suárez-Figueroa, M.C., Yakovyna, V., Mayr, H.C., Nikitchenko, M., Spivakovsky, A. (eds.) ICTERI 2018. CCIS, vol. 1007, pp. 298–321. Springer, Cham (2019). https://doi.org/10.1007/978-3-030-13929-2_15
12. Janarthanam, S.: Hands-On Chatbots and Conversational UI Development. Packt Publishing, Birmingham (2017)
13. Modrzyk, N.: Building Telegram Bots: Develop Bots in 12 Programming Languages using the Telegram Bot API, 1st edn. Apress, Berkeley (2019)
14. Trushar, B., Eytan, O.: Guide to Chat Apps. GitBooks (2015)
15. FAQ for the Technically Inclined. https://core.telegram.org/techfaq, Accessed 10 Oct 2021
16. 13Bots: An introduction for developers. https://core.telegram.org/bots/samples, Accessed 10 Oct 2021
17. 9 Best Chatbots in the Financial Services Industry. https://www.haptik.ai/blog/best-chatbots-in-financial-industry, Accessed 10 Oct 2021
18. Savchenko, S., Kobets, V.: Development of robo-advisor system for personalized investment and insurance portfolio generation. In: Ermolayev, V. et al. (eds.) Proceedings of 17th International Conference ICTERI, pp. 488–500. CEUR-WS, Aachen University (2021)

19. TIOBE Index for December 2021. https://www.tiobe.com/tiobe-index, Accessed 20 Dec 2021
20. Viber API Documentation. https://developers.viber.com/docs/api/java-bot-api, Accessed 20 Dec 2021

Author Index